

**SUMMARY TECHNICAL REPORT
OF THE
NATIONAL DEFENSE RESEARCH COMMITTEE**

This document contains information affecting the national defense of the United States within the meaning of the Espionage Act, 50 U.S.C., 31 and 32, as amended. Its transmission or the revelation of its contents in any manner to an unauthorized person is prohibited by law.

This volume is classified CONFIDENTIAL in accordance with security regulations of the War and Navy Departments because certain chapters contain material which was CONFIDENTIAL at the date of printing. Other chapters may have had a lower classification or none. The reader is advised to consult the War and Navy agencies listed on the reverse of this page for the current classification of any material.

UNCLASSIFIED

~~CONFIDENTIAL~~

08 7 07 001

Manuscript and illustrations for this volume were prepared for publication by the Summary Reports Group of the Columbia University Division of War Research under contract OEMsr-1131 with the Office of Scientific Research and Development. This volume was printed and bound by the Columbia University Press.

Distribution of the Summary Technical Report of NDRC has been made by the War and Navy Departments. Inquiries concerning the availability and distribution of the Summary Technical Report volumes and microfilmed and other reference material should be addressed to the War Department Library, Room 1A-522, The Pentagon, Washington 25, D. C., or to the Office of Naval Research, Navy Department, Attention: Reports and Documents Section, Washington 25, D. C.

Copy No.

129

This volume, like the seventy others of the Summary Technical Report of NDRC, has been written, edited, and printed under great pressure. Inevitably there are errors which have slipped past Division readers and proofreaders. There may be errors of fact not known at time of printing. The author has not been able to follow through his writing to the final page proof.

Please report errors to:

JOINT RESEARCH AND DEVELOPMENT BOARD
PROGRAMS DIVISION (STR ERRATA)
WASHINGTON 25, D. C.

A master errata sheet will be compiled from these reports and sent to recipients of the volume. Your help will make this book more useful to other readers and will be of great value in preparing any revisions.

UNCLASSIFIED
~~CONFIDENTIAL~~

①

SUMMARY TECHNICAL REPORT OF DIVISION 6, NDRC

VOLUME 20

LIBRARY
U. S. NAVY ELECTRONICS LABORATORY
SAN DIEGO 62, CALIFORNIA

BRANCH LIBRARY

FLUID DYNAMICS

SDTICD
ELECTE
JUL 07 1989

H

OFFICE OF SCIENTIFIC RESEARCH AND DEVELOPMENT
VANNEVAR BUSH, DIRECTOR

NATIONAL DEFENSE RESEARCH COMMITTEE
JAMES B. CONANT, CHAIRMAN

DIVISION 6
JOHN T. TATE, CHIEF



WASHINGTON, D. C., 1946

UNCLASSIFIED

~~CONFIDENTIAL~~

UNANNOUNCED

DISTRIBUTION STATEMENT A
Approved for public release
Distribution Unlimited

Accession For	
NTIS GRA&I	<input checked="" type="checkbox"/>
DTIC TAB	<input type="checkbox"/>
Unannounced	<input type="checkbox"/>
Justification	
By: <i>See AD221608</i>	
Distribution/	
Availability Codes	
Dist	Avail and/or Special
A-1	

NATIONAL DEFENSE RESEARCH COMMITTEE

James B. Conant, *Chairman*

Richard C. Tolman, *Vice Chairman*

Roger Adams

Army Representative¹

Frank B. Jewett

Navy Representative²

Karl T. Compton

Commissioner of Patents³

Irvin Stewart, *Executive Secretary*

¹ Army representatives in order of service:

Maj. Gen. G. V. Strong	Col. L. A. Denson
Maj. Gen. R. C. Moore	Col. P. R. Faymonville
Maj. Gen. C. C. Williams	Brig. Gen. E. A. Regnier
Brig. Gen. W. A. Wood, Jr.	Col. M. M. Irvine
Col. E. A. Routheau	

² Navy representatives in order of service:

Rear Adm. H. G. Bowen	Rear Adm. J. A. Furer
Capt. Lybrand P. Smith	Rear Adm. A. H. Van Keuren
	Commodore H. A. Schade

³ Commissioners of Patents in order of service:

Conway P. Coo	Casper W. Ooms
---------------	----------------

NOTES ON THE ORGANIZATION OF NDRC

The duties of the National Defense Research Committee were (1) to recommend to the Director of OSRD suitable projects and research programs on the instrumentalities of warfare, together with contract facilities for carrying out these projects and programs, and (2) to administer the technical and scientific work of the contracts. More specifically, NDRC functioned by initiating research projects on requests from the Army or the Navy, or on requests from an allied government transmitted through the Liaison Office of OSRD, or on its own considered initiative as a result of the experience of its members. Proposals prepared by the Division, Panel, or Committee for research contracts for performance of the work involved in such projects were first reviewed by NDRC, and if approved, recommended to the Director of OSRD. Upon approval of a proposal by the Director, a contract permitting maximum flexibility of scientific effort was arranged. The business aspects of the contract, including such matters as materials, clearances, vouchers, patents, priorities, legal matters, and administration of patent matters were handled by the Executive Secretary of OSRD.

Originally NDRC administered its work through five divisions, each headed by one of the NDRC members. These were:

- Division A—Armor and Ordnance
- Division B—Bombs, Fuels, Gases, & Chemical Problems
- Division C—Communication and Transportation
- Division D—Detection, Controls, and Instruments
- Division E—Patents and Inventions

In a reorganization in the fall of 1942, twenty-three administrative divisions, panels, or committees were created, each with a chief selected on the basis of his outstanding work in the particular field. The NDRC members then became a reviewing and advisory group to the Director of OSRD. The final organization was as follows:

- Division 1—Ballistic Research
- Division 2—Effects of Impact and Explosion
- Division 3—Rocket Ordnance
- Division 4—Ordnance Accessories
- Division 5—New Missiles
- Division 6—Sub-Surface Warfare
- Division 7—Fire Control
- Division 8—Explosives
- Division 9—Chemistry
- Division 10—Absorbents and Aerosols
- Division 11—Chemical Engineering
- Division 12—Transportation
- Division 13—Electrical Communication
- Division 14—Radar
- Division 15—Radio Coordination
- Division 16—Optics and Camouflage
- Division 17—Physics
- Division 18—War Metallurgy
- Division 19—Miscellaneous
- Applied Mathematics Panel
- Applied Psychology Panel
- Committee on Propagation
- Tropical Deterioration Administrative Committee

UNCLASSIFIED

CONFIDENTIAL

NDRC FOREWORD

AS EVENTS of the years preceding 1940 revealed more and more clearly the seriousness of the world situation, many scientists in this country came to realize the need of organizing scientific research for service in a national emergency. Recommendations which they made to the White House were given careful and sympathetic attention, and as a result the National Defense Research Committee [NDRC] was formed by Executive Order of the President in the summer of 1940. The members of NDRC, appointed by the President, were instructed to supplement the work of the Army and the Navy in the development of the instrumentalities of war. A year later, upon the establishment of the Office of Scientific Research and Development [OSRD], NDRC became one of its units.

The Summary Technical Report of NDRC is a conscientious effort on the part of NDRC to summarize and evaluate its work and to present it in a useful and permanent form. It comprises some seventy volumes broken into groups corresponding to the NDRC Divisions, Panels, and Committees.

The Summary Technical Report of each Division, Panel, or Committee is an integral survey of the work of that group. The first volume of each group's report contains a summary of the report, stating the problems presented and the philosophy of attacking them and summarizing the result of the research, development, and training activities undertaken. Some volumes may be "state of the art" treatises covering subjects to which various research groups have contributed information. Others may contain descriptions of devices developed in the laboratories. A master index of all these divisional, panel, and committee reports which together constitute the Summary Technical Report of NDRC is contained in a separate volume, which also includes the index of a microfilm record of pertinent technical laboratory reports and reference material.

Some of the NDRC-sponsored researches which had been declassified by the end of 1945 were of sufficient popular interest that it was found desirable to report them in the form of monographs, such as the series on radar by Division 14 and the monograph on sampling inspection by the Applied Mathematics Panel. Since the material treated in them is not duplicated in the Summary Technical Report of NDRC,

the monographs are an important part of the story of these aspects of NDRC research.

In contrast to the information on radar, which is of widespread interest and much of which is released to the public, the research on subsurface warfare is largely classified and is of general interest to a more restricted group. As a consequence, the report of Division 6 is found almost entirely in its Summary Technical Report, which runs to over twenty volumes. The extent of the work of a Division cannot therefore be judged solely by the number of volumes devoted to it in the Summary Technical Report of NDRC: account must be taken of the monographs and available reports published elsewhere.

Any great cooperative endeavor must stand or fall with the will and integrity of the men engaged in it. This fact held true for NDRC from its inception, and for Division 6 under the leadership of Dr. John T. Tate. To Dr. Tate and the men who worked with him—some as members of Division 6, some as representatives of the Division's contractors—belongs the sincere gratitude of the Nation for a difficult and often dangerous job well done. Their efforts contributed significantly to the outcome of our naval operations during the war and richly deserved the warm response they received from the Navy. In addition, their contributions to the knowledge of the ocean and to the art of oceanographic research will assuredly speed peacetime investigations in this field and bring rich benefits to all mankind.

The Summary Technical Report of Division 6, prepared under the direction of the Division Chief and authorized by him for publication, not only presents the methods and results of widely varied research and development programs but is essentially a record of the unstinted loyal cooperation of able men linked in a common effort to contribute to the defense of their Nation. To them all we extend our deep appreciation.

VANNEVAR BUSH, Director
Office of Scientific Research and Development

J. B. CONANT, Chairman
National Defense Research Committee

~~CONFIDENTIAL~~

UNCLASSIFIED

FOREWORD

SHORTLY AFTER Section C-4, later Division 6, was organized, the development of certain projectiles was undertaken. It soon became clear that additional data were required about how certain features of projectile design, such as shape, weight distribution, etc., affect projectile travel in the air, behavior during the water-entry period and subsequent travel in the water toward the target. It is generally true that a projectile should be designed to secure both accurate travel to the target and efficient utilization of the applied propulsive forces. Whether these objectives are met in a particular design depends in part upon performance determined by the resultant effect of the aerodynamic and hydrodynamic, or, to employ one term, *fluid dynamic force* to which it is subjected in its travel. This report describes laboratory facilities developed and methods employed to establish definite relationships between performance and design features, and the fluid dynamic forces to which the projectile is subjected. Also, the report records the results of investigations on many projectile models, and, in addition, discusses quite fully certain cavitation phenomena observed.

Following early studies, the Division in 1941 contracted with the California Institute of Technology to provide additional facilities in that Institution's Hydrodynamics Laboratory and to conduct tests

pertinent to the above objective. The facilities of the Hydrodynamics Laboratory were gradually expanded and methods for studying the dynamic behavior of projectiles were further developed. In addition to studies and tests upon projectiles being developed by Division 6, the laboratory was also able to undertake tests and supply data to other agencies also carrying on the development of projectiles.

The general project reported upon was under the direction of Dr. Robert T. Knapp to whom, together with his associate, Mr. Dailey, the Division is obligated for the preparation of this very complete report. The Division is also very appreciative of the fact that the Navy permitted the authors to complete this report after transfer of the project from Division to Navy support and direction.

The Division feels that while this report describes the work undertaken primarily for the use of the Armed Services, it also contains material of interest and value to civilian science and technology and it is hoped that steps can be taken to declassify substantial portions of the information presented.

JOHN T. TATE
Chief, Division 6

~~CONFIDENTIAL~~

UNCLASSIFIED

PREFACE

THIS VOLUME presents the results of the work of the Hydrodynamics Laboratory of the California Institute of Technology as part of the War Research Program from the fall of 1941 to the fall of 1945. The initial object of this work was to study the broad hydrodynamic aspects of the antisubmarine program. Later it was generalised to include the observation and analysis of the hydrodynamic forces of bodies moving through fluids and the development of satisfactory shapes for such bodies. These objectives and the development of the project are described in the first chapter.

The bulk of the work during this war period necessarily and properly pertained to specific projectiles. Little time was available for research along basic lines. When feasible more generalised data were obtained and presented. In spite of concentration upon specific projects, by the end of the contract their number and diversity had provided an immense amount of data suitable for much additional generalization. In preparing this volume, an attempt was made to organize and analyze this mass of data with the objective of ascertaining the basic factors involved. This was a lengthy process which required more time than was available during the closing weeks of the NDRC contract under which this project operated. Fortunately, however, the work of the

project was continued under the auspices of the Navy Bureau of Ordnance, which organization generously permitted the laboratory to complete the preparation of the report. Thus it was possible to present the data in a much more general fashion than could have been done otherwise. This general information is basic to the design of nearly all projectiles and allied bodies and contributes to the understanding of the hydrodynamic phenomena involved. Such information is of lasting value, not only to the problem of national defense, but to many other problems of industry and civilian technology.

In closing these remarks, the author wishes to take this opportunity to express his appreciation to the staff of the Hydrodynamics Laboratory without whose loyalty and sincere effort this report could not have been possible. In thinking of the staff of a research laboratory, one is apt to include only the highly trained technical personnel and to omit others who contribute very important and vital skills and efforts. This is not the writer's intention since he feels that all personnel made significant contributions which are hereby acknowledged.

ROBERT T. KNAPP
Editor

~~CONFIDENTIAL~~

UNCLASSIFIED

CONTENTS

CHAPTER	PAGE
1 Development of the Laboratory	1
2 Laboratory Facilities	7
3 Effect of Projectile Components on the Flow Diagram	69
4 Cavitation and Entrance Bubbles	96
5 Nose Cavitation—Ogives and Spherogives	118
6 Hydrodynamic Forces Resulting from Cavitation on Underwater Bodies	134
7 Cavitation Noise from Underwater Projectiles	155
8 Forces on Finless Body Shapes.	171
9 Stabilizing Surfaces on Nonrotating Projectiles	175
10 Effects of Projectile Components on Drag, Cross Force, and Lift	185
11 Effect of Projectile Components on Damping and Dynamic Stability	193
12 Effect of Experimental Variables on an Air- Launched Projectile Trajectory	201
13 Torpedoes.	203
14 Rockets and other Nonrotating Projectiles with Stabilizing Surfaces	230
15 Spin-Stabilized Rockets.	239
16 Depth Charges	245
17 Air Bombs	253
18 Two-Dimensional Bodies	259
19 Miscellaneous Investigations	271
Appendix	275
Glossary	281
Bibliography	283
Contract Numbers	286
Project Numbers.	287
Index	289

CONFIDENTIAL

UNCLASSIFIED

Chapter 1

DEVELOPMENT OF THE LABORATORY

1.1 PURPOSE AND HISTORY OF THE LABORATORY

1.1.1 Laboratory Objectives

DURING THE FOUR-YEAR period from the fall of 1941 to the fall of 1945, the Hydrodynamics Laboratory of the California Institute of Technology (CIT) devoted its entire resources to the prosecution of a war research program for the Office of Scientific Research and Development (OSRD) under the direction of Division 6 of the National Defense Research Committee (NDRC). The general assignment was to observe and analyze the hydrodynamic forces acting on bodies moving through fluid media, and to develop shapes for these bodies that would result in the specific performance characteristics desired. With very few exceptions, the bodies studied were projectiles. The larger part of the time and energy available was used in studying the behavior of projectiles whose trajectories were either partly or wholly under water. However, a very significant part of the laboratory activities was given over to work on air-flight projectiles operating at velocities enough lower than the velocity of sound so that the air could be considered incompressible. Much consideration was also given to the water entry problems associated with air-launched underwater projectiles such as aircraft torpedoes and antisubmarine rockets.

1.1.2 Historical Development of the Project

The need for this project developed in the New London Laboratory of the Columbia University Division of War Research (CUDWR-NLL). The initial task of this laboratory was to study the broad aspects of the antisubmarine program. In June 1941, Robert T. Knapp, a member of the CIT Mechanical Engineering Department, was requested to act as a consultant of the New London Laboratory on various hydrodynamic aspects of their research program.

Later in the summer the New London Laboratory became interested in the development of a streamlined depth charge which would have a much higher fall velocity in sea water than that of the Ashcan, the surface ship depth charge in use at that time. One of

the several disadvantages of the Ashcan was that its fall velocity was so low and its trajectory so erratic that the probability of securing a hit on a moving submarine operating at or below medium depth was very low. It was felt that a barrage of smaller, fast-sinking charges would have a much higher probability of securing a hit. Soon after the development of the high-velocity streamlined charge was begun, it became evident that serious problems concerning its stability and the prediction of its trajectory must be overcome if a satisfactory weapon was to be obtained. This meant that it would be necessary to determine the hydrodynamic characteristics of the various shapes proposed for the new charge.

Consideration was first given to use of a wind tunnel for such a study. However, it was soon found that existing wind tunnels were all heavily loaded with aerodynamic problems for the Army, Navy, and various manufacturers, and that it would be impossible to obtain results for as long a period and as rapidly as would be required. Furthermore, it was felt that there were some important phenomena such as cavitation that were peculiar to water and liquids in general and that would undoubtedly affect the performance of the projectile. This class of phenomena could not be studied directly in a wind tunnel. Therefore, in August 1941, the construction of a small water tunnel for the purpose of studying the underwater behavior of projectiles was proposed and approved. The project was undertaken by the Hydraulic Machinery Laboratory (CIT-HML) because much of the basic equipment of that laboratory could be adapted to the use of the water tunnel, and thus a working tool could be obtained more economically and in a much shorter time than if the project had to be built from the ground up.

A staff was immediately organized, which included a group to design the special apparatus and instruments needed, and the tunnel was put into operation early in the spring of 1942. It remained in continuous operation from that time to the termination of the contract in September 1945.

The same need for information that resulted in the sponsorship of the water tunnel was also responsible for the initiation of another small project—the design and construction of a polarized light flume. The

CONFIDENTIAL

1

UNCLASSIFIED

purpose of this development was to furnish a tool for use in studying the flow pattern around underwater projectiles. Recent work in the Chemical Engineering Laboratory of the Massachusetts Institute of Technology had demonstrated that dilute suspensions of certain varieties of bentonite exhibited the property of streaming double refraction to such a marked degree that they could be used to make flow visible. Permission was therefore requested and obtained from Davis R. Dewey II for the use of this development for the study of flow patterns.

Since the tunnel, and especially its associated equipment, had to be constructed with very little precedent, it underwent a continuous development during the entire time. For example, in the beginning the order of accuracy of the force measurements was relatively low but it was adequate to give the information required for the problems that presented themselves. The accuracy of the laboratory improved rapidly with experience and was able to keep pace with the needs of the program.

The first projectile that was studied in the tunnel was the streamlined depth charge that was responsible for its initiation. Before the work on this projectile was completed, a demand arose for the development of an instrument case to house some delicate equipment to be towed by a cable from an airplane. To secure satisfactory operation of these instruments it was necessary that this case should have a low drag, should be very stable, and should have slow responses to disturbing gusts in the air.

Early in the life of the laboratory a close liaison was set up and continuously maintained with the rocket program being carried out for NDRC Division 3 by CIT under Contract OEMar-418.

The first group of rockets to be studied were of the Mousetrap type of depth charge which were in the same general class as the small streamlined depth charges being developed by CUDWR-NLL. Later many other types of rockets were tested for Division 3, some of which were designed to have the final part of their trajectory under water, but most of which were regular air-flight rockets for general use against land or surface targets.

In the winter of 1942-1943 the laboratory assignment was expanded to include the first of a series of projectiles from Army Ordnance through requests originating at the Ballistic Research Laboratory at Aberdeen Proving Ground, Maryland. Included in this series was the bazooka. In the initial models this rocket had shown evidence of having insufficient sta-

bility in flight. A rather extensive program of tests resulted in the development of a series of stabilizing surfaces, generally of the ring-tail type, which improved the accuracy and reliability of the device.

Another rocket studied was the 4.5-in. which was equipped with folding fins. Investigations were also carried out for the same organization with a view to improving the stability of small mortar projectiles.

During 1942 the laboratory also made an investigation on the first of a long series of torpedoes of all types. The torpedo was the first projectile to be studied which had movable fins controlled by a steering mechanism. This required a much more elaborate series of tests and demanded higher accuracy than the rest of the program. In the latter half of 1943 the aircraft torpedo became a major part of the laboratory's activities.

The first problem to be presented concerned the stability of the Mark 13 torpedo and its behavior during water entry. The ensuing study resulted in the suggestion that the "ring tail" be added to the existing stabilizing fin structure. After a rapid but thorough series of full-scale laboratory and field tests, this suggestion was adopted. Torpedoes so equipped saw much field service before the close of the war.

The problems involved in the performance of the aircraft torpedo included not only its performance characteristics in the steady running state, but also its behavior in air, the phenomenon of water entry, and the behavior while operating within the cavity formed when it enters the water. These phases of the operation before the torpedo reached its steady running state involved phenomena which could not be studied adequately by the use of the water tunnel alone. Furthermore, by this time the original staff had increased tenfold, and the lack of suitable working space was so acute that the effectiveness of the organization was severely impaired.

The Office of Scientific Research and Development, therefore, authorized CIT to construct a new building and two additional pieces of major equipment for use of the project. The first item of new equipment was a variable-pressure launching tank designed for the purpose of studying the entry phase of the aircraft torpedo trajectory. The second item was a free-surface water tunnel for use in investigating shallow-water running operation within the cavity and the problems involved in underwater jet propulsion. The building was designed as a wing ad-

~~CONFIDENTIAL~~

joining the Hydraulic Machinery Laboratory, which made it possible to unify the laboratory and office work. Construction of the building was commenced in July 1944, and it was occupied in December of the same year. Design and construction of the equipment was started simultaneously with that of the building. The launching tank was completed and preliminary measurements were made in the spring of 1945. This development was continued up to the close of the contract. The construction of the free surface water tunnel proceeded more slowly due to the fact that top priority had been assigned to the launching tank. The major parts of the equipment were completed and assembly was started in the laboratory during the final month of the contract.

1.2 LABORATORY CAPABILITIES AND LIMITATIONS

One method of analyzing the capabilities and limitations of the laboratory consists in comparing the facilities with the details of the field of study assigned to it. This requires a specific statement of the problem. It may be outlined as follows: The main field of investigation of the laboratory has been the study of the interactions between air- or water-launched underwater projectiles and the media through which they travel, as these interactions affect the trajectory and the other external performance characteristics of the projectile. This study has been limited to the use of small-scale projectiles in the laboratory. Confirmation checks on full-scale projectiles have been carried out by other agencies. No studies have been undertaken in this laboratory concerning the mechanical strength of the projectiles, their internal construction, power plants, or explosive charges. In other words, the studies have been purely aero- and hydrodynamic in character.

1.2.1 Hydrodynamic Problems of Underwater Projectiles

In order to analyze the subdivisions of the work more closely it will be profitable to examine the trajectory of a typical projectile to see what problems present themselves along the path. The most versatile projectile studied by the laboratory has been the aircraft torpedo. It also presents the greatest number of problems. Therefore, the examination of the parts of its trajectory from the time it leaves the aircraft until it hits the selected target will serve to bring

out the general problems encountered by the laboratory.

The trajectory of the aircraft torpedo may be subdivided into four parts:

1. The air flight from the plane to the water surface.
2. Passage through the air-water interface and subsequent motion within the cavity formed during this passage.
3. The underwater run after the torpedo leaves the cavity.
4. The period of terminal ballistics beginning when the projectile hits the target.

A diagram of the trajectory showing these subdivisions will be seen in Figure 1.

The hydrodynamic problems involved in parts 1, 2, and 3 nearly all center around the external forces acting on the projectile and its resulting motion. Parts 1 and 3 have much in common since they are both concerned with the motion of the projectile in a homogeneous fluid. The differences that do exist can be traced to the great differences in density of the fluids involved, that is, air in part 1 and sea water in part 3. Satisfactory stability and damping characteristics are necessary for both parts of the trajectory. However, these characteristics differ widely for the two parts because, while the mass of the projectile remains constant, the external forces differ greatly in magnitude, although not in kind, due to this difference in fluid density. The problems peculiar to part 2 involve transient force systems rather than steady ones. Furthermore, the forces differ widely in magnitude, direction, and point of application from those existing either in parts 1 or 3. During part 2 the projectile no longer moves through a homogeneous fluid, but is acted on by both the air and the water. This results from the fact that a cavity is formed in the water during the passage of the projectile through the interface. This cavity is filled with air and persists for a considerable distance along the underwater trajectory. During part 3 the drag or resistance to forward motion becomes of more importance than in the preceding parts of the trajectory, because here it is the determining factor of the underwater speed and range of the projectile. Another problem arises in connection with part 3. Considerable noise may be produced by the projectile as it moves through the water. Although this noise does not affect the hydrodynamic operation of the torpedo, it may be undesirable for other reasons and hence presents a problem for study and elimination. In part 4 the hydrody-

UNCLASSIFIED

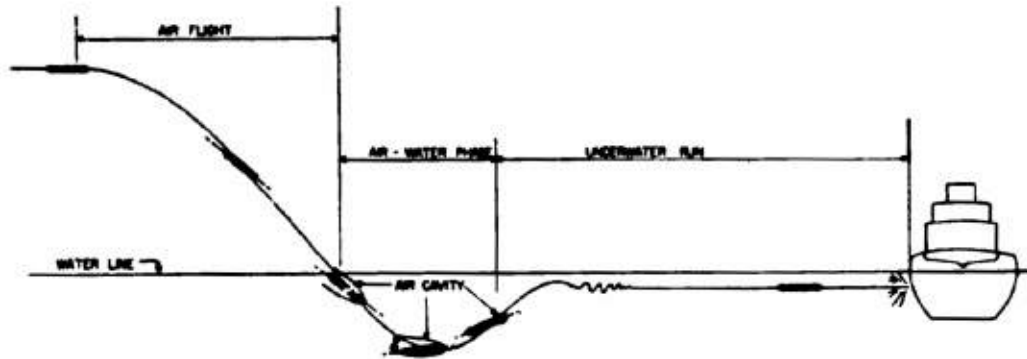


Figure 1. Typical aircraft torpedo trajectory.

dynamic problems no longer involve the forces and motions of the projectile, but are concerned with the forces resulting from underwater explosions.

12.3 Methods of Study Available in the Laboratory

The general method of attack used by the laboratory in studying projectile characteristics is the isolation and measurement of the individual properties one by one under controlled conditions with a view to obtaining the information necessary to understand the overall performance. The alternate method of attack is to observe the overall trajectory in order to determine the resultant forces by analyzing the corresponding motions at different instants along the path. When adequate facilities are available, the two methods can be worked together to good advantage, the one contributing to the other.

All of the work in this laboratory was carried on by the use of models, most of which were constructed to the standard diameter of 2 in. The main reason for using small models instead of full-scale projectiles is that the models require much less time to construct and test and, therefore, are peculiarly adapted to the pressure of a wartime research program. In addition, research with models is much less expensive, not only because the models themselves are much cheaper to construct, but also because the basic testing equipment costs only a small fraction of what it would for full-size tests. Another very appreciable advantage which is especially important in wartime is that the small-scale work requires a much smaller staff of trained personnel to achieve the same results. It should be noted that the word "model" by no means implies that the studies are restricted to empirical

investigation of specific projectiles. They can, of course, be used for all types of basic investigations as well. In fact, when basic investigations are considered, the terms "model" and "model scale" lose their significance.

The laboratory has available four major pieces of equipment. They will be described in some detail in the following chapter. However, a comparison of the general type of work for which they are suitable with the problems involved in the four subdivisions of the typical trajectory described in the preceding section will serve to show the capabilities and limitations of the laboratory in handling the problems assigned.

Figure 2 shows the typical trajectory of an air-launched underwater projectile. On it are superimposed symbols representing the four major pieces of equipment of the laboratory together with arrows indicating the fields of study for which each is adaptable.

HIGH-SPEED WATER TUNNEL

This is the most versatile piece of equipment in the laboratory and the one that has been in operation for the duration of the project. It was designed primarily for the measurement of the forces and moments acting on projectile shapes. As a result of various modifications and developments, it has been found suitable for the following types of measurements:

1. Steady-state forces and moments.
2. Damping forces.
3. Inception and development of cavitation.
4. Forces acting on cavitating bodies.
5. Noise produced by cavitation.
6. Powered model studies.

CONFIDENTIAL

7. The effect of exhaust gases on force and cavitation characteristics.

POLARIZED LIGHT FLUME

This is an auxiliary piece of equipment used principally to supplement the work of the high-speed water tunnel. Its chief characteristic is that it gives the visual picture of the flow around immersed bodies. These results are qualitative rather than quantitative. It has been employed chiefly for the following purposes:

1. The determination of hydrodynamically undesirable features of existing or proposed projectiles as evidenced by the formation of bad eddies, zones of separation, etc.
2. The design of stabilizing surfaces, especially ring tails, to set the flow pattern so as to reduce the resultant drag to a minimum.
3. The study of the action of various components of projectiles as evidenced by their effect on the flow.

CONTROLLED-ATMOSPHERE LAUNCHING TANK

This was especially designed to study the problems associated with the entry of the projectile into the water from the air and those of the phase immediately

following, in which the projectile is surrounded by the bubble that is formed during the entry. These problems differ in one important respect from those of the air flight and the steady-state underwater run in that in the two latter phases only one fluid is involved at a time, whereas in the entry and cavity phases, both the gas and the liquid are involved. It is for this reason that the launching tank is so arranged that the pressure can be varied at will. The use of this feature will be discussed more fully in Chapter 12. It is interesting to note that the final portion of the trajectory, i.e., the terminal ballistics, also involves phenomena in which the interaction of the gas and liquid phases are important. The underwater explosion produces a large volume of gas. The damage produced by underwater explosions is largely controlled by the behavior of this gas and its interaction with the hydrodynamic forces. The facilities embodied in the launching tank are adapted with little or no modification to a small-scale study of underwater explosions.

FREE-SURFACE WATER TUNNEL

This is the fourth and latest major piece of equipment of the laboratory. Its basic features are very similar to those of the high-speed water tunnel since it offers a working section in which bodies may be

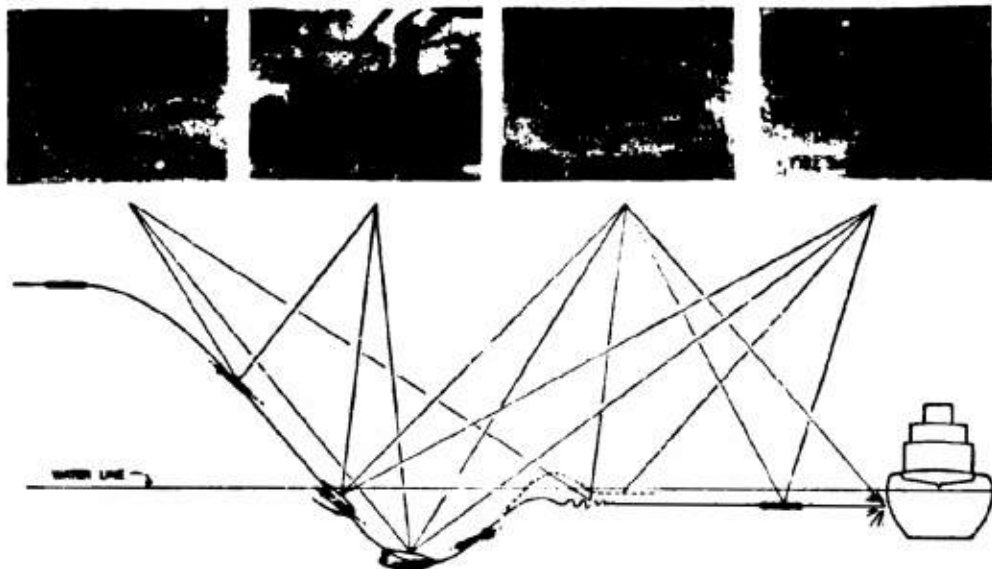


FIGURE 2. Application of laboratory equipment to study of torpedo behavior.

CONFIDENTIAL

UNCLASSIFIED

supported in a stream of flowing water so that measurements can be made of the force and other hydrodynamic characteristics. It has the unique feature, however, that the upper surface of the working section is not a solid boundary, but is a free surface, i.e., an air-water interface. The pressure at this interface may be maintained at any desired value from atmospheric down to about $1/10$ of an atmosphere. This makes it possible to study problems which cannot be dealt with effectively in the high-speed water tunnel. For example, if torpedoes of a certain design approach too close to the surface, they will broach and then run on the surface since the controls are inadequate to make them submerge again. These controls, however, appear quite adequate for the normal underwater run. This shows that the hydrodynamic forces acting on the body when it is near the surface are different from those acting during deep running. These forces and their variation with distance to the surface can be studied effectively in the free-surface water tunnel.

One of the unanswered questions involved in the use of jet propulsion in underwater projectiles is the effect of the jet on the resistance and the control characteristics of the projectile. The experimental

study of this effect requires the introduction of relatively large amounts of air or other gas into the working section in order to form a jet with the desired characteristics. Such a study cannot be undertaken in the high-speed water tunnel because it is not equipped to remove this large amount of gas after it leaves the working section. If it is not removed, it circulates with the water and in a very few seconds is back to the working section again. This is not permissible because it affects all the hydrodynamic forces and invalidates the measurements. The free-surface water tunnel, therefore, was designed with a high-capacity air-removal system to make it adaptable to detailed study of the effects of underwater jets.

The controlled-atmosphere launching tank was designed to give information concerning the overall behavior of the projectile during its passage through the interface and its run in the bubble. However, it was felt that it would be very helpful to be able to make force measurements and to observe cavity characteristics under steady-state conditions. This will be possible with the free-surface water tunnel since projectiles can be mounted on a balance above the water surface and the forces on them can be measured for any degree of submersion.

CONFIDENTIAL

Chapter 2

LABORATORY FACILITIES

2.1 PHYSICAL ARRANGEMENT OF LABORATORY

THE LABORATORY FACILITIES of the project are housed in the new Hydrodynamics Laboratory building and in the adjoining Hydraulic Machinery Laboratory. The Hydrodynamics Laboratory, which is shown in Figure 1, occupies three floors. Laboratory equipment is located on the basement and sub-basement floors, with offices on the ground floor. The Hydraulic Machinery Laboratory occupies four stories in the left-hand wing of the Guggenheim Aeronautics Laboratory building which appears in the background in Figure 1. The buildings are interconnecting on all three floors of the Hydrodynamics Laboratory.



FIGURE 1. Hydrodynamics Laboratory building.

Figures 2A, B, and C show the three floor plans and arrangement of major equipment and auxiliary facilities in both buildings. The total floor space available is approximately 19,000 sq ft. The high-speed water tunnel equipment occupies all four stories of the Hydraulic Machinery Laboratory area shown on the left in Figure 2. The working section and main operating level is on the first floor with circulating pump, water storage, and miscellaneous auxiliary equipment on the floors below. There is no floor at the second-floor level; the space is used for additional head room over the water tunnel. The controlled-atmosphere launching tank and the free-surface water tunnel, together with their storage tanks and auxiliaries, occupy two floor levels (basement and subbasement) in the adjoining new building. The polarized light flume is on the basement level.

It will be noted that in addition to the primary apparatus, space is provided for all the activities of the project auxiliary to the main experimental work. The first floor of the new Hydrodynamics Laboratory provides for administrative offices, design offices, and drafting rooms, computing rooms for reduction of experimental data, and quarters for analysis of results and preparation of technical reports. The basement floor contains photographic laboratories. The subbasement houses a machine shop for construction of test models. The electronics laboratory and shop are located adjacent to the water tunnel on the basement level.

2.2 HIGH-SPEED WATER TUNNEL

2.2.1 Purpose and Specifications

The high-speed water tunnel was designed and constructed to permit the determination of the hydrodynamic forces on projectiles when in the airborne or waterborne phases of the trajectory. The design of the apparatus is based on the relative-flow principle employed in wind tunnels wherein the flow pattern peculiar to the prototype moving through a stationary fluid is simulated by the flow pattern about a model immersed in a moving fluid. The essential components of the tunnel are:

1. A working section in which the model may be mounted and observed.
2. A circulating system consisting basically of a pump and piping by which the flow of water may be maintained through the working section.
3. A measuring system or balance by means of which the hydrodynamic forces on the model may be measured.

A general view of the high-speed water tunnel is seen in Figure 3. The essential features mentioned above will be seen and identification of most of the other components can be made by reference to the isometric drawing, Figure 4, and to the elevation drawing, Figure 5. The relationship of the high-speed water tunnel to the other main pieces of apparatus in the Hydrodynamics Laboratory can be seen on the floor plan, Figure 2.

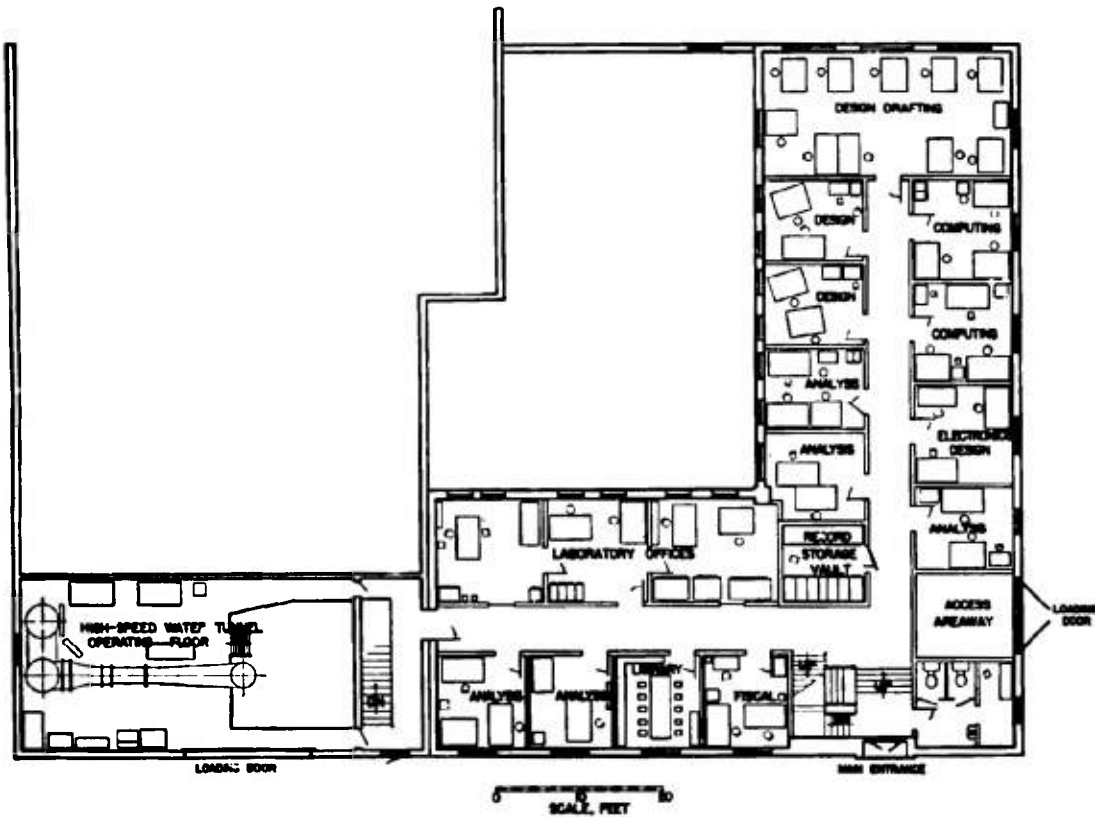


FIGURE 2A. Hydrodynamics Laboratory, ground floor level.

The construction of the tunnel centered around the existing equipment in the Hydraulic Machinery Laboratory. In addition to the general basic laboratory layout available for use, the following important components were available:

1. The electric dynamometer.
2. The dynamometer speed control system.
3. Special weighing-type pressure gauges.
4. The pressure control system.
5. The temperature control system.
6. The 60-in. diameter tank used as part of the main water tunnel circuit and for air-removal purposes.

The existence of this equipment was very important as a time-saving factor in getting the laboratory into productive work.

The specifications for the water tunnel were developed around the capabilities of the above-mentioned existing equipment and the needs of the National Defense Research Committee [NDRC]. An

enumeration of the main specifications of the water tunnel follows.

VELOCITY

The lower limit of the acceptable maximum velocity was set at 50 fps since it was felt that existing developments showed a definite trend toward higher and higher velocities for Service applications. The available horsepower in the electric dynamometer has permitted maximum speeds of 75 fps.

DIMENSIONS OF WORKING SECTION

A closed-type working section was decided upon because such a design reduces the energy loss, gives more stable flow, and results in a more definite and calculable boundary correction to the measurements as compared with other types of working sections.

CONFIDENTIAL

The acceptable model sizes and scales determine the size of the tunnel. It is axiomatic that models should be kept as small as compatible with desired accuracy and reliability of the test results, since smallness makes for economy, speed, and flexibility, and therefore increases the productivity of the laboratory. It was estimated that the prototype diameters of the bodies to be studied would vary from 2 to 24 in. Since the measurements were to be made in water, which is a fluid of high density and low viscosity, it was felt that a model diameter of 2 in. would result in forces of reasonable magnitude and at the same time the flow conditions would be comparable to service conditions. In other words, a 2-in. model tested in the high-speed tunnel gives sufficiently large Reynolds numbers to be comparable with prototype conditions.

On this basis it was decided that the working section should be 14 in. in diameter. This is in accordance with current wind-tunnel practice for dirigibles and similar symmetrical bodies, i.e., to have a model

diameter of about 15 per cent of that of the measuring section.

Aerodynamic practice has shown that the test chamber should be considerably longer than the model if accurate drag measurements are to be obtained. The maximum prototype length was estimated to be 8 to 10 diameters, with average length 4 to 6 diameters. This would make the average model length 8 to 12 in. with extremes to 20 in. For the NDRC work it was felt that a large working section would also permit more extensive observations of the wake. Therefore, a 72-in. working section was chosen.

BALANCE EQUIPMENT FOR FORCE MEASUREMENTS

The choice of the type of balance is one of the most difficult problems in connection with the tunnel. The balance is a necessary evil. The forces on the body under study must be measured, but any connection to the body to provide means of measuring these forces changes the forces themselves and thus a cor-

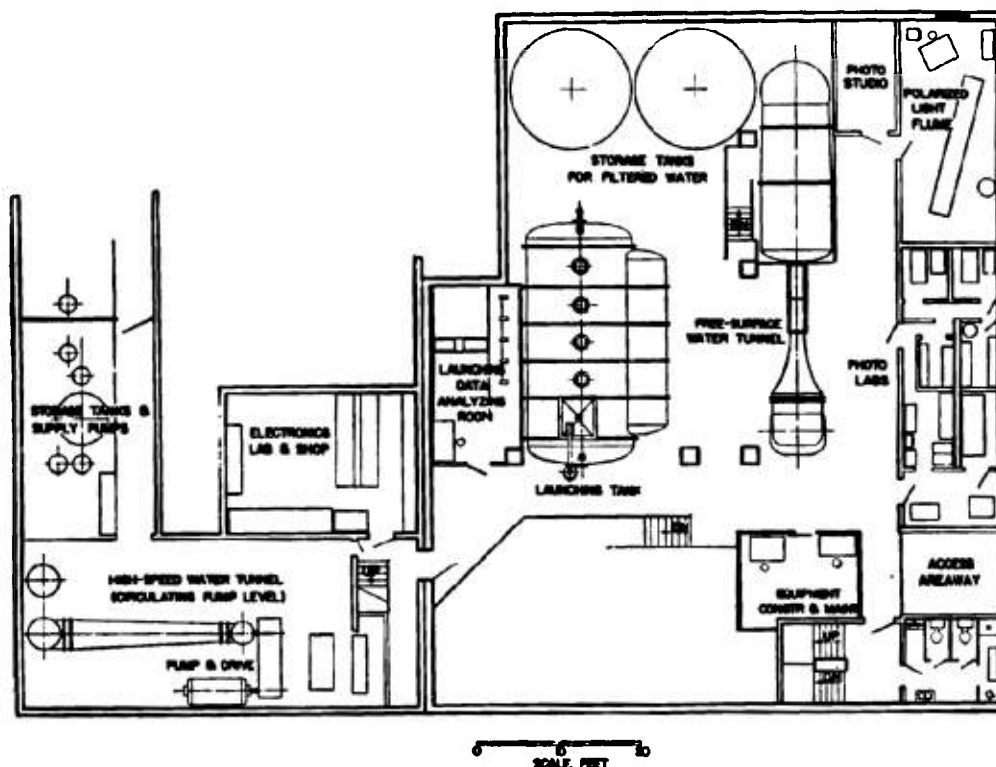


FIGURE 2R. Hydrodynamics Laboratory, basement level.

CONFIDENTIAL

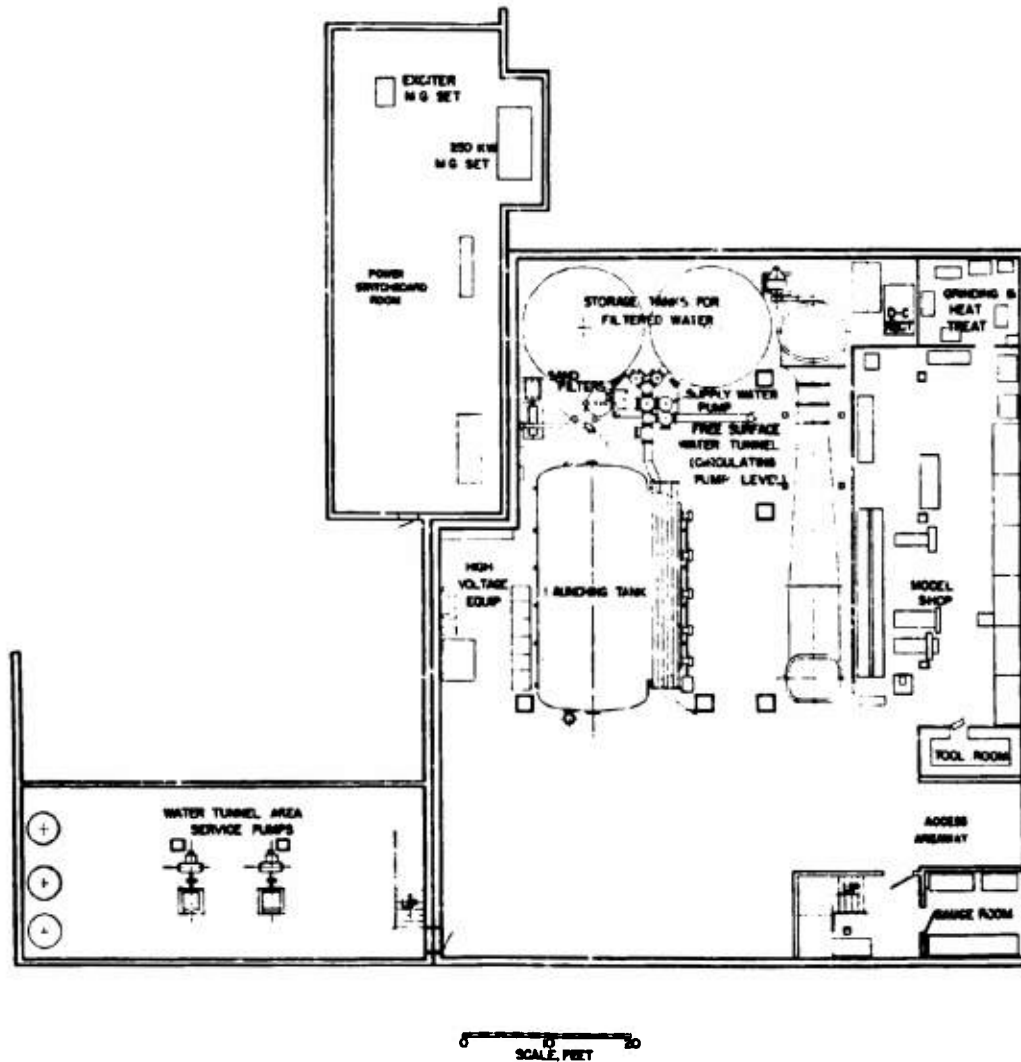


FIGURE 2C. Hydrodynamics Laboratory, subbasement level.

rection must be made. An analysis of the measurement desired shows that the balance system can be relatively simple, since the bodies to be studied have axial symmetry. A three-component balance, therefore, is capable of furnishing all the necessary information, since the possible forces acting on the body can be reduced to a drag force in the direction of flow, a cross force or lateral force, and a moment about an axis normal to the direction of flow. One additional factor entered into the selection of balance type. It

was anticipated that it would be necessary to study the characteristics of propelled bodies, whether the force of propulsion came from a propeller or a jet of fluid. This precluded the use of a balance which attaches axially to the rear of the body. The wire type of balance attachments was also eliminated because it provided no possibility for introducing a supply of fluid for the driving jet. Therefore, a single spindle-type balance was decided upon with the model axis normal to that of the spindle.

CONFIDENTIAL

REQUIREMENTS FOR CAVITATION STUDIES

If submerged bodies are required to travel at high speeds near the water surface, cavitation may result and produce serious deviations from the expected performance. In order to study the effects of cavitation in the model performance two additional requirements were introduced: (1) that the absolute pressure in the measuring section be variable without affecting the velocity of the flow, and (2) that provision be made for visual observation of the location and the action of the cavitation when it was produced.

1.1.1 Main Water Tunnel Circuit

FLOW CIRCUIT

The flow circuit can be traced in either Figure 4 or 5 by starting with the circulating pump. This is driven by a dynamometer through a multiple V-belt

drive having a speed reduction of 2 to 1. The pump discharges horizontally to the right through a diffuser section into the 5-ft diameter vertical tank. At this point, the flow is turned upward by vanes inside the tank and, at the working-section level, it is turned horizontally to the left by vanes into a short length of 34 $\frac{3}{4}$ -in. pipe. From there the flow passes through a honeycomb and a reducing nozzle to the 14-in. diameter working section. From the working section, the flow enters another horizontal diffuser which reduces its velocity considerably before entering the elbow. From the elbow the flow enters the diverging down-comer, which completes the deceleration before the flow reaches the inlet of the circulating pump.

CIRCULATING PUMP AND DRIVE

Figure 6 is a view of the circulating pump taken from the discharge end. Figure 7 shows the pump from the driving end and Figure 8 is a view into the

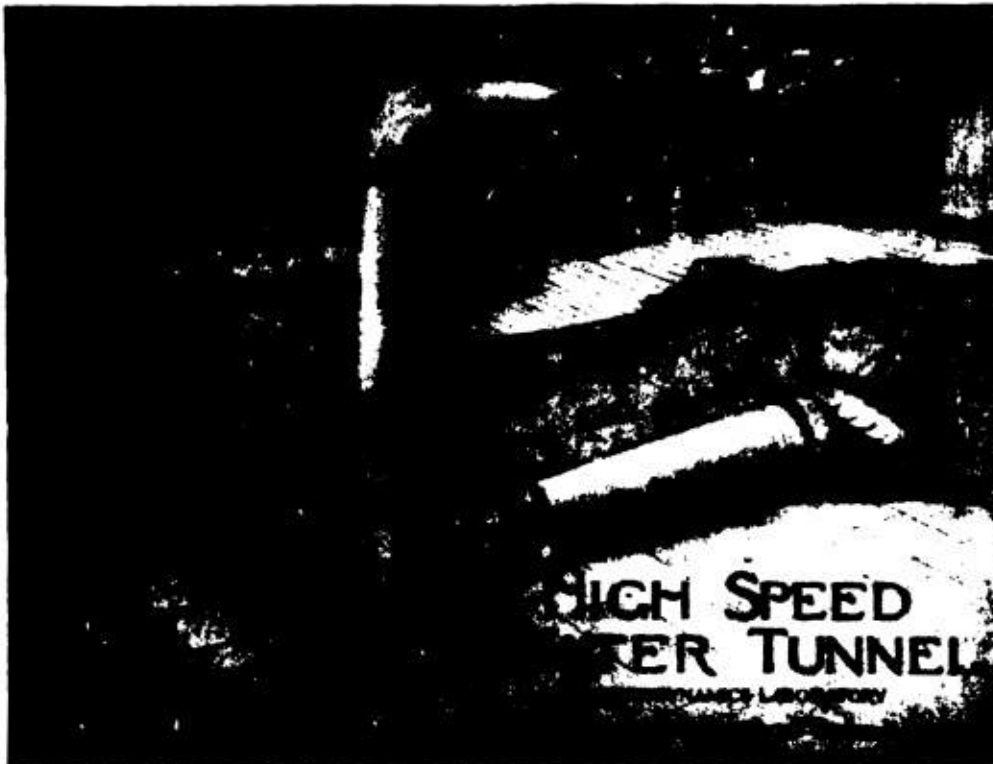


FIGURE 3. High-speed water tunnel. Hydrodynamics Laboratory, California Institute of Technology.

CONFIDENTIAL

shaft, therefore, turns at a speed proportional to the difference of the other two. This shaft actuates a phase shifter (in this case a selsyn motor driven through a friction clutch and limited in motion by

two systems. The speed-control gear box is shown in Figure 11. This control system permits a speed range for the dynamometer of from 100 to 5,000 rpm. For any given setting, the average speed is as ac-



FIGURE 8. Circulating pump for high-speed water tunnel. View into pump inlet, showing the straightening vanes.



FIGURE 9. Dynamometer for circulating pump for high-speed water tunnel. View from above.

steps) which controls the output of a battery of thyatron rectifiers. These furnish the excitation field for the shunt-wound dynamometer, and thus control its speed. It will be seen that any difference in speed between the dynamometer and the speed standard acts immediately to correct itself. The only position of equilibrium is absolute synchronism of the

curate as the quartz crystal controlling the standard-frequency source; about 1 part in 50,000. The instantaneous speed fluctuations are of the order of 1 rpm.

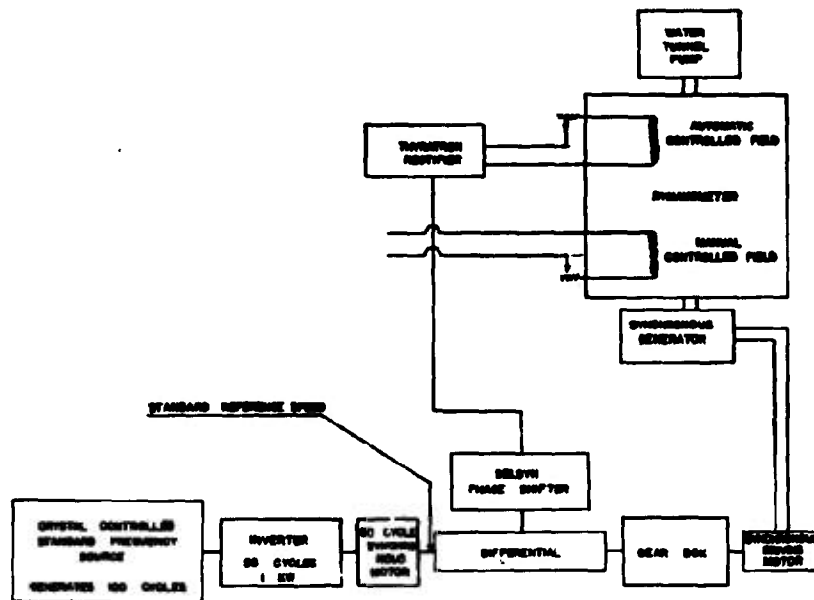


FIGURE 10. Block diagram of speed-control system for dynamometer, high-speed water tunnel.

AIR REMOVAL AND FLOW STRAIGHTENING

The 5-ft diameter tank, besides furnishing part of the primary flow circuit, provides a high point in the system for removal of accumulated air, as shown in Figure 12. The honeycomb is shown in detail in



FIGURE 11. Speed control gear box for dynamometer, high-speed water tunnel. View from above.

Figure 13 and its location in the circuit is shown in Figure 5. The honeycomb consists of a nest of axial channels $10\frac{1}{2}$ in. long and of triangular cross section, 1 in. on a side. This design is very easy to build out of light galvanized iron sheet and it has been a satisfactory means of removing the lateral-velocity components at the entrance to the nozzle.

NOZZLE

The nozzle is shown before assembly in the circuit in Figure 14 and after assembly in Figure 15. It re-

duces the flow cross section from $34\frac{3}{4}$ -in. diameter to the 14-in. diameter of the working section in a length of 47 in. The contour is designed to give a uni-



FIGURE 12. Five-foot diameter tank, high-speed water tunnel.

form velocity distribution across the flow at the entrance to the working section with no lateral-velocity components. This rather elaborate design was found necessary in order to eliminate local cavitation in the nozzle when the tunnel was being operated with low pressure and high velocity in the working section. The nozzle is fabricated steel plate machined to the specified contour, cadmium plated, and polished on the inside surface. Figure 15 shows the piezometer rings used to measure the pressure drop across the nozzle from which the velocity of flow in the working section is computed. Between the nozzle and the

working section is seen the 2 $\frac{1}{4}$ -in. thick dummy pitot tube block. This can be removed and replaced with an identical block drilled for the direction-finding pitot tube when a velocity traverse of the flow is to be taken.

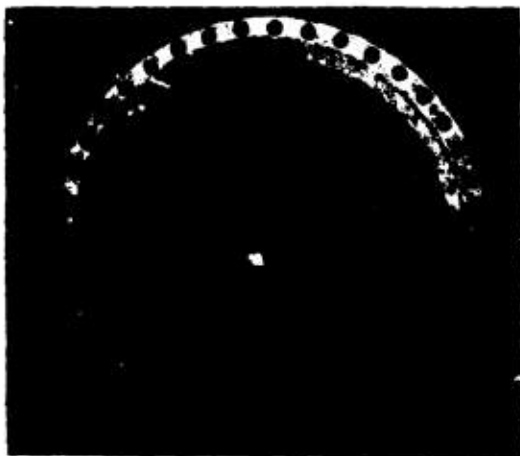


FIGURE 13. Honeycomb baffle. High-speed water tunnel.

WORKING SECTION

The working section used during the latter part of the project is shown before assembly in Figure 16 and after assembly in Figure 17. The bulkheads and reinforcing permit the use of the large Lucite windows for photographic purposes. The upstream end of the working section is bolted to the pitot tube block



FIGURE 14. Nozzle before assembly. High-speed water tunnel.

which, in turn, is bolted to the nozzle. Locating dowels are used to insure proper alignment. Unsupported-area type neoprene gaskets are used to permit metal-to-metal contact of the flanges and to eliminate any possibility of gasket material projecting into the flow. The downstream end of the working section is connected to the diffuser by a Victaulic coupling.

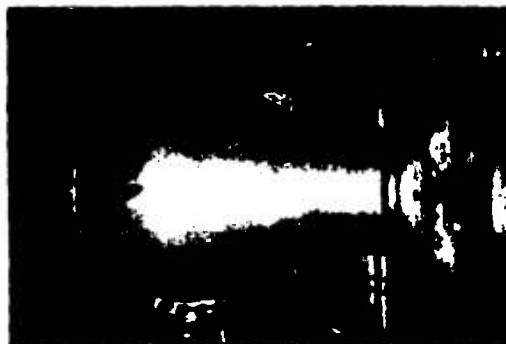


FIGURE 15. Nozzle after assembly. High-speed water tunnel.

This eliminates any mechanical stress on the working section and provides for small misalignments and thermal expansion.

223

Auxiliary Circuits

PRESSURE REGULATING CIRCUITS

Several auxiliary circuits are used in connection with the main circuit to obtain the desired operating flexibility. The water tunnel operates on a closed circuit in a completely filled system; therefore, it is possible to impose other minor flow circuits on this system without disturbing the main flow. This principle is used to obtain pressure control of the system.



FIGURE 16. Working section before assembly. Rear view. High-speed water tunnel.

CONFIDENTIAL

The pressure-regulating circuit pump is submerged in an open storage tank. The discharge goes to the 5-ft diameter tank through the horizontal pipe in Figure 5. Since the system is full, this same amount of water must leave the tank through the by-pass valve. The by-pass valve is motor-operated and is controlled from the working floor. The pressure in the 5-ft diameter tank varies with the amount of opening of this by-pass valve. When it is nearly closed, the tank pressure reached the maximum head which the pressure-regulating pump can develop, i.e., about 150 ft. Opening the by-pass valve reduces the head until atmospheric pressure is reached at that point. Since the working section is about 15 ft above the valve and since a large additional pressure drop is caused by the acceleration of the flow in the nozzle ahead of the working section, subatmospheric pressures can be obtained at the test station. However, if still lower pressures are desired, a booster pump located in the by-pass line, but not shown in this drawing, may be operated to pump water out of the system. The result is that cavitating conditions can be maintained in the working section for any desired test velocity. There is an air bleed line at the top of the 5-ft diameter tank, as shown in Figure 12. This is opened, upon filling the system, when the air in the tank is being displaced by water. For low-pressure operation a Nash Hytor vacuum pump is used in the bleed line to remove any accumulations of air that may gather in the system.

COOLING CIRCUIT

In the operation of the tunnel, up to 250 hp is continuously put into the system through the circu-

lating pump. This energy is all dissipated into heat; thus, unless the system is cooled, the temperature will rise to undesirable values. To maintain a constant temperature and therefore constant viscosity at the Reynolds number for testing, this heat must be removed. The method for doing this is also shown in Figure 5. A part of the return flow from the by-pass valve of the pressure-regulating system goes to the cooling water pump, which circulates it through a forced-draft cooling tower on the roof and returns it to the storage tanks. Thus cooling is obtained by continuously bleeding off heated water from the system and returning an equal amount of cooled water.

2.3.4

Balance

PRINCIPLE AND GENERAL ARRANGEMENT

As previously outlined, the balance is designed to measure three components of the hydrodynamic forces operating on the model. These are the drag force parallel to the flow, the cross force normal to the flow, and the moment about the axis of support. Note that these components are with reference to flow direction and not to the model orientation. Figure 18 is a diagram of the balance system. Basically, it consists of a vertical spindle supported near the center with a universal pivot that permits rotation through any axis about this point but allows no translation. The model is attached rigidly to the top of the spindle. This assembly is prevented from rotating under the action of the hydrodynamic forces by applying restraining moments about three mutually perpendicular axes intersecting at the pivot. These moments are applied by hydraulic pressure through the three



FIGURE 17. Working section after assembly. Front view. High-speed water tunnel.

CONFIDENTIAL

sets of pistons, cylinders, and yoke wires as shown in Figure 19. The three restraining moments correspond to the hydrodynamic forces acting on the model. In order to measure the forces acting on the model when it is inclined to the flow, the vertical spindle was made in two pieces. The model is attached to the upper

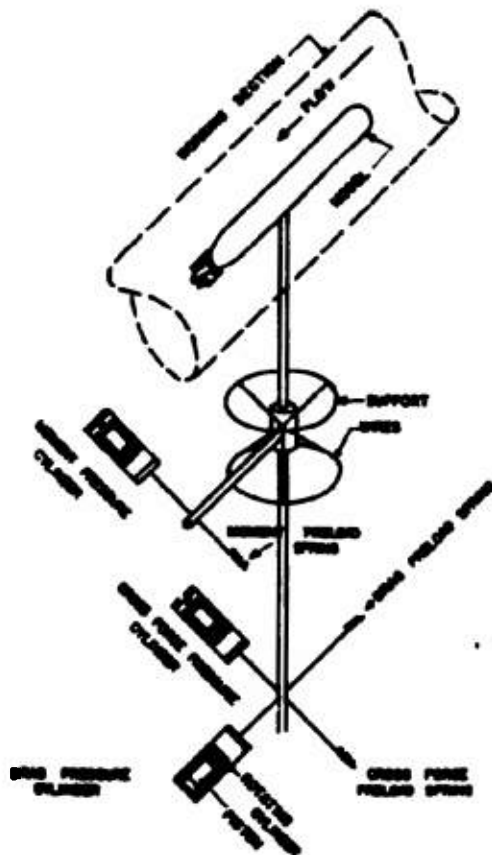


FIGURE 19. Diagram of balance system, high-speed water tunnel.

piece while the supporting pivot and pressure cylinders are attached to the lower piece. By rotating the upper spindle section with respect to the lower one and clamping it securely in place, the angle of yaw of the model is changed with respect to the flow but the direction of the balance restraining forces remains unchanged.

In order to keep the model position accurately fixed in the flow while the measurements are made, the limits of motion of the hydraulic pistons are

restricted to ± 0.003 in. This is equivalent to less than 2 minutes of angle. These small deflections require great structural rigidity, both of the spindle and of the supporting frame. Figure 15 shows how this rigidity has been built into the structure. The whole assembly is mounted on a hydraulic lift for ease in handling and adjusting. It is completely supported by this lift in the working section even when in position for measurements.

SPINDLE

The spindle which supports the model is seen projecting vertically upward from the top of the balance in Figure 20. This spindle is removable so that different types can be installed to meet the varying



FIGURE 20. View of balance showing application of moments by hydraulic pressure to balance system. High speed water tunnel.

needs of the different tests. The spindle pivot point lies at the center of the bronze ring seen at the top of the structure. The pivot is made up of two sets of three pairs of piano wire. Each set forms three equally spaced elements on the surface of a cone. The two vertices meet in a point on the centerline of the spindle. This means that for small deflections this point is the center of rotation for all three moments that are measured, and the resistance offered by the deflection of the support wires for slight angular movements of the spindle is small. Two pairs of wires can be seen in Figure 20.

SEAL

A watertight seal is provided between the balance spindle and the working section in the form of a soft rubber cylinder which is reinforced with concentric

steel rings vulcanized into it. This construction permits extreme flexibility and, at the same time, gives a structure which will resist both internal and external pressure. It operates satisfactorily from gauge pressures of 50 psi down to the vapor pressure of cold water. This seal is illustrated in Figure 21, which shows the deflection of the cylinder under the compression of a C clamp.

YAW ANGLE ADJUSTMENT

The angle of yaw of the model is changed by the rotation of the upper spindle with respect to the



FIGURE 20. Balance spindle. High-speed water tunnel.

lower spindle, over a range of about -20 degrees to $+20$ degrees. The two spindles are held together by a spring-loaded brake which has a resisting torque greater than any hydrodynamic moment within the design capacity of the balance.

The process of angle changing then requires that a torque be applied between the upper and lower spindles which will slip the friction brake. This torque is supplied by an electric motor mounted on the lower spindle. The motor operates a worm which engages a sector integral with the upper spindle, thereby slipping the brake and turning the upper spindle with respect to the lower spindle. The control buttons for angle changing are clearly shown in Figure 22, as well as the angle-changing motor.

The angular position of the model is indicated to the nearest 0.1 degree by a dial gauge attached to the lower spindle and having its deflection rod connected to the upper spindle by means of a flexible ribbon wound around the upper spindle. This dial gauge is the larger one shown in Figure 22.

FORCE- AND MOMENT-TRANSMITTING SYSTEM

The hydrodynamic moments on the upper spindle are balanced by the restraining wires at the bottom of the lower spindle as shown in Figure 19. The wires and yokes shown here transmit the forces to the hydraulic pistons. The length of the wires is great compared to the range of movement of the end of the spindle so that no error is introduced into the data.

At the extreme right of Figure 19 is seen a preloader. This device applies a spring preload of 50 psi



FIGURE 21. Watertight seal between balance spindle and working section. High-speed water tunnel.

to the oil in the cylinder and, at the same time, compensates for the small but undesired elastic resisting moment exerted by the spindle pivot wires on the spindle during the small angular deflections incident to the balancing operation. The preload is needed so that positive and negative forces may be measured by one piston. The cross force preloader is partially seen in Figure 19.

The pistons and cylinders are shown also in Figure 19. The piston and cylinder are lapped to a clearance of about 0.00004 in. To eliminate static friction the cylinders are rotated at constant speed by individual motors.

22.1 Pressure Gauges

PRINCIPLE OF OPERATION

The pressure in the cylinders on the balance are measured by weighing-type pressure gauges. A close-up view of one of these gauges is shown in Figure 23. The gauge consists essentially of a beam supported on a Cardon hinge pivot. The pressure to be measured is applied through a piston attached to this beam. This piston, like the balance pistons, is fitted in a cylinder which rotates to avoid static friction. The force exerted by the oil pressure on the piston is

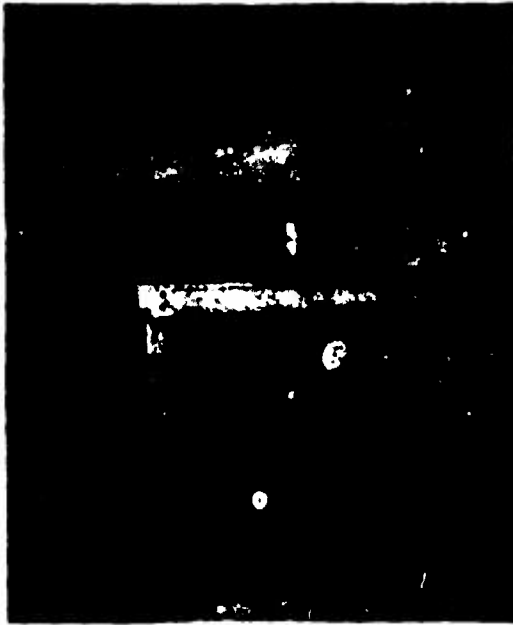


FIGURE 22. View of working section and balance mechanism. High-speed water tunnel.

balanced by pan weights applied to the end of the beam and also by a rider weight running on the beam. Unbalance of this beam results in unbalance of the optical-electrical control system which, in turn, starts a small electric motor and moves the rider weight until equilibrium is obtained.

PHOTOCELL CONTROL

The optical-electrical control of the equilibrium of the beam is obtained through use of a photocell system which is shown schematically in Figure 24. The pur-

pose of the photocell system is to obtain control of the beam by frictionless and nonfouling means and at the same time to obtain a response of the rider weight motor in proportion to the unbalance or deflection of

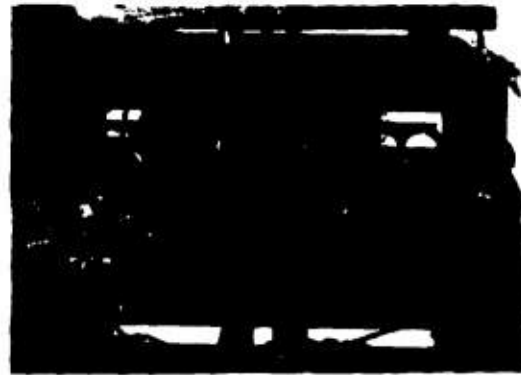


FIGURE 23. Weighing-type pressure gauge. High-speed water tunnel.

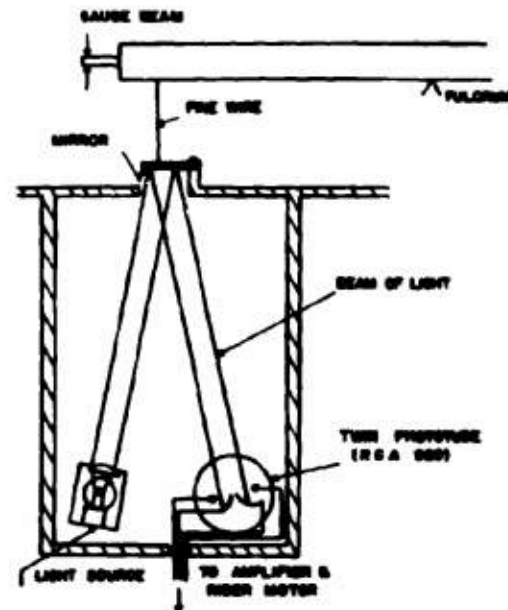


FIGURE 24. Schematic diagram of photocell control. High-speed water tunnel.

the gauge to avoid hunting. As can be seen by the schematic diagram, unbalance of the gauge causes a beam of light to move either to right or left and thus to give unequal illumination on the symmetrical halves of the phototube. This results in a voltage

which actuates a motor which moves the rider toward a balanced condition. At the balanced position, the two halves of the phototube are illuminated equally by the beam of light and thus there is no voltage to cause a movement of the rider. The position of the rider is indicated by a Veeder counter, and a scale is chosen such that the counter indicates the applied pressure directly in pounds per square inch to the nearest 0.01 psi.

SENSITIVITY AND RANGE OF SYSTEM

The length of the balance lever arms and the areas of the pistons in the system have been chosen so that the readings of the drag and cross force gauges in pounds per square inch are numerically equal to twice the hydrodynamic drag and cross force in pounds



FIGURE 25. Control panel. High-speed water tunnel.

and the reading of the moment gauge in pounds per square inch is numerically equal to the hydrodynamic moment expressed in inch-pounds. Pan weights are available in 50 psi units to a maximum of 500 psi, and the range of travel of the rider weight corresponds to 50 psi.

CONTROL PANEL

Figure 25 shows the instrument panel with the cross force, drag, and moment gauges just described and the differential pressure gauge, to be described later. In the center of the instrument group is a panel with lights indicating the state of balance of the gauges and other essential operating data. When all panel lights are out, a condition of gauge balance and general instrument readiness is indicated. Thereupon

a button is pushed which stops the gauge rider motors so that the pressure readings may be recorded.

HYDRAULIC TRANSMISSION SYSTEM

This hydraulic system composed of the balance pistons and cylinders, gauge pistons and cylinders,



FIGURE 26. Compensator. Assembled view. High-speed water tunnel.

and the connecting oil line is subject to slight leakage of the working fluid (light turbine oil) past the pistons. The leakage of the system is made up by compensators shown in Figures 26 and 27, so that the system is essentially a constant-volume one. The



FIGURE 27. Compensator. Disassembled view. High-speed water tunnel.

compensator is a small screw-operated piston which supplies oil to the system in a definite minute amount upon receiving an electric signal from the balance indicating that the amount of oil in the system has reached the minimum permissible. The indication of

the state of the oil system is made also by lights on the instrument panel.

2.2.6 Balance Sensitivities

In discussing the sensitivity of the balance system, two characteristics must be noted. The first is sensitivity defined as a change in the reading on the pressure gauge per unit change in force on the model. On this basis for the cross force and drag measurements, one dial division corresponds to 0.005 lb force on the model. For the corresponding moment readings, one dial division corresponds to 0.01 in.-lb torque on the model. The second characteristic is

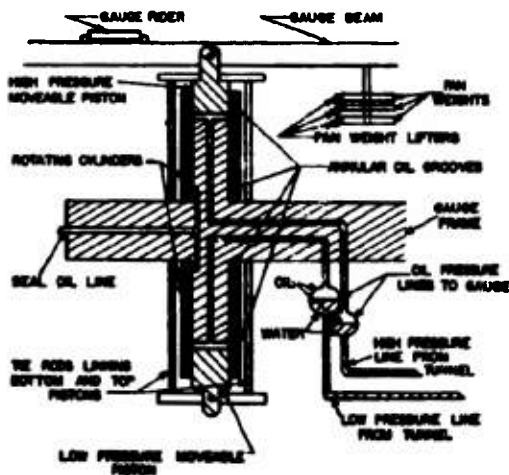


FIGURE 28. Schematic diagram of the differential pressure gauge, high-speed water tunnel.

responsiveness, which is defined as the magnitude of the minimum impressed force on the model necessary to cause a change in the gauge readings. This responsiveness is approximately 0.01 lb for cross force and drag measurements on the model and 0.02 in.-lb for moment.

2.2.7 Differential Pressure Gauge

PRINCIPLE OF OPERATION

A differential pressure gauge is employed which is very similar in appearance and design to the pressure gauges described above. The only difference is that the force applied to the beam is the result of the difference of two pressures applied to the

opposite ends of a piston. Figure 28 is a schematic diagram of this differential pressure unit. The two pressures are applied, one at the top and one at the bottom of a piston and the resulting force on the piston depends on the difference between the two pressures. This resulting force is transmitted to the beam and is measured in the same way as in the pressure gauges described above. The cylinders, like those used in the force measuring system, are rotated to avoid static friction. The gauge is actuated by oil connections from two bodies of oil floating on water surfaces in cylindrical separating pots beneath the gauge itself. The pressure leads from the water tunnel are connected into these separating pots. The pots are horizontal to permit a large change in volume with a relatively small change in elevation of the oil-water interface. This is necessary since, due to the different densities of oil and water, the reaction of the



FIGURE 29. Three-hole direction-finding pitot tube.

gauge will be affected by changes in the height of the oil columns. A cross connection between the two reservoirs permits initial leveling of the system.

APPLICATIONS

The principal application of this differential pressure gauge is in the measurement of velocity of flow in the working section by means of the pressure differences across the nozzle. Other applications are in the measurement of the pressure distribution on projectile models and in the measurement of the pressure and velocity distribution across the working section, which is obtained with the three-hole direction-finding pitot tube shown in Figures 29 and 30. Since this is essentially a zero volume-change device, the response of the gauge to pressure changes is very rapid.

2.2.8 Pressure Distribution Measuring Equipment

Since measurements are made on the model with a fluid flow having a pressure gradient along the work-

ing section and since the size and position of the model affects this pressure gradient, it is necessary to measure the pressure in the working section at closely spaced points along the wall. For this purpose the multiple differential manometer, seen in Figure 31, is employed. This is an air-water type with all columns having common air connections, and in general the pressure at the beginning of the working section is



FIGURE 30. Three-hole pitot tube mounted for use with high-speed water tunnel.

used for the reference pressure. Figure 31 also shows that the multiple differential manometer is well suited for photographic recording. Since the total pressure drop in the working section is of the order of 0.1 or 0.2 of a velocity head, great care has to be exercised in the construction of the piezometer openings to insure that the static pressure alone is measured, without measuring any of the velocity pressure.

1.2.3

Shields

In order to avoid corrections for hydrodynamic forces on the exposed spindle within the working section it is necessary to install streamlined shields



FIGURE 31. Multiple differential manometer.

around the spindle, firmly attached to the working section. This shield must be as small as possible in order to minimize disturbances in the flow, yet there must be sufficient clearance between the spindle and the shield so that there is no chance of the shield touching the spindle and absorbing a portion of the

CONFIDENTIAL

hydrodynamic forces applied on the model. The shield in present use for force tests is shown in Figure 32. This photograph shows the shield, spindle, and model installed, and Figure 33 shows a dummy shield,



FIGURE 32. Shield, spindle, and model installed in water tunnel.

termed an image shield, mounted above the model, and used in the tests to determine interference corrections. The shield is made in two sections, the section next to the model being much smaller



FIGURE 34. Shield used in connection with visual observation of cavitation.

than the section mounted on the tunnel wall. Both sections are Joukowski streamlined shapes. A splitter plate between the two sections acts to prevent cross flows. The purpose of the design, termed a duplex shield, is to secure a minimum flow disturbance near the model by use of the small upper shield, yet to allow use of a spindle size large enough to prevent undue deflection. The radial clearance be-

tween the spindle and the inside bore of the shield is about 0.015 in. Figure 34 is a photograph of a shield used for visual observation of cavitation. Since no forces are measured during visual cavitation tests,



FIGURE 33. Shield, spindle, and model group with added image shield (above model) installed within the tunnel.

the model is mounted rigidly to the shield and the large-diameter spindle is unnecessary. Therefore, this shield can be considerably more slender than the force shields. Note that the model is mounted di-

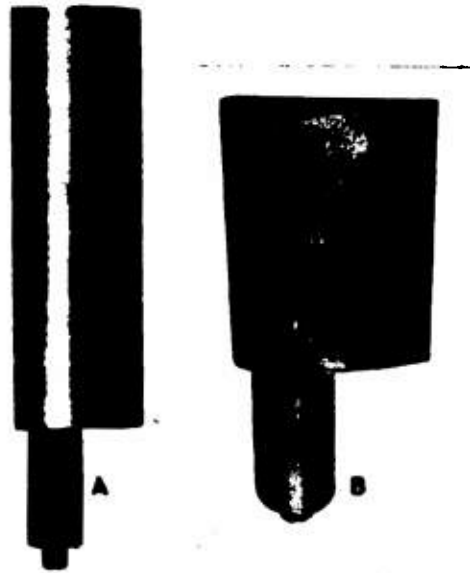


FIGURE 35A, B. Typical two-dimensional models, different lengths of an NACA 4412 airfoil.

rectly on the top of the shield and thus in effect the model is fastened rigidly to the working section. This shield is a streamlined, cavitation-resistant shape developed by the David Taylor Model Basin. In addi-

tion to the two types of shields described above, a shield has been developed for the simultaneous measurement of cavitation and force data. This shield also is a cavitation-resistant David Taylor Model Basin shape, and the spindle employed is elliptical in cross section so that for small angles of yaw the required rigidity is combined with the necessary slenderness.

2.2.10 Water Tunnel Operating Techniques

MODELS

The models used are exact geometric replicas of the prototypes within the tolerances of the precision machine shops employed. Most of the models have been three-dimensional but some two-dimensional testing has been done. Figure 35 shows two typical

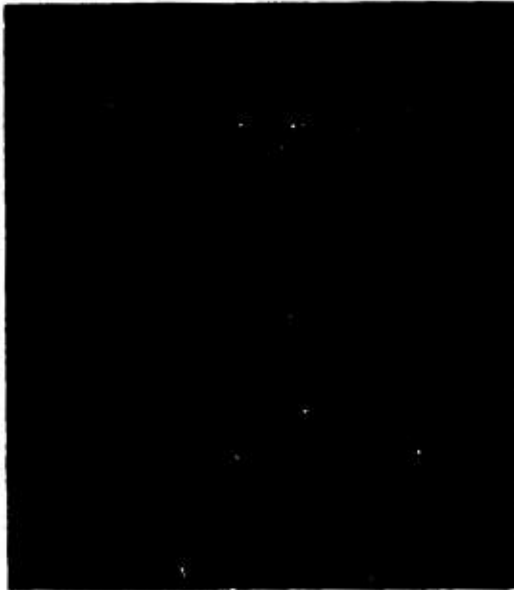


FIGURE 36. Typical 2-in. diameter model assembled about support section.

two-dimensional models, different lengths of a NACA 4412 airfoil. In this application, flat plates were installed in the bottom and top of the working section for the full length and the two-dimensional model spanned the distance between these two plates. This special setup was necessary in order to avoid end effects and thus secure pure sectional or two-dimensional data. The three-dimensional models are fas-

tened securely to the spindle in the following manner: A 2-in. diameter model section is silver-soldered to the end of the spindle and the remaining parts of the model are fastened to this center section by means of a through bolt.

Figure 36 shows a typical model and Figure 37 shows the individual components including the spindle and integral center section. A complete set of



FIGURE 37. Same as Figure 36 but with model parts separated. The central cylindrical section is fastened to the spindle.

cylindrical body sections from 0.10 in. to 0.20 in. long in 0.01-in. steps and from 0.20 in. to 4.00 in. in longer steps is available so that any cylindrical length may be readily made up. The necessary nose, afterbody, and tail members are fastened to the cylindrical part by means of a bolt through the whole assembly. The individual components have tongue and shoulder joints to secure precise alignment. A concentricity of about ± 0.0002 in. has been secured. When a design of a new body is submitted for test, a quick survey of the model parts shows what elements are available and what new parts must be made. In general the model parts are made of stainless steel to eliminate corrosion and to secure a reasonable hardness to prevent damage from handling. Special sections may be made of brass. Figures 38 and 39 show a typical powered model with an exhaust stack in which a flow of compressed air simulates the turbine exhaust. The motors used for the powered models are of a high-cycle induction type.

CONFIDENTIAL

OPERATING VARIABLES

The following quantities concerned with model performance may be varied conveniently with the existing equipment in the water tunnel: speed, pressure (submergence), pitch angle, yaw angle, rudder angle, and geometry of the model. Most of the tests conducted in the laboratory involve a systematic investigation of the effect of one of these variables while all the others remain constant.



FIGURE 38. Typical powered model with exhaust stack for compressed air simulating turbine exhaust.

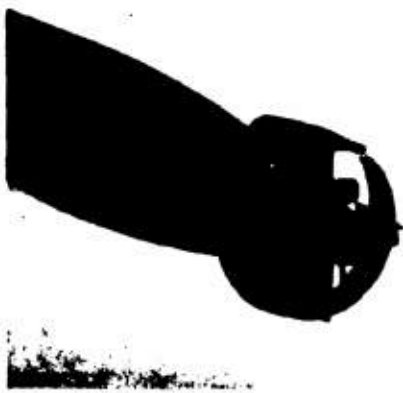


FIGURE 39. View of tail showing propeller and exhaust pipe.

FORCE TESTS

The fundamental test in the laboratory, termed a force test, involves a study of the hydrodynamic forces acting when speed, pressure, pitch angle, rudder angle, and geometry are constant, and yaw angle is the variable. In this test the yaw angle of the model is varied from about -15 degrees to +15 degrees in 2-degree increments and the forces (drag, cross force, and moment about the support point) are read simultaneously with the velocity on the pres-

sure gauges at the instrument panel. Instead of the yaw angle being the variable, the pitch angle may be made the variable by simply rotating the model about its longitudinal axis until the pitching plane of the model is horizontal. This test is then conducted in the same way as the yawing test. In addition, the

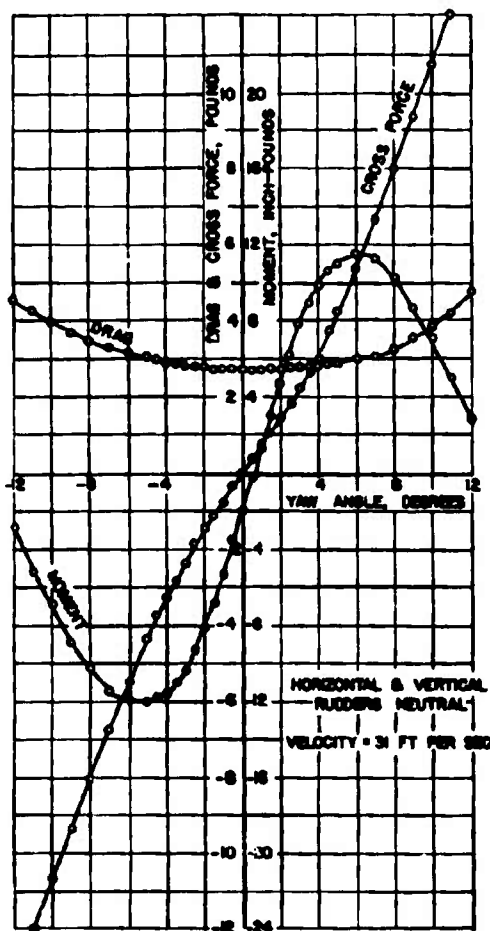


FIGURE 40. Typical plot of a force test.

rudder angles may be successively varied from up to down or from port to starboard to obtain this effect superimposed upon the effect of yaw or pitch angle. Studies may be made of models with successive changes in components such as nose shape or fin size in order to obtain the effect of the model geometry. The results of the tests are plotted as they are obtained. Figure 40 is a typical plot of force test.

SPEED TESTS

Tests are also made in which the principal variable is speed. In this case the hydrodynamic forces on the model are obtained for a speed range of from 10 to 70 fps, usually in 5-fps increments. Here again different model components may be tested in order to obtain

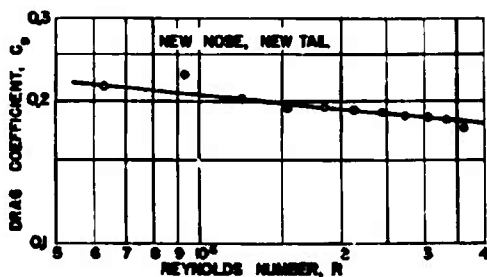


FIGURE 41. Typical plot from a speed run.

the effect of the model geometry upon the speed performance. Figure 41 shows a typical result of one of these tests.

CAVITATION TESTS

The effect of pressure (prototype submergence) may also be determined in the laboratory by the cavitation test. Usually this test is made with the model securely fastened to the working section and no forces are measured. The speed is held constant and the pressure in the working section is varied by means of the motor-controlled by-pass valve as explained in the description of the pressure-regulating circuit. The absolute pressure in the working section, at which various cavitation phenomena occur, is recorded both photographically and visually. Figure 42 illustrates typical photographs obtained in the cavitation tests. A series of such pictures clearly shows the nature of the cavitation on the projectile at the speed and depth indicated by the cavitation parameter K . In this way the cavitation performance of various model components may be studied or the occurrence of cavitation may be determined for various model parts as a function of yaw or pitch angle. Figure 43 is a plot showing cavitation parameter K at which cavitation occurs on the tail of a torpedo, as a function of the yaw angle of the projectile. In recent months a shield and spindle has been designed which permits the measurement of the hydrodynamic forces under cavitation conditions. In

such a test, in addition to the photographic records of cavitation obtained, the hydrodynamic forces are measured at the same time. Thus it is possible to test models where yaw or pitch angle and pressure are both variables.



FIGURE 42A, B, C. Typical photographs obtained in cavitation tests.

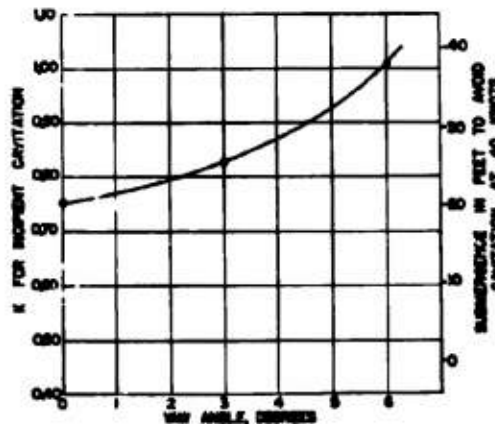


FIGURE 43. Plot showing the cavitation parameter, K , at which cavitation occurs on the tail of a torpedo, as a function of yaw.

PRESSURE DISTRIBUTION TESTS

Tests are also made to determine the pressure distribution about the surface of models. In this case the model is securely fastened to the working section through the shield as in the cavitation test. The sur-

face of the model has numerous pressure taps drilled normal to it and the pressure is transmitted from the model by means of small-diameter copper and rubber tubing through the shield to a manifold. From the manifold, copper tubing leads to the differential pressure gauge and, by means of appropriate valving, the pressure difference between the surface at any point and the pressure in the undisturbed stream may be obtained. The complete pressure distribution about the model is determined this way. A complete pressure distribution is usually made for successive yaw or pitch angles.

POWERED MODEL AND EXHAUST TESTS

Powered tests and exhaust tests have been conducted in the water tunnel in an effort to determine the interaction between exhaust jets and propellers. In this test the speed, pressure, yaw angle, and propeller revolutions per minute are held constant and photographic evidence of the interaction of jet and propeller is obtained for various air flows through the jet and various arrangements and dimensions of exhaust stack.

2.3 THE POLARIZED LIGHT FLUME

2.3.1 Comparison of the Polarized Light Flume with the High-Speed Water Tunnel and the Free-Surface Water Tunnel

The polarized light flume is essentially similar to the two large tunnels in that it furnishes a working section in which observations can be made on bodies immersed in a flowing liquid. It is so arranged that the upper surface of the working section can either be closed with a solid boundary like the high-speed water tunnel, or left free to the atmosphere as in the free-surface water tunnel. It is, however, a very much smaller piece of equipment as can be seen by the comparisons shown in Table 1.

TABLE 1. Comparison of flume and tunnel characteristics.

	Working section		Max velocity in fps	Max rate of flow in cfs	Max-imum hp
	Cross section in sq ft	Length in ft			
High-speed water tunnel	1	6	75	75	250
Free-surface water tunnel	3	8	25	75	75
Polarised light flume	1/2	4	6	3	2

2.3.2

Principle of Operation

The distinctive feature of this flume is that instead of pure water, the circulating fluid is a dilute suspension of bentonite. This is for the purpose of making the flow visible. Certain grades of bentonite have correlated physical and optical asymmetries. The physical asymmetries are such that if the particles are suspended in a stream of water, any relative shear between two adjacent filaments of water will tend to align the particles in a given orientation. The optical properties of the particles are such that if light is passed through the stream, the light waves will be rotated an amount proportional to the thickness of the fluid layer and to the degree of uniformity of the orientation of the particles. If the light used is polarized, the results will be a pattern of bands which is characteristic of the shear pattern existing in the fluid, and since this shear pattern is directly associated with the velocity distribution, the optical pattern gives a good approximation of the velocity field. Figure 44 is a diagrammatic sketch of the scheme of observation. It will be noted that polaroid screens are placed on either side of the working section. These may be used either with or without one-quarter wave plates since very similar results can be obtained with either plane or circularly polarized light. The polaroid screens can be so oriented with respect to each other that the pattern will be shown either in black and white or in color.

2.3.3

Construction of the Flume

Although only a very small amount of bentonite is required to produce a suspension having the desired characteristics, it introduces some very undesirable complications. The suspension reacts with a large number of metals. This results in corrosion, but an even more serious effect is that it causes the bentonite suspension to thicken and coagulate and thus destroys its use for the study. Unfortunately iron and nearly all its alloys, including stainless steel, react with the bentonite. Lead and tin mixtures also react, which eliminates the use of soldered joints. The polarized light flume, therefore, was constructed entirely of brass with silver-soldered joints, with glass walls in the working section. Figure 45 shows a photograph of the flume and Figure 46 is a line drawing of it. The suspension is circulated by a small propeller pump. This pump is a standard commercial design but made of brass instead of the cast iron usually employed. It

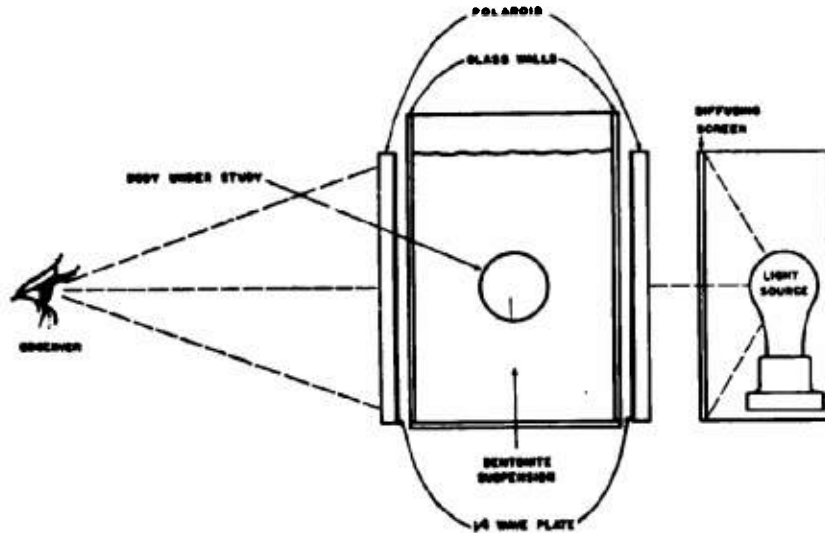


FIGURE 44. Cross section of polarized light flume.

is driven by a standard induction motor with an integral variable-speed V-belt drive which gives a speed range of 172 to 1,200 rpm. The velocity, of course, varies in the same ratio. Lower velocities are

obtained by adjusting a four-leaf pyramid type of valve which is installed on the inlet side of the propeller. Two views of this valve are shown in Figure 47. The pump discharges into a diffuser section

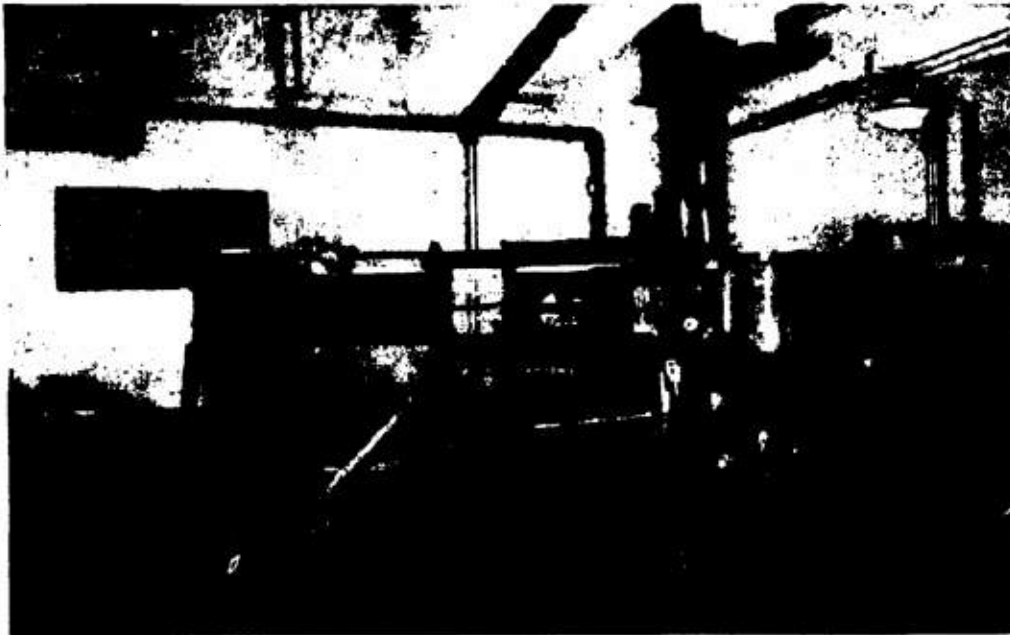


FIGURE 45. The polarized light flume.

CONFIDENTIAL

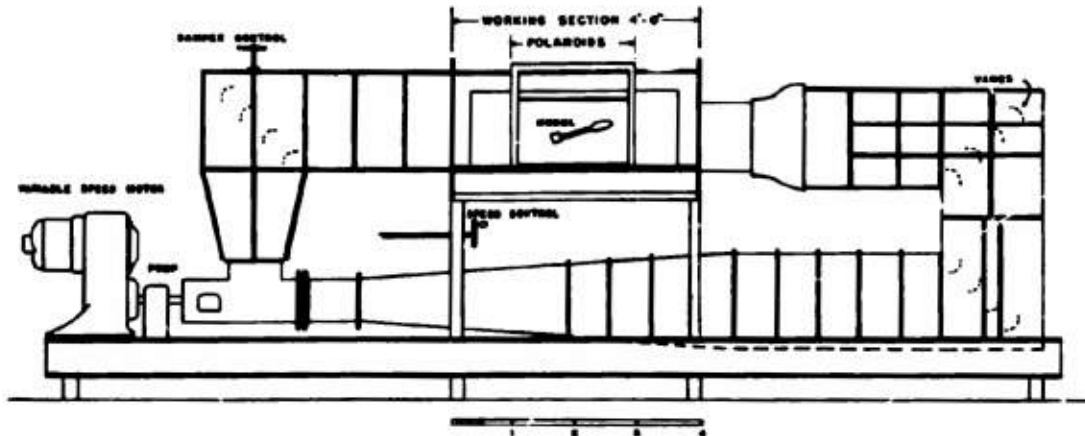


FIGURE 46. Elevation of polarized light flume.

which reduces the velocity to a very low value with a corresponding increase in cross section. The flow is brought to the working section at this low velocity by means of two vane elbows. The flow is accelerated to the velocity of the working section by a nozzle having a rectangular cross section. The contraction ratio of this nozzle is $4\frac{1}{2}$ to 1.

The working section is followed by a diffuser section which is operated with a free surface. An attempt is made to regain as much energy as possible in this section. This is done not so much to save the small amount of energy involved, but rather to eliminate all possible sources of disturbance which may carry around through the pump and passages to the working section. From the diffuser section the flow goes through the valve to the inlet to the propeller pump which has already been described.

2.2.4 Working Section

The working section employs glass plates for the two sides and the bottom. A Lucite cover has been constructed which can be installed as a prolongation of the upper surface of the nozzle when it is desired to operate the flume as a closed channel. It has been found more convenient for most studies to operate with the free surface to permit the easy insertion of auxiliary equipment for studying the details of the velocity distribution. A horizontal spindle has been mounted on the rear side wall to support the models. This is equipped with a streamlined shield of the same cross section as the one used in the high-speed water tunnel. The spindle can be rotated by a worm

and wheel on the front of the working section, thus permitting the observation of the flow pattern as it is affected by pitch or yaw. The degree of rotation is measured on a protractor which is an integral part of the rotating mechanism. This equipment can be seen in Figure 48, and also in Figure 49 which shows a close-up of the working section. The spindle is constructed so that the models used in the high-speed water tunnel may be installed in the polarized light flume without alteration. Although these models are made of stainless steel, it has been found that they can be used in the bentonite suspension without harm, either to themselves or to the suspension, if care is taken to leave them in for short periods only and if they are washed and dried thoroughly after each use. The two polaroid screens are supported, one on each side of the working section, by a carriage which rolls along guide rails mounted on the top of the flume. These screens are 12 in. high and 30 in. long, and thus provide a working area that is sufficiently large for most observations without the need of readjusting their position. Provision is also made for carrying the light source on the same carriage. A rear view of this light source is seen in Figure 50. For normal observations a battery of incandescent lights is used, but for special purposes high-intensity lights or high-voltage flash lamps may be employed.

2.2.5 Applications of the Polarized Light Flume

The majority of results of the studies made in this flume are reported in the form of sketches of the flow.

CONFIDENTIAL

In order to assist in the preparation of these sketches, the guide rulings of Figure 51 are mounted on the side windows of the working section. A miniature drafting machine of the steel-tape type is attached to the carriage as shown in Figure 52. It is used largely

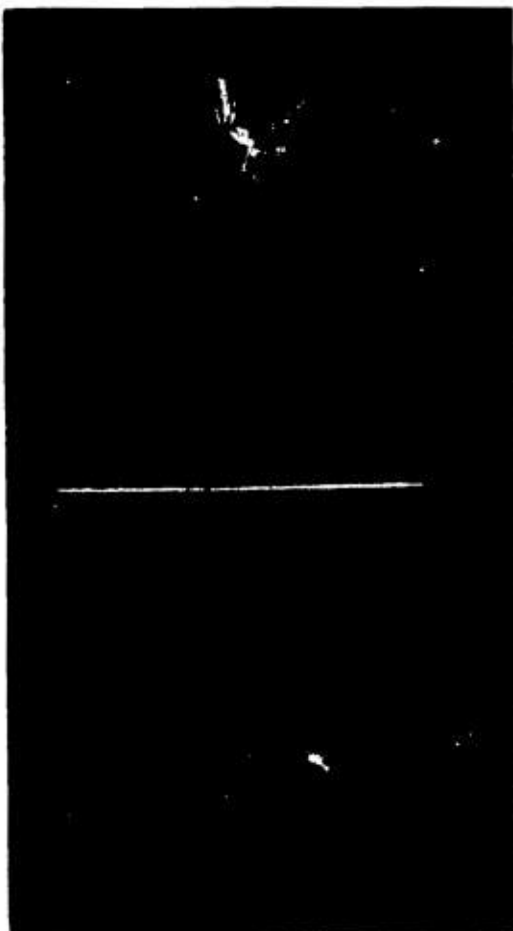


FIGURE 47. A, B. Four-leaf pyramid-type valve used with polarized light flume. (A) Closed. (B.) Open.

for determining the angles of flow in the various parts of the field. For detailed studies of the flow the indications of the polarized light patterns have been supplemented by other methods of delineating the flow. One of these is a mechanism for moving a small probe to any desired point in the working section. This probe carries a short section of light thread which streams out parallel with the flow and gives a

clear indication of the local flow angle. The mechanism, removed from the flume, is seen in Figure 53. Another technique that has been found useful is the introduction of minute air bubbles into the flow by the use of a very fine tube. At the velocities used for the studies the path of these air bubbles is very easily followed. Great care must be exerted to keep these bubbles small, however, since if their size becomes appreciable, their velocity of rise will become significant in comparison with the velocity of flow and thus distort their indications. Figure 54 shows the same typical bubble paths.



FIGURE 48. Pitch angle control and protractor for polarized light flume.

2.1.6 Principles of Operation

STREAMING DOUBLE REFRACTION

It is a well known fact that certain crystals possess the optical property of producing double refraction when a light beam is passed through them. The magnitude of the effect depends upon the length of the light path. A given length of light path could be obtained by the use of a single crystal of the proper dimensions or a series of crystals which, when added together, made up the required length. The total effect would be the same provided that in the case of the multiple crystals their optical axes were oriented in the same direction. If, however, their axes were oriented at random, no double refraction would be observed because the effects of the different crystals would cancel each other. If such a system of crystals were suspended in the fluid, double refraction would still take place. The magnitude of the effect observed

would depend upon the uniformity of the alignment of the axes of the crystals along the given optical path. It is apparent that if the optical alignment of the crystals were dependent upon some property of the flow of the fluid, a valuable tool would become available for the study of fluid flow. A brief consideration will show, however, that if a crystalline material is to fulfill the requirements, it must possess some unique characteristics. In the first place, the crystals must possess the property of double refraction. Second, the individual particles must be single crystals or masses of crystals so oriented that they behave optically as a single crystal, i.e., their optical axes must be parallel. Next, they must be insoluble in the fluid in which they are to be used. If the flow of the fluid is to have any effect on their alignment, they obviously must be physically asymmetrical. Furthermore, if this physical asymmetry is to be effective, it must have a uniform correlation with the optical asymmetry. If this phenomenon is to be used as a tool for the study of flow, it is necessary that the presence of the crystals should have little or no effect upon the flow. This means that the individual particles must be small, i.e., their dimensions should be of the same order or smaller than the least dimension required to measure the characteristics of the flow,

and their path must conform to that of the flow. This means either that the density of the crystalline material must be the same as that of the fluid or else that the individual particles must be so small that their fall velocity will be negligible as compared to the velocity of the fluid. The ideal case would be to have the particles so small that they would fall in the range of the Brownian movements and thus form a permanent suspension.

Assuming that such material were available, how could it be used? It would be very desirable if it could be made to indicate the velocity of flow. However, a brief consideration of the flowing suspension indicates that this is not possible. Consider a stream of this suspension flowing at a uniform velocity without turbulence. In this case all of the elements will be flowing at exactly the same velocity in parallel paths, and therefore will have no tendency to alter the orientation of the individual particles suspended in the fluid. This still holds true if the velocity of the entire flow is raised or lowered to any desired value. It is only when two adjacent layers of the fluid are considered to flow at different velocities that any force rises which can alter the orientation of the suspended particles. If the suspended particles are asymmetrical, say needle-like or plate-like in form, it is



FIGURE 49. Close-up of working section of polarized light flume.

CONFIDENTIAL

obvious that the difference in velocity between the two fluid layers will tend to produce uniform alignment of the particles lying in this boundary. It is reasonable to suppose that the number affected and degree of uniformity of alignment will be related to the magnitude of the difference in velocity of the two



FIGURE 50. Rear view of light source for polarized light flume.

layers. It will be seen from these considerations that the information which can be obtained by the use of this tool will concern the velocity differences or shear in the flow rather than the velocity itself. In general, the average velocity of the flow will be known or, at least, the velocity in some given location. If this is the case, then the knowledge of the velocity differences can be used to determine the velocity field over the entire flow. There are many limitations to the use of this method of flow study. The instrument used to obtain information from the flowing suspension is a beam of light which traverses the flow from one boundary of the channel to the other. The optical effect on the beam must be the summation of all the effects along the entire path. If these effects are uniform, the overall results will be measurable. If they are completely at random, the overall results will be nil. This indicates that the simplest use of streaming double refraction is for the study of two-dimensional flow. Furthermore, if the flow is turbulent, the turbulent components will introduce a random disturbance which will affect the observation. Experiment has shown that it is possible to use this method for quantitative measurements in two-dimensional laminar flow. To do this it is necessary to measure the relationship between the rate of shear and the double refraction obtained along a given length of path.

Qualitative measurements are possible in two-dimensional turbulent flow, although quantitative measurements are not yet feasible. At first glance it would appear that measurements of any kind would not be possible in three-dimensional flow, although experience has shown that good qualitative measurements can be made. In this connection it is interesting to observe that single photographs of three-dimensional flow are usually quite disappointing as compared with the results obtained from direct visual observation. There are apparently two reasons for this. One is that binocular vision makes it possible to differentiate between the flow characteristics at different distances in spite of the fact that each individual light ray gives only the integrated effect. The other is that persistence of vision gives quite a strong differentia-

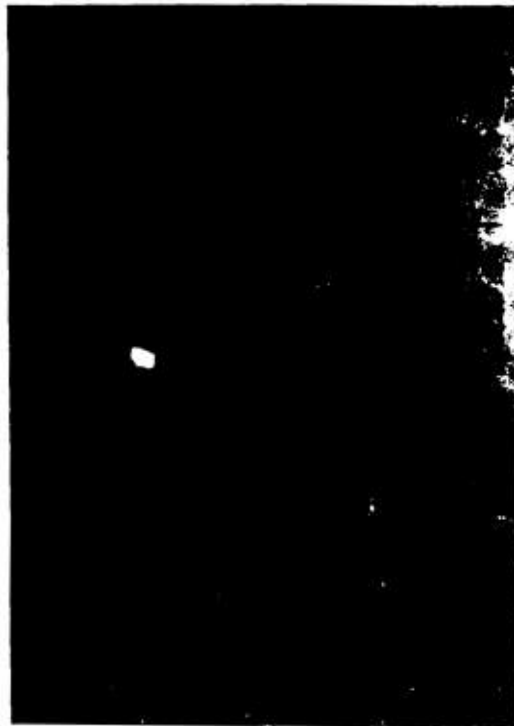


FIGURE 51. Guide rulings for polarized light flume.

tion between the steady flow pattern around the body and the random-motion characteristic of a turbulent motion which overlays the picture. Of course, the presence of turbulence is not a necessary accompaniment of three-dimensional flow. However, in all of the uses made of this method of study by the

CONFIDENTIAL

laboratory, it has been felt desirable to use turbulent flow since the indications obtained from purely laminar flow would have been of little practical value. As stated in the introduction to this section, the flow is actually observed through the use of circularly polarized light. The reason for this is that the phenomenon of streaming double refraction is essentially one of polarization. Therefore, if the flow is observed through a beam of light having a fixed image by polarization which can be produced by placing polarizing plates on each side of the flume, then any change in the degree of polarization produced by the suspension in the flume will be readily visible. Figure 55 shows the general appearance of the working section as observed by polarized light. Figure 56 shows the same model the instant after the motor was

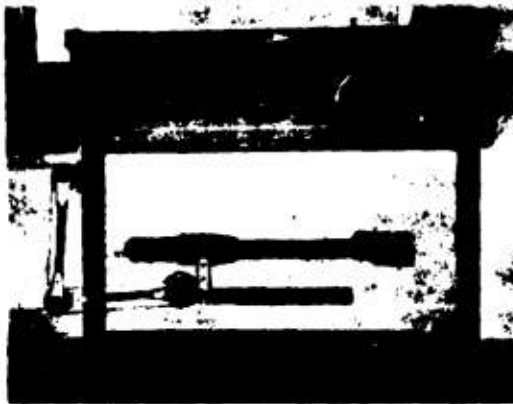


FIGURE 52. Miniature drafting machine attached to carriage of polarized light flume.

started, but before the general turbulence level had had time to form.

3.3.7 Development of the Use of Bentonite

DEVELOPMENT OF THE USE OF BENTONITE FOR STREAMING DOUBLE REFRACTION

There are undoubtedly many materials which possess the property of double refraction and which can be found or produced in suitable states to permit the necessary correlation between the physical and optical properties so that they can be used for streaming double refraction studies. Thus, for example, sesame-seed oil has this property to a limited extent. However, very few materials have as yet

been developed which possess the required properties to such a degree that they become convenient for use in flow studies. One of these materials is bentonite. This is a clay-like mineral which has several industrial uses. Its properties were studied rather intensively in the Chemical Engineering Laboratory of



FIGURE 53. Probe mechanism, removed from polarized light flume.

the Massachusetts Institute of Technology (MIT). One of the results of these studies was that certain samples of the mineral showed strong properties of streaming double refraction.

The MIT studies had indicated that different samples of bentonite showed widely varying amounts of streaming double refraction. At the beginning of the laboratory's use of the material it was believed that all bentonite found in the California mines possessed the property to a usable degree. This was soon found to be false. In fact, most of the samples tested from all sources showed too small an effect to be satisfactory. Because of a series of changes of distributors, the source of the material which had given such successful results was lost. However, it was finally traced and proved to be material marketed under the trade name of M. S. Eyrite. The reason for the wide variation of the properties of materials from different



FIGURE 54. Typical bubble paths observed in polarized light flume.

sources is not known. It is suspected, however, that it is connected with its method of formation or with its subsequent history as it has affected the correlation between the physical and optical asymmetries. Thus, for example, if the very fine individual particles have been formed by some grinding or disintegrating pro-

cess that largely destroyed the correlation between the physical and optical asymmetry, the material would show little streaming double refraction. The concentrations of the M. S. Eyrite required for use in the 6-in. wide laboratory flume have been quite low. The suspensions used for most of the work have contained approximately 0.1 to 0.2 per cent of the bentonite. In all cases the liquid used has been pure water. This amount of bentonite has the effect of increasing the viscosity slightly. During the useful life of the suspension it appears that the viscosity is about doubled. This increase, of course, is not enough to be detected by qualitative means. Experiments showed that the suspension was somewhat sensitive to the mineral content of the water used. Suspensions made with tap water in the laboratory had a very short life, since after a few days' use in the flume, when exposed to

in suspension. After purification the material is diluted to the proper concentration and is then ready for use.

2.1.1 Tobacco Mosaic Virus

The laboratory has been enabled to compare the properties of this bentonite with those of another material suitable for this use.* The second material is tobacco mosaic virus. Semiquantitative tests showed that the virus has much greater properties of streaming double refraction than does the best of the bentonites. For example, 0.3 mg per cc of the virus gives approximately the same results as 3 mg per cc of the M. S. Eyrite. No quantitative measure of the increase in viscosity was obtained but the indications were that the virus produced little, if any, increase. One in-



FIGURE 55. General appearance of working section of polarized light flume as observed by polarized light.

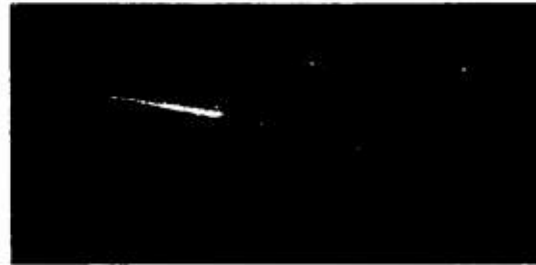


FIGURE 56. Same model as in Figure 55 but at instant after motor started and before formation of general turbulence.

the air, they commenced to flocculate. This was accompanied by a rapid increase in the viscosity and decrease in the streaming double refraction. The use of distilled water eliminated this difficulty and extended the life of the suspension to a couple of months. The deterioration of the suspension seems to be considerably accelerated by contact with air, since samples have been kept for long periods in closed glass bottles with no sign of deterioration.

The bentonite is obtained either in the form of a coarse powder or in lumps. However, it is readily dispersed in water by the use of a mixer of the Waring type. The individual particles of the bentonite are very fine, remaining in suspension indefinitely. However, the material contains a considerable percentage of impurities. These are removed by passing the concentrated suspension through a continuous super-centrifuge at a moderate rate of flow. The impurities separate out while the bentonite remains

interesting observation was that an increase in the concentration above 0.3 mg per cc produced no observable increase in the effect. This limited series of tests indicates that the virus is superior in several other characteristics to the bentonite. For equivalent suspensions the virus seems to be less cloudy and therefore transmits the light more effectively. Furthermore, the virus appears to be more stable, in that it did not show any signs of flocculation or change in properties with age, and its reaction to metals appeared quite neutral. On the whole, it was felt that the tobacco mosaic virus would be considerably superior to the bentonite for use on flow studies. Unfortunately there is no commercial source of the material and it has not been possible to obtain a sufficient amount of it for a filling of the polarized light flume.

* Through the courtesy of W. M. Stanley of the Rockefeller Institute for Medical Research.

2.1.9 Technique of Operation

STANDARD STUDIES

Most of the bodies studied in the polarized light flume were projectiles or projectile components. Standard studies consisted in delineating flow patterns for the projectile in two positions, i.e., with the axis parallel to and at an angle of 10 degrees with the flow. For determining the flow characteristics experience showed that the best visible indications were obtained when the velocity was about 1 fps. This low velocity, therefore, was used in the initial observations to establish the general flow pattern. After this had been established by the operator, the velocities were increased to 4 or 5 fps to observe the effect of the change in velocity on the flow pattern, and especially on wake angles and similar details. During the delineation of these flow patterns auxiliary methods of study were employed whenever necessary to clarify any details of the flow.

TROUBLE-SHOOTING STUDIES

In several cases the polarized light flume proved of value in locating the origin of disturbances, points of instability, etc., on projectiles which were giving unsatisfactory performance in the field. These studies followed the general pattern of the standard studies outlined, but detailed investigations were made on all points of possible trouble. Instead of making measurements for the two set angles only, it was often valuable to watch the flow as the angle of the axis with the stream was varied very slowly.

DESIGN OF STABILIZING SURFACES

The polarized light flume proved to be of assistance in aiding the designer to determine the optimum arrangement of certain types of stabilizing surfaces such as ring tails. In order to get the required stabilization with the permissible amount of drag, it is necessary to align the surfaces with the direction of flow at the place where it is desired to install them. Information was obtained in different regions by use of bubble streaks and thread probes. The angle of flow was measured by means of the small parallel-motion protractor installed on the permanent screen. Subsequent checks on models in the water tunnel showed that the angles determined in this manner were very reliable and that stabilizing surfaces installed to conform with the flow as measured in the

polarized light flume offered the minimum amount of drag, even when tested at velocities ten or more times higher than those at which the angles were determined.

FLOW DIAGRAMS

Owing to the difficulties outlined previously in obtaining good photographs of the flow pattern, the results of the studies have been presented in the form of line diagrams of the flow. These diagrams are always based on the actual observations and an effort was made to keep the flow directions correct. Figure 57 shows a typical flow diagram.

2.2 CONTROLLED-ATMOSPHERE LAUNCHING TANK

2.2.1 Purpose

The primary purpose behind the design and construction of the controlled-atmosphere launching tank is the securing of equipment that will permit the study of the hydrodynamic problems involved as a projectile enters the water from the air. All the specifications established at the beginning of the design were based on this objective. However, the equipment as it was finally constructed is useful for the investigation of other types of phenomena as well, in so far as they require the same facilities. The principal auxiliary use that is evident is the investigation of underwater explosions. Such a study is obviously limited to the use of small-scale explosions to insure that the equipment will not be damaged.

2.2.2 Analysis of Experimental Requirements

Before the design of the equipment was initiated, careful study was given to the type of measurements that would have to be made in order to carry out such a series of investigations in the laboratory. Because of obvious limitations of space, it is necessary to use only projectiles of small dimensions for the study. However, if the results are to be useful, they must be applicable to projectiles of any desired size. It is a well-known fact that the various factors affecting the forces and motion of a free body do not all necessarily vary at the same rate as the size of the body is changed. However, it is often possible, if care is taken in establishing the conditions of the experiment, to

obtain similar conditions for all the significant forces for two systems that differ widely in their geometrical size. Previous to the construction of the controlled-atmosphere launching tank most of the laboratory studies of water entry of an air-flight projectile had been made with small-scale projectiles launched into an open tank at atmospheric pressure. A consideration of the force systems shows that this does not produce conditions similar to those acting on larger projectiles when similarly launched. The primary reason for this is that in the period immediately after the projectile enters the water it is not operating in a

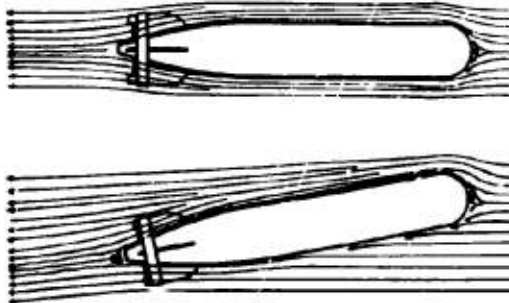


FIGURE 57. Typical flow diagram.

homogeneous fluid, but is acted upon by two fluids, that is, the water which touches it at the nose and possibly again at the tail, and the air bubble which surrounds the major part of the projectile surface. Now the shape and size of this air bubble is a function of the speed of the projectile which tends to keep the bubble open, and of the pressure in the surrounding water which tends to collapse it. This collapsing pressure is made up, not only of the hydrostatic pressure of the water at that point, but also of the superimposed pressure of the atmosphere acting on the interface. In the case of a small-scale projectile launched into a tank at atmospheric pressure, the effect of this atmospheric pressure will be relatively greater than it will be for a larger projectile. This can be seen readily from a consideration of a simple numerical case. Assuming that the atmospheric pressure is equivalent to a column of sea water 33 ft high, consider a projectile that is one-half this length, i.e., $16\frac{1}{2}$ ft, and imagine that this projectile enters the water from the air and dives to a depth of 33 ft. It is now 2 projectile lengths beneath the surface. The absolute pressure in the surrounding water will be 2 atmospheres, one due to its submergence and one due to the atmospheric pressure on top of the interface.

Next consider a projectile similar in every respect to the first one except that it is $16\frac{1}{2}$ in. in length instead of $16\frac{1}{2}$ ft, i.e., every dimension has been reduced to one-twelfth of the original. Assume that it is launched into a water tank at atmospheric pressure and dives to a similar depth. If the depth is similar, the geometric relation must appear the same. This means that the small projectile should be two projectile lengths under the surface, i.e., 33 in. However, the pressure in the surrounding water will no longer be equal to that of a column of water twice as high as the submergence, but to a pressure equal to the submergence plus 33 ft, i.e., to a column of water 13 times as high as the submergence. Thus it is obvious that if the pressures are to be similar, the atmospheric pressure must be scaled down in the same ratio as the geometric dimensions were reduced. If this is not done, then there is no reason to suppose that the bubble which forms at the surface and surrounds this small projectile will be similar in size and in its effect on the forces acting on the projectile as the one surrounding the large-scale projectile. This is the fundamental reasoning at the bottom of the decision to construct a launching tank in which the atmospheric pressure can be controlled to conform to the geometric scale of the projectiles being studied. Unfortunately the atmospheric pressure is not the only variable that may affect the behavior of a projectile at water entry. The density of the air is also a factor. Since the density of the water is constant, the density of the small projectile must be the same as that for the large one. This would indicate that the density of the gas forming the atmosphere should likewise remain constant. This requirement is in direct contradiction to that governing the change in pressure. The two can only be met by using a gas of great enough density so that when the pressure is reduced to correspond to the geometric scale, the density of the gas will be the same as that of air at atmospheric pressure. The conditions which make it possible to control the atmospheric pressure in the launching tank also make it possible to utilize gases other than air for the atmosphere over the interface. Another variable that may affect the characteristics at launching is the surface tension. Other factors may become evident upon further study of the problem. However, the initial considerations seem to indicate that of the various factors involved, the pressure is the one that is the most important and the density is next. It is anticipated that the other factors will be of relatively little importance.

CONFIDENTIAL

2.4.3 Summary of Design Specifications

In setting up specifications for this major piece of equipment it is convenient to subdivide it into four main components as follows:

1. The tank.
2. The launcher.
3. The trajectory recording system.
4. The data analyzing system.

These components of course, are related; for example some of the principal dimensions of the tank were determined by the decision to use photographic means for recording the trajectory. Again several types of launchers were eliminated because they were inherently too large and required too much space and adjustment to build them inside of a pressure vessel.

TANK

The basic specifications for the main tank were that it should permit a trajectory of approximately 25 ft with a water depth of approximately 10 ft. A distance of 12 ft was required from the launching plane to the camera windows, with this distance kept as clear as possible of all obstructions that would interfere with the clear view of the cameras. As indicated in the previous section, the physical requirements of the study called for scaling the atmospheric pressure down with the same ratio as the linear dimensions of the projectile study. Since projectile scales of 12 or 15 to 1 were contemplated, this established the requirement that the tank should stand an external pressure of a full atmosphere. The installation and operation of the launcher required that a large opening, which could be opened and closed rapidly, be provided in the top of the tank above the water line.

LAUNCHER

The requirements for the launcher were largely dictated by the specific needs of the study. It was decided to adopt for the launching tank the standard 2-in. model size used in the water tunnels. The maximum velocity of entry was set at 250 fps. It was considered desirable to make provisions for any trajectory angle from vertically downward to horizontal. Provisions were also required for launching the projectile at any desired angle of pitch between 10 degrees up and 10 degrees down from the trajectory angle. The desired accuracy of both the pitch and

trajectory angles was established as one-fourth of a degree or less. It was decided that no adjustment for yaw and no provision for the introduction of angular velocity and pitch should be incorporated in the original launcher design, but that if possible, the design should be laid out so that these adjustments could be incorporated later as they proved to be necessary.

TRAJECTORY RECORDING SYSTEM

It was realized that the models required for these launching studies would be more difficult and expensive to construct than the projectiles for the water tunnel because they would demand not only all the high accuracy required for the water tunnel studies, but also high dynamic accuracy, i.e., they would also have to have the correct weight, specific gravity, and moments of inertia. Furthermore, each launching would carry considerable danger of damage to the projectile as a result of striking the tank at the end of the trajectory. All these factors pointed to the necessity of developing a trajectory recording system that would secure all the data possible with each launching, even in the case of erratic trajectories. Therefore, the specification was established that the recording system should cover the entire underwater volume of the tank, as well as the above-water portion containing the trajectory from the launcher to the water surface. It was decided to make an attempt to determine five components of motion, i.e., horizontal, vertical, and lateral movement, and rotation in the pitch and yaw planes. Since high angular and linear accelerations are to be expected during parts of the trajectory, it was established that recorder readings should be taken at the rate of about 3,000 per second.

DATA ANALYZING SYSTEM

If detailed information is to be obtained from launching studies, it is unavoidable that each run will yield a large mass of data which must be analyzed. It was apparent that the analysis of the data would require either a large staff of computers or special mechanical devices. The decision was made to follow the latter course. The requirements for the mechanical analyzer were that it should transform the readings of the raw data into increments of motion along the path, analyzed into the five components outlined in the preceding paragraph, and, if possible, that this data should be plotted in the form of curves.

CONFIDENTIAL

1.4.4 Details of Construction

A general view of the equipment designed to meet the specifications for the first three components is seen in Figure 58. This is a rendition of the tank with the launcher and recording system in place.

MAIN TANK

As will be seen from Figure 58, the main tank consists of a large horizontal cylinder along one side of which is fastened a section of a small cylinder. The purpose of the smaller cylinder is to provide the necessary distance from the cameras to the launching plane to permit the photographic recording of the trajectory. The larger cylinder is 13 ft in diameter and 29 ft in length. It is made of $\frac{3}{16}$ -in. steel plate with $\frac{3}{4}$ -in. dished and flanged heads on each end. It has a 6-ft by 20-ft opening along one side over which is welded the section of the 6-ft diameter cylinder. Special provisions are required to carry the hoop stress across the opening formed by the intersection of the two cylinders. This is done through the use of longitudinal T beams 20 in. high and running the

entire 25 ft of the intersection. These beams transfer the loading into 2- by 12-in. vertical columns spaced at 54-in. intervals along the tank. The exact position of these columns was determined by careful study so as to place them to carry the load without eccentricity, but to keep them out of the field of view of the recording cameras. Four-inch H-beam ring stiffeners were welded around the circumference of the two cylinders in the plane of each column. To distribute the loading evenly over the floor of the laboratory, saddle feet were provided at each ring stiffener. Computation showed that with this method of support, no additional foundation would be required under the 6-in. reinforced concrete slab. The weight of the tank empty is approximately 40 tons, and when filled with water to the working depth of 10 ft, the weight is approximately 140 tons. Figure 59 is a sectional drawing of the tank.

It will be seen in Figure 58 that there is a large rectangular hatch opening on top of the tank near the left end. This opening is 48 by 55 in. and is designed to permit mounting the entire launcher mechanism on the hatch cover. This opening is off center to increase the distance from the launching plane to the

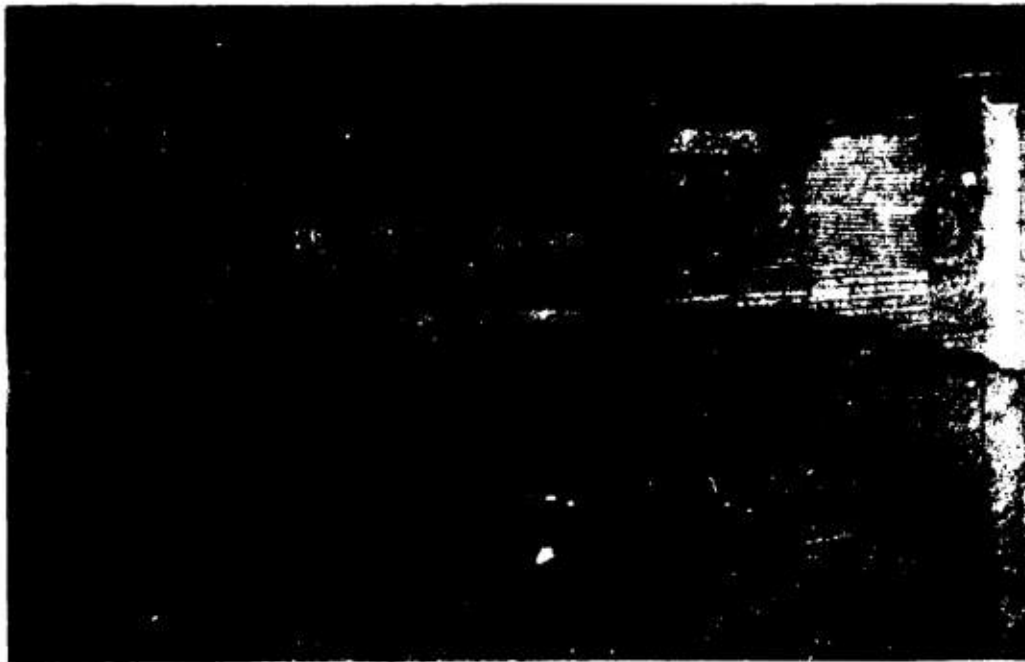


FIGURE 58. Controlled-atmosphere launching tank, Hydrodynamics Laboratory, California Institute of Technology.

CONFIDENTIAL

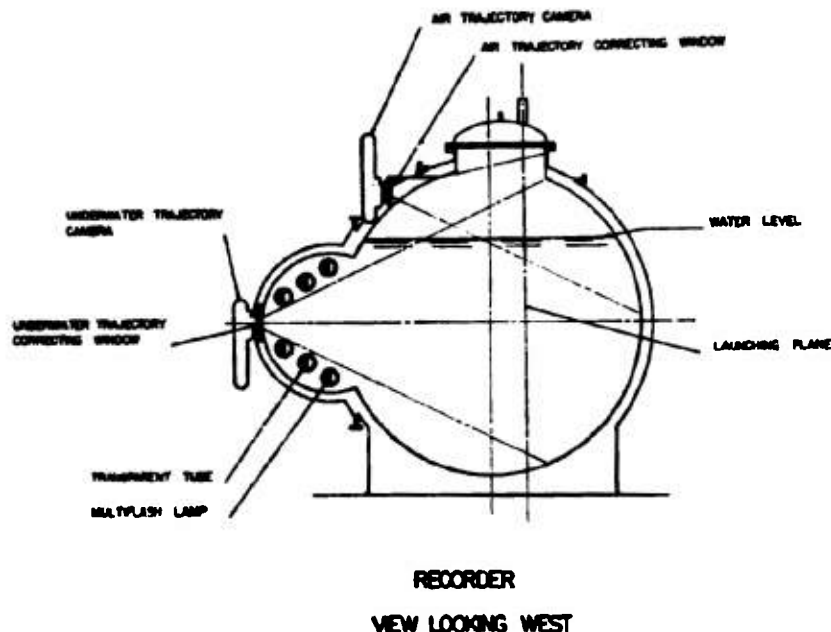


FIGURE 59. Sectional view of controlled-atmosphere launching tank.

camera. Very heavy reinforcing was required to carry the stress around this opening so as to prevent distortion when the tank is used with pressure or vacuum. The hatch cover is hinged to the left-hand edge of this opening. Provision for opening and closing it through a 90-degree arc is provided by a 12-in. hydraulic cylinder. When this cover is closed, a round rubber sealing ring recessed in the face of the cover prevents air leakage. This ring operates on the unsupported area principle. Heavy hydraulically operated C-clamp frames are provided on the two longitudinal edges of the opening. They serve to hold the cover rigidly in place under either pressure or vacuum conditions during testing. Figure 60 shows the cover and clamps. Six 8-in. nozzles are welded to each edge of the 6-ft cylinder to permit the installation of Lucite tubes running from end to end of the tank. These are required to house the underwater lighting system. The tank is fitted with ten 12-in. openings for the addition of the recorder cameras. Five of these are located on a horizontal line on the side of the 6-ft cylinder midway between the stiffening rings. Three of the openings are placed above the water line near the hatch opening to cover the air flight, and one is placed at the centerline of each of the main cylinders. Four 16-in. access openings are provided along the

upper portion of the main tank. Since the design of this tank was so unconventional, it was subjected after completion to a hydrostatic test of 60 psi. No signs of yielding were found at any point on the



FIGURE 60. Hatch cover and clamps. Controlled-atmosphere launching tank.

structure, using the standard brittle whitewash test as the indicator. Figure 61 shows the completed tank suspended from the crane as it is being lowered in the building excavation at the time of construction.

CONFIDENTIAL

Since the tank is to be used with a photographic recording process, it is necessary to take special precautions to maintain the water in excellent condition, eliminating anything that might decrease the light



FIGURE 61. Controlled-atmosphere launching tank being lowered into excavation for installation.

transmission. To assist in this matter, two corrugated galvanized steel storage tanks were provided for the clean water. Each is 14 ft in diameter by 19 ft high. These tanks are covered and air filters are installed

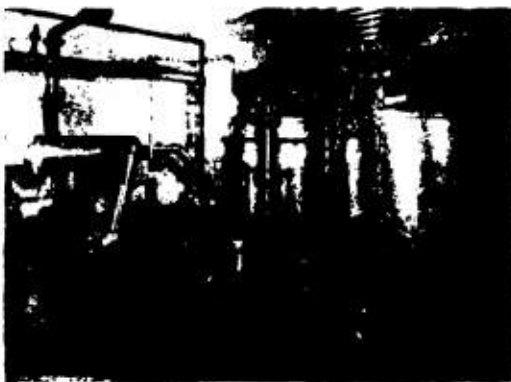


FIGURE 62. Controlled-atmosphere launching tank. Filter with one of storage tanks in background. Vacuum pump at left.

on all openings to prevent contamination. A commercial sand filtering system is provided for use in the initial purifying and subsequent reconditioning of the pure water to be used in the tank. Figure 62 shows the filter with one of the storage tanks in the background. On the left will be seen the large vacuum

pump used for maintaining the subatmospheric pressures required for the study.

THE LAUNCHER

After an extensive consideration of the possible launcher types, it was decided to use a centrifugal launcher because of the compactness possible with this design and also because of the advantages it offered in obtaining accurate control of the launching velocity, the trajectory, and the pitch angle. It consists basically of a rotating wheel which carries a model chuck near its periphery. The model is prevented from spinning about the chuck axis by a



FIGURE 63. Launcher mounted on open hatch cover with model in chuck.

planetary system of gears mounted on the wheel and connected to the hub. These gears are also used for setting the angle of the model with respect to the horizontal. Figure 63 shows the launcher mounted on the open hatch cover with a model in place in the chuck. Figure 64 gives a plan view of this installation with the chuck empty. Figure 65 shows the opposite side of the launcher wheel from that seen in Figure 63. This view shows one of the launcher controls. The component parts may be readily identified by comparing with the diagram of Figure 66. The launcher wheel is a steel plate, cadmium plated for protection against corrosion. It is $2\frac{1}{4}$ in. thick and, therefore, is heavy enough to provide sufficient fly wheel effect to insure very uniform velocities. The wheel is supported on a 4-in. stainless steel shaft which is mounted on four preloaded precision ball bearings running in an oil bath and is assembled in a quill to form an accu-

rately aligned unit. The launcher is driven by a 10-hp d-c motor whose speed is controlled electronically. The control is activated by means of a selsyn motor driven by chain from the launcher shaft. The planetary gear system which prevents the rotation of the chuck around its own axis is composed of specially cut fine-pitch precision gears. To insure maximum smoothness of operation and to eliminate any backlash, the center gear of this train is made in three parts, the outer two being spring loaded against the



FIGURE 64. Plan view of launcher with chuck empty.

central section by small tangential coil springs in the rim. The central gear and one outer one mate with the hub gear, whereas the central gear and the remaining outer one mate with the chuck gear. Of course the hub and the chuck gear have the same diameter. The hub gear is mounted rigidly to the pitch-angle arm. This, in turn, is mounted on and rotates with the trajectory-angle arm which is integral with the release arm. The trajectory-angle arm clamps to the trajectory scale and has a 90-degree adjustment. The pitch-angle arm can be adjusted to ± 10 degrees with respect to the trajectory-angle arm. Thus rotation of the trajectory-angle arm rotates both the hub gear and the release arm. The model chuck carries a trip lever which projects from its axis on the control side. The release arm carries a solenoid-operated release. In the normal position the striker finger of this release clears the trip lever of the chuck. When the solenoid is energized, the striker finger moves radially inward to a position which allows it to strike the

trip lever on the next revolution. This releases the model. The working of these controls may be seen from consideration of the following example. Assume that it is desired to launch the model at a trajectory angle of 15 degrees to the horizontal with the model having a 2-degree down pitch. Assume that both the pitch-angle arm and the trajectory-angle arm are set to zero on their respective scales, and that the model is clamped in the chuck. It will be seen that under these conditions the model will be horizontal for any position of the launcher wheel. First, the trajectory-angle arm is unclamped and rotated until its index is at 15 degrees. This rotates the hub gear 15 degrees which causes the chuck and model to rotate the same amount. The direction of rotation is such that the model is now tilted with the nose downward 15 degrees from the horizontal. Careful obser-



FIGURE 65. Launcher wheel from side opposite to that shown in Figure 63. Controlled-atmosphere launching tank.

vation will show that the release arm is now in such a position that the striker finger will trip the chuck so that the gear will release and free the model at the exact instant the chuck centerline is 15 degrees from its bottom position. Next the pitch-angle indicator is set at 2 degrees down. This rotates the hub gear, and consequently the chuck and model, 2 degrees more, but does not move the release arm. It will now be seen that when the release is operated, the model will leave the launcher at a downward angle of 15 degrees to the

CONFIDENTIAL

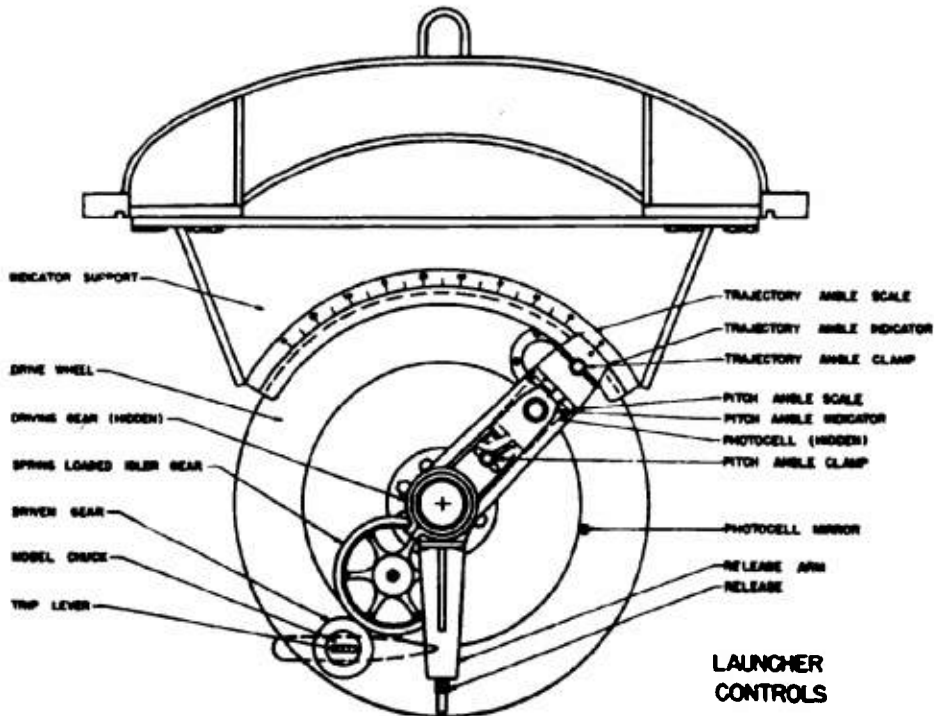


FIGURE 66. Launcher controls. Controlled-atmosphere launching tank.

horizontal and the model axis will have a 2-degree down pitch with respect to this trajectory.

The model chuck was designed with great care to insure accurate launchings. The detail of this construction may be seen in Figure 67. It consists basically of a support conforming exactly to the diameter of the model and covering the 135 degrees on the inside of the wheel or the upper side of the trajectory. It will be seen that at the instant of release the chuck seat and the model have exactly the same motion and subsequently the chuck lifts slowly away from the model without disturbing it. This seat is made as rigid and stiff as possible in order to store the minimum amount of energy which might affect the motion of the model at the instant of tripping. The model is held in the chuck by means of a finger. This finger falls away from the model at the instant of tripping, under the acceleration of a very stiff spring. The design is such that the finger always moves faster than the model and thus never interferes with it after the instant of release. The model is placed in the chuck with its center of gravity at the center of the seat. All the rotating parts of the launcher are dy-

namically balanced to insure vibration-free operation. The model itself is counterbalanced by means of an adjustable weight located in the plane of rotation of the model. No provision has been made to change the balance of the launcher after the release of the model because it has been determined experimentally that the entire structure is so massive and rigid that this unbalance causes no trouble for the short periods that the launcher remains rotating after the model has been tripped. Figure 68 shows a view of the chuck mechanism with the model clamped in position.

To determine the launching point or trajectory angle a photocell is used. A small polished stainless steel mirror is mounted on the launcher wheel and the photocell carried on the arm of the launcher tripper. A condenser discharging into a solenoid lifts the tripper into position to operate the launcher, the entire action taking under 4 msec.

TRAJECTORY RECORDING SYSTEM

The trajectory recording system is composed of a battery of synchronized high-speed motion picture

CONFIDENTIAL

cameras using standard 35-mm film. These cameras may be divided into two groups. The main battery is for the purpose of recording the underwater trajectory. It is made up of five cameras installed in a horizontal line along the 6-ft cylindrical tank. Two auxiliary cameras are used for recording the air-flight trajectory from the launcher to the water surface. These are installed in the proper two of the three camera windows provided above the water level in the main tank. A choice of location is provided for



FIGURE 67. Model chuck. Controlled-atmosphere launching tank.

these air-flight cameras because their field of view is limited by the fact that they are of necessity so much closer to the plane of launching. If low-angle launchings are to be studied, the cameras are placed at the center and the right-hand windows. If high-angle or vertical launchings are to be investigated, the cameras are placed at the center and the left-hand windows. Figure 58 shows the installation of these two batteries with the air-trajectory cameras installed for a low-angle launching. The cameras themselves are not visible in this picture because they are obstructed by the large vertical film magazines that are attached to the back of each camera.

The optical coverage of the underwater bank of cameras is shown in Figure 69. It will be seen that at the plane of launching the adjacent camera fields have a 60 per cent overlap. In the vertical direction the field of view covers the entire water depth. This coverage means that every point in the entire underwater space in front of the intersection of the ad-

acent fields of view is seen by two or more cameras. The purpose of this multiple coverage is to make it possible to use stereoscopic technique for the analysis of the recorded data. Difficulty was experienced in designing the system so as to get the desired coverage without the use of a prohibitive number of cameras. This difficulty was solved in part by the provision of the 6-ft diameter cylinder which increased the distance from the camera to the plane of launching, and hence increased the width of the field. However, even this was insufficient to permit the coverage of the entire underwater space with one line of cameras when equipped with the widest-angle lenses available. The reason for this was that the angular width of the field of view was substantially reduced by the refraction experienced by the light in passing from the air to the water. This reduction in field was finally eliminated by the use of spherical windows in front of each camera. The installation was carefully designed so as to put the front nodal point of the lens at the radius



FIGURE 68. Controlled-atmosphere launching tank chuck mechanism with model clamped in position.

of curvature of the window. The effect of such a system is to permit each light ray to pass through the interface at an angle of 90 degrees and thus suffer no refraction. These spherical windows are in effect additional lenses. They were, therefore, made of optical glass, ground and polished to optical standards. Care was taken to insure that the inner and outer surfaces were concentric. The auxiliary effect of this spherical window in contact with the water is that the apparent distance from the camera lens to the pro-

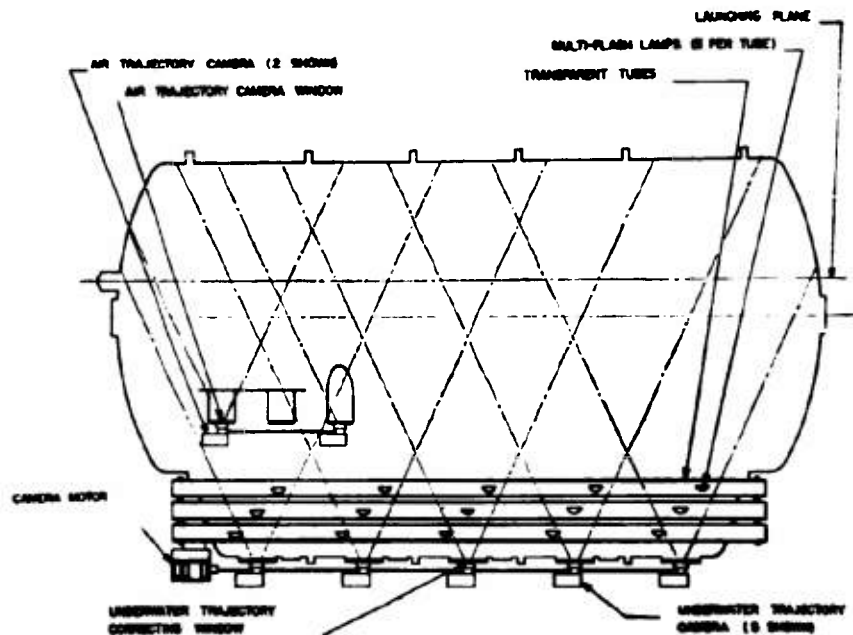


FIGURE 69. Recorder, plan view. Controlled-atmosphere launching tank.

jectile is greatly reduced, thus making necessary a very different focal setting of the lens from that which would have been used with a plane window. Careful computations were made to determine the optical distortions that might result from such an unconventional system using the design characteristics of the lens itself, which is a f 2.3 one-inch focal length Bausch and Lomb Baltar. These computations show that the optical characteristics for the underwater use would be at least as good as those of the lens alone in air, and in one or two characteristics, even better performance could be anticipated.

The design requirement of a maximum speed of 3,000 exposures per second imposed some very severe conditions on the photographic recording system. Such speed requires a continuous motion of the film as it is obviously impossible to stop the film 3,000 times per second. Two techniques have been developed for taking satisfactory motion pictures with a continuously moving film. The first one, which has several variations, is the introduction of some optical device to cause the image to move at the speed of the film during the exposure. The second one discards the conventional continuous illumination and substitutes in its place high-intensity flashing lights which act both as a source of illumination and as a camera

shutter. It will be recognized immediately that the success of the second system depends upon the procurement of a high-intensity light source whose flashes are of such short duration that the amount of movement of the image on the film during exposure is negligible. The only variation of the first method that could be applied to this recording system would require the insertion of a rotating prism or a rotating bank of mirrors in the light path between the lens and the film. The necessity for the use of short-focus, wide-angle lenses makes it impossible to apply this method simply because there is not space available between the lens and the film for the rotating system. Therefore, it was decided to adopt the high-speed flash illumination technique with the resulting simplified camera design. Figure 70 shows a simplified drawing of the camera and magazine mounted on the tank window flange with the spherical window in place. Due to the high speed required, it was decided to eliminate all sliding contact between the film and the camera, using only rollers for guides. This made it necessary to design a special roller-type gate to insure that the film would travel exactly in the focal plane during the exposure. Calculations showed that a final speed of 30 fps would be required, even after due allowance had been made for a very appreciable

CONFIDENTIAL

overlap of successive exposures. The requirements for the analysis of the film record indicated that it would be very desirable for the film to have a constant velocity during the recording. To obtain this with a conventional magazine using a supply and a take-up spool would be very difficult and also wasteful of film since such speeds would require a considerable acceleration time before the film would be up to speed. It was therefore decided to employ a special magazine so constructed that the required length of film could be spliced into an endless belt and laced over a series of rollers. This system would permit bringing the film up slowly to the exact speed required for the recording without danger of damaging the film during either the accelerating or decelerating periods. Figure 71 shows the rear elevation of one of these magazines with the cover removed so that the method of lacing of the endless belt of film is seen. Figure 72 is a similar view from the front

showing the camera in place on the magazine. Figure 73 shows the assembly with the cover in place.

The cameras are all driven by a single motor by means of a continuous line shaft which is directly connected to each drive sprocket. Figure 74 shows the underwater battery in place on the side of the tank with the drive motor at the left and the drive shaft running inside of its guard just below the observation window. Figure 75 shows a close-up of the camera drive motor. This motor drive is a very special installation designed to meet the peculiar needs of this camera system. In the first place, it is desired to synchronize the speed of the film with the speed of the light flashes to allow for projection and observation of the records as motion pictures. A synchronous motor is therefore used. An inverter unit has been designed to drive the motor. The inverter will operate at 62.5 cycles per second, and will be controlled by the laboratory constant-frequency

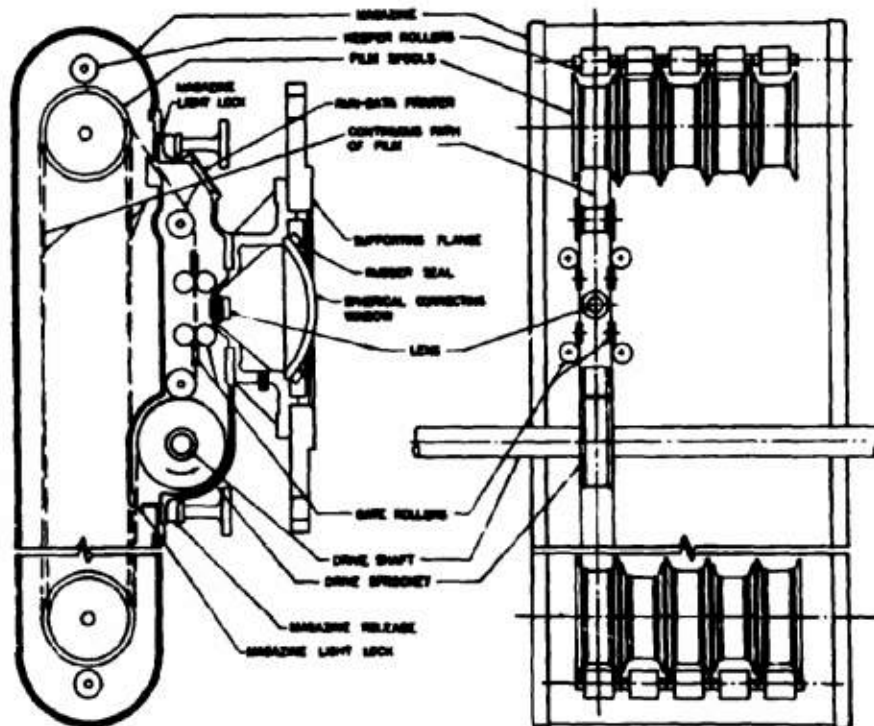


FIGURE 70. Drawing of high-speed camera and magazine mounted on tank window flange with spherical window in place. Controlled-atmosphere launching tank.

CONFIDENTIAL

set which will also control the flash rate of the lamp battery. With this combined operation, flash rates of 3,000, 1,500, 1,000, and 500 per second will correspond respectively to 6, 3, 2, and 1 exposures per standard $\frac{3}{4}$ -in. frame on the film. The inverter will



FIGURE 71. Rear of high-speed camera magazine with cover removed. Controlled-atmosphere launching tank.

deliver 1 kw of three-phase power. The motor is of the slotted rotor type and will deliver 1 hp at synchronous speed. To avoid damage to the film it is necessary to have smooth acceleration and deceleration over the entire speed range. To accomplish this with the synchronous motor, the motor frame is mounted on ball bearings so that it can rotate freely. The power is carried to it through a set of three slip

rings mounted on the outside of the frame. Two magnetic brakes are installed, one on each end of the motor. The brake drum of one is mounted on the motor shaft and that of the other on the motor frame. Before the motor is started the shaft brake is clamped and the frame brake is loosened. The power is then applied and the motor starts by revolving the frame, with the armature and consequently the shaft



FIGURE 72. Front view of high-speed camera and magazine with cover removed. Controlled-atmosphere launching tank.

and film drive standing still. The motor is brought up to speed and synchronized in this condition. When this is accomplished, the shaft brake is released. The frame brake is then applied gradually, thus decelerat-

CONFIDENTIAL

ing the frame and accelerating the film drive. When the frame is brought to a complete stop, the film drive is, of course, operating at a synchronous speed. The reversal of this procedure permits controlled deceleration as well. The torque applied to the frame brake can be varied at will to produce any rate of acceleration and deceleration for the film mechanism.

In order to permit the daylight loading of the magazines, a foot or two of the film on each side of

possible by the use of a magazine loader which consists of a film supply spool, a take-up spool, a splicer, and a precision footage counter. This is shown in Figure 76 as it appears mounted on the magazine in readiness for the reloading cycle. This cycle consists in breaking the film belt at the original splice, splic-



FIGURE 73. Camera and magazine with cover in place. Controlled-atmosphere launching tank.

the splice must be exposed to the light. It would obviously be undesirable to have this portion of the film pass through the camera during the actual recording period. Therefore, provisions have been incorporated in the drive to synchronize the film travel with the instant of launching. To do this for all of the cameras simultaneously required that each endless film belt should be exactly the same length, i.e., have the same number of sprocket holes. This is made



FIGURE 74. Underwater camera battery and motor. Controlled-atmosphere launching tank.

ing one end of this break to the film going to the take-up spool and the other end to that of the unexposed film coming from the supply spool. The light-tight lid is then closed and a measured amount of unexposed film is fed into the magazine while the exposed film is wound on the take-up spool. When the footage indicator shows the right amount, the door is opened and the film is spliced at the indicated sprocket holes after cutting the connections to the supply and take-up spools. The magazine is then



FIGURE 75. Close-up view of camera drive motor. Controlled-atmosphere launching tank.

ready for loading the camera. The cameras are all loaded with the film splice in the same position within a few sprocket holes. This insures that all of the splices pass through the camera at the same time. A counting mechanism is incorporated in the camera motor drive. This is used to give a signal at the time

that the film splices and the exposed film pass through the focal plane of the camera. This signal is electrically interlocked with the circuit which energizes the launcher release mechanism in such a way that the release mechanism can be operated only immediately after the splice in the exposed portion of the film has passed into the camera, thus insuring that the entire length of usable film is available for recording the launching. It is possible that at certain launching speeds the launcher and the film drive would be so synchronized that the model would never be in the correct position for launching during the short period

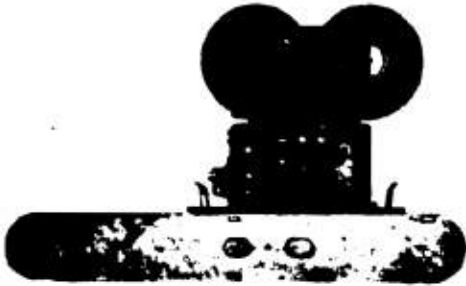


FIGURE 76. Magazine loader for high-speed camera. Controlled-atmosphere launching tank.

that the film splice position indicator permits launching to take place. To take care of these cases a small worm gear is provided on the film drive motor by means of which the motor frame can be rotated, thus changing the phase relationship between the film and the launcher. This mechanism can be seen at the extreme right of the motor shown in Figure 75.

It will be seen that about 250 ft of film are exposed by the camera battery of the recording system for each launching. An organized test program could be expected to produce several thousand feet of film per day. The necessity for rapid means of processing this film under conditions to produce the maximum density with the minimum grain size was the determining factor in the decision to install the continuous film processing equipment described in Section 2.6. This machine was designed to process from 400 to 1,000 ft of film per hour, depending upon the details of the developing cycle required.

Light Source. As previously indicated, the successful operation of this recording system is dependent upon the use of high-intensity flashing light sources of extremely short flash duration. A simple computa-

tion of the speed of the film and the projection ratio required for analysis showed that the maximum applicable effective flash duration would be between 1 and 2 μ sec if sufficiently sharp film images to give the required accuracy of measurement were to be obtained. This means that extremely high light intensity and quantity would be required to illuminate the test space sufficiently to obtain satisfactory records. This condition is aggravated by the fact that for these extremely short exposures, the photographic law of reciprocity seems to break down. For all normal ranges of photographic work satisfactory film exposures can be obtained if the product of the light intensity times the time of exposure is kept constant. This in itself is a severe requirement which can easily be seen from the consideration of an example. The normal high-speed motion picture camera takes pictures at the rate of about 64 frames per second for "slow motion" shots. With a good shutter this results



FIGURE 77. Special reflector for light source lamp. Controlled-atmosphere launching tank.

in the exposure time of approximately 0.01 sec. If instead of 0.01 sec, exposure flash illumination is used for a flash duration of 2 μ sec, the reciprocity law would require an illumination of 5,000 times the intensity to secure a film image of the same density. However, experiment has shown that an increase in the light intensity by a factor of 5,000 does not give satisfactory exposures. The intensity must be increased to several times this amount for good work.

A consideration of these requirements, together with the characteristics of existing flash lamps, indicated that a multiple battery of synchronized lamps

CONFIDENTIAL

would be required since there was little or no possibility of obtaining a single light source of sufficient intensity having such a short flash duration. The assistance of Harold Edgerton and his group of co-

workers at the Massachusetts Institute of Technology was enlisted because of his wide experience in the development and use of flash lamps. The system, consists of a battery of from 30 to 42 flash lamps, all operated in synchronism during the recording period. Measurements indicate that the individual lamps are synchronized with each other within less than $\frac{1}{4}$ μ sec.

Each lamp consists of a straight quartz tube about 8 in. long mounted at the focal point of a special cylindrical reflector. The cross section of this reflector is approximately ellipsoidal. The exact contours were calculated to provide the best illumination possible over the test area. The shape of this reflector was designed by I. S. Bowen, a member of the Physics De-



FIGURE 78. Four-unit light battery, rear view. Controlled - atmosphere launching tank.



FIGURE 79. Four-unit battery, front and side views. Controlled-atmosphere launching tank.



FIGURE 80. Batteries of lights installed. View from inside tank. Controlled-atmosphere launching tank.

partment of the California Institute of Technology. Figure 77 is a photograph of one of these reflectors. It is constructed of Lucite. The reflecting surface is aluminized by the standard sputtering technique. These lamps are assembled in batteries of four or more, as can be seen in Figures 78 and 79. Figure 78 shows the rear view of a battery. The ends of the quartz tubes and the electrical connections may be seen inside of the Lucite guards which house them. These guards are necessary because the glass-to-metal seals of the tubes are very fragile. The lamps are installed in the longitudinal Lucite tubes traversing the launching tank. Figure 80 shows thirty lamps installed in batteries of six in five of the tubes. This photograph was taken inside of the launching tank and also shows the heavy 2x12-in. vertical columns that carry the hoop stress across the opening at the intersection of the two longitudinal cylinders making

up the tank. Three of the spherical camera windows are seen along the horizontal centerline of the picture.

The power for the operation of each light is carried through an individual coaxial cable running from the light to the control panel. Each light is operated through an individual surge circuit which receives power from a large d-c power source. The power source operates at from 3 to 5,000 volts and the lights operate at twice this value through a voltage doubler incorporated in the circuit. The power consumption of each light is approximately 0.8 joules per flash. Thus, at 3,000 flashes per second, the battery of thirty lamps requires a continuous input of approximately 80 kw. It must be remembered that at this speed the lights are lit only about $\frac{1}{200}$ of the time. This means that the power input during the period of illumination is at the rate of better than 16,000 kw. The heat generated in the tubes themselves limits the length of operation since the tubes get quite hot and will collapse if they are operated too long. At flash rates of 1,000 per second and above, the only significant heat

dissipation is through radiation. Experiments have shown that 3,600 flashes per run are the maximum that can be employed for successful high-speed operation. At flash speeds of a few hundred, however, the average energy input becomes low enough so that conduction contributes a significant amount to the total energy dissipation. For such speeds the number of flashes per run can be increased and at flash speeds of 100 or 200 per second, the energy is dissipated rapidly enough to permit of continuous operation.

Spectroscopic analysis of the light shows it to be composed of discrete lines. Most of the energy lies between 4,000 and 4,600, which coincides with the wavelength at which the transparency of water is the greatest.

Figure 81 shows a final sketch of the tank with portions cut away to make it possible to see the interrelationship of the launcher, the air camera, the underwater camera bank, and the flash lamps. The central control station for the launching tank is located on the basement floor south of the tank. From

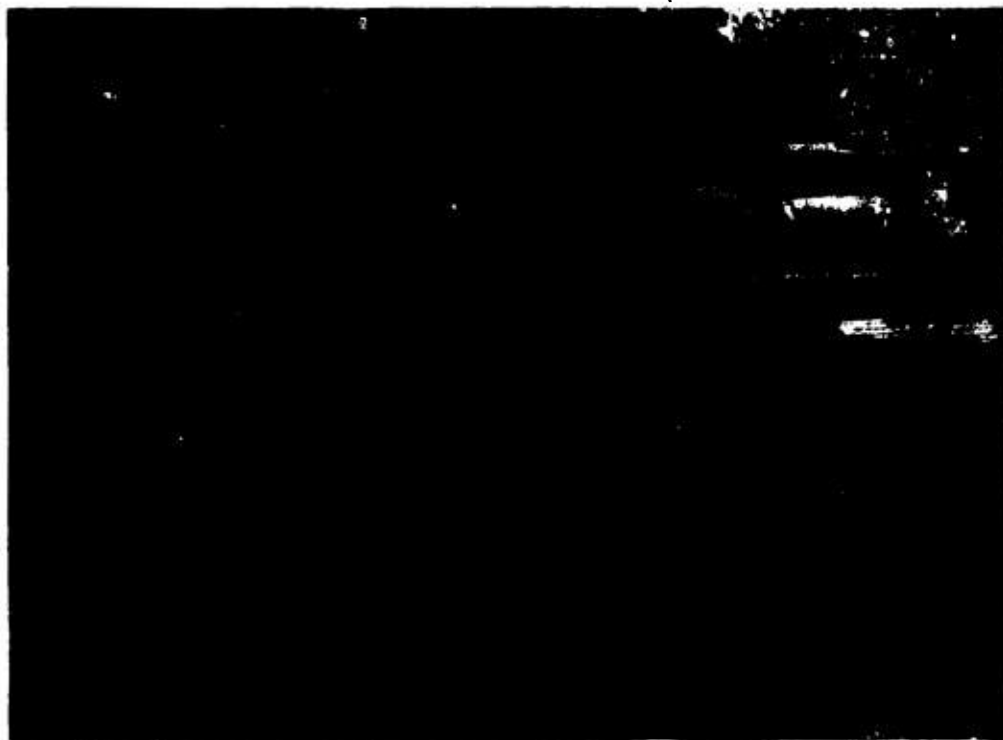


FIGURE 81. Cut-away drawing showing interrelation of parts. Controlled-atmosphere launching tank.

CONFIDENTIAL

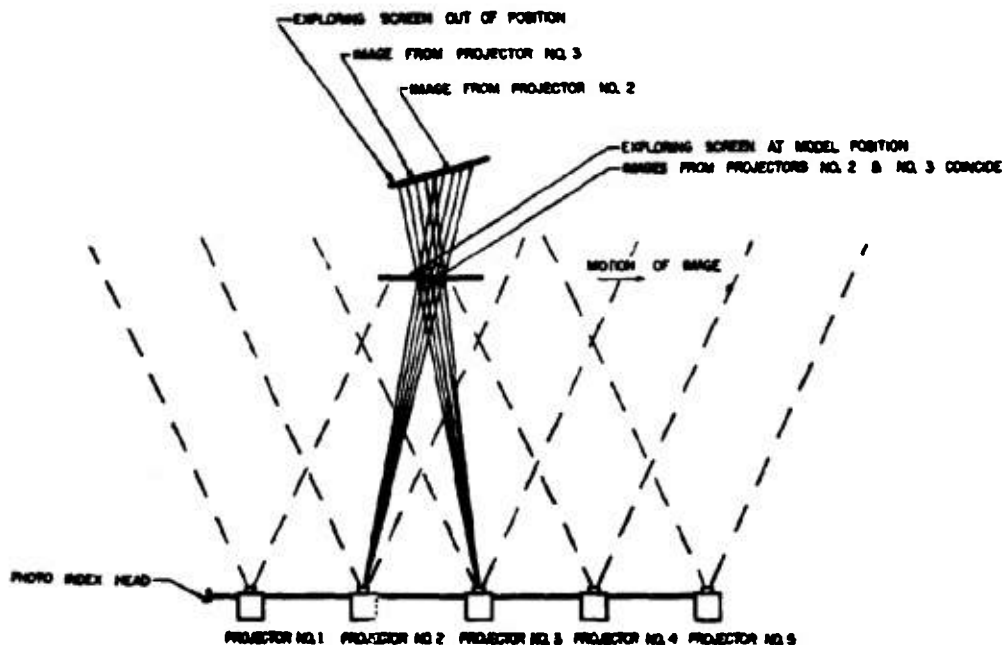


FIGURE 82. Line diagram of analyzer system. Controlled-atmosphere launching tank.

this point the launcher may be started or stopped and its speed set. The camera drive motor may be controlled, and the high-voltage power supply turned off and on. Also the vacuum pump and valve controls for adjusting the pressure within the tank are located here. An automatic interlock sequence prevents a launching from being made until all the accessories necessary to record the trajectory are in operating condition. When everything is in order, an indicating lamp shows that a launching can be made. When the launching control is actuated, the operation of all the equipment is fully automatic.

ANALYZER SYSTEM

Details of the analyzer system are not available because it is only in the initial stages of design and construction. However, the general lines of the development have been established and will be discussed. The basic principle of the analyzer essentially duplicates that of the recording system. Projectors will take the place of the cameras and a movable screen will replace the tank and the model. All of the films from one run of the recorder will be placed in the corresponding projectors with the film strips synchronized so that the corresponding frames taken at the

same time will be projected at the same time. The film drive of the projectors will be a continuous shaft so that once the film strips are synchronized, they will remain so during the projection of the entire run. Figure 82 shows a line diagram of the analyzer system. It represents a point on the trajectory in which the projectile was in the field of view of cameras No. 2 and 3 so that projectors No. 2 and 3 are projecting the two images into the analyzer space. It is obvious that there is only one position in this space in which the two images will coincide. The exploring screen of the analyzer is then maneuvered into such a position that the two images both show on it. Additional maneuvering will bring the screen into such a position that the images fuse into one. This will require movements in three linear directions and also in pitch and yaw. These movements will be transferred to a battery of counters. When the screen is finally in the exact position required for the precise fusing of the images, then the counters will record the position of the projectile in space. It is planned to build the analyzer to a scale of one-half that of the recording equipment.

The projectors for this analyzer will have to be precision instruments. As a first step in their construction, lenses were procured in matched pairs at

the time the cameras were constructed. One lens of the matched pair is to be used in the camera and the other lens in the corresponding projector. The gate mechanism will be designed to hold the film in the exact focal plane corresponding to that used in the camera. The light source will be kept at as low an intensity as is consistent with the required accuracy of the readings in order to reduce heat which might affect both the dimensions of the film and of the optical system. The temperature will be controlled further by the employment of water cells and individual air cooling. In order to check the location of each frame, it is planned to install a series of reference marks on the rear wall of the launching tank. These marks will be reproduced on a background screen at the rear of the analyzer, and before making a measurement, a check will be made to see that the image of the marks from the films in the projector fall on the corresponding marks on this screen. The exploring screen is designed to be mounted on a carriage suspended from longitudinal rails. This longitudinal carriage will, in turn, provide a set of transverse rails upon which will run the screen mount. The transverse carriage will carry an inverted pedestal which will provide the required vertical movement. The screen will be mounted on the lower end of the pedestal stem through a system which will provide the final pitch and yaw motions. Selsyn repeaters will be used as position indicators to transmit the required information to the operator's desk.

2.5 FREE-SURFACE WATER TUNNEL

The purpose behind the construction of the free-surface water tunnel was explained in Chapter 1. In general plan and in contemplated operation it is very similar to the main high-speed water tunnel. That is, it has a closed-circuit circulation system which is driven by a propeller pump powered by a variable-speed d-c motor. The circuit is arranged in a vertical plane with the working section in the upper horizontal run. The design specifications differ considerably from those of the high-speed water tunnel in that a much larger working section is to be provided. The cross section of the water jet is 20 in. square, which gives a cross section that is just under 3 sq ft as compared to the 1 sq ft of the high-speed water tunnel. It will be noted that the flow is square instead of circular in cross section. This is necessary to provide for the free surface of the jet in the working section which is the main distinguishing feature of this piece

of apparatus. The tunnel is designed to operate at velocities up to 25 fps. The exact maximum velocity will depend upon the equilibrium reached between the power available in the motor drive and the friction losses in the circuit. The tunnel is designed to permit the operation of the working section at controlled pressures. Since the jet has a free surface in this area, it is not possible to control the pressure by the simple means used in the high-speed water tunnel. Instead, it is necessary to control the pressure in the free gas space above the jet. This is done by connecting the tunnel to the same vacuum control system provided for use with the controlled-atmosphere launching tank. No operation is contemplated at pressures above atmospheric in the working section. The vacuum system will provide variations in pressure from 1 atmosphere down to $\frac{1}{2}$ to $\frac{1}{16}$ of an atmosphere.

Figure 83 shows a perspective sketch of the entire tunnel. The observer is shown watching the operation of a model mounted on the balance in the working section. The flow is from right to left as indicated by the arrow. From the working section the jet passes into a closed section which leads directly to a series of vane diffusers which increase the cross section and decrease the velocity in a series of four steps, each of which has a ratio of about 2 to 1. The flow leaves the last stage with a very low velocity and enters an especially designed air separator, the horizontal trays of which can be seen through the cut-away opening in the upper left-hand corner of the sketch. At the downstream end of the air separator the flow goes through a vane elbow which directs it vertically downward, and on leaving the lower level, goes through another vane elbow from which it enters the inlet of the main circulating pump. The discharge from the pump goes into a circular diffuser section which decreases the velocity. At the point of the maximum diameter of the diffuser, a transition section is entered which gradually changes the cross section from round to square. This leads to a third vane elbow which deflects the flow vertically upward. The acceleration of the flow to the working velocity begins in the vertical section above this third elbow. The channel section contracts in one dimension only. This contraction is completed by the fourth vane elbow which is so designed as to produce a considerable acceleration. The flow leaves this vane elbow in a horizontal direction. It now has a rectangular cross section 20 in. high, which is the depth required in the working section, but with a full width of the main

CONFIDENTIAL

diffuser. The final acceleration is carried out in a two-dimensional nozzle designed in the same careful manner as the one used in the high-speed water tunnel to avoid any local areas of low pressure. At the nozzle exit the flow cross section has been reduced to the 20-in. square dimension of the jet in the working section.

The working section is provided with Lucite windows on all faces. These are held in a comparatively light steel framework designed to take the stresses involved in the low-pressure operation. The windows are divided into two sections, each about 4 ft long, by steel columns, thus giving a total working section of about 8 ft. A 10-in. air space is provided over the free surface of the jet. The side windows are, therefore, 30 in. high, whereas the top and bottom windows are only 20 in. wide. In order to eliminate deflections these large windows are made of very thick Lucite procured to laboratory specifications. The side walls are 4 in. in thickness and the top and bottom windows are 3 in. thick. Provisions are to be made for mounting balances either in the bottom panels or the top panels of the working section. An adjustable lip will be required at the end of the nozzle to provide a clean interface from the closed channel to the free surface. Likewise it is planned to install an adjustable entrance vane at the downstream end of the

working section to provide a smooth transition from the free-surface operation back to the closed channel. Many of the investigations contemplated will result in disturbances of the free surface which may produce splash and spray. Provisions are made to collect the water thus involved which does not re-enter the closed channel at the lower end of the working section and to return it by means of a pump into the main circulation system. It is contemplated that the standard three-component balance used in the high-speed water tunnel will be usable in this tunnel as well. However, special balances will also be required which will permit of a vertical adjustment of the model so as to allow testing at various distances below the free surface. A balance with a similar vertical adjustment mounted in the top window will permit of supporting the body under test above the free surface and of adjusting its degree of immersion to any desired amount. It is felt that a four-component balance will give sufficient flexibility for the required measurements. Separate adjustments will be necessary for pitch and yaw since the effect of one cannot be simulated by a simple rotation of the model of 90 degrees from the plane in which the other was measured.

Figure 84 shows a drawing of the battery of deceleration vanes. It will be noted that the entry and



FIGURE 83. Free-surface water tunnel. Hydrodynamics Laboratory, California Institute of Technology.

CONFIDENTIAL

exit cross sections are fixed, which means that the overall velocity reduction ratio is set independent of the velocity of operation of the tunnel.

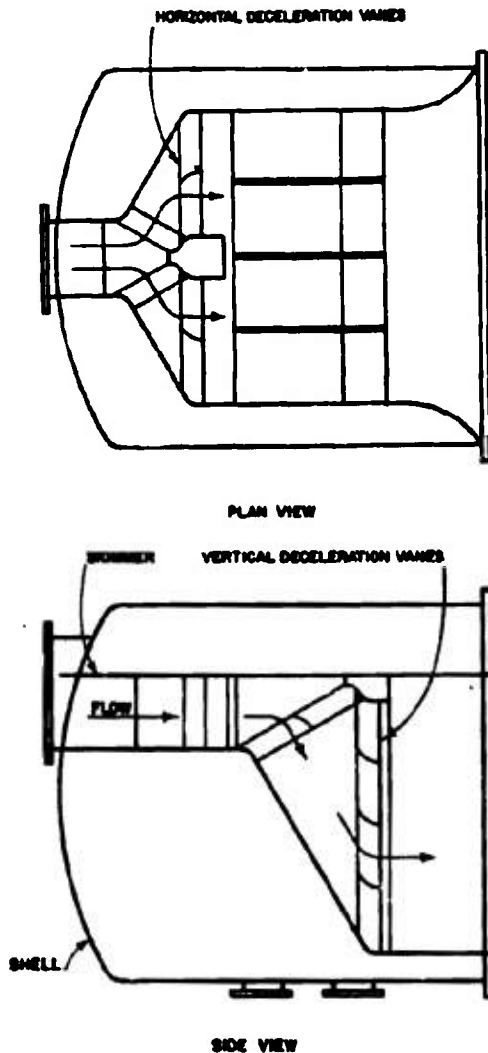


FIGURE 84. Battery of deceleration vanes. Free-surface water tunnel.

Design of an air separator for a system of this kind has presented a great many difficulties. It is contemplated that a rather large amount of air will be introduced into the working section from time to time and this air may appear in the form of rather fine bubbles,

many of which may be in the lower levels of the working section. The rate of rise of such bubbles is rather small. This means that either a long time or a short distance to a free surface is required if adequate separation is to be obtained. Although the velocity at which the flow leaves the battery of deceleration vanes will probably be under 2 fps, the depth will be very great, too great to permit of the rise of a small bubble to the surface before the flow reaches the vane elbow and is directed down away from the free surface towards the circulating pump. It was, therefore, decided to divide the air separator section into a series of shallow channels and to provide access along the upper surface of each channel to the free surface. This is accomplished by the use of a series of double wall trays at the upper surface of which is a flat plate. The lower surface is made up of expanding metal, thus permitting free access of any bubble to the space within the tray. This space connects directly with channels leading to the free surface that is continuous throughout the air separator section. These trays are approximately $\frac{1}{2}$ in. thick and are spaced with a 2-in. vertical separation which makes the net thickness of the flowing stream $1\frac{1}{2}$ in. The average time of passage for the flow through the tray section for the maximum velocity of operation will be approximately 5 sec. This means that bubbles with an effective rate of rise of $\frac{1}{4}$ ips or greater will be separated from the flow. In order to assist this separation, arrangements have been made to provide a slight pressure drop which will cause a small flow from the main stream up through the trays and out through the channels to the free surface. This flow will be collected in a system similar to the one used for taking care of the spray from the working section. It will then be returned to the main flow through another pump which injects it upstream from the air separator.

It proved advantageous in the construction of the air separator to give a slight inclination downward in the direction of flow to the cylindrical case. The result of this is that the vane elbow following the air spacer is slightly elliptical in cross section. Special reinforcing rings were designed to take care of the asymmetric stresses caused by this shape when the tunnel is being operated at subatmospheric pressures. The lower vane elbow is likewise elliptical and requires the same treatment. The section is transformed into a circular one, however, by the time that the flow reaches the pump. The pump is a standard Peerless 42-in. propeller pump of the same type as that

CONFIDENTIAL

used in the high-speed water tunnel. The mechanical design of the bearings and shaft seal were modified, however, for use in the closed circuit of this type, with horizontal drive and with a possibility of negative pressures tending to cause air leaks in the seal. Although the pump is physically much larger than the one used for the high-speed water tunnel, and although it circulates approximately the same quantity of water, the head requirements of this tunnel are so much lower due to the low velocity in the working section that the power requirements are greatly reduced. Therefore, the pump is driven by a 75-kw

the details of the contours. These contours were machined very accurately using a carefully constructed



FIGURE 85. Upstream view of pump bowl, propeller in place. Free-surface water tunnel.

rectifier set which has both armature and field controls for precise speed adjustment. Figures 85 and 86 show upstream and downstream views of the pump bowl with propeller in place. Figure 87 is a photograph of the 75-kw rectifier set. Figure 88 shows a photograph of the transition and third vane elbow. Figure 89 shows the accelerating vane elbow to which is bolted the two-dimensional nozzle. Special care was taken with the alignment of the vanes in both of these elbows in order to insure the proper direction of flow, since disturbances introduced in these points by improper alignment would be difficult to remove before the working section was reached. Figure 90 is a photograph of the two-dimensional nozzle, and Figure 91 is the working drawing showing



FIGURE 86. Downstream view of pump bowl, propeller in place. Free-surface water tunnel.



FIGURE 87. Seventy-five-kilowatt rectifier set for free-surface water tunnel.

wooden template. Both the top and bottom plane surfaces and the side contours were worked until

they were smooth and then all of the component parts were cadmium plated and polished. These precautions were taken because the nozzle is the most critical part of the circuit as it is the determining

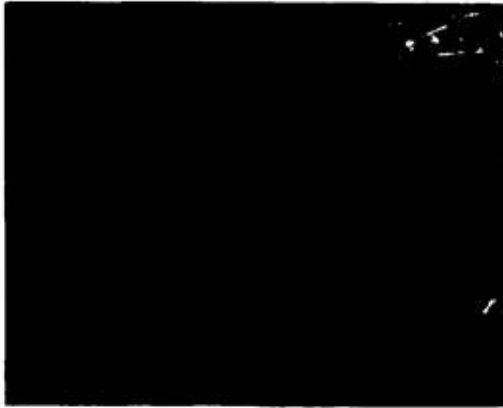


FIGURE 88. Transition and third vane elbow. Free-surface water tunnel.



FIGURE 89. Accelerating vane elbow. Free-surface water tunnel.

factor of the quality of the flow in the working section itself.

The preceding description represents the present state of the design and construction of this tunnel. It will be seen that there are several design problems

yet to be solved. Furthermore, it is anticipated that some minor operating difficulties will be encountered at the time the tunnel is put into service because there is little precedent available concerning the behavior of the free-surface jet. With a depth of 20 in., the velocity of a wave on the free surface is about $7\frac{1}{2}$ fps. Most of the operations contemplated will be

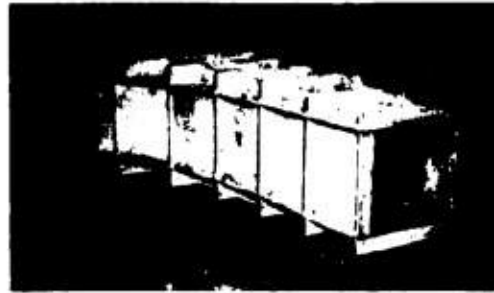


FIGURE 90. Two-dimensional nozzle. Free-surface water tunnel.

at velocities well above this figure. For example, at 25 fps, there will be enough energy in the jet to produce a hydraulic jump of appalling magnitude as compared to the air space in the working section. For this and similar reasons it is anticipated that great care will be necessary during the initial period while the laboratory staff is learning the operating characteristics of this new tool.

2.4 PHOTOGRAPHIC EQUIPMENT

2.4.1 Photographic Equipment and Processing Facilities

In any research laboratory, photographic equipment is probably the most important and most used facility outside of the basic apparatus of the laboratory itself. The specialized requirements of a hydrodynamic research program call for equipment to record high-speed phenomena under a wide latitude of lighting conditions. Such equipment must include, in addition to specific purpose cameras like those used with the controlled-atmosphere launching tank, a variety of plate and roll film cameras and movie cameras of both normal-motion and high-speed type. Suitable darkroom and processing facilities are necessary to handle film and produce final prints and enlargements. The following paragraphs contain a brief description of the facilities and more important

CONFIDENTIAL

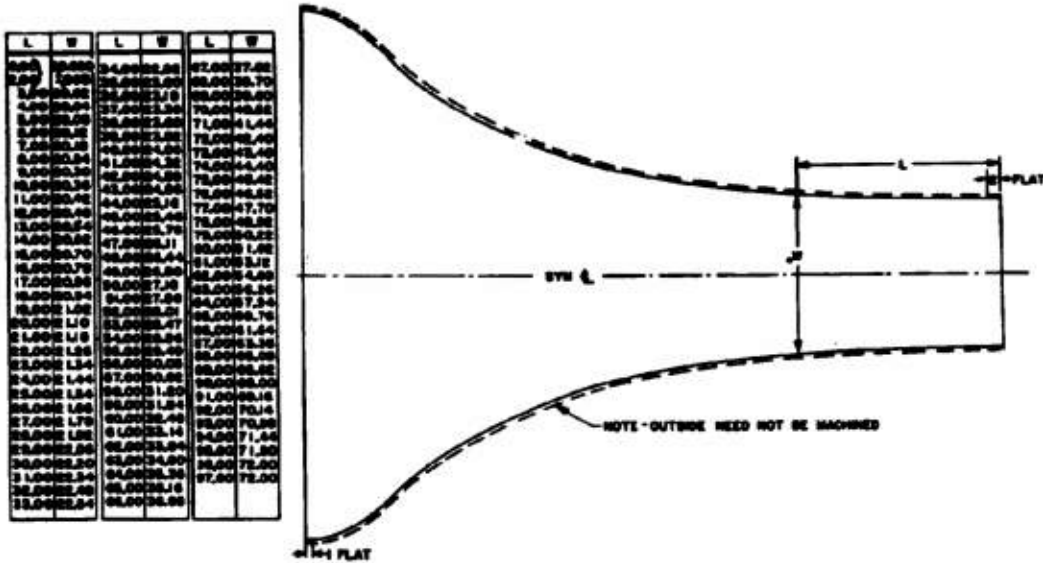


FIGURE 91. Details of contours of two-dimensional nozzle. Free-surface water tunnel.



FIGURE 92. Type K-17-B aircraft camera, "A" in position to take pictures through side window of working section "B." A view camera, "C," is mounted above the working section to record the view from the top. The intervalometer, "D," is resting upon the power supply, "E," for the three spark lamps, "F," used in this setup.

CONFIDENTIAL

items of portable equipment available to the Hydrodynamics Laboratory.

2.4.1 Portable Camera Equipment

The laboratory is equipped with still camera equipment which will meet all the demands from the routine copying of drawings, photographs, and printed

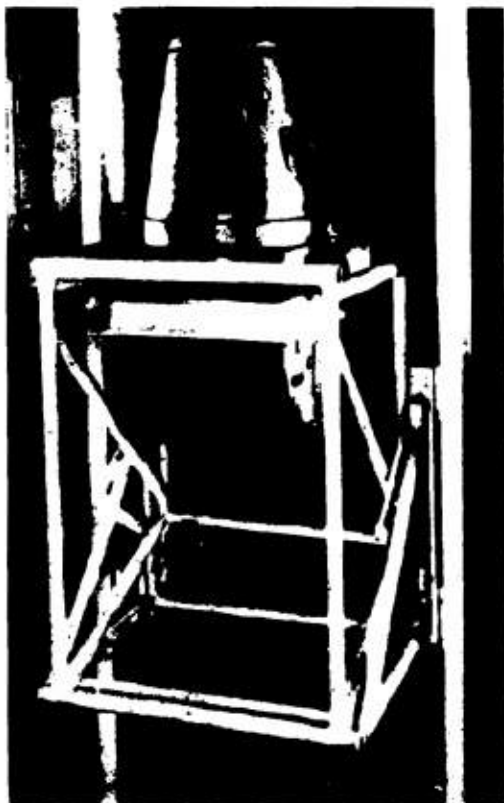


FIGURE 93. Aircraft camera in stored position.

matter to stopping the motion of speeding objects, and from photographing buildings, laboratories, and apparatus to recording minute imperfections in delicate instruments. In addition to a group of standard cameras, including all sizes and types from 35-mm for roll film to 8x10-in. view type for cut film and plates, the laboratory has two Fairchild K-17B serial cameras using 9-in. roll film. These cameras may be used for single pictures or, in conjunction with an intervalometer, to make a series of exposures

automatically at time intervals ranging from 3 to 120 sec.

The lighting used with the still equipment includes continuous illumination from photoflood, tungsten arc, or high-intensity mercury vapor lamps, or flash illumination from a General Radio Strobolux or from Edgerton-type short-duration flash lamps. (See Section 2.4.4.)

An arrangement for making spark photographs of high-speed phenomena in the water tunnel is shown in Figure 92. For this use the aircraft camera is operated with the usual electric drive on the shutter and film wind, although this type may be operated manually. The camera illustrated has been modified so that it will discharge a group of spark lamps when its shutter is opened to full aperture and so that it will advance the film 3, 4½, or 9 in. per frame. Note that it is kept near the working section of the water

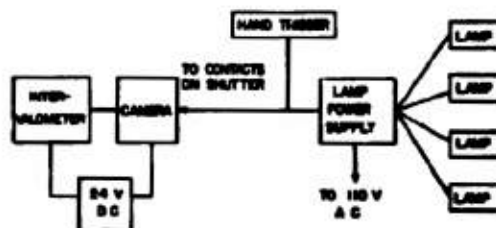


FIGURE 94. Block diagram showing electrical hookup for aircraft camera and spark lamp.

tunnel and ready for immediate use. It has been mounted in a lightweight tubular steel framework which is hinged to fold upward against the wall for storage as shown in Figure 93.

Frequently it is advantageous to photograph the same action simultaneously from two angles. This is being done in Figure 92, in which it will be noticed that a view camera has been placed above the working section of the tunnel. The photographer holds the shutter of the view camera open by pulling a cord, then presses a switch to operate the aircraft camera, the shutter of which discharges the lamps. The block diagram, Figure 94, shows that a trigger switch also may be used to test the lights or to take pictures with the view camera when the aircraft camera is not in use.

The available motion picture equipment permits recording a wide range of the very high-speed hydrodynamic phenomena under investigation, as well as all the normal-speed motions encountered. The former is accomplished with a General Radio high-



FIGURE 95. Half-frame, high-speed motion pictures made with the General Radio camera. Sequence of exposures is from top to bottom and from left to right. The pictures cover a period of approximately $1/80$ second; individual exposures were less than 5 microseconds.

CONFIDENTIAL



FIGURE 96. Photographic laboratory and studio facilities.

speed 35-mm camera. This camera is used in conjunction with the Edgerton-type lamps which can be flashed at rates up to 3,000 times per second while the duration of a single spark is somewhat less than $5 \mu\text{sec}$. In this camera the film moves continuously past a shutterless lens and over a large sprocket on the side of which a series of electric contacts are so spaced that a circuit will be completed each time the film has advanced one frame. The extremely bright spark is of such short duration that it is unnecessary to stop the film for each exposure and no shutter is needed. At 1,600 standard frames per second the film moves 100 fps or approximately $1/200$ in. during the flash. This is almost negligible in the majority of cases, but not when fine detail is desirable. By making pictures of the usual width but only half the standard frame height, the laboratory has been able to secure high-speed motion pictures of remarkable

sharpness. The pictures reproduced in Figure 95 were obtained in this manner.

2.2.3 Darkrooms, Processing, and Printing Equipment

Five darkrooms, fully equipped, are provided for processing film, making prints, enlargements, and lantern slides. A studio, a chemical mixing room, drying and mounting rooms, and refrigerated storage space for unused film complete the photographic department. Figure 96 is a plan showing the arrangement of the rooms and the location of major items of equipment.

Cut and roll films are loaded and processed in the developing room which is equipped with trays, six water-jacketed tanks, film hangers, viewing light, drying cabinet, and storage space for film holders and

film. Cut film is developed in hangers which are provided for the various sizes including 8x10 in., and roll film is processed on adjustable reels. The equipment permits aircraft film to be handled in lengths up to 150 ft.

In the two darkrooms labeled "35 mm" and "16 mm," motion picture film is processed by machines which perform the entire operation, including drying. These rooms also contain equipment for loading and editing film and tanks for the storage of developing and fixing solutions. The laboratory does not have machines for printing motion picture positives. In the printing room are four printers on which contact prints of any size up to 11x14 in. can be made. One printer is designed especially for use with rolls of negatives from the aircraft cameras. All four are supplied with power at a constant voltage and with automatic timing devices. Prints are washed in a machine of the rocker type.

The enlarging room is equipped with an autofocus and a precision enlarger. Negatives from 9x12 cm to 5x7 in. can be enlarged to slightly more than four diameters, smaller negatives to fifteen diameters. Adjoining the printing and enlarging rooms is the drying room which houses a drum-type dryer for prints and the machine in which aircraft film is dried. This room also contains a print straightener and equipment used in treating prints before they are dried.

In the office and mounting room there is a densitometer, a safe in which negatives are stored, cabinets for prints and photographic notes, tables with transparent illuminated panels, and suction plates for use in preparing prints for the dry-mounting press. In addition to the usual trimming boards there is a paper-cutting knife for trimming prints in batches of 100 or less.

Provision is made in the studio for the photography of instruments and models. A camera stand and easel facilitate making copies, or photographing line drawings and printed material. Miscellaneous equipment includes fluorescent, spot and flood lights, lightstands, backgrounds, tripods, and unipods. The microphotographic camera is housed in the studio.

A room adjoining the developing and film processing rooms is set apart for the storage of chemicals and the mixing of all solutions. There are scales for weighing chemicals, graduates and pipettes for measuring liquids, a metering device for water, and both large and small mixing vessels equipped with mechanical

stirrers. This room and all darkrooms are equipped with stainless steel sinks and supplied with hot, cold, and iced water.

27 ELECTRICAL ACCESSORIES

Most of the electrical and electronic equipment of the laboratory form an integral part of the main pieces of apparatus, and have been described in connection with them. However, there are a few general facilities that are described in the following paragraphs.

The laboratory is equipped with a source of constant frequency of the quartz-crystal type. It consists of a 100-kilocycle GT-cut low thermal drift crystal in a stabilized oscillator circuit. Means are provided for adjusting the frequency of the oscillator to zero beat with WWV, the standard-frequency station of the National Bureau of Standards. Following the oscillator is a tripler to produce 300 kilocycles and multi-vibrator-type frequency dividers which provide 3,000-cycle per second output. The 3,000-cycle per second signal is distributed about the laboratory.

At the water tunnel the 3,000-cycle per second signal is put into a frequency dividing unit which puts out 100- and 120-cycle per second positive pulses. This pulse output is used to drive a parallel inverter of the thyratron type at either 50 or 60 cycles per second. The inverter can feed a 500-watt load, and is used to power the synchronous motor that provides the standard for control of dynamometer speed. The inverter may be used to drive any small timer of the synchronous motor type anywhere in the laboratory whenever greater precision of timing than is available from the power lines is desired.

At the launching tank the 3,000-cycle per second signal from the constant-frequency set is run into a set of frequency divider and pulse generators which provide positive pulses at 3,000, 1,500, 1,000, and 500 cycles per second for operation of the stroboscopic lights. The inverter which supplies power to the synchronous motor driving the cameras is also driven from the same 3,000-cycle per second constant-frequency source.

The laboratory has available a frequency changer capable of supplying "high-cycle" power. The frequency range of the machine is 0 to 300 cycles per second at 1.22 volts per cycle. A maximum of 7.5 kw may be delivered to a suitable load. One use of this machine is to power the motors driving the propellers of water tunnel models.

For the operation of special equipment requiring a d-c power source, 24 volts direct current is provided throughout the laboratory. This makes it possible to use a 14-channel recording oscillograph (Consolidated 5-101) anywhere in the building.

As indicated in the description of the free-surface water tunnel, the laboratory has a high-voltage power supply for the operation of the high-speed, high-intensity flash lamps. This power supply is of the rectifier type, and operates over a range of from 4 to 12 kw. Its maximum output is 100 kw. Arrangements are being made to provide utility and control facilities together with the necessary power lines, to make it possible to utilize this power at each of the major pieces of equipment to operate banks of flash lamps and to take high-speed motion pictures.

A small shop is available for the maintenance of the electrical and electronic equipment, and for the construction of the special apparatus required for the project. This shop is provided with the necessary tools and instruments for carrying on this work.

2.0 SOUND-MEASURING EQUIPMENT

The development of acoustically operated homing projectiles has required a knowledge of the various self-induced supersonic noises. Cavitation is one of the important causes of such high-frequency noise, and the laboratory is equipped to measure the intensity and frequency distribution of sounds from this source.^{1,2} Design details of the equipment described in the following paragraphs will be found in the reports. Submerged bodies are subjected to cavitating conditions and the resultant noise in various bands from 1 to 160 kilocycles can be measured by hydrophone units located either inside or outside the bodies. Such measurements are possible, because, although the water tunnel itself produces high noise levels, it is relatively "quiet" in the range above 6 kilocycles. Background levels in the high-frequency range are so low as to introduce errors of only a few per cent.

2.0.1 Receiving Equipment

Two arrangements are used for receiving the noise emitted by cavitating projectiles. In one a crystal hydrophone receiver is mounted external to the water tunnel and is focused through a window toward the cavitating zone by means of a suitable reflector or "mirror." This system eliminates possible disturb-

ance to the flow and accompanying extraneous noise which a submerged hydrophone housing would cause. In the other, a receiver is mounted inside the 2-in. diameter projectile model itself.

HYDROPHONES

Brush Development Company type C11-A1 and AX90 crystal hydrophones are used. These sensitive units are of very small size and can be adapted with

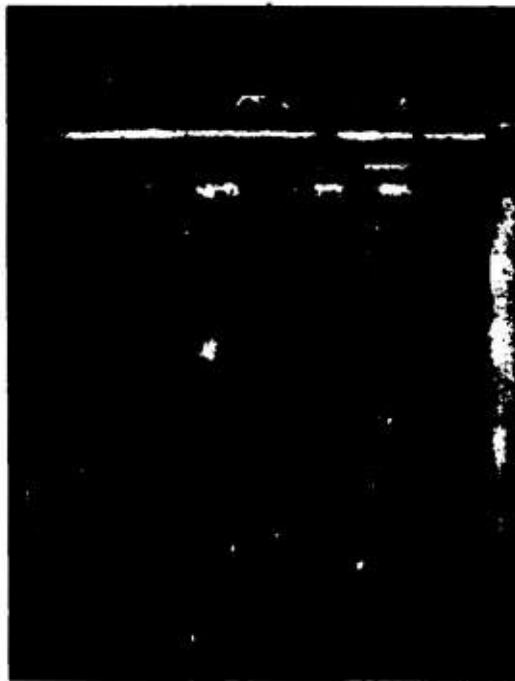


FIGURE 97. Ellipsoidal reflector and C11-A hydrophone assembled in water tank at working section window. Noise coming through Lucite window is brought to focus in the hydrophone crystal.

few changes to installation inside the small models and to use with the focusing reflectors described below.

METHOD OF ASSEMBLY

In the arrangement with the receiving system external to the tunnel, the hydrophone is placed at the focal point of spherical or ellipsoidal reflectors and the assembly submerged in a water-filled tank attached to the side of the working section. Figures

97 and 98 show the installation with an ellipsoidal reflector focused to pick up noise from a model (whose tip can be seen projecting past the reflector in Figure 98). The noise originating from cavitation on or near the projectile surface is transmitted through a water medium continuous, except for the Lucite window, to the reflecting surface and back to the hydrophone. The setup is spaced so that the hydrophone is at one focal point of an imaginary ellipsoid of revolution and the cavitation is at the other. Provisions are made for focusing from any

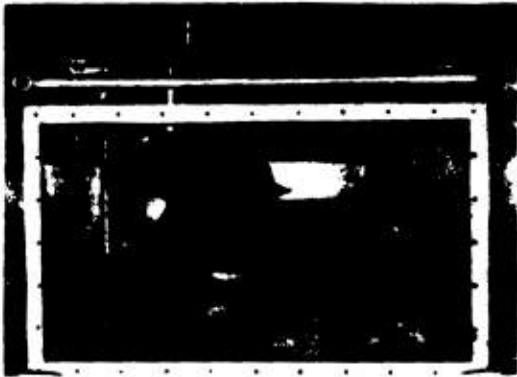


FIGURE 98. Hydrophone-reflector assembly focused to receive noise from cavitation on projectile surface. Note that assembly can be positioned at any point within the external water tank.

position inside the exterior tank. The focusing helps isolate the source of noise and concentrates more of the total sound energy at the hydrophone.

SOUND REFLECTORS

Three sizes of ellipsoidal mirrors are available. Each has a focus-to-focus distance of 16.2 in. The aperture diameters are 10, 5, and 3 in., respectively. These are shown in Figures 99A, B, and C. A single spherical mirror with a 10-in. aperture is also available. This is shown in Figure 100.

The mirror construction is based on the fact that the reflection of sound takes place when the waves strike a discontinuity in the transmitting medium. The per cent of the incident sound pressure which is reflected is the ratio

$$\frac{\rho_1 c_1 - \rho_2 c_2}{\rho_1 c_1 + \rho_2 c_2}$$

where ρ_1 and ρ_2 are the densities of mediums 1 and 2,

and c_1 and c_2 are the velocities of sound in mediums 1 and 2.

The greater the difference between the products ρc , the greater will be the reflection. Consequently, to obtain good reflection of sound traveling at high velocity in a dense medium, the reflector should be a

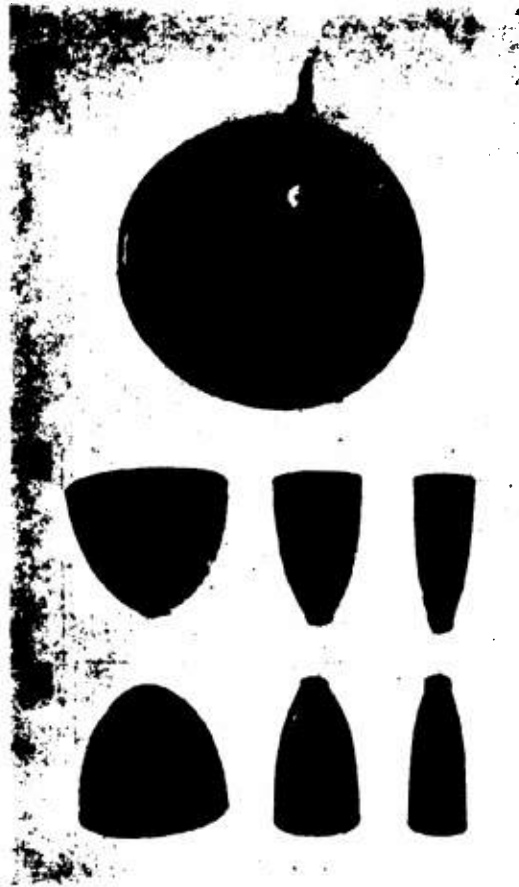


FIGURE 99A, B, C. Ellipsoidal reflectors with apertures of 10, 5, and 3 in.

surface which forms a boundary with a low density substance in which sound travels slowly. The reflectors just described use air as the medium at the reflecting surface. In the ellipsoidal construction two concentric copper shells are separated by an air pocket. The face of the aluminum spherical reflector is covered with a $\frac{1}{8}$ -in. thick layer of sponge rubber with nonintercommunicating air pockets.

INTERNAL RECEIVERS

For mounting within the model, the AX90 hydrophone is used. This unit is without integral pre-amplifier and requires less space than the C11-A1 unit. For this installation, the models are made up of 0.020-in. wall aluminum shells.

In addition to commercial hydrophones, one special receiver was constructed with ammonium di-



FIGURE 100. Face view of spherical surface reflector. Note surface covering of sponge rubber with nonintercommunicating air cells.

hydrogen phosphate crystals cemented directly on to the inside surface of a 0.020-in. wall aluminum nose.^b The X-ray photograph of Figure 101 shows the crystal locations. Four crystals are mounted on the inner surface of the nose at $\frac{1}{4}$ -in. intervals in a line parallel to the projectile axis. Another crystal is cemented in place at 90 degrees around the circumference of the shell. This unit is designed for an investigation of the location of the source of noise for various stages of cavitation on the hemisphere nose.

^b The crystals in this model were cut and mounted at the Underwater Sound Laboratory of the University of California, Division of War Research, at San Diego.

FREE-FIELD CALIBRATIONS

Equipment is available for determining free-field directivity patterns and frequency-response calibration curves of the hydrophones and hydrophone-mirror assemblies. For these calibrations, the AX90 hydrophone is used as a projector. It acts as an approximate point source, because of its small physical size. The geometrical arrangement between source and receiver used in the actual water tunnel measurements are duplicated. Thus, for the ellipsoidal reflectors, the two crystal units are separated by the distance between the conjugate foci of the ellipsoidal shape. For these tests a rig consisting of holders for

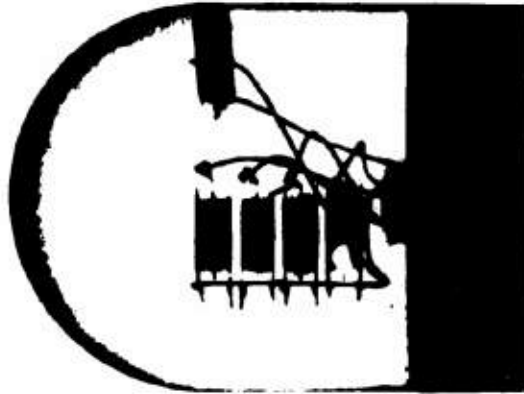


FIGURE 101. X-ray photograph of crystal pickups cemented to inside surface of aluminum nose.

the projecting and receiving units with provision for rotating the projector in a circle whose center is at the receiving crystal is submerged to a 20-ft depth in a large reservoir (Morris Dam).

Figure 102 shows the rig arranged for calibration in a plane normal to the receiving hydrophone stem. By rotating the hydrophone and mirror with respect to its support, calibrations can be obtained in other planes, for example, at 90 degrees, as shown in Figure 103. Examples of the directivity patterns and calibrations obtained with this equipment are shown in Chapter 7.

AMPLIFYING AND FILTERING EQUIPMENT

Two amplifying systems are in use. One is a unit specially constructed in the laboratory. The other is a modified Naval Ordnance Laboratory Mark 3 Acoustical Unit.

CONFIDENTIAL

The laboratory-built equipment is designed to amplify the output of a detecting hydrophone in selected frequency ranges between 1 and 100 kc and to indicate the amplified voltage on a meter. With this unit a voltage gain of 90 db can be obtained with no variation over the range of 20 to 100 kc. The gain is adjusted with attenuator pads, having a total of 100 db in steps of 1 db. Two sets of filters are included to analyze the noise spectrum. One is a high-

160 kc. Each amplifier is equipped with an attenuator with a range of 50 db in 10-db steps. All the amplifiers have flat response from 10 to 160 kc. The filters in this equipment separate the input into four octaves: 10 to 20 kc, 20 to 40 kc, 40 to 80 kc, and 80 to 160 kc. Each amplifier drives an Esterline Angus graphical



FIGURE 102. View in aperture of 10-in. ellipsoidal reflector as assembled for field calibration. The AX-90 hydrophone in foreground is used as a source and rotated in a plane normal to the receiving hydrophone stem.

pass type with optional cutoff frequencies of 1, 5, 10, 20, 30, 40, 60, 80, and 100 kc. The other is a low-pass type with the same optional cutoff frequencies. With this arrangement channels of different widths and boundary frequencies can be chosen. The actual sound pressure in dynes per square centimeter is proportional to the voltage recorded. The block diagram of the equipment is shown in Figure 104. Photographs of the racked units are shown in Figure 105.

The Mark 3 equipment includes a hydrophone pre-amplifier and four other amplifiers to analyze the spectrum of the input signal over the range of 10 to



FIGURE 103. Same as Figure 102 but assembled at 90 degrees for calibration in a plane containing the receiving hydrophone stem.

recorder, so a continuous record of all four octaves can be kept. The gain of each amplifier is about 80 db. Front- and rear-view photographs of this equipment are shown in Figure 106.

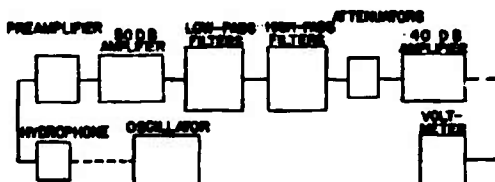


FIGURE 104. Block diagram of laboratory noise measuring system.

For calibration of either amplifier system a known voltage is inserted in the circuit at the connection to the hydrophone crystals. The output produced by this calibrating voltage is measured and the readings are converted to equivalent sound pressure from a hydrophone calibration chart supplied by the manufacturer.

CONFIDENTIAL

2.9 SHOP FACILITIES

The construction of the apparatus, instruments, and experimental test models used by a research laboratory requires the services of a variety of shop and erection facilities. While all types of work are involved, the most important and the most difficult



Figure 105. Front and rear views of laboratory amplifying and filtering equipment for 1- to 100-kc range.

- | | |
|--------------------|--------------------------------|
| A. Preamplifier | E. Voltmeter |
| B. 40-db amplifier | F. Hewlett Packard oscillator. |
| C. Attenuator | G. Low-pass filter |
| D. 50-db amplifier | H. High-pass filter |
| I. Hydrophone. | |

to obtain in volume is precision machine work. Instruments and models particularly require the use of specialized equipment and skills not readily available in most general shops. Ordinary construction and

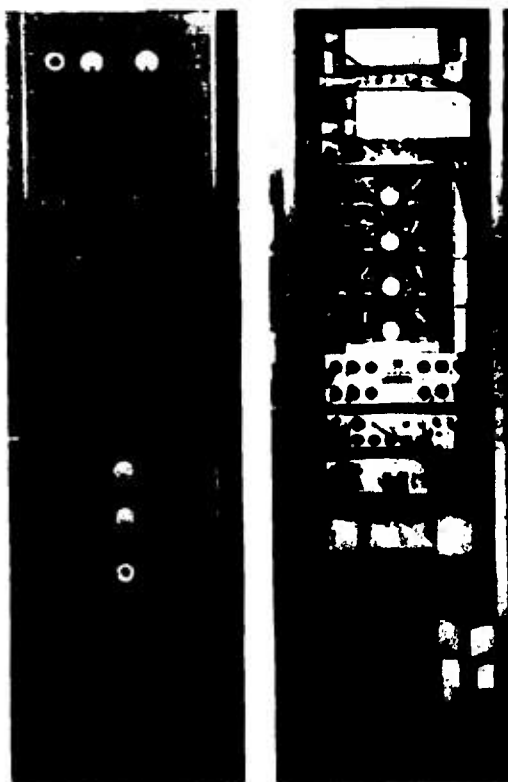


Figure 106. Front and rear views of Naval Ordnance Laboratory Mk 3 acoustical unit.

machine work can be done in most general shops, but the special handling associated with single jobs causes difficulty in maintaining a continuous flow of work. Therefore, some shop equipment directly under the laboratory supervision becomes a necessity.

2.9.1 Model Shop

The shop facilities of the Hydrodynamics Laboratory were designed to handle the specialized needs of a research program. In addition to the normal facilities for handling the general maintenance and rough work, a model and instrument shop is available which is equipped to do all types of lathe and mill work, pantograph reproductions, and precision drilling, and

CONFIDENTIAL

to take advantage of casting and other metal forming procedures. A general view of this shop is shown in Figure 107. Among its special features are the three-dimensional Gorton pantograph machine for construction of apparatus and models requiring scaled duplications of curved and warped surfaces, surface grinders and grinding attachments for holding surface finishes to desired tolerances, and electric and induction furnace equipment for specialized casting and heat-treating operations.

To control the accuracy of the work the shop is equipped with a toolmaker's microscope for precise measurements and a binocular microscope for use while working on small precision parts. Johannson gauge blocks are used for miscellaneous precision setups as well as for standardizing micrometer equipment.

SPECIAL TECHNIQUES

Special adaptations and attachments for the machine tools have been developed to meet the particular requirements of model construction. As an ex-

ample, the technique used in forming model bodies will be described in more detail. A primary spline jig four times model size is produced on the Gorton pantograph machine from data giving the two coordinates of the body shapes and the angle of the normals to the curve. In this operation, as shown in Figure 108, the milling table is set to the coordinates and the drill-guide jig on the tracer table is set to the angle of the normal. By this method a double line of dowel holes is accurately drilled and reamed in one operation along the shape curve. Steel dowel pins pressed into these holes securely hold a spring steel spline in the proper curve. From this primary spline jig a model-size cam plate is produced on the same machine, as shown in Figure 109.

In turning the model part the cam plate is mounted on a jig attached to one of the lathes and guides the cross feed by means of an air-operated piston, while the carriage is moved along by the power feed. Two views of this setup are shown in Figure 110.

The advantage of this technique is that the personal element in smoothing in curves from coordinate data



FIGURE 107. General view of model shop.

CONFIDENTIAL

is reduced to a minimum and any number of accurate duplicate model shapes may be produced quickly.

MAINTENANCE AND REPAIR

The general repair and maintenance of the heavier and rougher apparatus is handled by a maintenance



FIGURE 108. Gorton pantograph machine.



FIGURE 109. Production of model-size cam plate.

shop using different equipment. Lathe and drill press equipment, in addition to portable power tools and hand tools, are available here.

General carpentry and cabinet work is carried on in a shop operated jointly with the Soil Conservation Service Laboratory on the CIT campus. Miscellaneous power tools are available there.

OUTSIDE SHOPS

During the course of the NDRC sponsored projects, it has been necessary to rely on the services of many outside shops to supplement the volume of



FIGURE 110. Two views showing cam plate in use.

work handled in the Hydrodynamics Laboratory shop itself. The additional organizations which contributed most effectively in the program include the Mount Wilson Observatory shop in Pasadena, whose facilities were made available on a cost basis through the courtesy of the Carnegie Institution of Washington; the Fred C. Henson Company, a maker of scientific instruments in Pasadena; and the Astrophysics Machine Shop and Optical Shop, both located on the CIT campus.

CONFIDENTIAL

Chapter 3

EFFECT OF PROJECTILE COMPONENTS ON THE FLOW DIAGRAM

3.1 INTRODUCTION

THE HYDRODYNAMIC BEHAVIOR of submerged moving bodies is dependent upon the pattern of relative motion of the fluid with respect to the body. All the forces arising from such a system of motion are caused by the interaction between the body and the fluid. The changes in momentum in various directions caused by the reactions between body and fluid are measures of the forces. With each body shape there results a particular field of fluid velocities and therefore a particular set of forces. Thus there are two ways to obtain hydrodynamic forces for the analysis of a body's behavior in motion. First, by direct measurement; second, by observing what happens to the fluid whose motion the body affects. In many respects the latter method, while much the more difficult, is the more important. In general, direct measurements give overall results. Special measurements may indicate but do not explain the role played by the various components of a body shape. However, a realization of the ways by which various shapes affect the flow leads not only to an evaluation of the forces but to the ability to predict the force changes obtained by shape modification.

The laboratory has found in the flow line diagrams produced in the polarized light flume the means of visualizing, qualitatively at least, the relation between body geometry and the resulting flow.³ Thus even though the picture is too incomplete to permit actual evaluation of forces and moments, it represents an extremely important design aid. For these reasons the assemblage of flow line diagrams for various projectiles and projectile components which grew up in the course of this project is included in this chapter, prefacing several general discussions of submerged body behavior. It can be used as a reference chapter in which the reader's picture of fluid motion about various shapes can be refreshed from time to time.

The diagrams are constructed from actual experimental determinations of the flow. The zones of local separation and turbulence generation are drawn from visual observation of the bentonite suspension. Shear patterns are made visible by transmitted polarized light, and local flow directions are determined

through explorations with needle probes and thread streamers. The diagrams are intended to represent flow directions only. Furthermore, they are, in general, limited to the flow in the plane containing the axis of symmetry of the body shape. While this representation does not give the entire picture of the flow around yawed three-dimensional bodies, it does provide an essentially accurate picture of the sense and relative magnitudes of the velocity changes introduced by yawing different shapes. In cases for bodies with stabilizing and control surfaces, the flow over these surfaces is indicated for planes away from the axis.

The scheme of presentation of diagrams in this chapter is based on separation of the projectile into its components, the nose, body, afterbody, and tail structure, for individual and systematic study. While the exact final diagram for any complete body is the result of a complex interaction between the effects of each component, examples will show how it is still possible, with judicious interpretation, to assemble a qualitative picture for the whole. For each component several series of diagrams for certain basic families are given, followed by diagrams for specific designs that were devised by modifying the basic profiles. For all bodies the flow is shown around the unyawed shape and around the body yawed to 10 degrees.

3.1 NOSE SHAPES

3.1.1 Basic Design Shapes

Selection of the projectile nose shape depends upon the requirements of load-carrying capacity (volume), length for a given diameter, fluid friction resistance, and cavitation limits. The effects of each of these requirements are very conveniently studied by systematically investigating families of shapes. While the families possible are numberless, the ones included here stem from the most familiar and commonly used shapes; ellipsoids, ogives and spherogives, hemispheres, cones, and various truncated shapes including the square-end cylinder. Within each of these families will be found a wide range of all the variables just listed so that a series of flow

Figure 2 shows the flow line diagrams for a group of these ellipsoid noses. In this series note that for all shapes finer than the hemisphere, smooth flow without separation is obtained. With the hemisphere and blunter noses separation occurs near or ahead of the maximum diameter.

OGIVES

The ogive as commonly defined is pointed. Blunt ogives can be obtained if the geometrical definition is modified slightly by assuming that for radii less than 0.5 caliber (the hemisphere) the nose face is a flat disk drawn tangent to the ogive arc. The limiting case is then the square-end cylinder where the ogive radius is zero. Figure 3 shows the pointed series, and Figure 4 the blunt or small-radius series. Pointed ogives result in smooth flow patterns without visible

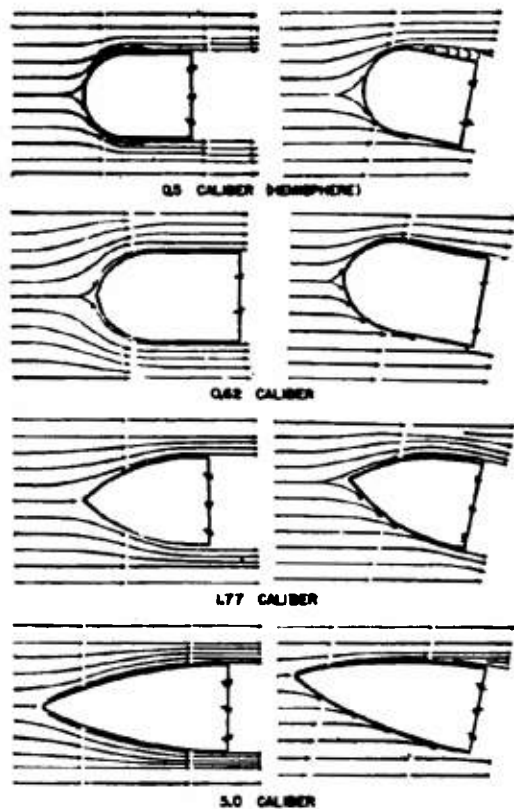


FIGURE 3. Ogives.

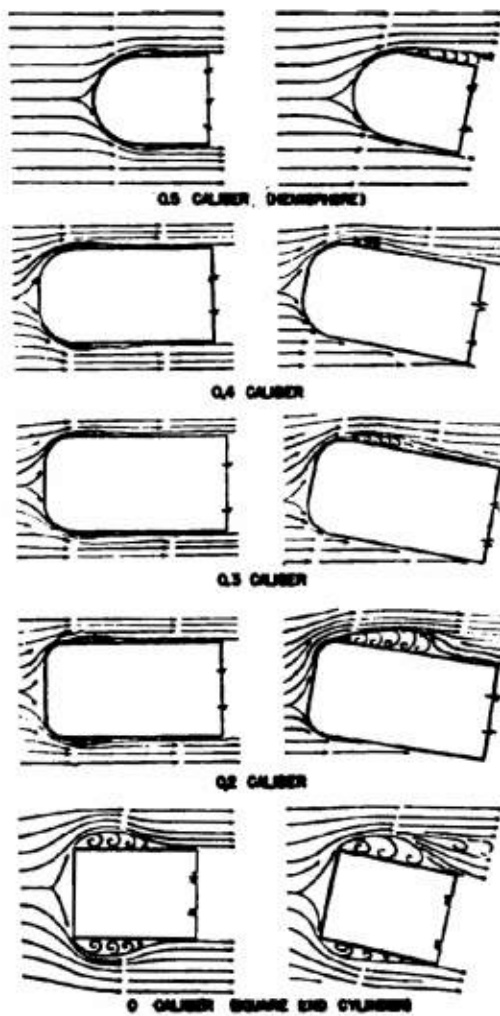


FIGURE 4. Small radius ogives.

separation even when yawed at 10 degrees. The hemisphere and the small-radius series, however, show increasing separation to the maximum obtained with the square-end cylinder.

Beginning with the largest radius ogives, the drag should be high because of extra skin friction. As the radius is reduced, however, a minimum should be reached, beyond which for shorter radii the drag should grow again as a result of separation and consequent increase in form drag. For the square-end cylinder, the drag is all form drag and no skin friction.

SPHEROGIVES

The pointed ogive is the shape normally used for noses on artillery shells and small arms ammunition. For those cases where the velocity is above sonic, the sharp point is important in reducing the drag resulting from shock waves. For velocities below the critical sonic values, however, ogives often may be shortened, while still maintaining the basic advantages of the slender nose, by replacing a portion of the point with curves forming blunt tips. If the spherical segment is used there results the spherogive. For any given ogive a series of noses can be formed by drawing in spherical segments with larger and larger radii. Each will include a greater and greater "half angle" measured between the axis and the point of tangency of the sphere and the ogive. Such a family is shown in Figure 5. If the sphere half angle is maintained constant, the nose assumes different proportions as the ogive

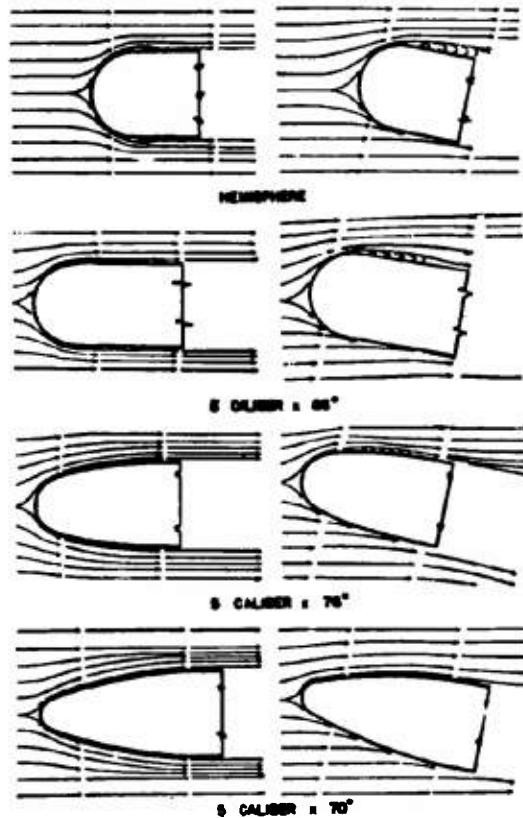


FIGURE 5. Spherogives with constant caliber ogives.

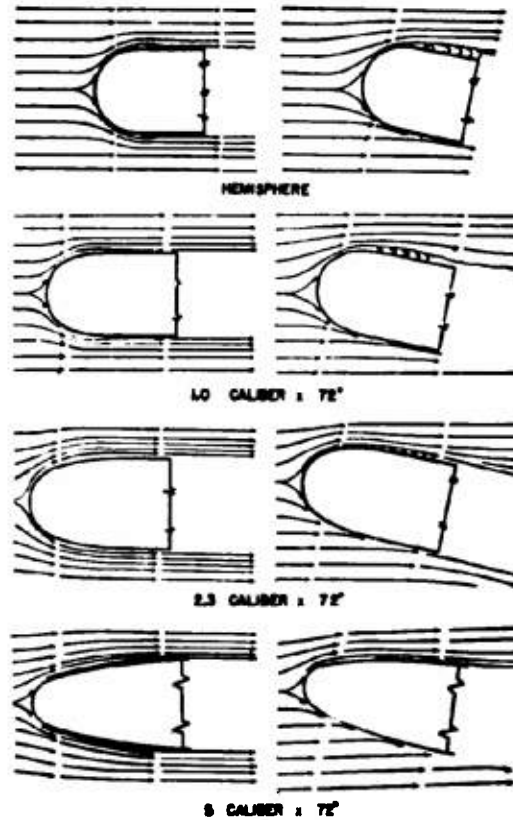


FIGURE 6. Spherogives with constant sphere half angle.

radius is varied. Figure 6 illustrates this family. In both Figures 5 and 6 the hemisphere appears as the limiting case.

Several things are apparent on examination of Figures 5 and 6. First, for the 5-caliber series, separation of the flow around the yawed projectile occurs for sphere half angles larger than 72 degrees. (Note bottom diagram in Figure 6 as well as Figure 5.) Second, for the constant 72-degree half-angle series, separation becomes successively worse as the ogive radius is decreased. Note also that all the spherogives shown permit smooth flow at zero yaw without separation so that for bodies which will operate with small yaws the spherogive offers a possible way of obtaining lower length in calibers or a larger volume for given overall length.

On bodies with sharp curvatures separation occurs where the curvature requires too rapid a deceleration for the flow to follow the body. Separation from this

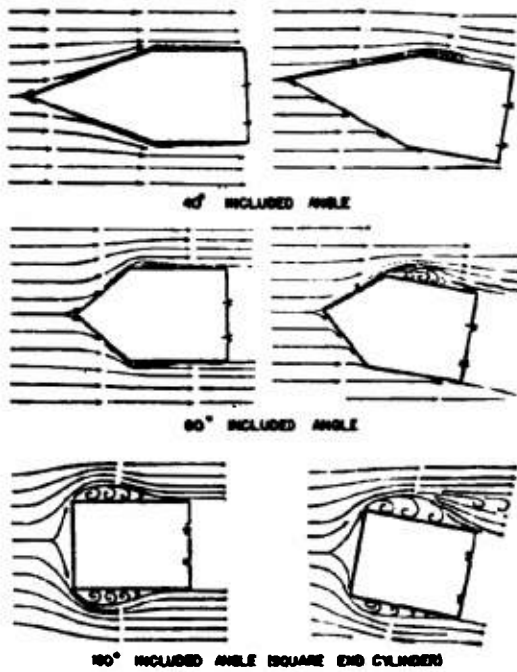


FIGURE 7. Conical tapers.

cause is also an indication of the probable tendency to cavitate since low pressures will be obtained in the zones of maximum flow curvature usually occurring just ahead of the separation zone. Thus the examples in Figures 5 and 6 indicate that within limits the length of nose can be shortened by using spherical tips without affecting the cavitation behavior.

CONICAL TAPERS

Tapers in modified forms are used on many pro-



FIGURE 8. Conical tapers and truncated ogives.

jectiles. Simple cones are not regarded as satisfactory because of the flow separation at the juncture with the cylindrical section, even for very small included angles. Figure 7 shows examples of this shape with the square-end cylinder as the terminal condition. These same shapes with examples of truncated ogives are shown in Figure 8.

TRUNCATED OGIVES

Flat-faced noses formed by truncating ogives have

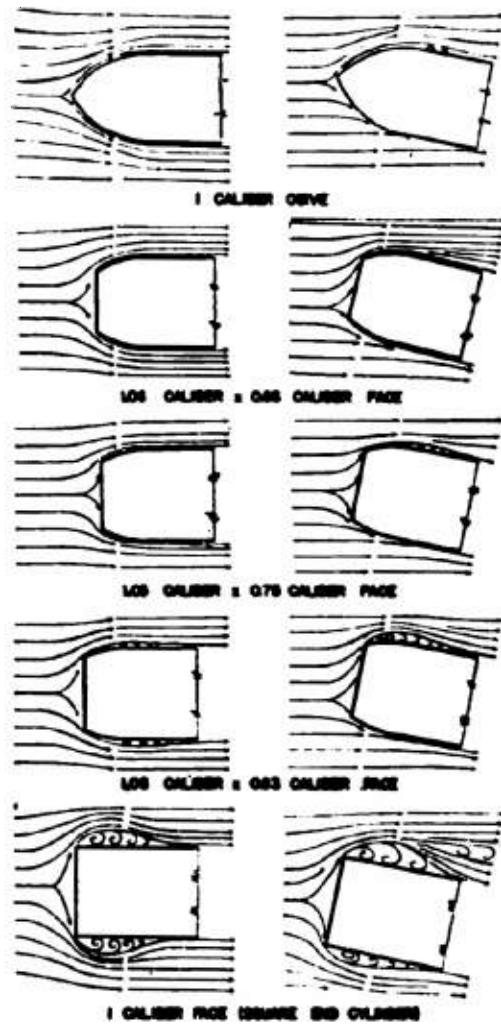


FIGURE 9. Truncated ogives. These noses are described by the radius of the circular ogival arc and the diameter of the flat face, both measured in calibers.

proved important in permitting satisfactory water entry for air-launched projectiles. On striking the

surface the flat face with its relatively sharp edge aids in creating a cavity of proper diameter to envelop the projectile and to avoid interference between the tail and water. In addition, as a nose of this type yaws the flat face deflects fluid in the direction of yawing, giving a reaction in the opposite direction. This effect, which occurs whether the nose is completely submerged or is wetted only on the disk, gives a stabilizing moment that tends to keep the projectile



FIGURE 10. Modified hemispheres.

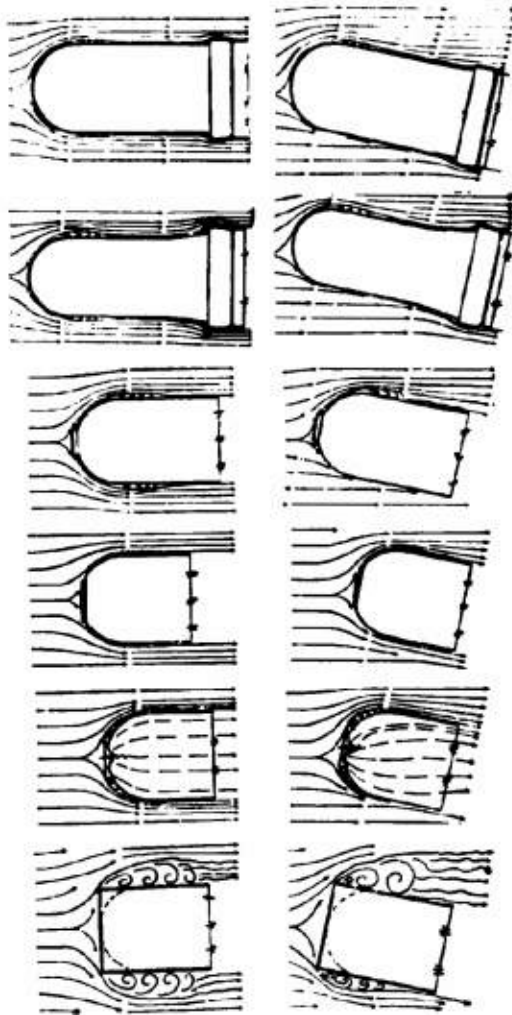


FIGURE 11. Modified hemispheres.



FIGURE 12. Modified ogives and spherogives.

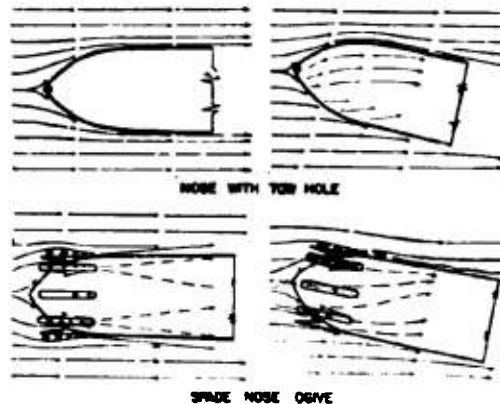
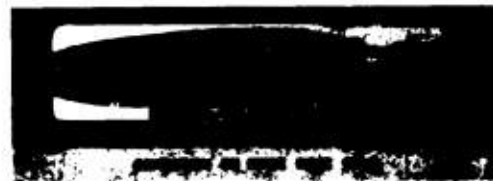


FIGURE 13. Modified ogives.

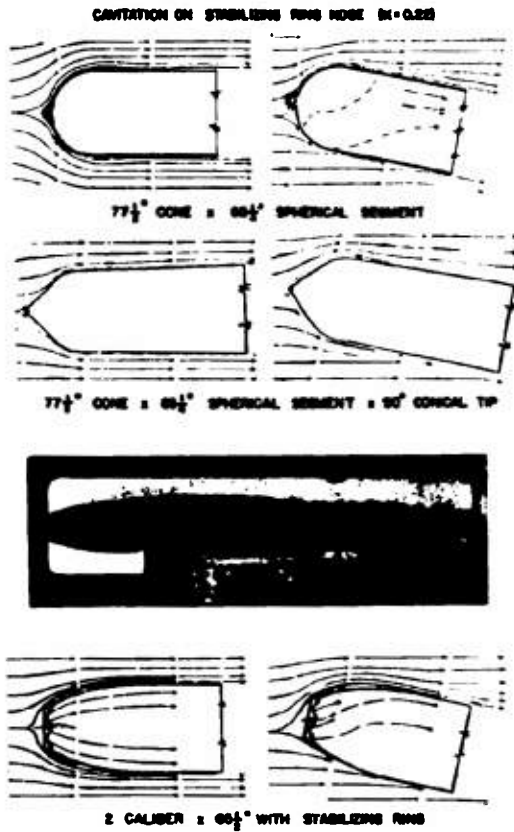


FIGURE 14. Modified spherogives.

on course. This effect of the nose on the flow is shown clearly in Figure 9 for completely submerged conditions.

Figure 9 also illustrates the effect of truncating an ogive to form successively larger disks. Note that for the submerged case if the velocity and pressure conditions are such that cavitation does not occur, relatively large disk areas can be used without excessive flow separation at the edges and consequent relative increase in form drag.

These noses provide a very low l/d ratio (relatively large volume) when drag and cavitation are unimportant.

MODIFIED HEMISPHERES

The hemisphere in modified form is one of the most widely used shapes for all types of projectiles. In Figures 10 and 11 are shown several, including the

extreme example of the "pickle barrel," a cylindrical shell extending the full length of the normal nose. Reading down in Figure 11, the third and fourth diagrams are noses with fuse projections, the fifth shows a version of a Kopf ring.

The pickle barrel is designed to stabilize an air-launched torpedo during its air flight. It has some of the characteristics of the truncated ogives and the square-end cylinder in that on yawing a stabilizing moment results from the pressures arising on the nose as the air is deflected laterally in the direction of

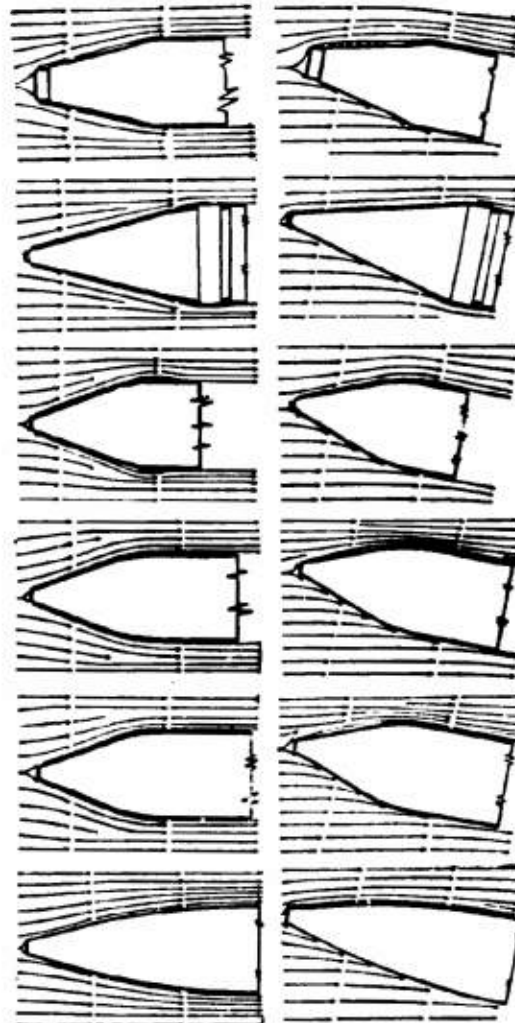


FIGURE 15. Modified tapers.

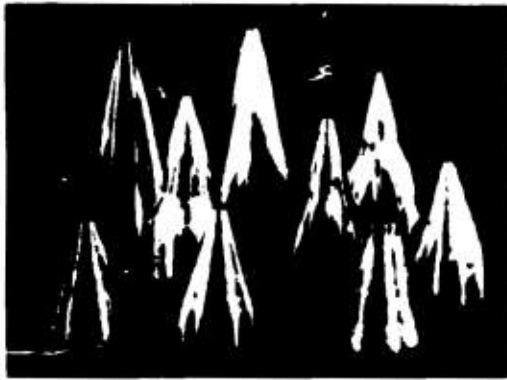


FIGURE 16. Modified tapers.

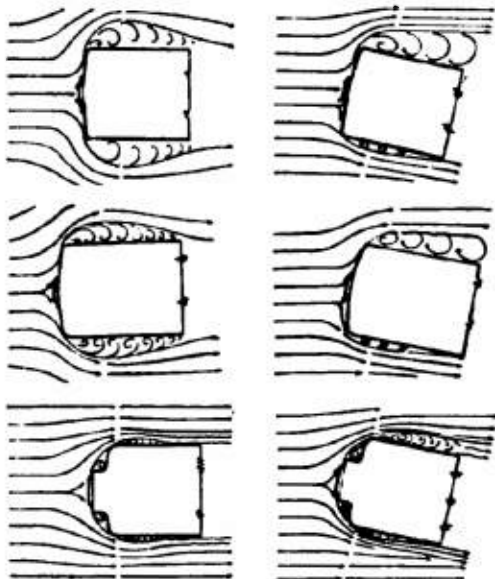


FIGURE 17. Modified square-end cylinders.

yawing. This barrel is destroyed on entry and hence does not influence the underwater run. The Kopf ring is designed to improve the air-water entry of an air-launched projectile. It does so by creating a clean cavity of the proper diameter to contain the projectile and avoid undue interference and by a tendency to produce a stabilizing moment for small yaws in much the same manner as the square-end cylinder. It is clear from the flow line diagrams that on becoming submerged the extra turbulence created by this ring will increase the drag of the projectile.

MODIFIED OGIVES AND SPHEROGIVES

Examples of modified ogives and spherogives are shown in Figure 12, with flow diagrams in Figures 13 and 14. Included with these noses are two modifications designed to improve water entry, the spade nose in Figure 13 and the Kopf stabilizing ring in Figure 14. The flow line diagrams show that both devices introduce extra turbulence and drag. Photographs of

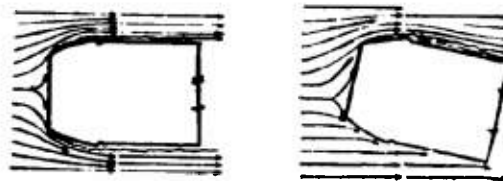


FIGURE 18. Modification of a truncated ogive.

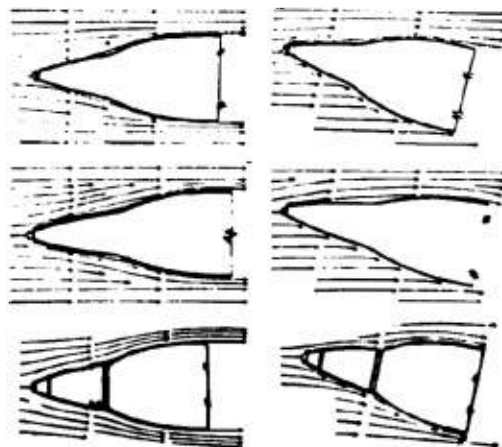


FIGURE 19. Compound-taper ogives.



FIGURE 20. Noses with common length.

CONFIDENTIAL

full cavitation bubbles are shown for both. As is discussed in Chapter 4, cavitation cavities so produced are similar to the air cavities obtained on entry. Note that the cavity actually forms on the Kopf ring and tends to envelop the projectile. On the other hand, note that each spade forms an individual cavity but that the projectile as a whole is not enveloped so that considerable interference and resultant side force can be expected during entry.

MODIFIED TAPERS

While simple conical tapers are not used normally for projectiles, tapers modified mainly by eliminating the sharp discontinuity at the base of the cone are used. The examples in Figures 15 and 16 are for a series of low-velocity rockets. Note that with moderate radii at the juncture of cone and cyl-

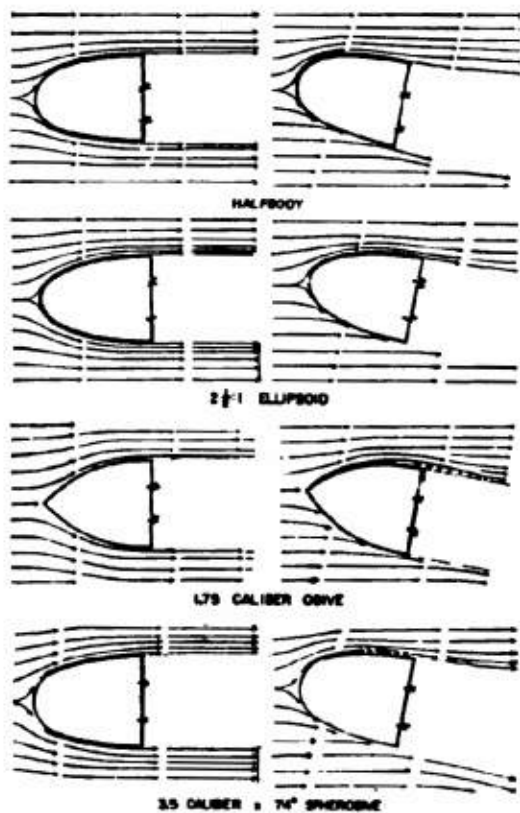


FIGURE 21. Noses with the same l/d back to the maximum diameter.

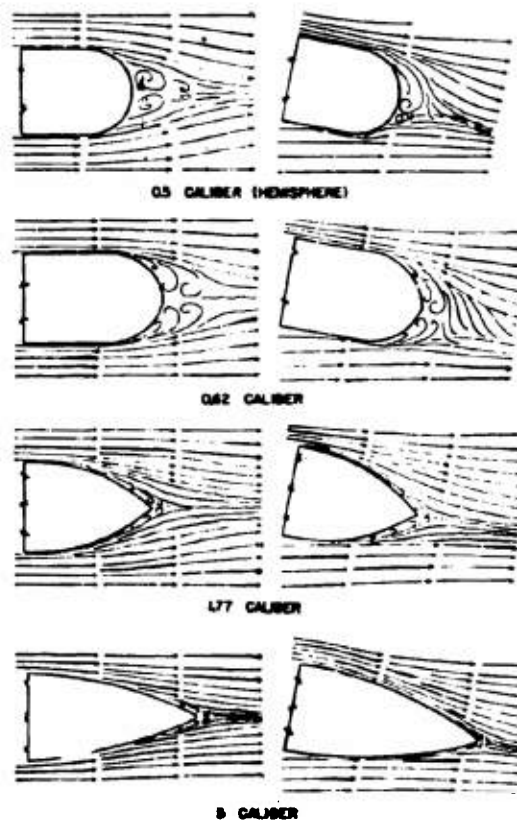


FIGURE 22. Ogives.

inder, smooth flow without separation can be obtained.

MODIFIED SQUARE-END CYLINDERS

Eliminating the sharp corner reduced the degree of separation and hence the drag. Noses with moderate drag coefficients, but still providing for good water entry and also having the desirable stabilizing moment for small yaw angles when submerged, can be obtained this way. These noses, illustrated in Figure 17, are all for air-launched depth charges.

MODIFIED TRUNCATED OGIVE

Compared with Figure 9 the diagrams in Figure 18 show little influence of the small irregularities of the

nose profile. The edge of the blunt face provides sufficient separation (even though small in magnitude) and hence disturbance in the boundary layer so that there are no extra contributions from the downstream projections.

COMPOUND-TAPER OGIVES

These noses are used for high-velocity projectiles. Consequently their flow line diagrams are of interest

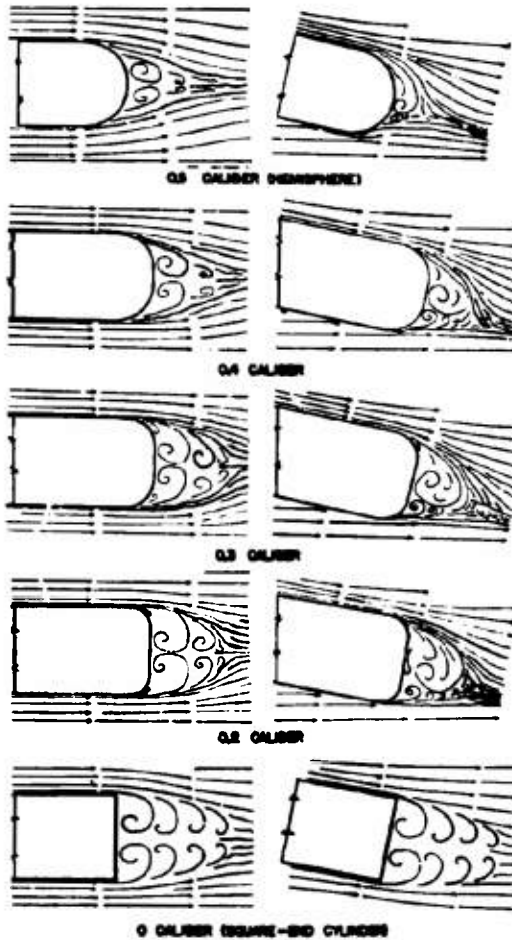


FIGURE 23. Small-radius ogives.

only for the short period of acceleration when the velocity is below the velocity of sound. The flow diagrams of Figure 19 which are for such noses merely show that when yawed the fluid is deflected in the

opposite direction so that cross forces and destabilizing moments in the direction of yaw can be expected. Projectiles with such noses must be stabilized, at least during this accelerating period, with fins or by spinning.

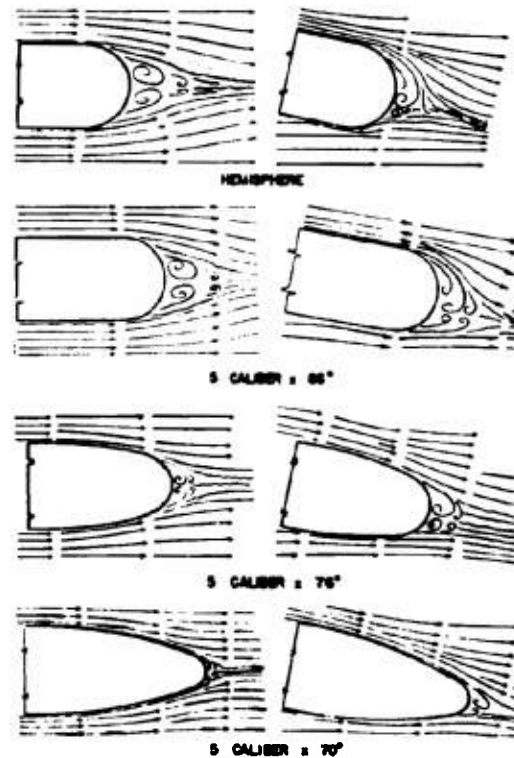


FIGURE 24. Spherogives with constant caliber ogives.

NOSES WITH COMMON LENGTH

A simple example of application of the flow line diagram is shown in Figure 21 for the noses pictured in Figure 20. The four noses are selected to give the same length in calibers, l/d , from the tip back to the maximum diameter. The prismatic coefficient, the ratio of the nose volume to the volume of a circular cylinder of length l and diameter d , is listed for each as follows:

Half body	0.74
2½-to-1 ellipsoid	0.67
1.75-caliber ogive	0.56
3.5-caliber by 74-degree spherogive	0.79

The only significant difference in the diagrams occurs

for the yawed condition. Note that separation occurs for the two bodies having the maximum and minimum volumes. The ogive radius is so sharp that separation occurs on the ogive itself. The spherogive tip is so large that it causes separation. This example makes it clear that "fineness" alone is not a sufficient criterion for selecting a low drag, anticavitating nose.

OGIVES

In this and succeeding series the effect of bluntness on the wake formed by separation is emphasized. Note that even for the 5-caliber ogive shown in Figure 22 the flow leaves the body surface before the tip is reached. The extreme condition, of course, is for the square-end cylinder in the small-radius series shown in Figure 23.

(Comparison with Figures 3 and 4 emphasizes that a shape suitable for application as a nose may not be satisfactory as an afterbody. For example, the 1.77-caliber ogive when used as a nose causes no serious disturbance but, when used as an afterbody causes an undesirable eddying wake. Thus it is necessary that the afterbody be finer than the nose to produce a

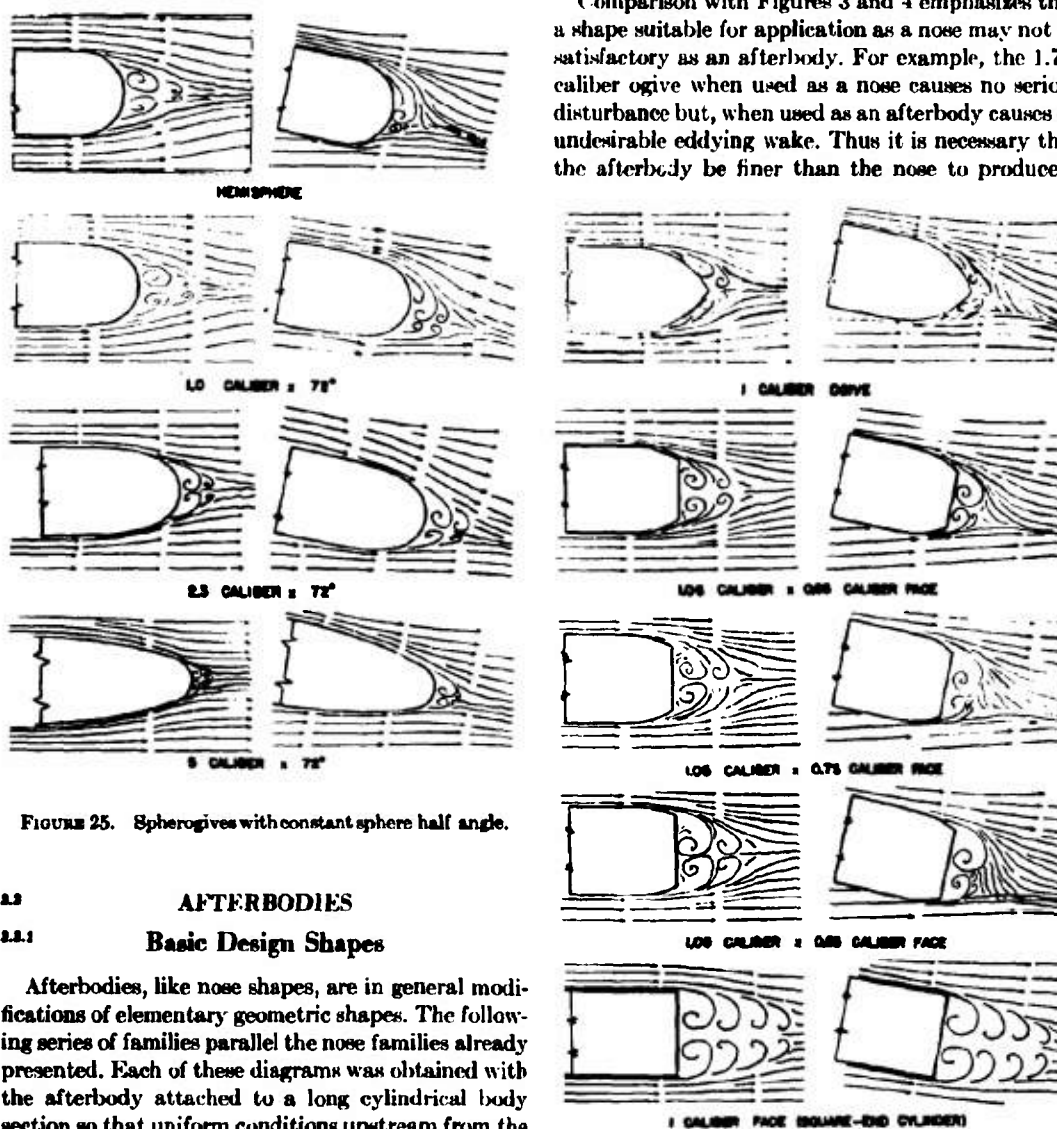


FIGURE 25. Spherogives with constant sphere half angle.

FIGURE 26. Truncated ogives.

2.2 AFTERBODIES
2.2.1 Basic Design Shapes

Afterbodies, like nose shapes, are in general modifications of elementary geometric shapes. The following series of families parallel the nose families already presented. Each of these diagrams was obtained with the afterbody attached to a long cylindrical body section so that uniform conditions upstream from the afterbody existed.

balanced design with equally satisfactory flow over both ends of the projectile.

SPHEROGIVES

The diagrams in Figures 24 and 25 show some similarity to those for the ogives in Figure 22. Note particularly that rounding off the 5-caliber ogive tip (Figure 22) to form the 5-caliber by 70-degree spherogive (Figure 24) produced very little effect on the flow diagram, particularly at zero yaw.

TRUNCATED OGIVES

The top two diagrams in Figure 26 show that some large portion of the ogive tip can be removed without affecting the flow appreciably. This is similar to the effect already observed in forming the spherogives.

Comparison of Figure 26 with Figure 22 indicates that truncating the 1.05-caliber ogive to a face as large as 0.75 caliber produces a disturbance whose magnitude is about equal to that for a 0.62-caliber ogive.

CONICAL TAPERS

Tapers with small included cone angles show marked improvement over blunt afterbodies. Figure 27 serves to emphasize, however, that severe dis-

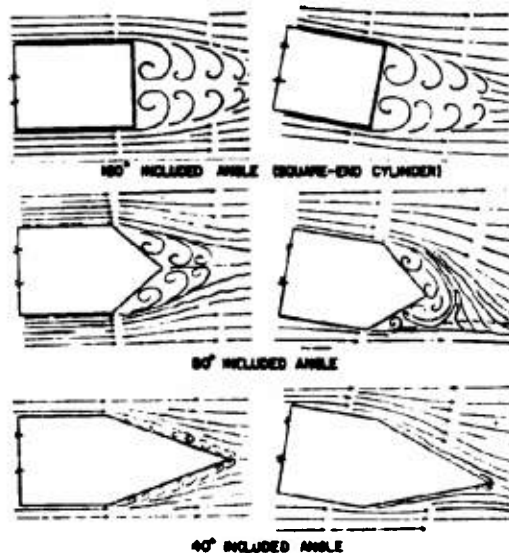


FIGURE 27. Conical tapers.

turbance and consequent undesirable hydrodynamic effects are still obtained unless precautions are taken to eliminate the sharp discontinuity at the base of the cone.

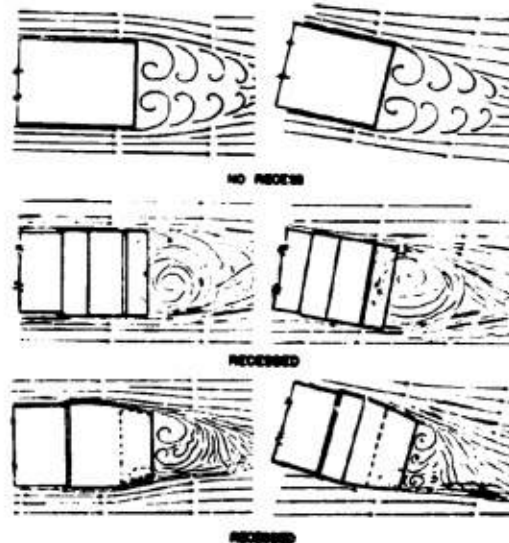


FIGURE 28. Spiral flow produced by recesses.



FIGURE 29. Afterbodies followed by booms.

RECESSED AFTERBODIES

Recesses in blunt afterbodies produce an asymmetrical condition that results in a definite spiral to the flow in the wake. This effect, which is in contrast to the normal wake obtained with the square-end cylinder, has been observed for a variety of shapes with large recesses at the trailing end, as shown in Figure 28.

2.3.3 Specific-Purpose Afterbodies

AFTERBODIES FOLLOWED BY BOOMS

Various projectiles, particularly rockets, employ

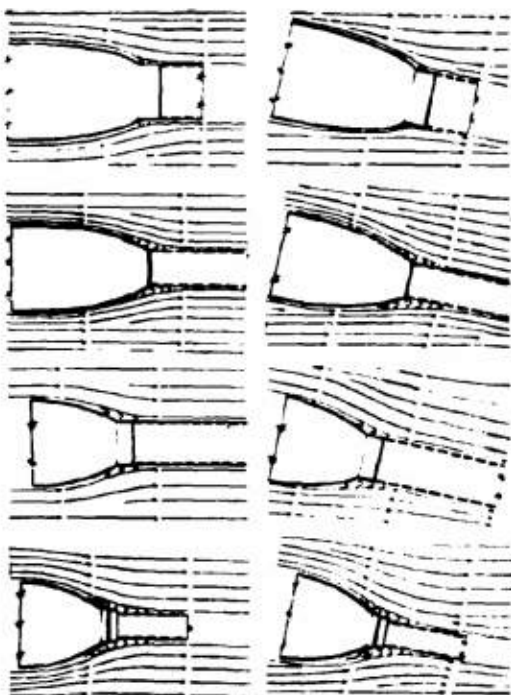


FIGURE 30. Modified ogive afterbodies followed by boom.

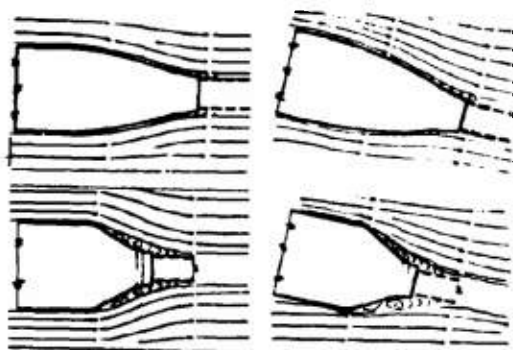


FIGURE 31. Modified taper afterbodies followed by boom.

booms between the main body and the tail surfaces. Figure 29 shows a series of afterbodies designed for use with booms. Some of these are modified ogives and some are more properly classed as tapers. The flow diagrams were all obtained with the booms in place. As the diagrams in Figures 30 and 31 show, the

flow separation in each case occurs along the surface of the afterbody proper so that irregularities at the boom connection contribute little additional disturbance.



FIGURE 32. Fine afterbodies.

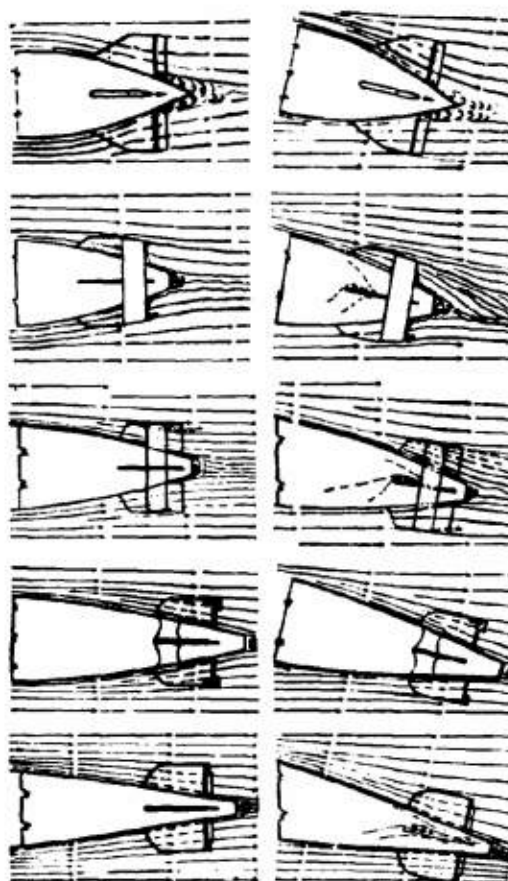


FIGURE 33. Fine afterbodies.

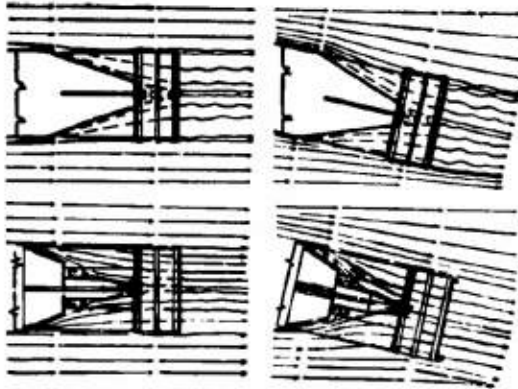


FIGURE 34. Modified conical afterbodies.

FINE AFTERBODIES

Several torpedo afterbodies whose shapes are approximately ogival, or ogival with conical tips, are shown in Figure 32, with their flow diagrams in Figure 33. The importance of using the longer, finer shapes for afterbodies is emphasized here. A relatively fine body is necessary before flow is obtained without appreciable disturbance ahead of the trailing tip.

Figure 34 shows two depth bomb afterbodies of modified cones. The relative magnitudes of the disturbances and the resulting wakes are indicative of the degree to which discontinuities in the surface profile have been suppressed.

The influence of tail structures such as shown in these figures will be discussed in a later section in this chapter.

ROCKET NOZZLES

Rocket nozzles are located either at the end of a boom, and hence are of a smaller diameter than the main body, or are incorporated as part of the afterbody proper. Nozzles on booms are shown in Figures 35 and 36. Nozzles in afterbodies are shown in Figure 37.

Elimination of disturbances by streamlining can be readily accomplished in various degrees up to the point where the nozzle area equals the boom diameter (compare last diagram in Figure 35 with Figure 36). It should be noted, however, that such streamlining of the flow is not a desirable feature for all cases. As will be discussed in more detail with respect to tail structures, the drag from the disturbances such as

shown in Figure 35 produces a stabilizing moment when the projectile is yawed. Consequently for certain low-velocity projectiles, where drag is relatively unimportant, this effect may be a desirable contribution.

The diagrams in Figure 37 illustrate examples with various degrees of streamlining. The effects of the tail surfaces (fins and ring) such as shown in Figures 35, 36, and 37 will be discussed later.

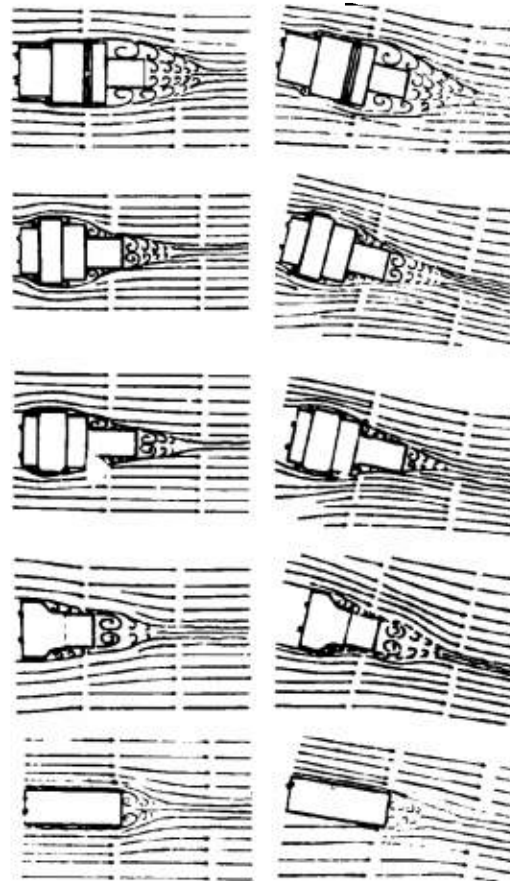


FIGURE 35. Rocket nozzles.

EFFECT OF COMPONENTS OF A NOZZLE ASSEMBLY

Figure 38 illustrates a typical example of varying one of the components of a tail nozzle assembly.

Figure 39 shows the effects of step-by-step additions to a complete assembly. As stated in the intro-

duction, the flow diagram for the complete projectile is not necessarily the summation of the diagrams for the individual components. In this example each component introduces a radical change in the diagram.

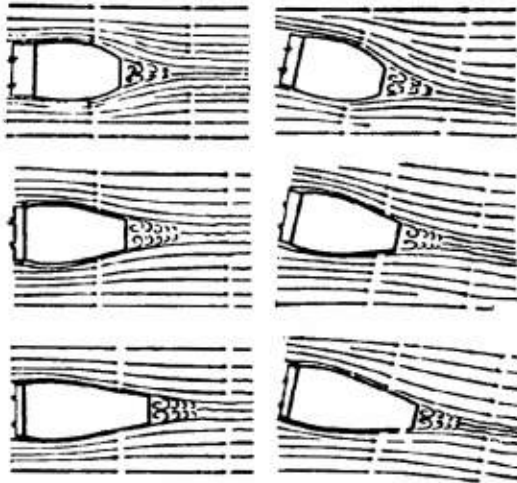


FIGURE 36. Rocket nozzles.

3.4

TAILS

3.4.1

Purpose of Tails

Generally speaking it is the purpose of tail surfaces to provide an otherwise unstable projectile with a desired degree of static and dynamic stability. In the case of certain missiles, such as torpedoes, adjustable tail surfaces permit control of the projectile trajectory as well.

3.4.2

How Tails Work

Tail surfaces are effective in producing static stability because, when a projectile yaws, the tail deflects some fluid and as a result is subjected to a force proportional to and in the opposite direction to that at the change in the fluid momentum. This force will have a lateral or cross force component and a drag component. The resultant of this force and the skin friction drag on the tail will cause a moment about the projectile's center of gravity. The fact that both drag and cross force components can be made to produce stabilizing moments leads to two methods of creating a required moment. It can be obtained either by a high-drag (and usually low-lift) shape or by a

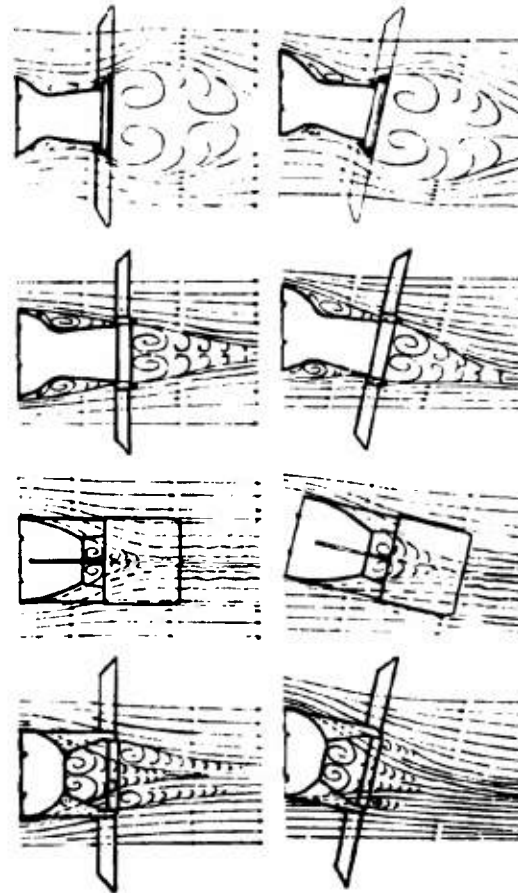


FIGURE 37. Rocket nozzles.

high-lift (and usually low-drag) shape. Vector diagrams illustrating these two combinations are shown in Figure 40. It is clearly seen that for the same resultant force the moment is much larger if a high cross force rather than a high drag is obtained. Nevertheless, some designs do make use of high drag as a means of getting additional stabilizing moment. The normal designs of fin tails, ring tails, and square box tails are structures intended primarily to produce large cross forces with yaw.

In addition to producing moments as described, when a projectile yaws, stabilizing surfaces also provide additional damping forces, and hence damping moments, to contribute to the dynamic as well as static stability. This effect cannot be studied by the flow line diagrams which are for the static, or steady-

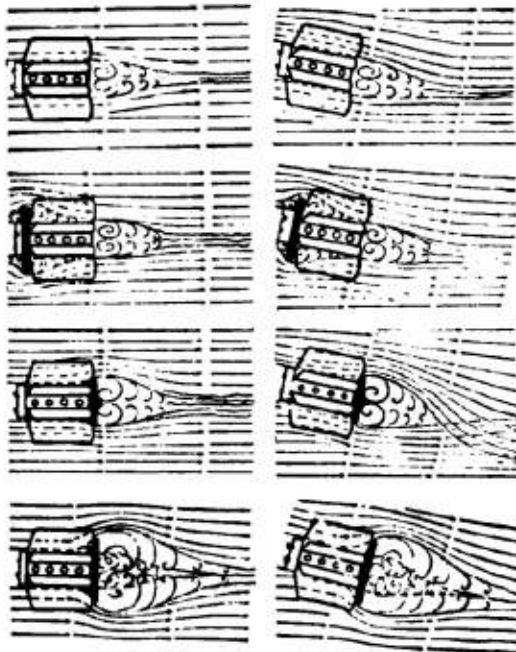


FIGURE 38. Effect of tail disks on terminal disturbance.

state, conditions only. A more thorough discussion of stabilizing surfaces and static and dynamic stability, together with quantitative test data, is given in Chapters 9 and 11.

3.4.3 Plain Fin Tails

FIXED AND COLLAPSIBLE FINS FOR ROCKETS

Figures 41 and 42 illustrate four very different types of fin tails for rockets. Fins on the first three are fixed, fins on the last (bottom diagram) are designed to fold forward for insertion into a launching tube of the diameter of the main body of the projectile. On launching, the fins fly open as shown for air travel.

At zero yaw, tail fins are ineffective. When yawed, the diagrams illustrate how the fluid is given a change in direction producing a lateral force on the fin surface. Within certain limits a given force can be obtained by a long fin with a short span, or by a very narrow fin with a wide span. The collapsible fins are of the latter type. Figures 43 and 44 show three designs of collapsible fins for the bazooka rocket

suggested to replace the original tail shown second from the top in Figure 44. Both radial and raked fins are illustrated. Actually the radial fins in these figures produce much more cross force than the original tail. The only essential difference in the flow picture is caused by the flanged fin tips in the top two diagrams. With the radial fins the flange is in-

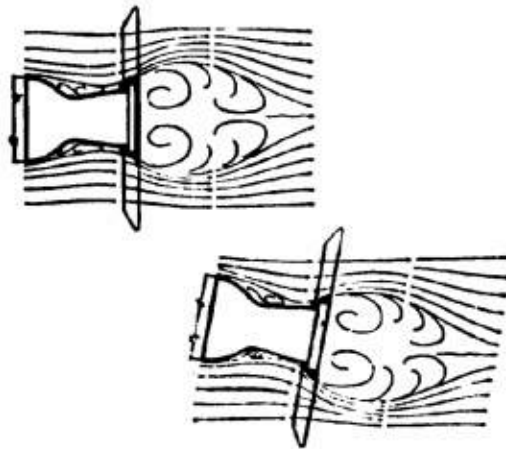
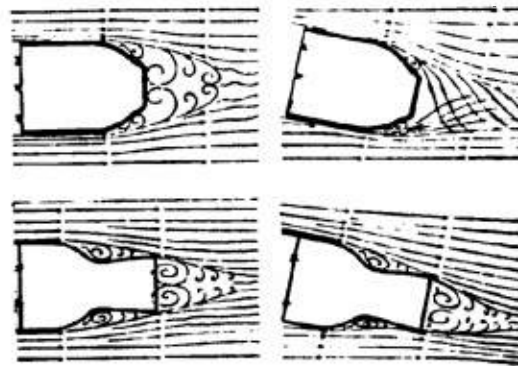


FIGURE 39. Effect of components of rocket nozzle afterbody.

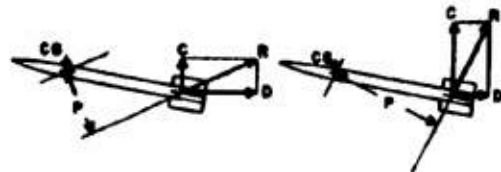


FIGURE 40. Diagram showing the effect of change of moment arm P as cross force and drag change even though resultant force on tail remains unchanged.

clined to the flow resulting in some disturbance at zero yaw. The raked fins are tilted back until the flange is in line with the flow and hence causes no disturbance.

The long narrow vanes used on collapsible fin tails are subjected to severe bending forces during the initial launching period before the fins unfold. Figure 45 shows the flow over a typical folded tail, a typical diagram of the forces produced with yaw, and a photograph of a fin which was bent from the folded position during tests in the water tunnel. As the vector diagram indicates, a large normal force is easily obtainable on the fin at some distance forward of the hinge. The resulting bending moment can easily damage an unreinforced fin. Note that two of the tails in Figures 43 are constructed with fins reinforced with longitudinal flutes.

FIN TAILS WITH ADJUSTABLE RUDDERS

Torpedoes require adjustable tail surfaces to create the variations in cross forces and moments necessary for the control of the projectile motion. Figure 46 shows three different designs with fixed fins followed



FIGURE 41. Plain fin tails.

by movable rudders. Zero- and 10-degree yaw diagrams for rudders neutral and rudders down are shown. The added effect of the very small rudder area is small for these cases. In addition to showing how the fins and rudders act to produce a lateral force, the diagrams emphasize the desirability of maintaining close clearance between the rudder and fin. In the bottom diagram considerable flow through the wide gap and hence loss in cross force results on yawing.

1.4.4 Ring Tails and Square Tails

RINGS WITH OGIVAL AFTERBODIES

The cross force developed on a ring tail as a projectile is yawed occurs when the ring surface is at an

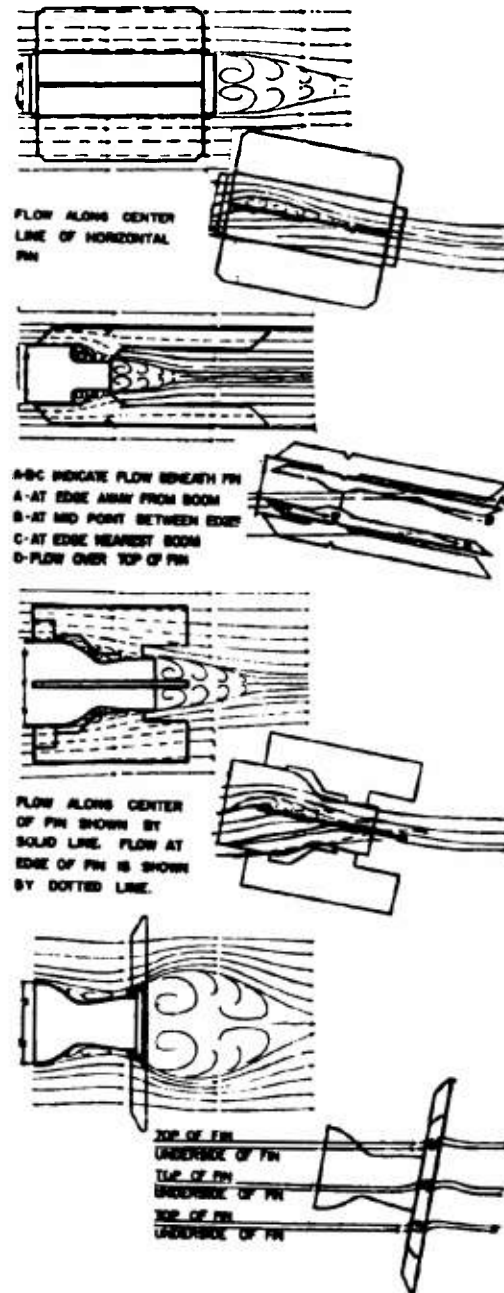


FIGURE 42. Four types of fin tails on rockets.



FIGURE 43. Collapsible fin tails.

“angle of attack” with respect to the flow past it. At zero yaw, on the other hand, additional undesirable drag is obtained unless the ring surface matches the flow lines around the ringless afterbody. Thus, depending on the shape of the afterbody, the ring may be cut from either a right cylinder or a cone. For the various ogival and tapered afterbodies, the cone angle can be adjusted to meet the flow conditions. The cone angle is defined as the included angle between the inner chords of the ring on an axial cross section; thus it is twice the angle of the flow measured from the projectile axis.

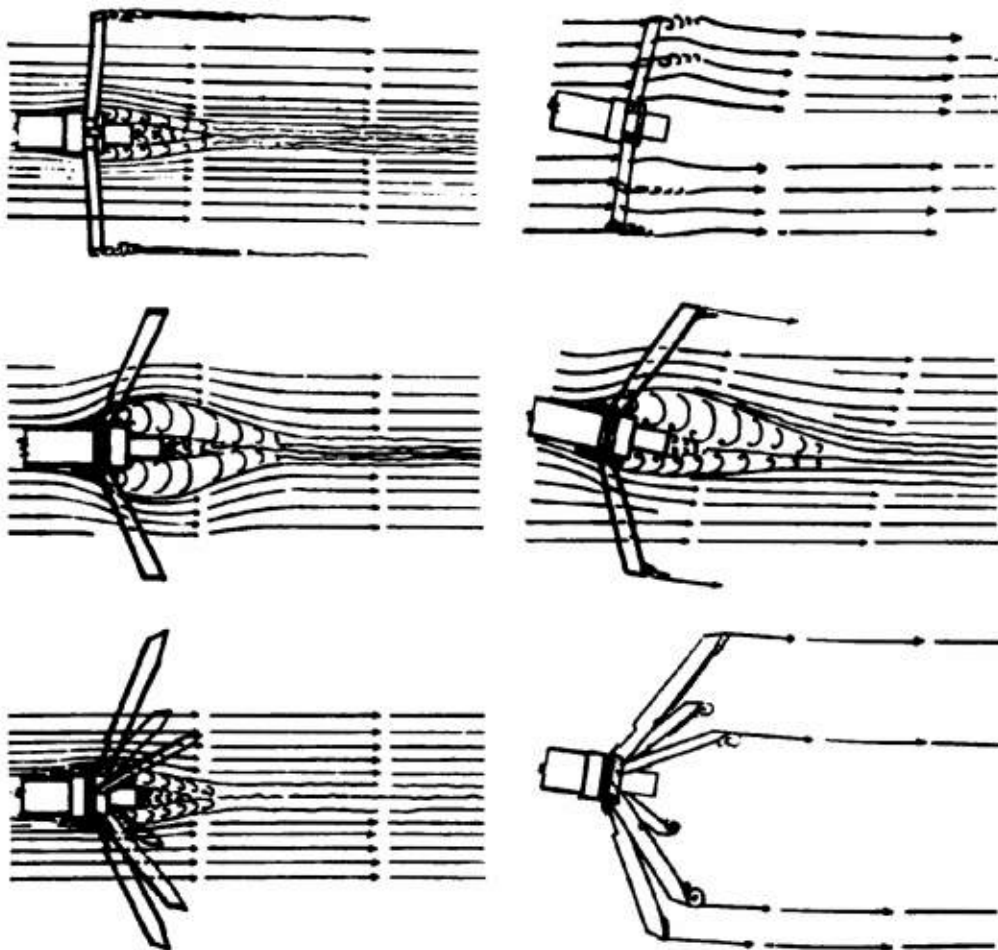


FIGURE 44. Collapsible fin tails—radial and raked fins.

CONFIDENTIAL

An example of the matching of ring tails to flow lines is shown in Figure 47. The flow past the ringless afterbody shows an angle of 4 degrees at the fin tip where the ring is to be placed, calling for an 8-degree conical ring. The best fit to the flow lines was actually obtained with this cone angle as may be seen by comparing the flow lines for the cylindrical ring and the 8-degree and 16-degree rings shown in Figure 47. Photographs of the same three rings are shown in Figure 48. Additional examples are shown in Figure 49 of rings fitted to afterbodies finer and also blunter than those in Figure 47. The cylindrical ring on the blunt afterbody causes a disturbance of the flow lines which is avoided with the correctly matching 12-degree ring. Note that all the rings shown were constructed with true cylindrical or conical inside surfaces. The outside surface was machined to make the

cross section of the ring, taken through the cone axis, a streamlined shape.

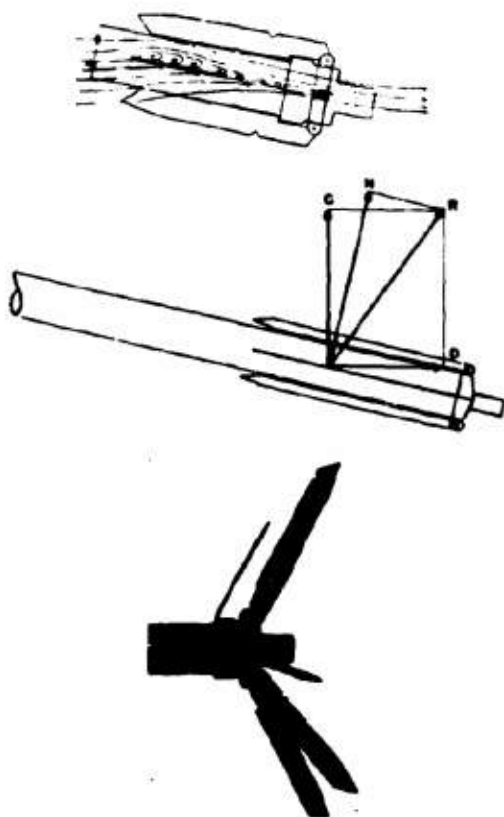
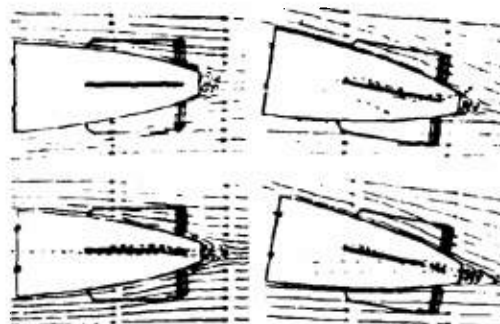


FIGURE 45. Large bending forces exist on folded fin.

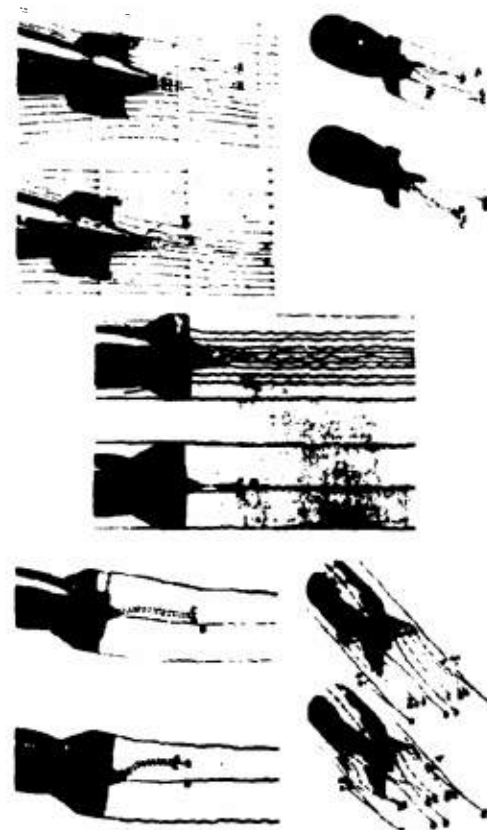


FIGURE 46. Fin tails with adjustable rudders—each pair shows rudders neutral and rudders down.

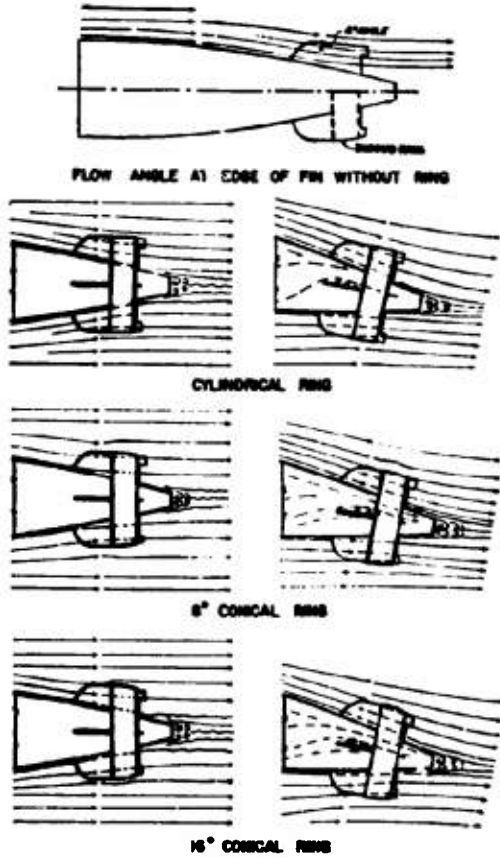


FIGURE 47. Matching ring tails to flow lines.

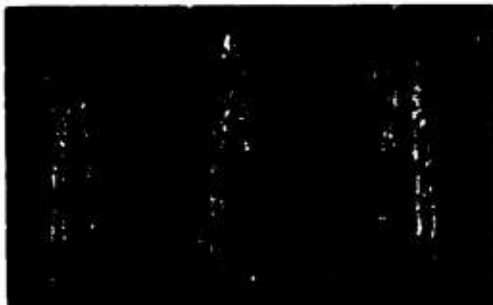


FIGURE 48. Matching ring tails to flow lines.

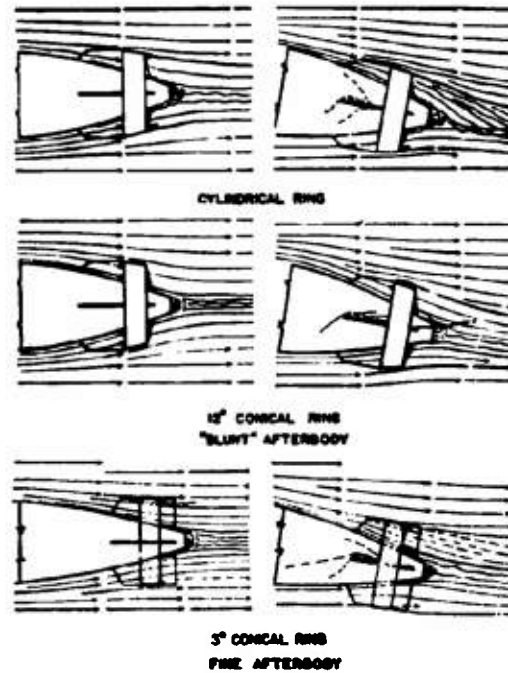


FIGURE 49. Matching ring tails to flow lines. Ring section is streamlined with conical inside surface and curved outside surface as shown.



FIGURE 50. Ring tails.



FIGURE 51. Ring tails.

RINGS ON ROCKET BOOMS

The effectiveness of a ring (as well as the simple fin) depends on it being located so as to extend beyond the zone of fluid decelerated by the body into the high-velocity fluid. The location as well as the design of the ring therefore will depend on the body shape. Typical rings for rockets with cylindrical booms, tapered afterbodies, and irregular nozzles on booms are shown in Figures 50 and 51, and with flow diagrams in Figures 52, 53, 54, and 55.

In Figure 52 the effect of ring diameter (width),

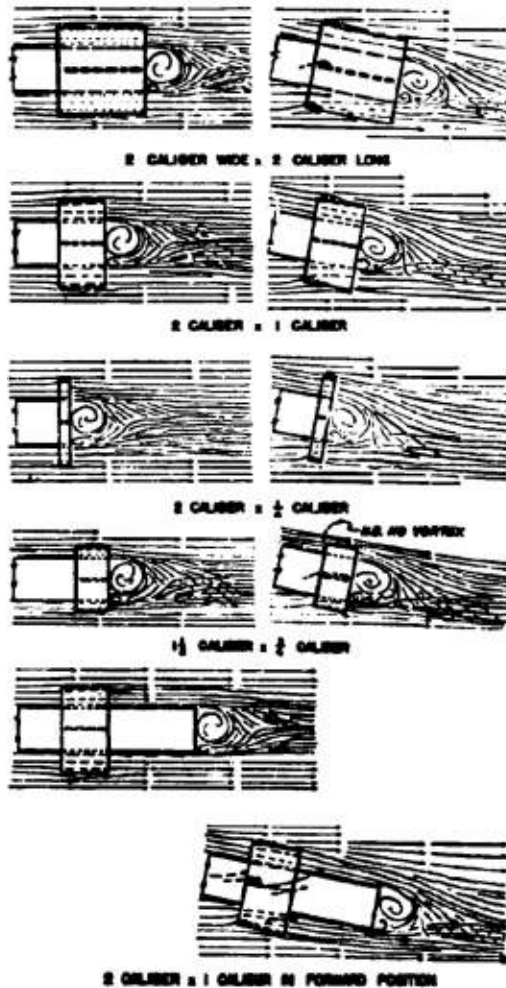


FIGURE 52. Ring tails on cylindrical rocket boom.

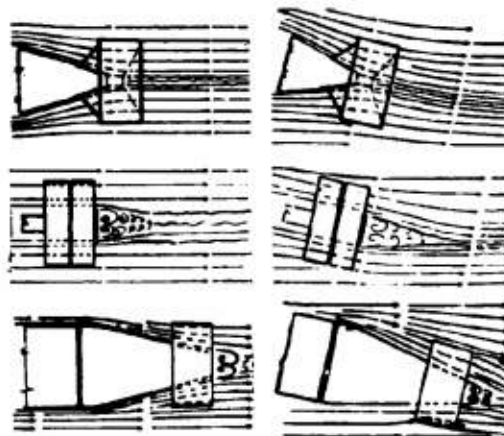


FIGURE 53. Three applications of ring tails to rocket-propelled bodies.

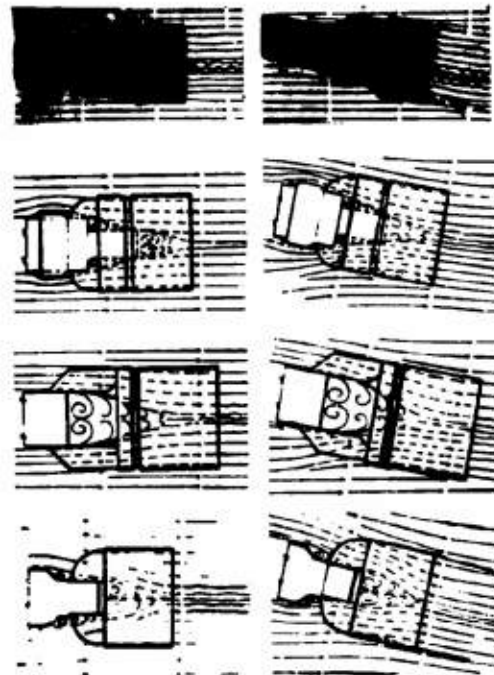


FIGURE 54. Ringtails on rocket booms.

length, and ring location are illustrated for cylindrical booms. The top two diagrams show about the same effect on the flow pattern. This is a qualitative indication that for a given diameter the effectiveness of

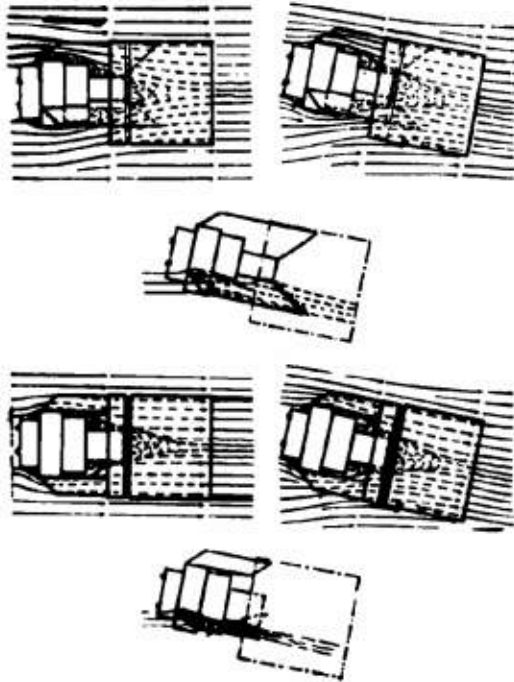


FIGURE 55. Effect of supporting fin area and snugness to body.

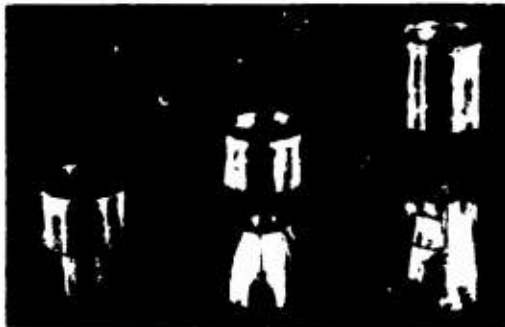


FIGURE 56. Ring tails on extended interior fins.

the tail is not improved if a certain optimum length is exceeded. This fact is borne out by actual measurements (see discussions in Chapters 9 and 14). The resistance to flow through the narrow passage left inside the small diameter ring shown in the fourth diagram causes some of the fluid to by-pass the ring and hence reduces the cross force. The small arrow at the top of the yawed ring marks a disturbance resulting from the flow "spilling out." The tail with the

ring moved forward as shown in the bottom diagram is less effective than for the same ring at the end of the boom, also because there is greater resistance to flow through the annular space inside the ring. In Figure 54, the effects of different attachments to rocket nozzles are shown. These show the advantage of providing large passage and good access to encourage as much fluid as possible to pass through the ring. The effectiveness of the increased supporting fin area in deflecting the fluid is shown by comparing the top three diagrams with the lower three in Figure 55.

RING MOUNTED ON EXTENDED FINS

Ring effectiveness can be increased if the ring can be supported aft of the projectile proper. Not only

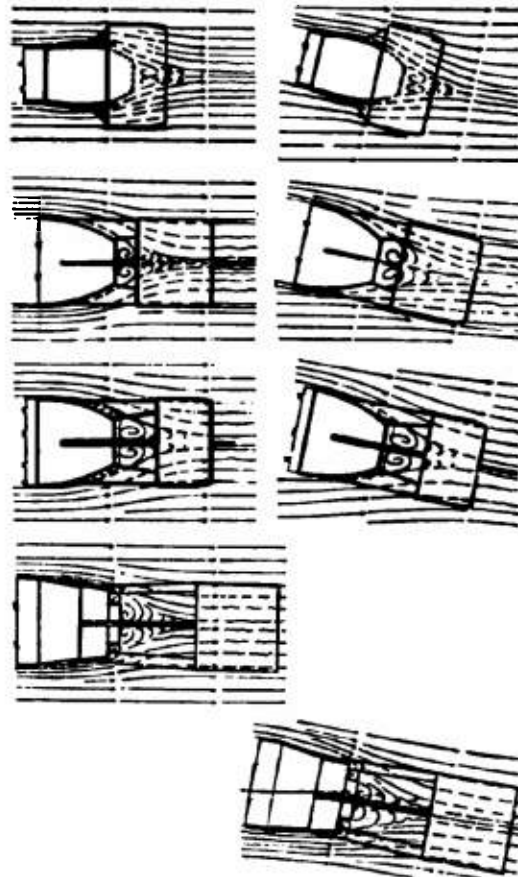


FIGURE 57. Ring tails on extended interior fins.

is the distance to the center of gravity of the projectile increased, but on yawing the ring extends outside the wake of the projectile body into high-velocity fluid. Figures 56 and 57 are examples where the fins,

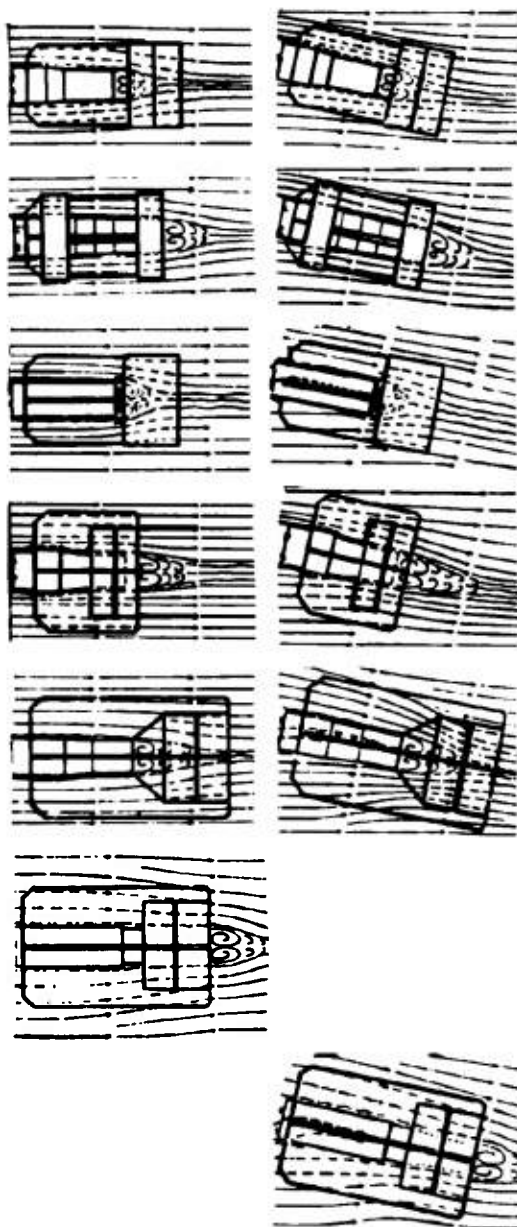


FIGURE 58. Ring tails on extended exterior fins.



FIGURE 59. Ring tails designed for high drag.

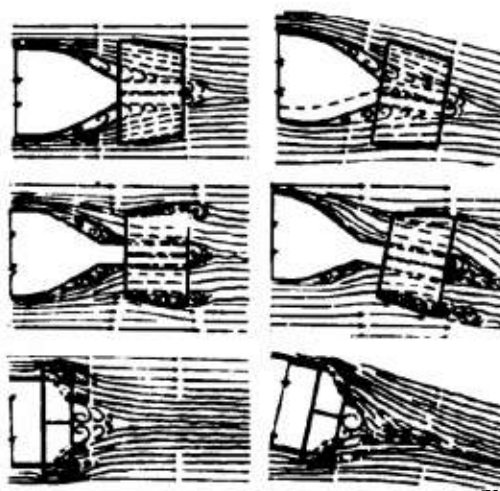


FIGURE 60. Ring tails designed for high drag.

which are primarily supporting struts, and the rings are restricted to the diameter of the projectile body. Note that in the first three cases the fins must be arranged to provide for expanding exhaust gases.

Where an extra large cross force and restoring moment is required, large fins can be used which extend from the ring radially or longitudinally. Examples are shown in Figure 58. Some of these tails are poorly designed for their purpose. The second design with the two separated rings is less effective than if a single ring of twice the length were used at the end of the boom. This construction, however, does add to the mechanical strength. Similarly if there are no clearance limitations a much more effective design

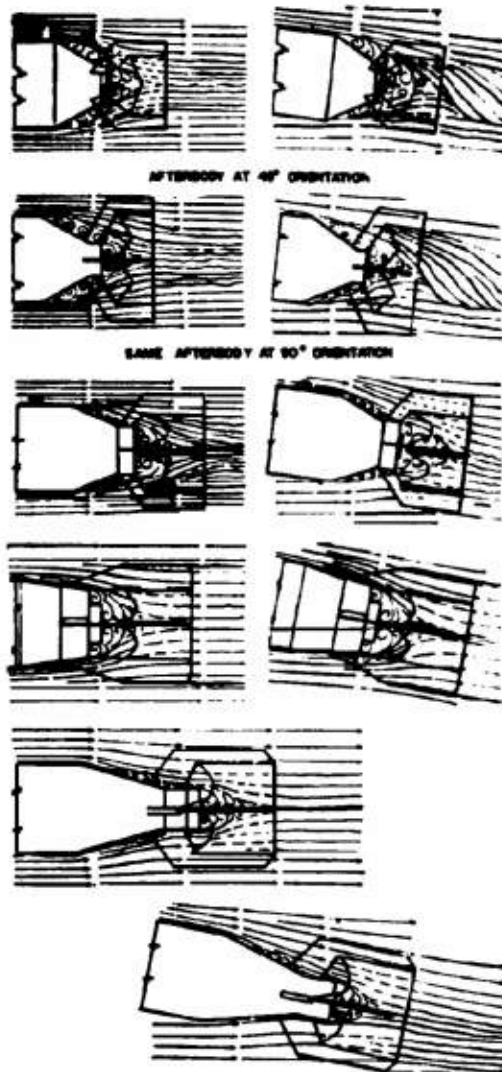


FIGURE 61. Square (box) tails following conical afterbodies.

can be obtained than shown in the lower diagrams, by increasing the ring diameter as well as the fin span.

RING TAILS FOR HIGH DRAG

As already discussed, a high-drag tail is not an efficient means of providing a stabilizing moment.

However, it probably represents the best method of maintaining a low terminal velocity. High drag due to any other component of the projectile reduces the stabilizing moment under yaw. This is particularly important if the sonic velocity range is approached. The formation of shock waves on the nose should result in increased sensitivity to yaw.

Figure 59 shows two designs, one of which can be oriented in either direction, as shown in flow line diagrams of Figure 60. The drag of the cone with the small-diameter end forward greatly exceeds the drag of the other two examples.



FIGURE 62. Square tails.

SQUARE TAILS

The principles for design of square tails parallel those for ring tails. Examples of these box tails on the conical afterbodies of several Service bombs are given in Figure 61. Models of two of the versions are illustrated in Figure 62.

24.5

Special Application

RING TAIL WITH EXHAUST STACK

Torpedo exhausts carried through the propeller hub complicate the mechanical design. Figure 63 shows the diagram for a design using the ring tail and its supporting fin as an exhaust duct. For this arrangement the diagram makes it clear that a tail pipe is necessary to extend the exhaust aft of the propeller disk so as to avoid interference with the propeller and consequent loss of thrust.

CONFIDENTIAL

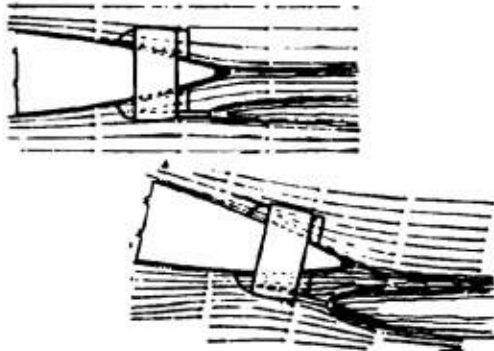


FIGURE 63. Ring tail with exhaust stack.

2.5 THE USE OF FLOW DIAGRAMS IN DESIGN

2.5.1 Effects of Subassemblies on Assembled Units

As discussed in the introduction to this chapter, the flow diagram for a complete projectile represents all the interdependent effects of the components. To be sure, certain details can often be examined separately, resulting in conclusions independent of the shape of the whole. Care must be taken, however, to assure that this is true. For example, Figure 64 shows

local flow disturbances around rivets and suspension fittings as examined separately. Figure 65 shows the flow diagram for similar suspension fittings on a complete torpedo. There is no essential difference in the conclusions reached about the effects of these fittings on the flow and drag. Figure 66, on the other hand, shows such fittings on a depth bomb. A discontinuity at the junction between the nose and the full diameter body results in flow separation and a wake which completely envelops the suspension fittings. As a result, extra drag should not be expected from these protrusions in the latter case. This conclusion was verified by water-tunnel measurements.

The cases where complete diagrams can be assembled from those of the components are numerous, however. An example is shown in Figure 67.

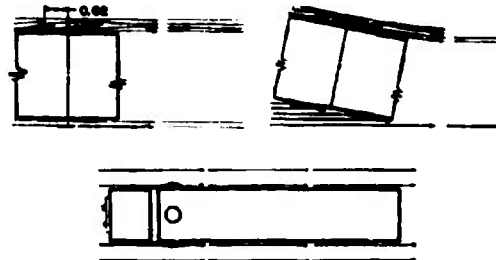


FIGURE 64. Local disturbances by rivets and suspension fittings.

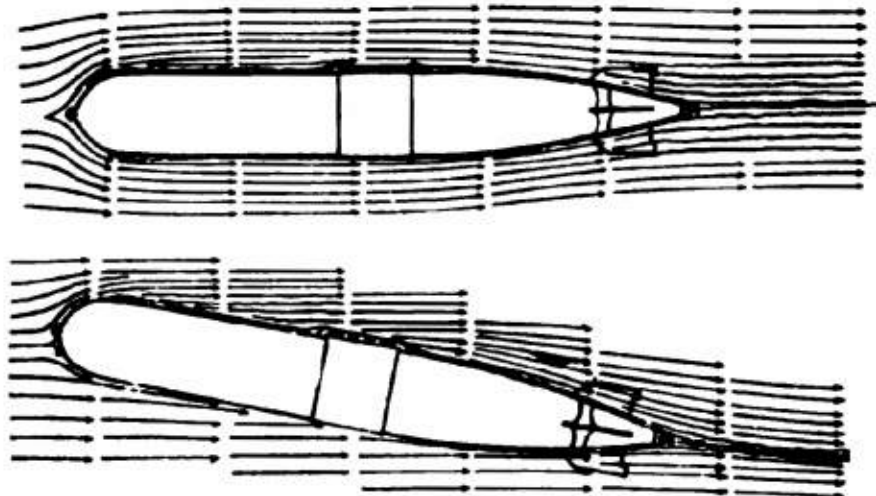


FIGURE 65. Suspension fittings on streamlined projectile.

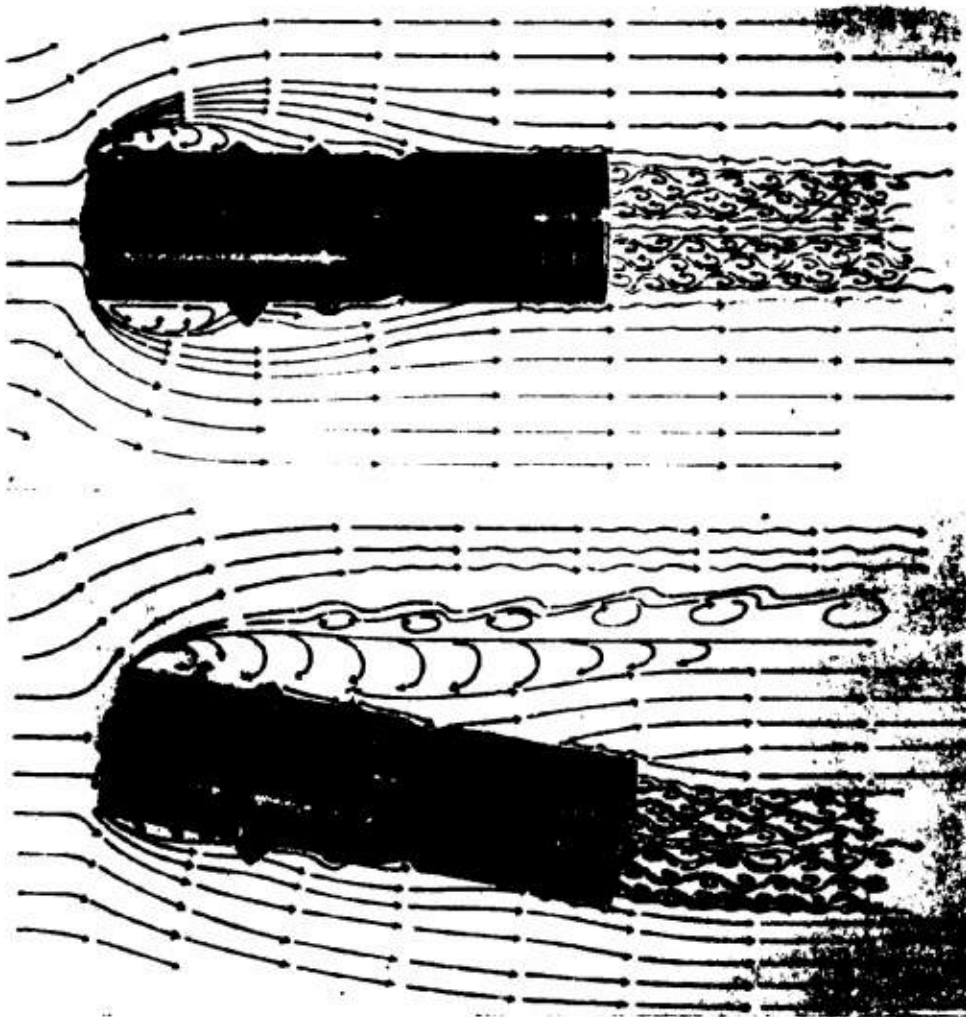


FIGURE 66. Suspensio fittings in wake of blunt nose.

CONFIDENTIAL

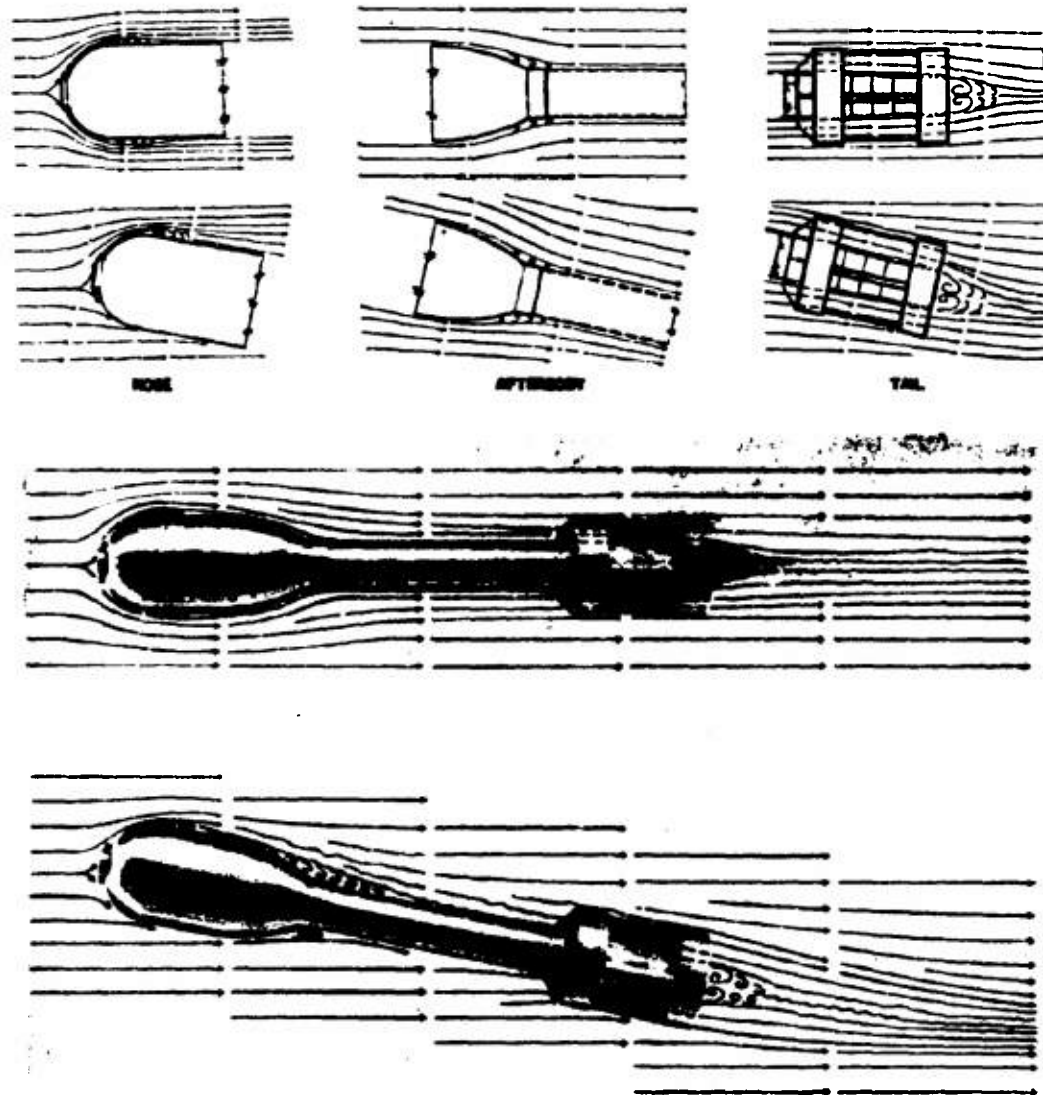


FIGURE 67. An example of the use of flow diagrams in combining projectile flow components.

CONFIDENTIAL

Chapter 4

CAVITATION AND ENTRANCE BUBBLES

4.1 INTRODUCTION

AN AIR-WATER PROJECTILE, such as an aircraft torpedo, in the course of its trajectory from the airplane to the underwater target, passes through at least one, and possibly two, transient conditions in which its entire performance may be affected significantly by phenomena involving both a gas and a liquid. The first of these begins at the instant of water impact, and continues as long as the air that has been carried down into the water by the projectile stays with it as a bubble that covers at least a portion of the projectile surface. The second condition occurs if, during the subsequent underwater run, the reduction of pressure resulting from the velocity of the body becomes, at some points on the projectile, equal to the vapor pressure of the water at the existing temperature. If this happens, evaporation will occur at these points, forming small vapor-filled bubbles. These small bubbles, under certain conditions, may be formed in increasingly higher numbers covering an increasingly larger surface. If conditions become more favorable to their formation, they combine to produce a large cavity or bubble which normally appears as a band encircling the projectile. If conditions become still more favorable, the cavity may grow until it envelops the entire downstream portion of the body. This phenomenon is called cavitation and its different stages are known as incipient, partly developed, and fully developed cavitation. Any of these stages may be the equilibrium stage and thus prevail for any length of time, and, therefore, be subject to study. Unlike this, the different stages of the air bubble formed at the water entrance of the projectile are continually changing, thus making the phenomenon transient in the strictest sense. The direct investigation of this transient phenomenon is far more difficult. Furthermore, cavitation can be studied on a stationary body surrounded by a moving fluid, but, even in the laboratory, entrance bubbles must be studied on moving bodies.

On the other hand, the similarity of the air envelope formed after the entrance of the projectile into water, and the vapor envelope of fully developed cavitation suggests that they are, in many respects, manifestations of the same basic phenomenon, even

though in the past they were considered as wholly unrelated.

In view of the similar characteristics of the two manifestations and the relative difficulty of making quantitative studies on moving bodies, the main basic investigations were carried out in the cavitation field. However, to form a basis for discussing the application of the cavitation results to the water-entry problem, the main features of the entrance bubbles will be reviewed first, so that during the presentation of the results of the cavitation study, it will be possible to point out the similarities and differences of the entrance and cavitation bubbles.

4.2 ENTRANCE BUBBLES

As a projectile, having a moderate or high speed, first touches the surface of the water, the latter is forced away from the point of contact. This action is so violent that it gives rise to the common description that the projectile "blows a hole for itself in the water." This cavity may be considerably larger in diameter than the projectile, and many times its length. During its formation it is open to the atmosphere and, therefore, is filled with air at or slightly below atmospheric pressure. As the projectile penetrates farther into the water, the cavity continues to lengthen until a point is finally reached where the water closes in, severing the connection between the cavity and the atmosphere, and changing the cavity from an open tube into a closed bubble. This bubble continues to travel forward with the projectile. However, from the instant of closure, the amount of air within the bubble diminishes because it is entrained by the water through which it is moving until it finally disappears completely. Figure 1* shows such a cycle. This cavity, from the instant of its inception as the tip of the projectile first touches the water until its final disappearance as the last particle of air is swept away from the surface of the projectile, is commonly referred to as the entrance bubble.

As the projectile touches the water the drag goes up tremendously, primarily because of the great increase in density of the water over the air, and

* These pictures were taken in the model tank at the Naval Ordnance Laboratory, Washington.

secondarily because, as far as the water is concerned, the shape of the projectile is that of the entrance bubble, and this in general is less streamlined than the projectile, and thus has a higher form drag, as well as a larger cross section. Furthermore, the entire force distribution on the body is radically altered. During the air flight, the aerodynamic forces are the result of the skin friction and the pressure distribution over the entire body, whereas in the entrance bubble the only existing forces of significant magnitude are applied in the very small areas of contact between the projectile and the water. In the initial

phenomenon. Its superficial similarity with cavitation may be recognized by comparing the cavitation pictures, shown in Figure 2, with the entrance bubbles of Figure 1.



FIGURE 1. Entrance bubble cycle from model tank.

stages of the bubble formation, the nose is the only point of contact. Hence the point of application is ahead of the center of gravity, and for any normal nose shape the condition is unstable. The lateral component of this force acts to produce a rotation about a transverse axis through the center of gravity, and this rotation continues until a restraining force is developed when the afterbody or tail structure comes in contact with the wall of the bubble. Since all of these forces are large, they greatly affect both the velocity and the direction of the motion of the projectile.

We note the entrance cavity is an air bubble, and although there may be traces of water vapor or other gases present, they play no significant part in the

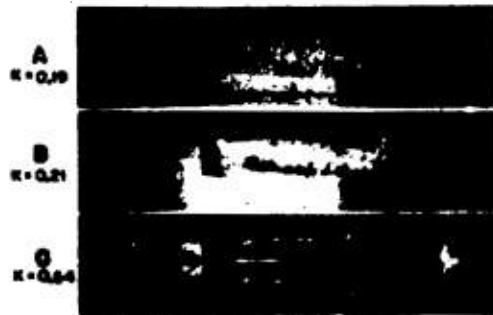


FIGURE 2. Cavitation bubbles.

6.3

CAVITATION

6.3.1

Definition of Cavitation

In this discussion cavitation will be taken to mean the generation of a gas space, or bubble, in a liquid, this space being filled primarily with the gas phase of the liquid, at the same temperature as the liquid, and at the equilibrium pressure for that temperature. So far all of these requirements could be filled by gas

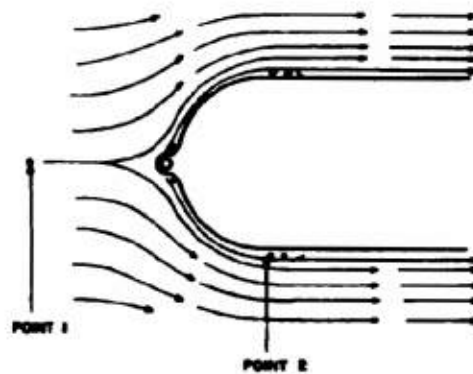


FIGURE 3. Flow diagram. Mk 13 Torpedo nose.

bubbles formed in a boiling liquid. This is not surprising, since the cavitation voids are filled with gas by evaporating a portion of the surrounding fluid, i.e., by boiling. However, in most processes where a

liquid comes to a boil the liquid is either stationary with respect to the container or moving at a velocity so low that it has no appreciable effect on the pressure. Thus, the pressure is sensibly the same throughout the liquid, varying only with the depth. In cavitation, however, the velocities in the cavitating zone must be high, because they are the cause of the drop in pressure from the static pressure, which is well above vapor pressure, down in vapor pressure itself at the point where the cavity is formed. This drop in pressure which accompanies an increase in velocity is in accordance with the principle of the conservation of energy, as expressed in the Bernoulli equation. Consider a stream tube in the flow pattern in Figure

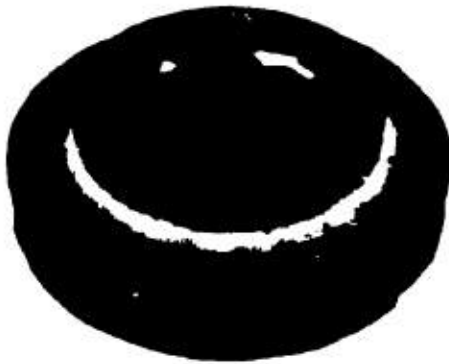


FIGURE 4. Cavitation damage to runner of centrifugal pump.

3. If the Bernoulli equation is written between points 1 and 2, which lie in a horizontal plane, it becomes

$$p_1 + \rho \frac{v_1^2}{2} = p_2 + \rho \frac{v_2^2}{2}$$

or

$$p_2 = p_1 + \frac{\rho}{2} (v_1^2 - v_2^2)$$

where ρ is the density of the fluid, and p_1 and p_2 are the pressures, and v_1 and v_2 the velocities, at points 1 and 2, respectively. Another striking difference between the cavitation phenomenon and usual boiling is seen when the possibility of collapse of a vapor bubble is examined. In the boiling liquid a gas bubble, once formed, tends to rise due to its buoyancy, and as it rises, the pressure on it decreases due to the decreasing hydrostatic head. Thus, even though no more vapor passes into the bubble, it will expand until it reaches the surface. Now, a vapor bubble formed by cavitation will also tend to rise due to buoyancy. However, in most cases, the upward velocity due to

the buoyancy is negligibly small compared to the velocity of flow of the surrounding liquid. Therefore, the path of the bubble is determined by the flow of the liquid. If the liquid carries the bubble to a region where the pressure is higher, the bubble will collapse because the vapor is no longer in equilibrium with the liquid, i.e., it condenses. Since in this condensation the vapor disappears entirely into the liquid phase, there is no gas to cushion the collapse. Therefore, when the liquid surfaces meet or when a liquid surface collapses against a solid surface forming a part of the bubble boundary, the "water hammer pressure" which results can be extremely high. These high forces are probably responsible for the pitting of metal surfaces that is commonly associated with continued cavitation. An extreme case of cavitation damage on the runner of a centrifugal pump is shown in Figure 4. However, the principal objective of this discussion is to investigate the phenomenon of cavitation itself and not the damage resulting from it. Therefore, cavitation damage will be given no further consideration.

4.2.2

Location of Point of Cavitation Inception

From the preceding description of the nature of cavitation, it is obvious that if the pressure distribution is known, then the point of cavitation inception can be determined immediately. Cavitation obviously will occur first at the point of minimum pressure on the body. It will commence when this pressure reaches the vapor pressure of the fluid. If the surface of the submerged body be thought of as a deflecting or guiding surface for the flowing fluid, a rough estimate can be made of the critical points on the body where low pressures might be expected. Thus, parts of the surface which deflect the flow away from the body will be regions of high pressure and, therefore, will not be susceptible to cavitation. Conversely, those parts of the surface which fall away from the flow and thus deflect it so that the flow lines are concave toward the body are low-pressure regions, and hence zones in which cavitation may be expected to appear. Consider a typical projectile, such as the torpedo shape which is shown, together with its pressure distribution, in Figure 5. The tip of the nose is always the high-pressure region because it is deflecting the flow away from the body. However, considerably before the cylindrical portion is reached, the nose surface is falling away from the lines of flow, and hence, a low-

pressure region can be anticipated. If cavitation occurs in this region, as shown in Figure 6, it is usually referred to as nose cavitation. The amount of lowering of the pressure below that of the neighboring undisturbed liquid is, for a given velocity, de-

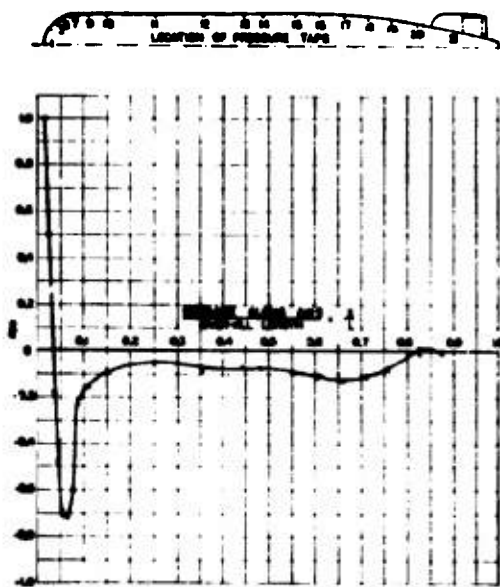


FIGURE 5. Mk 25 torpedo shape. Pressure distribution along longitudinal section. Yaw angle 0 degree.

termined by the shape of the nose. It is to be expected that the cylindrical part of the body will be a zone of rather uniform pressure since it has no means for causing any radical change in the flow direction. However, as soon as the body starts to decrease in diameter towards the tail, another low-pressure re-

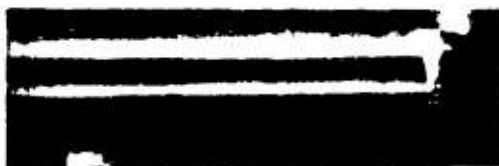


FIGURE 6. Nose cavitation.

gion will be formed. If this has a lower pressure than the corresponding region on the nose, cavitation will first occur here, as in Figure 7. Finally, a high-pressure zone can be expected toward the aft end where the flow lines that follow the tapering after-

body come together and are forced to lose their radial component of velocity.

If the body has fixed or movable fins, the leading edges will be high-pressure regions. However, by



FIGURE 7. Afterbody cavitation.

analogy to the flow around the nose, these edges will be followed immediately by low-pressure regions, and hence, as in Figure 8, will be another possible source of cavitation. If the projectile is a torpedo, the propellers will offer another possible location for cavitation, as seen in Figure 9; a very likely one in fact, because they are nothing more than moving fins, and



FIGURE 8. Fin cavitation.

their rotation means that they have a higher velocity with respect to the water than do the fins. This higher velocity may result in correspondingly lower pressures, and hence, additional cavitation regions. It is possible to conceive of a body so designed that each of these four zones would have the same pressure and



FIGURE 9. Propeller cavitation.

hence, when the pressure field was lowered they would all reach vapor pressure at the same instant, and four independent zones of cavitation would be formed. Figure 10 shows a body upon which cavi-

tion starts in several different zones at nearly the same time. In practice, however, this is rarely the case. One zone usually has a lower pressure than the other and cavitation becomes evident there first. If the pressure field continues to drop, the zone of next lowest pressure will start to cavitate, and so on. Often, however, the growth of the cavitation bubble at the first zone is so rapid that it envelops the other zones before they would have reached cavitation conditions if the flow had remained undisturbed. This growth of the bubble will be discussed in more detail later.

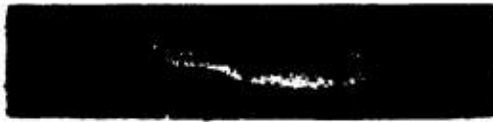


FIGURE 10. Body with several points of simultaneous cavitation.

It may have been inferred from the previous remarks that visible cavitation always occurs at the point of minimum pressure on the body. This is not strictly true. When the minimum pressure point coincides with a geometric discontinuity, the visible cavitation usually appears at the same location. However, if the discontinuity is sharp enough, the cavitation may even appear first in the fluid at some distance from the body. For shapes with reasonably large radii of curvature, the visible cavitation usually appears somewhat aft of the point of minimum pressure.

4.2.3 Cavitation Parameter

In order to describe quantitatively the conditions under which cavitation occurs, the cavitation parameter K has been defined as follows:

$$K = \frac{P_L - P_B}{\rho \frac{v^2}{2}}, \quad (1)$$

in which P_L = absolute pressure in the undisturbed liquid,

P_B = absolute pressure in the bubble or cavity,

v = velocity of the projectile with respect to the undisturbed liquid,

ρ = density of liquid.

Note that any homogeneous set of units can be used in the computation of this parameter. It is often convenient to express this parameter in terms of the head, i.e.,

$$K = \frac{h_L - h_B}{\frac{v^2}{2g}}, \quad (1a)$$

where h_L = the submergence plus the barometric head, in feet of liquid;

h_B = absolute pressure in the bubble, in feet of liquid;

g = acceleration of gravity, in feet per second per second;

$v^2/2g$ = the velocity head, in feet of liquid.

Any unit of length can be used in equation (1a) instead of feet. It will be seen that the numerator of both expressions is simply the net pressure or head acting to collapse the cavity or bubble. The denominator is the velocity pressure or head. Since the pressure reduction at any point on the body is proportional to the velocity pressure this may be considered as a measure of the pressure available to open up a cavity. From this point of view, the cavitation parameter measures the ratio of the pressure available to collapse the bubble to the pressure available to open it. If the K for incipient cavitation is considered, it can be interpreted to mean the maximum reduction in pressure on the surface of the body, measured in terms of the velocity pressure. From this it follows that, if a body starts to cavitate at $K = 1$, the lowest pressure at any point on the body is 1 velocity pressure below that of the undisturbed fluid. Figure 5 presents a concrete example of this relationship. It shows the measured pressure distribution on the surface of a torpedo, expressed in terms of the velocity pressure. The lowest pressure occurs at the junction between the spherical nose and the conical section. The pressure at this point is 0.72 of a velocity head below that in the undisturbed fluid. Under cavitation tests in the water tunnel, this same shape cavitates first at this location, and the measured K for incipient cavitation is 0.67.

It will be seen that the K for incipient cavitation is a measure of the resistance of the body to cavitation, or in other words, an indication of the excellence of the shape. Thus, the lower the K for incipient cavitation, the greater the cavitation resistance, and the better the shape from this viewpoint.

It should be borne in mind that the cavitation characteristics of a given body are not defined by a

single value of K . For example, a specific torpedo shape might show signs of incipient cavitation on the nose at a particular value of K_1 . With a slightly lower value K_2 , cavitation might commence on the fixed fins. Careful examination of the propellers might demonstrate that cavitation had commenced on them at a value K_3 , which was even greater than K_1 . A value K_4 might be recorded at the start of cavitation on the afterbody. At K_5 , the length of the cavitation bubble on the nose might be observed to be equal to 2 body diameters.

The preceding paragraphs illustrate the fact that the cavitation parameter K , has many uses. Two of these should be noted explicitly. The first one is that for a given projectile, each specific bubble configuration from the point of inception to the development of a bubble of "infinite" length corresponds to a specific value of K . It thus serves to define, for one given shape, the degree of cavitation. The second use is that in comparing different projectiles or different parts of the same projectile, it serves as a yardstick for the evaluation of their relative performances. This use has been demonstrated in the two preceding paragraphs.

It may have been noted that in defining the cavitation parameter there has been no discussion concerning what determines the pressure within the bubble. This was done deliberately because the pressure in the bubble may be determined by a number of different factors which have no effect on the interpretation of the parameter. Thus, it is quite immaterial whether the bubble contains air under pressure, products of combustion, or water vapor in equilibrium with the surrounding water. However, if the cavitation void is filled only with water vapor in equilibrium, then the phenomenon is that of "true cavitation" as normally defined. In this case, P_B becomes the pressure of the vapor, which can be determined from tables of the vapor pressure of sea water or fresh water, as the case may be. Figure 11 has been constructed to assist in the determination of K for such cases. This diagram clearly shows the effect of depth, or submergence, and velocity. (Also see Appendix.)

It should be noted that although, under service conditions, the pressure on the water surface can vary only by the normal barometric fluctuations, very different conditions can be established in the laboratory, where, for example, the "atmospheric" pressure is completely under control. Thus, in the high-speed water tunnel, shapes can be made to cavitate at much lower velocities than would be possible

in the free ocean, simply by reducing the system pressure until the K is reached at which the desired degree of cavitation is obtained. For example, take the case of a projectile which runs in the ocean at 5-ft submergence and has a K for incipient cavitation of 0.45. The velocity at which cavitation commences is given by equation (1a).

$$v = \sqrt{\frac{2g(h_L - h_v)}{K}} = \sqrt{\frac{64.4(33.2 + 5 - 0.4)}{0.45}} = 73.8 \text{ fps}^b$$

If a model of this projectile is tested in the water tunnel, and if the tunnel pressure, h_L is reduced, say, to 15 ft abs, the velocity for incipient cavitation reduces to

$$v = \sqrt{\frac{64.4(15 - 0.4)}{0.45}} = 45.7 \text{ fps.}$$

A further reduction of h_L to 5 ft abs, would cause the cavitation to start at 25.6 fps. If with h_L equal to 5 ft abs the velocity were maintained at 45.7 fps, K would be reduced to 0.14 and extremely heavy cavitation would be caused, resulting in a bubble several times as long as the projectile.

4.3.4 Degrees of Cavitation

One of the most significant cavitation characteristics of a body is its K for incipient cavitation. However, this by no means describes its entire cavitation performance even if consideration is given only to the single zone in which cavitation first commences. For example, Figures 12A to G represent the development of cavitation on a typical body with a hemispherical nose. It will be observed that as the cavitation parameter decreases, the cavitation zone lengthens. It has been found in the laboratory that for a given shape of body and constant yaw angle, the relationship between the length of the zone and the value of K is a fixed function of that shape, thus, as suggested earlier in this section, K can be used to describe the degree of cavitation as well as the beginning of it.

Since, for a given value of K , the cavitation bubble has a fixed size and location with respect to the body, from the point of view of the liquid, the shape of the body has been altered by it. Thus, as far as the liquid is concerned, it is flowing around an object which has the overall shape of the original body plus the cavi-

^b 33.2 ft of sea water at 50 F = 1 atm. At this temperature its vapor pressure is 0.4 ft.

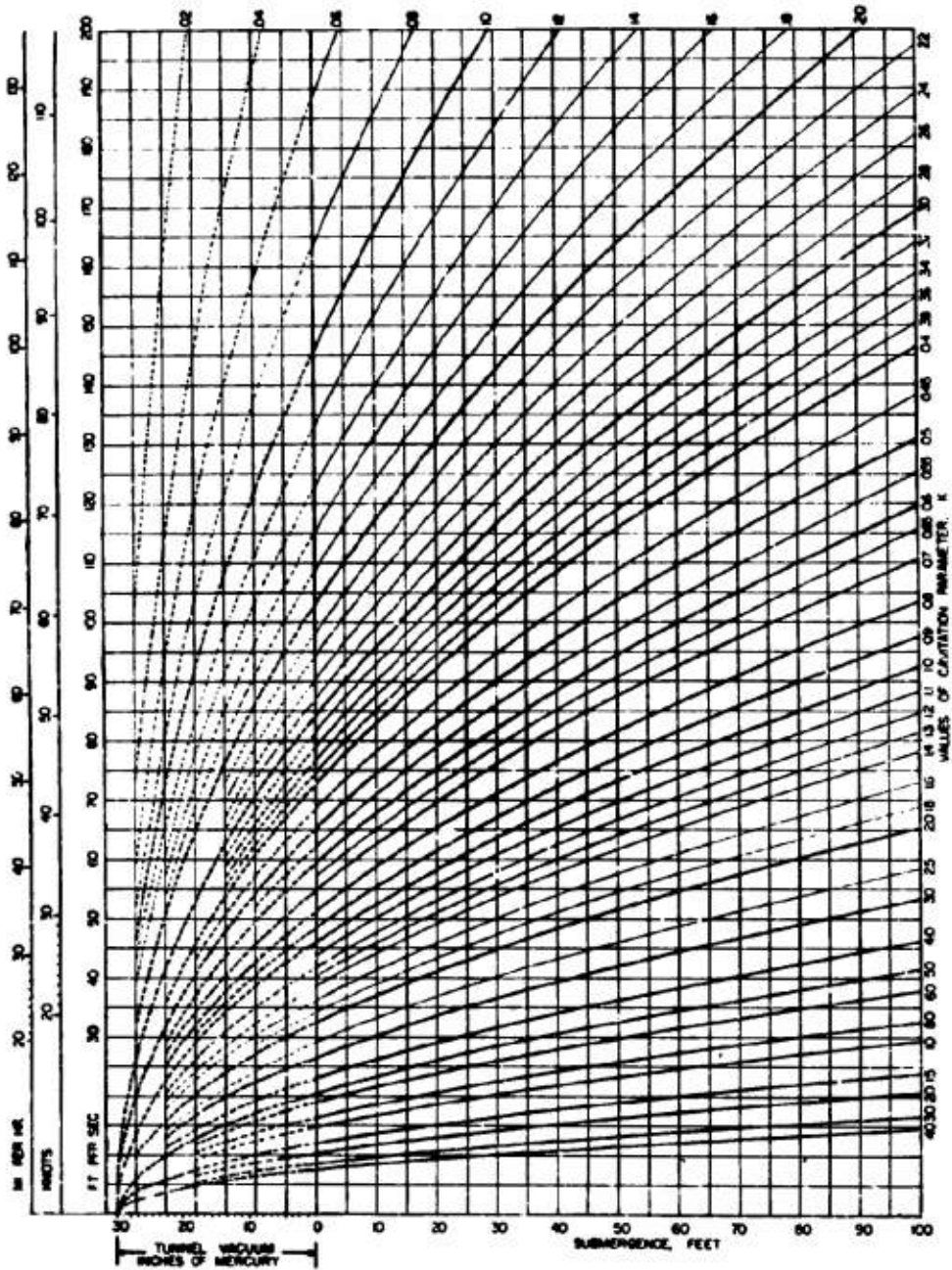


FIGURE 11. Chart showing relation between velocity, submergence, and cavitation parameter.

CONFIDENTIAL

tation void. Therefore each change in shape of the bubble produces corresponding changes both in the velocity and the pressure fields surrounding the body. Another way of saying this would be that each value of K corresponds to a given effective body shape. However, there is one unique characteristic of the

bubble will deform until it is. Thus the interface between the bubble and the liquid is an isopiestic surface.* From this it might seem that if the pressure distribution around the body were measured or computed, the isopiestic surfaces would define the shape and course of growth of the cavitation bubble. This is not true because of the changes in the pressure fields produced by changes in the bubble shape. However, it is reasonable to suppose that for a given state of development of the cavitation bubble, the adjacent isopiestic surface in the flow will be a good indication of the direction of growth of the bubble as the pressure is lowered.

Cavitation is often thought of as a very localized phenomenon which occurs in narrow zones such as those shown in Figures 12A and B. However, as seen in Figures 12C to G, if the pressure is reduced sufficiently, the cavitation grows to enormous proportions and may become many times the volume of the original body. This complete envelopment of a projectile by a vapor or a gas bubble is easily possible if the velocity is high enough or if the pressure in the bubble is sufficiently great. Thus, in Figure 12G it is seen that only a portion of the hemispherical nose of the body is in contact with the water. The flow breaks away from the body before the full diameter of the projectile is reached. This is, of course, a typical bubble condition which occurs when the projectile enters the water from the air.



FIGURE 12. Development of cavitation bubble. Hemispherical nose. This is an example of fine-grained cavitation.

part of the effective body that is formed by the bubble. The original solid body was unaffected by a variation in pressure on it, i.e., the variation in pressure produced no change in the body shape. On the other hand, the bubble is incapable of resisting any appreciable difference in pressure over its surface. In other words, the pressure on the entire surface of the bubble must be uniform since in case it is not, the

4.3.5 Types of Cavitation

If a shape that has a relatively poor cavitation resistance such as a hemispherical nose, is studied, it will be observed that when cavitation commences it occurs in a sharply defined zone. It appears as a white band, which, upon closer examination, seems to be made up of a series of very small bubbles. As the pressure is lowered and the cavitation zone spreads, the zone remains quite sharply defined, especially at the leading edge, and the character of the surface stays approximately the same. This might be called "fine-grained cavitation." A typical case of this type is seen in Figure 12. In contrast to this, if a shape having more cavitation resistance is subject to a similar scrutiny, as, for example, a long elliptical or more pointed nose, cavitation will appear first as a series of individual and comparatively large droplike bubbles.

* This statement ignores the minute pressure gradient that may exist due to gas circulation in the bubble. This factor is discussed in Section 4.3.7.

As the pressure is reduced, these bubbles grow more numerous until they cover the entire surface, but they retain their individual character over a wide range of cavitation conditions. This we will term "coarse-grained cavitation." A characteristic example of this class is seen in Figures 13A to C which show cavitation development on an ogive having a radius of curvature equal to 2.0 body diameters.



FIGURE 13. Development of cavitation bubble. Two-caliber ogive nose. This is an example of coarse-grained cavitation.

One possible explanation of the reason for the difference in the appearance of these two variants of the cavitation phenomenon may be found in an examination of the pressure distribution occurring on the two shapes. In the case of the hemispherical nose the pressure gradient is relatively steep, and therefore, the zone in which the pressure becomes equal to the vapor pressure is quite sharply defined. Consider two elements of liquid moving abreast in parallel paths along the body. Both enter the cavitation zone at the same instant so that there is no time available for the

change in flow produced by the presence of the gas bubble formed in one element to affect the pressure, and hence the evolution of gas in the adjacent element. Therefore, cavitation occurs simultaneously in the two elements, and consequently around the entire circumference of the nose. On the other hand, on the long ogive nose, the pressure gradient is much smaller. Therefore, the exact point on the path of the liquid element at which the pressure reaches the vapor pressure is much less sharply defined. Thus, it is possible to imagine that, owing to localized fluctuations in velocity that are always present in turbulent flow, or possibly in some instances due to a minor surface imperfection, such as a scratch on the body, one element of the fluid would reach the vapor pressure slightly before the corresponding one on the neighboring parallel path. The resulting gas bubble would cause the liquid to be deflected around it, which might result in a slight increase in pressure on the liquid in the adjacent element and thus delay vaporization from it until it has moved a short distance further downstream. This explanation is very tentative and is offered without any background of quantitative experimental confirmation.

4.3.6

Effect of Cavitation on Underwater Performance

Comparatively little quantitative information is available about the effect of cavitation on the performance of underwater projectiles. The exceptions to this statement include (1) the case of propeller cavitation, since much study and analysis has gone into the investigation of the effect of cavitation on propeller performance, and (2) measurements of the forces on a group of cavitating projectiles. (See Chapter 5.) For further details reference should be made to the publications of the David Taylor Model Basin, the Department of Naval Architecture at the Massachusetts Institute of Technology, etc.

The presence of the cavitation bubble on the main body of the projectile would be expected to modify the normal hydrodynamic forces of drag, cross force, and moment. The nature and magnitude of these effects are discussed together with those of the entrance bubble in Section 4.5. However, there is one effect, probably peculiar to the inception of true cavitation, that will be mentioned here. There is some evidence to indicate, on certain body shapes, that there is a very small reduction in drag just before or during the inception of cavitation. This re-

duction seems to be followed by a quite rapid increase in drag as the cavitation zone develops to an appreciable magnitude. If the normal division of the total drag into skin friction and form drag is considered, it is not very difficult to find an explanation for this anomalous behavior. It would be expected that the presence of the cavitation bubble would affect the two components of the drag in opposite manners. The skin friction should be reduced, since the total area of the projectile exposed to the flow of the liquid is decreased. Furthermore, the first traces of cavitation may possibly inhibit the growth of the boundary layer. One would expect the form drag to

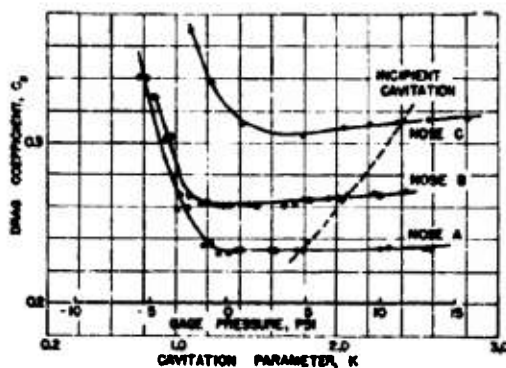


FIGURE 14. Drag coefficient versus cavitation parameter.

increase, since it would be a rare case indeed in which the presence of the bubble could be expected to improve the hydrodynamic form of the body enough to overbalance the increase in drag which would result from the larger effective diameter due to the presence of the bubble. Through the interplay of these two opposing effects, it is possible that at the inception of cavitation, the skin friction is reduced more than the form drag is increased; whereas, as the cavitation develops, the increase in form drag overtakes and then completely masks the reduction of skin friction. Figure 14 gives the results of a drag test which shows this effect.

4.1.7 Gas Cycles in Cavitation

In general, little attention has been paid to the behavior of the vapor which fills a cavitation bubble. For many purposes it has been adequate to consider the space as if it were a complete vacuum. Actually it is gas filled. That part of the surface which is

bounded by the liquid is moving rapidly with respect to the gas. The gas is produced by vaporization of the liquid through this interface. Since the heat for this vaporization comes from the sensible heat of the liquid itself, the process must result in a decrease in temperature of the liquid. As the percentage of liquid that is vaporized must be extremely small, this decrease in temperature is probably negligible for any of the present considerations. It might be assumed that the downstream boundary of the cavitation zone is a region of condensation where the vapor collapses back to the liquid state. However, observation of actual cavitation quickly shows that, although this may be partially true, it does not describe the phenomenon completely. The downstream end of the cavitation zone can be seen to be a region of very rapid entrainment of elements of the gas by the rapidly moving liquid. This is especially evident in photographs taken with very short-duration flash illumination. In such pictures it is possible to see not only clouds of minute bubbles being swept far downstream from the end of the cavitation zone, but large individual bubbles can be observed in the process of entrainment and transportation downstream. All the cavitation photographs presented here are taken with such flashes which give a resulting exposure time between 1 and 25 μ sec. Figure 15 shows this entrainment quite clearly. Furthermore, within the main cavitation bubble there must be a rather intense circulation of the gas, since a large part of the surface is formed by the moving liquid, which must induce a corresponding flow in the gas. Since all of this gas cannot be entrained at the downstream end, there must be a resulting forward counter flow along the surface of the projectile to complete the circulation, as shown on the sketch in Figure 16. It is probable that one result of this circulation pattern is that there is a minute pressure difference which exists between the upstream and downstream end of the bubble, the higher pressure being at the upstream end.

The appearance of some of the well-advanced cavitation bubbles points to the existence of this gas circulation and pressure difference. Thus Figures 17A to D show the various stages in the development of cavitation on a projectile having a nose of low cavitation resistance. In the beginning the entire surface of the bubble appears milky or frothy and seems to be made up of a series of minute bubbles. It might be assumed that the entire space was filled with this froth. However, it must be remembered that rapid evaporation is taking place from the liquid through

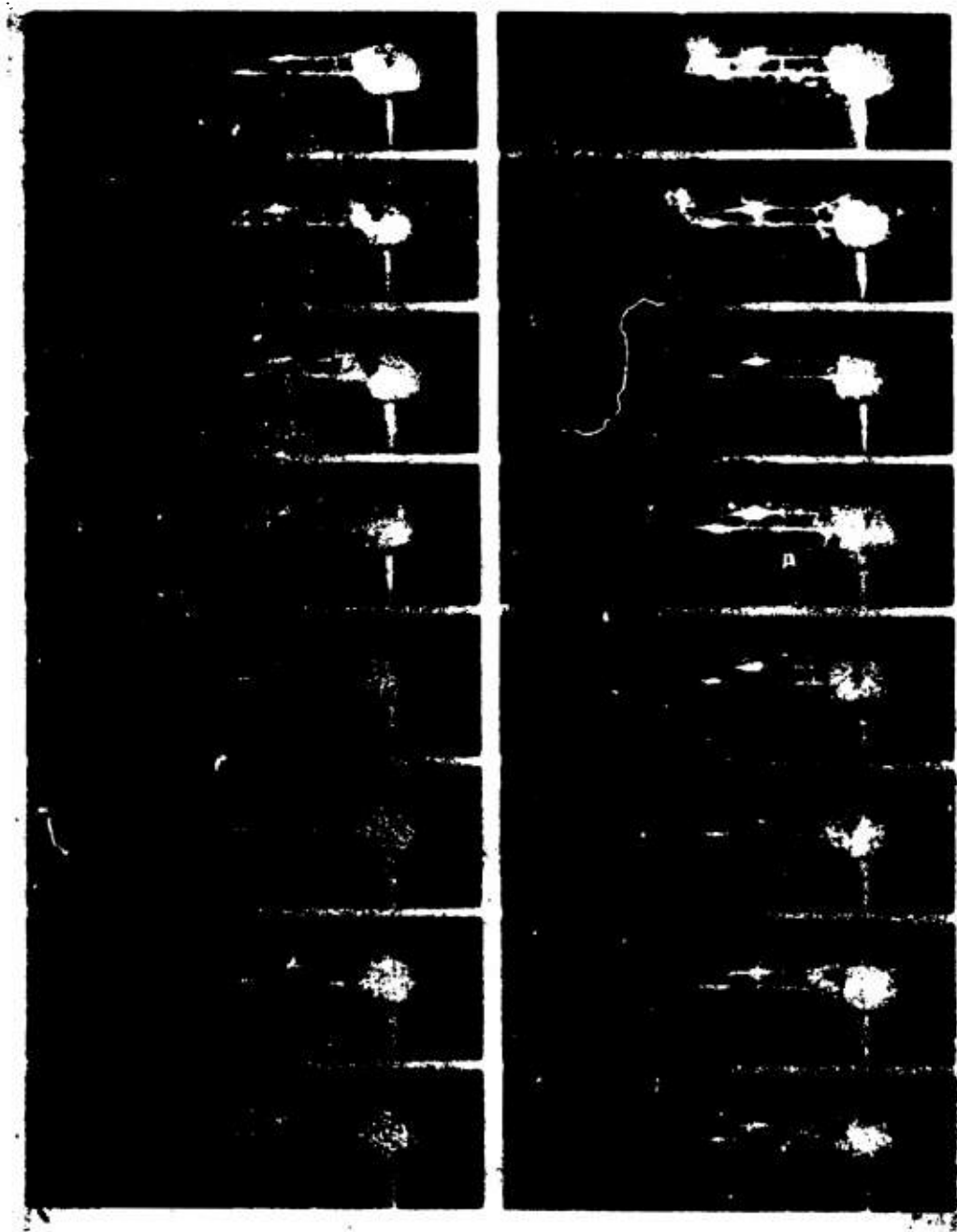


FIGURE 15. Entrainment from cavitation bubble. Flow velocity 60 feet per second. Interval between pictures approximately $1/750$ second. Note arrows showing beginning of second and third breaks.

CONFIDENTIAL

the interface into the gas space. The observer is looking from the liquid side and very probably sees only the breaking bubbles at the surface. Since the rate of entrainment at the downstream end of a cavitation zone is obviously high, the rate of vaporization is equally high in order to supply the required

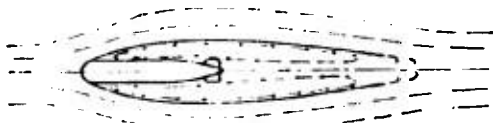


FIGURE 16. Gas circulation within bubble.

amount of gas. However, as the surrounding pressure decreases and the size of the bubble increases, the amount of the surface through which vaporization can occur appears to increase more rapidly than the entrainment. This is shown by the fact that the forward part of the bubble begins to have glassy zones through which the projectile can be seen. As the bubble size increases further, this smoothing of the surface, i.e., the decrease in vaporization through it, spreads downstream until the entire length of the projectile is visible, as in the case of Figure 17D. Now, if the pressure within the bubble were uniform, it would be expected that the rate of vaporization would be decreased uniformly over the whole interface. However, the photographs show that this is not the case and that the vaporization disappears first at the forward end of the bubble. The easiest explanation is the one previously offered, i.e., that the gas circulation has produced a slight pressure gradient with a higher pressure at the upstream end.

4.4 ENTRANCE AND CAVITATION BUBBLES

4.4.1 Similarities and Differences

The discussion of entrance and cavitation bubbles at the beginning of this chapter and occasional references later on have indicated that the two phenomena belong to the same family. However, it is constructive to examine the specific points of similarity and difference between them.

If the two bubbles are compared on the basis of the cavitation parameter K , it will be found that for the same value of K on a given projectile, the cavitation

bubble and the entrance bubble will be of the same size and shape within reasonably close limits, i.e., they are geometrically alike. It must be remembered that in computing the value of K for the entrance bubble, the pressure of the air inside the bubble must be used for P_b , in place of the vapor pressure of the water. As the air pressure is much higher than the vapor pressure, a given value of K is obtained at

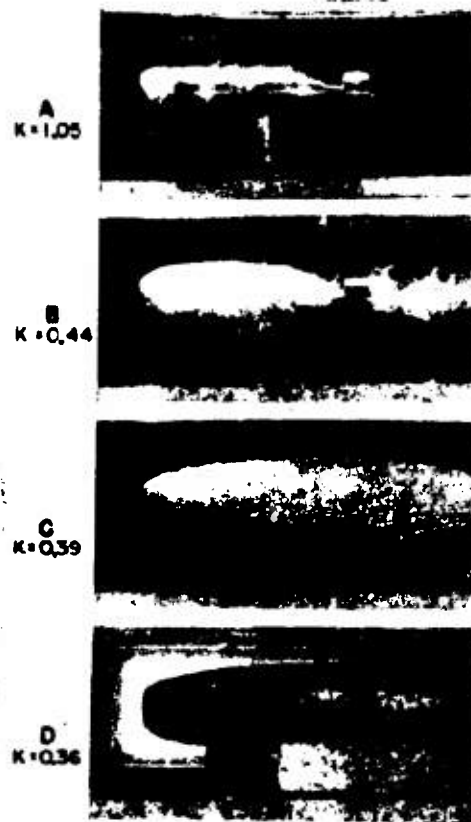


FIGURE 17. Development of cavitation on a blunt nose, showing transition to clear bubble.

much lower velocity for an air-filled bubble than for a true cavitation bubble. Since the bubbles are similar, their effect on the drag coefficient and on the coefficients of the other hydrodynamic forces should be the same. It should be noted that force coefficients are specified rather than the forces themselves because the velocities involved for the same values of K are quite different in the two cases.

CONFIDENTIAL

The gas supplies for the two cases are quite different. The cavitation bubble has an unlimited gas supply through the vaporization of the surrounding water, whereas the entrance bubble has a very limited supply. When a projectile enters the water from the air, the supply of air to the bubble is cut off when the air tube to the surface closes. Henceforth, as the gas is pumped away through entrainment at the downstream end, either the bubble must get smaller or the pressure within it must drop. This process must continue until the bubble is completely consumed. However, for corresponding K 's the gas circulation and the entrainment should be comparable to that of the cavitation bubble. For the air bubble the interface will always be clear and transparent since no vaporization takes place across it.

Under some conditions the cavitation bubble can be considered a steady-state phenomenon. For example, a projectile running at a constant depth and a constant velocity could maintain continuously a cavitation bubble corresponding to the existing value of K . The entrance bubble, on the other hand, is inherently transient because it has no continuous supply of gas. It is, of course, possible to imagine conditions on a torpedo in which the exhaust gases from the power plant could act as the source of supply. Likewise, the products of combustion from a jet-propelled torpedo might furnish sufficient gas to maintain an entrance bubble. However, it appears that for the normal projectile shapes and arrangements, these points of discharge are not very favorable for the maintenance of the bubble. This is very fortunate, since it would be impossible to secure acceptable performance if a bubble large enough to envelop the body were maintained during the entire run.

4.4.1 Entrance-Bubble Formation

An examination of the cavitation parameter shows that at the point of passing through the interface, every projectile entering the water from the air is operating with a K of zero, since at that point $P_L = P_B$. Therefore, every projectile shape, no matter how excellent, must produce a bubble at water entrance. However, K rapidly assumes a finite value as the depth of submergence increases, even though an open passage is maintained from the projectile to the surface through which the air can continue to enter. This is because P_L always increases directly with the submergence.

The entrance phenomenon starts when the projectile first touches the water. From this point on and continuing during the first diameter or two of travel the change in the phenomenon is so rapid that it has no significant effect during the rest of the life of the bubble. The initial accelerations imparted to the water are very high, and in the case of oblique entry the forces on the projectile are asymmetrical. Therefore, during this beginning part of the phenomenon, there is probably little similarity between the behavior of the entrance bubble and the bubble observed under steady-state conditions. However, the flow pattern rapidly becomes established and the rates of change of the conditions decrease so that soon the differences between the transient and steady-state conditions are not of major importance. Since this discussion is largely based on the results of experiments and analysis of steady-state conditions, the conclusions are inherently limited to this second phase of the entrance phenomenon. It would seem that as a rough approximation this second phase might be thought of as beginning at about the time the projectile has traveled three or four diameters from the point of contact.

The entrance bubble is apparently formed for the same dynamic reasons that the cavitation bubble is formed. The water is forced out of the path of the moving projectile by the nose, thus giving the water a radial component of velocity. If the flow is to conform to the shape of the body a point is soon reached when an acceleration must be produced towards the body. If the pressure difference between the fluid and the surface of the body is not sufficient to produce this acceleration, then the flow will not follow the body surface. If there is a supply of gas available, the intervening space will be filled by it. This is, of course, what happens when the projectile enters the water. The water is forced away from the projectile and at the surface there is no restoring force; hence, only the forward part of the projectile is in contact with the water and the bubble forms aft of this point. As the nose penetrates below the surface, the hydrostatic pressure builds up and acts to restrict the size of the bubble. It should be noted that the only force acting outward away from the projectile is supplied by the wetted portion of the nose. From this zone aft, all the forces act to produce an acceleration toward the body, thus tending to decrease and later to reverse the outward radial velocity component. If the velocity of entrance is low, it is possible for the hydrostatic forces to close the bubble either on the mid- or

CONFIDENTIAL

after-section of the projectile. However, if the entrance velocity is increased, the hydrostatic forces will require a longer time to close the bubble. In this case the length of the bubble will be increased due to two factors, (1) the bubble is open longer and (2) the projectile is going faster, thus creating greater length per unit time. Since the forces at the surface tending to cause closure are very low, closure will normally take place at some point below the surface. Then a residual tube of air from the point of closure to the surface will be expelled, causing considerable surface disturbance.

From the point of view of the above analysis, it will be seen that the maximum diameter of the entrance bubble for a given trajectory angle will depend upon two factors, (1) the shape of the nose and (2) the speed of the projectile. These control the magnitude of the outward acceleration and hence the size of the bubble, since the restoring force, i.e., the submergence, is constant.

4.4.4

Bubble Decay

The mass of air present in the entrance bubble reaches a maximum at the instant of its closure. From that point on, the bubble steadily loses air to the surrounding liquid. In discussing the gas cycle within the cavitation bubble, it was pointed out that the downstream end of the bubble is a region of very rapid entrainment of the gas. This is equally true of the entrance bubble. The surrounding water acts as an ejector to pump the air out of the bubble by breaking off or entraining its elements. Thus, the mass of gas continues to decrease. The volume of the bubble, however, is determined not only by the mass of the gas within it, but also by the pressure at which this mass is at equilibrium with its motion relative to the liquid. This pressure, in turn, is a function both of the velocity of the projectile and the submergence, and, in addition, is affected by the shape of the nose. In short, it is governed by the value of K , just as was the case when the bubble was filled with water vapor. It will be seen that, if a projectile is submerged and running with constant velocity at constant depth within an entrance bubble, as the air is pumped out of the bubble P_s will decrease and hence the value of K will increase until the bubble disappears. This statement assumes further that, at the time that the last trace of air is entrained, the value of K is greater than the K for incipient cavitation. If this is not the case, the water will vaporize and the bubble will gradually

turn into a pure cavitation bubble in which the void is filled entirely by water vapor. In the case of high-speed entry, it is very probable that this actually occurs, i.e., that the air-filled entrance bubble merges gradually into the vapor-filled cavitation bubble before the velocity is reduced sufficiently to eliminate the cavitation. Such a condition would be more apt to occur on a shallow-diving than on a deep-diving projectile, since, for similar velocity conditions, the latter projectile has a higher K .

If it is assumed that the projectile under consideration either is without power or is driven by propellers, the entrance bubble phase of the trajectory will be one of continually decreasing axial velocity. This decrease, in effect, acts as a compressing force on the air-filled bubble since it is tending to raise the value of K , and hence, to decrease the size of the bubble. If the submergence is increasing at the same time, this effect is accelerated. This compression alone probably tends to increase the mass rate at which the gas is pumped out of the bubble, simply because there is more mass carried away in a given volume of gas.

4.5

PROJECTILE DYNAMICS WITHIN CAVITATION AND ENTRANCE BUBBLES

A certain superficial similarity exists between the forces acting on underwater projectiles when enveloped in a bubble and the air flight of a similar projectile traveling at supersonic velocities. In both cases, assuming zero yaw, the principal force acts on the nose alone, and in general its point of application is well ahead of the center of gravity. Furthermore, in both cases the nose shape is of prime importance in determining the magnitude of the force for a given velocity. However, there is little point in pursuing this similarity very far since the mechanics of the two phenomena are quite different.

The forces on the projectile within the bubble are, as in the case for any other portion of the path, the result of the reaction from the change in momentum produced in the surrounding fluid by the presence of the projectile. Thus, if the movement of the water surrounding the projectile and its bubble were known, the projectile forces could be calculated. Since the surface of the bubble defines the path of the adjacent layer of water, the bubble shape can be used as an indication of the character of the flow. Since a change in the force on the projectile is the result of a change

CONFIDENTIAL

in the momentum imparted to the water by the projectile, such a change must be accompanied by a change in the bubble shape, i.e., in the path of the water adjacent to the bubble. Investigations⁴ of the performance of a certain special type of underwater projectile for Division 3 have led to the hypothesis that the bubble diameter at a given distance back of the head is an effective measure of the drag on the projectile, the force varying roughly as the diameter to the fourth power. This hypothesis assumes that the skin friction is negligible, since the wetted surface area is negligible, and that the drag force is directly

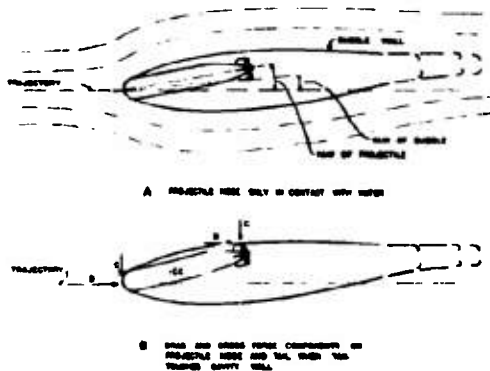


FIGURE 18. Projectile with yaw in entrance bubble.

proportional to the radial force imparted to the water to get it out of the way of the projectile. This latter statement implies a constant "efficiency" of the nose as a deflector, or in other words, all noses producing the same diameter of bubble are acted upon by the same force. This is probably true only within reasonable limits. For example, it would seem that in the case of a square nose, part of the axial force might be used to impart an appreciable axial component of velocity to the water; whereas a long ogive, or fine ellipse, might produce the same diameter bubble, but would impart practically no axial velocity to the liquid. For detailed measurements of the drag and other forces acting on a few specific body shapes, see Chapter 5.

4.4.1 Cross Force in Bubble

In the preceding paragraph, the shape of the bubble was used as a basis for some of the conclusions regarding the drag. Bubble shape is equally helpful in the investigation of the cross force. Thus, if the bub-

ble is symmetrical, it is reasonable to suppose that the resultant force acts along the axis of symmetry of the bubble. If the axis of symmetry of the bubble coincides with the trajectory there should be no resultant cross force on the projectile. If the axis of the bubble makes an angle with the trajectory, then a cross force should be expected and its magnitude should be about equal to the drag force multiplied by the sine of the angle between the axes. In most cases, however, it will be observed that when the axis of the bubble does not coincide with the trajectory, the bubble is asymmetrical. For this case the bubble axis is not significant, so the resultant force must be used. Its line of action is determined by the condition that in any plane containing this line, the amount of momentum change in this plane must be equal and opposite on each side of the line of action.

4.5.1 Equilibrium Yaw Angles within Enveloping Bubbles

Figure 18 is a diagrammatic sketch of the conditions which exist when a projectile is surrounded with a bubble, and is traveling with a pitch or yaw with respect to its trajectory. In the preceding paragraph it was pointed out that the cross force on a projectile is a function both of the force resisting the motion and the angle that the force makes with the trajectory. It will be seen from Figure 18A that this angle can be defined by two others: (1) the pitch or yaw angle of the projectile with the trajectory, and (2) the inclination of the bubble axis or line of action with the projectile axis. It should be remembered in computing the cross force that the accepted definition is that the cross force is normal and the drag force is parallel to the trajectory, regardless of the angle between the projectile axis and the trajectory.

Some further simple deductions can be made concerning the forces acting on the projectile while it is surrounded by the bubble.

1. The forces can act only on those portions of the projectile that are in contact with the water. Therefore, it is obvious that the moment produced by the hydrodynamic forces on the nose is usually a destabilizing one, since its point of application is always ahead of the center of gravity. Thus, unless the line of action of the nose force makes a greater angle with the trajectory than does the axis of the projectile, the resulting moment will be in a direction to increase the yaw.

CONFIDENTIAL

2. If continuous rotation of the projectile is to be prevented, a moment of equal and opposite magnitude must be applied. The forces which can produce such a moment first come into play when other points of the projectile touch the bubble interface. In projectiles of normal shapes the afterbody and the tail structure will be the points that will touch first. Since such points of contact lie well aft of the center of gravity, as shown in Figure 18B, the moments resulting from the forces applied at these points are stabilizing.

3. If the stabilizing moment from these forces increases faster with increasing yaw than does the destabilizing one from the nose force, an equilibrium yaw angle can be reached at which these two moments will be balanced. Since under these conditions the cross forces will not balance, the projectile will be forced into a curved path. If this condition persists long enough to obtain equilibrium, the radius of curvature of the path will be such that the centrifugal force just balances the hydrodynamic cross force.

4.3 Relation between Size of Bubble and Equilibrium Yaw Angle

Some qualitative conclusions can be drawn concerning the interaction between the various parts of the projectile.

1. Other things being equal, the curvature of the path will depend upon the magnitude of the cross force.

2. For a given nose and location of center of gravity, the cross force will depend on the equilibrium angle of yaw and the distance aft from the center of gravity to the points at which the forces that furnish the stabilizing moment are applied.

3. From this it follows that the longer the afterbody and the larger the diameter of the tail structure, the greater will be the radius of curvature, or, in other words, the less will be the deviation of the projectile from a straight path. The reasoning is as follows: The bubble size and shape is a function of the nose shape alone. Therefore, for a yawing projectile, the farther aft the afterbody and tail structure extends from the center of gravity, the sooner they will come in contact with the wall of the bubble. Thus, the longer the afterbody and tail, the smaller will be the equilibrium angle and the less will be the cross force on the nose. Furthermore, the amount of

tail cross force required to produce the necessary stabilizing moment will decrease as the points of contact of the afterbody and tail move aft.

4. The same line of reasoning leads to the statement that the radius of curvature of the path of a projectile of given construction can be changed simply by changing the shape of the nose. Two factors enter into this: the size of the bubble produced and the amount of cross force for a given yaw. Thus, if a change in the nose is made which results in a larger bubble but leaves the relationship between cross force and yaw unchanged, the effective cross force at equilibrium will, nevertheless, increase. This is because the projectile will have to rotate to a larger yaw angle before the afterbody and tail come in contact with the bubble surface and are forced into it far enough to develop the moment required to balance the destabilizing moment of the nose. This larger yaw angle means a greater cross force on the nose as well as a greater cross force on the tail, and hence, a shorter radius of curvature to produce the centrifugal force required to balance this larger cross force. The result would be the same if the nose were changed in such a manner that the size and shape of the bubble would be unaffected, but that the resulting cross force would be larger for a given yaw angle. In general, it is very difficult to modify the bubble shape without affecting the cross force and vice versa, since, as previously pointed out, the bubble shape and the nose forces are intimately related.

5. It will be seen from the interrelation of these factors that any change in the design of a given projectile that affects the shape of the nose, the shape of the afterbody and tail surfaces, or the position of the center of gravity, will result in a change in the performance of the projectile while it is in the bubble. Conversely, when the relative behaviors of these various factors are known and understood, it may be possible to design a projectile with any desired behavior in the bubble phase.

4.4 CHARACTERISTICS OF SPECIFIC NOSE SHAPES

Chapter 5 contains a discussion of the detailed characteristics of a group of specific nose shapes, and Chapter 6 presents measurements of the forces acting on projectile bodies when operating under various stages of cavitation. The present discussion will be limited to a few general comments on the significance

of nose cavitation with respect to the behavior of the projectile.

4.4.1 Hemispherical Noses

If the bubble produced by a hemispherical nose is observed from its inception until it develops to a length of many times that of the projectile, it will be seen that when it first appears it is located nearly at the junction between the hemisphere and the cylinder. As it grows longer and longer, the point at which it springs clear from the nose slowly moves forward until, when the bubble is fully developed, it leaves the hemisphere considerably forward of the point of tangency of the sphere with the cylinder. This is

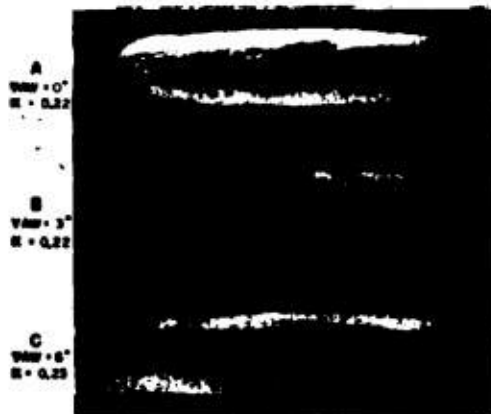


FIGURE 19. Cavitation. Hemispherical nose. Yaw 0, 2, and 6 degrees.

clearly shown in Figure 12. If, when the bubble is fully developed, the projectile within it is yawed a few degrees, the shape of the surface in contact with the water is unaltered since it always remains a segment of a sphere. Figures 19A to C show this behavior. Note especially that the line of contact of the bubble with the projectile nose always remains perpendicular to the direction of flow, that is, to the trajectory. This property of preserving the same contact surface, independent of the pitch or yaw angle, is unique to the sphere. The result is that the bubble is unaffected in shape or alignment with the trajectory by moderate pitches or yaws, and consequently, the resultant force on the projectile is unchanged in magnitude and direction with respect to the trajectory. Hence, for small angles the cross force

is zero and the moment is directly proportional to the yaw.

4.4.2 Ellipsoidal Noses

If the development of the bubble on a projectile with an ellipsoidal nose is observed in the manner just described, it will be seen that the superficial behavior is similar, i.e., as the bubble grows, its point of contact moves forward on the nose. However, in

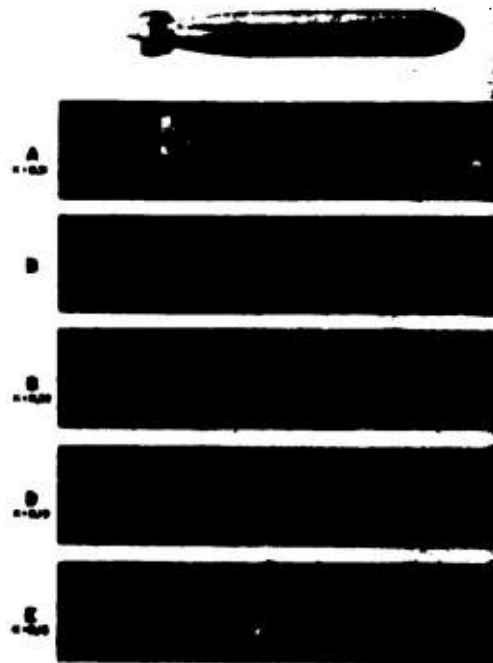


FIGURE 20. Development of cavitation; 2-to-1 ellipsoidal nose.

the case of the ellipsoid, the amount of forward movement is considerably greater than that on the hemisphere. This movement can be observed in Figure 20. If, while the bubble is fully developed, the projectile is again yawed slightly, it will be seen that the wetted surface becomes asymmetrical and causes the bubble to alter its shape and alignment. This change appears to be in the direction to increase the cross force and the moment, largely as the result of swinging the axis of the bubble. Figure 21 shows top views of fully developed cavitation on the nose shape shown in

Figure 20, comparing the bubble shapes with and without yaw. Note particularly that with the elliptical nose, the line of contact of the bubble with the projectile swings from perpendicular to the flow at

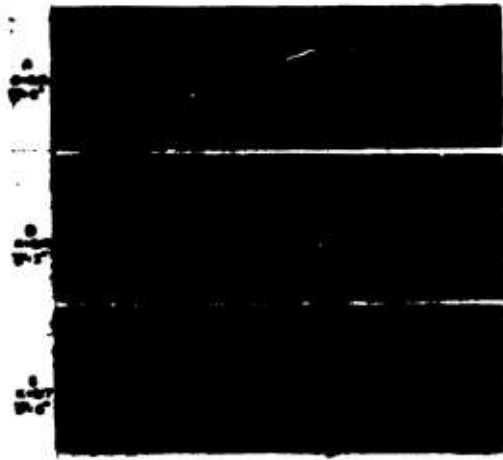


FIGURE 21. Full cavitation with yaw, 2-to-1 ellipsoidal nose. Top view.

zero yaw, to a deviation from perpendicular of from two to three times the yaw at 6 degrees, and that this rotation is in the opposite direction to that of the yaw.

4.6.3 **Ogives**

The behavior of simple ogives, i.e., nose shapes generated by the rotation of an arc of a circle which is tangent to the cylinder, is about the same as that of the family of ellipsoids. Other nose shapes which are finer than the hemisphere have a similar type of behavior, i.e., finite cross forces exist even at small yaws and both cross force and moment increase more rapidly with yaw than they do with the hemisphere.

4.6.4 **Resistance of Noses to Inception of Cavitation**

The resistance of many nose designs to the inception of cavitation appears to depend upon the radius of curvature of the nose at the point of tangency with the cylindrical portion of the body. Apparently, cavi-

tation follows the laws of geometrical similarity. This means that the radius of curvature must be measured in relative rather than in absolute units, i.e., in calibers or diameters of the body. For simple shapes, such as ogives and ellipsoids, the greater the radius of curvature at the point of tangency, the higher will be the cavitation resistance, i.e., the lower will be the parameter K at the inception of cavitation. Figure 22 shows the results of the experimental determination of K for inception on various ellipsoids and ogives. It should be noted that although these two series of shapes look quite different, the K 's are about the same for equal curvatures at the point of tangency.

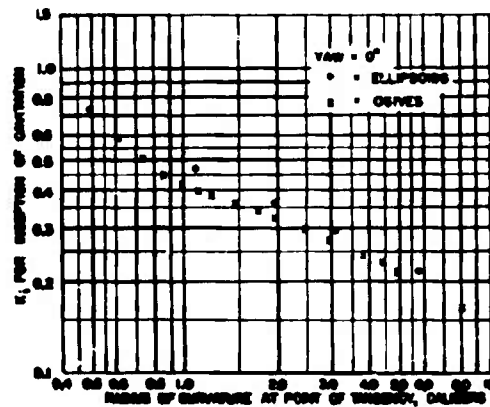


FIGURE 22. Cavitation parameter, K_i , versus curvature.

4.6.5 **Entrance Bubble and Cavitation Performance Characteristics for Successful Overall Flight**

In much of the previous discussion very little attempt has been made to distinguish between the characteristics of the entrance and the cavitation bubbles. The primary reason for this lack of distinction is, of course, that they are felt to be two aspects of the same phenomenon. However, in considering the overall trajectory, it must be remembered that generally speaking, if both manifestations occur, they are not concurrent, but appear one after the other. Therefore, it is necessary to examine the projectile shape from two separate viewpoints, i.e., to see if it will give satisfactory performance (1) in the entrance bubble and (2) in the subsequent underwater run.

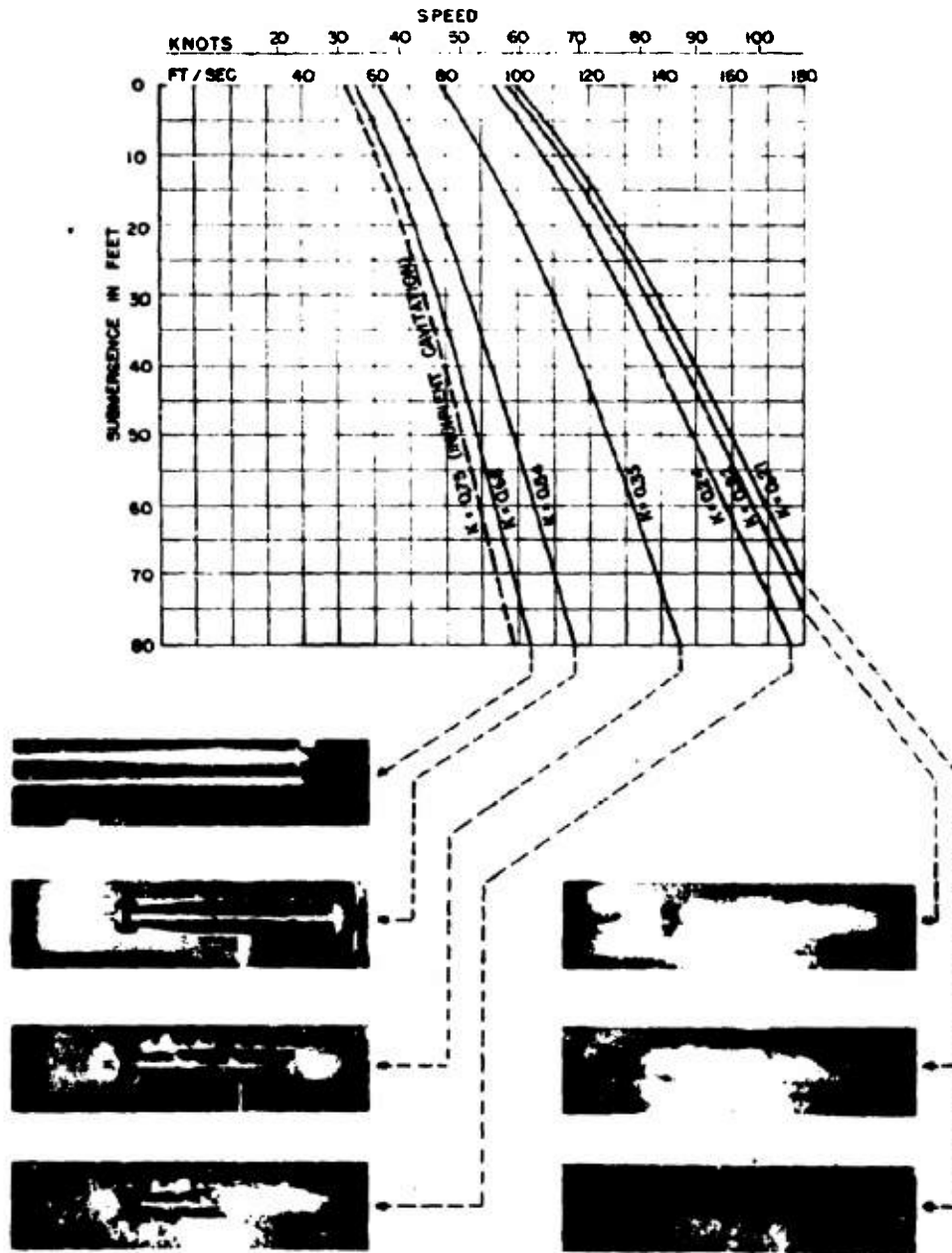


FIGURE 28. Hemispherical nose. Cavitation development related to depth and speed.

At first sight it might appear that the best entrance bubble would be none at all. However, the previous discussion has shown that at the water surface every nose shape will form an entrance bubble; that it is very difficult to design the nose so that at a given speed this bubble will be exactly the size of the projectile; and that even if this were achieved for one speed, the bubble would be longer and larger as the speed was increased. Furthermore, the entrance bubble may serve the very useful purpose of increasing the curvature of the path in the vertical plane so as to reduce the maximum depth of dive and shorten the distance from the point of entrance to the beginning of the normal part of the run. Satisfactory performance in the bubble phase must include the following items:

1. The decelerating force, and hence, the drag in the bubble, must be kept below the point at which structural damage occurs.
2. The projectile must remain on course in the horizontal plane.
3. The combination of the cross force and the pitch in the bubble must result in a curvature which prevents deep dives, but does not permit the projectile to "broach."

The most desirable cavitation characteristic for a torpedo or similar projectile is that cavitation does not occur on any part of it during its normal steady-state run. If this is impossible to achieve, then for satisfactory performance to be obtained, the cavitation effects must stay within the following limitations:

1. The drag must not be increased appreciably.
2. The change in the cross force and moment must not affect the stability adversely.
3. The cavitation must not blanket or reduce appreciably the effect of the control surfaces.

4. The propulsive efficiency must not be reduced.
- These limitations mean essentially that if cavitation does occur, it must be extremely limited, especially in the regions of the control surfaces and propellers.

4.6.6 Selection of Nose Shape for Satisfactory Overall Performance

A review of the discussion of the effect of nose shape on the performance within the entrance bubble

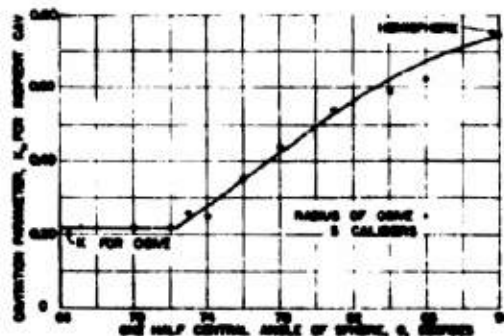


FIGURE 24. Family of 5-caliber spherogives. Cavitation parameter, K_c , versus angle of sphere.

indicates that, in general, the fine noses, such as long ellipsoids and ogives, produce such high cross forces that the projectile is very hard to control while in the bubble, is liable to broach badly, and on the other hand, may make deep dives if at the water-entry point there is an appreciable down pitch. These undesirable characteristics may be alleviated by increasing the effective length of the projectile, either

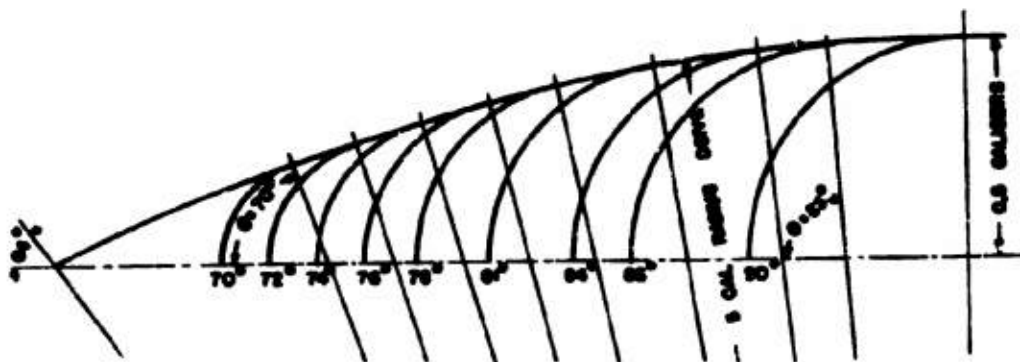


FIGURE 25. Family of 5-caliber spherogives.

by actually lengthening the body or by applying a shroud ring to the tail. However, hemispherical or

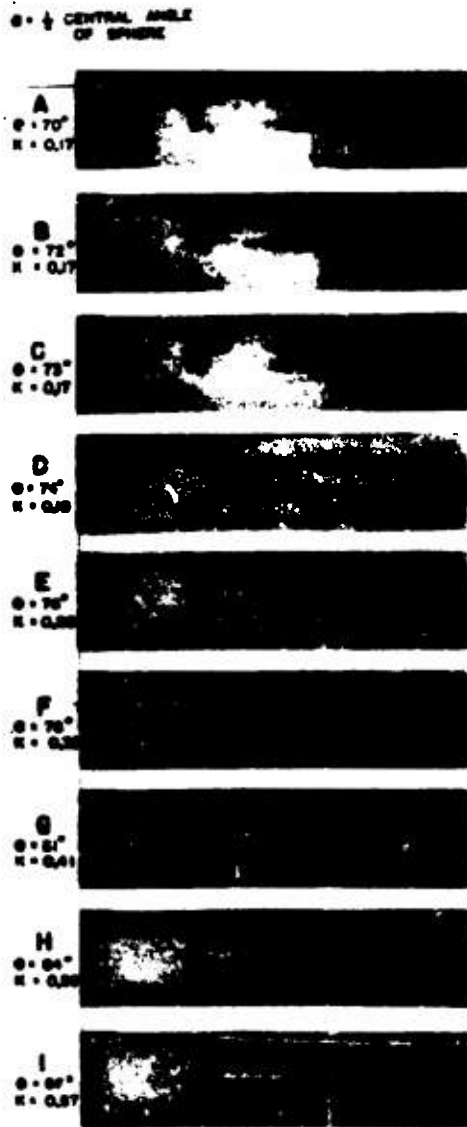


FIGURE 26. Family of 5-caliber spherogives cavitation photographs.

"near" hemispherical noses show more desirable entry characteristics, particularly for small entry

angles. Further improvement appears possible by using even blunter shapes. On the cavitation side of the picture conditions are exactly the reverse. The finer the nose, the better the cavitation resistance. It will be seen from Figure 23 that cavitation begins to appear on the hemispherical nose at 50 knots and 40-ft submergence, and increases rapidly if either the speed is increased or the submergence decreased. Blunter noses show even poorer performance. It is obvious that the hemispherical nose is not satisfactory for a modern high-speed torpedo, and it can be anticipated that future requirements will call for even higher speeds and lower minimum submergences. It thus appears that the nose shape requirements for satisfactory performance within the entrance hubble and satisfactory cavitation performance during the normal run are diametrically opposed.

4.4.1

Spherogive Noses

One promising approach to the problem of satisfying simultaneously these conflicting requirements has been made. This is in the development of the so-called spherogive nose, a nose shape which consists of a tip formed by a segment of a sphere and a transition section which consists of a single-radius ogive tangent to the sphere and to the cylindrical section of the projectile. This shape was investigated first to see if it offered a simple substitute for an ellipsoid. However, a series of measurements showed that it possessed some unique cavitation characteristics. For example, Figure 24 shows the performance of a family of spherogives constructed in accordance with the outline drawing of Figure 25. It will be seen that in the entire family the transition ogive has a constant radius. The only difference occurs in the radius and angle of the spherical segment which forms the tip. It will be observed that from the viewpoint of cavitation resistance as measured by the K for incipient cavitation, there is no significant difference between performance of the simple pointed ogive and all of the spherogives in this particular family in which the spherical tip has a half angle of 72 degrees or less. However, when the half angle of the spherical tip exceeds 72 degrees, the cavitation resistance continues to decrease, reaching the value of the hemisphere when the central angle is 90 degrees. Figure 26 shows the appearance of these various noses while cavitating. For all of the series with tips smaller than 72 degrees, cavitation starts at the point of tangency with the ogive of the cylinder. For all the members

CONFIDENTIAL

having spherical tips larger than 72 degrees, cavitation starts on the sphere, whereas, for the member having the spherical tip of 72 degrees, cavitation appears simultaneously on the sphere and at the point of tangency with the cylinder. One further item should be noted. All of the members of the series had better cavitation resistances than the hemisphere, and all of those having tips of 77 degrees or less had very good cavitation resistance. For example, they could all operate without cavitating under such severe conditions as a speed of 50 knots and 10-ft submergence.

Reference to the discussion concerning the characteristics of the hemispherical nose in the cavitation bubble shows that its good performance is attributed to the fact that the line of action of the force with respect to the flow was unaffected by small angles of pitch or yaw, because the shape of the nose in contact with the water, and hence, the shape of the bubble was unaltered by the change in angle. Thus it would appear possible for a properly designed spherogive to have good performance both within the entrance bubble and also during the subsequent steady-state running conditions. In the series under discussion, spherogives having tip angles between 72 degrees and 77 degrees would seem to offer good possibilities, since the cavitation bubble, and hence, the entrance bubble, always leaves the nose from a point on the spherical tip. Under these conditions the projectile should be insensitive to pitch and yaw; whereas for steady-state running conditions there should be no cavitation on the nose for any speed below 50 knots at submergence greater than 10 ft.

One further physical factor must be considered. If the projectile is to be insensitive to yaw or pitch while in the entrance bubble, the bubble must be large enough so that it does not touch the body of the projectile at any point, after leaving the spherical tip, until it reaches the afterbody or the tail. This means that the bubble produced by the spherical tip must have a diameter larger than that of the projectile. A spherogive tip can be so designed that cavitation starts on the sphere, but that the sphere is so small that the bubble produced by it will not be so large as the diameter of the projectile. Hence, the bubble will touch on the ogive part of the nose and thus be opened out to an adequate diameter. If this happens, the insensitivity to yaw is forfeited.

It is, of course, realized that the spherogive is probably not the best shape that can be constructed to satisfy the conflicting requirements of the entrance-bubble and the cavitation characteristics. The ogive section can be improved, for example, by substituting a curve of continuously changing curvature which has infinite curvature at the point of tangency with the cylinder. Improved characteristics may also be obtained by modifying the spherical tip to produce even less change in moment with pitch or yaw. However, the basic principle involved, that of securing a good cavitation resistance by making the overall shape of the nose effectively fine, while designing the forepart so that the wetted surface at the head of the bubble has the correct shape for satisfactory bubble performance, seems to hold much promise for future developments.

CONFIDENTIAL

Chapter 5

NOSE CAVITATION—OGIVES AND SPHEROGIVES

5.1 INTRODUCTION

THIS CHAPTER covers the progress of an investigation of cavitation on various projectile nose shapes. It is apparent that a very extensive series of tests will have to be made in order to cover the ground in a satisfactory manner. Only the tests of ogive and spherogive noses will be described. A total of about fifty models of these two types of nose shape have been tested. However, all data in this chapter must be considered as preliminary only and subject to corrections based on future tests. The work so far done has furnished a fairly comprehensive overall picture of the performance of these two types of nose, even though the test data are rather meager.

In order to obtain consistent results, it has been found necessary to make the models to very close tolerances. All linear dimensions are held within ± 0.001 in. Especial care is exercised to be certain that the curves forming the nose are truly tangent and match within 0.001 in. or less. The angle of the spherical segment forming the tip of a spherogive nose must be held to within a quarter of a degree as, in some cases, a variation of 1 degree will cause a change of 15 per cent in the value of the cavitation parameter.

5.2 METHOD OF TEST

One of the primary objects of the investigation was to determine the point of incipient cavitation for the various nose shapes. This was done by mounting the model in the high-speed water tunnel and observing the first evidence of cavitation as the pressure in the tunnel was lowered. The water velocity during these tests was, in general, held at a constant value of approximately 60 fps. The cavitation parameter K , for the point of incipient cavitation, is calculated from the velocity and pressure in the tunnel as described in Chapter 4. This value of K for incipient cavitation will, hereafter, have the symbol K_i .

After the point of incipient cavitation had been determined, the pressure in the tunnel was lowered, corresponding to decreasing values of the cavitation parameter, and high-speed photographs were taken of

the development of the cavitation bubble. These photographs, which furnish valuable data regarding the nature, location, and extent of the cavitation effects for each nose shape, appear throughout this chapter and are discussed in the text.

5.3 OGIVE NOSES

Sixteen ogive nose shapes of different proportions have been investigated. The ogive nose profile is formed by two equal arcs tangent to the cylindrical portion of the projectile and meeting at a point. Figure 1 is a drawing of the family of 16 ogive noses that were tested. The radii of these ogives varied from 0.5 to 8.12 calibers, a caliber being the maximum diameter of the projectile.

In Table 1 are given the observed values of K for incipient cavitation for the ogive noses, and these values are plotted in Figure 2. From the smooth curve in Figure 2, the value of K_i for each ogive has been determined and is shown in Table 1. These latter values will be referred to throughout this chapter as the K_i 's for incipient cavitation for ogive noses. The values of K_i can also be plotted against the curvature ($1/\text{radius}$) of the ogive. Figure 3 shows this curve in which the values of K_i have been taken from the smooth curve of Figure 2.

TABLE 1. Incipient cavitation parameter K_i for ogive noses.

Ogive radius r in calibers	Curvature = $1/r$ in calibers	Observed K_i	K_i from Fig 2
0.5	2.0	0.75	0.75
0.625	1.60	0.61	0.60
0.75	1.33	0.53	0.52
0.875	1.14	0.46	0.46
1.0	1.00	0.40	0.43
1.125	0.89	0.40	0.41
1.25	0.80	0.39	0.39
1.50	0.67	0.37	0.37
1.75	0.57	0.37	0.35
2.0	0.50	0.34	0.33
2.5	0.40	0.31	0.30
3.0	0.33	0.27	0.28
3.875	0.26	0.26	0.25
4.5	0.22	0.21	0.24
5.0	0.20	0.21	0.22
8.12	0.12	0.17	0.17

1.6 HEMISPHERICAL NOSE

The hemispherical nose is the limiting case of an ogive nose with minimum radius. It is interesting to compare the development of the bubble on this nose with that of the 2.0-caliber ogive just discussed. Figure 12 of Chapter 4 shows the development of cavitation on a hemispherical nose with values of K ranging from 0.71 to 0.21, incipient cavitation on this nose occurring at a value of $K_i = 0.75$. In this series of pictures it is seen that the cavitation bubble is of a

different type, termed "fine-grained cavitation." The cavitation effect begins as a band of very fine bubbles having a homogeneous appearance, a form which persists throughout the development of the bubble proper.

1.7 TRANSITION ZONE

It has already been pointed out that the curve of K for incipient cavitation plotted against ogive radius shows a rather abrupt change in slope in the region of

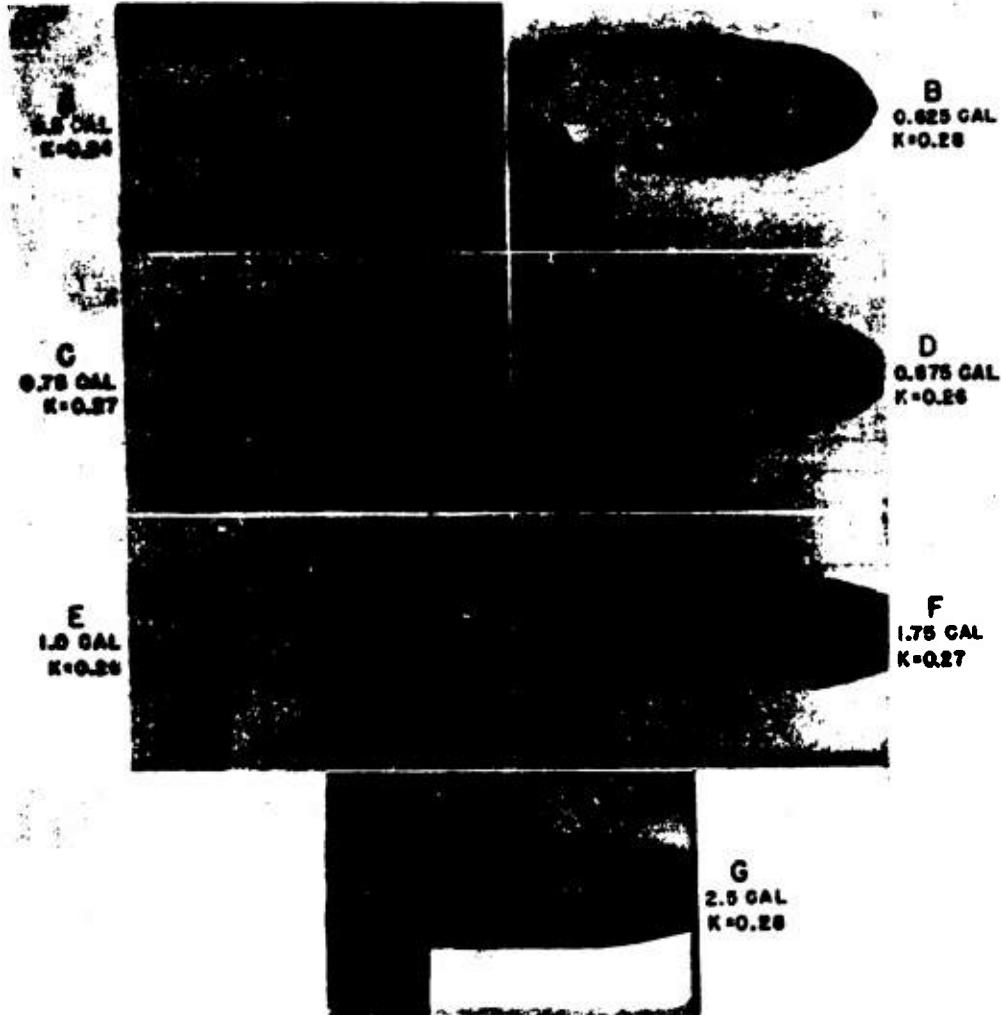


FIGURE 4. Variation in cavitation developed on various ogives at K_i approximately 0.26. (Note that longer ogives extended to the right outside the camera range and appear cut off in these and subsequent photographs.)

CONFIDENTIAL

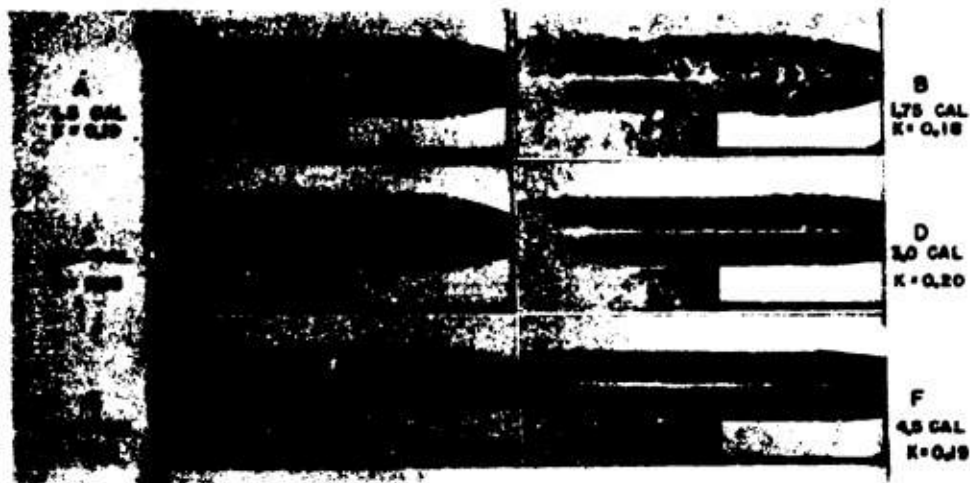


FIGURE 5. Variation in cavitation developed on various ogives at $K \approx 0.19$.

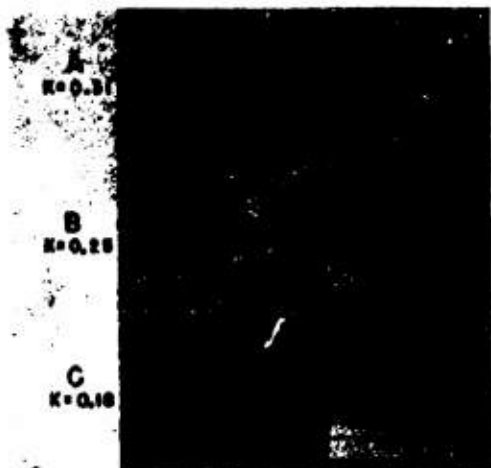


FIGURE 6. Development of bubble; 2.0-caliber ogive.

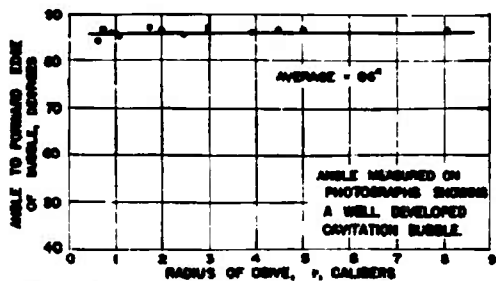


FIGURE 8. Angle to forward edge of well-developed cavitation bubble, ogive noses.

1.0-caliber radius. It is interesting and probably significant to note that the type of cavitation bubble also undergoes a change in this region. Noses of less than 1.0-caliber radius show a distinct fine-grained cavitation bubble, and those of greater radii than 1.0 caliber have a coarse-grained bubble.

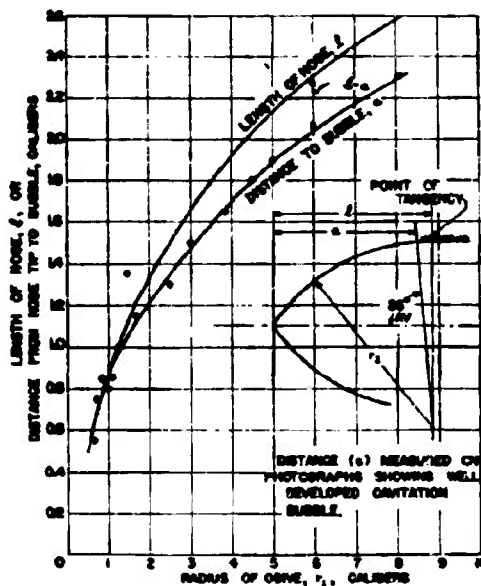


FIGURE 7. Distance of cavitation from tip of nose for well-developed bubble on ogive noses.

Figure 9 shows pictures of three ogive noses having radii of 0.875, 1.00, and 1.125 calibers at three stages of cavitation, roughly for K 's of 0.40, 0.33, and 0.26. In the 0.875 series (A, B, and C), it is seen that the cavitation is of the fine-grained nature throughout, although some of the coarse-grained bubbles are

appearing at the lowest value of K . The 1.0-caliber series, (D, E, and F), shows the typical fine-grained cavitation band at the highest value of K (D), and somewhat of a mixture of fine and coarse grain in E and F. The 1.125-caliber series, (G, H, and I), shows the typical coarse grain throughout.

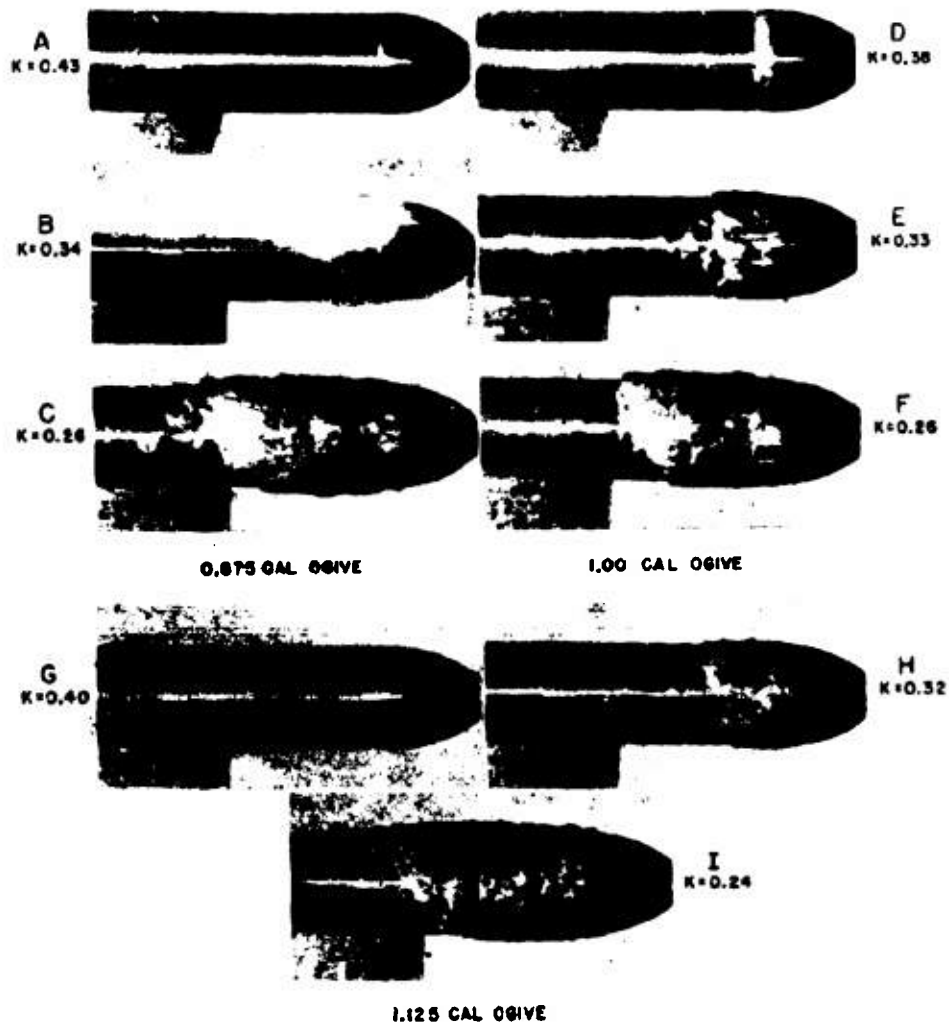


FIGURE 9. Influence of nose shape on formation of fine-grained and coarse-grained cavitation at different K values.

CONFIDENTIAL

6.3 EFFECT OF YAW

It is intended to investigate the effect of yaw on the cavitation bubble for the full range of noses included in this series. To date, however, results can be reported for the hemispherical nose only. Observations of the value of K for incipient cavitation were made at yaws of 0, 3, and 6 degrees, and these results are shown in Figure 10. It is seen that there is a rapid increase in K , with increasing yaw angle. The significance of this is made more apparent by the scale on the right of the diagram, which gives the submergence necessary to avoid cavitation with this hemispherical nose at a speed of 40 knots. With zero yaw, at 40 knots, cavitation will be avoided with a submergence of 20 ft, but the submergence will have to be increased to 25 ft should the yaw be 3 degrees, and with a yaw of 6 degrees, cavitation could not be avoided at any submergence less than 37 ft. Of course, as the speed is increased or decreased, the submergence would have to be increased or decreased accordingly.

Figure 11 shows photographs of the hemispherical nose at yaws of 0, 3, and 6 degrees, each for two dif-

ferent values of K . These pictures show clearly the effect of yaw on the shape and position of the cavi-

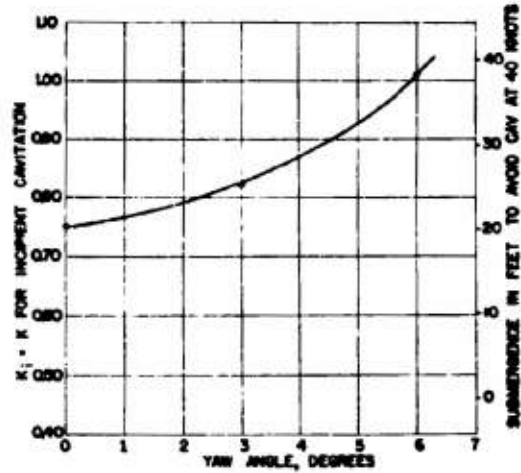


FIGURE 10. Cavitation parameter versus yaw. Hemispherical nose.

ferent values of K . They also show quite conclusively that the plane of the forward edge of the cavitation bubble



FIGURE 11. Effect of yaw on bubble. Hemispherical nose.

CONFIDENTIAL

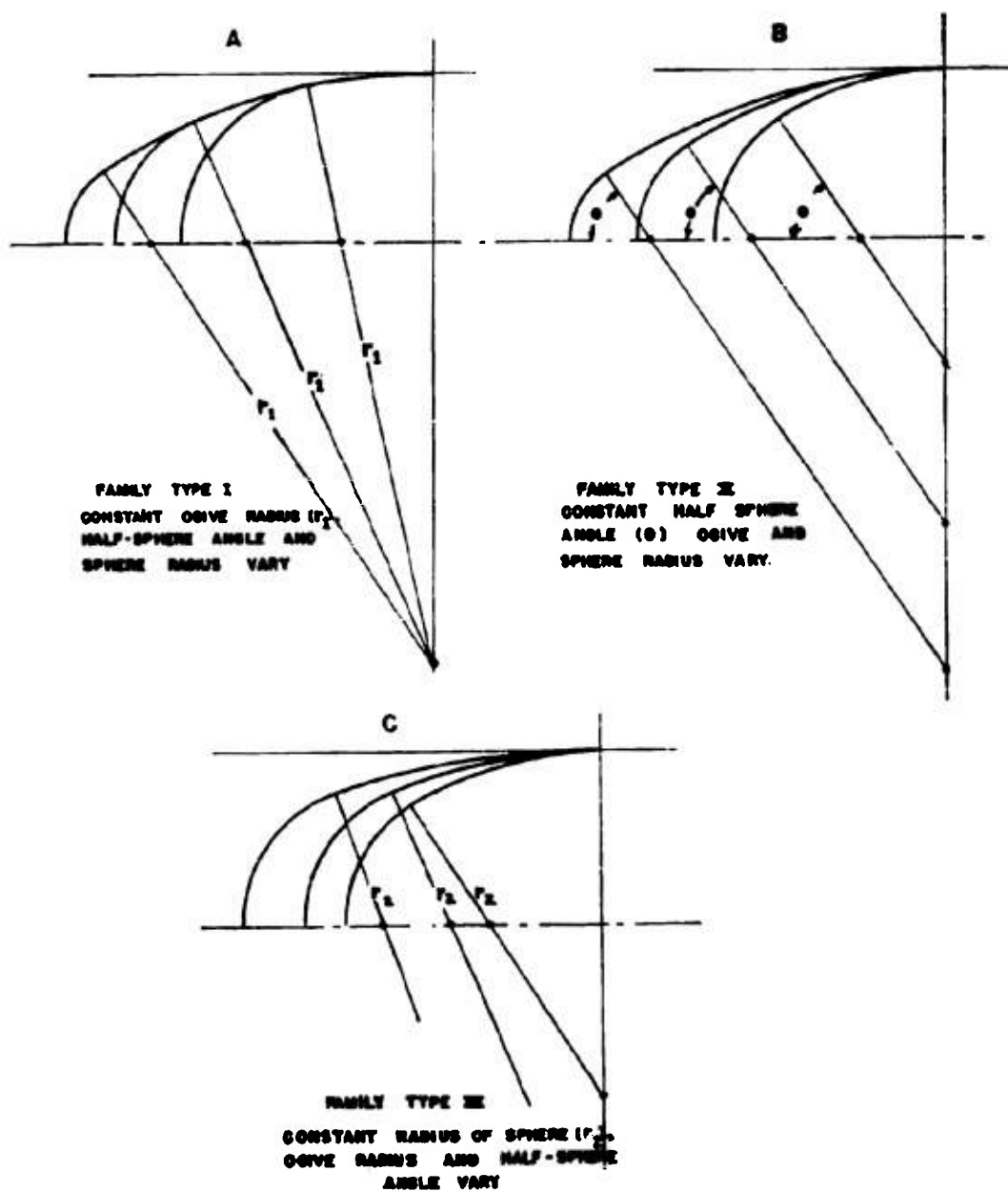


FIGURE 12. Method of construction. Families of spherogives.

CONFIDENTIAL

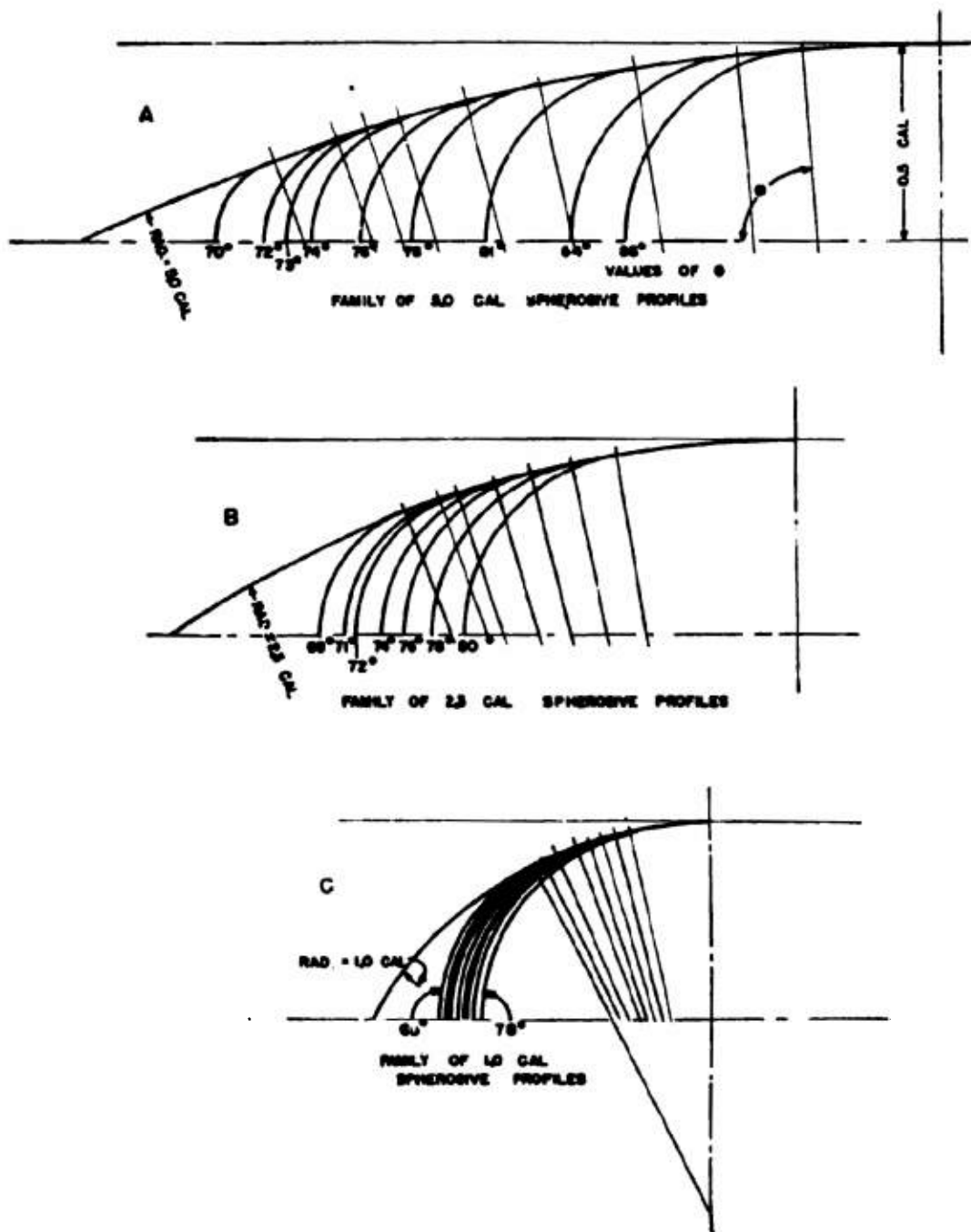


FIGURE 13. Spherogive profiles arranged as Type 1 families.

CONFIDENTIAL

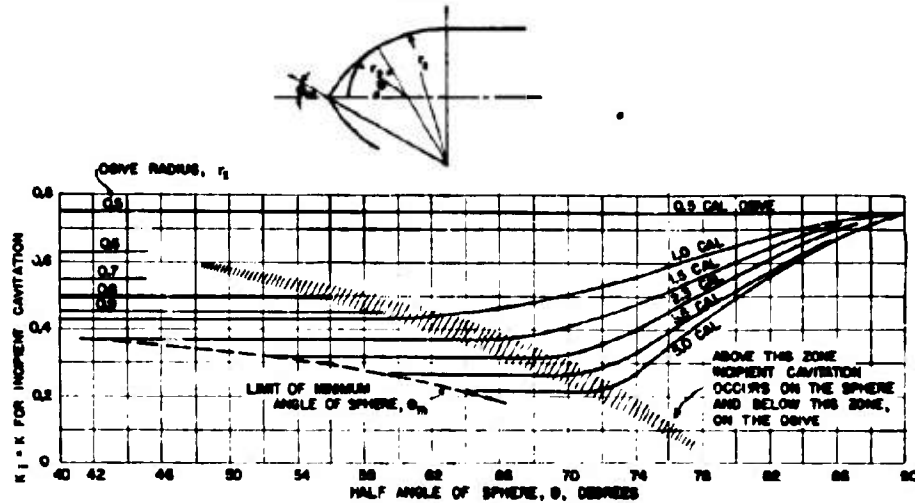


FIGURE 14. Cavitation parameter, K , versus sphere angle, spherogive nose.

remains practically at right angles to the direction of travel regardless of the yaw, at least for yaw angles up to 6 degrees. This is considered one of the inherent properties of the spherical nose tip.

5.8 SPHEROGIVE NOSES

Thirty-five spherogive noses of various proportions have been tested thus far. The tests on this number of noses have furnished interesting and instructive data but are not by any means sufficient to predict definitely the performance of any given spherogive nose. It is believed that enough information is now available to permit some general conclusions regarding the properties of the spherogive family of noses, but much yet remains to be done.

A spherogive nose shape is made by terminating an ogive in a segment of a sphere, the curves of the sphere and ogive, of course, being tangent at their junction. Figure 12 shows that a family of spherogives can be constructed in three ways: (1) by maintaining the radius of the ogive r_1 constant, which gives a series of spheres of varying radii r_2 and also varying half-sphere angle θ ; (2) by maintaining the half-sphere angle θ constant, resulting in varying values for the radii of both the sphere and ogive; (3) by maintaining the radius of the sphere r_2 constant, resulting in varying values for the radius of the ogive and the half-sphere angle. Some interesting tests of families of noses constructed in this manner will be discussed.

The program contemplated tests on five families of spherogives based on ogives having radii of 5.0, 3.5, 2.3, 1.5, and 1.0 calibers. Only a few models were made for the 3.5- and 1.5-caliber series and the test results on these were not very consistent so emphasis will be placed mainly on the 5.0-, 2.3-, and 1.0-caliber series. Figure 13 shows profiles of these three families of spherogives drawn to scale so their relative shapes can be easily observed. Table 2 gives the observed values of K for incipient cavitation for the spherogive nose shapes tested.

These values of K have been plotted against the half-sphere angle θ for each nose and faired curves drawn through the points as shown in Figure 14, from which some interesting observations can be made. The horizontal portions of the curves represent the incipient cavitation parameter for the ogive alone, corresponding to those given by the curve in Figure 2. This shows that the sphere can be increased in size without affecting the incipient cavitation parameter until some critical value of the half-sphere angle is reached. This region is represented by the shaded zone at the break in the curves. This shaded region represents a transition from cavitation on the ogive to cavitation on the sphere. In other words, all nose shapes represented by the curves in the region above the shaded zone will cavitate first on the sphere and all below this zone will cavitate first on the ogive. The line of demarcation is not definite, for, as might be expected, cavitation can occur on the ogive and on the sphere simultaneously.

CONFIDENTIAL

TABLE 2. Incipient cavitation parameter K_i for spherogive noses.

Ogive radius r_i in calibers	Half-sphere angle θ in degrees	Observed K_i	K_i for ogives only
5.0	70	0.22	0.22
	72	0.22	
	73	0.26	
	74	0.27	
	76	0.35	
	78	0.44	
	81	0.54	
3.5	74	0.33	0.26
	77	0.45	
	80	0.54	
	80 ^{1/2}	0.58	
2.3	69	0.33	0.32
	71	0.35	
	72	0.35	
	74	0.40	
	76	0.45	
	78	0.50	
1.5	72	0.46	0.37
	74	0.47	
	76	0.53	
	78	0.54	
1.0	63	0.49	0.43
	65	0.51	
	67	0.49	
	70	0.52	
	72	0.53	
	74	0.55	
	76	0.60	
	78	0.63	

Figure 14 can be used for the design of spherogive noses to fit varying requirements for bluntness and incipient cavitation.

The data given in Figure 14 make possible the plotting of another chart showing the relation between the radii of the sphere and ogive, the half angle of the sphere and the cavitation parameter. This chart appears as Figure 15 and covers the whole field of possible spherogives, although available data permit the plotting of only a portion of the curves involved. As will be seen, this chart gives the radius of the sphere corresponding to any half-sphere angle and several values of ogive radius. In addition, there appear dotted lines of constant K values for incipient cavitation. The shaded zone is similar to that in Figure 14 in that it represents the region of transition from cavitation on the ogive to cavitation on the sphere.

An inspection of Figure 15 shows a surprisingly small region in which the cavitation is governed by

the sphere. It also shows that the longer the ogive radius, the larger the half-sphere angle can be without increasing the incipient cavitation parameter. The shaded zone, representing the region of transition from cavitation on the ogive to cavitation on the sphere, appears to intercept the horizontal axis at about an 80-degree half-sphere angle, indicating that cavitation will always be on the sphere for angles above 80 degrees regardless of the ogive radius.

4.20 BUBBLE DIMENSIONS FROM PHOTOGRAPHS

4.20.1 Hemispherical Nose

The water tunnel is equipped for making photographs of a model during the various stages of cavitation. These can be taken from the side, as in Figures 16 and 18, or from the top, as in Figure 17, when the effect of yaw is to be shown. As can be seen, these photographs give very clear and distinct details of the cavitation bubbles so they can be measured for the determination of bubble dimensions. A few illustrations of the utilization of the measurements of photographs will be given for a model equipped with a hemispherical nose.

In Figure 16 is shown one of a series of photographs of the bubble, produced by a hemispherical nose, for various values of the cavitation parameter K . These photographs were measured to determine the length of the bubble from the point of the beginning of cavitation to the end of the bubble proper (miscellaneous small bubbles in the wake of the main bubble are neglected). The results of these measurements are plotted in Figure 19 as K against bubble length in calibers. Considering the many inaccuracies involved in determining the actual bubble size, it is believed the results are satisfactory. This figure shows that there is little change in bubble length at the higher values of K but the increase is very pronounced as the lower values of K are approached.

The variation in bubble length with yaw is shown in Figure 20. In this case the length of the bubble was measured on the starboard side and the yaw angle was positive, in other words, the nose was deflected to the starboard side. The points are not as consistent as could be desired but they do show that the bubble length increases about 20 per cent when the yaw is increased from 0 to 6 degrees.

Figure 17 is a top view of the model at 6-degree yaw and with $K = 0.27$, and Figure 18 is a side view

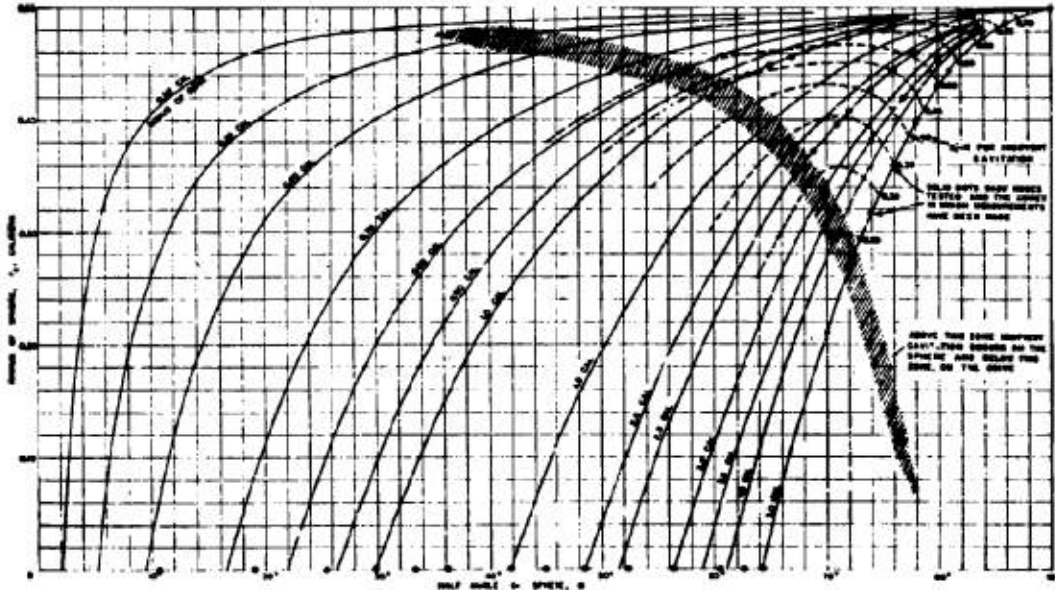


FIGURE 15. Relation between radius of sphere, radius of ogive, half angle of sphere and incipient cavitation parameter for ogives and spherogives.

taken simultaneously. A series of these top and side view photographs was measured to determine the length of the bubble on the starboard side as well as



FIGURE 16. Hemispherical nose; 0 degree yaw. $K = 0.24$. Side view.



FIGURE 17. Hemispherical nose; 6 degree yaw. $K = 0.27$. Top view.

the maximum diameter of the bubble and the distance from the nose tip to the point at which the maximum diameter occurred. The bubble length was

taken from the side views of which Figure 18 is a sample. The maximum bubble diameter and its distance E from the nose tip were measured as shown in Figure 17. One-half the maximum diameter of the bubble was taken as the distance from the centerline of the spherical nose to the edge of the bubble. Figure 21 shows the variation of the distance E with the cavitation parameter K , for yaws of 0, 3, and 6 de-



FIGURE 18. Hemispherical nose; 6 degrees yaw. $K = 0.27$. Side view.

grees. It is seen that the point of maximum bubble diameter recedes rapidly from the nose tip with decreasing values of K . The yaw angle seems to have little effect on E , at least for values less than 6 degrees.

Figure 22 shows the value of the maximum diameter of bubble for yaws of 0, 3, and 6 degrees. Here again the maximum diameter of bubble increases with decreasing K and the yaw angle has little effect.

Referring to Figure 17, it is seen that when the projectile is yawed, the bubble tends to follow the direction of the line of travel and in doing so the edge of the bubble on the top of the projectile forms a definite angle α with the line of travel. Many of these

diameter, in calibers, obtained. In the entire group of noses measured the sphere radius varied from a minimum of 0.211 calibers to 0.500 calibers, the maximum for the hemisphere.

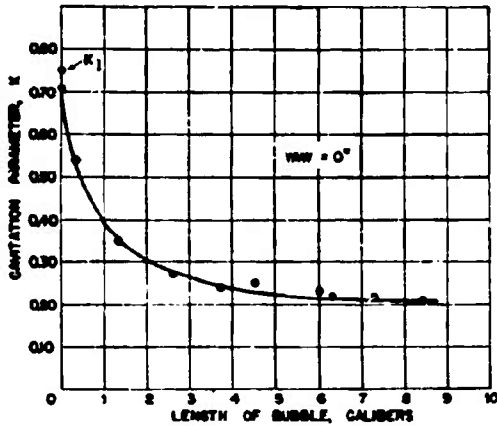


FIGURE 19. Cavitation parameter, K , versus length of bubble, (0 degree yaw). Hemispherical nose.

angles were measured for various values of K and yaw and the results are plotted in Figure 23. No attempt has been made to investigate this phenomenon further or to determine its significance.

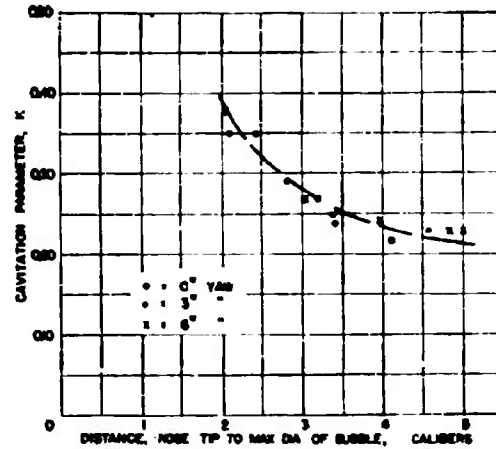


FIGURE 21. Cavitation parameter, K , versus nose tip to maximum diameter of bubble. Hemispherical nose.

In Figure 24 the maximum bubble diameter has been plotted against the radius of the sphere, both in calibers. It is remarkable to note that there appears to be a linear relationship between these two quantities, although it must be remembered that the meas-

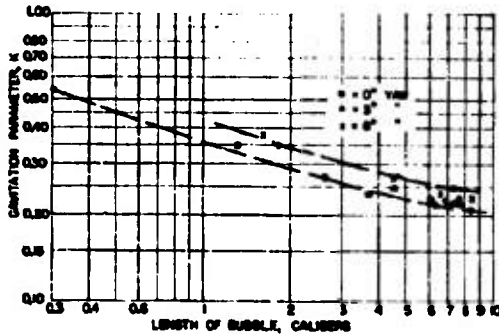


FIGURE 20. Cavitation parameter, K , versus length of bubble, (0, 3, and 6 degrees yaw). Hemispherical nose.

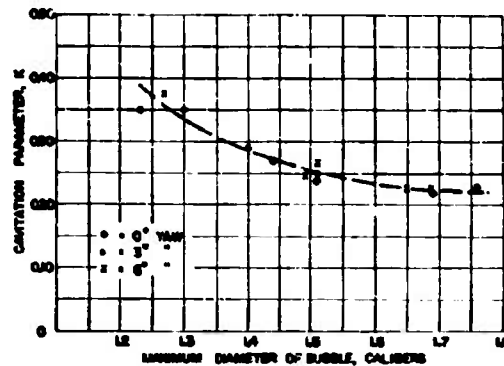


FIGURE 22. Cavitation parameter, K , versus maximum diameter of bubble. Hemispherical nose.

8.20.3

Spherogive Noses

An attempt was made to determine the effect of the radius of the sphere on the maximum diameter of the full cavitation bubble. Photographs of the 1.0-, 2.3-, and 5.0-caliber spherogive noses under full cavitation were carefully measured and the bubble

urement of these small photographs is subject to many errors.

The 5.0-caliber series is the only one in which it was possible to make measurements of the bubble diameter for values of the sphere radius in the region

where cavitation occurred on the ogive only. There are two noses with sphere radii of 0.211 and 0.268 calibers which have the same bubble diameter. This is not unexpected as this is the bubble diameter for the ogive, the sphere having no effect. The dotted horizontal lines indicating the bubble diameters for 2.3- and 1.0-caliber ogives are assumptions, although they are believed to be fairly accurate as they are drawn to correspond approximately to the bubble diameters for noses close to the transition point. No photographs have been taken of the full bubble produced by ogive noses, so the diameters of these could not be determined by measurement.

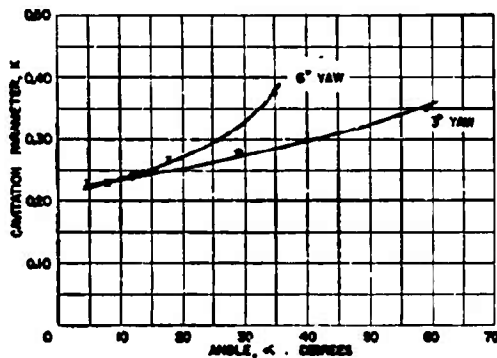


FIGURE 23. Cavitation parameter, K , versus angle α , of bubble with flow. Hemispherical nose.

Figure 24 furnishes good evidence to support the theory that the full bubble diameter is determined by the sphere radius. (See Chapter 4.)

5.11 EFFECT OF THE SPHERE SIZE

It has been shown that the full bubble diameter is determined by the radius of the sphere. The curves in Figure 14 show that incipient cavitation is governed by the half angle of the sphere θ for a given ogive. It is also true that the half angle of the sphere determines the extent and nature of the cavitation bubble during its development after the point of incipient cavitation has been passed. In Figure 25 have been assembled photographs of cavitation effects on spherogive noses having ogive radii of 1.0, 2.3, and 5.0 calibers and half-sphere angles of 72 and 76 degrees.

Comparing photographs A and F of Figure 25, of the 1.0-caliber series for a K of 0.21, it is seen that increasing the half-sphere angle θ from 72 to 76 degrees greatly increases the size of the cavitation bubble.

The 72-degree sphere produces a bubble only slightly longer than the projectile, whereas the 76-degree sphere produces practically a full cavitation bubble. A comparison of B and G for a higher value of K shows a decided increase in the extent of the bubble for the larger sphere angle. A like comparison can be made with the photographs of the 2.3-caliber and 5.0-caliber series; in every case there is a pronounced

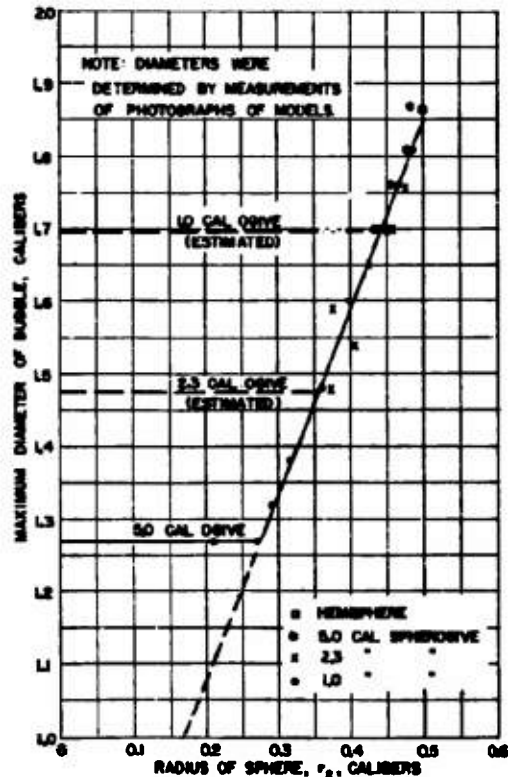


FIGURE 24. Radius of sphere versus diameter of fully developed bubble on spherogive noses at zero yaw.

increase in the cavitation effect due to increasing the half-sphere angle with the cavitation parameter remaining constant.

In connection with Figure 25, it is interesting to note that photographs B, H, I, and J show cavitation on both the sphere and the ogive.

Figure 26 shows how the cavitation bubble is affected by variations in the ogive and sphere radii, the half-sphere angle remaining constant. Photographs A, B, C, and D show the bubble for four spherogive noses with a half-sphere angle of 72 de-

degrees and K remaining constant at 0.21. It is seen that there is an increase in the size of the cavitation bubble as the nose becomes more and more blunt. The four pictures on the right, E, F, G, and H were selected to show approximately the same degree of cavitation, and it should be observed that the value of K , for this condition, increases as the bluntness of the nose increases.

The effect of varying the half-sphere angle is shown in Figure 26 of Chapter 4, which is a series of photographs of a family of 5.0-caliber spherogives. In this case the 74-degree sphere appears to be at the transition point as cavitation is occurring on both the ogive and the sphere. The noses with spherical angles less than 74 degrees cavitate on the ogive and for angles of greater than 74 degrees the cavitation is on the sphere only. The last five photographs have been selected to show approximately the same degree of

cavitation and it is seen that as the noses increase in bluntness, i.e., from 76 to 86 degrees for the half-sphere angle, the value of K increases from 0.25 to 0.57. Stating this in terms of submergence and speed, the 76- and 86-degree noses would have the same degree of cavitation at a speed of 60 knots with a submergence of 57 ft for the 86-degree nose and only 7 ft for the 76-degree nose.

5.11 COMPARISON OF OGIVE AND SPHEROGIVE BUBBLES

Comparisons have already been made between the cavitation parameters for ogives and spherogive noses at the point of incipient cavitation. It would be instructive to observe the development of the cavitation bubble on the two types of nose for values of K lower than that for incipient cavitation.

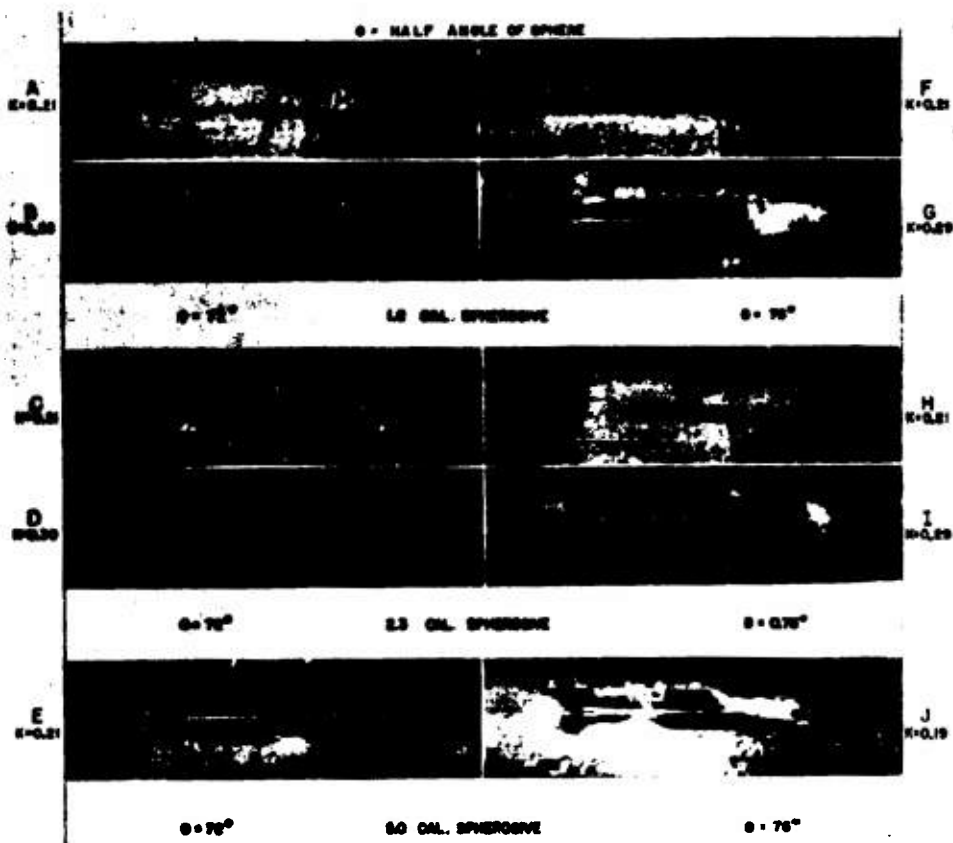


FIGURE 25. Effect of size of sphere on cavitation parameter. Spherogive noses.

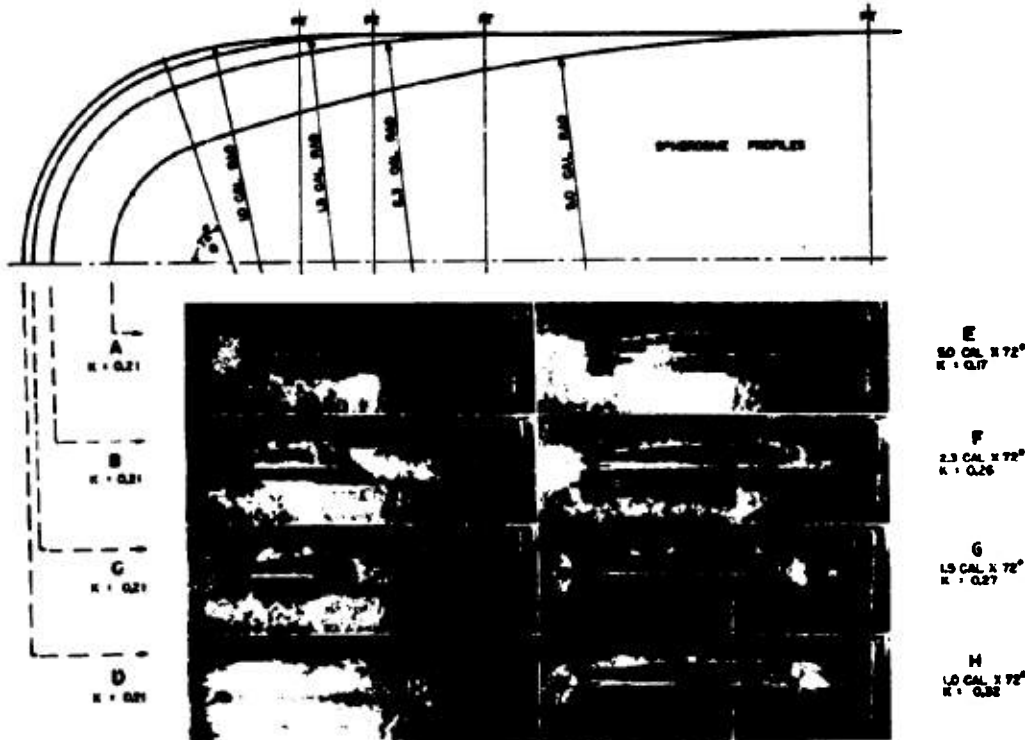


FIGURE 26. Cavitation bubbles; 72-degree spherogives.

The first series of photographs in Figure 27A to C, shows the cavitation bubbles at a K of approximately 0.25 for the following nose shapes: 1.0-caliber ogive, and 1.0-caliber by 6.5-degree, 2.3-caliber by 76-degree, 3.5-caliber by 77-degree, and 5.0-caliber by 78-degree spherogives. All these shapes, excepting the 1.0-caliber by 65-degree spherogive, have approximately the same K for incipient cavitation (0.43 to 0.45). The 1.0-caliber by 65-degree spherogive has a somewhat higher K , and it has been included as it was the best available photograph showing a spherogive cavitating on the ogive only. It will be seen that the bubbles for the three spherogives C, D, and E are of about the same size, and that cavitation is taking place on both the sphere and the ogive. The 1.0-caliber by 65-degree spherogive (B) is cavitating on the ogive only as the spherical segment is so small that it has no effect. It is of interest to note that the bubbles in photographs A and B are of the same size, which should be the case as both are for 1.0-caliber ogives at a K of 0.26.

The second series of photographs in Figure 27 (F to I), shows the cavitation bubbles at a K of approxi-

mately 0.19 for the following noses: 1.5-caliber ogive, and 2.3-caliber by 72-degree, 3.5-caliber by 74-degree, and 5.0-caliber by 76-degree spherogives. All of these noses have nearly the same K ; (0.34 to 0.37). In this series also it is observed that the bubbles for the spherogives are of practically the same size, while that on the ogive is of much smaller size.

From these preliminary data it seems reasonable to draw four conclusions subject to revision after more complete test results are available:

1. Spherogive noses with spherical segments larger than the critical angle and having the same K , will have practically the same size and type of bubble at lower values of K .

2. If an ogive and a spherogive with a spherical segment larger than the critical angle have the same K , the bubble formed at lower values of K will be shorter for the ogive than for the spherogive.

3. If an ogive and a spherogive have the same radius for the ogive, the values of K , and the size of the cavitation bubbles will be the same for both noses if the spherical segment is smaller than the critical angle.

4. The cavitation bubble originating on a spherical tip develops faster as K is reduced than one starting at the same K , which originates on a surface of larger radius of curvature such as an ogive.

5.13 MEASUREMENTS OF PHOTOGRAPHS

All models have been made 2.00 in. in diameter so this can be used as the unit of length for measurements made on photographs. Owing to the unequal horizontal and vertical distortion caused by the Lucite window in the tunnel, the diameter of the model will represent 2 in. in the vertical direction and 1.83 in. in the horizontal direction.

5.14

CONCLUSIONS

Although based on incomplete data, the following conclusions seem to be justified:

1. The incipient cavitation parameter K_i for ogive noses drops rapidly as the ogive radius is increased from 0.5 to 1.0 caliber, the decrease being much less pronounced for radii between 1.0 and 8.0 calibers.
2. The ogive radius drawn to this forward edge of a well-developed cavitation bubble makes an angle of about 86 degrees with the axis of the nose. This angle seems to be constant for all noses investigated.
3. The incipient cavitation parameter K_i increases rapidly with an increase in yaw angle. For a hemispherical nose K_i increases from 0.75 for zero yaw to

1.01 for 6 degrees yaw.

4. Photographs of well-developed bubbles on a hemispherical nose indicate that the plane of the forward edge of the bubble remains practically at right angles to the direction of travel for yaw angles up to at least 6 degrees.

5. When the sphere segment on spherogive noses is large compared to the ogive, cavitation occurs first on the sphere so that the inception and subsequent growth of the cavitation bubble depend only on the sphere size. When the sphere segment is small compared to the ogive, cavitation occurs first on the ogive, and the inception and subsequent bubble growth depend on the ogive and are independent of the sphere size. The critical sphere size dividing the two behaviors is different for different spherogive families. For the 5.0-caliber family of spherogives, this critical sphere size corresponds to a half-sphere angle θ of about 72 degrees, and for the 1.0-caliber family, this angle is about 60 degrees.

6. Based on measurements of photographs, it appears that the maximum diameter of the full cavitation bubble on spherogive noses varies directly with the radius of the sphere regardless of the ogive radius.

7. For a given family of spherogives, based on a constant ogive radius, the value of K for incipient cavitation, K_i , will be determined by the half-sphere angle. The blunter the nose, the higher the K_i value.

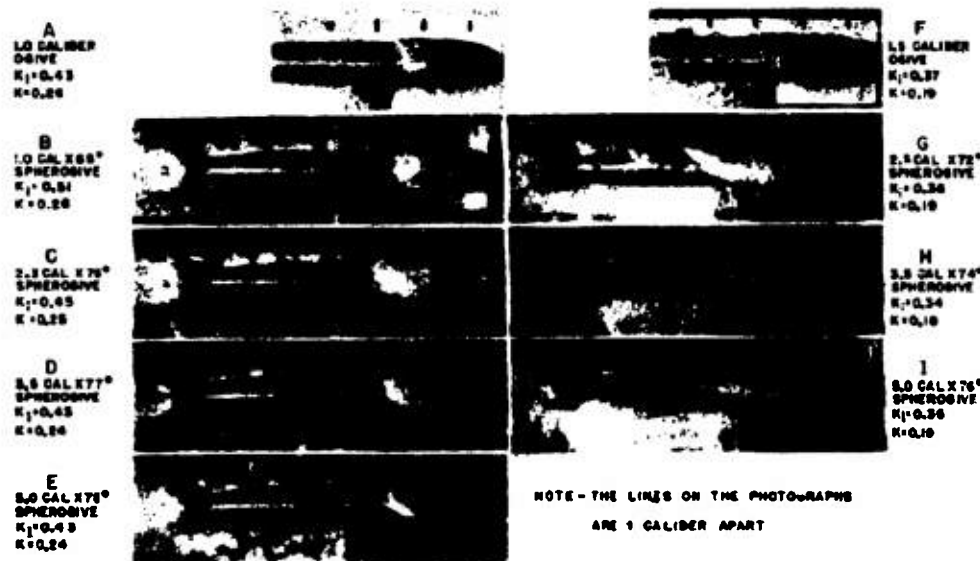


FIGURE 27. Comparison of ogive and spherogive bubbles.

Chapter 6

HYDRODYNAMIC FORCES RESULTING FROM CAVITATION ON UNDERWATER BODIES

PURPOSE AND SCOPE OF INVESTIGATION

WITH THE INCEPTION and growth of cavitation, the distribution of velocities and pressures around a moving body are changed, and the hydrodynamic forces are different from those existing under cavitation-free conditions. In the case of underwater projectiles, most interest is in the two extreme conditions—the initial stages immediately after the onset of cavitation and the fully developed stage when a large portion of the cavitating body is enclosed in a vapor cavity. For the initial stages, it is important to know how far cavitation can develop before affecting the forces and moments appreciably, as well as the magnitude of the resulting forces. This phase applies to the steady underwater run of all high-velocity torpedoes. For the fully developed condition, a knowledge of the forces and moments and the physical conditions of flow affecting these forces are important. This phase also applies to the air-water entry problems arising for various projectiles where the air cavity which is obtained at entry is similar, if not identical, to the vapor cavity which is obtained with cavitation.

In order to investigate these different aspects, measurements of forces and moments were made for a variety of bodies subjected to cavitating conditions in the high-speed water tunnel. Complete projectiles with different noses and tail structures were tested to determine the total performance for the incipient and more developed stages of cavitation. Short bullet-shaped models with different noses were tested to obtain the effect of the nose shape alone, primarily for fully developed cavitation.

In addition to the measurements on three-dimensional bodies, that is, bodies of revolution, tests were made for cavitating and noncavitating flow of the drag of a cylinder with its axis normal to the direction of motion. The drag of this two-dimensional case and of two of the three-dimensional shapes are compared with values calculated from measured pressure distributions on the body surface.

6.1 THE EFFECT OF CAVITATION ON DRAG

6.1.1 Physical Growth Necessary to Change the Drag

The amount of cavitation necessary to cause a measurable change in drag is dependent somewhat on the shape of the body, the kind of cavitation that is formed, and the relative magnitude of the drag without cavitation. The results of measurements on several different bodies, and photographs of the cavitation at various stages of development are shown in Figures 1 to 11. The pictures were obtained with exposures of the order of $20 \mu\text{sec}$ so that the flow was effectively "stopped." The drag measurements are presented as curves of the drag coefficient C_D plotted against the cavitation parameter K . Decreasing values of K represent conditions for increased cavitation. The methods of evaluating and correcting the test data and a list of symbols and definitions are given in the Appendix.

HEMISPHERE NOSE

The first two sets of data were obtained with a cylindrical body having an ogival tail or afterbody with a hemisphere nose in one case, and with a square-end nose in the second. With this simple form a good comparison of the effect of nose shape should be obtained. Flash photographs of cavitation on the hemisphere are shown in Figure 1. The outline of the projectile can be seen in the first photograph, while in the second photograph, a small band of fine-grained cavitation is seen just aft of the junction between the hemisphere and the cylinder. In the bottom two photographs, the entire body is enveloped in a cavitation cavity. The drag coefficient of this body is shown in Figure 2 as a function of the cavitation parameter K . On this figure the dashed curve represents C_D values calculated from measured pressure distributions and will be discussed in detail later. The curve of measured C_D values shows that there is no sudden increase in drag with the onset of cavitation.

Instead, with increasing cavitation (decreasing K) the resistance increases very slowly until a K of about 0.5 is reached, when the cavitation zone on the nose is about $\frac{1}{2}$ caliber long, as can be visualized by interpolation between photographs. With further development of cavitation, however, C_D rises rapidly to

develops, but increases very slowly until the wispy formation coalesces to form the white plume. This increase is at about the same rate as observed for the hemisphere, but is a much smaller percentage of the total drag. Here, in order to increase the drag materially above its already high value, it is necessary that enough cavitation be formed to displace the flow away from the body further than for noncavitating flow separation and to increase the turbulent wake downstream.

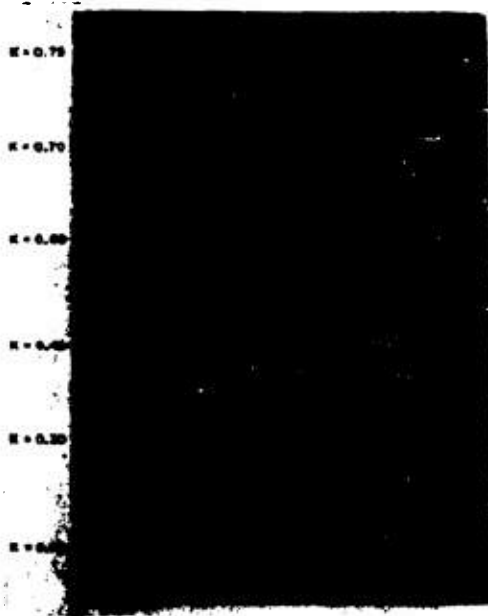


FIGURE 1. Cavitation on cylinder with hemispherical nose and ogival tail. Yaw = 0 degree.

several times its initial value. A peak value is reached after which C_D tends to decrease as the trend of the calculated dashed curve would predict.

SQUARE-END CYLINDER

In Figures 3 and 4, data are shown for the cylinder with the square end. This "nose" produces the wispy type of cavitation at inception which develops into a fine-grained white plume and ultimately to a clear-walled cavity extending back from the separation point in the sharp edge as cavitation increases.

The drag without cavitation is initially nearly ten times the value for the hemisphere. It is almost completely form drag caused by separation of the non-cavitating flow from the body at the sharp corner of the nose. As in the case of the hemisphere, the drag does not change suddenly as cavitation forms and

VARIOUS NOSES ON A TORPEDO

Measurements for a ring-tailed torpedo with exhaust stacks in the ring are shown in Figure 5. No photographs were obtained with the test, but the development of cavitation at various points on the

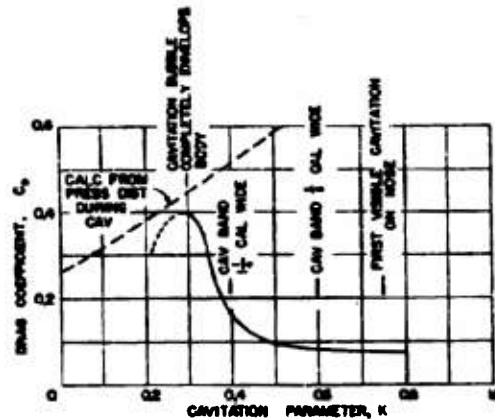


FIGURE 2. Effect of cavitation on drag of cylinder with hemispherical nose and ogival tail. Yaw = 0 degree.

projectile is described by notes on the curves. Two noses were used with this projectile. One, the so-called Mark 13 nose, is composed of a $2\frac{1}{4}$ -degree included angle cone, tapering down from full diameter to 0.92 degree of the maximum diameter, with a spherical segment tip having an $88\frac{3}{4}$ -degree half angle. The other, a 2.3-caliber by 78-degree spherogive, is formed by replacing the pointed tip of a 2.3-caliber ogive with a spherical segment which becomes tangent to the ogive surface at a half angle of 78 degrees.

The Mark 13 nose is very little different from a hemisphere and produces the same type of cavitation just aft of the tangent point with the conical surface. Inception is obtained at a K of about 0.66 instead of

0.75, however. The tail structure and the nose begin to cavitate at about the same time. There is no measurable change in drag on this projectile immediately after the onset of cavitation. C_D increases materially only after a moderate band is developed on the nose (less than for the hemisphere on the cylindrical body, however) and pronounced cavitation develops on parts of the tail structure.

The spherogive nose has much better characteristics than either the hemisphere or the Mark 13 and, consequently, does not cavitate until K is reduced to

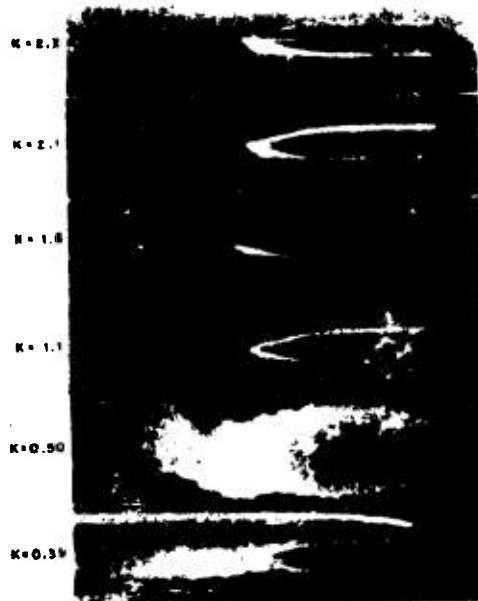


FIGURE 3. Cavitation on square-end cylinder with ogival tail. Yaw = 0 degree.

approximately 0.5. As a result, tail cavitation is well developed before nose cavitation appears and causes the drag to increase while the nose cavitation is still in its early stages.

BLUNT NOSE ON A DEPTH BOMB

A depth bomb with a ring tail and a blunt nose was tested and the results are shown in Figures 6 and 7. The nose is a 1-caliber ogive truncated so the diameter of the face is $\frac{3}{8}$ caliber. The edge of the flat face is rounded slightly. The initial cavitation on this projectile forms on the ogival surface at the junction

with the flat face and is very fine-grained in character. The tail surfaces begin to cavitate soon after inception on the nose. The cavitation-free drag of the projectile is about three times the value c_v , the drag of the simple body with hemisphere nose shown in Figure 2. With the onset of cavitation, there is, if anything, a slight tendency for the drag to drop off. An increase is obtained, however, with a relatively small amount of cavitation on the nose and the tail. In fact, the rapid increase in drag of this particular projectile occurs with less visible cavitation than on any of the other models discussed thus far.

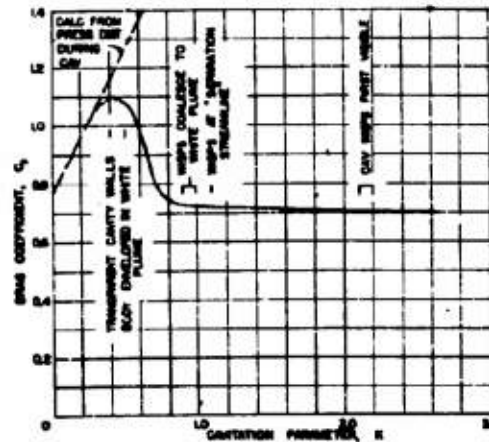


FIGURE 4. Effect of cavitation on drag on square-end cylinder with ogival tail. Yaw = 0 degree.

EFFECT OF YAW

A set of data showing the effect of cavitation with yaw is shown in Figure 8 for the Mark 13-2 torpedo with a hemisphere nose, the Mark 13 nose, and a 5-caliber by 76-degree spherogive nose. Photographs of the cavitation are shown for each nose in Figures 9, 10, and 11. The curves of Figure 8 show results similar to those already observed at zero yaw. With the hemisphere and Mark 13 nose very little change in drag occurs until cavitation is fairly well developed on both the nose and the tail surface. Actually cavitation appears first on the tail ring at about $K = 0.9$ and later on the lee side of the hemisphere at $K = 0.83$. The drag with the hemisphere nose is only 10 per cent greater at $K = 0.62$ when the cavitation band on the nose has grown to a length of about $\frac{1}{2}$ caliber. With the Mark 13 nose, nose cavitation appears at lower K as does the sharp increase in drag. Here the influence of the tail cavitation becomes more im-

portant. With the 5-caliber by 76-degree spherogive, nose cavitation does not appear at all until after cavitation on the tail and, in this case, on the afterbody also, has caused the drag to rise. The principal effect of the yaw seems to be that all stages of cavitation occur earlier, that is, at higher values of K than

amount of cavitation formed at this point occupies an appreciable physical volume.

6.2.3 Effect on Boundary Layer and Skin Friction

In general, the drag of bodies is the sum of skin friction and form drag. As cavitation develops, the relative proportions of the two components are changed. Finally for fully developed cavitation where

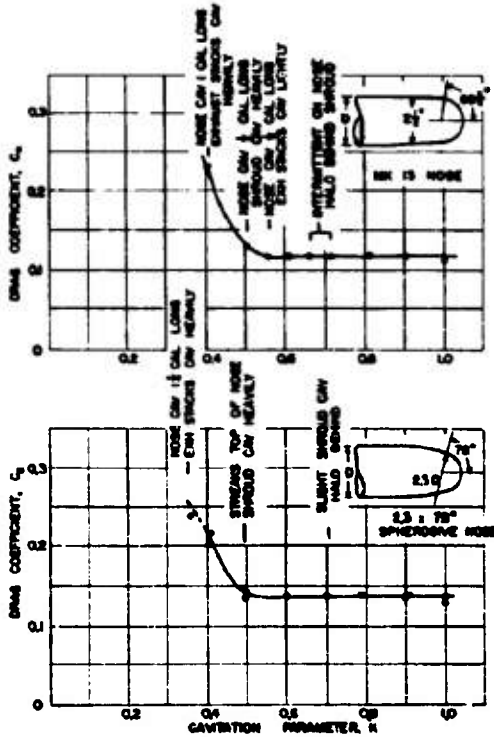


FIGURE 5. Effect of cavitation on drag of ring tail torpedo with 4 exhaust stacks. Yaw = 0 degree.

do the corresponding stages on the body with zero yaw. The result is that for any constant value of K less than K_c , the drag increases more rapidly with yaw than it does for the noncavitating condition.

6.2.3 Summary

To summarize, these examples show the common effects that the onset of cavitation as observed visually does not result in an immediate sharp increase in drag. Instead, the drag increases slowly, and in one case actually tends to drop off slightly, until sufficient cavitation is formed to change the basic flow pattern around the object. For all cases except one, the

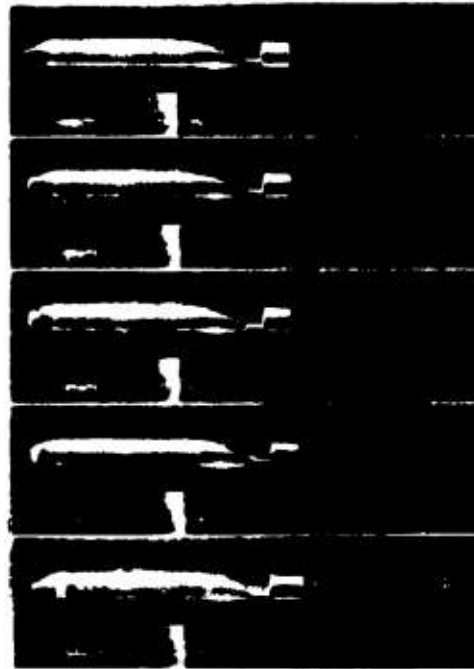


FIGURE 6. Cavitation on blunt-nosed depth bomb (1-caliber ogive truncated to 2 1/2-caliber flat face with edge rounded). Yaw = 0 degree.

the projectile is completely enclosed in a cavity, and contacts the fluid only over a small area at the nose tip, the drag becomes almost 100 per cent form drag. The kind of effect cavitation produces will depend on the body shape which determines the ratio of form drag to skin friction for noncavitating conditions. The influence of cavitation in affecting the form drag can be visualized rather clearly, since the effective shape of a body is, of course, changed by the bubble formation. The physical mechanism of its effect on skin friction can be explained qualitatively by com-

parison with local separation and its effects on the boundary layer development.^{5,6,7,8}

For cases where the drag is due primarily to skin friction, it will be highest when the boundary layer is turbulent. At a given Reynolds number (based on the

or discontinuities in the curvature at the surface that will cause local separation of the flow, and hence introduce turbulence.

For the types of cavitation already discussed, a definite similarity exists between the cavitation and separation. Reference to Figure 1 shows that fine-grained cavitation forms a ring just aft of the junction between the hemisphere tip and the cylinder. Figure 3 shows thin wisps forming in eddies well

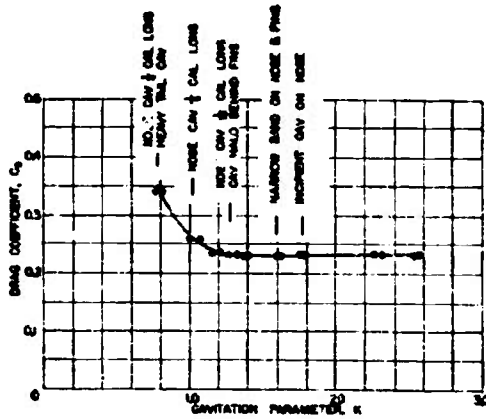


FIGURE 7. Effect of cavitation on drag of blunt-nosed depth bomb (1-caliber ogive truncated to 3/4-caliber flat face with edge rounded). Yaw = 0 degree.

length of the projectile in direction of motion), if an appreciable portion of the boundary layer is laminar, C_D will be much lower. Any influence which causes an early transition to a turbulent layer will tend to

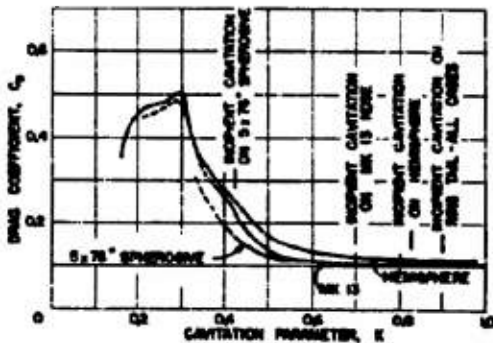


FIGURE 8. Effect of cavitation on drag of Mk 13-2 torpedo with three different noses. Yaw = 3 degrees.

increase C_D . In noncavitating flow, this can be accomplished by increasing Reynolds number and/or increasing the turbulence in the surrounding fluid. It can also be accomplished artificially by providing roughness or obstructions on the surface of the body,

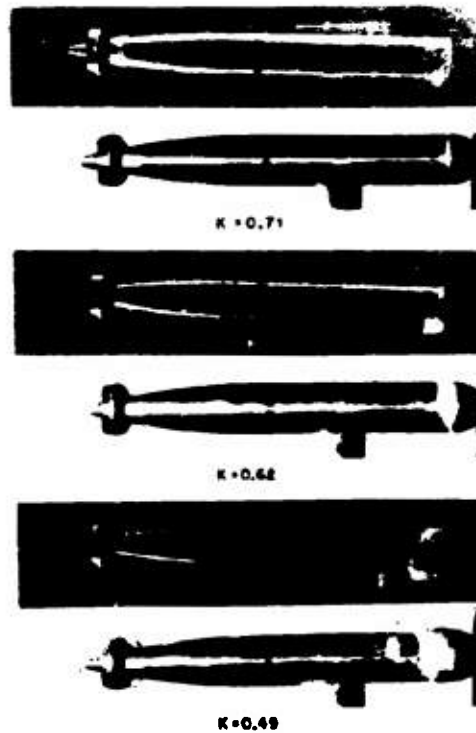


FIGURE 9. Hemisphere nose on Mk 13-2 torpedo. Yaw = 3 degrees. Top and side views.

away from the projectile surface. Figure 6 shows fine-grained cavitation appearing at the discontinuity between the flat-face and the ogive surface of the nose. Each of these has the common characteristic that cavitation appears first at or near a discontinuity in surface curvature.

In Figure 12, in the left column, are flow line diagrams for these same noses on which the zone of separation is shown. These diagrams were drawn from actual observations in the polarized light flume^{2,3} at

very low Reynolds numbers, so the separation effects are exaggerated. However, it is clear that for these cases, both separation and cavitation occur in the same general vicinity. In the initial stages, therefore, cavitation must be similar to separation in its effect on the drag. This idea is in agreement with the cases discussed thus far.

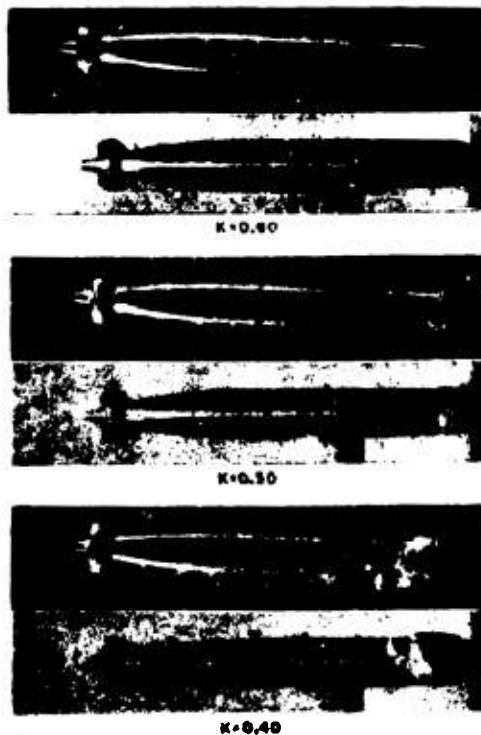


FIGURE 10. Standard Mk 13 nose on Mk 12-2 torpedo. Yaw = 3 degrees. Top and side views.

With the blunt-nosed bodies, the form drag is initially high due to severe separation. Incipient cavitation occurs in the same zone as the separation and has practically no effect on the drag. With bodies having sharp discontinuities in surface curvature such as that between the hemisphere and the cylinder, the boundary layer probably starts as predominantly turbulent, so that cavitation alters the conditions only slightly. C_D increases materially only with the development of enough cavitation to establish a new effective shape for the body, and hence alter both skin friction and form drag.

With more streamlined noses, separation does not occur under normal conditions and the boundary layer remains laminar over a longer distance from the tip of the nose. The minimum pressure on the body surface usually occurs at some point ahead of the maximum diameter so that it is possible that, on small projectiles at least, cavitation occurs in the normally laminar zone. The bottom diagram in Figure 12 for the semiellipse illustrates this possibility.

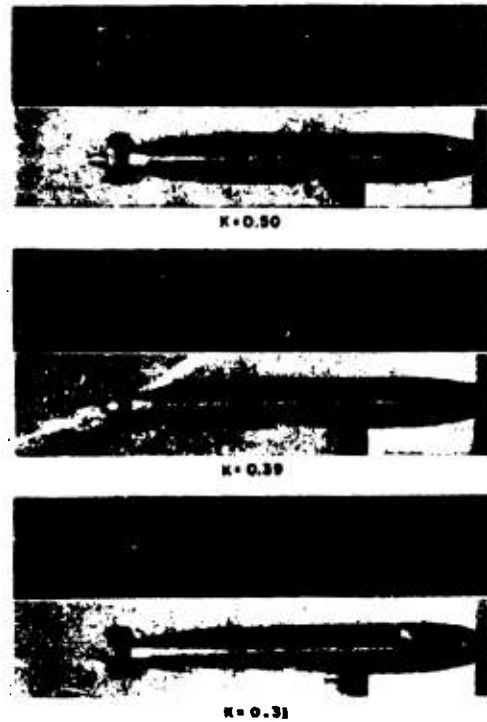


FIGURE 11. Five-caliber by 76-degree spherogive nose on Mk 12-2 torpedo. Yaw = 3 degrees. Top and side views.

Cavitation under these conditions should result in a transition to a turbulent boundary layer with a change in drag. For large projectiles the boundary layers for most velocities are almost completely turbulent so that this condition is of secondary importance. Also, with increased body fineness, the type of cavitation changes to coarse-grained so that, while turbulence is introduced, it is somewhat different from that formed by local separation and the analogy may not hold so closely.

CONFIDENTIAL

As cavitation grows, it effectively changes the shape of the body and thereby alters the form drag. Simultaneously, the skin friction should decrease because there is less high-velocity fluid in contact with the surface. Ultimately, if the cavitation envelops the body completely, there remains only form drag due to the difference between the pressure forces on the

depth bomb with a truncated ogive nose indicates a slight decrease in C_D with initial growth of cavitation. Knapp has suggested¹⁰ that with growth of cavitation in the early stages after inception the interplay between the increase in form drag and possible decrease in skin friction might result initially in such a decrease. A similar phenomenon has been measured in the case of some centrifugal pumps where measurable increases in head and efficiency have been observed when the pump impeller began to cavitate.^{11,12}

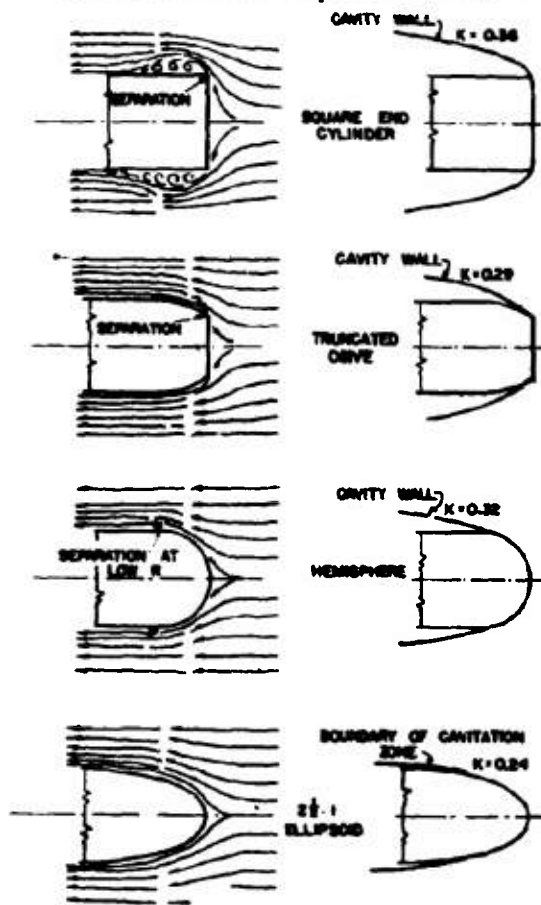


FIGURE 12. Flow line diagrams and cavity silhouettes.

small wetted area of the nose and the gas pressure in the bubble. The pressure distribution along the surface of the solid body is altered completely, while the effective body is enlarged by the extent of the cavitation bubble. The right-hand diagrams in Figure 12 show the full cavity conditions for the noses already discussed. These were obtained by scaling the cavity silhouettes from photographs.

The drag coefficient curve shown in Figure 7 for a

6.3.4 Drag in the Cavity

With a completely enveloping bubble such that contact with the water is made only over a small area at the forward portion of the body, skin friction can be neglected and all of the drag can be assumed to be form drag. This assumption will certainly hold for Reynolds numbers (based on diameter) greater than 10^4 on spheres, cylinders, and blunter bodies. For more streamlined shapes skin friction will cause a small correction. With enveloping bubbles the magnitude of C_D is not a single value but depends on the stage of bubble development. The total pressure (static plus dynamic) acting over the wetted portion of the body will depend on the velocity and on the static pressure in the undisturbed fluid while the "back pressure" acting over the after portion of the body will be independent of the velocity or pressure in the undisturbed fluid. This back pressure will be constant and equal to the vapor pressure for pure cavitation. An expression for C_D in the cavity stage showing its variation with bubble growth (and hence K) can be obtained by neglecting the skin friction and integrating the normal forces acting over the entire body surface as follows.

Writing the pressure or form drag as a summation of all components of the pressure forces taken parallel to the direction of motion gives

$$D = \int P \cos \theta da \quad (1)$$

where D = the pressure force acting in the direction of motion.

P = the unit normal pressure at any point on the body, also

= the static pressure in the undisturbed flow plus the pressure resulting from dynamic effects,

da = an element of area on the body surface,

θ = the angle between an area element da and the direction of motion.

This expression must be integrated over the wetted area of the body and the area enclosed by the bubble so that

$$D = \int_{\text{wetted area}} P \cos \theta da + \int_{\text{enveloped area}} P \cos \theta da. \quad (1a)$$

Simplifying the expression by writing $\cos \theta da = dA$, an element of area projected on to a plane normal to the direction of motion, gives

$$D = \int_{\text{wetted area}} P dA + \int_{\text{enveloped area}} P dA. \quad (2)$$

In this normal projection, the net projected area of the wetted surface and the bubble-enclosed surface are equal and can be denoted by A_w . Assuming now that $P = P_b = \text{constant}$ inside the bubble and adding and subtracting P_0 , the static pressure undisturbed flow, from the total pressure P , one obtains after simplifying,

$$D = \int_{A_w} (P - P_0) dA + (P_0 - P_b) A_w. \quad (2a)$$

Dividing by $(\rho v^2 A)/2$ gives the drag coefficient

$$C_D = \frac{D}{\frac{\rho v^2 A}{2}} = \frac{1}{A} \int_{A_w} \frac{P - P_0}{\frac{\rho v^2}{2}} dA + K \frac{A_w}{A} \quad (3)$$

where A = the area of the maximum section of the body projected normal to the direction of motion,

$$K = (P_0 - P_b) / (\rho v^2 / 2).$$

The first term in equation (2) is the integral of the pressure intensity caused by dynamic effects. The second is merely the difference between the hydrostatic pressure in the undisturbed fluid and the bubble pressure. When converted into a coefficient as in equation (3) the first term becomes a function of the dimensionless dynamic pressure distribution and the second a function of the cavitation parameter K . When $K = 0$ the limiting C_D equals the first term of equation (3). As the cavity decreases from the full bubble stage with increasing K , C_D will increase primarily because of the increase in $P_0 - P_b$. Usually the variation in wetted area and pressure distribution on the body will have a secondary effect. This trend persists until the cavity no longer envelops the body and hydrodynamic forces begin to act on the after portion as well as the nose or leading edge. Depending on the

body shape and attitude with respect to the flow, the drag may increase somewhat farther. Finally, however, as the bubble becomes smaller and smaller, C_D must approach the normal cavitation-free value. For streamlined objects, like most projectiles, this will be less than for the cavity stage. For nonstreamlined objects, like a cylinder normal to the flow, the cavitation-free drag may exceed the cavity drag.

Actual numerical evaluation of C_D from equation (3) requires that the pressure distribution denoted by the function P be known. An evaluation based on actual measurements of the pressures on the surfaces of cavitating bodies will be discussed in a later paragraph.

3.3 Effect of Body Shape on Cavity Drag

To investigate the effect of body shape on drag in the cavity, a series of measurements was made using models short enough to insure that the entire body could be completely enveloped by the cavitation pocket at the lowest value of K obtainable in the water tunnel. Six different noses were tested on short cylinders with either a blunt afterbody or with an ogival afterbody. The three basic types of nose shapes tested were:

1. Noses tipped with spherical segments, including the hemisphere, the Mark 13, the 2.3-caliber by 78-degree spherogive, and the 5-caliber by 76-degree spherogive.
2. Blunt noses, including the square-end cylinder and the truncated ogive.
3. "Streamlined" noses typified by a $2\frac{1}{2}$ - w -1 semiellipsoid.

DESCRIPTION OF CAVITIES

Typical top and side view pictures of the cavities formed by these shapes are shown in Figures 13 and 14. These photographs are not all for the same value of K nor for the same degree of bubble development. However, the essential features of the influence of nose shape can be seen, since further reductions in K do not change appreciably the forward portion of the cavity. In Figure 13 it will be noticed that for these models the cavity separates on the spherical tip so that the water is in contact with only a portion of the tip. For the blunt noses shown in Figure 14 the cavity separates from the body at the sharp edge so that water is in contact with only the flat face of the body. For the semiellipsoid, also shown in Figure 14, the

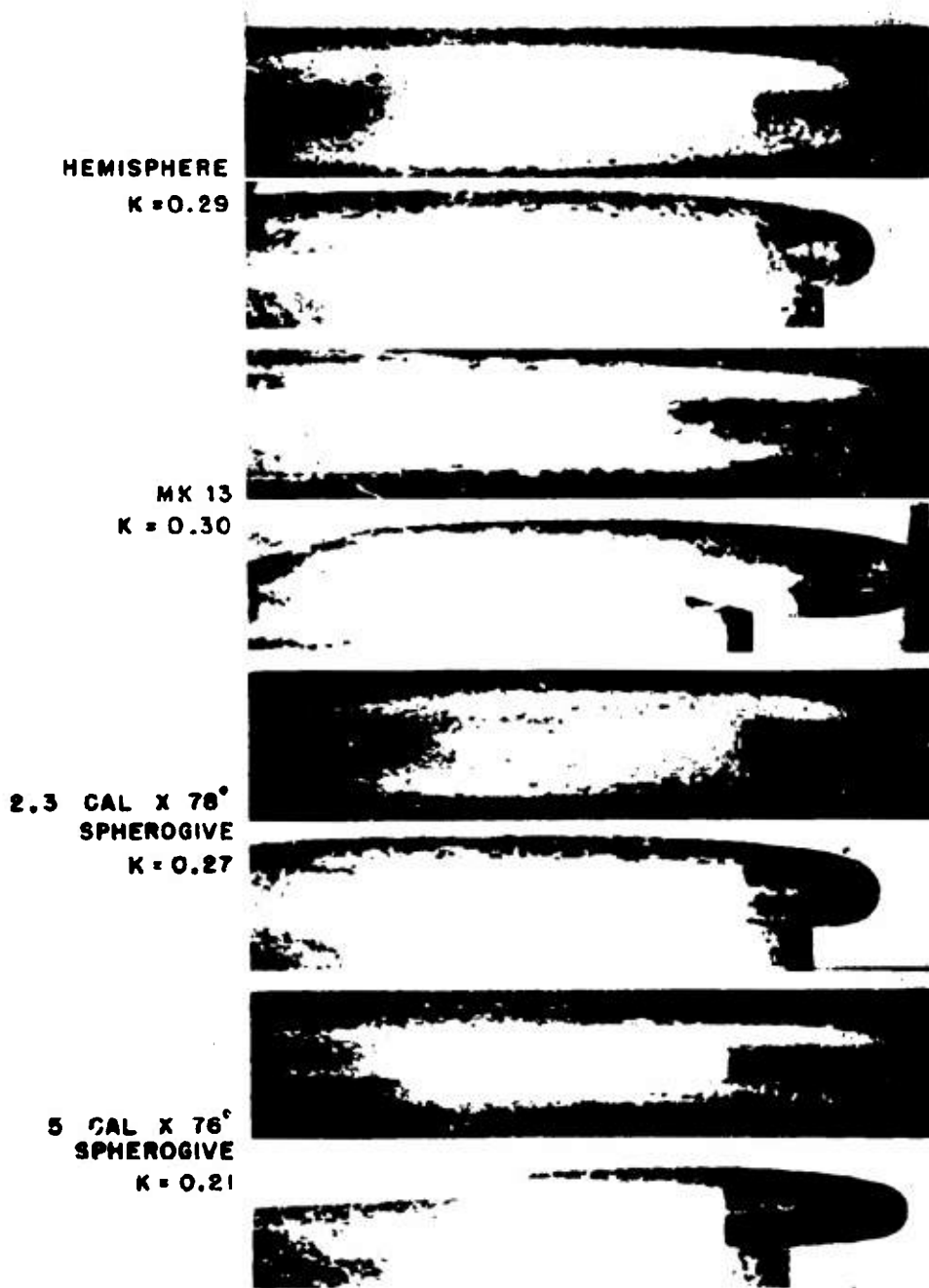


FIGURE 13. Cavitation bubbles on spherical-tipped noses. Yaw = 0 degree.

CONFIDENTIAL

cavitation is of the coarse-grained type and clean separation is not obtained even though most of the body is enveloped so that only the nose proper is in contact with the water. The pictures also show the expected result that the cavity diameter increases with bluntness of the nose. Thus the square-end cylinder produces the largest cavity, and the 5-caliber by 76-degree spherogive or the $2\frac{1}{2}$ -to-1 semiellipsoid,

the smallest. It is interesting to note that the truncated ogive produces a bubble which at a given distance from the separation point has about the same diameter as that produced by the hemisphere nose in spite of its bluntness. This is no larger because the diameter of the face is only $\frac{3}{8}$ caliber and because, further, the edge of the flat face is rounded off to a small radius.

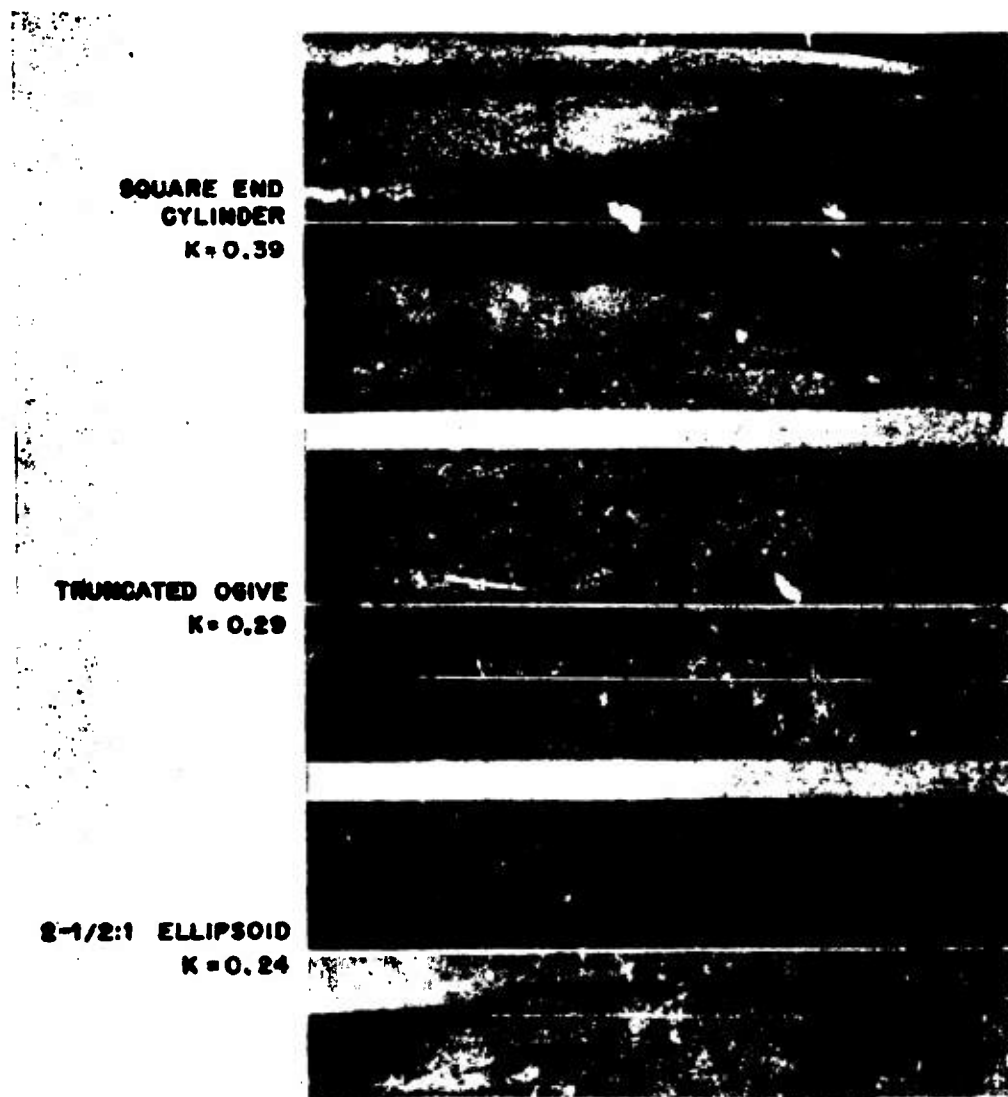
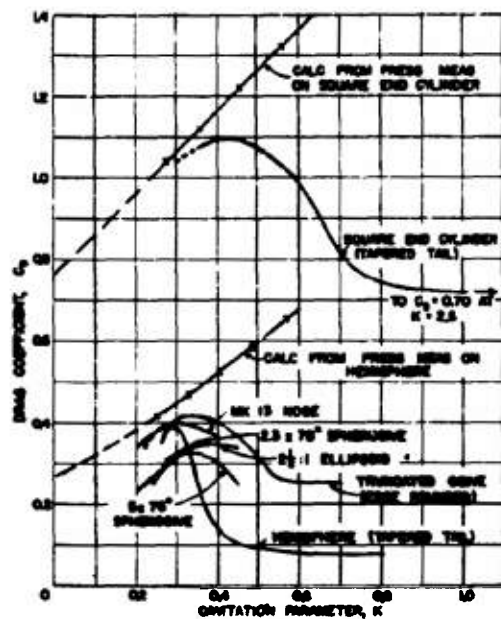


FIGURE 14. Cavitation bubbles on flat-faced and ellipsoidal noses. Yaw = 0 degree.

CONFIDENTIAL

DRAG VERSUS K

The measured values of C_D for these shapes are shown in Figure 15 plotted against the cavitation parameter K . Interest is centered mainly on the low- K end of each curve which is shown by a heavier line to indicate that the body is completely enveloped in the cavitation bubble. On this same diagram are plotted the same calculated values for the square-end



NOTE: BODY COMPLETELY ENVELOPED BY CAVITATION BUBBLE IN ZONE MARKED BY HEAVY CURVE.

FIGURE 15. Effect of nose shape on drag in the cavity. Yaw = 0 degree.

cylinder and the hemisphere as were shown in Figures 2 and 4. These were calculated using equation (3) above, and the measured pressure distributions on the surface of these noses.¹² The calculated coefficients are extrapolated from the points indicated by crosses down to zero K .

For a given value of K the measured magnitudes of C_D reflect the difference in bubble size already observed, the square-end cylinder showing the largest and the 5-caliber by 76-degree spherogive and the 2 3/4-to-1 ellipsoid the smallest. This is a necessary relationship since the cavity diameter is a measure of the momentum change imparted to the water as the

nose pushes it aside and hence is proportional to the drag. Thus C_D also is measured by the cavity diameter relative to the projectile diameter. This dependence of C_D on the bubble diameter does not hold, however, if one compares cavity sizes produced by the same projectile at different values of K . As K is reduced, it is easier for a body to make a cavity because the momentum required is reduced in proportion to the pressure forces, represented by $P_0 - P_B$, which must be overcome. Consequently, C_D becomes smaller with reductions in K even though the bubble grows larger.

The truncated ogive has a lower drag than would be calculated normally for the equivalent-sized square-end cylinder because of the slight rounding of the corner. Its drag coefficient is calculated to be about 50 per cent greater with a sharp edge. In all cases, as equation (3) states, a reduction in drag coefficient with reduction in K is discerned soon after the body is completely enveloped. The measurements for the hemisphere and the square-end cylinder with the enveloping cavity are both slightly lower than the calculated values. It is interesting to note that the calculated values extrapolated to $K = 0$ give $C_D = 0.76$ for the cylinder and 0.27 for the hemisphere.

The formation of an enveloping cavity has a particularly effective stabilizing influence on blunt-nosed bodies. In the case of both the square-end cylinder and the truncated ogive, the "bullets" tested were dynamically unstable in the water as long as cavitation was suppressed. The resultant oscillations about the support point loaded the model support system excessively. With the growth of cavitation, however, both bodies quieted down and with the formation of the full clear cavity shown in Figure 14, no oscillations existed and the hydrodynamic forces were uniformly steady.

6.24 Drag of a Cylinder in the Cavity

The two-dimensional case of a circular cylinder aligned with its axis normal to the flow was investigated also. A 3/4-in. diameter rod spanning the 14-in. diameter working section of the water tunnel was tested at velocities of 47.5, 50, and 55 fps for a range of the cavitation parameter that assured a well-developed cavity. A line made by inlaying a 0.010-in. wide copper strip extended along the length of the rod so that with the aid of the balance mechanism for yawing models, the rod could be turned about its

CONFIDENTIAL

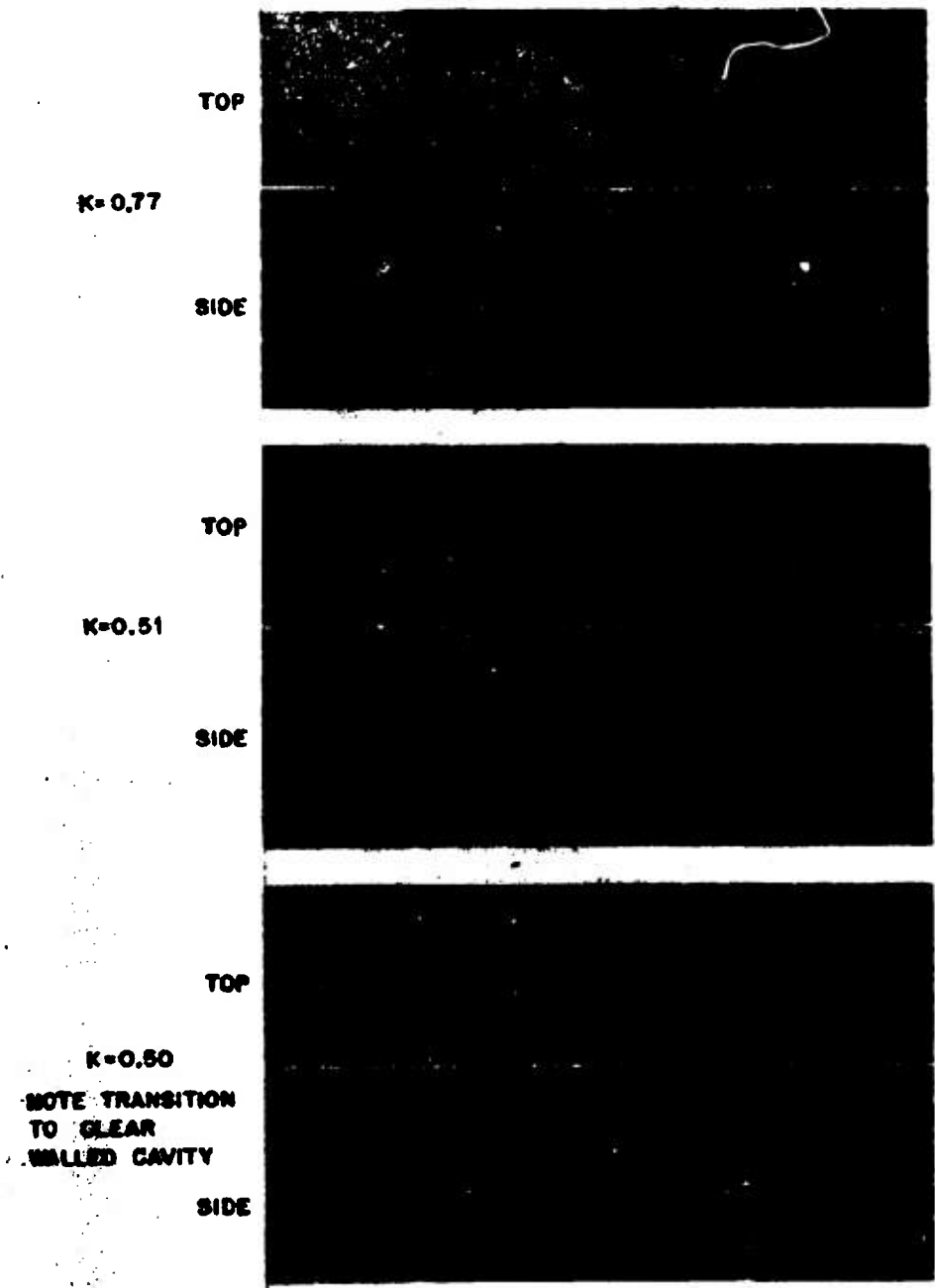


FIGURE 16. Three-quarter-inch diameter circular cylinder in cavity.

CONFIDENTIAL

axis and the angular position of the separation point observed.

Photographs showing the end view of the spindle and the cavity outline as seen through the top transparent window of the working section, and simultaneous side views showing the length of the spindle are presented in Figure 16.

DESCRIPTION OF CAVITY

It is seen that for the early stages of cavitation the bubble surface is opaque and milky, and is composed of the so-called fine-grained cavitation. At a critical K of about 0.50, however, the cavity wall suddenly

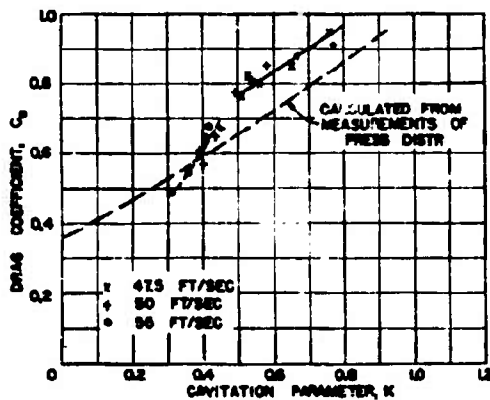


FIGURE 17. Drag coefficient for $\frac{3}{4}$ -in. diameter circular cylinder.

becomes clear and transparent. This is indicated by the glossy texture of the cavity shown in the bottom photograph. At the same time the width of the cavity is reduced somewhat, as can be seen by comparison of the end views of the spindle for $K = 0.50(+)$ and $0.50(-)$. Note also that the cavity boundary extending back from the point of separation at the cylinder is sharply defined by a clear-cut line after the transition occurs. In the side view photographs, the separation of the flow at the cylinder surface is indicated by the irregular line in the center of the highlight. Ahead of this highlight the forward portion of the cylinder is shown in dark relief, while downstream from the highlight the cylinder is enveloped by the cavity and cannot be seen until the cavity wall becomes transparent as in the bottom photograph. The point at which the flow separates from the cylinder surface was observed to shift forward slightly towards the stagnation point as K is reduced. At the critical K the

separation point apparently makes a small rearward shift as the cavity wall clears and then moves forward again. This behavior agrees qualitatively with the observed decrease in cavity width. The angle of separation measured back from the stagnation point falls between approximately 76 degrees and 80 degrees for the range of K from 0.45 to 0.80.

DRAG VERSUS K

Figure 17 shows measured drag coefficients and theoretical coefficients calculated from wind-tunnel measurements of pressure on the cylinder surface.¹⁴ As predicted by the theoretical values, the measured C_D decreases with increasing cavitation. The variation is approximately linear down to the critical K when the trend of the measurements changes sharply. The lower C_D value after the transition to the clear-walled cavity is also consistent with the observed decrease in cavity width. The measurements show C_D to fall below the theoretical curve as K is reduced further and the cavity elongates. However, the accuracy of the measurements at lower K is questionable because of the difficulty of preventing accumulation of air in the tunnel working section.

COMPARISON WITH CALCULATED C_D

Above the critical K the curve of measured drag coefficients parallels the theoretical curve but shows higher values. The theoretical coefficients were calculated using equation (3). The limits of integration of the pressure intensity term were determined from assumed points of separation from the cylinder surface. For the limiting condition of $K = 0$, separation was assumed to occur where the dimensionless pressure term $(P - P_0)/(\rho v^2/2)$ became zero for the wind-tunnel determinations. For higher K 's (less cavitation) separation was taken to occur where the reduction in pressure below P_0 gave values of $(P - P_0)/(\rho v^2/2)$ equal to assumed values of K . This method indicated separation points much farther forward than actually measured, which causes the lower theoretical drag coefficient curve shown in Figure 17. Such a discrepancy in the point of separation is not unexpected because the flow with a cavity is actually quite different than the noncavitating flow in the wind tunnel. With the cavity some change in the pressure distribution on the part of the body must be necessary to provide the extra forces required to open up the cavity.

WALL EFFECTS

Some deviations from the truly two-dimensional case exist. There is a small wall effect because the cylinder occupies 7.3 per cent of the tunnel cross section. Also, the ratio of channel width to the cylinder diameter is 19 to 1 at the maximum section, but is reduced towards each end of the cylinder. The change is slow, however, so that all of the cylinder except the extreme end is at a good distance from the wall. Probably the boundary layer caused by the tunnel wall, which is of the order of $\frac{1}{2}$ in. thick, will have a predominant influence in this zone. Thom¹⁵ reports that the presence of channel walls parallel to the axis of a cylinder causes a correction to the velocity of the order of 1 per cent for a ratio of channel width to cylinder diameter of 20 to 1 and less than 2 per cent for a ratio of 10 to 1. It is unlikely that a ratio of 19 to 1 for the circular tunnel cross section will cause a correction greater than the 2 per cent for the 10-to-1 ratio with parallel walls.

ALTERNATING FORCES

The measurements shown in Figure 17 were confined to cavitating conditions because, without the cavity, excessive lateral vibration of the cylinder prohibited operation at these high velocities. This was due to the alternating cross force resulting from the shedding of vortices of the von Kármán trail. But with the cavity completely stable conditions were obtained, permitting operation at even the maximum velocity of the water tunnel. To get to the high velocity without vibrations severe enough to damage the balance equipment, it was necessary to cause the cylinder to cavitate at low velocities and then to raise the speed while maintaining the cavitation bubble. An indication of the alternating forces of the vortices generated for noncavitating flow is given by the observed lateral deflections of approximately $\frac{3}{8}$ in. at 25-fps velocity. A uniform static load of about 8 psi, or a total of about 110 lb, is necessary to cause this. With cavitation at 58 fps, as shown in the top picture of Figure 16, a deflection was observed only in the direction of motion. A maximum deflection of the order of $\frac{1}{4}$ in. ($\frac{1}{3}$ of the cylinder diameter) for a measured total drag of 150 lb was obtained. The deflection in the direction of motion can be seen in the top views of the cylinder by comparing the position of its axis with the neutral position indicated by a line drawn between the two arrow points. Note that the

maximum deflection is obtained in the top photograph for the highest K . This deflection also accounts for the inclination of the cylinder observed in the side views.

NONCAVITATING DRAG

Measurements were obtained for noncavitating conditions in a velocity range of 10 to 25 fps, or a Reynolds-number range of 55,000 to 160,000. C_D was constant and equal to 1.13 ± 0.03 . This agrees with published data on the drag of a cylinder of infinite-aspect ratio.

6.3 THE CROSS FORCE AND MOMENT IN THE CAVITY

6.3.1 Effect of Body Shape on Cavity Cross Force and Moment

CAVITY SYMMETRY VERSUS NOSE SHAPE

The spherical-tipped noses shown in Figure 13 have the common characteristic that the cavitation bubble is formed by separation of the flow well forward on the tip so that water is in contact with only a portion of the spherical segment. The bubble shape should therefore be independent of yaw as long as the after part of the body does not reach over and touch the cavity walls. Top views of these same noses in fully developed cavitation bubbles are shown in Figure 18 yawed at 3 degrees. Note that in each case separation occurs along a sharp line normal to the direction of motion, and the resulting cavity, while displaced laterally as viewed from above, is symmetrical about a line parallel to the flow. In the case of the 5-caliber by 76-degree spherogive the cavity does not completely envelop the body, yet it retains its symmetry back to a point where it intersects the body surface.

In contrast, the shapes shown in Figure 14 all present an asymmetrical obstruction to the flow when yawed. Consequently, separation of the flow cannot occur symmetrically and the resulting cavity must be asymmetric. Views of cavitation bubbles in Figure 19 formed by these noses in yawed positions show this effect clearly. The cavities for the two blunt noses have trailing bubbles displaced slightly in the direction of yaw, while the ellipsoid has a trail of bubbles displaced slightly opposite to the direction of yaw.

CONFIDENTIAL

FORCES VERSUS CAVITY SYMMETRY

The characteristics which determine whether or not the bubble is symmetrical are important in determining the hydrodynamic forces that will act on the body under yaw. Since the resultant force must be equal and opposite to the momentum change of the water deflected by the body, the symmetry or asymmetry of the cavitation cavities determines the existence and sense of moment and cross force. Thus, for

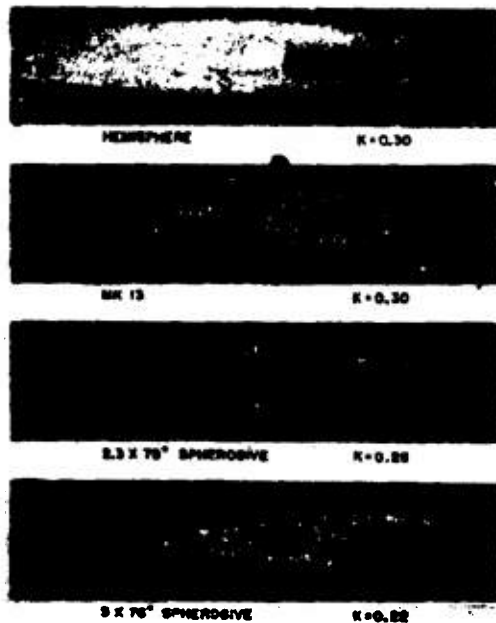


FIGURE 18. Cavitation bubbles on spherical-tipped noses. Yaw = 3 degrees.

the spherical-tipped noses used in these experiments, the cross force should become zero and the moment should be due only to the drag acting through the center of curvature of the spherical segment forming the nose tip. On the other hand, a finite cross force should exist on the other noses, causing a definite upsetting or destabilizing moment in the case of the ellipsoid, with a stabilizing moment tending to counteract the destabilizing effect of the drag in the case of the blunt noses.

MEASURED COEFFICIENTS

The cross force and moment coefficients C_C and C_M

measured for these noses are shown in Figure 20, plotted as functions of the cavitation parameter K . The moment coefficients are calculated for direct comparison with the coefficients for a reference projectile 7.18 calibers long with the center of gravity at 42 per cent of the length back from the nose tip. The data are not corrected for support interference effects because it was found that the effect, if any, on the cross force C and moment M was very small once the full cavity was developed. On the other hand, as the curves indicate, both C and M are much larger just before the cavity is formed than

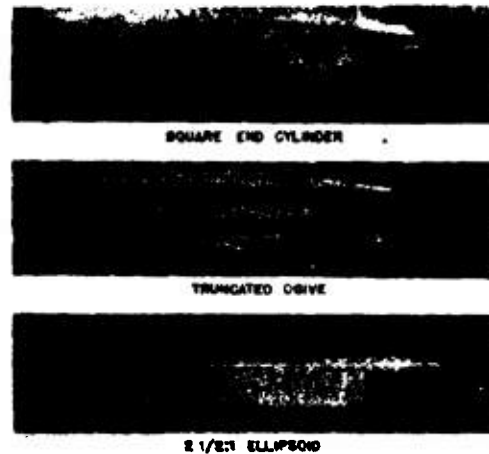


FIGURE 19. Cavitation bubbles on flat-faced and ellipsoidal noses. Yaw = 3 degrees.

after. Since the values for other than the cavity stage are of significance only for indicating trends, no corrections were made.

In general, the trends shown by the curves as K is reduced and the test conditions approach a full cavity verify the qualitative deductions just stated. The hemisphere nose on which a big cavity was developed at the K 's of the test shows zero cross force and a moment for normal cavitation-free operation of about $\frac{1}{6}$ that of the reference projectile without fins, or about $\frac{1}{3}$ of that of the reference projectile with fins. This measured moment can be approximated with fair accuracy from the drag measurement. For the 2.3-caliber by 78-degree spherogive, the cross force is finite but very small, and the moment is also reduced from the cavitation-free value of the reference projectile. Both C_C and C_M are decreasing rapidly with

CONFIDENTIAL

increasing bubble size so that in the light of the observed bubble symmetry in Figure 18, it is probable that C_C will eventually become zero.

For the other two spherical-tipped noses, the Mark 13 and the 5-caliber by 76-degree spherogive, both show relatively high cross force and moment. This is attributed to the extra length of these noses and the difficulty of getting a cavity large enough to assure no interference at points aft of the separation zone.

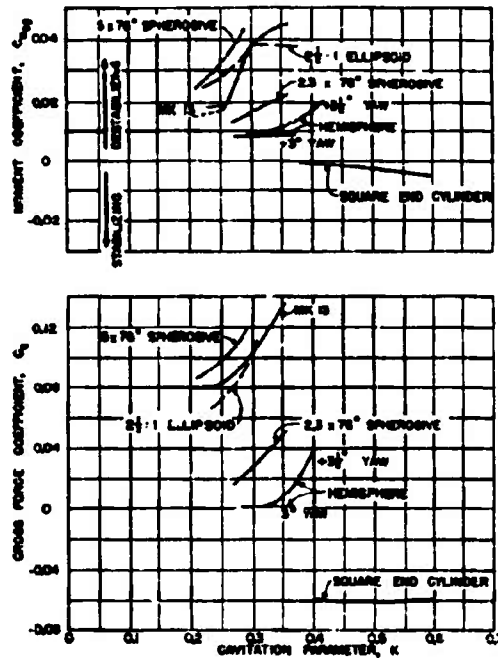


FIGURE 20. Effect of nose shape on moment and cross force in the cavity.

This is especially severe in case of the spherogive because of its high resistance to the inception of cavitation. A similar result was obtained with the hemisphere nose when the bullet was elongated to the point that there was some question as to whether the cylindrical portion interfered with the cavity wall. By shortening the bullet, however, this was eliminated. It is not possible to assemble these two noses in shorter units so the results from these tests are included with this reservation. The trend shown is consistent, however, with the symmetry of the cavitation bubble, and C_C should eventually fall to zero for both units.

The 2½-to-1 semiellipsoid nose also results in high C_C and C_M but for different reasons. While the cavitation pictured in Figure 19 is well developed, the cavity is not formed by clean-cut separation as on the spherical-tipped models. Instead, the coarse-grained cavitation bubbles appear intermittently over a broad zone on the nose surface, and form a close-fitting sheet over the surface of the body. In a sense, therefore, a cavity is not really formed on this shape. As a result, the trailing bubble is inclined to the direction of flow, and in light of this asymmetry, it is not expected that C_C will vanish or that C_M will be reduced to the low value shown for the hemisphere.

The square-end cylinder produces both a cross force and moment that is stabilising in effect. This is because the pressure on the flat face acts normal to the face and, hence, has a lateral component tending to reduce the angle of yaw. But for asymmetry in the pressure distribution across this face, the resultant vector would coincide with the axis of the cylinder and zero moment would result. The existence of a small moment is an indication of a slight shift in the stagnation point in a direction opposite to the sense of the yawing.

6.3.3 The Cross Force and Moment on a Complete Projectile during Cavitation

DESCRIPTION OF CAVITIES

It will be recalled that the projectiles pictured in Figures 9, 10, and 11 are equipped with three of the spherical-tipped noses just discussed. Figures 21, 22, and 23 show additional pictures of these same projectiles for more advanced stages of cavitation. The same characteristics observed in the photographs of the short bullets are observed when these shapes are used with a full body. Separation occurs on the spherical segment along a clear line which is normal to the flow. Consequently, the bubble is formed with an initial symmetry. This symmetry is maintained back to the point where the body and tail slice through the bubble interface. For the 5-caliber by 76-degree spherogive the higher resistance to inception of cavitation results in less bubble growth at the same value of K than for the hemisphere or the standard Mark 13, so that at $K = 0.25$, the nose bubble is scarcely more developed than at $K = 0.35$ on the hemisphere.

Even for the partially developed conditions shown, however, separation occurs along a line normal to the flow on the spherical tip of the nose.

MEASURED COEFFICIENTS

Measurements of the cross force and moment coefficients for these three models are shown in Figure

the very small destabilizing effect of the nose. The latter, according to the measurements on the short bullets, is reduced once most of the nose is enclosed in cavitation, thus contributing also towards a stabilizing trend. The curves also show a tendency towards a reduced cross force when the bubble is well developed. It will be noted by comparing the photographs in

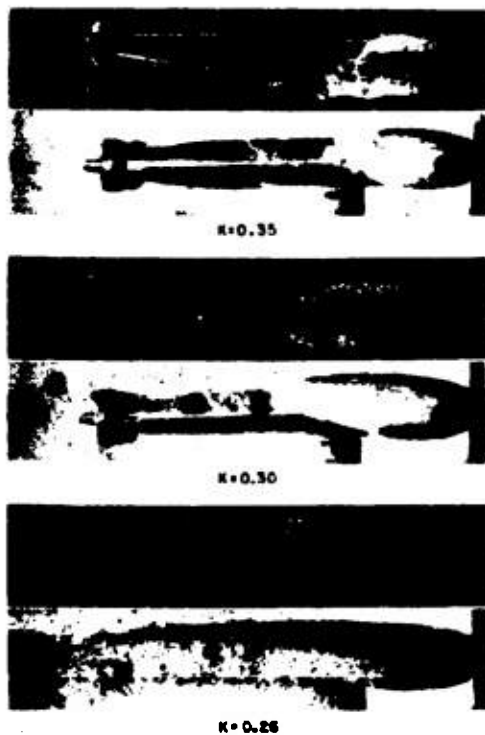


FIGURE 21. Hemisphere nose on Mk 13-2 torpedo. Yaw = 3 degrees. Top and side views.

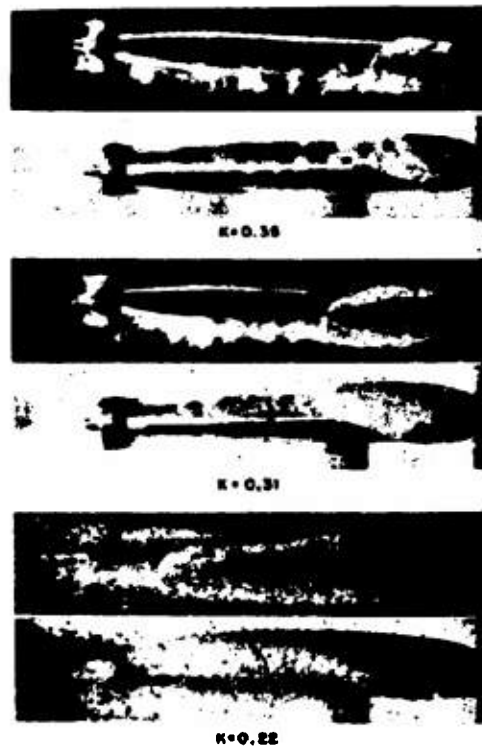


FIGURE 22. Standard Mk 13 nose on Mk 13-2 torpedo. Yaw = 3 degrees. Top and side views.

24. Because these measurements include primarily the intermediate range between no cavitation and complete cavitation, corrections for support interference are necessary, if the results are to be compared with the corresponding values without cavitation. The results show that for the advanced stages obtained on the hemisphere and Mark 13 noses, a zero or stabilizing moment is obtained. There is also a tendency for the cross force to be reduced. In these cases the stabilizing effect is caused by the tail and afterbody "biting" into the water and overcoming

Figures 21 and 22 that a larger cavity is obtained on the hemisphere than on the Mark 13 at the same values of K . Thus the hemisphere results in a more pronounced effect on the cross force and moment as shown. These curves extend to a high enough K to include also the noncavitating performance and the effect of the initial stages of cavitation on the performance. In the case of the hemisphere and the Mark 13, both the cross force and the moment drop off with the onset of cavitation on the nose and on the tail structure. As cavitation develops the cross force

CONFIDENTIAL

increases again to slightly above its noncavitating value. Apparently there is a differential effect so that the increase is greater at the nose, because the moment begins to increase slightly at the same time. With continued growth the distorted flow pattern causes a complicated additional fluctuation of both C and M until the cavitation envelops most of the body. At this stage the reduced moments and cross

moment which is caused primarily by the high drag of the tail.

6.4 SUMMARY OF OBSERVATIONS AND CONCLUSIONS

The main findings of the investigation of the forces and moments acting during cavitation are summarized as follows:

1. There is no sudden rise in the drag coefficient with the inception of cavitation.

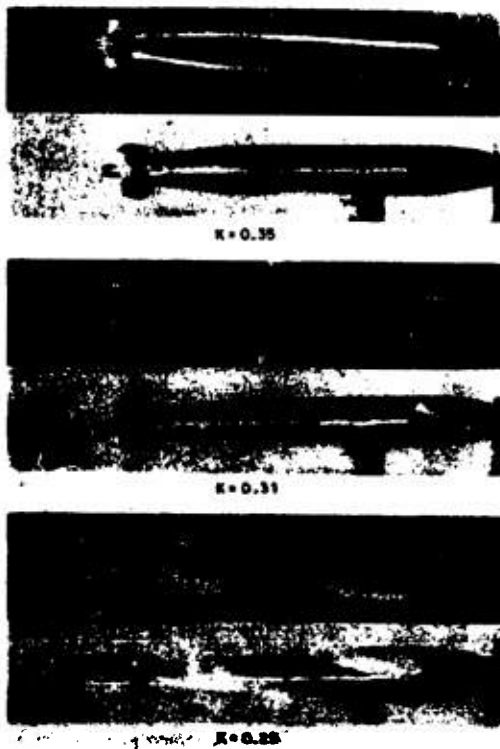


FIGURE 23. Five caliber by 76-degree spherogive nose on Mk 13-2 torpedo. Yaw = 3 degrees. Top and side views.

forces already mentioned are obtained. The curves for the 5-caliber by 76-degree spherogive nose begin at $K = 0.72$ when cavitation is already present on the tail structure. The nose does not begin to cavitate until K is approximately 0.42. At the lowest K of the tests, and the maximum bubble development, Figure 23 shows that nose cavitation is still confined to the lee side of the body although there is strong cavitation on the afterbody and the tail. For these conditions both moment and cross force show a tendency to drop off. This is more pronounced in the case of the

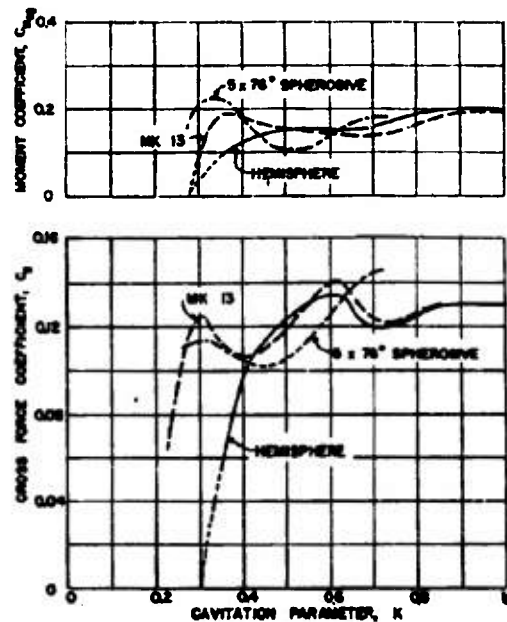


FIGURE 24. Effect of cavitation on moment and cross force of ring tail projectile with three different noses. Yaw = 3 degrees.

2. Enough cavitation must develop to alter appreciably the normal flow pattern before the drag is affected materially. When this occurs the amount of cavitation as observed visually occupies an appreciable physical volume.

3. Between inception and the marked increase in drag the coefficient may increase slowly, may remain unchanged, and in some cases has been observed to decrease slightly.

4. A qualitative comparison between cavitation and separation indicates:

a. For blunt bodies with severe separation under noncavitating conditions the appearance of

CONFIDENTIAL

cavitation does not immediately alter the flow pattern around the body, and hence introduces no immediate effect on C_D .

- b. For other bodies with a normal boundary layer, cavitation and local separation both have the same basic effect on the flow in the boundary layer, and hence on the skin friction components of C_D .

5. As cavitation develops beyond the inception point, the skin friction component is probably reduced because there is less high-velocity fluid in contact with the surface.

6. Drag is proportional to the change in momentum imparted to the water so that at a given value of K , drag in the cavity is proportional to the bubble size relative to the diameter of the body. For a given body, as K is reduced the cavity drag coefficient decreases, although the cavity size grows, because the momentum required to form the cavity is reduced in proportion to the pressure forces, represented by $(P_0 - P_B)$ which must be overcome.

7. For the square-end cylinder and hemisphere, C_D in the cavity agrees within a few per cent with values calculated from the measured pressure distribution.

8. The effect of rounding the corners on noses with sharp edges, such as obtained with a flat face, results in a smaller cavity and less drag. For the case of the truncated ogive with rounded edge, C_D in the cavity is reduced to about $\frac{3}{5}$ the value calculated for a sharp edge.

9. Cross force and moment depend upon the cavity shape and hence upon the shape of the wetted portion of the body.

10. With spherical-tipped noses proportioned so that the cavity always separates on the spherical segment, not only at zero but at the maximum yaw, the cross force is zero and independent of yaw, and the moment is caused by the drag only.

11. With bodies which do not have spherical-tipped noses, the cavity produced is asymmetric and a definite cross force exists.

The sense of this cross force depends on the sign of the lateral momentum imparted to the water, and hence on the direction of the cavity asymmetry.

12. With a complete projectile a reduced cross force and a zero or stabilizing moment are obtained when most of the body is enveloped in a cavity, but the tail projects through the cavity wall into the water.

13. For intermediate stages between full and no

cavitation the growth of cavitation alters both the cross force and the drag contributions from various parts of the projectile body.

The shift in magnitude, direction, and point of application of the resultant hydrodynamic force causes simultaneous variations in C_M .

6.5 REMARKS ON APPLICATION OF OBSERVATIONS AND CONCLUSIONS

The basic problems around which this research has centered have been connected with underwater projectiles and consequently applications of the results to this field are most direct. Consider first the normal underwater operation of high-speed torpedoes.

HIGH-SPEED TORPEDOES

Cavitation is known to be detrimental and in the absence of definite information regarding the limits of its effect, every effort is normally made to keep the operating velocities below those for incipient cavitation. However, the present results show that appreciable cavitation can be tolerated on typical torpedo shapes before the drag increases as much as 10 per cent. In the examples shown in Figures 5 and 8 an increase of about 10 fps or 10 to 15 per cent above the cavitating velocity was allowable. Thus it may easily be worth some sacrifice in power to increase the speed by such an amount. Admittedly, the simultaneous effect of cavitation on the cross force and moments can not be ignored. For example, normal operation with a negative buoyancy calls for an angle of attack to support the load. Since the torpedo shape with the hemisphere nose in Figure 8 showed about a 10 per cent loss in cross force at 3 degrees yaw for the same K at which the drag increased 10 per cent, cavitation could cause difficulty in maintaining the proper depth. With the decrease in cross force (lift in the vertical plane), the depth mechanism would operate the rudders to give the body the increased angle of attack necessary to carry the load. This trend would persist until a new set of equilibrium conditions was obtained. Under these conditions higher drag would result. Variations in the moment and cross force will result in other variations in maneuverability. For example, the turning radius will be rather unpredictable if excessive cavitation exists, so that behavior on angle shots will not be consistent. The selection of shapes for the projectile components such that cavi-

CONFIDENTIAL

tation occurs as uniformly as possible on the lee and windward sides will tend to reduce the unbalanced effect on the hydrodynamic forces.

All these effects are particularly serious when the projectile operates without much submergence and K is correspondingly reduced. In fact, for very low submergence, cavitation will occur first on the top side of the projectile even with no angle of attack. A torpedo seeking depth can easily be subjected to intermittent cavitation as it rises and falls along its course and the resultant unbalance in hydrodynamic effect should certainly contribute to delay in reaching equilibrium conditions. It is possible also that cavitation of this type could increase the oscillations of the projectile and make it break surface.

AIR-WATER ENTRY

Reference has already been made to the similarity of cavitation bubbles to the cavities obtained at air-water entry. A basic difficulty in translating these results to entry problems is the unsteady character of the latter. However, qualitative conclusions can still be used to obtain some useful concepts regarding the effect of shape and consequent cavitation development on the behavior at entry. The most obvious application is the effect of nose shape in the cavity on cross force and moment, and hence on the tendency of the projectile to yaw and drift. The spherical-tipped noses, of which the spherogive series is typical, have the special properties of giving zero cross force, if proportioned to assure separation of the cavity on the spherical segment. In this case the only moment is that due to drag. Blunter noses, it was observed, actually produced a large stabilizing cross force and a resulting moment that overcomes the effect of the drag and thus results in a net stabilizing moment. It should be possible to design a nose shape slightly blunter than a hemisphere which would produce a similar effect and make C_M stabilizing or equal to zero within a desired yaw range. Cavitation characteristics which are better than those of the hemisphere at inception and during the early stages of development have been obtained for a shape differing only slightly in size or volume from a hemisphere, by making the slope and curvature of the surface profile continuous over the nose proper and at the junction between the nose and the cylindrical body. With judicious treatment of the profile up to the zone of separation at least, good results should also be obtainable for the cavity stage. The insensitivity of

moment and cross force to yaw will contribute toward less sensitivity to yaw or pitch at entry, and tend to reduce deflections from the set trajectory during the cavity stage.

Any nose shape should be investigated for its behavior on impact at entry, since the projectile breaks the surface with one side of its nose, resulting in a nonsymmetrical cavity and nonsymmetrical forces in this stage. However, qualitative conclusions for this condition can be obtained also from steady-state cavitation data since, neglecting the additional apparent mass effects, the sense and point of application of the resultant forces immediately after impact must be the same as the corresponding forces measured with a large cavitating bubble. If the launching conditions are such that the whip or pitching velocity induced on impact is serious, the shape of the initial cavity formation, and hence the forces acting on the projectile, can be modified by changing the nose shape. This procedure has been tried to some extent on full-size torpedoes.¹⁶

The existence of moment and cross force in the cavity results in two well-known effects. First, the moment causes the projectile tail to go to one side of the cavity where it sticks through the bubble until enough stabilizing moment is built up to offset the destabilizing moment from the nose. Second, the cross force produces a lateral motion of the center of gravity and causes a curved trajectory. It has been reported¹⁷ that even for long projectiles the resultant curve is dependent primarily on the nose shape. Hemispherical noses cause little cross force and the curvature is practically infinite. Noses with sharper ogives than 2.0 calibers result in large cross forces and short radii of trajectory curvature. The beneficial effect on drag in the cavity of reducing the area contacted by the water is well known. This idea has been applied to blunt-nosed projectiles particularly where the reduction in drag is appreciable. Spherogives and other combination forms can be used to produce the same effect with basically low-drag shapes.

LIFTING SURFACES

The loss of lift and increase in drag associated with the onset of cavitation is a serious problem in applications to lifting surfaces of various types. The fixed and adjustable guide surfaces on projectiles, submarines, and surface ships are vulnerable to cavitation, particularly for conditions of yaw such as obtained during a maneuver. The shroud ring tail on

CONFIDENTIAL

the typical torpedo already discussed is one example. Movable rudders of course are the most likely to cavitate, and in some cases can be rendered quite ineffective by large cavitation zones. In general, it is probable that there will be less loss in lift if the cavitation is of the coarse-grained type and the development of a full cavity on the low-pressure side of the surface can be avoided.

HYDRAULIC MACHINERY

Pumps, turbines, and propellers are basically lifting surfaces that are also subjected to cavitating conditions. In general, cavitation causes a loss of head or thrust and torque. However, an actual increase in head, torque, and efficiency has been observed with the onset of cavitation in some radial-flow type pumps.¹¹ It has been suggested that this effect is caused by a slight reduction in skin friction as cavitation grows. The effect of vane shape controls this behavior, just as in the case of the three-dimensional

bodies investigated. Shaping the vanes to give coarse-grained cavitation should prove beneficial on two counts. First, inception should be delayed, since it was the more highly resistant forms that gave this type of bubble formation. Second, with the more advanced cavitation there probably will be less loss in lift on the blades.

In the case of pumps and turbines, the "lattice" effect of the vanes will modify the cavitation behavior over that obtained with a single blade. The modifications are similar to "wall effects" obtained in the water-tunnel tests, but of great magnitude. The main deviations will be in the advanced stages of cavitation where the vapor occupies an appreciable fraction of the total volume between blades, and hence seriously restricts the water passage. For the initial stages the concepts presented here of the similarity between the effects of cavitation and separation on the boundary layer and, hence, on the general flow around the blade should apply with good accuracy.

Chapter 7

CAVITATION NOISE FROM UNDERWATER PROJECTILES

1.1 PURPOSE AND SCOPE OF NOISE MEASUREMENTS

THE SONIC AND SUPERSONIC noise emitted during the onset and development of cavitation on various parts of underwater bodies has become important for several reasons. For example, the noise produced by a cavitating propeller on a ship is easily detected and the ship's position ascertained by underwater sound locating devices. On the other hand, if the vessel carrying the sound gear has a cavitating propeller, the noise produced interferes with the operation of the listening equipment. The importance of this cavitation noise in connection with other acoustical applications can be visualized readily. It was the purpose of the investigations in the water tunnel to measure the noise produced in the 20- to 100-kilocycle frequency range by certain body shapes and to determine the variation of sound emitted with the beginning and growth of cavitation. A further aim was to determine, if possible, the distribution of the noise in the various frequency bands. In addition an investigation was made to identify the exact location of the source of the sound during cavitation.^{1,2}

High-frequency noise measurements were possible in the water tunnel working section because, although the circulating pump and other associated equipment produced a high noise level in the range of sonic frequencies, they produced but few high-frequency components. Consequently, the tunnel circuit was "quiet" in the range above 6 kilocycles.

1.2 THE APPARATUS

The noise measurements were made in the working section of the water tunnel using the regular 2-in. diameter models mounted on a streamlined strut. The hydrophone and recording equipment used is the same as that described in Section 2.8. Two systems of mounting the receiving hydrophone were used. In one case the hydrophone was placed in a water-filled plastic blister clamped to the Lucite window of the working section as shown in Figure 1. The second method made use of focusing reflectors or "mirrors" in connection with the hydrophone, with both the mirror and hydrophone submerged in a water-filled

tank attached to the side of the working section. Photographs of this arrangement with spherical and ellipsoidal reflectors are shown in Figures 2 and 3. Provisions were made for directing and focusing the hydrophone mirror assembly from any position within the side tank. Except for the Lucite window both arrangements provide a continuous water path from the noise source to the hydrophone, or to the reflecting surface and back to the hydrophone.

The focusing system has the advantages of increasing the gain at the hydrophone, and limiting the reception from other than the focused direction, thus tending to reduce possible interference from other sound sources and from sound reflected from the tunnel walls. Typical directional characteristics of the reflector system³ are shown by the directivity patterns of Figures 4 and 5 which are for the hydrophone alone and the hydrophone with an ellipsoidal reflector.⁴ The *directivity pattern* is a polar diagram showing the sound pressure, in decibels relative to that on the axis of symmetry of the mirror, measured for different angles between the noise source and the axis of symmetry. While the hydrophone alone shows but slight directional characteristics, the addition of the ellipsoidal reflector gives a directivity index of -28 db at 50 kilocycles and -31.4 db at 70 kilocycles. The *directivity index*, which can be calculated from the three-dimensional directivity patterns of the hydrophone system, is the ratio in db of the acoustic pressure averaged over all directions to the pressure measured on the axis of symmetry. These calibrations, made with a fixed distance between the noise source and the focal points of the reflectors, duplicated the geometrical arrangement used for the water tunnel tests except that the Lucite window between the source and the receiving hydrophone was not included. This window has a flat outside surface and concave cylindrical inside surface. A comparison of the free-field directivity patterns obtained from measurements with and without the Lucite window is shown in Figure 6. Very little distortion is caused by the Lucite in the plane normal to the curved inside surface of the window. During the calibrations the effect of changing the distance between the noise

³These calibrations were made by the Calibration Group of the University of California, Division of War Research.

source and the focal point of the ellipsoidal mirror was investigated also. It was shown that the focusing obtained when the noise source moved along the axis of symmetry of the mirrors was only $\frac{1}{4}$ to $\frac{1}{2}$

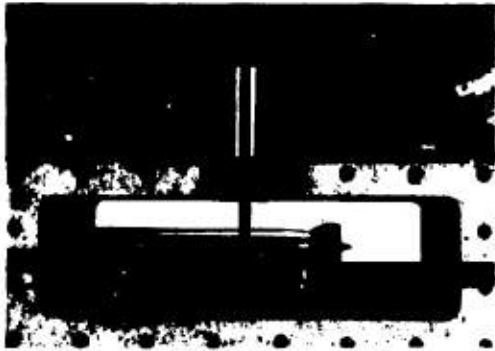


FIGURE 1. Hydrophone mounted in water-filled blister on side of working section.

as good as when the source moved normal to this axis and that the best focusing along the axis of symmetry was obtained when the sound source was slightly short of the conjugate focus of the ellipsoid.



FIGURE 2. Spherical reflector and hydrophone assembly focused on projectile inside working section.

1.3 BACKGROUND NOISE

The measurements of sound from cavitating projectiles in the tunnel working section include a certain amount of background noise generated by the tunnel flow circuit and its mechanical drive. To be sure that, over the frequency range of interest, the magnitude

of this noise was small relative to the cavitation noise, a series of measurements was made without the model or its supporting strut in the working section. With the hydrophone first mounted in the Lucite blister on the working section window and later used with the mirrors and focused on a fixed point on the tunnel axis, noise was measured over a wide frequency range for a series of different constant velocities. Examples of measurements with the reflectors are given in the following paragraphs. Aside from effects on gain due to the focusing features of the mirrors, these measurements are typical for both types of installations.



FIGURE 3. Ellipsoidal reflector and hydrophone assembled in water tank at working section side window.

EFFECT OF VELOCITY AND PRESSURE

The typical curves shown in Figure 7 illustrate the magnitude of the background noise and the effect of velocity and pressure on the noise. In this figure measurements for velocities of 40 to 70 fps are plotted as a family of curves of sound pressure in dynes per square centimeter (with linear decibel scale) vs the cavitation parameter K . The data were obtained from tests taken with the spherical mirror focused on the centerline of the working section and with the sound filters set to include the entire 20- to 100-kilo-cycle band. These curves show the same characteristic trends as were obtained by the earlier measurements^{1,2} without a reflector. For each velocity, as the pressure is reduced from an initially high value, the

increased cavitation and flow separation in various parts of the flow circuit caused an increase in noise until at a low K a peak is reached and the level drops off. The sudden reduction in noise level shown in this figure coincides with cavitation in the contracting nozzle at the entrance to the working section, and an accumulation of vapor and air bubbles which clouded the working section and probably acted as sound screen between the hydrophone and the noise.

EFFECT OF TUNNEL CIRCUIT VARIABLES

The data plotted in Figure 7 could be duplicated as long as tunnel conditions remained the same. How-

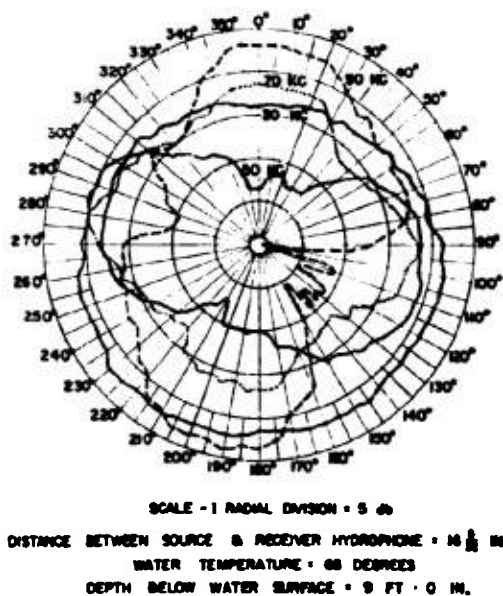
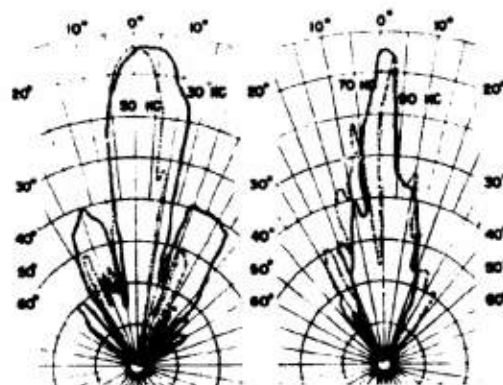


FIGURE 4. Directivity patterns for C-11A hydrophone in plane normal to hydrophone spindle.

ever, changes in the condition of the circulating pump, in the relative settings of the valves in the pressure control circuits auxiliary to the tunnel, or in the flow circuit itself, caused some variation in the magnitude of the background noise. Differences of as much as 10 db have been observed for different combinations of these variables.

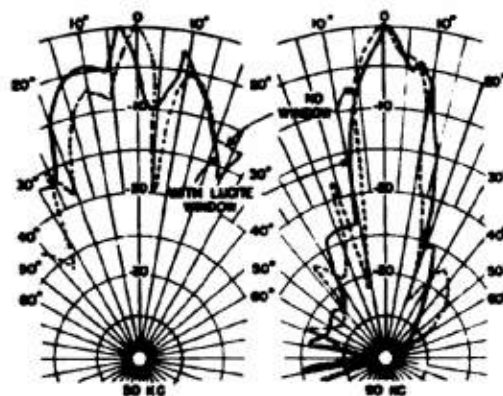
Figure 8 shows the background noise level curves obtained with the same spherical mirror assembly after an improved contracting nozzle was installed at the inlet to the working section. These curves are similar to those in Figure 7 but show from 2 db to 5

db lower noise levels at the same K . The peaks are higher, however, because lower K 's are reached before the noise drops. With the original nozzle the



DISTANCE BETWEEN SOURCE & RECEIVER HYDROPHONE = 16 1/2 IN.
 WATER TEMPERATURE = 68 TO 69 DEGREES
 DEPTH BELOW WATER SURFACE = 9 FT - 0 IN.

FIGURE 5. Directivity patterns for C-11A hydrophone with 10-in. aperture ellipsoidal reflector in plane normal to hydrophone spindle.



DISTANCE BETWEEN SOURCE & RECEIVER HYDROPHONE = 16 1/2 IN.
 DEPTH BELOW WATER SURFACE = 30 FT - 0 IN.

FIGURE 6. Effect of Lucite window on directivity patterns with 6-in. aperture ellipsoidal reflector. Patterns are for plane normal to hydrophone spindle and containing axis of cylindrical surface of window.

noise was interrupted when cavitation, accompanied by an almost simultaneous accumulation of air bubbles, appeared at the nozzle throat. With the new

nozzle, cavitation in the nozzle proper does not occur within the experimental range. However, with the sustained operation at the low absolute pressures corresponding to the lowest K values obtainable, air does accumulate in the tunnel and the noise level drops.

BACKGROUND NOISE COMPARED WITH CAVITATION NOISE

The highest sound pressure measured in the clear tunnel was about 420 dynes per sq cm. This was obtained at 70 fps, which is the maximum velocity at which noise from projectiles was recorded. As will be discussed later, pressures of 1,000 to 2,000 dynes per

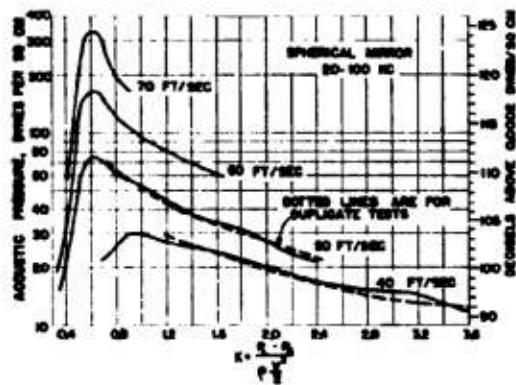


FIGURE 7. Background noise level. No model or strut in tunnel. Spherical mirror focused on a point on the center line of the working section 21 inches from inlet. Old nozzle at inlet to working section.

sq cm were measured with the spherical mirror as cavitation developed on the projectile shapes. Since the recorded level is approximately the root-mean-square value of all the sound contributions, the background noise has no significant effect on these pressures. It is possible also, for the same reason, to ignore the relatively small effect of background noise variations caused by different tunnel setups as illustrated by Figures 7 and 8.

Similar background noise measurements made using the ellipsoidal mirror showed 5 db to 8 db higher levels than with the spherical mirror. However, peak noise pressures of 5,000 dynes per sq cm or greater were measured from cavitating projectiles with this reflector, thus making the background noise even less significant. It is interesting to note that for the par-

ticular test conditions of Figures 7 and 8, and for K values above those at which the peaks occur, the background sound pressure is approximately proportional to the fourth power of the water velocity and inversely proportional to the hydraulic pressure. For low K values nozzle cavitation or air accumulation changes this relationship.

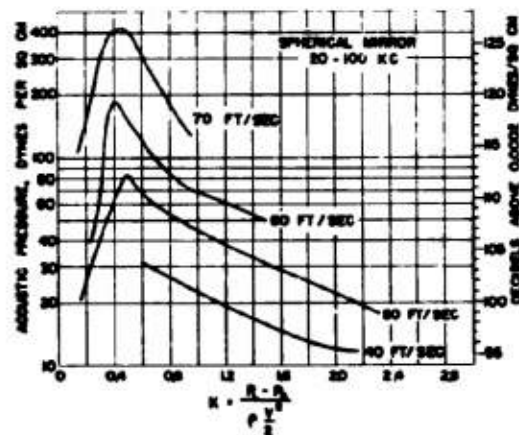


FIGURE 8. Background noise level. No model or strut in tunnel. Same as Figure 7 except that new nozzle installed at inlet to working section.

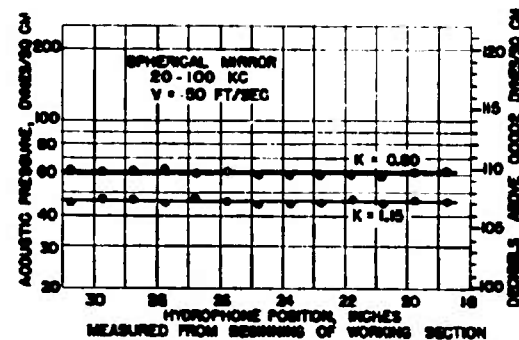


FIGURE 9. Background noise level at different positions along center line of tunnel. No model or strut in tunnel.

UNIFORMITY OF BACKGROUND NOISE

A comparison of the background noise obtained at different positions along the centerline of the tunnel is shown in Figure 9. These measurements were made with the velocity and pressure fixed ($K = \text{constant}$) by moving the hydrophone and mirror parallel to the

tunnel axis. They show the same noise level throughout the length of the working section normally occupied by the model.

BACKGROUND NOISE WITH PROJECTILE IN TUNNEL

In order to verify that these "clear-tunnel" measurements gave the same background noise that would be obtained with actual test installations, a survey was made for noncavitating flow with a projectile installed in the working section. All the other test conditions used to obtain the data in Figure 7 were duplicated as nearly as possible and measurements made of noise vs distance along the tunnel axis at $v = 40$ fps and $K = 3.74$. With such a high value of K no cavitation existed at any place on the model. These measurements, shown in Figure 10, gave an average noise level within 2 db of the clear-tunnel noise shown for the same K in Figure 7.

7.4 MEASUREMENTS OF NOISE PRODUCED BY CAVITATING PROJECTILES

7.4.1 Correlation with the Beginning and Growth of Cavitation

CAVITATION TYPES AND INFLUENCE OF PROFILE SHAPE

During observations of various projectiles in the water tunnel, it was noticed that as cavitation first appeared, the formation and collapse of the cavitation bubbles were different for varying degrees of abruptness of the body at the cavitation zone. When the profile was not too abrupt, the zone of cavitation bubbles appeared to form, grow, and collapse right on the surface of the body. For more abrupt bodies the bubbles seemed to form at the surface of the body, but to spring clear of it before collapsing and disappearing. For some very abrupt shapes the cavitation vapor pocket originated and collapsed in the stream away from the disturbing surface, with no visible connection to the body itself. Consequently, in studying the correlation of sound generated with the beginning and growth of cavitation, the several different forms of cavitation were investigated by using several body shapes. The four bodies for which measurements are reported here and the type of incipient cavitation obtained are:

- | | |
|-----------------------------------|---|
| 1. Hemisphere nose | Cavitation forms and collapses on the surface of the projectile. Similar to hemisphere nose. |
| 2. Semiellipsoid nose | |
| 3. Truncated hemisphere nose | Cavitation vapor bubbles originate at the sharp edge but collapse in the stream away from the projectile surface. |
| 4. Tail rudder tilted into stream | No visible connection between cavitation bubbles, which form and collapse in water, and the rudder surface. |

A comparison of the shapes of the four bodies and the types of flow about each for noncavitating conditions are shown by the scale drawings in Figure 11. The three noses and the upturned rudder present to the flow successive changes from smooth to blunt and

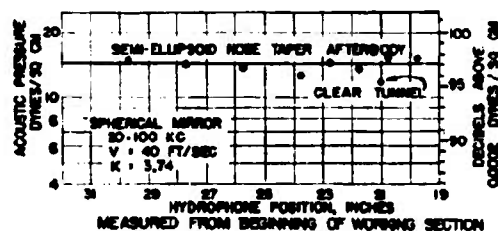


FIGURE 10. Background noise with model in tunnel. Semiellipsoid nose. No cavitation.

abrupt profiles. The flow line diagrams were drawn from detailed observations of the actual flow in the polarized light flume.⁹ They are useful for determining qualitatively the velocity field around the projectile and, hence, locating the zones of low pressure where cavitation is most likely to occur. Wherever the flow, which has been pushed aside by the projectile surface, begins to curve back around the body (concave towards the body), local reductions in pressure are affected. The greater this curvature, the lower the pressure and the greater the possibility of developing cavitation. The flow lines show the maximum curvature near the junction between nose and cylinder for the hemisphere and semiellipsoid noses, at the sharp edge on the truncated hemisphere, and at the tip of the rudder on the finned afterbody. In addition, the diagrams show varying sharpness in

maximum curvature, indicating earliest cavitation for the truncated hemisphere nose or upturned rudder, and later cavitation for the semiellipsoid and hemisphere noses.

SOUND PRESSURE VERSUS CAVITATION GROWTH

With the hydrophone and spherical mirror focused on the zone of incipient cavitation and varying the pressure while maintaining the velocity constant, measurements showing the variation in sound pres-

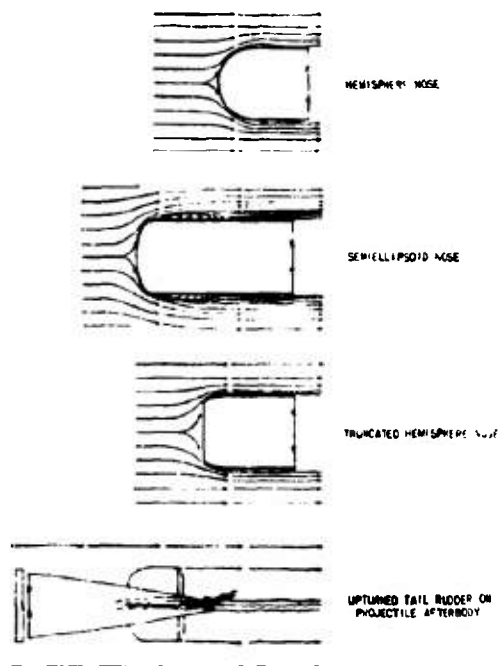


FIGURE 11. Projectile profiles with flow diagrams.

sure with the stage of cavitation were obtained for each projectile. A corresponding series of photographs showing the successive stages of cavitation development were also made. All tests were made with zero yaw and zero pitch. The results are shown in Figures 12, 13, 14, and 15 where the sound pressure is plotted against the cavitation parameter. A scale for the sound level in decibels is also shown. The photographs included in the same figures are arranged in the order of decreasing values of K and each is marked with the corresponding measured sound level. Note that in all cases the total sound pres-

sure in the 20- to 100-kilocycle band is shown, but that the data for each nose were obtained at a different constant velocity.

Each set of curves and photographs in Figures 12 to 15 show the following common characteristics:

1. With reduction in the cavitation parameter K , the sound pressure rises sharply to several times the magnitude of the background noise in the tunnel as soon as the slightest trace of visible cavitation is observed.

2. The rise in sound begins with the appearance of minute cavitation bubbles and reaches a peak value while the ring of bubbles is still very narrow.

3. The sound pressure decreases with continued development of cavitation until, for fully developed conditions, the noise is but a fraction of the peak magnitude. In some cases it drops to approximately the same level as the tunnel background noise.

These characteristics are shown clearly by examining Figure 12 for the hemisphere nose. For high values of K at which no cavitation occurs on the projectile, the measured noise is only that due to background disturbances. However, as K is reduced by reducing the hydraulic pressure or increasing the velocity, and cavitation begins, the noise rises sharply to a high value. In this instance the increase is from 95 to 1,700 dynes per sq cm, a gain of about 25 db. With continued growth of cavitation the noise peaks and then falls off until, with very large bubbles enveloping the body, the measured level equals the background noise level. During tests at the K corresponding to Figure 12A, only small intermittent bubbles of cavitation could be discerned by careful visual examination. They were too small to be detected photographically. Figure 12B shows a small amount of cavitation along the top half of the body at the junction between the hemisphere and the cylinder. Note that it is a very narrow band, yet as the noise curve shows, it is between this condition and the slightly more developed one shown in the next photograph that the maximum noise is measured.

Examination of Figure 13 shows the semiellipsoid nose to cavitate at a higher K , but otherwise to exhibit the same characteristics. Because the background noise was very low for this 40-fps test, the noise gain at the inception of cavitation is nearly 37 db. Again, as indicated in Figures 13B and C, the maximum noise is measured when only a thin ring of cavitation appears near the junction between the cylindrical body and the nose contour. A second small noise peak of undetermined cause is evident at

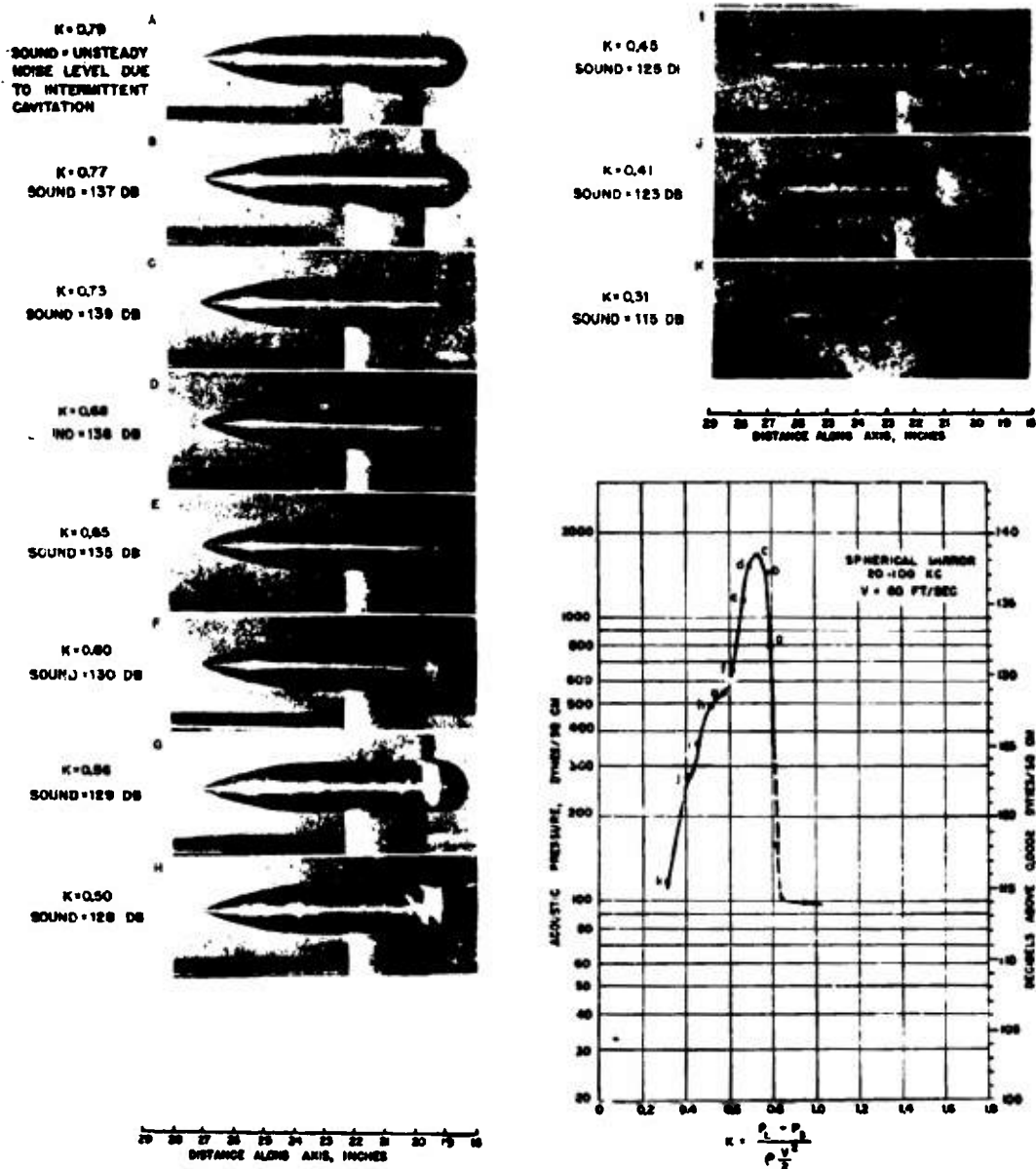


FIGURE 12. Cavitation on hemisphere nose.

CONFIDENTIAL

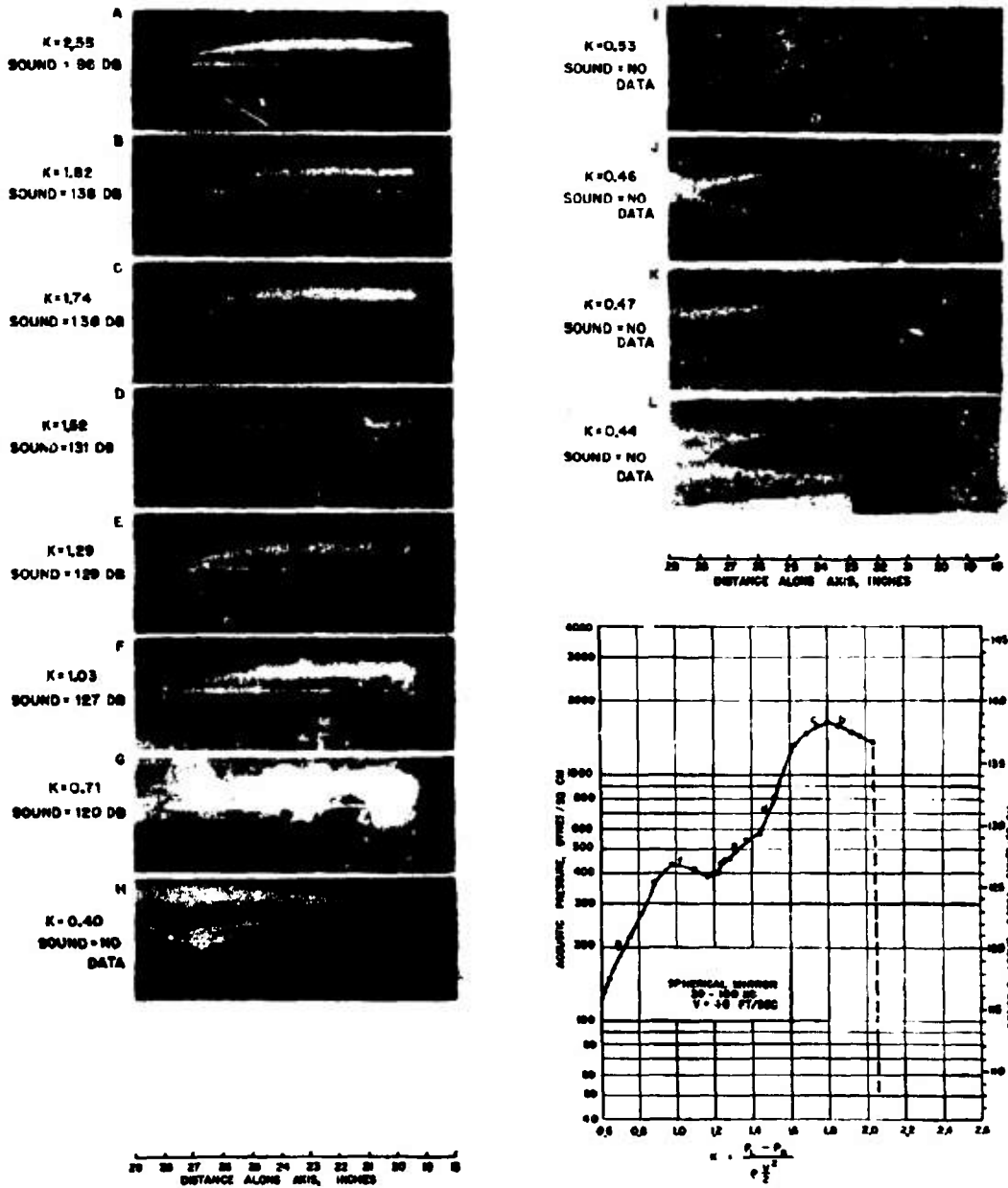


FIGURE 13. Cavitation on semiellipsoid nose.

CONFIDENTIAL

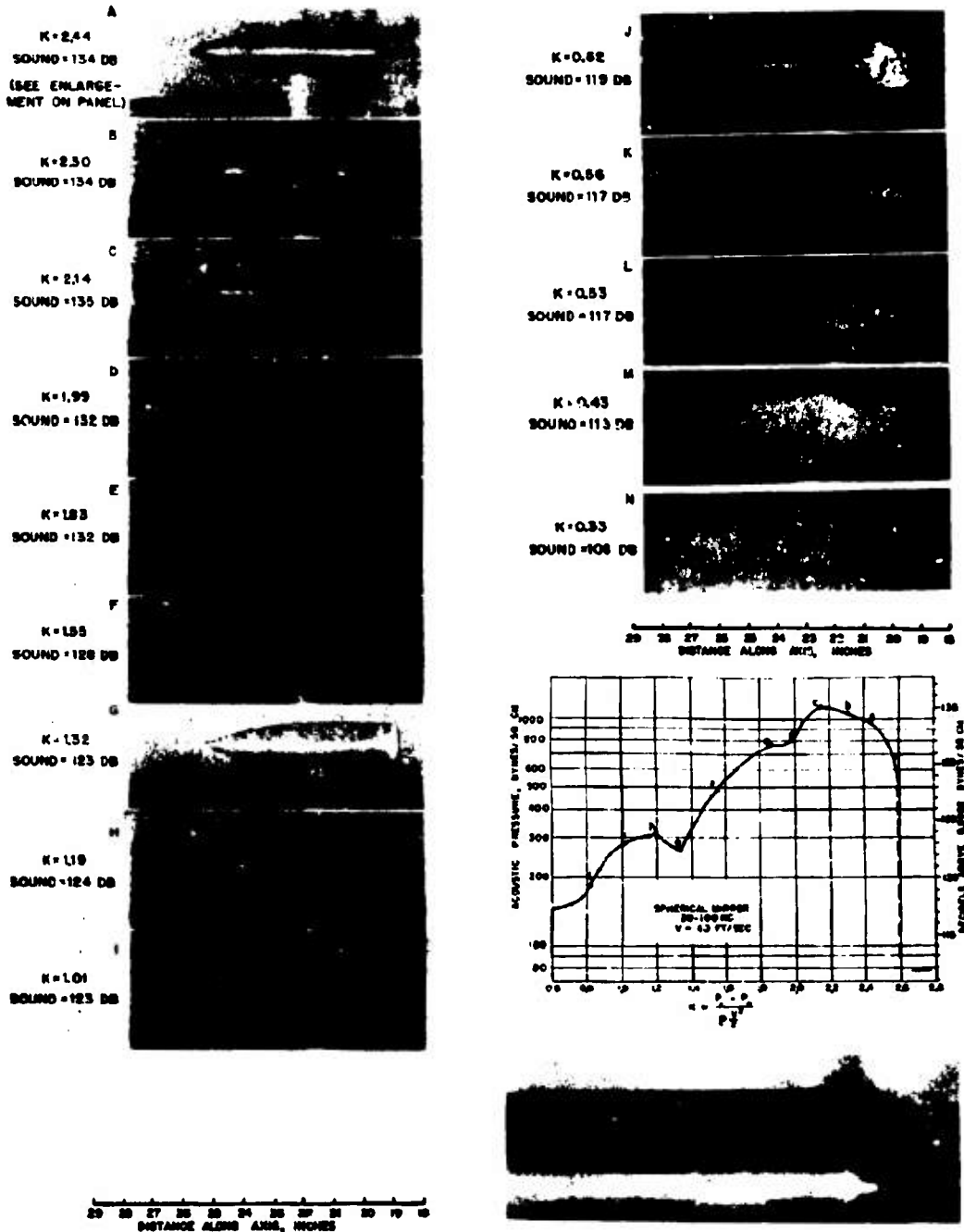


FIGURE 14. Cavitation on truncated hemisphere nose.

CONFIDENTIAL

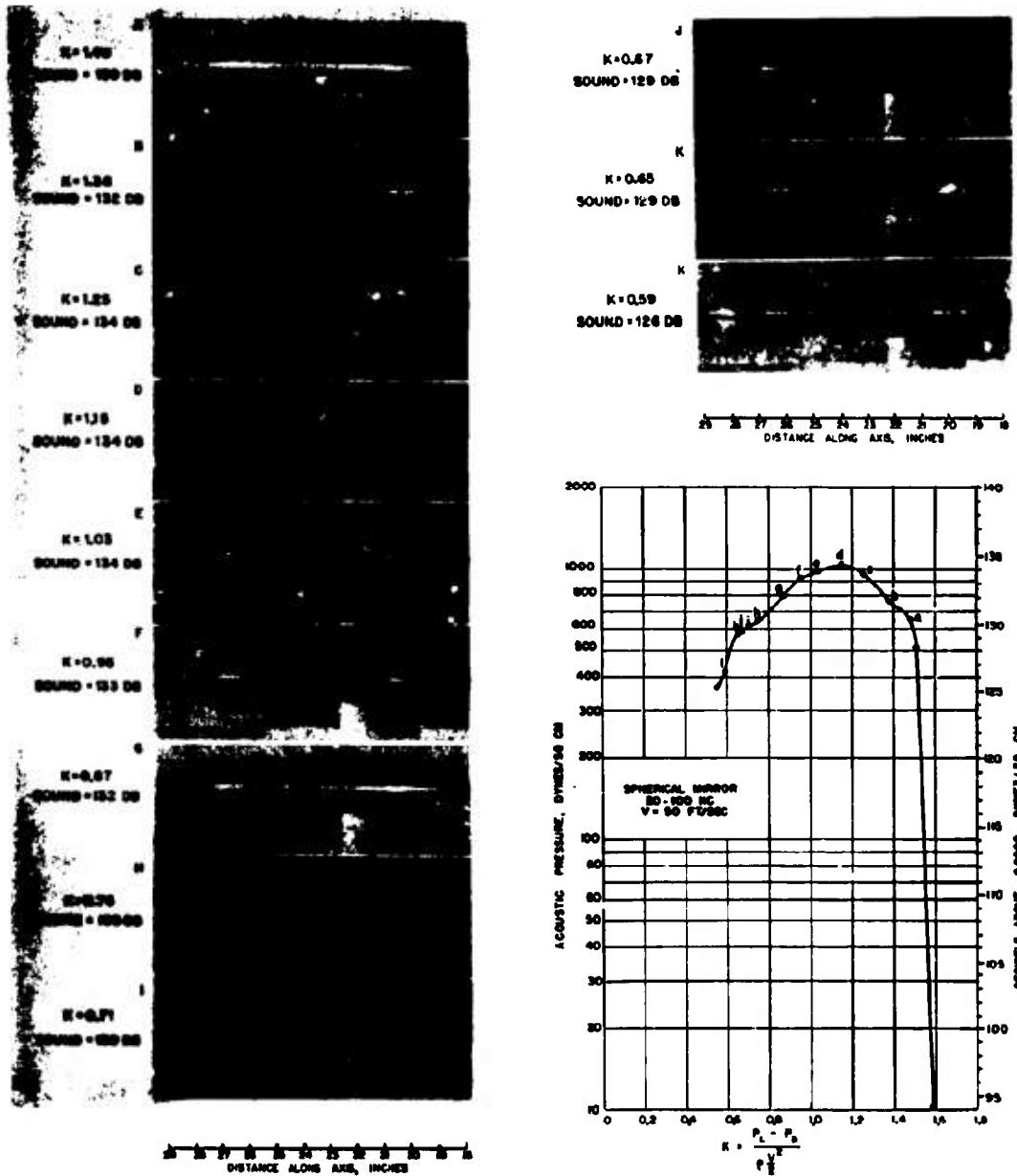


FIGURE 15. Cavitation on upturned rudder of fin tail.

CONFIDENTIAL

the advanced stage of cavitation shown when $K = 1.03$ in Figure 13F.

Figures 12 and 13 both show similar types of incipient cavitation where the bubbles lay close to the body surface. Figure 14 for the truncated hemisphere nose, shows the second type of cavitation where the bubbles collapse in the water away from the body. Figures 14A and B illustrate this clearly. The trailing ends of the small cavitation wisps which originate at the sharp edge on the nose are separated from the body by a definite space. With continued growth of cavitation, the bubble zone becomes more dense and this characteristic is less discernible. The same trends in measured sound were obtained as for the other two noses with about a 23-db increase in level as cavitation began.

Figure 15 shows sound measurements and photographs for a tail rudder tilted up into the stream. As the first photographs of the series show, the initial cavitation occurs at the rudder post as well as at the tip and finally, at very low K values, the entire wake behind the tilted rudder becomes filled with vapor. The noise curve shows the characteristic increase to a peak value and then reduction with cavitation growth. Note that, as Figure 15D shows, the peak noise, a 40-db gain over the background, is obtained with very little visible cavitation.

It might be noted that surface condition is very critical in making the cavitation measurements. The noise measurements and cavitation photographs of the four noses were made after carefully polishing the assembled models and wiping the surface and joints between body sections with a waxed cloth. These precautions caused the onset of cavitation to be more uniform by eliminating early cavitation at isolated points around the periphery of the projectile.

SOUND PRESSURE AND BUBBLE COLLAPSE

The fact that for all three types of cavitation the maximum sound was measured when the visible cavitation was small, and that the magnitude was reduced with the growth of the bubbles, might be tied in with the concept that the noise originates primarily at the bubble collapse. With small cavitation bubbles which form and collapse cleanly and sharply within a small physical zone, the energy release and, hence, the noise is of high intensity. As the zone of cavitation grows, the bubbles collapse throughout a larger space, and mutual interference and absorption due to

the damping properties of the bubbles themselves reduce the intensity of the noise radiated.

COMPARISON OF THE FOUR BODIES AT SAME VELOCITY

It should be noted again that each set of data in Figures 12 to 15 is for a different velocity and, furthermore, the inception of cavitation occurs at a different pressure for each body. Consequently, there is no satisfactory basis for comparison of the magni-

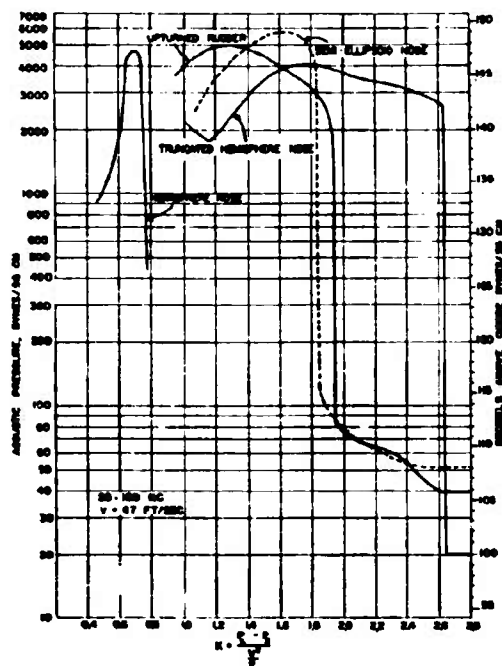


FIGURE 16. Noise caused by cavitation on four different bodies.

tudes of the sound levels measured. Measurements of the noise produced by each of the projectiles at the same velocity of 47 fps were obtained using the ellipsoidal reflector instead of the spherical mirror. These results are shown in Figure 16. The increased effectiveness of this reflector over the spherical mirror is apparent. For example, the hemisphere nose curve shows a maximum sound pressure of 4,800 dynes per sq cm for this 47-fps test, as against about 1,100 shown in Figure 12 for a 60-fps test with the spherical mirror. Similarly higher peaks are obtained for the others. These curves show some difference in the magnitudes of the noise peaks for the different bodies.

CONFIDENTIAL

There is also some difference in the shapes of the curves, the peak occurring at a K somewhat lower than the inception value for the two most abrupt shapes, the truncated hemisphere and the upturned rudder. For the hemisphere and the semiellipsoid the peak occurs soon after the inception point. For both the truncated hemisphere and the upturned rudder, the determination of the beginning of cavitation was very critical so that sound measurements in that region were difficult to obtain. With the other two noses, however, the increase, although sudden, could be traced, and with extreme care, measurements could be made at levels intermediate between the background and highest pressures.

NOISE VERSUS VELOCITY

Figure 17 shows the change in noise with velocity for the hemisphere nose. For the velocity range of 40

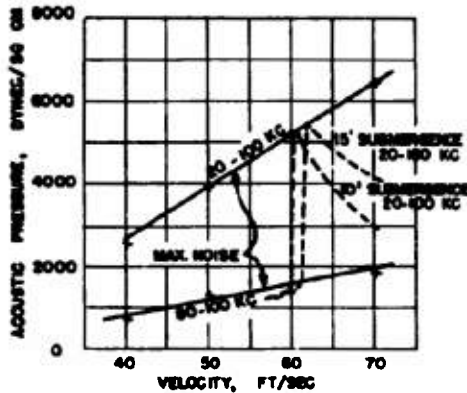


FIGURE 17. Noise versus velocity. Hemisphere nose.

to 70 fps the increase in maximum noise for each speed is approximately linear. This holds for both the 20- to 100-kilocycle and 80- to 100-kilocycle frequency bands. Note also that the ratio of increase with velocity is the same, both bands indicating that probably the composition of the total noise produced at the maximum may be the same at all velocities. This maximum noise is not obtained at the same pressure (submergence) for all speeds, but rather at a nearly fixed value of the cavitation parameter K . If a projectile travels under water at a constant depth, the maximum noise represented by the straight lines in Figure 17 will be generated only at one velocity where K assumes the above fixed value. For all other

velocities the noise will be less than the maximum. The other curves in Figure 17 show the variation in noise in the 20- to 100-kc band for this nose submerged to 10 ft and 15 ft. It will be noted that the noise level is low up to the critical velocity for the inception of cavitation. Then it increases several fold until it reaches the maximum level curve. Beyond this peak the noise level drops. Cavitation is postponed to higher velocities as submergence increases, but when cavitation does occur, the peak noise is higher also. It might be noted that the data from

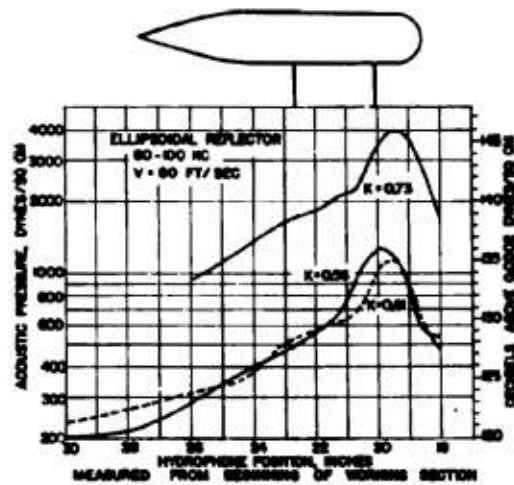


FIGURE 18. Movement of noise source with growth of cavitation on the hemisphere nose. Compare with Figure 12C, F, G.

which these curves were drawn were obtained with a different arrangement in the water tunnel setup, so the magnitudes of the maximum noise are not directly comparable to those illustrated in Figure 16.

NOTE ON MAGNITUDE OF MEASURED NOISE

It should be emphasized that the absolute magnitudes of the sound levels measured in the water tunnel bear no particular relation to what might be obtained in the field. In any event, in either laboratory or field measurements the hydrophone receives only such a portion of the total sound emitted as the geometry of the setup permits. The magnitudes reported here are good for comparative purposes only.

CONFIDENTIAL

7.4.3 Location of Noise Source during Cavitation

VISIBLE CAVITATION AND THE NOISE SOURCE

It is generally believed that at the point of collapse of a cavitation bubble the energy concentration is appreciable, resulting in a local pressure intensity that is very high. In a collapsing zone the pressure waves produced at a very high rate are the cause of the mechanical damage commonly known as cavitation corrosion and of noise, both acoustic and supersonic.¹⁹ That the source of noise measured is concentrated at the zone where cavitation is visible is clearly

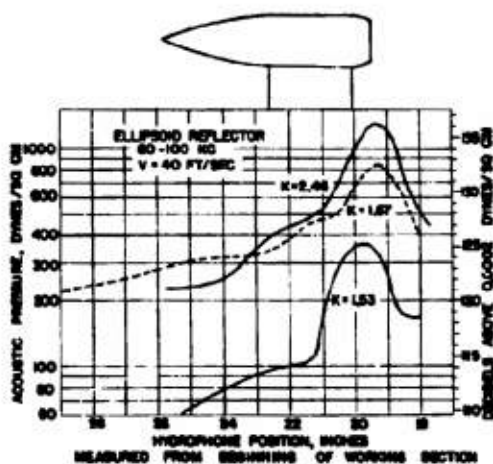


FIGURE 19. Movement of noise source with growth of cavitation on the truncated hemisphere nose. Compare Figure 14A, F.

shown by traverses giving the sound pressure as the hydrophone is moved parallel to the water tunnel axis. As the examples for the hemisphere nose in Figure 18 show, the maximum noise level is obtained when the hydrophone is positioned to focus on the cavitation zone as shown in the photographs of Figures 12C, F, and G. At 1 in. on either side of this position the sound is reduced 3 to 5 db. The ring source shown in the photographs appears as a line to the hydrophone receiver so that, as might be expected, focusing of the hydrophone in a position 1 in. above or below the centerline of the working section gives less than 1-db reduction in the level. Because the sharpest focusing was obtained at the higher frequencies the measurements in Figure 18 are for the 80- to 100-kilocycle band.

MOVEMENT OF SOURCE WITH SHIFTING ZONE OF COLLAPSE

If it is assumed that the bulk of the total noise measured from a cavitating object is obtained from the collapse of the bubbles, the physical observation that the collapsing zone moves downstream with the growth of cavitation should indicate the downstream movement of the noise source. The curves in Figure 18 also indicate this trend. The peak obtained for a cavitation parameter K of 0.56 is approximately $\frac{1}{2}$ in. farther back than the peak for $K = 0.73$, whereas

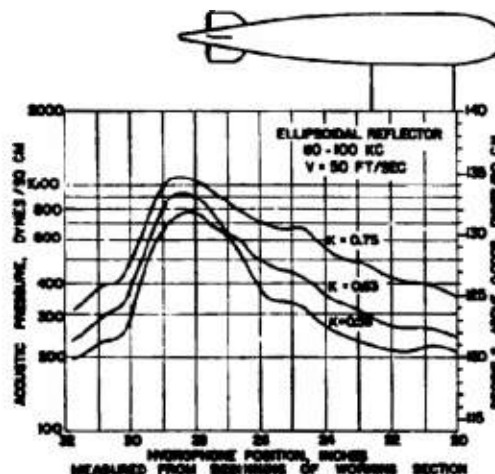


FIGURE 20. Movement of noise source with growth of cavitation on upturned rudder of fin tail. Compare Figure 15H, K, L.

photographs of Figures 12C and G indicate about 0.6-in. downstream elongation of the cavitating zone.

It has been suggested that growth of the sound source could indicate an apparent shift in its location, or that some combination of the effects of the screening and reflections peculiar to the projectile and tunnel configuration could explain the measured shift. It is felt, however, that the agreement between length of cavitation bubble and movement of the sound peak measured in this and other cases is good evidence that the noise source is moving with the zone of the collapsing bubbles.

Measurements for the truncated hemisphere nose in Figure 19 show the same typical trends observed with the hemisphere nose. Figure 20 shows the results obtained with cavitation on the upturned rudder.

CONFIDENTIAL

These curves do not indicate a consistent shift in peak, even though cavitation at the lowest K is much more severe than at the highest. Reference to Figures 15H and L shows, however, that the visible zone of vapor on the lee of the rudder was changed very little as K was reduced. With more severe conditions, more and more vapor was entrained by the water and swept downstream to collapse outside the range of the hydrophone system, but the main cavity shown was almost uninfluenced.

In mounting the hydrophone-reflector assembly precise angular adjustment in the horizontal plane was very difficult. However, as shown in Figures 2

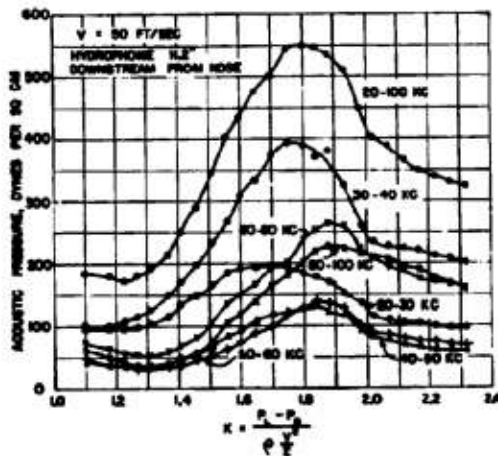


FIGURE 21. Frequency distribution of cavitation noise from truncated hemisphere nose.

and 3, the whole assembly was attached to a carriage which, after focusing adjustment, was moved parallel to the tunnel axis on machined rails. As a result, while the relative portions of the noise peaks were determined accurately, the absolute locations were apt to be in error by the amount of any angular misalignment multiplied by the distance between the noise source and the hydrophone. For the earliest stages of cavitation the location of the peak can be accurately checked because the noise undoubtedly originates from the very narrow visible band. If all the traverses are taken without further adjustment this correction will apply to all measurements. This procedure was followed for determining the absolute location of the peaks in Figures 18, 19, and 20.

The effect of the movement of the sound peak with the growth of cavitation has a secondary effect on the

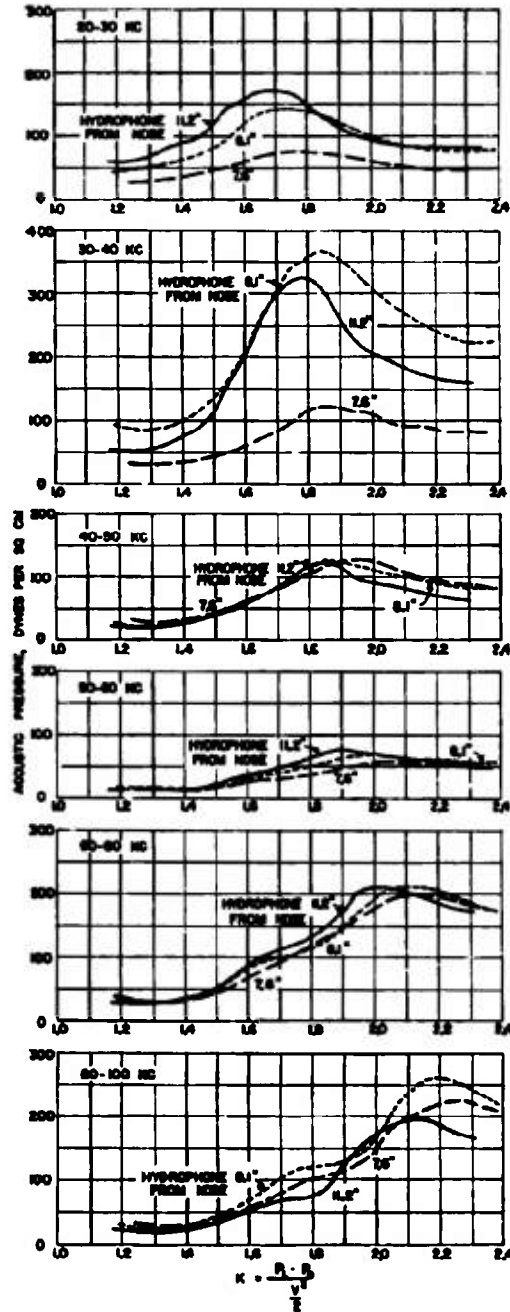


FIGURE 22. Effect of relative position of hydrophone and noise source on measured frequency distribution. $V = 41$ feet per second.

accuracy of the sound versus K curves shown in Figures 12 to 16, which were obtained with the hydrophone in a fixed position. With the growth of the cavitation zone beyond the stage giving the maximum noise, the level measured by the fixed hydrophone is slightly low. This effect is small, however, being less than 2 db for the hemisphere nose at $K = 0.56$ or the truncated hemisphere at $K = 1.51$. Consequently, it does not alter the peculiar characteristics of the measurements shown, nor change the conclusions already presented.

It is interesting to note that in Figures 18 to 20 the sound-pressure location curves for the hemisphere nose and tail rudder show more gradual reductions in noise on the side of the maximum which was toward the body of the model. This asymmetry became more pronounced at lower K values, while at high K 's, as obtained with the cut hemisphere nose in Figure 19, no definite asymmetry is observed. Examination of the photographs in each figure shows that at the lowest K 's, cavitation is occurring at the junction between the streamlined strut which supports the projectile and the cylindrical projectile body. It is thought that this secondary cavitation is contributing to the measured sound and is responsible for the asymmetry observed.

7.4.3 Frequency Distribution of Cavitation Noise

One of the objectives of this investigation was to measure the distribution of the high-frequency noise when cavitation occurs. Obtaining significant measurements of this type is very difficult, since the hydrophone is separated from the sound source by water and the Lucite tunnel window, and since the geometry of the installation may cause reflection patterns that will bias the determinations. Even the use of focusing reflectors does not eliminate this possibility because even though the directivity may be good, standing waves may still bias the results. In addition, field calibrations have shown that the response of the reflectors themselves is not uniform over the frequency range of interest. As a result the relative position of the hydrophone and the sound source has an important influence, and a single set of measurements for one installation cannot be relied upon to indicate accurately either the magnitude or the distribution of the actual noise generated in the working section. This handicap was not present for the measurements that have been discussed in the

previous sections because the main interest lay in the relative amount of noise obtained over a wide frequency band with and without cavitation. Neither the absolute magnitudes of the measured intensities nor the distribution within the band covered was of particular significance there.

Because of the above considerations a series of experiments were made in which the relative position of a cavitating nose and the hydrophone was varied using the simple arrangement of the hydrophone inserted in a Lucite blister clamped to the face of the working-section window. The noise level was recorded in each of several bands within the 20- to 100-kilo-

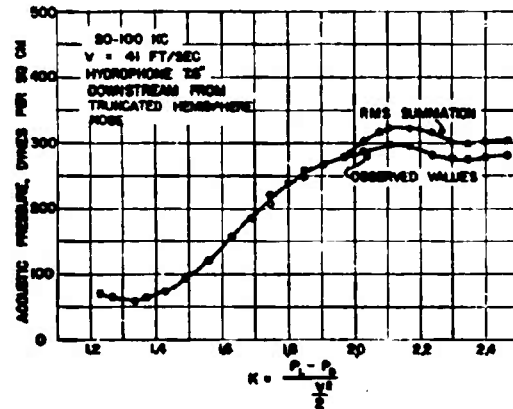


FIGURE 23. Noise in 20- to 100-kc band by measurement and by rms summation from narrower bands.

cycle range as well as for the entire range. The results of these measurements are shown in Figures 21, 22, and 23. Figure 21 gives the distribution measured on the truncated hemisphere nose at a velocity of 50 fps with the hydrophone located 11.2 in. downstream from the cavitating nose of a projectile (2-in. diameter model in 14-in. diameter working section). The measured levels in the various frequency bands are not uniform, the most predominant sound pressures being obtained in the 30- to 40-kilocycle band. Figure 22 shows comparisons of the noise measured at 41 fps in each band and for the hydrophone at 11.2, 8.1, and 7.6 in. aft of the model nose. For any band of frequencies although the location of the peak pressure and the shapes of the curves are similar for all hydrophone positions, there are changes in the magnitude of the sound in some bands. This is definite indication of existence of some complex standing wave pattern caused by reflections from the tunnel walls. As cavi-

tation grows and the falling noise level approaches the background level, the curves tend to converge, giving a more nearly uniform response over the entire frequency range independent of hydrophone position. Such differences as do occur are most noticeable in the 30- to 40-kilocycle band. Note that all of these measurements were made at velocities and hydraulic pressures corresponding to K values at which there was no liberation of air from the main flow to cause attenuation of the noise.

An interesting comparison is shown in Figure 23 by the two curves for the noise in the entire 20- to 100-kilocycle range. One was obtained by plotting the observed points, the other by plotting the square root of the sum of the squares of the sound pressures observed in individual bands. Aside from differences of about 10 per cent at the higher K range, which can be accounted for by filter cutoff characteristics, the agreement is very good.

Chapter 8

FORCES ON FINLESS BODY SHAPES

8.1 INTRODUCTION

THE HYDRODYNAMIC FORCES acting on the finless bodies of fin-stabilized projectiles are of interest to the designer because a knowledge of the magnitude and distribution of these forces forms a basis for understanding the overall forces acting on the complete projectile and, as is shown in Chapter 11, aids in clarifying the relationship between the lift, moment, damping force, and damping moment. The effect of the body shape on the drag is discussed in Chapter 10. This chapter will be devoted to a discussion of the lift and moment and the relationship between them.

8.2 DISTRIBUTED FORCES AND RESULTANT FORCES

The structural designer of the shell of a projectile or an airship needs information on the *distribution* of forces over the surface of the body. On the other hand, in dealing with the external ballistics of the body shape it is usually sufficient to know the *resultant* of these distributed forces. For example, in the case of a well-streamlined body of revolution the dynamic pressure acting on the nose (parallel to the direction of motion) is nearly balanced by the dynamic pressure on the afterbody, and the two taken together contribute but little to the total drag of the body. To determine the overall drag, which consists of the pressure drag (or form drag) plus skin friction drag, it is not necessary, therefore, to know the magnitude of the nose pressure or the afterbody pressure. However, to the structural designer these pressures may be important since the body structure must transmit them from one end of the body to the other.

In the design of frail structures such as airship hulls, the distributed forces are of major importance. In the case of projectiles such as bombs, rockets, and torpedoes, the shells are usually made strong enough, because of other considerations, to withstand the hydrodynamic pressures encountered in a normal run. Therefore, we are usually interested only in the resultant forces and moments such as are measured

in the wind tunnel or water tunnel. However, a better understanding of the behavior of the resultant forces may be gained by studying their origin in the distributed forces.

The distributed forces acting on a body moving through a fluid medium may be divided into two groups: normal pressures acting at right angles to the surface and shear forces acting parallel to the surface. The shear forces contribute mainly to the drag, while the normal forces may contribute to the drag but are more important in determining the moment and lift or cross force. In the following discussion we will, therefore, deal mainly with the normal pressures.

8.3 STREAMLINED SHAPE IN A FRICTIONLESS FLUID

For the purpose of this discussion it is convenient to start with the forces acting on a streamlined shape moving through an ideal frictionless fluid. Such a fluid does not exist since all real fluids are viscous to some extent. The force distribution with a frictionless fluid, therefore, cannot be measured but may be calculated from potential flow theory. The actual forces acting on the forepart of a well-streamlined shape moving at high Reynolds numbers through a real fluid are almost identical with those calculated for the ideal fluid.

In Figure 1 is shown a streamlined body of revolution moving rectilinearly with velocity v and angle of attack α . The solid line curve shows the transverse force distribution *calculated* for such motion through a frictionless fluid.²⁰ The ordinate at each point along the axis gives the resultant force obtained by integrating the vertical component of the pressures acting on the surface of the body per unit of axial length at that station. It is seen that the forces on the forebody are directed upward and on the afterbody downward, giving rise to a large upsetting moment, i.e., a moment which tends to increase the angle of attack α . Since the areas enclosed by the curve above and below the axis are equal, it is evident that this force distribution results in zero transverse force or lift but produces a pure couple only.

2.4 STREAMLINED SHAPE IN A REAL FLUID

In Figure 1 is also shown the force distribution calculated from pressure-distribution measurements made on the same body, which is a model of the airship R101. These data²⁰ are shown by the circled points and dotted curve. It is seen that, on the forebody, the measured forces are in very good agreement with the calculated values. On the afterbody the values measured with a real fluid are less than those calculated for the ideal fluid. It is known that this difference is due to the fact that, with a real viscous fluid, separation and vortex formation which occur

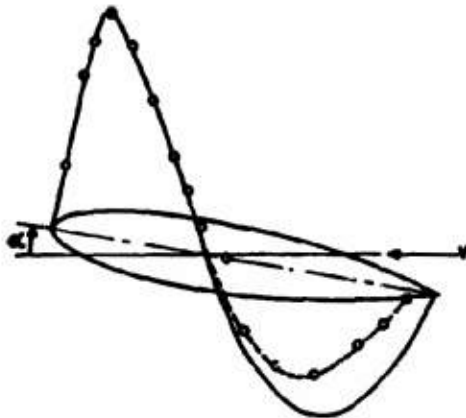


FIGURE 1. Calculated and measured transverse force distribution.

near the tail alter the force distribution on the afterbody.²¹

This force distribution, unlike that of the ideal fluid, does give rise to a resultant lift, since in this case the downward force on the afterbody is not as large as the upward force on the forebody. The resultant lift is equal to the difference between the areas enclosed by the experimental curve above and below the axis; or, equal to the area enclosed between the solid and dotted curves on the afterbody.

In addition to the lift, the body is also subject to an upsetting moment. However, in the case of the real fluid this upsetting moment is not as large as with the ideal fluid because the force on the afterbody is smaller. Nevertheless, a comparison of the areas under the curves of Figure 1 shows that the magnitude of the moment is still large in comparison with

the resultant lift. That is, the moment is due to real forces acting directly on the body which are considerably larger than the resultant lift.

2.5 RESOLUTION OF FORCES

In dealing with the external ballistics of projectiles we are usually interested only in the resultant forces and moments, since the motion of the body as a whole is determined by them. These resultants are easily determined by direct measurement in water or

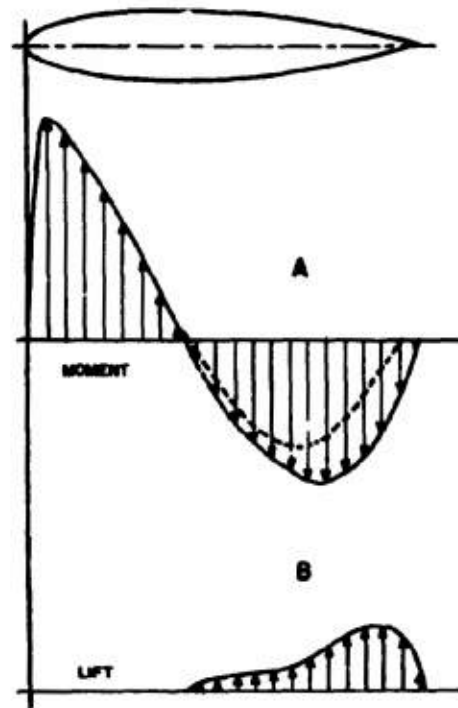


FIGURE 2. Resolution of forces.

wind tunnel or towing tank. The determination of the force distribution, on the other hand, requires laborious processes involving integration from pressure-distribution measurements and evaluation of the skin friction drag.

Direct force measurements give the magnitudes of the moment and of the lift, but not the force distribution. To establish a relationship between the moment and the lift, it is usually assumed that the moment is a direct result of the lift force acting at some point

called the center of pressure CP . To determine the location of CP with reference to the center of gravity CG , we divide the moment M about CG by the lift force L , this ratio giving the lever arm l_{CP} , i.e.,

$$l_{CP} = -\frac{M}{L}. \quad (1)$$

This conventional method of resolution leads to some incongruities. For instance, in the case shown in Figure 1, the moment tends to turn the body clockwise and the lift acts upward. If the moment is attributed to the lift, then the lift must be acting at some point ahead of CG . Also, since in this case the lift is small and the moment is large, l_{CP} comes out so large that the lift appears to act 0.8-body-length ahead of the nose. Obviously, a transverse force cannot be transmitted to the body through the water from a point ahead of the body. Furthermore, if we were to modify the body shape so as to increase the lift, for instance by making the tail more blunt or by adding fins, we would thereby decrease the moment. Again we arrive at an incongruity, i.e., the moment, which supposedly is due to the lift, diminishes as the lift grows. With the oversimplified relationship embodied in equation (1), this is explained by saying that l_{CP} becomes smaller or even changes sign, i.e., the center of pressure is moving aft along the body axis.

The forces may be resolved in a different manner which gives a clearer and more consistent picture of the true conditions. Instead of taking, for the case of the real fluid, the force distribution shown by the experimental curve in Figure 1, we may say that there are two sets of forces acting on the body, as shown in Figure 2. One (shown at A) is the same as the calculated force distribution of Figure 1, which results in a pure couple and zero lift. The other distributed force is as shown in Figure 2B, equal to the difference between the calculated and experimental curves of Figure 1. The area under this curve represents the lift force. It is seen that the moment about CG of this lift is of opposite sense to, and partially balances, the moment due to the force distribution shown at A. The resultant moment acting on the body in a real fluid is then equal to the difference between the upsetting moment of the ideal fluid and the righting moment of the actual lift force.

The several inconsistencies which were seen to arise from the conventional force resolution are now eliminated. All forces now act directly on the body. The lift force is seen to act on that part of the body where the physical phenomena (separation and vortex for-

mation) which give rise to it actually occur. The fact that as the lift force grows the resultant moment tends toward greater stability is also consistent. Any tail surfaces that may be added would contribute an additional lift increment acting approximately at the same location and in the same direction as the hull lift.

EVALUATION OF THE THEORETICAL MOMENT

To determine the line of action of the lift force by the method outlined above, it is not necessary to

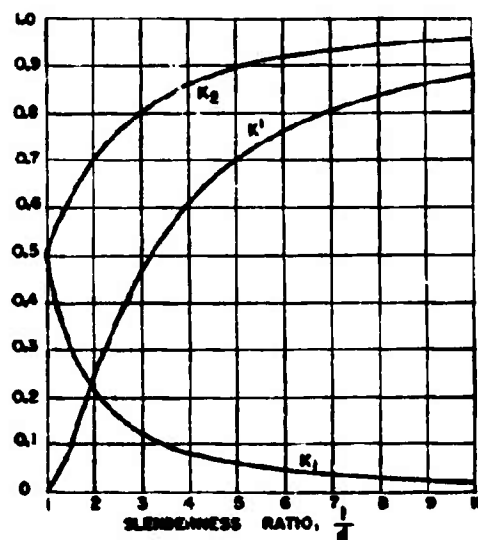


FIGURE 3. Inertia coefficients of an ellipsoid moving in a fluid, K_1 , axial; K_2 , transverse; K' , rotation.

know the theoretical and actual force distributions over the entire body. Only the resultant magnitudes of the theoretical moment and the actual moment and lift are required. The righting moment of the lift is equal to the difference between the theoretical and actual moments. The ratio of this righting moment to the lift force gives the distance from CG to the line of action of the lift.

The resultant theoretical moment for a streamlined body of revolution without fins may be determined with sufficient accuracy for most practical needs by a simple calculation sometimes used in airship work. This is based on the assumption that the theoretical moment for a well-streamlined shape is

equal to that of an ellipsoid of revolution having the same volume and length. For an ellipsoid, the theoretical hull moment H is given by^{2a}

$$H = \frac{1}{2} \rho v^2 (k_2 - k_1) V \sin 2\alpha \quad (2)$$

where k_1 and k_2 are the coefficients of apparent mass of ellipsoids of revolution for longitudinal and trans-

verse motion, respectively, as calculated by Lamb,^{2b} and V is the volume of the projectile. The only possible source of inaccuracy involved is in the selection of the equivalent ellipsoid. This error, however, is very small for projectiles of slenderness ratio (l/d) of 7 or more, since, as may be seen in Figure 3, the values of k_1 and k_2 change but slightly in this range.

Chapter 9

STABILIZING SURFACES ON NONROTATING PROJECTILES

9.1 PURPOSE OF STABILIZING SURFACES

A SYMMETRICAL PROJECTILE, supported at its center of gravity and situated in a completely uniform flow, should be in a position of equilibrium and the moment coefficient C_M should be zero. If this projectile position be altered slightly and the projectile itself be free to move under the new distribution of forces, it is said to be statically stable when it tends to return to the equilibrium position; statically unstable, when it tends to move farther away; neutral when it remains in the new position. In the first case, the resultant of all the pressures will act as though it were being applied aft of the center of gravity; in the second, as though it were ahead. It is possible for this resultant to act as though it were being applied at such a distance forward of the center of gravity as to be in front of the nose.

The purpose of a stabilizing surface is to provide a desired degree of static stability in a projectile which would be inherently unstable without it. It does this by creating a cross force some distance aft of the center of gravity which produces the righting moment. The cross force arises because the stabilizing surfaces will deflect some of the surrounding fluid when the projectile yaws or pitches. Stabilizing surfaces also provide additional damping forces and, hence, damping moments to give dynamic as well as static stability.

9.2 FORM AND ACTION OF STABILIZING SURFACES

Stabilizing surfaces are usually fins, rings, or box tails. Fins are essentially flat surfaces set in planes which contain the longitudinal axis of the projectile. Ring or box tails are made with all surface elements parallel either to the projectile axis or to the normal local flow direction. The stabilizing surfaces may be attached directly to the body or afterbody or to booms extending back from the body proper. The fin span, the ring diameter, or the diagonal length of box fins must not exceed the body diameter of any projectile launched from tubes or gun barrels but may be greater when launched by other means. A special case is the collapsible fin tail for which the fins are

folded initially to permit tube launching, unfolding thereafter to give a much larger span with greater effectiveness. Most stabilizing surfaces are immovable. However, certain projectiles, such as torpedoes, are equipped with movable rudders in addition to fixed fins and rings and hence, through the action of suitable control engines, can be steered in any desired direction.

Fundamentally, the magnitude of the cross force developed by a stabilizing surface depends upon the lateral momentum imparted to the fluid. The force is proportional to the amount of fluid deflected and the magnitude of the deflection as measured by the simultaneous change in the velocity vector. Thus, a given force can be obtained by deflecting a small amount of fluid through a large angle or by deflecting a greater amount through a smaller angle. These effects, which have been discussed qualitatively, with the aid of flow diagrams, in Chapter 3, are the basis for geometric differences in tail designs. Actually, the drag of stabilizing surfaces also contributes to the stabilizing moment. However, in general, the drag coefficient is held to a low value since a large drag coefficient is undesirable in all but very low-velocity projectiles.

9.3 EFFECT OF DESIGN VARIABLES

Standard types of tails—fin, ring, and box—have been mentioned above. Additional design variables are the fin span which is the dimension equivalent to ring diameter and box diagonal; the fin, ring, or box length which is measured in a direction parallel to the projectile longitudinal axis; boom locations for stabilizing surfaces as opposed to location on the body or afterbody; and the overall length of the projectile itself. Specific projectiles will be discussed later in some detail, but the main conclusions as to the effects of these design variables are presented now.

9.3.1 Conclusions

1. The ring tail is far more effective in producing stability than the fin type when physical dimensions only are considered.
2. An increase in the outside diameter (or span) of either the ring or fin tail causes a very marked in-

crease in the stabilizing moment because of the larger quantity of fluid affected and the lessening relative effect of body interference and tip losses.

3. An increase in the (axial) length of fins beyond about two-thirds of the fin (diametrical) span produces very little, if any, increase in stability.

4. The critical length of a ring, beyond which little increase in stability occurs, lies between one-half and two-thirds of the ring diameter.

5. Stabilizing surfaces separated from the main body by a boom cause increased moments because of

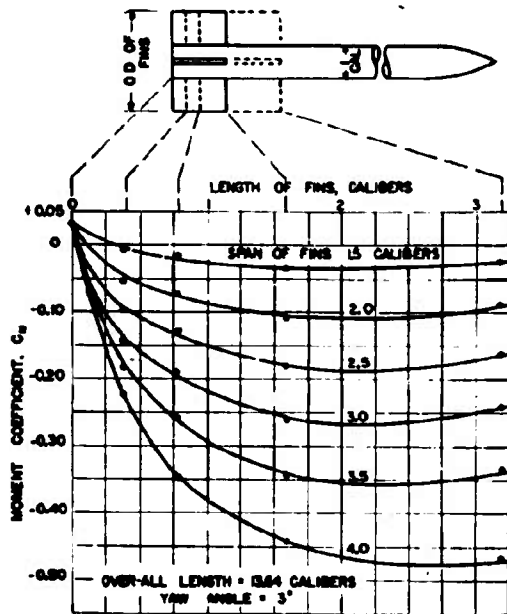


FIGURE 1. Moment coefficient versus fin length and diameter. Fin tails.

the increased lever arm to the center of gravity and because body influence of the flow at the tail surfaces is reduced.

6. Varying the overall length of a given projectile from 7 to 14 calibers (by adding to the cylindrical body section and keeping the percentage distance of the center of gravity from the nose a constant) gave, for the same fin or ring tail, a restoring moment directly proportional to the overall length. In other words, the moment coefficient was constant. This means that the contribution of the tail surfaces to the restoring moment is also proportional to the projectile length or that the actual forces on the tail surfaces are independent of the length.

9.2.2

Fixed Fin Tails

The manner in which the moment coefficient C_M is affected by changes in fin proportions is well illustrated by tests on the 5-inch HVAR rocket.²⁸ Figure 1 shows how the moment coefficient changes with varying length and span of the fin. This curve sheet covers fins with spans up to 4 calibers and lengths increasing (from the after end forward) up to 3.2 calibers. It may be seen that an increase in fin length produces relatively little increase in the moment coefficient after a length of about two-thirds of the span dimension has been reached. Additional length does not increase the effectiveness of the fin in deflecting the fluid but results in nearly the same angular deflection and, hence, the same cross force. The center of pressure on the fins moves forward as the tail is lengthened. This decreases the lever arm of the stabilizing cross force and tends to reduce the moment coefficient C_M . For fin lengths below two-thirds



FIGURE 2. Sixty-millimeter mortar projectile.

the span, this decrease in lever arm is, relatively, much smaller than the increase in cross force due to the lengthening. For excessively long fins, the reverse is true.

It may also be seen from these curves that as the span of a given length fin tail is increased, the gain in moment coefficient is greater than the change in fin area. Furthermore, the gain is more pronounced for a unit increase when the span is short. Apparently a unit fin area near the body surface is affected by body interference and the tip losses are relatively higher.

The influence of body interference on the effectiveness of fin tails is shown by the performance of a tail having the same outside diameter as the projectile body. The example chosen is the 60-mm mortar projectile²⁸ with a tail of eight fins attached directly to the tapering afterbody as shown in Figure 2. In order to increase the stability, tests were made with the tail mounted on booms of different lengths. The increases obtained are shown by the force coefficient curves in Figure 3. A curve is also included showing the per

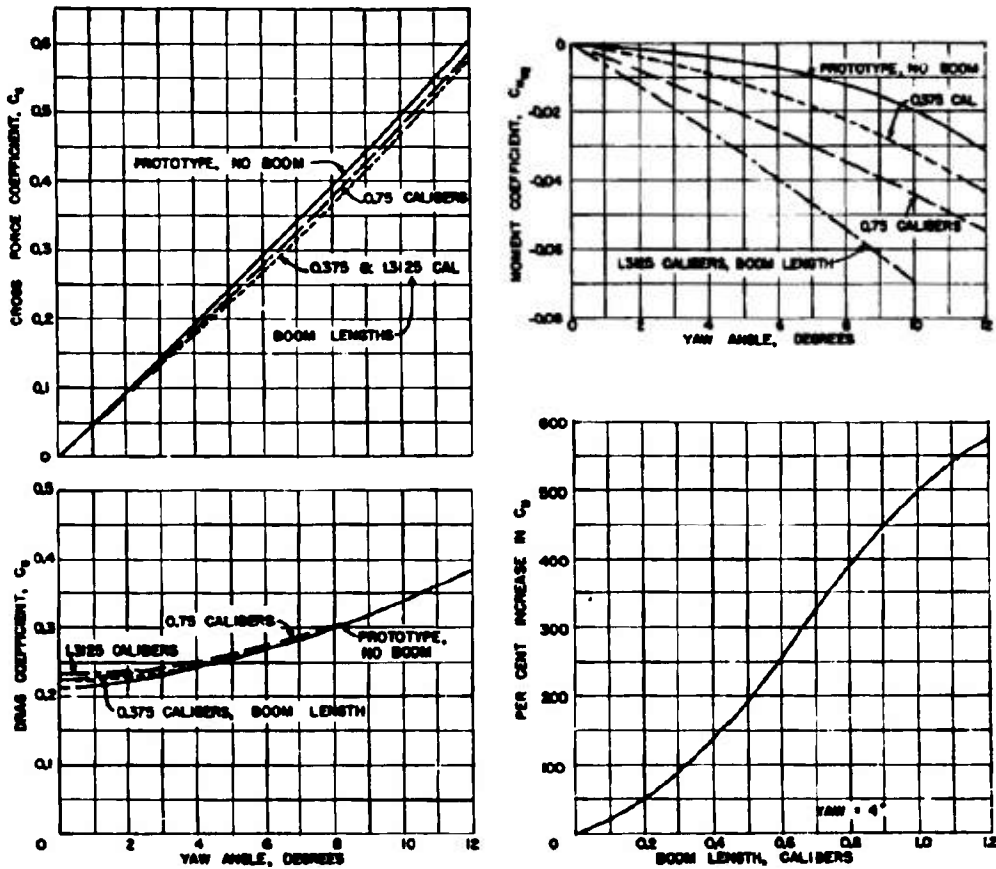


FIGURE 3. Moment and force coefficients. Sixty-millimeter mortar projectile.

cent increase in stabilizing moment coefficient plotted against boom length in calibers for a yaw angle of 4 degrees. Note that C_M increases at first at a rate greater than the linear change that would be due to increasing the boom length alone. The extra effect is due to the fact that better flow conditions are obtained over the fins because of the increasing distance from the afterbody. The very large magnitude of the percentage increase in C_M with increasing boom length is due, in this case, to the fact that the boom makes up a relatively large percentage of the overall length.

9.1.1

Ring Tails

Typical effects from varying the length and diameter of ring tails are shown by the performance of

a group of tails having a diameter larger than the body of the projectile. Figure 4 shows the moment coefficient for the 5-in. HVAR projectile with a series of ring tails having diameters of 1.5 to 2.5 calibers, and lengths varying from 0.25 to 2.5 calibers. These curves show only a slight change in moment for any increase in ring length beyond one-half to two-thirds of the ring diameter.

The data in these curves also illustrate a rapid increase in moment coefficient with ring diameter similar to that shown for increasing the span of plain fin tails.

The performance of ring tails having the same diameter as the projectile body is similar to that of fin tails no larger than the body diameter. Because changes in ring length show relatively small effects, the most satisfactory way to increase stability in this

CONFIDENTIAL

case is by means of a boom, as for fin tails. Many tests made to determine the suitability of the ring tail for the 4.5-in. rocket^{28,29} illustrate this point. Figure 5 is a photograph of the model of the 4.5-in. rocket with a ring tail and boom. Figure 6 shows the corresponding performance curves and curves giving the per cent increase in moment coefficient due to the boom. As was observed for the fin tail on the 60-mm mortar projectile, the increase is greater than can be accounted for by the increase in lever arm due to the

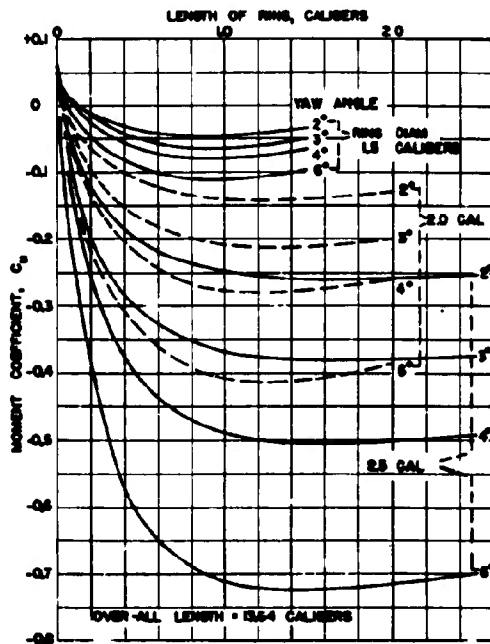


FIGURE 4. Moment coefficients versus ring dimensions; 5-in. HVAR ring tails.

added length, indicating that the tail is more effective in producing cross force with the longer boom. The increase in C_M with boom length is very much less than was the case with the 60-mm mortar projectile, this, of course, being due to the fact that the 4.5-in. rocket is a long projectile and the boom length is relatively small in comparison.

The 7.2-in. chemical rocket,²⁷ shown in Figure 7, is, in effect, a projectile with a ring tail of the same diameter as the body mounted on a boom 0.43 caliber in diameter and 3.87 calibers long. This will serve to illustrate the effect on stability of a boom of great length. The moment coefficient for the rocket with

the standard ring tail (No. 61 in Figure 7) is approximately 0.056 at 3 degrees yaw. This is a much greater moment coefficient than is usually found when the ring diameter does not exceed that of the body. The addition of fins to this projectile resulted in a considerable increase in the stabilizing moment. The fins were 1.39 calibers in diameter and 1.18 calibers in length, shown as tail No. 62 in Figure 7. Inasmuch as these fins project beyond the ring, the increase in moment coefficient is not unexpected. The curves in Figure 8 indicate how the stability is affected by the addition of fins, and it is seen that the moment coefficient is increased approximately 50 per cent.

An illustration of the effect of body shape on fin effectiveness is given by tests to determine the feasibility of applying a ring tail to the Mark 13 torpedo.²⁸ These rings were of the same diameter as the torpedo body and were mounted on fins attached to the tapered afterbody. Figure 9 gives the moment coefficient for the torpedo with three types of ring

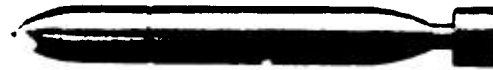


FIGURE 5. Four and one-half-inch rocket with ring tail and boom.

tails; a cylindrical ring, a ring with a 16-degree included cone angle, and one with an 8-degree included cone angle. The 8-degree ring conforms to the angle of flow as determined by studies in the polarized light flume. The resulting flow line drawing is shown in Figure 10.* The 16-degree cone angle causes a converging flow through the ring, and the cylindrical section causes a diverging flow through the ring as compared to the normal flow without the ring.

In the diagrams of Figure 9, the positive moment coefficients denote a destabilizing static moment, and the negative coefficients stable moments. An examination of the curves discloses that with one exception the addition of the ring gives an additional righting force. With the 16-degree conical ring the effectiveness of the tail surfaces is actually reduced if the ring width is large. In general, the stabilizing effect of the ring increases with decreasing cone angle, so that the greatest stabilizing effect is obtained with the cylindrical ring. This is due to both large cross

* A complete description of the determination of flow angles over this afterbody is given in Chapter 3.

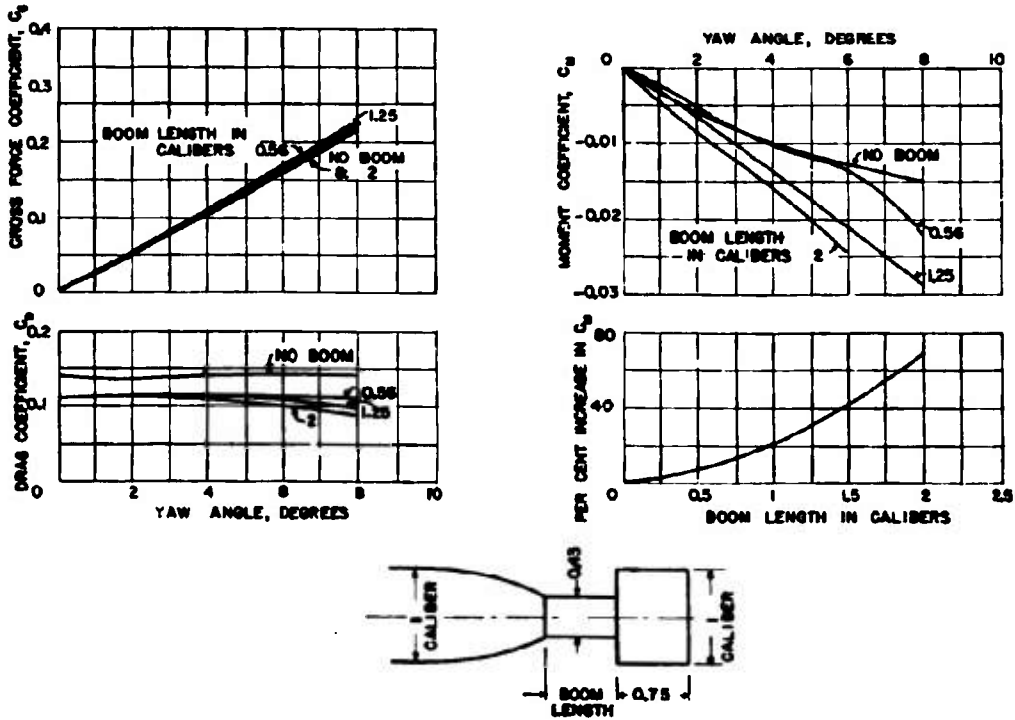


FIGURE 5. Moment and force coefficients; 4.5-in. rocket with ring tail and boom.

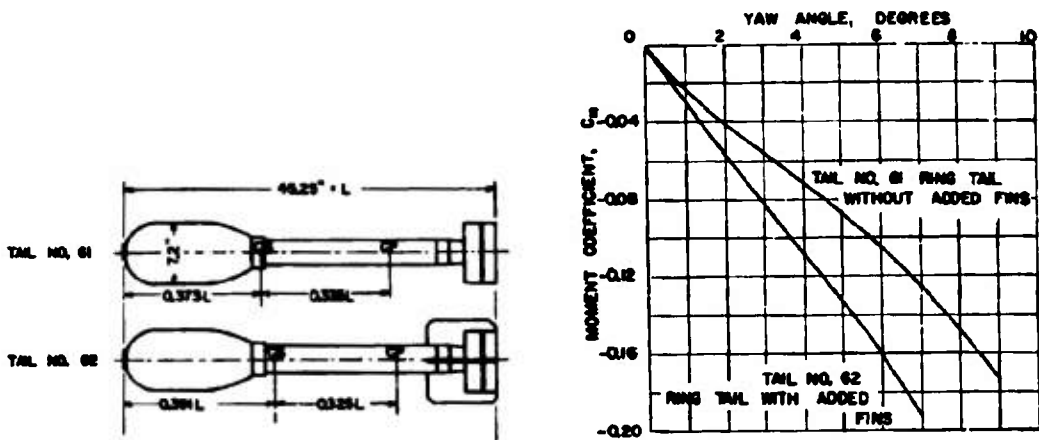
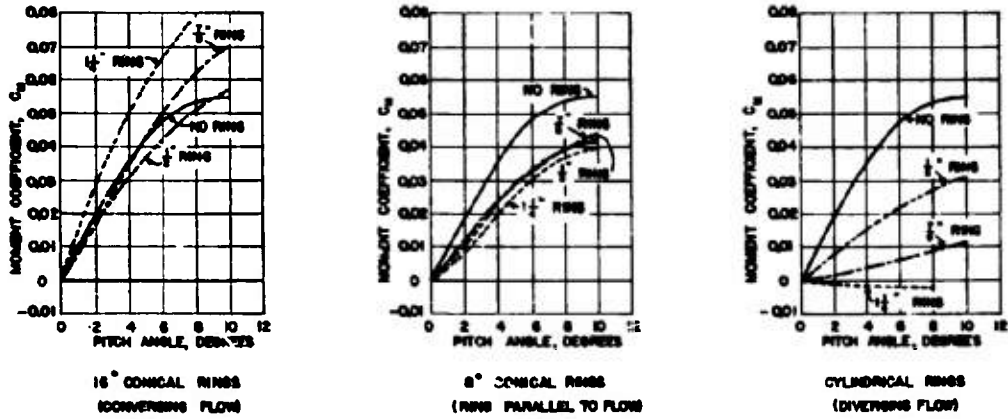


FIGURE 7. Chemical rocket (7.2-in.) with and without fins.

FIGURE 8. Moment coefficients. Chemical rocket (7.2-in.).



NOTE: FOR DIMENSIONS IN CALIBERS, DIVIDE DIMENSIONS ON CURVES BY 2

FIGURE 9. Moment coefficients, Mk 13 torpedo with ring tails.

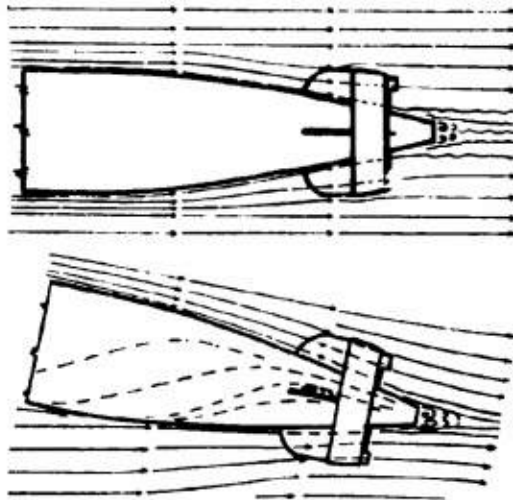


FIGURE 10. Flow line drawing, Eight-degree ring tail on the Mk 13 torpedo.

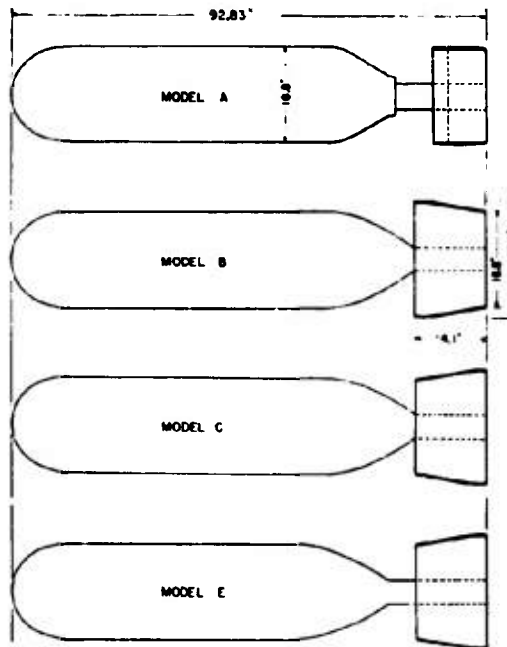


FIGURE 11. High-drag ring tails.

force and high drag. As shown in Chapter 3, when the projectile is yawed, the windward ring surface of this tail will act at a larger angle of attack and will cause more lateral deflection of the fluid it contacts than does the leeward surface. However, even at zero yaw the ring does not match the flow and the drag is high; consequently, this is not the normal method of obtaining a large cross force and moment. The effect of the cylindrical ring increases with length. Apparently it was not carried to the point of diminishing returns obtained in the tests with the 5-in. HVAR rocket. It should be noted that the stability of the cylindrical ring as shown is not typical of actual torpedoes since with adjustable rudders complete static stability is not necessarily desirable.

9.2.4 High-Drag Ring Tails

A special adaption of the ring tail to produce high drag is of interest. Here the tail was intended to limit the terminal velocity of a bomb to prevent deep penetration on impact, and at the same time supply sufficient moment for good stability. Figure 11 shows a straight ring tail, a conical ring set approximately to the flow lines, and two conical rings expanding in the aft direction. As shown by the coefficient curves of Figure 12, the cylindrical and normally tapered rings have about the same drag, the value being approximately what would be expected for this type of tail. However, when the taper of the ring is reversed, as in models C and E, the drag is increased about $2\frac{1}{2}$ times. Tail E is the same as tail C except that it is installed on a short boom. As in the case of the results obtained with the Mark 13 torpedo, the greatest cross force is given by the designs that cause the most deflection of the fluid, tails A, C, and E. Of these, tail E is most effective because interference from the body is reduced. It is better than tail A which is also on a boom, because it is more effective in deflecting the surrounding fluid. Tail B, with the cone angle aligned approximately to the normal flow, presents the least obstruction and, with yaw, causes the least lateral deflection. The resultant moment coefficients are roughly in agreement with the cross force trends.

9.2.5 Effect of Body Length

One remarkable effect noticed in connection with the investigation of ring tails is that the moment coefficient for a given tail is practically constant for

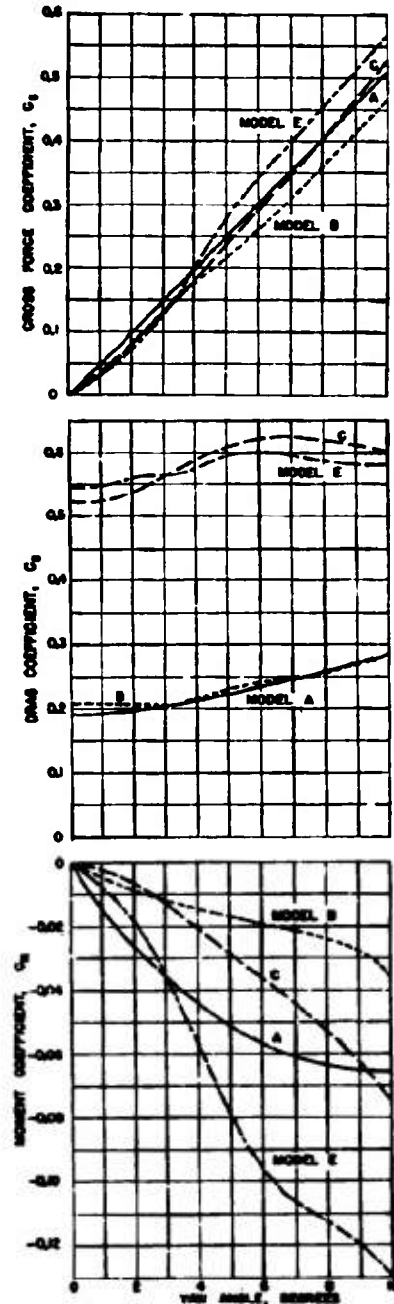


FIGURE 12. Moment and force coefficients. High-drag ring tails

CONFIDENTIAL

overall projectile lengths between 7 and 14 calibers. This refers to bullet-shaped projectiles, with the diameter of the ring tail greater than the body diameter, and for which the center of gravity is assumed at a fixed per cent of the overall length from the nose tip.

Figure 13 gives the moment coefficient versus overall length of projectile for ten ring tails of various

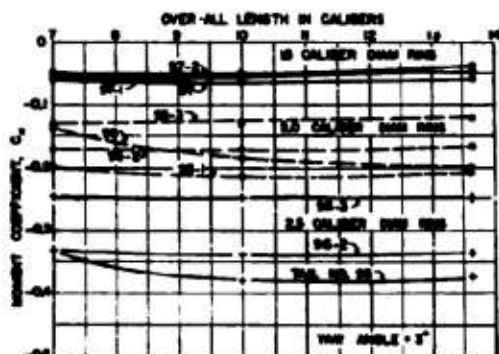


FIGURE 13. Moment coefficients versus projectile length; 5-in. HVAR ring tails.

lengths and diameters. It is seen that all but two of the curves show a practically constant value for the moment coefficient. The abnormal performance of the two tails for body lengths between 7 and 10 calibers has not been investigated.

Tests of finless body shapes (see Chapter 8) have shown, in the few instances where only the length was varied, that the moment coefficient for the body alone increases very slightly for yaw angles of 3 degrees or less, even with large increases in length, if the

shortest projectile is not less than 4 calibers long. Thus it can be concluded that the forces on the tail surfaces in Figure 13 remained sensibly unchanged throughout. This conclusion is logical since the body shape ahead of the tail remains fixed as the

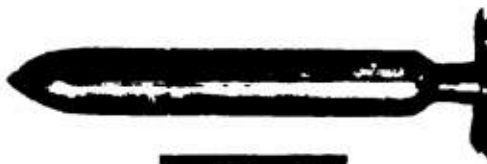


FIGURE 14. Four and one-half-inch rocket with original collapsible fin tail.

length is increased so that the flow into the tail probably is also unaffected. As already seen in the case of the 4.5-in. rocket, this result is not obtained if the length is changed by boom additions so that body interference is reduced.

Fin tails on this same projectile also show a tendency toward a constant value of coefficient with

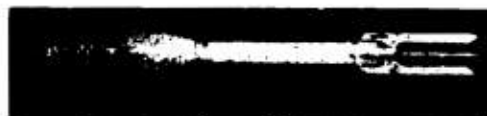


FIGURE 15. Rocket (2.36-in.) with original fixed fin tail.

varying body length, but the effect is not so pronounced as with ring tails. For a given yaw angle and a given tail the moment coefficient is quite constant for body lengths between 10 and 14 calibers. As the length changes from 10 to 7 calibers, the moment

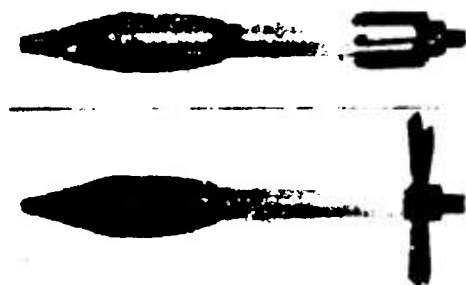


FIGURE 16. Rocket (2.36-in.) with No. 2 collapsible fin tail.



FIGURE 17. Rocket (2.36-in.) with No. 5 collapsible fin tail.

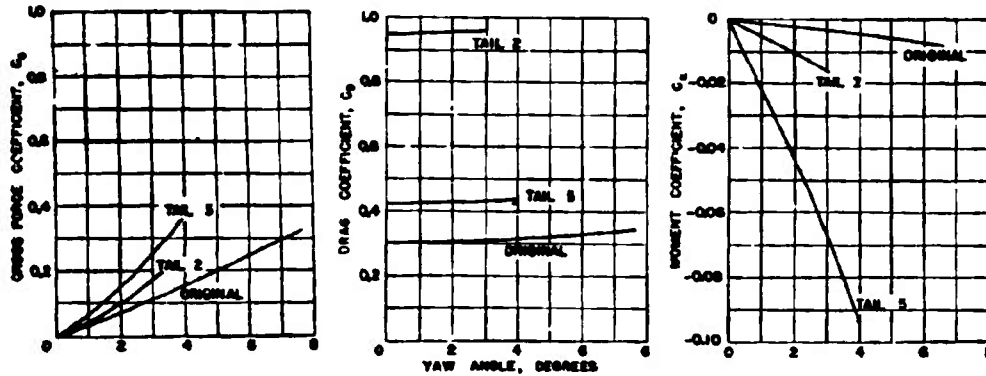


FIGURE 18. Moment and force coefficients. 2.36-in. rocket.

coefficient will decrease between 5 and 20 per cent depending on the yaw angle and tail design.

9.4.6

Collapsible Fins

Many designs of collapsible fin tails for rockets have been made as these have some advantages over other types. The collapsible design allows the use of as great a fin span as desired and still permits the launching of the rocket through a tube of the same diameter as the body. However, owing to the many moving parts of this type of tail, it is not, mechanically, as desirable as a simple fin or ring form.

Figure 14 is a photograph of the original collapsible fin tail of the 4.5-in. rocket.^{22,23} This tail gave a stabilizing moment considerably greater than other types of fin and ring tails that were designed for this projectile. The efficacy of this type of tail is in agreement with the general discussion on fin tails in that it takes advantage of a rather large span for the fins, which is very effective in producing both a cross force and a drag at the tail and, hence, a stabilizing moment.

The most extensive and reliable data on collapsible fins are those relating to the 2.36-in. rocket.^{22,23} This projectile was originally designed with long, parallel fixed fins having an outside diameter equal to the diameter of the body. Figure 15 is a photograph of the original design of this rocket. In order to increase the stability, several different tail designs were made and tested. Figures 16 and 17 show two of the designs which were given the laboratory designations of tail No. 2 and tail No. 5. It is apparent that the span of the extended fins has been greatly increased over the original design and, as a conse-

quence, a considerable increase in the stabilizing moment would be expected. Figure 18 shows curves of the force coefficients for this rocket equipped with

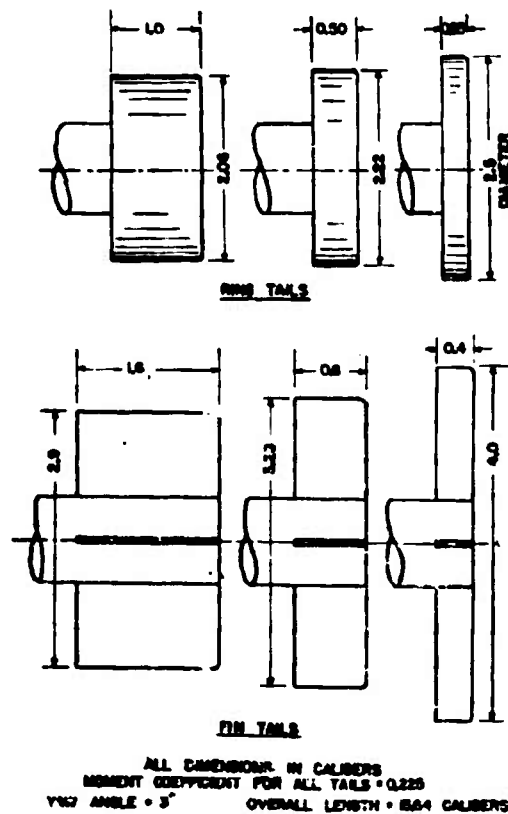


FIGURE 19. Fin and ring tails all having the same moment coefficient.

CONFIDENTIAL

the original fixed fins and also with the two types of collapsible fins. The collapsible fins have resulted in an increase of several hundred per cent in the stabilizing moment. The moment for tail No. 5 is much greater than that for tail No. 2 because its outside diameter is 9.15 in., with only 7.25 in. for tail No. 2.

It should be noted that a material increase in drag results from the use of the collapsible fin tail. Except for a very high drag, however, the drag effect on the stabilizing moment is usually not important. This can be shown as follows:

The moment (about the center of gravity) acting on a projectile is given by the expression

$$M_{CG} = Nel$$

in which N = the sum of the components of the drag and cross force acting normal to projectile axis, or

$$N = \text{drag} \times \sin \psi + \text{cross force} \times \cos \psi.$$

ψ = yaw angle,

l = length of projectile,

e = center-of-pressure eccentricity expressed as a percentage of l .

From the equation for N it is seen that for low values of drag and yaw angle, the term involving drag will be small compared to that involving the cross force and can, therefore, be omitted with only a small error. In other words, only comparatively large values of drag can be considered as affecting the moment.

3.1.7 Ring versus Fin Tails

It is instructive to compare the dimensions of various fin and ring tails that have been designed to give the same stabilizing moment coefficient.

In Figure 19 are shown the proportions of three ring tails and three fin tails all giving a moment coefficient of 0.225 when applied to the 5-in. HVAR projectile. It is very apparent from Figure 19 how much the length of either fins or rings must be increased to counteract the effect of a decrease in fin span or ring diameter. Also the smaller physical dimensions of the ring tails in all cases show how much more effective the ring is than the fin in producing stability.

Chapter 10

EFFECTS OF PROJECTILE COMPONENTS ON DRAG, CROSS FORCE, AND LIFT

10.1 INTRODUCTION

THE USE OF STABILIZING SURFACES ON nonrotating bodies and forces on finless body shapes were discussed in Chapters 8 and 9. This chapter extends consideration to the effects of projectile components on drag, cross force, and lift.

10.2 DEFINITIONS

Drag D is the force in pounds exerted on the projectile parallel with the direction of motion, that is, it is the resistance offered to relative motion between the projectile and the surrounding fluid. The drag is positive when acting in a direction opposite to the direction of motion.

The cross force C is the force in pounds exerted on the projectile normal to the direction of motion and in a horizontal plane. A positive cross force acts to the right for an observer facing in the direction of travel.

The lift L is the force in pounds exerted on the projectile normal to the direction of motion and in a vertical plane. It is positive when acting upward.

It may be seen, by reference to Figure 1, that these forces act along the intersections of the horizontal and vertical planes through the longitudinal axis of the projectile and the plane perpendicular to these two through the center of pressure for zero yaw and pitch angles.

10.3 FORMULAS

$$D = C_D \left[\frac{\rho v^2 A_D}{2} \right] \quad (1)$$

$$C = C_C \left[\frac{\rho v^2 A_D}{2} \right] \quad (2)$$

$$L = C_L \left[\frac{\rho v^2 A_D}{2} \right] \quad (3)$$

$$R = \frac{l v}{\nu} \quad (4)$$

where D = drag force, in pounds;

C = cross force, in pounds;

L = lift force, in pounds;

ρ = mass density of fluid in slugs per cubic foot;

$$\rho = \frac{\text{weight per cubic foot}}{32.2} = 1.94 \text{ for fresh}$$

water and 1.99 for sea water at 60 F;

v = mean relative velocity between water and projectile in feet per second;

A_D = area in square feet at the maximum cross section of projectile taken normal to its longitudinal axis;

R = Reynolds number;

l = overall length of projectile, in feet;

ν = kinematic viscosity of fluid in square feet per second (value: from tables or graphs, about 1.057×10^{-5} sfs for fresh water at 70 F).

10.4 DISCUSSION OF THE FORMULAS

It may be seen that the bracket portion of the first three formulas is identical. The term $(\rho v^2/2)$ represents the kinetic energy of a unit volume of the fluid. For a given projectile in water of a given kind and temperature, this term will be a constant and the formulas will become

$$D = C_D K v^2 \quad (5)$$

$$C = C_C K v^2 \quad (6)$$

$$L = C_L K v^2 \quad (7)$$

where K is the constant $(\rho A_D/2)$.

The terms D , C , L , and v are measured directly in the water tunnel and from these values (K being known), the coefficients C_D , C_C , and C_L may be determined for Reynolds numbers corresponding to the velocities obtainable. The Reynolds number for the full-size projectile is generally very much higher than for a model. The problem then reduces to a determination of the effect of projectile components on the coefficients as functions of Reynolds numbers. To estimate the effect on full-size bodies the results from tunnel measurements are extrapolated to full-scale Reynolds numbers.

20.5

DRAG

The total drag D and the total drag coefficient C_D are, ordinarily, the only drag values measured or calculated. However, this total drag may be thought of as being composed of two parts, called the form drag and the skin friction drag.

20.5.1

Form Drag

The form drag arises from the pressures normal to a body and may be determined by integrating the components of the pressures parallel to the direction of motion. It is proportional to the velocity squared and to the projected area, for a given Reynolds number. The resistance of a flat plate normal to the

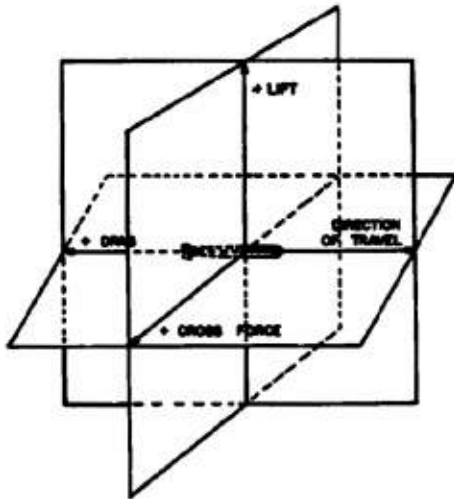


FIGURE 1. Illustration of force terms.

flow is practically all form drag and is due to the difference in pressure on the two sides.

20.5.2

Skin Friction Drag

The skin friction drag arises from the shear stresses on the body surface and its value can be determined by integrating these stresses over the wetted surface of the projectile. This drag is caused by the viscosity of the fluid and therefore is a function of the viscosity as well as the velocity. It is usually expressed as a function of Reynolds number. A flat plate parallel to the flow is an example of a body with nearly pure skin friction drag. This skin friction drag is influenced

by the type of flow which may be laminar or turbulent, or in a transition zone between. With laminar flow, the fluid layers slide smoothly over those nearer the body with relatively small friction or shear between layers. Turbulence, strictly speaking, is a condition of irregular fluctuations, which is distinct from vortex motion in general, and which results in a continuous interchange of fluid between streamlines and hence, a relatively high friction between different layers of fluid. Therefore, under conditions of turbulent flow, the drag is higher than when the flow is laminar. Flow conditions are turbulent for full-scale projectiles and for nearly all models used in tests such as are described in this volume. A few highly streamlined models have shown values of the drag coefficient which were in the transition zone between laminar and turbulent flow conditions.

20.5.3

Skin Friction Coefficient

The skin friction coefficient of a flat plate, for which sensibly all of the drag is due to the skin friction, is

$$C_F = \frac{2F}{\rho v^2 S} \quad (8)$$

where F = the frictional drag force, in pounds, and
 S = the area of the wetted surface, in square feet.

Figure 2 is a logarithmic plot of this skin friction coefficient against Reynolds number for smooth plates for both laminar and turbulent flow conditions.²¹ Three of the possible types of transition curves, between the laminar and turbulent flow, are also shown.

Formula (8), above, cannot be used directly for projectile models and the method of calculation based on pressure distribution involves special construction and numerous measurements. Frequently, an approximate evaluation of the skin friction drag and form drag coefficients is all that is necessary and these may be readily calculated if we assume that the skin friction coefficient for the model is the same as that for a flat plate of the same length and area. If, to distinguish between them, we call the skin friction coefficient of the model C_{DF} and that of a flat plate C_F (as before), then the former, which is based on the cross-sectional area A_D , is

$$C_{DF} = \frac{2D}{\rho v^2 A_D}, \quad (9)$$

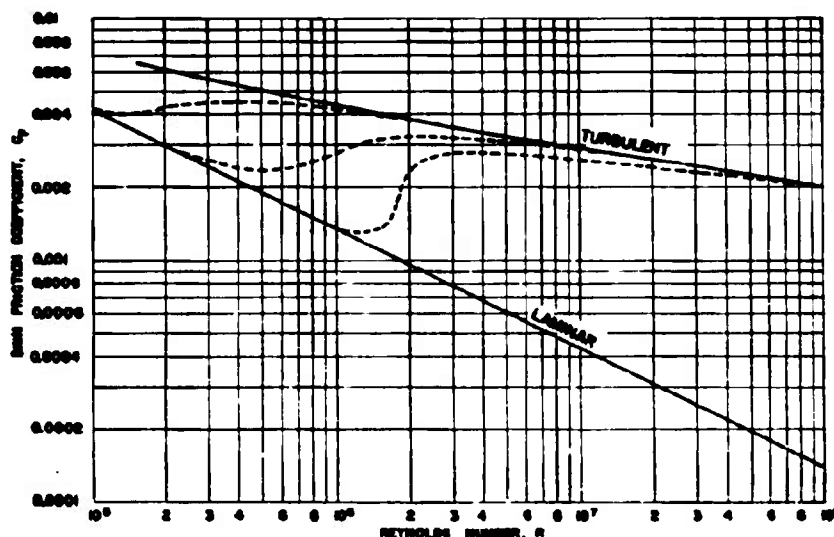


FIGURE 2. Effect of flow types and Reynolds number on the skin friction coefficient of a flat plate parallel to the flow.

and the latter, based on total wetted surface is

$$C_F = \frac{2F}{\rho v^2 S} \quad (8)$$

or

$$F = \frac{C_F \rho v^2 S}{2} \quad (10)$$

Substituting this value of F for D , which it is now assumed to equal for drag due to the skin friction, gives

$$C_{DF} = \frac{S}{A_D} C_F \quad (11)$$

This provides the simple relation between the two objects, which says, in words, that the skin friction coefficient of the models is equal to the skin friction coefficient of the flat plate multiplied by the ratio of the total wetted area of the model to its maximum cross-sectional area (in a plane perpendicular to its longitudinal axis). These areas may be calculated from the model dimensions and the C_F values taken from Figure 2. The values obtained in this manner will be somewhat different from those which actually exist because the original assumption neglects the fact that, without separations, the fluid velocities over the greater portion of the surface of a body of revolution will be higher than those for a plate in the same original velocity flow due to the accelerations necessary in passing such an object. If separation does occur, the surface velocities are low and may even reverse direction so the contribution to skin

friction is small. It is affected, in addition, by differences in the rate of growth of the boundary layer. These inaccuracies are usually small, and the formula provides a simple way to obtain generally satisfactory information on this factor.

2.1.4 Form Drag Coefficient

The form drag coefficient can now be evaluated as the difference between the total drag coefficient and the skin friction drag coefficient at the same Reynolds number. Of course, when the skin friction drag coefficient is obtained in the manner described, the form drag coefficient values will be governed by the same assumption.

No instance is at hand when there has been an increase in the form drag coefficient with increased velocity of water flow. The value could remain constant with increased Reynolds number only if the flow pattern remained the same, so that pressures normal to the surface, expressed as fractions of the dynamic pressure, remained unchanged. Thus, the normal tendency will be for the form drag coefficient to be reduced by higher velocities as any existing separations in the flow will be reduced in extent at higher Reynolds numbers.

2.1.5 Drag in Relation to Flow

Usually a low drag is desired and this is obtained

through "streamlining,"* that is, by having a shape primarily with minimum form drag. The essential point is that drag is intimately related to the nature of the flow produced and that this flow results from the entire body shape, starting with the nose. Thus, it would be practically meaningless to say that a certain tail had 10 per cent less drag than another unless the conditions of flow about the projectile ahead of the tail were known. This might be true for a certain Reynolds number and a model with a streamlined nose, yet it is possible that there would be no differences in the measured drag of these tails at the same R value if a blunt nose were used. As an illustration of the importance of flow character, we may consider the AN-Mark 41 bomb (see Chapter 16). The prototype tested had a very blunt nose and several lugs and other protrusions from the cylindrical body. When all these protrusions were removed and the drag was measured, no change was recorded. The very blunt nose caused the high-velocity water to separate at the junction between the nose and cylindrical body and form an envelope of relatively stagnant water. Since this enclosed the protrusions, they had no measurable influence on the drag under these flow conditions. When a less blunt nose was used, the flow clung more closely to the body, high-velocity water did strike the protrusions and the difference in the drag with this nose for the body with and without protrusions was more than 10 per cent at the same R value.

10.1.4

Nose Influence

Since the flow pattern starts to form at the nose, we may begin to discuss the nose effect by considering a circular plate perpendicular to the flow, since such an object is, in a loose sense, all nose. Somewhat more accurately, it is an object with a blunt nose and blunt afterbody but no body. It has been found to have a drag coefficient of 1.12 over a wide range of R values.²⁴ If now we give this plate a length, converting it to a cylindrical body with sharply blunt nose and afterbody, the drag coefficient will first diminish by about 25 per cent when the length is three times the diameter and then gradually increase again with further length increments. In general, the original decrease is due to reduction of form drag and the

* A streamlined body is one so shaped that the transformation of velocity head into pressure is so gradual that separation does not occur at all or only on a very small region at the extreme end.²⁵

subsequent increase is due to increase in skin friction drag resulting from the larger wetted surface. The length of a cylinder with blunt ends that will give minimum drag is approximately three times the diameter but this ratio does not remain true with other shape changes. Other considerations besides the drag alone are involved in proportioning a desired volume, such as manufacturing simplicity, handling, and release or launching limits on dimensions and similar matters. Among low-drag projectiles the United States Shoe Machinery Hydrobomb, Design No. 8, has a length-to-diameter ratio of 4.65; the Westinghouse Hydrobomb, 7.15; the Mark 13 torpedo, 7.18; the Mark 14-1 torpedo, 11.7; and the Mark 15 torpedo, 13.7. (See Chapter 13.) When a slenderness ratio of length divided by diameter is being chosen, it is sometimes convenient to express the drag coefficient as a function of volume V , rather than of cross-sectional area. In this case

$$C_{DV} = \frac{D}{\frac{\rho}{2} v^2 V^1} \quad (12)$$

Comparison of this coefficient for different body shapes will provide an indication of the optimum proportion for a body of a given volume. The ordinary expression will not reveal this.

It is possible to have a nose with a higher drag than that of a flat plate. A hollow hemisphere with the hollow side upstream has a drag about 19 per cent higher.²⁶

Seemingly small roundings of sharp edges meeting the flow head-on result in material drag reductions. If rounding is carried to the extent of putting a hemisphere on the upstream end of a cylinder 3 diameters long, the drag coefficient will be reduced to approximately 0.25 at R about 3×10^4 , with similar reduction for longer cylinders.²⁶ Still greater refinements of nose shapes are, of course, possible. Many so-called families, such as the spherogives, have been investigated and numerous noses based on special formulas have been designed and tested. The effect of some representative noses on the drag coefficient of a specific projectile will be described below in connection with other components.

Reduction in drag, as must be apparent, is obtained by reducing the violence of flow changes. Better noses lessen this violence at the forward end of the projectile and better afterbodies will improve conditions at the rear. Nose improvements, however, are relatively much more important than rear-end

changes when both conditions are bad, but this statement is not necessarily true under other conditions. Thus, as mentioned above, the addition of a hemispherical nose to a 3-caliber cylinder gave a C_D of 0.25; the addition of a tapered afterbody while the nose remained "square," gave 0.70. The combination of a hemispherical nose and hemispherical afterbody reduced the drag coefficient to 0.135.^{4a} This indicates, again, the importance of the type of flow around structural portions behind the nose in the possibility of percentage improvement. It is repeated that, unless these parts are in high-velocity flow, changes will have only a minor effect, if any.

3.3.7 Interrelated Body, Afterbody, and Tail Influences

Low-drag afterbodies are, compared to diameter, generally long and tapering^b since small changes in curvature are necessary so that the fluid may close smoothly about the body. The taper may be a conical surface or some curved surface such as an ogive. When it is conical, there is customarily a transition curve connecting it to the cylindrical body portion. There is also, generally, a truncated end of relatively small diameter. Some afterbodies have booms, that is, small diameter cylindrical extensions, for the usual purpose of getting the tail surfaces into a more advantageous position. The Mousetrap projectiles have rather long booms; the Squid, a shorter one.

As mentioned in Chapter 3, tails may consist of vanes alone, vanes with rudders, vanes with shroud rings, vanes with rudders and shroud rings, and other designs such as box tails. Some rockets have collapsible fins while, of course, spin-stabilized rockets have no tails at all in the sense the word is here used. Tail diameters are usually the same as the body but there are numerous exceptions, particularly some rockets which have very large diameter vanes. The primary purpose of the tail is to give stability and control. It is obvious that the tail should be no larger or more complicated than necessary to function adequately as anything additional will be only a disadvantage. The large wetted area (some 37 per cent in the case of the Squid) of the tail surfaces contributes materially to the skin friction drag, while the numerous sharp edges in the flow produce a form drag which may also be a considerable part of the total for the projectile.

^b For a sphere at $R > 3 \times 10^5$, C_D has been given by Rouse as 0.20 and for a 1-to-3 ellipsoid at $R > 2 \times 10^5$, $C_D = 0.06$.

Merely rounding all leading edges in the tail of one Squid model reduced the total drag by 20 per cent. Shroud rings will add unnecessarily to the drag unless they are constructed with the optimum angle to the flow at their location. This angle is not yet calculable from formulas and has generally been determined by polarized light flume observations checked, subsequently, by water-tunnel performance tests. (See Chapter 3.)

High-velocity flow must pass over or along all tail surfaces for these surfaces to have maximum effectiveness. This means that the afterbody design must be such as to direct it there and that the opening between any shroud ring and the afterbody be large enough to permit its free flow through the tail.

The "body" is generally a cylindrical portion between the planes where the nose curvature becomes zero and where afterbody curvature begins. These sections may be short or long. Increased length of body section, other things being equal, increases the total drag mainly by the additional skin friction. In rare cases there have been projectiles with abrupt changes of diameter in the body section (unrelated to the nose or afterbody). Such changes will, of course, have an effect on the drag.

As an example of the interrelation and effect of various components on the drag coefficient, we may consider some investigations of the British Squid (depth bomb).

Figure 3 shows an outline drawing of the prototype, of another model with a special nose, new cone afterbody and new tail, and of an earlier type nose referred to as the No. 45 nose. There were, actually, two new tails; they were alike except that one had a 0-degree shroud ring (a true cylinder) while the other had a conical ring with a 2-degree cone angle. All parts were interchangeable except that the new tails could be used only with the new afterbody and the prototype tail only with the prototype afterbody.

The upper graph of Figure 4 shows the influence of nose shape on the drag coefficient with variation of Reynolds number for the 0-degree tail models. Measurements extended to $R = 4 \times 10^6$ and the lines were extrapolated therefrom to full-scale values. The top-most three lines are, from the top, for progressively better noses all with the new afterbody and new 0-degree tail. They show progressively lower drags, particularly at full-scale R . The lowest curve of this group was obtained by the simple substitution of the special nose on the original model and gave the best

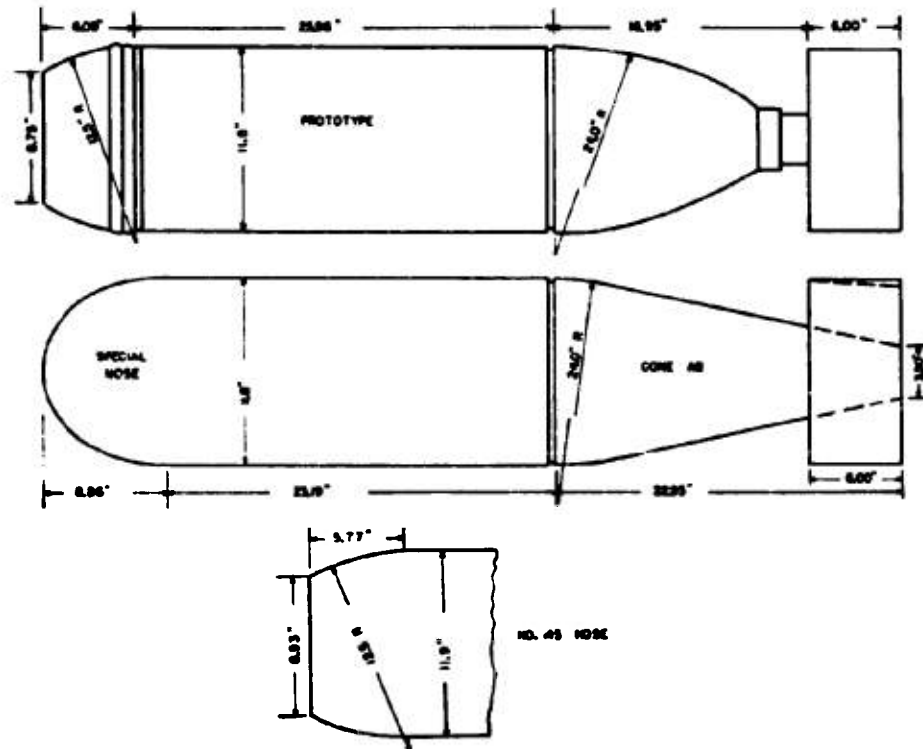


FIGURE 3. Outline drawing of British Squid and major modifications.

results of any combination tried. This nose profile is based on the formula

$$\left(\frac{x}{1.5}\right)^2 + y^2 = 1.$$

The lower graph is, similarly, for the same three noses and the new afterbody with 2-degree tail. A similar reduction in drag was also obtained. It may be noted that the 2-degree tail gave, with each nose, a lower drag than the 0-degree tail, the afterbodies being the same.

The cone afterbody with 0-degree tail was inferior to and, with the 2-degree tail, no better than the original afterbody and tail when all were used with the prototype nose. It is believed this is due to insufficient clearance between the shroud ring and new afterbody but it has not yet been checked experimentally.

It should not be deduced from these curves that an improvement in nose shape will always result in proportionally less drag as R is increased. The opposite effect seemed to hold in a similar series of nose tests

for the Mark 13-1 torpedo. Of course, an improvement with nose refinement occurred at any R in both cases. The difference in the two cases is that the per-

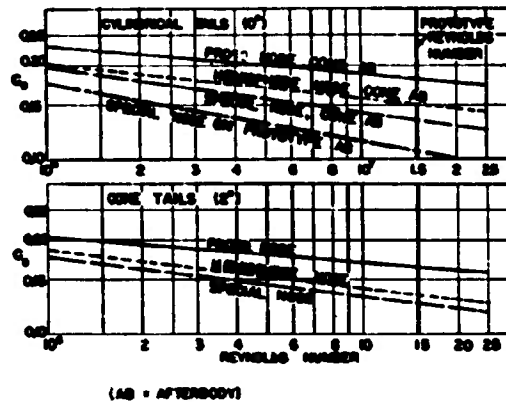


FIGURE 4. Influence of nose shape on C_D with variations of Reynolds number for British Squid and modifications. Top: Cylindrical tails (0 degree); bottom: Cone tails (2 degree).

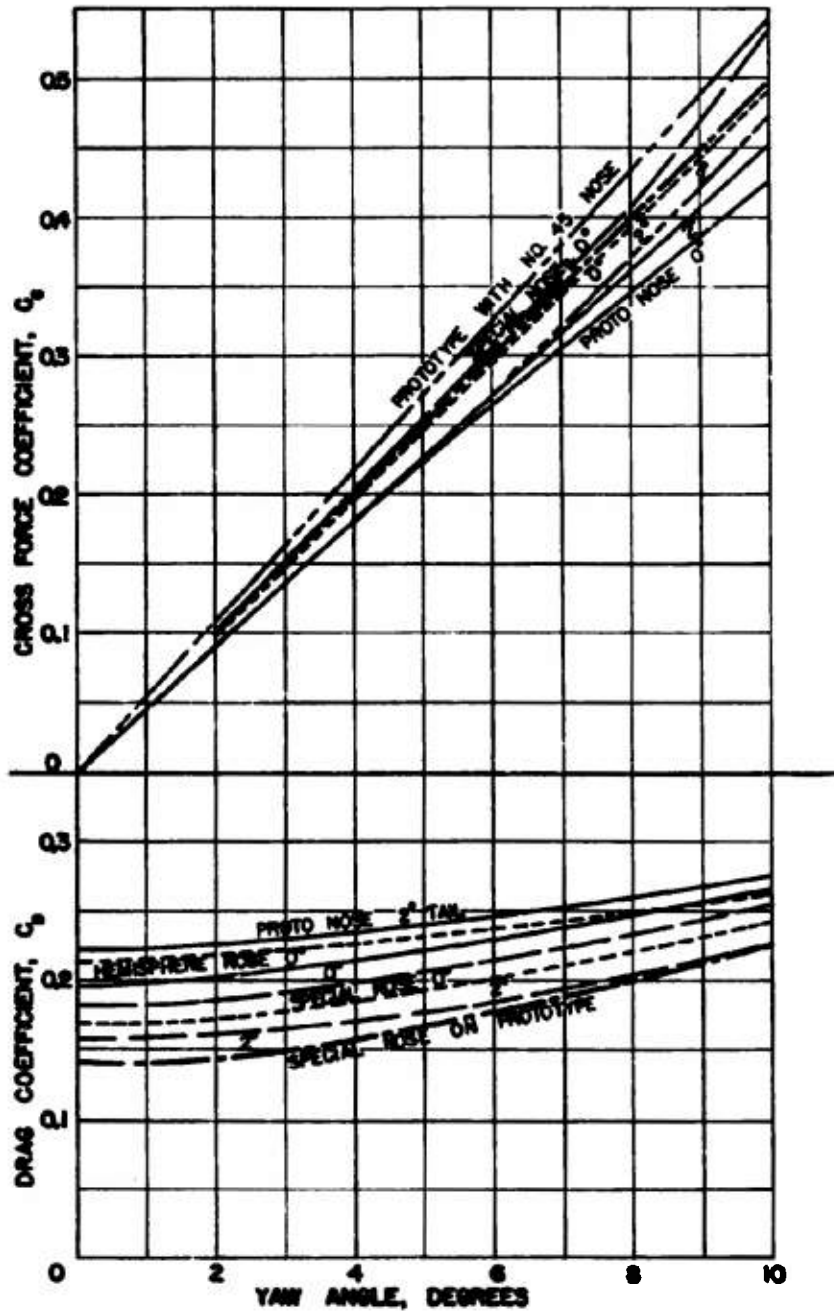


FIGURE 5. Effect of yaw on C_D and C_y for British Squid and modifications.

CONFIDENTIAL

centage improvement increased with R for the Squid and decreased for the Mark 13-1. The explanation is believed to be as follows. Granted a perfect afterbody and tail structure, the form drag coefficient for those parts would have an absolute minimum value. Form drag improvement, therefore, would be confined to, and dependent upon, the nose shape. A blunt nose will have a relatively high form drag and, hence, there will be a greater opportunity for its reduction at higher Reynolds numbers. Finer noses, producing less turbulence, have less opportunity to improve at higher velocities. The Mark 13-1 afterbody has a low form drag compared to that of the Squid afterbody, hence, the effects are akin to those produced by the perfect afterbody and tail. When a fine nose is used with the Squid afterbody and tail, the nose form drag is decreased but there is also more turbulence near the tail which will be reduced by the more advantageous flow conditions produced there at high Reynolds numbers.

A discussion of drag under conditions of cavitation appears in the chapter on cavitation.

10.6 INFLUENCE OF YAW OR PITCH ON DRAG AND CROSS FORCE OR LIFT

Previous discussion has dealt with drag when the projectile had a zero pitch and yaw angle. Under these conditions, both the cross force and lift force will be zero for symmetrical projectiles. However, some degree of asymmetry will exist in individual projectiles, designed to be symmetrical, because of manufacturing tolerances, deformations from handling, and similar causes. If it be anticipated that such unintentional asymmetries will have a materially adverse effect upon projectile performance, they may be avoided by setting the tail vanes at a slight angle, as in the case of the British Squid, which produces a slow rotation of the projectile, thereby averaging out the effects. Rudders may be considered as devices intended to produce asymmetry for purposes of course control of the projectile and will, by their action, also overcome the effect of other unintended asymmetry.

When the projectile yaws or pitches, a different aspect of the shape is presented to the flow, almost always one which will have a greater resistance. The effect of positive yaw angle to 10 degrees on the drag coefficient is shown in the lower graph of Figure 5 and on the cross force coefficient in the upper graph. All curves shown are for the Squid. Since the design of this projectile is symmetrical, the lift-coefficient curves plotted against pitch angle would be the same as those for the cross force coefficient.

Values for negative yaw and pitch angles generally are the same as for positive angles except that the cross force coefficient will be negative.

In general, a model with a lower drag at 0-degree yaw will also have a lower drag at greater positive or negative angles, although this is not invariably the case as may be seen even in the illustrative group. These drag-coefficient vs yaw-angle curves are, essentially, parabolas.

10.7 EFFECT OF PROJECTILE COMPONENTS ON CROSS FORCE AND LIFT

Serious study of the effect of projectile components on the cross force and lift has been limited mainly to a consideration of the effect of horizontal and vertical rudder action and of fins and shroud ring at the tail. Numerous specific illustrations of their effect are given in this volume, particularly in Chapters 8 and 9. In general, the most important requirements are that the fin and rudder surfaces be sufficiently large and arranged in the most effective locations and proportions to achieve necessary stability and control without introducing unnecessary drag. The latter can be further avoided by rounding all edges, as previously mentioned. Properly designed shroud rings are often, but not invariably, a material aid in course control. These matters are intimately connected with the moment coefficient about the center of gravity and are discussed further under that subject.

A comprehensive study of the effects of all the various components on cross force and lift is now being made but the results are not ready for report.

Chapter 11

EFFECT OF PROJECTILE COMPONENTS ON DAMPING AND DYNAMIC STABILITY

11.1 INTRODUCTION

THE BEHAVIOR of a free-flying, nonspinning projectile without rudder controls depends entirely on its dynamic stability and on the motion of the fluid through which it is traveling. The behavior of a controlled projectile also depends on these factors and, in addition, on the characteristics of its controls. To evaluate the dynamic stability of a tail-stabilized projectile it is necessary first to determine at least four of its hydrodynamic coefficients; namely, the coefficients of lift, moment, damping force, and damping moment. It can be shown theoretically that, for normal projectile shapes, these four coefficients are intimately related, and that the damping coefficients may be determined without direct measurement if the lift and moment coefficients are known. Also, the dynamic stability is a simple function of the lift and moment coefficients. It is obvious that these relationships, if substantiated by experiment, would materially reduce the volume of preliminary tests and investigations required in order to design a projectile shape to meet given performance specifications.

It is the purpose of this chapter to indicate the relationships among the various hydrodynamic coefficients and their relationship to the dynamic stability of tail-stabilized projectiles; also, to show which of the various components of the projectile shape are the main factors in determining the hydrodynamic characteristics of the projectile.

11.2 DAMPING FORCE AND DAMPING MOMENT

11.2.1 Definition

When a projectile is traveling rectilinearly under steady-state conditions, the forces acting on it are functions of the velocity and angle of attack alone. However, when the projectile is oscillating or turning about a transverse axis, the forces acting on it are no longer determined by the velocity and instantaneous angle of attack alone, but are modified by reaction whose magnitudes depend on the instantaneous value

of the angular velocity. For convenience in dealing with this latter case, the forces are resolved into two terms, one of which is equal to the force that would act if the projectile were traveling on a straight line with the same angle of attack at the center of gravity, and one which depends on the angular velocity. The sense of the second term, called the damping term, is always such as to oppose the angular velocity, thus changing the force system from a conservative system to one having energy dissipation through a "hysteresis loop."

11.2.2 The Mechanics of Damping

When the projectile deviates from rectilinear motion, the angle of attack is no longer constant but varies from point to point along the axis. The flow about the body is then different from that of straight motion and, consequently, the forces are different. The method used in estimating the damping forces is based on the knowledge that, although the angular velocity modifies the force distribution about the entire body, the only changes which affect the resultant force occur at the tail.

Figure 1, taken from reference 7b, shows the theoretical force distribution about the bare hull of an airship in curved flight through a frictionless fluid, resolved into three terms. Part A shows the attitude of the ship in relation to its path, with bow turned inward and stern outward, and with yaw angle ψ at center of hull. The first term of the force distribution, shown at B, is the same as in straight flight with angle of attack ψ . This gives rise to a destabilizing moment (tending to increase the yaw angle) but has no resultant force. The second term C, sometimes called the "negative centrifugal force," is due to the fact that the ship, traveling with its bow turned into the curve, displaces air in an outward direction and is subject to a reaction directed inward. This is most pronounced at the middle of the hull. The third term D, represents forces concentrated near the ends, and their sum in magnitude and direction is equal to the lateral component of the centrifugal force of the displaced air. These forces are due to the fact that the angle of attack at the bow is smaller than ψ , while at

the stern it is larger than ψ . The sum of the second and third terms gives neither a resultant force nor a resultant moment. Thus, the resultant forces acting on the bare hull in curved flight in a frictionless fluid are the same as those in straight flight.

The forces acting on a streamlined finless body in rectilinear motion were analyzed in Chapter 8 of this volume. It was shown that in an ideal fluid such a body is subject to a destabilizing moment but develops no lift, and that in a real fluid the finless body does develop some lift and that the destabilizing moment is smaller than in an ideal fluid. It was also shown that the lift developed in a real fluid is due to vortices forming near the tail and, therefore, the lift

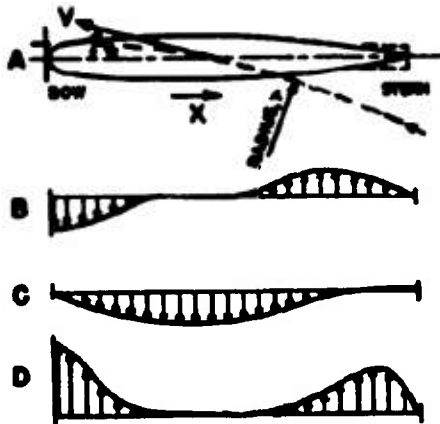


FIGURE 1. Airship in curved flight and forces developed.

of the finless body should be considered as acting at the tail. When fins or other tail surfaces are added, the additional lift developed by them also acts at the tail. It may be said, therefore, that for a streamlined body with tail surfaces the total lift acts at the tail and is determined by the effective angle of attack at the tail.

In the preceding analysis of the curved motion of a finless hull in a frictionless fluid it was shown that the body is subject to a destabilizing moment equal to that of rectilinear motion with the same angle of attack at the center of the body. The problem of dealing with the curved motion of a streamlined hull with fins in a real fluid may be greatly simplified by resolving the forces into two terms: the theoretical moment of the hull, which is a function of the angle of attack at the center of the hull; and a lift force acting at the tail, which is a function of the angle of

attack at the tail. For the motion shown in Figure 1A, the angle of attack at the tail is larger than that at the center. The lift, therefore, would be larger than for rectilinear motion with the same angle of attack at the center. This *increase* in the lift is, by definition, the damping force, and the moment of the damping force about the center of the hull is the damping moment.

12.3 Estimate of Damping Coefficients from Steady-State Data

The projectile in Figure 2 is shown moving in the direction of its axis with velocity v and, in addition, is turning about a transverse axis through the center of gravity with a small angular velocity ω . The center of pressure of the tail force CP_T then has a small downward velocity $\omega\lambda$, and the angle of attack at the tail is $\tan^{-1} \omega\lambda/v$, where λ = the distance from CG



FIGURE 2

to CP_T . For small disturbances from the mean path, the angle of attack may be taken as $\omega\lambda/v$ radians, and the force due to that may be taken as proportional to the angle of attack. The damping force then is

$$F = \frac{\omega\lambda}{v} C_l \frac{\rho v^2}{2} A, \quad (1)$$

where $C_l = (\partial/\partial\alpha)C_{L_0}$ or the slope, in units per radian, of the curve representing the coefficient of lift, as measured in the water tunnel or wind tunnel, plotted against the angle of attack α . The moment of this force about CG is the damping moment, which may be written

$$K = F\lambda = \frac{\omega\lambda^2}{v} C_l \frac{\rho v^2}{2} A. \quad (2)$$

If we define a damping force coefficient C_F , and a damping moment coefficient C_K as

$$C_F = \frac{F}{\frac{1}{2}\rho v\omega A l} \quad (3)$$

$$C_K = \frac{K}{\frac{1}{2}\rho v\omega A l^2} \quad (4)$$

where ρ is the density of the fluid, A the maximum

cross-sectional area of the projectile, and l its overall length, then we get

$$C_r = C_{l_l}^{\lambda} = C_r e_r, \quad (5)$$

and

$$C_K = C_l \left(\frac{\lambda}{l} \right)^2 = C_r e_r^2 \quad (6)$$

where e_r is the eccentricity of the tail force.

To determine the damping coefficients it is necessary, therefore, to know the slope of the lift curve and the eccentricity of the tail force. The latter may be evaluated when both the lift and moment coefficients are known, as outlined in Chapter 8 of this volume.

The oscillating projectile in Figure 2 is shown at the instant when the angle of attack at CG is zero. When the angle of attack at CG is not zero, there are the normal cross force and normal moment due to the angle of attack at CG and, in addition, the damping force and damping moment due to the fact that the angle of attack at the tail is different from that at CG by $\pm \omega \lambda / v$. For computations involving oscillations about zero yaw, the damping coefficients are determined from the slope of the cross force coefficient curve and the eccentricity of this force at zero yaw. For oscillations about a definite angle of attack, such as when a torpedo is traveling with dynamic lift or when circling, the slope and eccentricity should be taken at the mean value of the angle of attack.

In the preceding analysis, the contribution of the drag force to the moment was neglected. For low-drag projectiles and for small angles of attack, the error introduced by this omission is very small. Actually the normal component of the hydrodynamic forces is $(L \cos \alpha + D \sin \alpha)$, where L is the cross force, D is the drag, and α is the angle of attack. For small values of α this may be taken as $(L + D\alpha) = \frac{1}{2} \rho v^2 A (C_L + C_D \alpha)$. In equations (1), (2), (5), and (6), C_l then becomes

$$C_l = \frac{\partial}{\partial \alpha} C_L + C_D.$$

11.3 DYNAMIC STABILITY OF PROJECTILES

Any object in motion is said to be stable if it tends to continue in its present mode of motion. In ballistics we are usually interested in directional stability, i.e., whether a projectile, fired or launched in a given direction, continues to travel close to the original line of motion. When any projectile is disturbed from its line of motion it does not actually return to the origi-

nal line, but the motion may be considered stable if the deviation is small. With respect to stability requirements projectiles may be divided into three groups: (1) spin-stabilized; (2) tail-stabilized without rudder control; (3) tail-stabilized with rudder control. The stability of spinning projectiles is treated in Chapter 15 of this volume. In the following paragraphs we will discuss the stability of tail-stabilized projectiles such as bombs, rockets, and torpedoes.

Although the *stability requirements* of rudder-controlled projectiles usually differ from those of rudderless projectiles, the *degree of dynamic stability* in either case is determined without reference to rudder action. That is, the dynamic stability of a rudder-controlled projectile is determined by its hydrodynamic properties with rudders fixed in neutral position.

11.3.1

Definition

A projectile is said to be dynamically stable if, when disturbed from its linear motion, it will return to motion on a straight line without benefit of rudder action. The new line of motion is not an extension of the original line, but makes some angle with it. The magnitude of this change in direction depends on the degree of dynamic stability, the greater the stability the smaller the course deviation.

A projectile that is dynamically unstable, when disturbed from linear motion, does not (in the absence of rudder control) return to motion on a straight line. Instead, it travels on a gradually tightening spiral and eventually settles down to circular motion. The diameter of the circle depends on the degree of dynamic instability, the greater the instability the smaller the diameter of the circle.

As a corollary of the above definition it may be said that a dynamically stable projectile without rudder control cannot run on a circle. With rudder control a dynamically stable projectile can be made to circle, but can be brought back to linear motion merely by returning the rudder to neutral position, i.e., without applying opposite rudder. To bring a dynamically unstable projectile out of circular motion, it is necessary to apply opposite rudder. Returning the rudder to neutral position would merely increase the diameter of the circular path.

11.3.2

Criteria for Dynamic Stability

A criterion for the dynamic stability of a projectile

may be derived very simply from a consideration of the conditions required for equilibrium on a circular path. This is based on the principle that any deviation from a straight path may be regarded as a tendency to swing into a circular path.²⁰ If the projectile (with rudders, where present, locked in neutral position) can attain equilibrium on a circular path, then it is dynamically unstable. If it cannot attain equilibrium on a circular path, it will return to linear motion and, therefore, is dynamically stable.

In Figure 3 is shown a projectile, with rudders locked in neutral position, traveling on a circular path of radius R , with velocity v and with angle of attack α (exaggerated in the figure) at C_G . The forces are resolved into the theoretical moment of the bare hull H and a lift force acting at the tail. This tail

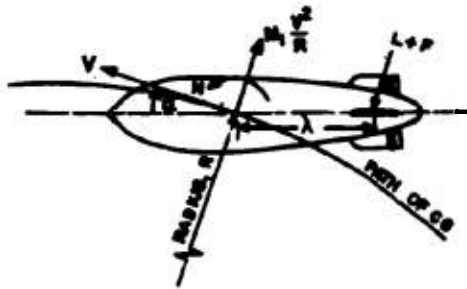


FIGURE 3. Equilibrium on a circular path.

force includes the normal lift L and the damping force F . In addition there is the centrifugal force $M_1 v^2/R$ acting at C_G . M_1 stands for the mass of the projectile M plus the apparent mass for longitudinal motion $k_1 \rho V$, where V is the volume of the projectile, and k_1 the coefficient of apparent mass for longitudinal motion. The correct value of the apparent mass in this case is $(k_1 \cos^2 \alpha + k_2 \sin^2 \alpha) \rho V$,²¹ but for small angles of attack $k_1 \rho V$ may be used.

For equilibrium on the circular path, we have

$$L + F - M_1 \frac{v^2}{R} = 0, \quad (7)$$

$$H - \lambda(L + F) \cos \alpha = 0. \quad (8)$$

For small values of α ,

$$L = C_L \frac{\rho v^2}{2} A = C_L \alpha \frac{\rho v^2}{2} A,$$

$$H = C_H \frac{\rho v^2}{2} A l = C_H \alpha \frac{\rho v^2}{2} A l.$$

From equations (3) and (5)

$$F = C_{F2} \rho \omega A l = C_{F2} \frac{\rho}{2} V \omega A l.$$

We define a mass coefficient m_1 such that

$$M_1 = m_1 \frac{\rho}{2} A l.$$

Substituting in equation (7) and dividing by $\rho v^2 A/2$, we get

$$C_L \alpha + C_{F2} \frac{\omega l}{v} - m_1 \frac{l}{R} = C_L \alpha + (C_{F2} - m_1) \frac{l}{R} = 0$$

or

$$\alpha = \frac{(m_1 - C_{F2}) \frac{l}{R}}{C_L}. \quad (9)$$

Substituting in equation (8) and dividing by $\rho v^2 A l/2$, we get

$$C_H \alpha - v C_L \alpha - \lambda C_{F2} C_L = 0$$

or

$$\alpha = \frac{\lambda C_{F2} C_L}{C_H - v C_L}. \quad (10)$$

Equating (9) and (10) and solving for C_{F2} , we have

$$C_{F2} = \frac{m_1 C_H}{m_1 + C_H}. \quad (11)$$

It is seen that for equilibrium on a circular path, C_{F2} [$= C_F$, from equation (5)] must have a definite value. If this requirement is fulfilled, the projectile will be indifferent to angle of attack and to circling radius as long as the angle of attack is within the limits wherein the forces are proportional to it. That is, the projectile may travel with zero angle of attack in which case R would be infinite, or it may assume some small angle of attack and circle on a radius corresponding to that angle of attack. If C_{F2} has a value greater than that indicated in equation (11), that is, if the moment of the tail force is larger than required to balance the hull moment, then the path of the projectile will straighten out. If C_{F2} is smaller, the angle of attack will continue to increase until it exceeds the value wherein the forces are proportional to it. Since for large angles of attack C_L increases faster than linearly, equilibrium will be established eventually and the projectile will continue to circle.

It is apparent, therefore, that the condition represented by equation (11) marks the borderline between dynamic stability and instability, and may be used as a criterion. That is, for dynamic stability

$$C_{F2} - \frac{m_1 C_H}{m_1 + C_H} > 0. \quad (12)$$

Taking the ratio of the two sides of equation (11) we get another criterion which is somewhat quantitative in that it shows the ratio of the actual tail moment

($C_{\rho r}$) to that required to just barely attain dynamic stability, i.e., for dynamic stability

$$\frac{C_{\rho r}(m_1 + C_L)}{m_1 C_L} > 1. \quad (13)$$

The value of these criteria lies in the fact that it is not necessary to measure the damping force and damping moment, but only the so-called static lift and moment. Also, the quantity on the right side of equation (11) may be evaluated as soon as the shape of the projectile body and its overall weight are selected, and before any tests are made. This tells us how large the quantity $C_{\rho r} = C_{\rho}$ must be in order to attain the desired degree of dynamic stability. Since data are available on the moment and lift coefficients of a large number of projectile shapes with various tail structures, it should be possible to select a tail structure which, when mounted on the given projectile, will produce very nearly the desired degree of dynamic stability.

Another criterion for dynamic stability of ships and projectiles, developed by a different method from the one used above, has the form²³

$$C C_K - m C_m > 0 \quad (14)$$

where C_L , C_m , and C_K are as defined in this chapter, and $m = m_1 - C_{\rho}$. By substituting for C_m , C_{ρ} , and C_K their equivalents as indicated in this chapter, i.e., $C_m = C_L - C_{\rho r}$, $C_{\rho} = C_{\rho r}$, and $C_K = C_{\rho r}^2$, this expression may be reduced to equation (12).

It should be noted that the dynamic stability of a projectile depends not only on the overall shape of the projectile, but also on its mass and on the density of the medium through which it travels. The stability criteria of equations (13) and (14) contain hydrodynamic coefficients C_L , C_m , C_{ρ} , C_K , and c_r , and a mass coefficient m_1 . For projectiles operating at high Reynolds numbers, the hydrodynamic coefficients are functions of the body shape alone. The mass coefficient, however, depends on the mass and shape of the projectile and also on the density of the surrounding fluid, since

$$m_1 = \frac{M + k_1 V}{\frac{1}{2} \rho A l}$$

where M = mass of projectile, k_1 = coefficient of apparent mass for longitudinal motion, ρ = density of fluid, A = maximum cross section, l = overall length and V = volume of projectile. For elongated projectiles k_1 is small (0.01 to 0.05). The value of m_1 , therefore, is nearly proportional to M , and inversely proportional to the density of the surrounding fluid.

ρ . Examination of equation (14) shows that the dynamic stability decreases with increasing mass of projectile, and increases with increasing density of the fluid. Thus, for instance, an aircraft torpedo which may be dynamically stable during its underwater run may not possess sufficient stability for its air flight. This is usually overcome by adding larger tail surfaces (air stabilizer) which are stripped off the torpedo on water impact.

11.2.3 Relation between Static and Dynamic Stability

The static stability of a projectile is determined by its shape alone, i.e., it is independent of the mass of the projectile or the nature of the fluid through which it is traveling. A projectile is said to be statically stable if, when restrained from moving laterally and given an initial yaw angle, the projectile tends to return to zero yaw. The projectile is said to be statically unstable if the moment resulting from the initial yaw angle is such as to tend to increase the yaw. (In accordance with the sign convention used in this volume, a projectile is statically stable if C_m , the derivative of the moment coefficient, is negative, and it is statically unstable if C_m is positive.) The static stability in itself, therefore, merely describes the behavior of a projectile if it were used as a weathercock but it does not describe its behavior in free flight, while the dynamic stability does indicate in a general way the behavior of the projectile in free flight. Nevertheless, for a projectile of given shape and weight traveling through a given fluid, the dynamic stability and static stability are directly related.

The relation between the static and dynamic stabilities of a projectile will be illustrated by using, as an example, the Mark 14-1 torpedo without propellers. The test data used herein are shown in Figure 4, and are taken from water tunnel tests made on a propellerless model of the Mark 14-1 torpedo.²⁴ Only one of these curves, the one showing the moment coefficient of the finless body in an ideal fluid, was calculated. All others are test results. Taking the slopes of these curves for small pitch angles ($\pm 1^\circ$), we get the values of C_L for the finless hull in an ideal fluid, and of C_L and C_m for the finless hull, hull with fins, and hull with fins and ring tail, in a real fluid.

With C_L , C_m , and C_L known, the eccentricity of the tail force, c_r , may be evaluated for each case. With c_r known, the damping coefficients C_{ρ} and C_K may

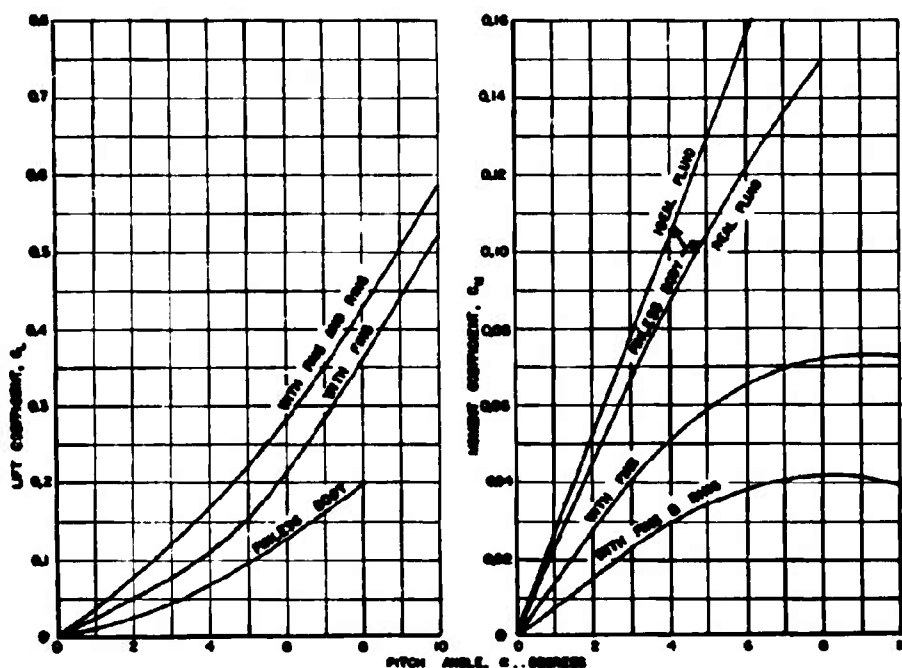


FIGURE 4. Mk 14-1 torpedo without propellers. Rudders neutral.

be determined. Adding the value of the coefficient of mass m_1 (for this torpedo in salt water $m_1 = 2.04$), we can evaluate the criteria of dynamic stability of equations (13) and (14). Table 1 shows all these values, as well as C_l , the derivative with respect to pitch angle of the coefficient of moment about CG due to the tail force ($C_l = C_A - C_m$), for the finless body, body with fins, and body with fins and ring tail. It is seen that for these three conditions, respectively, the tail force acts at points 48, 50, and 51 per cent of the overall length aft of CG . If we take an average value

for e_T , in this case 0.50, then all the hydrodynamic properties of the projectile listed in Table 1 become linear functions of the lift coefficient derivative C_l .

Figure 5 shows the variation of the different hydrodynamic coefficients of the Mk 14-1 torpedo as functions of C_l . The condition $C_l = 0$ is equivalent to the finless hull in a frictionless fluid, which is subject to a pure moment C_A . As C_l grows, the stabilizing moment due to it grows and the resultant moment, $C_m = C_A - C_T e_T$, diminishes. C_T , C_K , and the dynamic stability criteria of equations (13) and (14) increase linearly with C_l . It is seen that dynamic stability in water is reached when $C_l = 1.77$ [$C_l C_K - m C_m = 0$ or $C_T e_T (m_1 + C_A) / m_1 C_A = 1$], and static stability is attained when $C_l = 3.0$ ($C_m = 0$). To attain dynamic stability in air this torpedo would require a C_l of 3. Coincidentally, in this case, the same value of C_l gives both static stability and dynamic stability in air. In general, the value of C_l required for dynamic stability in air does not differ much, for most projectiles, from that required for static stability. This forms the basis for the arbitrary rule that aircraft bombs and rockets must be statically stable.

TABLE 1. Hydrodynamic properties of Mark 14-1 torpedo without propellers.

Coefficient	Hull with fins and ring		
	Hull alone	Hull with fins	Hull with fins and ring
C_A	1.50	1.50	1.50
C_m	1.26	0.78	0.43
C_l	0.24	0.72	1.07
C_T	0.50	1.43	2.09
e_T	0.48	0.50	0.51
C_P	0.24	0.72	1.07
C_K	0.12	0.36	0.54
$C_T e_T (m_1 + C_A) / m_1 C_A$	0.24	0.83	1.24
$C_l C_K - m C_m$	-2.21	-0.51	+0.71

CONFIDENTIAL

The values of C_L actually measured in the water tunnel for this torpedo are indicated in Figure 5. It is seen that neither the hull alone nor the hull with fins are dynamically stable in water. It is believed that, with propeller drive, this torpedo when equipped with fins is dynamically stable in water. The hull with fins and ring would be dynamically stable even without propeller drive.

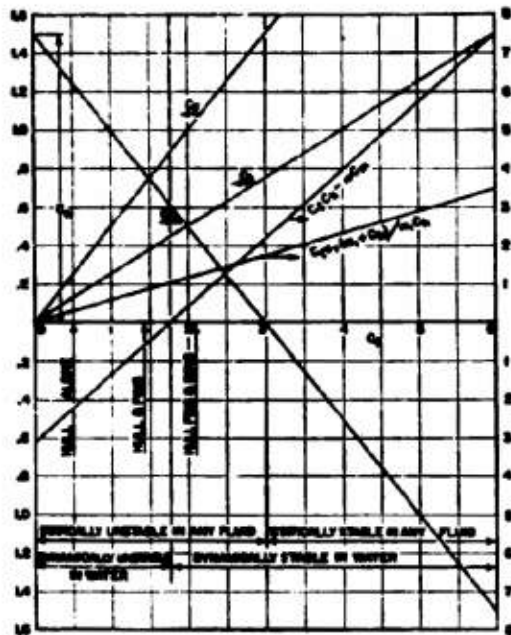


FIGURE 5. Hydrodynamic properties as functions of lift coefficient derivative. Mk 14-1 torpedo without propellers.

11.4 EFFECT OF VARIOUS COMPONENTS

From the preceding analysis it is clear that the damping and dynamic stability of normal, tail-stabilized projectiles are directly related to the static stability. By *normal projectiles* is meant relatively clean bodies of revolution, with fairly streamlined nose shapes (hemisphere or finer), with lift-producing appendages at the tail only, i.e., without fins, spoilers, Kopf rings, or any other prominent appendages ahead of the tail. For these projectiles it may be said that any modification of the body shape which increases the lift force, or shifts the point of application of the lift force aft along the body, also increases the damping coefficients and the dynamic stability. The effect of such modifications on the damping and dy-

amic stability may, therefore, be inferred from their effect on the steady-state forces measured in the water tunnel or wind tunnel.

11.4.1 Nose Shape

Measurements made in the water tunnel on a torpedo model with several different nose shapes ranging from a hemisphere to a $2\frac{1}{2}$ -to-1 ellipsoid, and including the standard noses of the Mark 13 and Mark 14 torpedoes, showed that the lift and moment coefficients were practically unaffected by the nose shape.²² Similar tests with other projectiles gave the same results. It may be concluded, therefore, that the damping and the dynamic stability of a projectile will vary but little with changes in nose shape, as long as the nose is a fairly streamlined body of revolution.

11.4.2 Afterbody

The afterbody shape has a pronounced effect on the hydrodynamic properties of the projectile. In Chapter 8 of this volume it was shown that the lift of a finless body is due to separation and vortex formation near the tail. It is evident, therefore, that any modification of the afterbody which increases the vortex formation will also increase the lift of the finless hull. It is known that abruptly tapering or truncated afterbodies produce higher lift than finely tapered shapes. When fins are added, the effect of the afterbody shape on the total lift depends on the location of the fins with respect to the zone of flow separation. If the fins are within that zone, the flow velocity over the fins will be low and, consequently, the lift developed by them will be low, and this may more than offset the increase in the lift of the bare hull. This usually occurs on a torpedo with a rapidly tapering afterbody, since the fins are located aft of the zone where separation on the afterbody begins. On the other hand, with a rocket, where the fins are usually attached to the cylindrical portion of the body and the tapering or abrupt termination of the afterbody occurs ahead of the fins, the fin lift is not reduced by the separation while the body lift is increased thereby.

11.4.3 Tail Structure

The use of stabilizing surfaces on non-rotating projectiles was treated in Chapter 9 of this volume,

where the effect of the various design factors on the lift and moment coefficients was shown. Again, any modification of the tail structure which increases the lift or the static stability of the projectile also increases the dynamic stability.

11.4.4

Propellers

On propeller-driven projectiles, the propellers have a pronounced effect on the lift and moment acting on

the projectile. This is partly due to the fact that the flow velocity over the tail structure is increased, but mainly because the propeller itself produces a transverse force or lift when yawed in the stream.³⁶ Tests made on such projectiles without running propellers do provide valuable information for their design. However, any measurements made to determine accurately the hydrodynamic properties of the complete projectile should be made with power-driven propellers.

Chapter 12

EFFECT OF EXPERIMENTAL VARIABLES ON AN AIR-LAUNCHED PROJECTILE TRAJECTORY

DURING THE DEVELOPMENT of the plans for initiating launching studies for the purpose of investigating the water entry of projectiles, considerable thought had been given to the technique required for making laboratory studies in order that the results would be applicable to field conditions. The following section is devoted to the discussion of some of the conclusions that have resulted from these considerations. Two different points of view present themselves in the consideration of such a laboratory study: (1) that the study should be organized as a "model study" of specific projectile shapes and characteristics; (2) that the study should be an investigation and a clarification of the physical phenomena involved. At first glance it would appear that these two viewpoints would be quite widely separated. However, further consideration shows that, in general, satisfactory model experiments are possible only in case the experimenter has a good qualitative or semiquantitative understanding of the physical phenomena. The philosophy back of the ideal model experiment is that experiments shall be carried out under conditions that are similar in all respects to those existing in the prototype. This is strictly possible only in very rare cases, usually those in which only one simple physical process takes place. For the average case, however, the study involves the simultaneous action of several different physical processes, and analysis generally shows that the conditions for similarity of the model and the prototype are different for the different phenomena involved. The result is that practically all model studies have to be carried out under conditions in which the similarity laws and certain of the existing phenomena are disregarded completely. Under such conditions successful results can be obtained only if the experimenter is in a position to evaluate the relative importance of each phenomenon involved. He must also be enabled on this basis to devise an experiment in which similarity is obtained for all of the major phenomena and is violated only for minor phenomena.

In many cases the experimenter is not in this advantageous position. He is then forced, if he is to carry on a sound program, to carry on his experi-

ments with both objectives in mind, that is, to study the problem so as to delineate and evaluate the phenomena involved and as this knowledge becomes available, to proceed as rapidly as possible to the determination of the various specific results desired for the given prototype condition. A consideration of the knowledge available concerning some laboratory and field studies of the water entry of air-launched projectiles indicates that it is in this latter condition that there is not enough information available concerning the relative magnitude of the various factors which affect water entry to make it possible to plan a laboratory model study with assurance that the results will be applicable to prototype conditions. Therefore, it seems inevitable that the work must be carried on step by step, gaining knowledge as rapidly as possible concerning the physical processes involved and applying it to the study of known projectiles as fast as the knowledge becomes available.

Certain conditions can be established in the beginning. The study is basically a dynamic one, i.e., the study of the motion of a free body under the action of a system of forces. From this fact it follows that as the dynamic characteristics of the body must be carefully controlled, i.e., the specific gravity, the center of gravity, and the moments of inertia about the three axes, these are the properties of the body that determine its reaction to the force system. The greatest lack of knowledge apparently comes in the delineation and evaluation of the different forces that operate during entry. Cavitation studies in the water tunnel have much in common with the studies of the projectile behavior in entrance bubbles. Cavitation studies have shown very clearly the extreme importance of precise geometric similarity of the body shape. It has been found that small deviations from true contours can, under certain conditions, have very significant effects on the magnitude and direction of the forces acting on the body. This means that a very precise workmanship is required for the construction of the bodies to be tested in the laboratory, accompanied by precise measurements of the completed bodies. Tunnel tests have also shown that bubble shapes may be affected by small surface irregularities or changes in texture. All of the force

measurements in the water tunnel have demonstrated that the force system on such bodies is very sensitive to axial asymmetries or misalignments, i.e., to nose or tail structures that are out of line with the main body axis. An analysis of experimental data from various sources representing both laboratory and field investigations shows that the behavior of a body at water entry is greatly affected, both by the angle of a trajectory with respect to the water surface and by the pitch or yaw of the projectile with respect to its trajectory. This means that a laboratory study to investigate satisfactorily the entry problem must be in position to control accurately these variables and to obtain any desired combination of them at will. Some of the problems of a laboratory model study at

water entry were pointed out in Chapter 2 in conjunction with the description of the controlled-atmosphere launching tank. The most serious difficulties arise from the fact that water entry is a two-phase problem, i.e., it concerns both a gas and a liquid. This means that it is extremely difficult to set up experimental conditions which will not be affected by the size or scale of the experiment. It is clear that the gas density, gas pressure, liquid viscosity, and surface tension are all factors that can affect the force system acting on the entering body. It is felt that the possibility of successful model studies depends, to a large degree, upon the experimenter's ability to secure sufficient knowledge concerning these factors to enable him to evaluate their relative importance.

Chapter 13

TORPEDOES

13.1

INTRODUCTION

UNDER THE TERM "torpedoes" are included all those underwater projectiles which, throughout their underwater run, travel under their own power and are continuously guided by devices which maintain or regulate their course and depth. Investigations in this laboratory are confined almost exclusively to the exterior ballistics, which are not affected by the interior construction of the torpedo, the type of power plant (turbine, reciprocating engine, electric motor, or jet propulsion), or the type of steering mechanism control. For these investigations the most convenient classification is by method of launching into two groups: aircraft torpedoes and totally water-borne torpedoes.

AIRCRAFT TORPEDOES

Aircraft torpedoes are launched from aircraft traveling at high speed and relatively high altitudes, and as a result, they have a long air trajectory and hit the water at a high velocity. The impact opens up a cavity in the water which fills with air forming an elongated bubble which travels with the torpedo to a considerable depth, eventually separating and rising to the surface in a series of smaller bubbles. Upon emerging from the entry-bubble cavity, the torpedo rudders and propellers become effective, causing the torpedo to recover from the dive and finally to level off to its normal steady run.

TOTALLY WATER-BORNE TORPEDOES

Totally water-borne torpedoes are launched from submerged tubes or from the decks of surface vessels. In the latter case the air trajectory is relatively short, the impact velocity low, and the dive shallow. Hydrodynamic investigation of these torpedoes is limited to those characteristics affecting the underwater run only.

Figure 1 shows, to the same scale, outline drawings of all of the torpedoes investigated. Table 1 shows weights and principal dimensions. The various torpedoes are briefly described in the following paragraphs. For fuller description, detail dimensions, and discussion of the test results, reference is made to specific reports covering each torpedo.^{23, 24, 25, 27-32}

13.1.1 Aircraft Torpedoes

MARK 13 SERIES

All the torpedoes of the Mark 13 series have identical body shapes and dimensions. The various modifications differ from each other in the weight of the explosive charge, the running speed, and in the tail structure. The original Mark 13 torpedo had its rudders mounted aft of the propellers, supported by struts extending from the outer edges of the fins which were forward of the propellers. This arrangement was abandoned because of the inherent struc-

TABLE 1. Dimensions and weights of various torpedoes.

	Overall length in inches	Maximum diameter in inches	Maximum weight in pounds	Displacement in pounds	Speed in knots
Aircraft torpedoes					
Mark 13 series	161	22.42	2127	1703	33.5-40.5
Mark 25 series	161	22.42	40.5
Hydrobomb; Westinghouse design	160.125	22.42	3360	1770	40
Hydrobomb; USMC Design No. 39	119.57	28	61
Hydrobomb; USMC Design No. 8	150	28	3500	2052	61
Water-borne torpedoes					
Mark 14 series	246	21	3185	2516	30.5-47.5
Mark 15 series	268	21	3347	3045	27.4-46
Mark 26 series	245.88	21	3350	2630	30-45

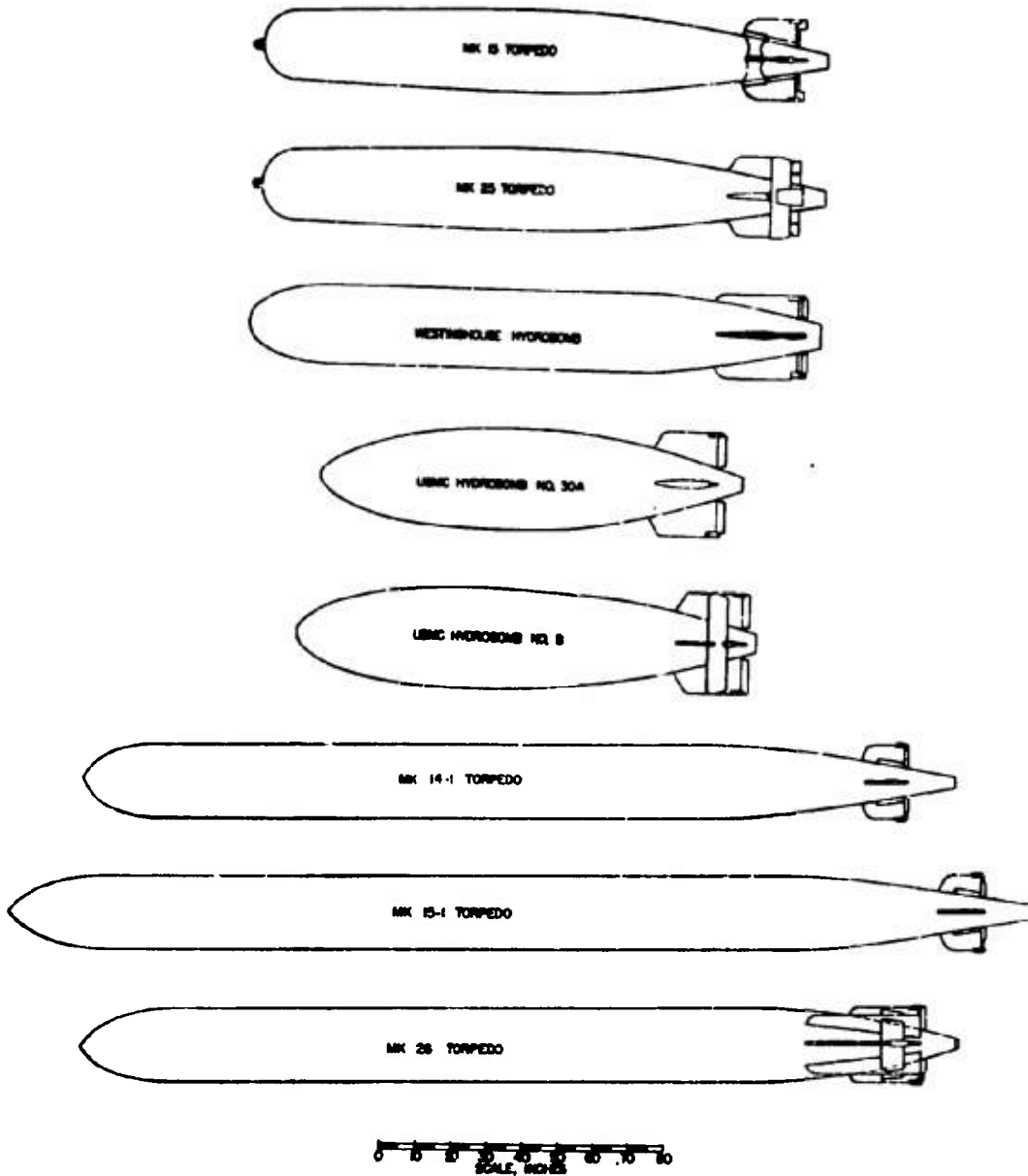


FIGURE 1. Outline dimensions of torpedoes.

tural weakness and the added drag. It was superseded by the Mark 13-1 in which the rudders are forward of the propellers, and immediately aft of the fins. Later modifications increased the speed and weight of explosive and strengthened the afterbody,

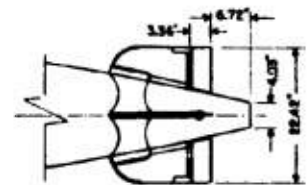
without, however, changing the external dimensions. In other modifications, shroud-ring tails were added to improve the stability and behavior in water entry. Figure 2 shows the principal dimensions and Figure 3 is a photograph of the 2-in. diameter model.

CONFIDENTIAL

MARK 25 TORPEDO

This torpedo has the same overall dimensions and body shape as the Mark 13. It was designed structurally to withstand drops from aircraft at higher speeds and altitudes than were possible with the

ings, both with and without shroud rings, to determine the arrangement which would cause least interference with rudder and propeller action. Figure 4 shows the model with the exhaust opening in one of the fins and Figure 5 shows the tail structure with one of the subsequent modifications in which the



HORIZONTAL RUDDER

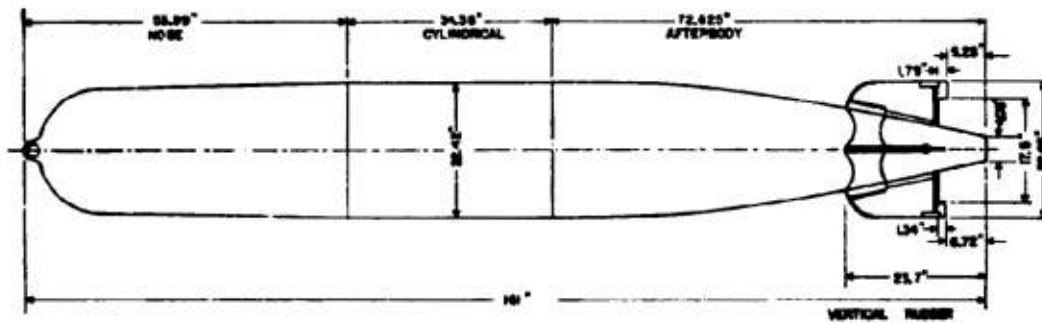


FIGURE 2. Principal dimensions of Mark 13-1 torpedo.



FIGURE 3. Two-in. diam. model of Mark 13-1 torpedo.

Mark 13-1. It is equipped with a later design of power plant in which the exhaust gases, instead of discharging through a hollow propeller shaft, are discharged through two passages in the fins. In addition to the usual hydrodynamic tests, the investigation covered various arrangements of the exhaust open-



FIGURE 4. Mark 25 torpedo model with exhaust opening in top of fin.

gases are discharged through a stack attached to the shroud ring.

HYDROBOMB—WESTINGHOUSE DESIGN

This is a jet-propelled torpedo having the same overall length and diameter as the Mark 13 and the Mark 25. The nose is somewhat sharper and the afterbody has a more abrupt taper than the Mark 13. The fins and rudders for both course and depth control are considerably larger than on the Mark 13 or

Mark 25. The depth control fins are symmetrical and have a total span 2 in. greater than the maximum body diameter. The course control fins are unsymmetrical, the lower fin projecting 1 in. beyond the maximum body radius and 1 in. more than the upper

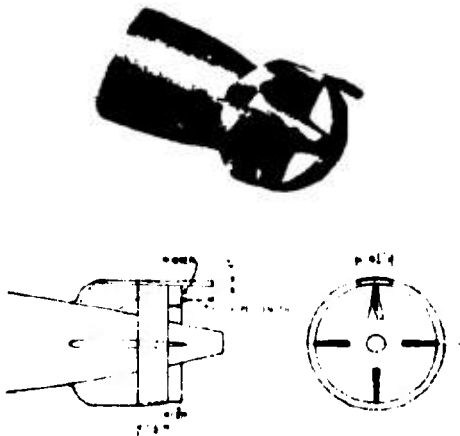


FIGURE 5. Mark 25 torpedo with ring tail and single exhaust pipe.

fin. The fins are of appreciable thickness (2 in. maximum) and both fins and rudders have rounded edges and are well streamlined. No modifications of this shape were tested. Figure 6 shows the outline dimensions, and Figure 7, a photograph of the model.

HYDROBOMB—UNITED SHOE MACHINERY CORPORATION DESIGN NO. 30

This hydrobomb is jet propelled and intended to travel at an underwater speed of 60 knots. It is 119 in. long and 28 in. in maximum diameter; shorter and of greater diameter than the Westinghouse design. The fins are relatively thick (2½ in. maximum) and are larger compared to the body size than on the Westinghouse design. The maximum thickness of the fin is at about 80 per cent of their length from the leading edge. The rudders are relatively smaller than on the Westinghouse design, particularly the vertical or course rudders. The nose is a long (3.13 to 1) ellipsoid and the afterbody tapers rather abruptly. Figure 8 shows the principal dimensions and Figure 9 is a photograph of the model.

HYDROBOMB—UNITED SHOE MACHINERY CORPORATION DESIGN NO. 8

This is also a jet-propelled hydrobomb, designed for an underwater speed of 60 knots. It is 130 in. long, 11 in. longer than the Design 30 and the afterbody has a more gradual taper. The fins are somewhat smaller relative to the body size than on the

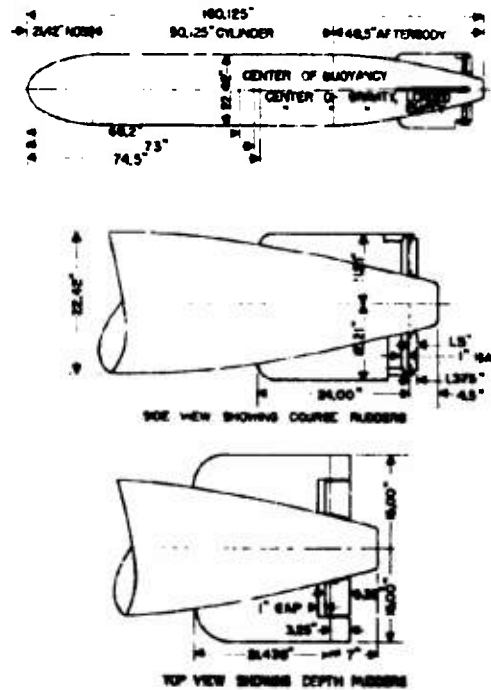


FIGURE 6. Outline dimensions, Westinghouse hydrobomb.



FIGURE 7. Two-in. diam. model of Westinghouse hydrobomb.

Design 30 and the rudders, both horizontal and vertical, relatively larger. Two fin arrangements were tested, differing in that the span of the horizontal or depth fins was 28 in. on one and 34 in. on

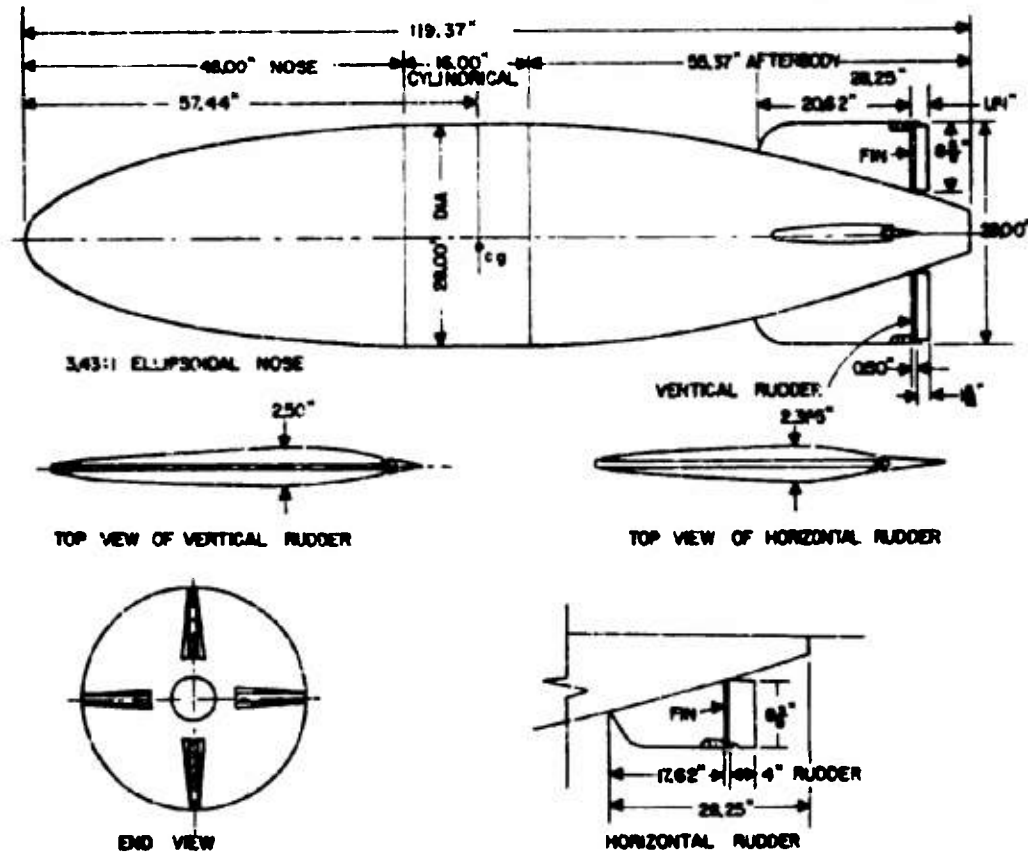


FIGURE 8. Outline dimensions, United Shoe Machinery Corporation hydrobomb, Design 30.

the other; the vertical fin span was 29 in. on both. Both models were also tested with shroud rings added on the fins. Figure 10 shows the principal dimensions and Figure 11 is a photograph of the model with the 34-in. dep^h fin span and shroud ring.

12.1.3 Water-Borne Torpedoes

MARK 14 AND MARK 15 SERIES

The torpedoes of these two series are all 21 in. in diameter, made up with heads and afterbodies having the same external shape and dimension and are all equipped with identical fin and rudder assemblies. The only differences, externally, are in their overall length, due to the different lengths of their cylindrical midsections. Models of only one torpedo in each series, the Mark 14, Modification 1 and the Mark 15,

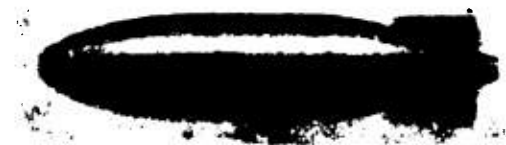


FIGURE 9. Two-in. diam. model of United Shoe Machinery Corporation hydrobomb, Design 30.

Modification 1, were investigated. Relative to the size of the body, the fin and rudder areas of these torpedoes are considerably smaller than on the aircraft torpedoes. Tests were also made on these models with shroud rings added to the fins. Figure 12 shows the outline dimensions of the two torpedoes and Figure 13 is a photograph of the model of the Mark 14-1 torpedo.

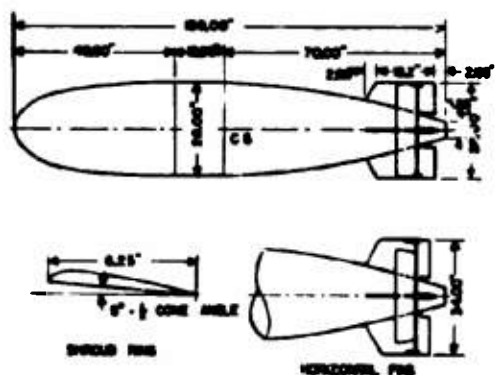


FIGURE 10. Outline dimensions, United Shoe Machinery Corporation hydrobomb, Design 8



FIGURE 11. Two-in. diam. model of United Shoe Machinery Corporation hydrobomb, Design 8 with 34-in. depth fin span and shroud ring.

MARK 26 TORPEDO

This torpedo is electrically driven, designed for speeds of 39 and 45 knots. In overall length and diameter it is the same as the Mark 14. It has a somewhat blunter shape and the displacement is slightly greater than for the Mark 14. The original design as received in the laboratory showed an afterbody with eight fins and a shroud ring. The shroud ring had an overall diameter 2 in. less than the torpedo body diameter in order to clear the latching device in the launching tube. The fins were considerably longer than on the Mark 14 and 15 and the rudders were relatively larger than on the Mark 14 and 15. Three successive modifications of the fin structures were investigated by water tunnel tests. The original design was designated by the laboratory as the Mark 26-1. On the Mark 26-2, the shroud ring was omitted. On the Mark 26-3 the shroud ring and the four 45° fins were omitted. On the Mark 26-1, 26-2, and 26-3 the horizontal or depth fins are inclined to the longitudinal axis of the torpedo, the forward edges being raised so that the fins are at an angle of about $1\frac{1}{2}^\circ$ to the torpedo axis, giving a slight down-

rudder effect. On the Mark 26-4 the fins are all shorter than on the other three models and the depth fins are in the plane of the torpedo axis. The design was based on results of tests of other projectiles which indicated that the greater part of the stabilizing effect is obtained from the aft portion of the fins and

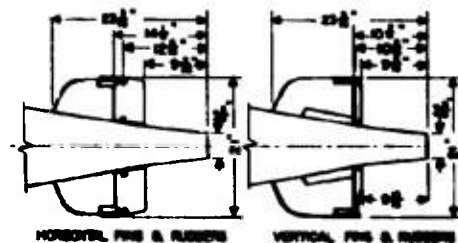
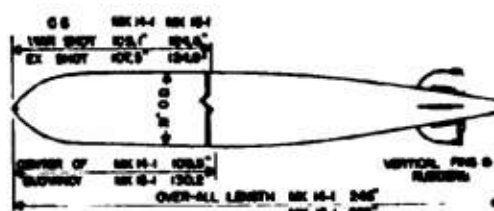


FIGURE 12. Principal dimensions of Mk 14-1 and 15-1 torpedoes.

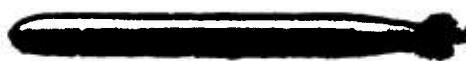


FIGURE 13. Model of Mark 14-1 torpedo.

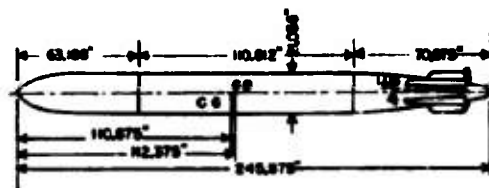


FIGURE 14. Outline dimensions of the Mk 26-2 torpedo.

that the gain in stability by extending the fins forward is very slight. The fins on the Mark 26-1 are closely comparable to those of the Mark 14. The rudders on all four models are the same. Figure 14 shows the outline dimensions of the Mark 26-2 torpedo. Figures 15 and 16 show the tail structures of

the Mark 26-1 and Mark 26-4, respectively. Figure 17 is a photograph of the model of the Mark 26-1 and Figures 18 to 21 show photographs of models of the four different tail fin designs.

tively, from observation of the cavitation characteristics of the projectile in the high-speed water tunnel. Pressure distribution measurements provide additional information that is useful in understanding the behavior of the projectile during the entry phase.

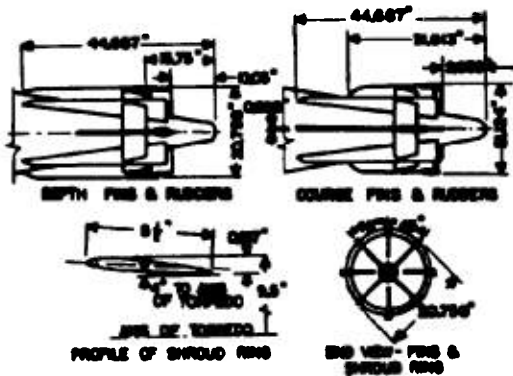


FIGURE 15. Fins and rudders of the Mk 26-1 torpedo.

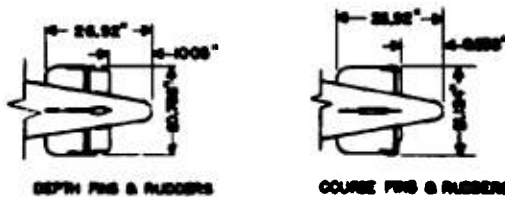


FIGURE 16. Fins and rudders of the Mk 26-4 torpedo.

12.2 TYPES OF TORPEDO STUDIES

12.2.1 Water Entry

The controlled-atmosphere launching tank⁴⁴ was designed and built specifically for investigating the behavior of air-launched underwater projectiles during the water-entry phase. The methods used are described in Chapter 12 of this volume. Because of the similarity of the entrance bubble to the fully developed cavitation bubble (see Chapter 4), some knowledge of the behavior of the projectile in the entrance bubble may be inferred, at least qualita-

12.2.2 Force Measurements

The force studies made in the water tunnel on torpedo shapes include the measurement of drag, cross

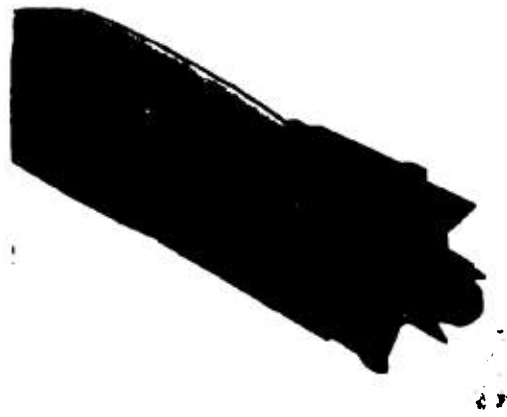


FIGURE 18. Model afterbody of Mark 26-1 torpedo.

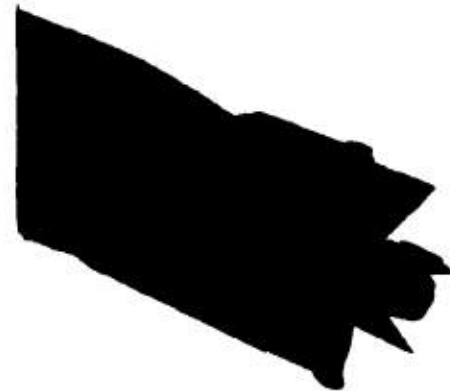


FIGURE 19. Model afterbody of Mark 26-2 torpedo.



FIGURE 17. Model of Mark 26-1 torpedo.

force, lift, and moment as functions of the pitch (angle of attack), yaw, and rudder angle. These tests are made under steady-state conditions and, there-

fore, give directly only the steady-state hydrodynamic forces and moments, but not the damping forces and moments which arise when the projectile is rotating or oscillating about a transverse axis. The data thus obtained are sufficient for solving various problems not involving angular velocity, e.g., the power requirements, the degree of static stability, the ability of the torpedo to carry excess weight over buoyancy, and the pitch angle and rudder setting at

problems involving angular velocities. Reference is made to Chapter 11, in which the relationship between the static and dynamic coefficients is discussed.



FIGURE 20. Model afterbody of Mark 26-3 torpedo.



FIGURE 21. Model afterbody of Mark 26-4 torpedo.

which the torpedo must travel in order to maintain a horizontal path under any given loading condition. The steady-state force and moment data form part of the information required in dealing with dynamic

problems involving angular velocities. Reference is made to Chapter 11, in which the relationship between the static and dynamic coefficients is discussed. For well-streamlined shapes, such as torpedoes, the cross force, lift, and moment coefficients are practically independent of the Reynolds number. The drag coefficient, however, does vary materially with the scale of the tests and, therefore, the investigations usually include a study of the drag coefficient as a function of Reynolds number.

The models for the force tests were complete in all details except for the omission of minor surface ir-

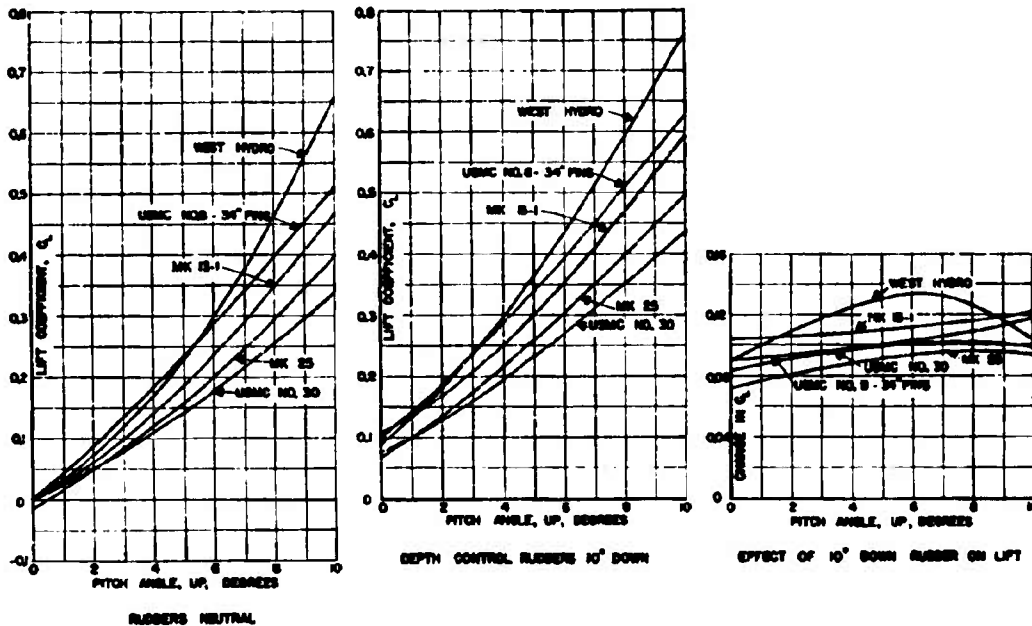


FIGURE 22. Comparison of lift coefficients, aircraft torpedoes.

regularities and the omission of the propellers. The propellers were omitted because, unless driven at the proper speed, they would only obstruct and disturb the flow on the afterbody. The action of the propellers undoubtedly modifies to some extent the forces and moments acting on the torpedo. However, data taken on propellerless models are useful in studying

torpedo behavior, in calculating certain equilibrium conditions, and in comparing the effect of modifications in design.

LIFT, CROSS FORCE, AND MOMENT

The lift, cross force, and moment characteristics as

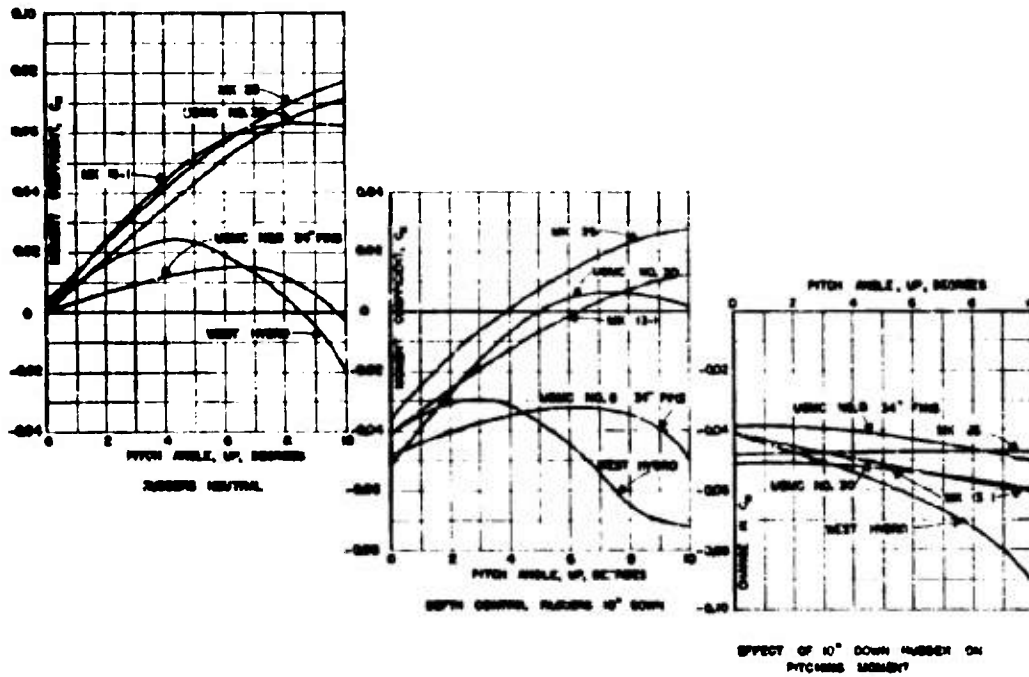


FIGURE 23. Comparison of pitching moment characteristics, aircraft torpedoes.

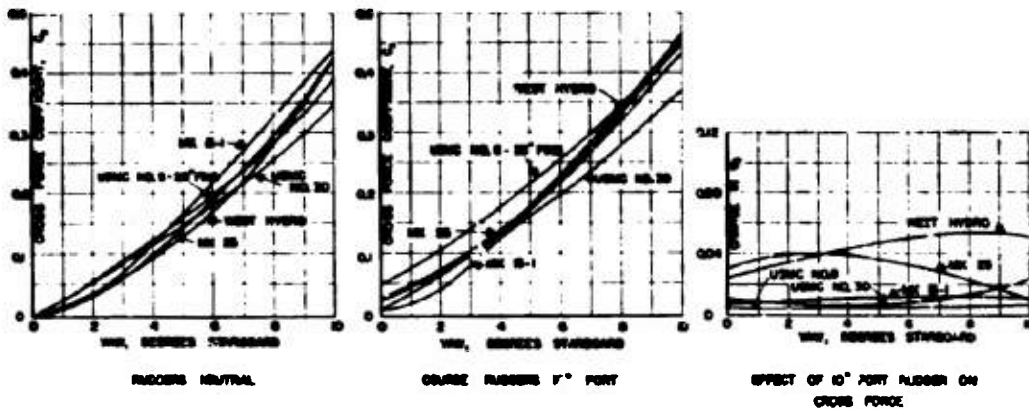


FIGURE 24. Comparison of cross force coefficients, aircraft torpedoes.

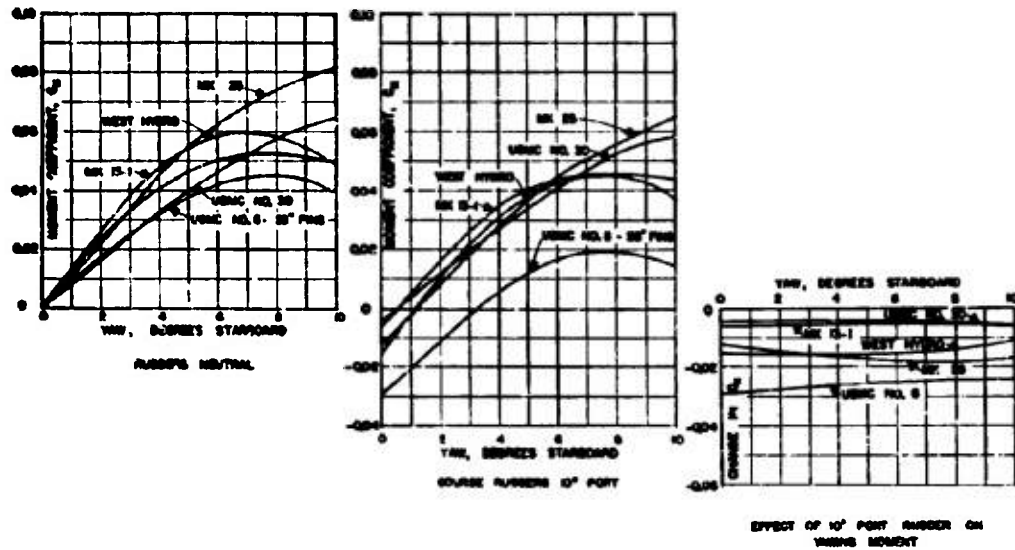


FIGURE 25. Comparison of yawing moment coefficients, aircraft torpedoes.

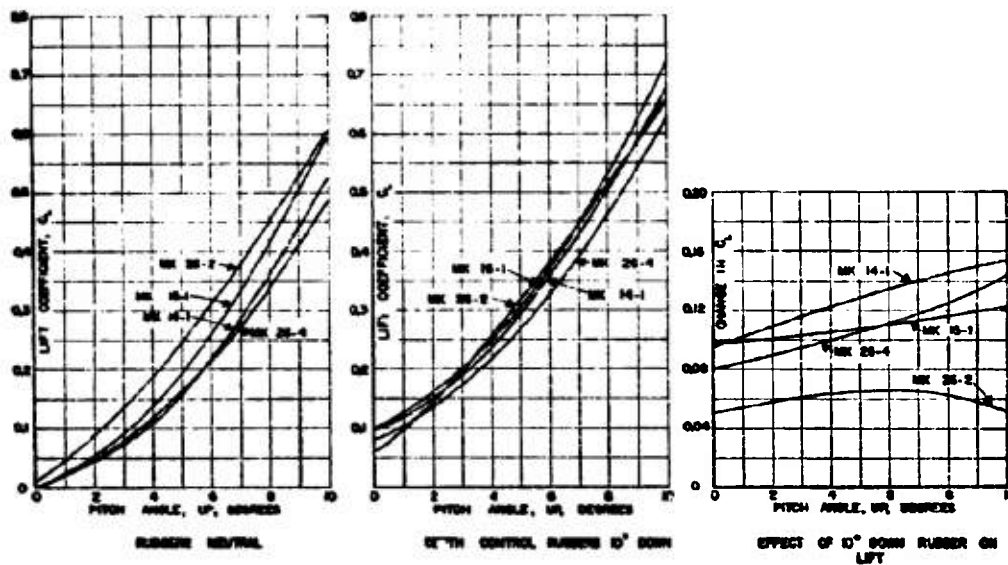


FIGURE 26. Comparison of lift coefficients, water-borne torpedoes.

functions of positive pitch and yaw (upward pitch and starboard yaw), with rudders neutral and set at 10 degrees down or port are plotted in Figures 22 to 25 for aircraft torpedoes, and Figures 26 to 29 for water-borne torpedoes. Definitions of the terms and

symbols used in these and succeeding figures are given in the Appendix.

The differences in the force and moment characteristics and rudder effect of the various torpedoes depend not alone on the size of the fins and rudders, but

also on the contour of the torpedo, the shape of the fins and rudders, and the interference effects between the torpedo body and the fins and rudders, as well as the location of the center of gravity

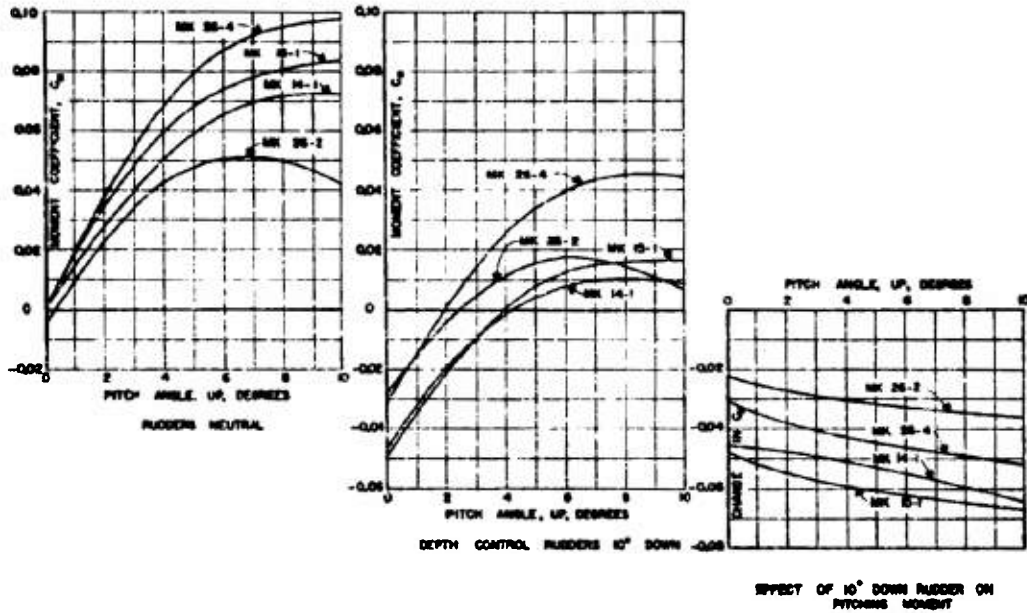


FIGURE 27. Comparison of pitching moment characteristics, water-borne torpedoes.

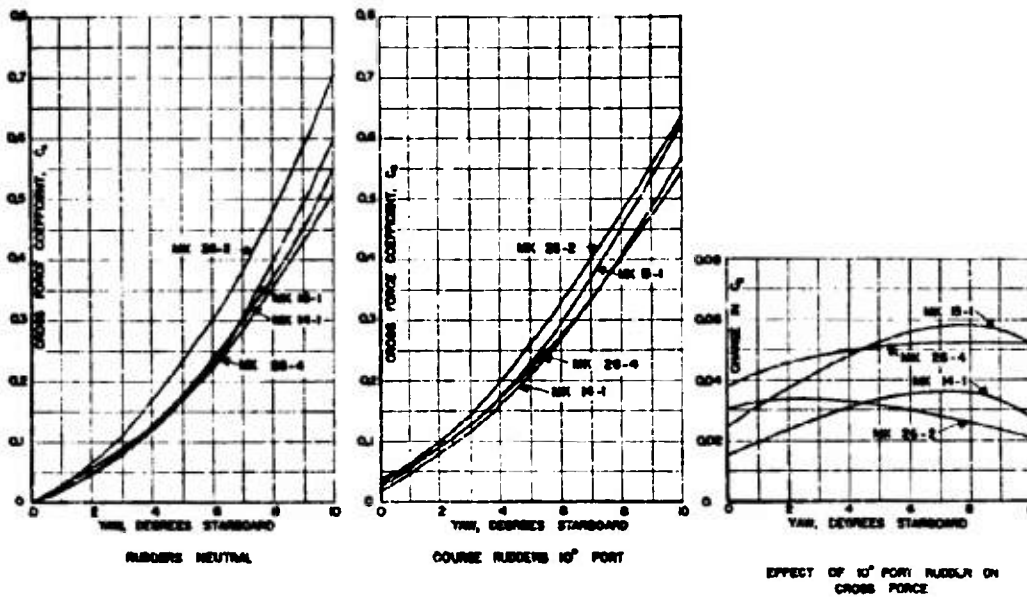


FIGURE 28. Comparison of cross force coefficients, water-borne torpedoes.

CONFIDENTIAL

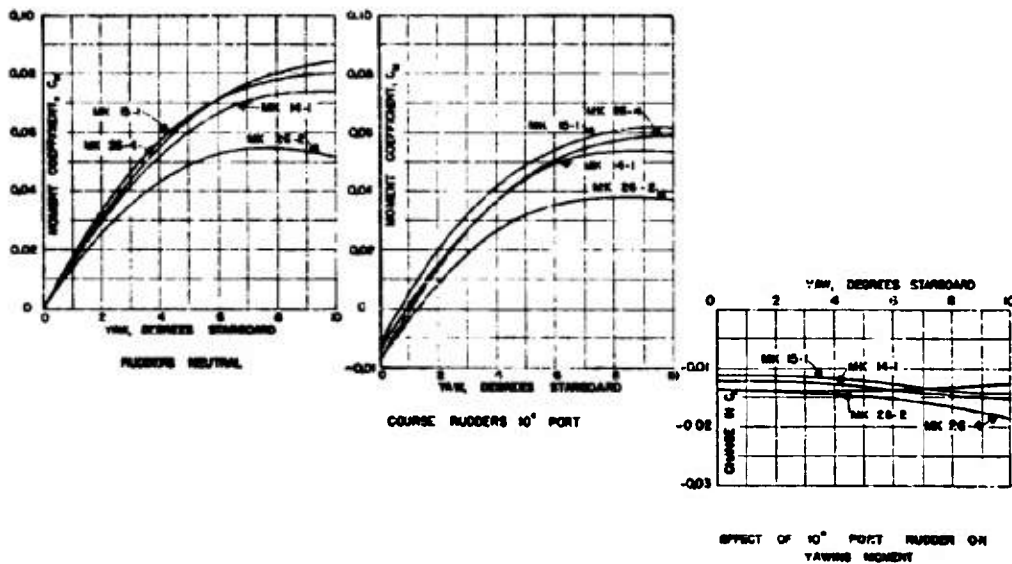


FIGURE 29. Comparison of yawing characteristics, water-borne torpedoes.

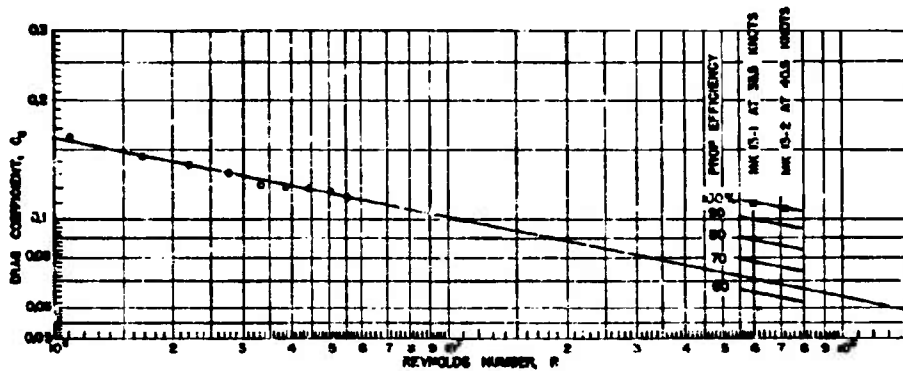


FIGURE 30. Relation between drag coefficient and Reynolds number, Mk 13-1 torpedo.

of the torpedo. In comparisons of similar body shapes having stabilizing surfaces of considerably different areas, the larger surfaces produce more lift and a greater stabilizing moment. This is illustrated by comparing the lift and pitching moment coefficient curves of the Mark 13-1 torpedo and the Westinghouse hydrobomb in Figures 22 and 23. The depth fins of the hydrobomb are much wider than on the Mark 13 torpedo and result in a greater increase of lift with pitch for the hydrobomb and a small destabilizing moment. In comparing the two United

Shoe Machinery Corporation [USMC] designs of hydrobomb, the Design No. 8, with its larger fin area shows a similar difference in lift and moment. These comparisons, however, are not quantitative; that is, there is no direct relation between fin size and the lift or moment, even on very similar body shapes. The rudder effect is a function not only of the size of the rudders, but of their disposition relative to the fins and afterbody and of the shape of the rudders. One extreme example is the comparison of the effect of a 10-degree port rudder on yawing moment between

the USMC Design No. 30 and Design No. 8 hydrobombs. On the Design No. 30, the course rudders are extremely small and located directly aft of rather thick fins, and show a very slight effect on the moment at all yaw angles. In the Design No. 8, the fins are thinner and the rudders considerably larger, and the effect on the yawing moment is several times as great.

VARIATION OF DRAG COEFFICIENT WITH REYNOLDS NUMBER

Tests to determine the variation of the drag coefficient as a function of Reynolds number were made on 1½-in. and 2-in. diameter models in the high-speed water tunnel at velocities between 10 and 70 fps. Figures 30 to 33 show C_D as a function of R

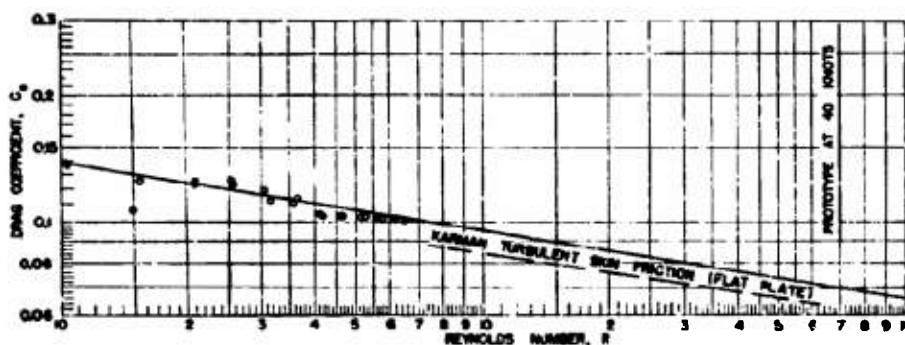


FIGURE 31. Relation between drag coefficient and Reynolds number, Westinghouse hydrobomb.

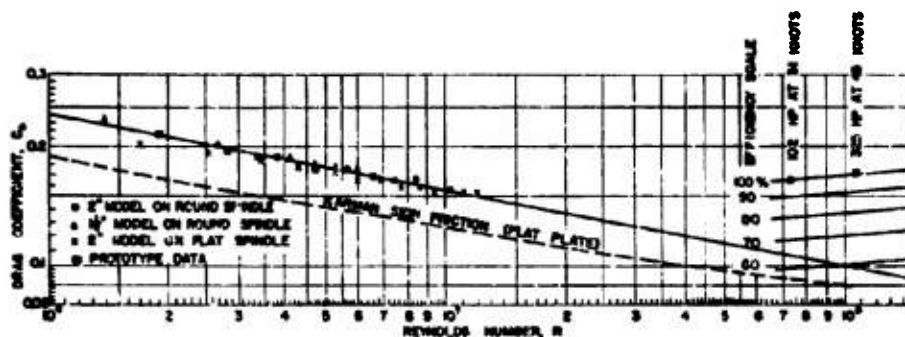


FIGURE 32. Relation between drag coefficient and Reynolds number, Mk 14-1 torpedo.

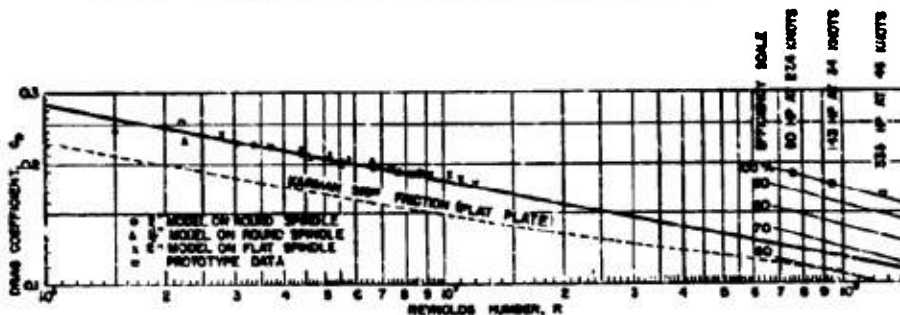


FIGURE 33. Relation between drag coefficient and Reynolds number, Mk 15-1 torpedo.

plotted on logarithmic paper. It is evident that straight line extrapolation on these diagrams is all that is justified by the experimental data. As a comparison, the von Karman curves for turbulent skin friction only, for flat plates of the same surface area and length as the torpedoes have been plotted in Figures 31, 32, and 33. If a power law is assumed for the variation of the drag coefficient with Reynolds number, it may be expressed by the equation:

$$C_D = mR^{-n} \quad (1)$$

If the coefficients in equation (1) are evaluated from the curves drawn on Figures 30 to 33, the resulting equations are the following:

Mark 14 torpedo	$C_D = 3.32R^{-0.10}$
Mark 15 torpedo	$C_D = 3.94R^{-0.10}$
Mark 26-1 torpedo	$C_D = 2.93R^{-0.18}$
Mark 26-4 torpedo	$C_D = 1.56R^{-0.14}$
Mark 13 torpedo	$C_D = 2.54R^{-0.20}$
Westinghouse hydrobomb	$C_D = 1.28R^{-0.16}$

The slope of the curves, indicated by the exponent of R , varies from about $-1/7$ to $-1/5$, with most of the experimental data tending toward the negatively larger value, i.e., a steeper slope. The Reynolds number obtained at 60 to 70 fps with 2-in. diameter models is, for most torpedoes, between $1/6$ and $1/12$ of the Reynolds number corresponding to the prototype operating condition. The scatter of the test points is such that repeated experiments might easily justify a change in the slope exponents and, consequently, in the extrapolation to prototype conditions.

The fineness ratio of a streamlined shape such as a torpedo is commonly expressed as the ratio of length to diameter, l/d .

The drag coefficient C_D , usually calculated on the basis of the maximum transverse cross-sectional area, may also be calculated on the basis of volume V to the $2/3$ power, resulting in the expression:

$$C_{D_V} = \frac{D}{\frac{\rho}{2} V^{2/3}}$$

When calculated on this basis, the coefficient for a given Reynolds number shows less variation with the fineness ratio l/d .

In Figure 34, the drag coefficients of most of the torpedoes investigated, calculated from the test results on the basis of both area and volume, have been plotted as ordinates against values of l/d as abscissas,

for a constant Reynolds number of 6×10^6 . It will be noted that the curve of C_{D_V} vs l/d has a long flat minimum. This indicates that, for a given volume, a series of torpedoes could be designed, all having the same volume and requiring approximately the same horsepower to produce a given speed, but covering a wide range of length-to-diameter ratios.

It must be remembered that these results are from a series of bodies all having good streamlining. Their resistance is largely due to skin friction, with a relatively small contribution of form drag. Changes in nose and afterbody profiles, and in the form of appendages such as tail structure, can affect appreciably the form drag and thus the overall resistance. Structural variations of this type account for the scatter of the points shown on Figure 34.

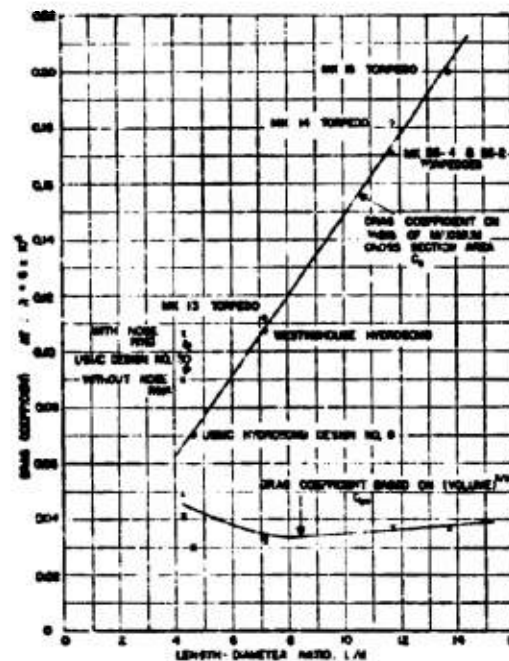


FIGURE 34. Relation of drag coefficient to length/diameter ratio for constant Reynolds number.

DRAG AND POWER REQUIREMENTS

The drag determined by model tests is useful in estimating the horsepower requirements of the full-size torpedo, even though extrapolation of the drag coefficient to prototype conditions may not be very

exact. For propeller-driven torpedoes, if the propulsion efficiency is known, it is possible to estimate the shaft horsepower required. Conversely, if the shaft horsepower of a given torpedo is known, the extrapolated drag coefficient curve makes it possible to estimate the propulsion efficiency. Thus in Figures 30, 32, and 33 scales for propulsion efficiency are shown based on shaft horsepower measurements from dynamometer tank measurements. This calculation assumes that the drag force obtained by extrapolating water tunnel measurements is a true indication of the propeller thrust required to drive the torpedo. This neglects the change in flow over the afterbody caused by the propeller.

The following approximate expression may be used to estimate the shaft horsepower required by a well-

tion to the $1/2$ to $1/3$ power of the Reynolds number (see Figures 7 to 10). For simplicity, the $1/2$ power was used, although $1/3$ corresponds more nearly to most test results and would result in higher estimated power at high speeds. For a torpedo of a given size, therefore, if the drag coefficient varies as the -0.2 power of the speed, the drag force is proportional to the 1.8 power of the speed and the horsepower to the 2.8 power of the speed. Also, as shown by Figure 34, the drag coefficient, when computed on the basis of V^2 instead of cross-sectional area, is more nearly independent of the shape and length-to-diameter ratio and is, therefore, assumed constant in the above formula. For convenience the displacement was used instead of the volume because data on torpedoes usually are given in terms of displacement (buoyancy).

TABLE 2. Calculated and observed horsepower of several torpedoes.

Torpedo	Displacement in lb	Speed in knots	Drag coefficient at rated speed from Figures 30 to 33	Shaft horsepower		
				Calculated for 65% prop. efficiency	Calculated from equation (2)	By test (average)
Mark 14	2430	31.5	0.107	108	106	102
Mark 14-1	2516	46	0.098	309	303	325
		31.5	0.107	108	107	102
Mark 15 1	3045	46	0.068	309	310	325
		27.4	0.122	82	82	80
Mark 25-1	2630	34	0.117	149	151	142
		46	0.110	347	352	335
Mark 26-1	2630	39	0.110	212	200	...
		45	0.106	314	300	...
Mark 26-4	2630	39	0.123	237	200	...
		45	0.120	355	300	...
Mark 13-1	1765	33.5	0.071	101	100	96
Mark 13-2	1765	40	0.066	160	165	170
Westinghouse hydrobomb	1770	40	0.069	163	(jet propelled)	

streamlined, propeller-driven torpedo at speeds within present torpedo practice:

$$\text{hp} = 0.369 \times 10^{-4} (\text{speed})^{2.8} (\text{displacement})^1 \quad (2)$$

in which the speed is in knots and the displacement is in pounds.

The constant 0.369×10^{-4} of equation (2) was evaluated from data on the displacement, speed, and shaft horsepower from dynamometer tank tests of torpedoes of the Mark 13, Mark 14, and Mark 15 series taken from U. S. Navy Ordnance pamphlets 629A, 635, and 642, respectively.

The form of the above equation was chosen because drag tests show that the drag coefficient is not constant but varies approximately in inverse propor-

Table 2 shows the comparison for several torpedoes of the shaft horsepower (1) computed directly from the extrapolated drag coefficient assuming a propulsion efficiency of 65 per cent, (2) calculated from equation (2), and (3) as determined by dynamometer tank tests.

EQUILIBRIUM RUNNING CONDITIONS

The weight of a torpedo is normally greater than its buoyancy, and the center of gravity CG is usually ahead of the center of buoyancy CB and slightly below the axis of symmetry. Therefore, in order to travel on a horizontal path, the torpedo must assume a pitch angle and a rudder setting such that the lift

will balance the excess weight over buoyancy and the hydrodynamic moment will balance the static moment due to the displacement of *CG* from *CB*. For any given conditions of speed, weight, and *CG* location, there is only one pitch angle and one rudder setting which will satisfy these conditions. The following paragraphs present one of several methods for determining the pitch and rudder angles required for equilibrium.

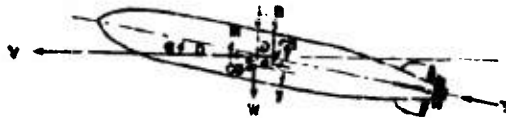


FIGURE 35. Forces acting on torpedo in straight run.

Figure 35 shows the forces acting on a torpedo when running on a straight horizontal path with a pitch angle α . The hydrodynamic forces are resolved into a lift L acting at right angles to the path, a drag D acting parallel to the path, and a moment M . The lift and drag are taken as acting at the point O , on the torpedo axis and above the center of gravity. In addition, there is the propeller thrust T assumed to be acting along the axis, the weight W acting vertically downward at the center of gravity, which is a distance y below the axis, and the buoyancy B acting vertically upward at the center of buoyancy, which

is on the axis and a distance a aft of the center of gravity. The equilibrium equations may then be written:

$$\text{Vertical forces: } L + B - W + T \sin \alpha = 0. \quad (3)$$

$$\text{Horizontal forces: } D - T \cos \alpha = 0. \quad (4)$$

$$\text{Moments about } O: M - Ba \cos \alpha - Wy \sin \alpha = 0. \quad (5)$$

From equation (4)

$$T = \frac{D}{\cos \alpha}.$$

Substituting for T in (3) and rearranging

$$L + D \tan \alpha = W - B. \quad (6)$$

Since both the distance y and the pitch angle α are small, equation (5) may be written

$$M = Ba. \quad (7)$$

Dividing equation (6) by $\frac{1}{2} \rho v^2 A$ and (7) by $\frac{1}{2} \rho v^2 Al$, we get

$$C_L + C_D \tan \alpha = \frac{W - B}{\frac{1}{2} \rho v^2 A} \quad (8)$$

and

$$C_M = \frac{Ba}{\frac{1}{2} \rho v^2 Al} \quad (9)$$

Dividing (9) by (8), we have

$$\frac{C_M}{C_L + C_D \tan \alpha} = \frac{Ba}{(W - B)l} \quad (10)$$

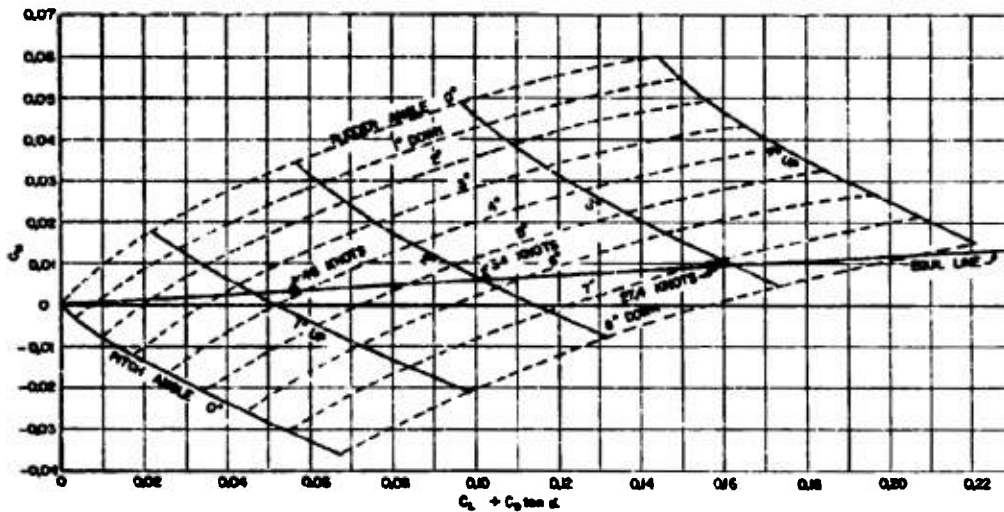


FIGURE 36. Mk 15-1 torpedo. Pitch angle and rudder setting for equilibrium.

CONFIDENTIAL.

To simplify the solution of the above equations, the water tunnel data is plotted in the form of C_M against the quantity $(C_L + C_D \tan \alpha)$ as shown in Figure 36 and the constant pitch angle and constant rudder angle lines are drawn. Here C_M is the moment coefficient, C_L the lift coefficient, C_D the drag coefficient, and $C_D \tan \alpha$ represents the vertical component of the propeller thrust. The data shown in Figure 36 is for the Mark 15-1 torpedo and was taken from Figure 20 of the report on this torpedo²⁴ with the 1-degree rudder setting intervals drawn in by interpolation. From equation (10) it can be seen that, for a given set of loading conditions, the locus of equilibrium points for all speeds on the diagram in Figure 36 is a straight line through the origin with a slope equal to $Ba/(W - B)l$. In order to determine equilibrium conditions for any speed it is necessary only to determine the quantity $(C_L + C_D \tan \alpha)$ by means of equation (8) and to locate the corresponding point on the straight line locus of equilibrium conditions. The equilibrium values of pitch angle and rudder setting for the speed represented by the point so located can then be read directly from the pitch angle and rudder setting curves of the diagram. Figure 36 shows the solutions for the Mark 15-1 at three different running speeds under conditions at the start of a run, i.e., fully loaded with fuel and explosive.

For a low-drag torpedo the term $(C_D \tan \alpha)$ is small in comparison to C_L (about 5 per cent for the Mark 15) and, therefore, the solution for equilibrium conditions may be further simplified by neglecting the term and plotting C_M against C_L instead of against $(C_L + C_D \tan \alpha)$.

Table 3 shows the equilibrium pitch and rudder angles for several torpedoes calculated by the above method.

TABLE 3. Equilibrium pitch angles and rudder settings for various torpedoes in straight horizontal run.

Torpedo	Speed in knots	Pitch angle, up, in degrees	Rudder setting, down, in degrees
Mark 13-2	40.5	0.7	1.1
Mark 14-1	45	1.1	3.1
	31	2.2	5.4
Mark 15-1	46	1.2	3.8
	34	2.0	5.6
	27.4	2.9	7.1
Mark 28-2	45	0.8	2.0
	39	1.0	3.3
Mark 26-4	45	0.7	3.2
	30	1.0	4.2

11.2.1

Pressure Distribution

The forces acting on a projectile traveling through any fluid are due to the distributed fluid pressures acting normal to the surface, and to the shear stresses in the fluid adjacent to the surface (skin friction) acting tangentially. The tangential forces make up most of the drag, but the moment and cross force are practically unaffected by them. Therefore, with the pressure distribution about a projectile completely known, it is possible to calculate the resultant moment, cross force, and lift, and also the contribution of the normal pressures to the drag (form drag). With most torpedoes, however, the pressures acting on the tail surfaces cannot be measured because of the thinness of these sections on the small models. Consequently, only the forces acting on the bare hull can be computed from the pressure distribution.

LABORATORY PROCEDURE

Two-inch diameter scale models were used for the pressure distribution measurements. Piezometer holes $\frac{1}{32}$ in. in diameter with the entrance edges

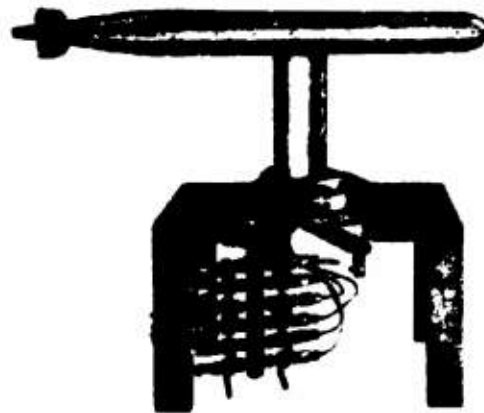


FIGURE 37. Model of Mark 14-1 torpedo assembled on streamlined strut with base plate and tube manifold ready for installation in the water tunnel.

rounded to 0.005-in. radius were drilled normal to the surface of the torpedo and each connected by a small rubber and nickel-silver tube to one side of a differential pressure gauge. The other side of the gauge was connected to static pressure in the tunnel working

section and the differential pressure read directly on a weighing beam-type balance reading to 0.01 psi. All piezometer openings were in a single plane through the longitudinal axis of the torpedo. The pressure distribution was explored by setting the plane of the piezometer openings at a given angle with the vertical and measuring the pressure at each tap for yaw angles of 0, ± 3 , and ± 6 degrees. In most cases the angles of the plane of the taps were varied in 15-degree steps from 0 to 90 degrees from the vertical. Because of the symmetry of the torpedo, these measurements give the pressure distribution about the entire body. Most of the tests were made with a velocity of 40 fps and a static pressure of 10 psi. Tests at other velocities and pressures showed that within the range of the tests there was no measurable change in the relative pressure distribution. Figure 37 is a view of the Mark 14-1 model mounted ready for test.

TEST RESULTS

The test results are presented in terms of p/q , where $p = P - P_0$,

p = normal pressure on the torpedo surface in pounds per square foot,

P_0 = static pressure in undisturbed water at same level as torpedo centerline in pounds per square foot,

$q = \rho v^2/2$ = dynamic pressure of water in pounds per square foot,

ρ = mass density of water in slugs per cubic foot,

v = mean relative water velocity in feet per second.

Figures 38 and 39 show typical pressure distribution and location of pressure taps for torpedo shapes

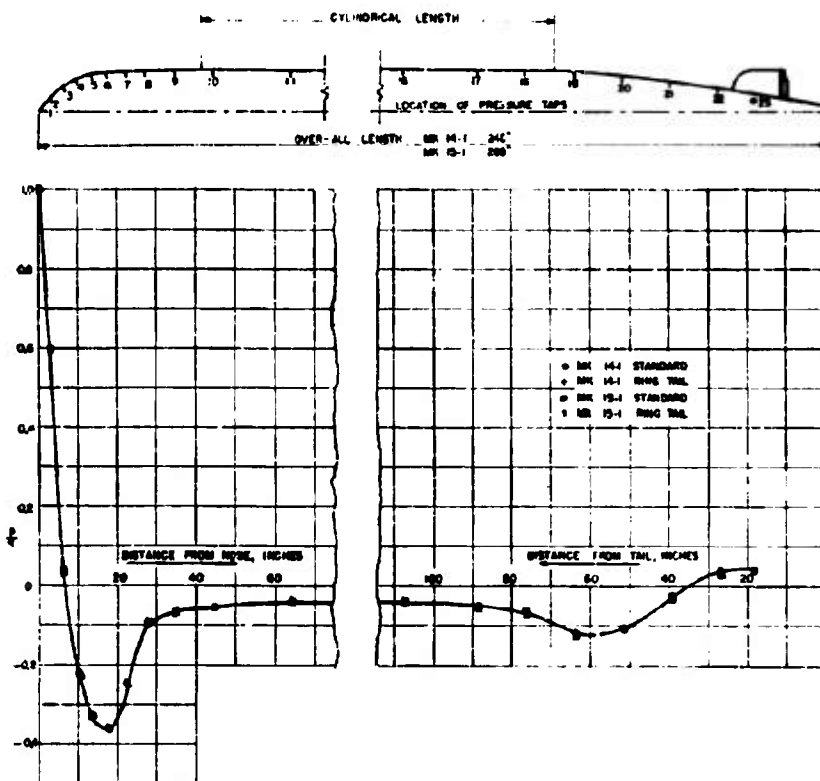


FIGURE 38. Mk 14-1 and 15-1 torpedoes. Longitudinal pressure distribution on nose and afterbody at zero yaw.

CONFIDENTIAL

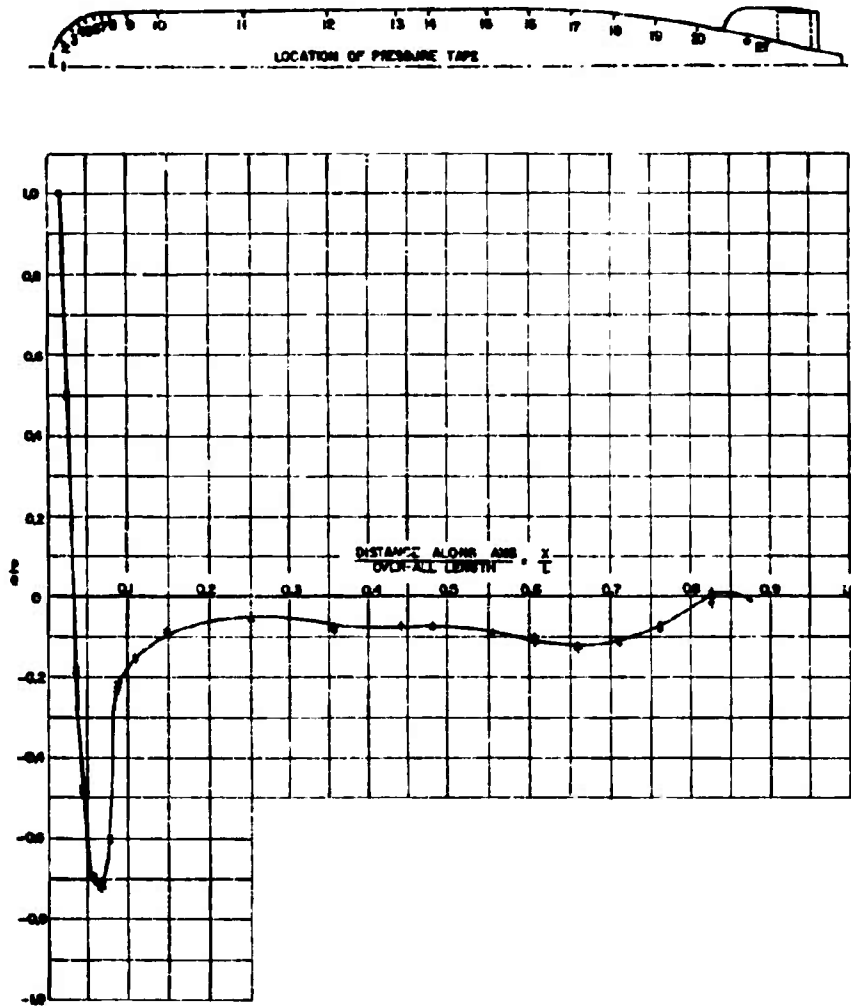


FIGURE 39. Mk 25 torpedo. Pressure distribution along longitudinal section at zero yaw.

on a longitudinal section at zero yaw. Figure 40 shows the effect of pitch or yaw on the pressure distribution in a plane at right angles to the plane of pitch or yaw. Figures 41 and 42 show the effect of pitch or yaw on the pressure distribution in the pitching or yawing plane, for the windward and lee sides of the Mark 14-1 torpedo. Figures 43 and 44 show the effect of pitch or yaw variation in pressure around the torpedo at points on the nose and afterbody.

These measurements show two interesting common characteristics. First, the pressure on the body sur-

face is higher than the static pressure in the undisturbed fluid, P_0 , only over a small portion of the nose and a small portion of the afterbody and tail. Everywhere else the pressure is less than P_0 . Second, over the cylindrical body section the magnitude of the relative pressure, p/g , is seemingly unaffected by body length and is only slightly affected by the kind of nose and hence by pressures ahead of the midsection. Figure 38 shows that with the same nose and afterbody shapes the pressure along the body cylinder of the Mark 14-1 and Mark 15-1 torpedoes is exactly

the same. Comparison of Figures 38 and 40 show that despite the very much greater reduction in pressure on the spherical tip of the Mark 25 torpedo, p/q along the cylinder is only -0.08 compared to -0.05 for the Mark 14-1.

The minimum value of p/q obtained at the nose is a function of the nose profile and the consequent curvatures and accelerations of the flow around it. Note that if the torpedo operates under a combination of velocity and submergence such that the minimum pressure P on the nose equals the vapor pressure P_v , then

$$\frac{p}{q} = \frac{P_v - P_0}{\frac{\rho v^2}{2}} = -K$$

where K is the cavitation parameter. Increasing numerical values indicate an increasing tendency for cavitation to occur early.

In the examples shown p/q increases gradually along the afterbody section to slightly positive values. The rate of increase and the final magnitude ob-

tained depends upon the profile and the tendency, if any, for the flow to separate from the body surface. These measurements are all for well-streamlined afterbodies so that there is no discontinuity in the curves up to the point where the pressure is influenced by the presence of the tail surfaces. Note the slight reduction in p/q , for all examples, caused by the sudden change in curvature at the transition from the cylindrical body to curved afterbody section.

Pressure distribution data on torpedoes are useful mainly for determining the best location and arrangement for the pressure intake to the hydrostatic diaphragm of the depth control mechanism. If this mechanism is to keep the torpedo at the set depth under all normal operating conditions, it is necessary that the pressure impressed upon the diaphragm be at all times equal to the static pressure of the undisturbed water at the actual running depth of the torpedo. This is best accomplished by locating the pressure intake to the hydrostat at a point on the body where the pressure at the surface, under all conditions of speed, yaw, and pitch, is equal to the

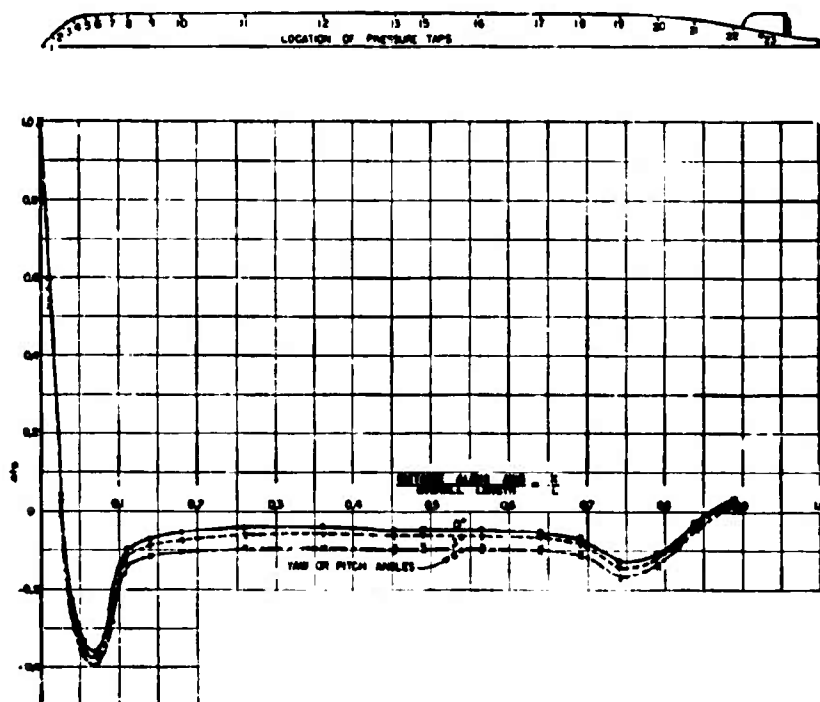


FIGURE 40. Mk 14-1 torpedo. Pressure distribution along longitudinal section at right angles to plane of yaw or pitch.

CONFIDENTIAL

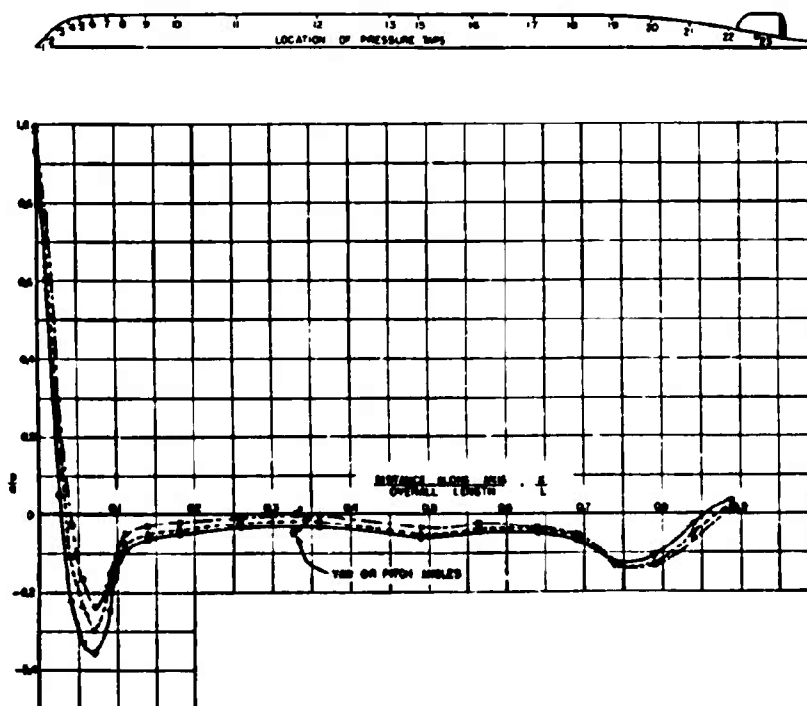


FIGURE 41. Mk 14-1 torpedo. Pressure distribution along longitudinal section in plane of yaw or pitch. Wharward side of body.

static pressure of the water. Also, the intake opening should be flush with the surface, at right angles to it, and with smooth edges. Experience has indicated that piezometer openings with slightly rounded edges (to a radius of about $\frac{1}{8}$ the bore diameter) are more accurate and reliable than sharp-edged openings.

With the pressure intake located where the pressure at the surface is not equal to the static pressure, the hydrostatic diaphragm would, for a given yaw or pitch angle, be actuated by a pressure which differs from true static by a fixed fraction of the velocity head. For a single-speed torpedo, the pressure impressed on the diaphragm would then differ from static pressure by a constant number of feet, and this can be taken into account in the calibration of the depth-setting mechanism. In a multispeed torpedo, this method of correction cannot be used since it would require a different calibration at each speed. Another method of correcting for mislocation of the pressure intake is to so design the intake that the

pressure transmitted to the diaphragm differs from the normal pressure at the surface by the required fraction of the velocity head. This can be done by drilling the pressure taps at some angle other than normal to the surface or by using scoops or baffles. These methods, however, are likely to be highly sensitive to changes in yaw or pitch.

The requirements outlined above in connection with the location and design of the pressure intake for the depth control mechanism apply also to the pressure intake for the hydrostatic diaphragm of the *depth and roll recorder* [DRR], if the instrument is to record true running depth.

Re-examination of the longitudinal pressure distribution curves shows that the pressure at the surface equals the static pressure ($p/q = 0$) at two stations on the body, one on the head and one on the afterbody. The transverse pressure distribution curves show that on the afterbody, in the region near the station where $p/q = 0$ (e.g., stations 21 and 22, Figure 44), the pressure is practically independent of

yaw or pitch. This position, therefore, meets the requirements for the location of the pressure intake for the depth control diaphragm. On the other hand, at the station on the forebody where $p/q = 0$, the pressure varies greatly with yaw or pitch (see stations 3 and 4, Figure 43). Therefore, it is not advisable to locate the intake to the DRR diaphragm at that station. Remote connection of the DRR to the position on the afterbody where $p/q = 0$ will probably be ruled out because of the physical difficulties involved. It appears, therefore, that the best procedure remains to determine the error of the DRR, and to apply a correction to the depth record obtained with the instrument in its present location.

It should be pointed out that unless the pressure intakes for both are located where the effect of pitch, yaw, and roll are negligible, the depth control mechanism and the depth and roll recorder should not be used as primary instruments to check each other, as in this case it is possible to have the torpedo run at some depth other than set depth and, at the same time, to obtain a depth record which indicates a run

at or near set depth. As has already been mentioned, the pressure over most of the surface of the torpedo is lower than static pressure (see Figures 38 to 42). It is possible that the pressures impressed on both depth control and depth and roll recorder diaphragms are lower than static pressure. In this case, the torpedo would run below set depth but the DRR would indicate a depth shallower than the actual running depth; thus the error may not be detected.

13.2.4

Cavitation

The general phenomenon of cavitation on underwater projectiles, and the similarity between the fully developed cavitation bubble and the entrance cavity of air-launched projectiles, were discussed in Chapter 4 of this volume. The effect of nose shape on the inception and development of cavitation is covered in Chapter 5. The effect of cavitation on the forces acting on the projectile is treated in Chapter 6, and Chapter 7 deals with the noise generated by cavitation on the underwater projectiles. For the purposes

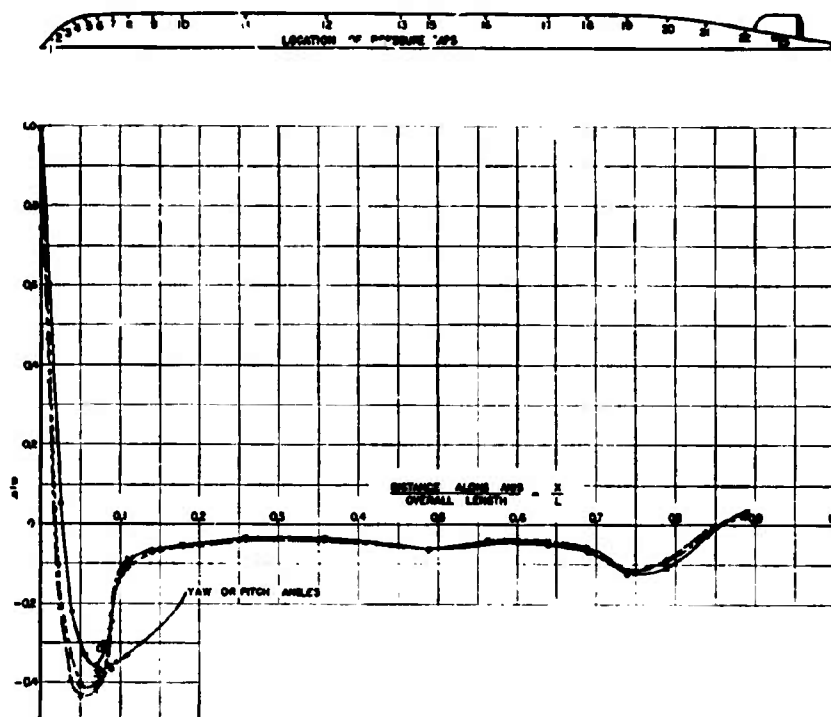


FIGURE 42. Mk 14-1 torpedo. Pressure distribution along longitudinal section in plane of yaw or pitch. Lee side of body.

CONFIDENTIAL

TABLE 4. Cavitation parameter K for incipient cavitation on nose and tail structure, and speed in knots at 5-ft submergence above which further cavitation will develop.

	Yaw angles in degrees		
	0	3	6
Mark 13-1 torpedo			
Cavitation on nose			
K for inception	0.73	0.81	0.89
Speed in knots at 5 ft submergence	34	33	31
Cavitation on tail structure			
K for inception	0.92	1.46	2.02
Speed in knots at 5 ft submergence	31	24	21
Westinghouse hydrobomb			
Cavitation on nose			
K for inception	0.31	0.37	0.41
Speed in knots at 5 ft submergence	52	48	46
Cavitation on tail structure			
K for inception	0.80	0.86	1.14
Speed in knots at 5 ft submergence	33	32	27
Mark 14-1 torpedo			
Cavitation on nose			
K for inception	0.34	0.36	0.38
Speed in knots at 5 ft submergence	50	48.50	47
Cavitation on tail structure			
K for inception	0.42	0.74	1.14
Speed in knots at 5 ft submergence	43	33.50	27
Mark 26-4 torpedo			
Cavitation on nose			
K for inception	0.38	0.38	0.44
Speed in knots at 5 ft submergence	49	49	46
Cavitation on tail structure			
K for inception	0.60	1.00	1.80
Speed in knots at 5 ft submergence	38	29	22

of this chapter, it is sufficient, therefore, to indicate the specific reasons for studying the cavitation characteristics of torpedoes in particular.

Cavitation on torpedoes during the normal part of the run is objectionable because of the sharp increase in drag with the development of cavitation, because of the detrimental effect on stability and control, and because of the noise generated by the formation and subsequent collapse of the cavitation bubbles. In addition, cavitation originating on the tail structure may spread to the propellers and interfere with their function. The various components of the torpedo should, therefore, be so designed that cavitation will not occur when operating under design speed and shallowest submergence normally used. This involves a study of the conditions leading to the inception of cavitation, which is normally carried out on each torpedo under investigation by this laboratory. A study of the size and shape of the fully developed cavitation bubble and its behavior when the projectile is yawed is also useful in understanding the behavior of aircraft torpedoes while in the entrance bubble.

The noses and forebodies of torpedoes running at underwater speeds up to 50 knots and even higher offer no difficult problems in design to avoid objectionable cavitation. The tail structures, particularly the leading edges of the stabilizing fins and the attachments forming the supports for the rudder pivots, usually develop cavitation at lower speeds for a given submergence than the nose. At the higher speeds, unless set to run at considerable depth, the cavitation on parts of the tail structure may be sufficient to interfere seriously with the action of the rudders and propeller. Table 4 shows, for several of the torpedoes investigated, the speeds, at 5 ft submergence, that are permissible to avoid nose or tail cavitation altogether. Considerably higher speeds, at the same submergence, are permissible before there is serious interference with steering or stability. This is illustrated by Figure 45 which shows, at 3° yaw, the visual appearance of cavitation on the Westinghouse hydrobomb at successively lower K values of 0.34, 0.29, 0.25, and 0.18 corresponding respectively to speeds at 5-ft submergence of 50, 54.5, 58.5, and 69 knots. At 50 knots, there would probably be a high

level of cavitation noise, but no interference with rudder effect. At 54.5 knots the cavitation effects on the afterbody might affect the rudders and be sufficient on the forebody to increase the drag and affect the stability. The higher speeds, corresponding to the two lowest K values doubtless could not be obtained in underwater propulsion because of greatly increased drag and the entire change in hydrodynamic characteristics.

12.1.5 Specific Modifications

Several investigations were made to determine the effect on the hydrodynamics of certain torpedoes resulting from various modifications of their external

shape. Some of these modifications were suggested by this laboratory or by others to overcome some undesirable characteristic such as high drag or insufficient stability, while other modifications were designed to meet some requirement apart from hydrodynamic considerations as, for example, suspension fittings designed to facilitate the installation of torpedoes in aircraft, or a modification of the exhaust gas discharge system. In these latter cases, the studies made in this laboratory were concerned with the possible effects of such modifications on the hydrodynamics of the torpedo.

The most fruitful in this group of investigation was the one which led to the addition of the shroud ring to the tail structure of the Mark 13 series torpedoes.

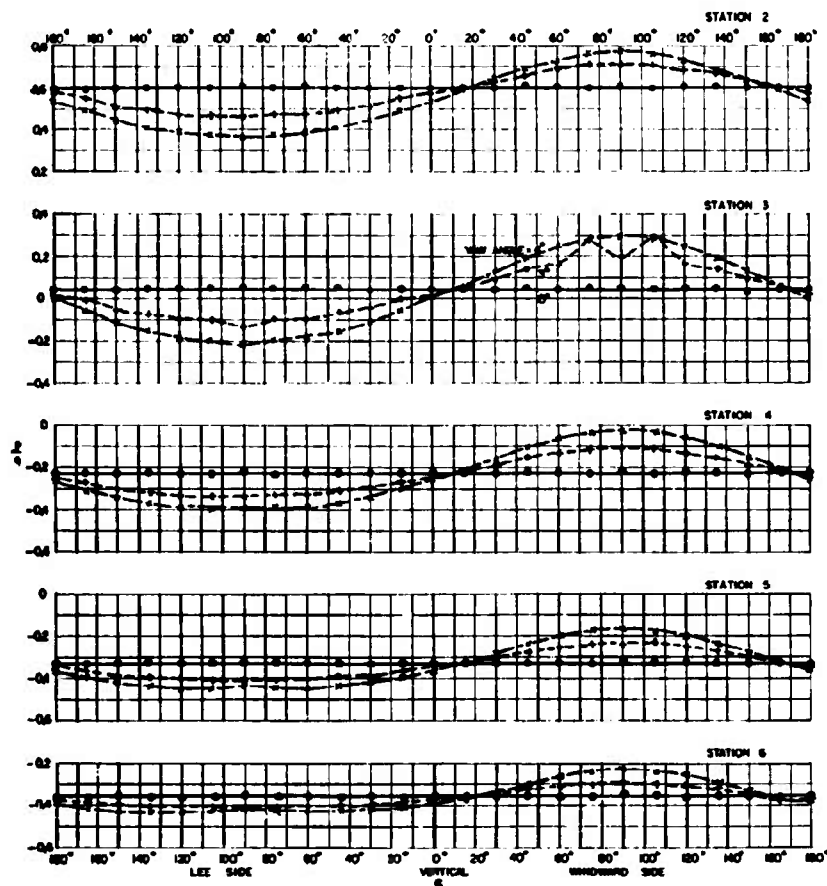


FIGURE 43. Mk 14-1 torpedo. Pressure distribution about normal cross section. Stations on forward part of nose.

CONFIDENTIAL

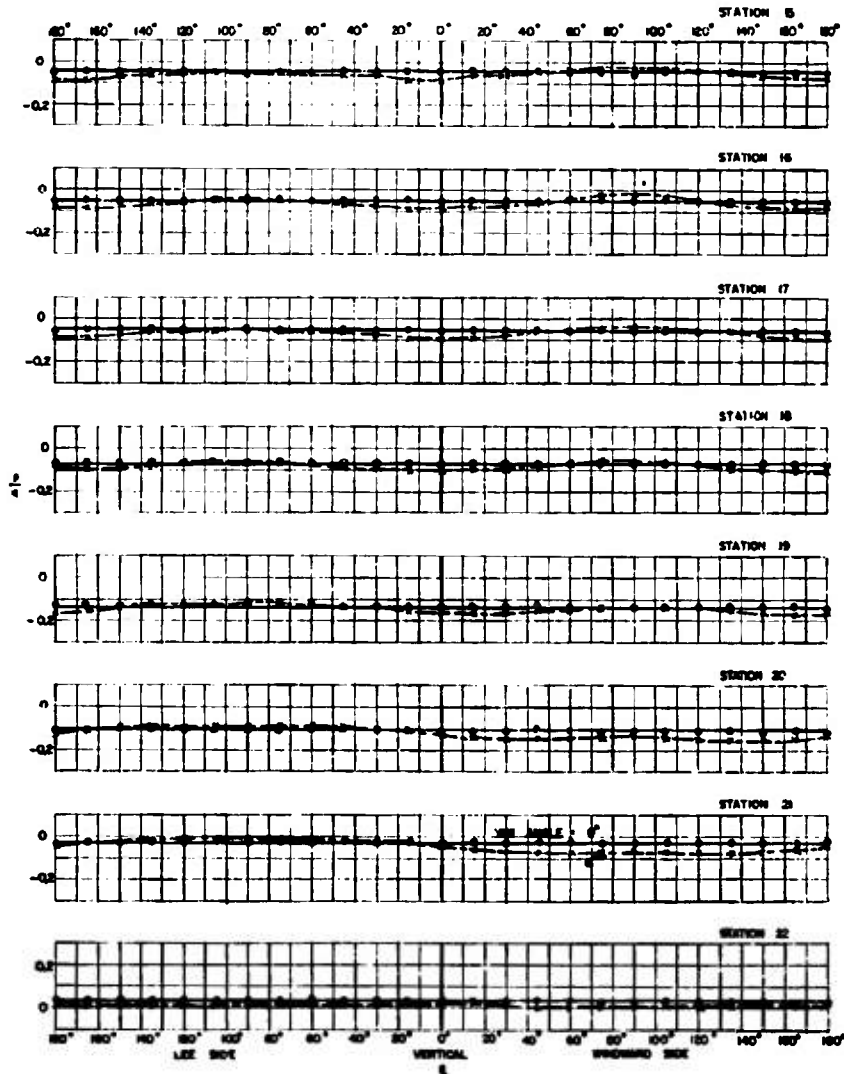


FIGURE 44. Mk 14-1 torpedo. Pressure distribution about normal cross section. Stations on afterbody.

Prior to this modification, these torpedoes ran somewhat erratically, in that they often broached and hooked after entering the water, and had a periodic roll of considerable amplitude and a wavy depth line during the steady run. A preliminary study of the hydrodynamic characteristics of these torpedoes indicated that the broaching might be due to excessive instability with a consequent short turning radius and could be corrected by the addition of a shroud

ring. This laboratory then investigated a systematic series of shroud rings for these torpedoes and recommended one of the designs tested. A model with this ring is shown in Figure 46. This ring was installed on full-scale torpedoes which were fired at the Morris Dam Launching Range, and showed less tendency to broach and roll. Later test drops from aircraft at San Diego and at Newport confirmed these findings and the shroud-ring tail was finally adopted.

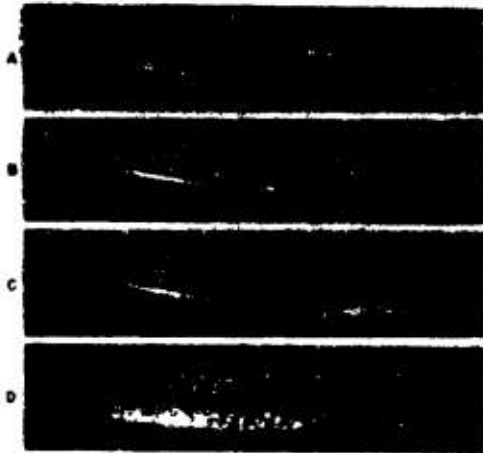


FIGURE 45. Westinghouse hydrobomb. Development of cavitation at 3 degrees yaw. (A) $K = 0.34$, 50 knots at 5 feet submergence. (B) $K = 0.29$, 54.5 knots at 5 feet submergence. (C) $K = 0.25$, 58.5 knots at 5 feet submergence. (D) $K = 0.18$, 69 knots at 5 feet submergence.

The addition of a shroud ring to the tail fins of a torpedo modifies the hydrodynamic characteristics of the torpedo in several ways.

First, by increasing the tail surface area, the cross force at any angle of attack is increased. Since this increment of cross force is concentrated at the tail, it is evident that the resultant moment increment is a stabilizing one. Therefore, a torpedo with ring tail usually has less static instability than the same torpedo without ring. By the same reasoning, it may be concluded that the ring tail also increases the dynamic stability.

Second, the ring usually decreases the roll amplitude and thereby reduces cross steering.²⁴ This is accomplished both by the increased resistance to roll due to the additional skin friction of the ring itself, but, mainly, by the increased effectiveness of the fins due to the prevention of circulation around their outer edges where they are covered by the ring. With reduced cross steering and increased stability, a smoother trajectory with respect to both course and depth line is obtained.

Third, if the ring is so placed that it overlaps the rudders or comes very close to them, it may cause a change in the effectiveness of the rudders. This may, in some cases, be detrimental to control; in all cases this and the increased stability result in larger turning radii. In the case of the Mark 13 series torpedoes,

the shroud ring reduced the static instability to about one-half of its value without ring and the rudder effect to about 62 per cent of its former value.²⁵ This did cause an increase in turning radius²⁶ but improved the overall performance on straight runs.

Fourth, if the ring is so designed that it fits the flow lines about the afterbody of the torpedo, it should cause no appreciable increase in the drag. As a matter of fact, the ring may even reduce the drag somewhat by improving the flow around the afterbody and by preventing separation. An improperly designed ring, however, may cause an appreciable increase in drag and a consequent reduction in speed.

On the Mark 26 torpedo, several modifications of the tail structure, as suggested by this laboratory, were investigated by model tests (see Figures 18 to 21). The original design embodied a shroud ring, but the limitation imposed, i.e., the reduced diameter, and the necessity of locating the ring forward of the rudder supports, were such as to place the ring too close to the afterbody and to cause it to interfere with the rudder effect. No beneficial action could be attributed to the ring, as was evidenced by the results



FIGURE 46. Model of Mark 13-1 torpedo with shroud ring tail.

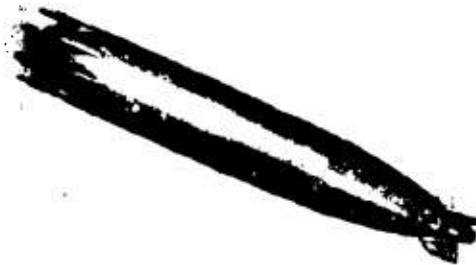


FIGURE 47. Model of Mark 13-1 torpedo with 8 spades.

of tests on the same model with the ring omitted. Also the original design had eight stabilizing fins, all considerably longer than on similar torpedoes which

were known to operate successfully. Models with four of the eight fins removed, and one with the four remaining fins shortened were made and tested with the result that the last model, with the four shortened

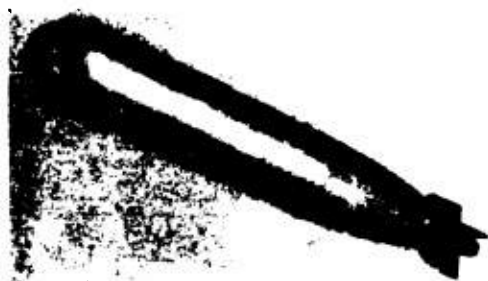


FIGURE 48. Model of Mark 13-1 torpedo with hemispherical nose and stabilizer ring.

fins, showed hydrodynamic properties that indicate satisfactory running performance together with simpler fabrication in the prototype.

Other specific modifications investigated were various modifications of nose shapes on the Mark 13 torpedo and attachments to the nose of various devices intended to improve the water-entry behavior.



FIGURE 49. Model of Mark 13-2A torpedo with suspension band Mark 11.

Two examples are shown in Figures 47 and 48. The effects of various suspension attachments to aid in aircraft launching were also investigated for the Mark 13. One version tested is shown in Figure 49.

Numerous arrangements for discharging exhaust gases from the tail structure of the Mark 25 torpedo were studied, especially noting the cavitation performance and the combined effects of cavitation and gas exhaust on the action of the rudders and propeller. For the latter tests, a power model was tested in which the propeller was rotated at speeds corresponding to the propeller speed of a full-size torpedo.

Chapter 14

ROCKETS AND OTHER NONROTATING PROJECTILES WITH STABILIZING SURFACES

14.1 GENERAL FEATURES

VARIOUS FORMS of stabilizing surfaces applied to nonrotating projectiles were discussed in Chapter 9. The general statements of principles therein presented apply to stabilizing surfaces on rockets, although the selection of the particular form of these surfaces is subject to some necessary limitations and qualifications on account of the inherent properties of rocket projectiles.

The shape of a fin-stabilized rocket and consequently its external ballistics vary according to the combination of the several components making up a rocket, namely, the explosive charge, the rocket motor, and the stabilizing device. The rocket motor shape depends on the size and type of the explosive charge and on the velocity required. The best form for the stabilizing device depends on the proportions of the charge and motor and the method of launching. For tube-launched projectiles the maximum dimension of any component must be limited to the bore of the tube. One result of this is the folding-fin type of tail. For rack-launched units no such restrictions are necessary. If the combination of charge weight and range is such that a relatively small motor is necessary, it can be housed in a small diameter boom extending aft from the main charge. Tail surfaces attached to such a boom were found in Chapter 9 to be very effective so that, in general, the maximum tail span or diameter can be held to a small dimension. On the other hand, a projectile requiring a motor of the same diameter as the main charge introduces limitations in the stabilizing tail proportions. Interference from the body reduces the tail effectiveness so much that, in general, such units require tail spans exceeding the projectile diameter.

The various fin-stabilized rockets tested in the laboratory were for a wide range of application and consequently included all types of shapes and arrangements of components. In the following sections will be reviewed briefly the various fin-stabilized rockets tested by this laboratory which are fairly representative of the varieties of rockets now in use. Profile diagrams of these rockets are shown in Figure 1.

14.2 7.2-INCH CHEMICAL ROCKET

The following physical data apply to this projectile:

Body and ring tail diameter	7.2 in. = 1 caliber
Ring tail length	4.0 in. = 0.55 caliber
Overall length	45.25 in. = 6.3 calibers
Weight without propellant	47.9 lb
Explosive charge	19.5 lb
Distance, nose to CG, the center of gravity (without propellant)	0.391 × length
Moment of inertia about CG	
Without propellant	35.7 lb-ft ²
Radius of gyration	1.167 ft
Velocity	680 fps

This rocket is a good example of one having a ring tail no larger in diameter than the body of the projectile. In effect the ring tail is mounted on a greatly extended boom. As discussed in Chapter 9, the mounting of the tail on a boom will increase effectiveness of the tail surfaces and, hence, the static stability.

In Figure 1 is shown the outline of the original design of this rocket.²⁷ Many tests were made to determine whether the addition of fins to the ring tail would increase stability. Three of the fin and ring tails, as well as the original design, are shown in the photographs in Figure 2. Figure 3 gives the cross force, drag, and moment coefficients for these four tail designs.

From the curves it is seen that the addition of fins increases the stabilizing moment from 20 to 50 per cent. The great increase obtained with tail No. 67 is due to the additional length as well as to the fin surfaces. It is interesting to note that tails No. 68 and 62 have about the same stabilizing moment coefficient, showing that when fins are extended forward, the increase in moment is not at all proportional to the increase in fin surface.

14.3 5-INCH HVAR ROCKET

The following physical data apply to this projectile:

Overall length	68.60 in. = 13.64 calibers
Maximum diameter	5.03 in. = 1 caliber
Outside diameter of fins	15 in. = approx 3 calibers
Length of fins	8 in. = approx 1.6 calibers

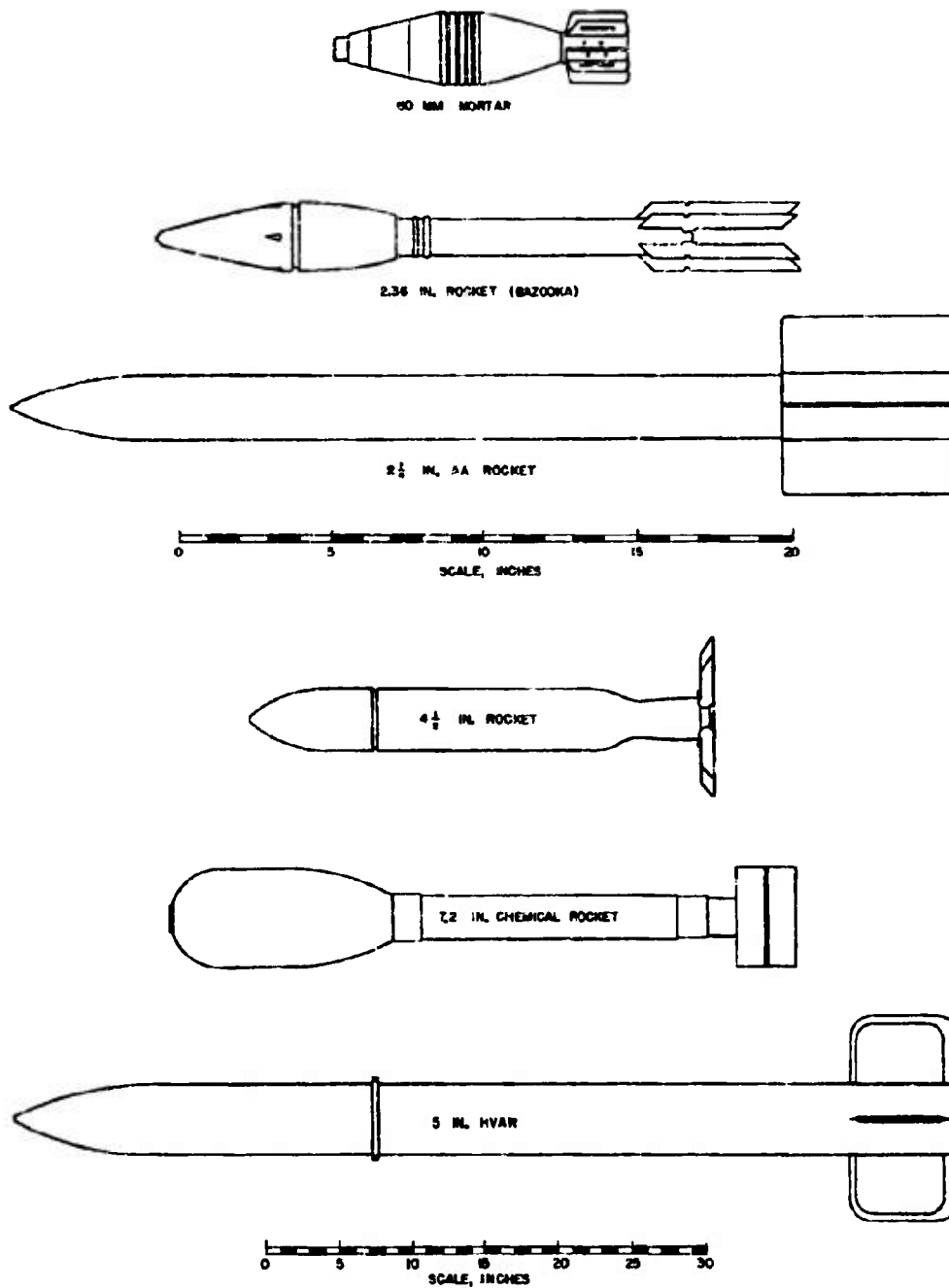


FIGURE 1. Outline drawings of fin-stabilized rockets.

CONFIDENTIAL

Loaded weight	136.5 lb
Weight without propellant	112.5 lb
Radius of gyration	1.82 ft
Velocity	1,375 fps
Distance, nose to CG	0.467 × length

As will be seen in the outline drawing, Figure 1, this rocket²³ is a bullet-shaped projectile with fins having a span greater than the body diameter. This is a most effective way to obtain a high stabilizing moment. The tests indicate that the moment increases much more rapidly with increasing span of the fins than with increasing fin length. This point is clearly illustrated in Figure 1 of Chapter 9 which shows the variation in moment coefficient with in-



FIGURE 2. Ring and fin tails, 7.2-in. chemical rocket; reading down, tail 61, 62, 67, 68.

creasing fin span and length. These curves indicate that practically no increase in stability is obtained by extending the fin length forward more than 1½ calibers.

Eleven ring tails of widely differing proportions were tested in order to determine their performance compared to the fin tails. The ring type of tail has many advantages, especially from the standpoint of mechanical strength and smaller physical dimensions. In Figure 4 of Chapter 9 are given the moment coefficients for ring tails having diameters of 1.5, 2.0, and 2.5 calibers, and lengths up to 2.5 calibers. These curves show how rapidly the moment increases with increasing ring diameter and also that little increase in stability results from making the ring length more than one-half the ring diameter.

In order to show more graphically the comparison of fin and ring tails, Figure 4 has been prepared. This gives the dimensions of fin and ring tails of different proportions, each of which produces the same moment coefficient. Figure 5 is a photograph of a ring tail and a fin tail for the 5-in. HVAR rocket which produce the same moment coefficient. These draw-

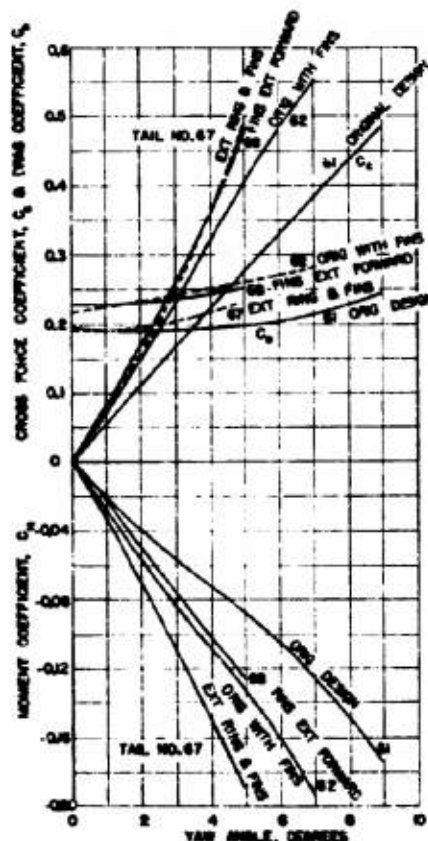


FIGURE 3. Force and moment coefficients; 7.2-in. chemical rocket.

ings show very clearly that the ring-tail design is more compact.

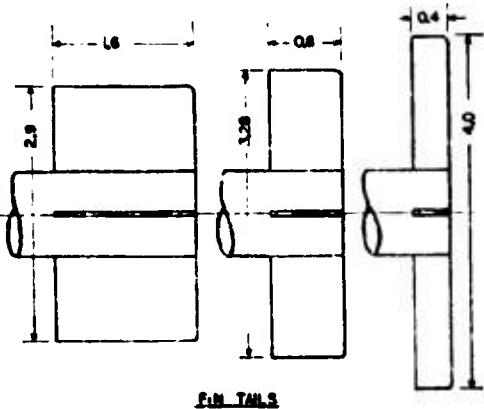
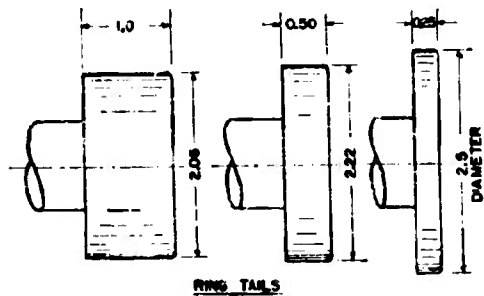
4.4 4½-INCH ROCKET PROJECTILE

The original design of this rocket^{24,25} is shown in Figure 1 and in the photograph of Figure 6. The blunt afterbody was fitted with six collapsible fins which produced a fairly high stabilizing moment. As

this rocket was to be launched through a tube, the maximum fin span or ring diameter of the tail could not exceed the body diameter. For this reason collapsible fins were used. An alternate collapsible-fin design is shown in Figure 7.

It was felt that the reliability of the rocket could be increased if it could be stabilized by fixed surfaces-

In order to divert more of the flow through the ring, and thereby increase the stability, a ring tail 1.0 caliber in diameter and 0.75 caliber long was



ALL DIMENSIONS IN CALIBERS
MOMENT COEFFICIENT FOR ALL TAILS = 0.225
YAW ANGLE = 3°
OVERALL LENGTH = 0.64 CALIBERS

FIGURE 4. Fin and ring tails all having the same moment coefficient.

instead of the collapsible fins. As the ring type of tail seemed to offer the most possibilities, considering the limitations imposed by tube launchings, several of these designs were tested. Tail No. 24, shown in Figure 8, consisted of a 1.0-caliber diameter ring 0.89 calibers long mounted on four vanes extending not far from the blunt afterbody. Tests indicated that the projectile was unstable with this tail due, no doubt, to the blunt afterbody preventing the diversion of much of the flow through the ring.



FIGURE 5. Ring and fin tails for the 5-in. HVAR giving equal moment coefficients.



FIGURE 6. Four and one-half-inch rocket with No. 10 collapsible fin tail.

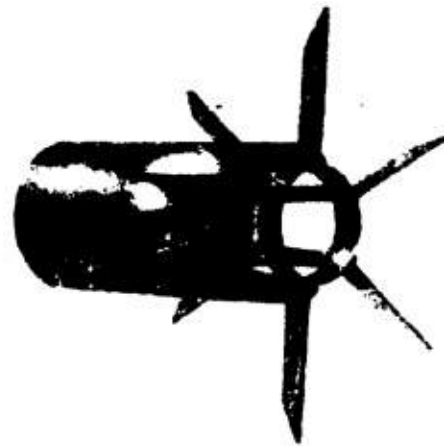


FIGURE 7. No. 25 collapsible fin tail for 4.5-in. rocket.

mounted on booms of various lengths. Figure 9 shows this ring tail mounted on a boom 1.5 calibers in length. Many other combinations of ring, boom, and

fins were tried, but the arrangement shown in Figure 9 gave the greatest stability.

In Figure 10 are shown the drag and moment co-

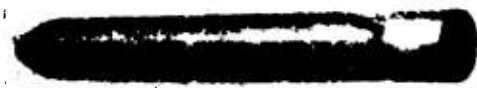


FIGURE 8. Four and one-half-inch rocket with No. 24 ring tail.

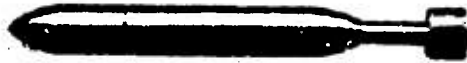


FIGURE 9. Four and one-half-inch rocket with ring tail 0.75 caliber long on boom 1.5 calibers long.

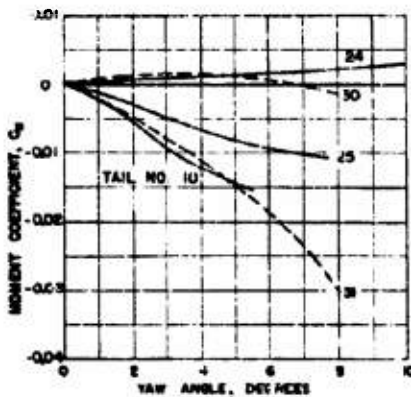
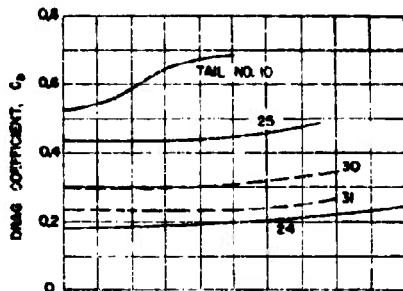


FIGURE 10. Drag and moment coefficients; 4.5-in. rocket with various tails.

efficients for the projectile fitted with the original fin tail (No. 10), the fin tail attached by means of vanes (No. 25), the ring 0.89 caliber in length attached with fins (No. 24), the ring 0.75 caliber in length without a

boom (No. 30), and the same ring attached to a boom 1.31 calibers in length (No. 31). These curves emphasize the fact that a ring tail of the same diameter as the projectile body, if mounted too close to the after-body, will produce little if any stabilizing moment

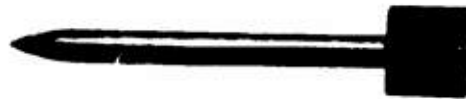


FIGURE 11. Two and one-quarter-inch AA rocket.

By mounting the ring on a boom, a good degree of stability can be obtained. It is seen from Figure 10 that a ring 0.75 caliber long will produce practically

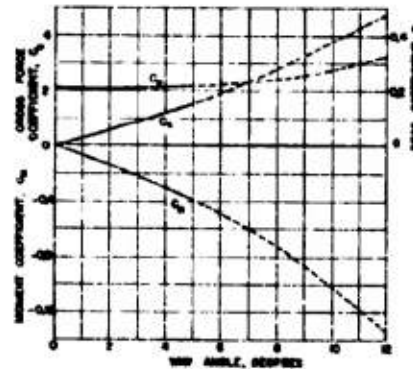


FIGURE 12. Force and moment coefficients; 2 1/4-in. AA rocket.

the same stabilizing moment as the long-span collapsible fins (Tail No. 10) if it is mounted on a boom a little over 1 caliber in length.

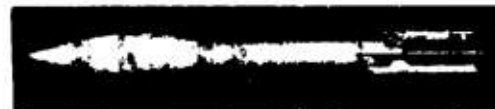


FIGURE 13. Original design of 2 3/8-in. rocket. Conical nose and fixed fin tail.

24.5

2 1/4-INCH AA ROCKET

The 2 1/4-in. AA rocket,²⁶ shown in Figures 1 and 11, is similar in design to the 5-in. HVAR rocket in that the fins are attached directly to the bullet-shaped body. The physical data of this rocket are as follows:

Overall length	14.5 calibers
Fin span	2.8 calibers
Fin length	2.5 calibers
Velocity	680 fps

The moment, drag, and cross force coefficients for this projectile are given in Figure 12. It is of interest to note that the curves in Figure 1 of Chapter 9, which show the moment coefficients for a family of fin tails for the 5-in. HVAR projectile, give practically the identical value for the moment of a tail having the dimensions just noted above.

16.8 2.36-INCH ROCKET (THE BAZOOKA)

Many tests were made on models of this rocket,^{20, 27-29} which is the well-known bazooka, in order to determine the effect on performance of various types of fin and ring tails as well as different nose shapes. In addition to the outline drawing in Figure 1, photographs of various modifications are shown in Figures 13, 14, and 16. This is a low-velocity, short-range rocket launched from a tube, and for these reasons the drag is relatively unimportant and tail design must be such that it will not exceed the body diameter. Figure 13 is a photograph of the original design of this rocket with conical nose and fixed-fin tail.

Five designs of collapsible-fin tails, as shown in Figure 14, were tested. These were similar in that they consisted of six fins that could fold for passing through the launching tube and which opened in flight. These five tails had the following dimensions:

Tail number	Span of unfolded vanes in inches	Vane angle back from radial
1	5 $\frac{1}{4}$	5°
2	7 $\frac{1}{4}$	5°
3	5 $\frac{1}{4}$	40°
4	8	40°
5	9.19	28°

Table 1 gives the data available on the force coefficients for these collapsible-fin tails compared with the original fixed-fin tail.

TABLE 1. Force and moment coefficients for 2.36-in. rocket with various fin tails.

Tail	Drag coefficient C_D at 0° yaw	Cross force coefficient C_C at 4° yaw	Moment coefficient C_M at 4° yaw
No. 1	0.52	0.23	-0.020
No. 2	0.95	-0.022
No. 3	0.76
No. 4	0.77
No. 5	0.42	0.37	-0.092
Original fixed fin	0.30	0.16	-0.004

The remarkable increase in the stabilizing moment obtained with the collapsible fins is in accord with the discussion in Chapter 9 where it was shown that the stability increases very rapidly with increase in fin span. As would be expected, the collapsible fins cause a great increase in drag, but this is of relatively

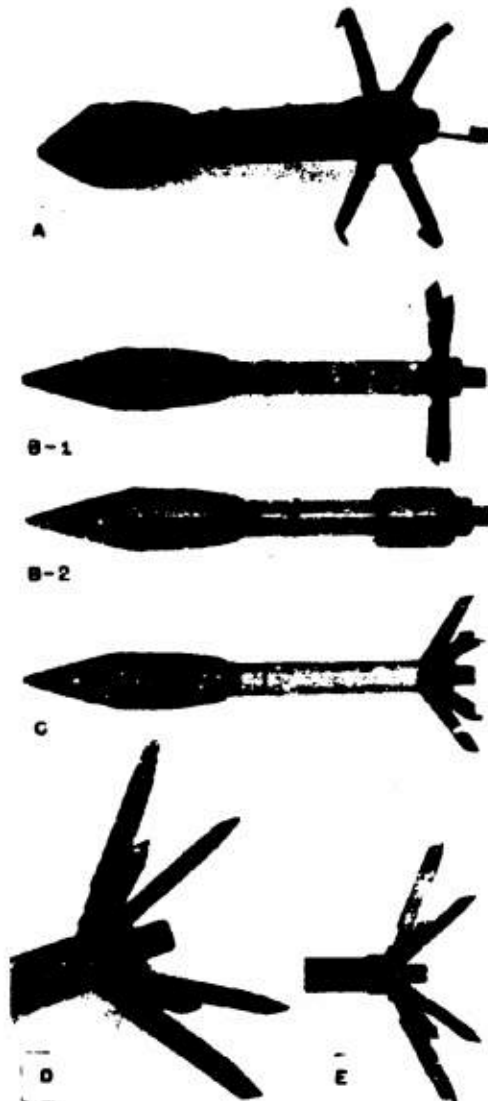


FIGURE 14. Collapsible fin tails, 2.36-in. rocket. (A) Tail No. 1, (B) tail No. 2, (C) tail No. 3, (D) tail No. 4, (E) tail No. 5.

little importance because of the short range of the rocket.

Partly on account of the high drag, but largely because of the mechanical complication and fragility of the collapsible fins, an effort was made to design a

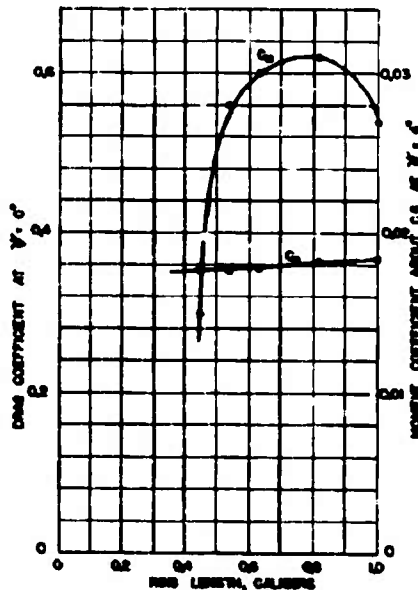


FIGURE 15 Drag and moment coefficients versus ring length; 2.36-in. rocket.

ring tail that would provide the required stability. The ring tails considered were of two types: One had streamlined leading and trailing edges on the ring as well as streamlined propellant nozzles, while the other was made of commercial grade stampings and channel shapes. A series of tests was also run to determine the effect of the length of the ring on performance.

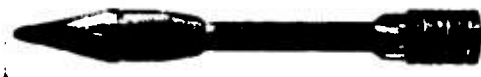


FIGURE 16. Variation in length of ring tail; 2.36-in. rocket.

In Figure 15 are given the drag and moment coefficients for a series of rings varying in length from $1\frac{1}{8}$ to $2\frac{3}{8}$ in. or from 0.45 to 1 caliber. There is a very rapid increase in moment as the ring length increases from 0.45 caliber until the maximum stability

moment is reached at a ring length of 0.8 caliber. The drag decreases only about 5 percent as the length of the ring is reduced from 1.0 to 0.45 caliber. Figure 16 is a photograph of the model showing the variations in the length of the ring tails in this series.

Of all the ring tails tested, the three types of construction that gave the highest stabilizing moment are those shown in Figure 17. Descriptions of their



FIGURE 17. Rocket (2.36-in.). Three types of construction giving high stabilizing moments. (A) Tail No. 21, (B) tail No. 35 (construction identical to No. 32 but shroud ring length = 0.51 caliber), (C) tail No. 47 (construction identical to No. 48 but shroud ring length = 1.19 calibers).

construction differences, as well as the results of the tests, are shown in Table 2. Note that tail No. 21 as tested is identical to the photograph of Figure 17A. Tails No. 32 and 48 as tested are the same as shown

TABLE 2. Force and moment coefficients for 2.36-in. rocket with three good ring tails and original fixed-fin tail.

Tail description	Ring length in calibers	Drag coefficient C_D at 0° yaw	Cross force coefficient C_C at 4° yaw	Moment coefficient C_M at 4° yaw
No. 21 Streamlined nozzle, ring and vanes	1	0.17	0.19	-0.013
No. 32 Plain ring, channel-shaped vanes and stepped nozzle	0.82	0.37	0.19	-0.034
No. 48 Plain ring, channel-shaped vanes, and plain boom nozzle	0.82	0.22	0.22	-0.048
Original fixed fin	0.30	0.16	-0.004

in Figures 17B and C except that the length of the shroud ring was 0.82 caliber for each.

Only one of the above ring tails has a higher drag than the original fixed-fin tail and two of them have considerably less drag. There is not much change in the cross force but the increase in moment due to the ring tails is very great, varying from three to twelve times that of the original tail. Comparing Table 2 with Table 1, it is seen that the drag, in general, is considerably less for the ring tails than for the collapsible-fin tails, and the stabilizing moment is of about the same order.

Diameter	2.362 in. = 1 caliber
Overall length	9.54 in. = 4+ calibers
Distance, nose to CG	0.49 × length
Weight as fired	2.90 lb
Velocity, cartridge only	225 fps
Range at 45°, cartridge only	488 yd
Velocity, cartridge plus 4 wafers	518 fps
Range at 45°, cartridge plus 4 wafers	1,984 yd

Figure 3 in Chapter 9 shows the force coefficients with the fin tail mounted on booms of various lengths. The material increase in stability which can be obtained by using a boom with a fin or ring tail is very apparent in this case.

It was thought that the extended boom might be

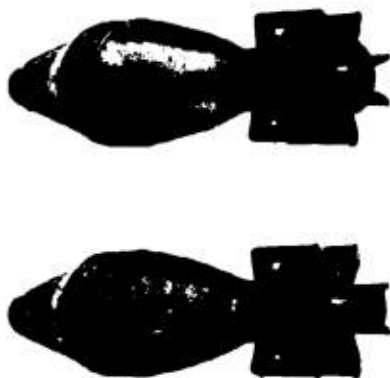


FIGURE 18. Mortar projectile (60 mm) with plain and notched disk behind tails.

14.7 60-MM MORTAR PROJECTILE

Although the 60-mm mortar projectile²⁴ is not properly a rocket, it is somewhat similar in design and performance and a brief description of it is therefore included here. An outline drawing of the mortar is shown in Figure 1, and a photograph is shown in Figure 2 of Chapter 9. This projectile is fired by dropping it into the mortar tube. When it strikes the bottom of the mortar, a cartridge in the aft end of the projectile is ignited, thus projecting the missile. Greater velocity and range are obtained by attaching wafers of powder to spring clips provided on the tail fins.

The following physical data pertain to this projectile:

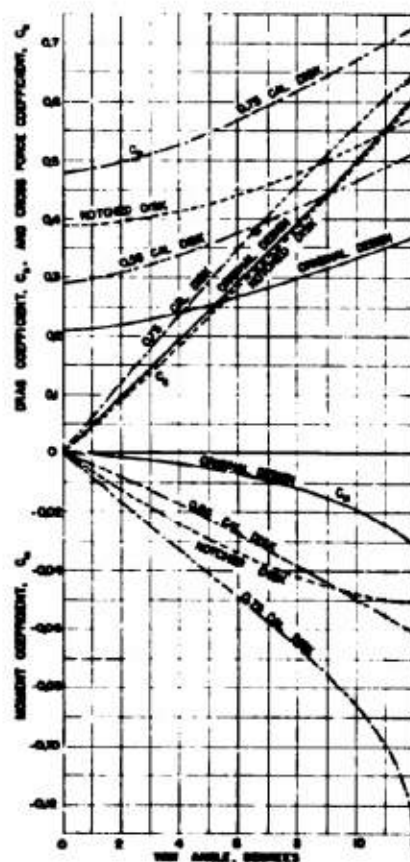


FIGURE 19. Drag and moment coefficients; 60-mm mortar projectile. Fin tail with disks.

objectionable, so other means for increasing stability were sought. The installation of a disk immediately aft of the fins proved to be quite effective. While this illustrates the fact that, in many cases, the stabilizing moment can be increased by increasing the drag, it should be noted that the large gains obtained here are



FIGURE 20. Mortar projectile (60 mm). Flow line drawing for original tail design.

not due to drag alone but to an added cross force as well. Figure 18 shows the model with a plain and a

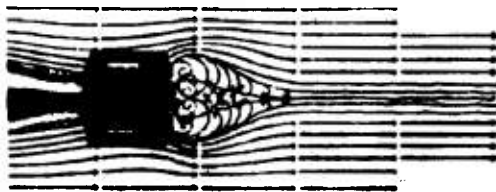


FIGURE 21. Mortar projectile (60 mm). Notched disk behind tail.

notched disk, both of which greatly increased stability. In Figure 19 are given the force coefficient curves for this projectile with the original fin tail, also with the addition of plain disks 0.56 and 0.75 caliber in diameter, as well as a notched disk. From these curves it is seen that at small yaw angles the disk 0.75 caliber in diameter increases the drag about 120 per cent while the moment coefficient is increased 700 per cent. The corresponding figures for the 0.56-caliber disk are 75 and 330 per cent.

The flow line drawings of this projectile show very clearly the effect of the added disks. Figure 20 is the flow line drawing of the prototype in which is seen the typical disturbance in the wake of the blunt boom on which the fins are mounted. The great increase in disturbance caused by the disks is indicated in Figures 21 and 22, showing the 0.56-caliber and notched disks. This added disturbance caused by the disks is consistent with the observed increase in drag.



FIGURE 22. Mortar projectile (60 mm) with 0.56-caliber disk behind tail.

Chapter 15

SPIN-STABILIZED ROCKETS

GENERAL FEATURES OF SPINNER ROCKETS

TWO DISTINCT MEANS are used to give stability to a rocket. In one case fins, or other stabilizing surfaces, are attached to the outside of the rocket body or else mounted on a boom aft of the body; in the other no stabilizing surfaces are used, the stability being achieved solely by the spinning of the rocket as with a rifle bullet. With spin-stabilized rockets the spin is imparted to the projectile by setting the propellant nozzles at a definite angle with its axis. When stabilizing fins are used, the propellant is generally discharged through a single axial nozzle. As a rule, spin-stabilized rockets operate at velocities ranging from a little below sonic (700 or 800 fps) to 1,500 fps or more.

With increasing velocity, drag has an increasing effect on the range of a projectile. Consequently, it is important to reduce the drag by maintaining as smooth a body shape with as few projecting surfaces as possible. This is particularly true for velocities near sonic where compressibility effects become important. In these cases spin stabilization with the elimination of tail surfaces is advantageous.

15.1.1 Effects of Propellant Burning

It is easily seen that as the propellant is used up, the rocket weight and center of gravity location are changed with a resultant change in its behavior during flight. This must be taken into account in designing the projectile and some effort has been made to reduce the effects of propellant consumption to a minimum as in the case of the 15-cm German spinner shown in Figure 5. With this rocket the propellant nozzles are located around the offset in the body, ahead of the main charge. In general the propellant burning time is of the order of 1 sec. Any effect on stability due to changing weight or shifting of the center of gravity *CG* or any effects on the yaw and lateral displacement due to malalignment of nozzles will be felt during this accelerating period. If the propellant is consumed before the rocket

has left the launcher, these effects will be largely eliminated.

15.1.2 Applicability of Water Tunnel Tests

Water tunnel tests are valid for air-flight projectiles operating at velocities in the range where the air may be assumed to be incompressible. This range extends to about 750 fps or somewhat below sonic velocity. As spin-stabilized rockets generally have velocities greater than this, the water tunnel tests will apply directly only to the portion of the accelerating period below a velocity of 750 fps. This accelerating period is quite important in determining the performance of the projectile during its subsequent flight because the dispersion of the projectile is dependent on the type of oscillatory motion set up initially. Water tunnel data can be used to calculate the period of oscillation of a projectile in subsonic flight as well as the maximum lateral displacement during an oscillation.

15.1.3 Hydrodynamic Characteristics

Spin-stabilized rockets are usually plain bullet-shaped bodies with ogival noses and blunt ends. The hydrodynamic forces on such bodies are discussed in Chapter 8 and generalized conclusions are given there. The salient features of drag, cross force, and moment are summarized briefly as follows:

1. The drag coefficient for a wide variety of bullet-shaped bodies has a moderate value in the neighborhood of 0.25.
2. The cross force coefficient increases approximately linearly with yaw.
3. The moment about the center of gravity is generally destabilizing, although on some projectiles, depending on the nose and afterbody shapes, there may be a slight stabilizing moment for yaws of about 1° or less.

The latter result is important since, if the rocket is spin-stabilized, it is desirable to eliminate this slight stability near zero yaw. Tests of modifications of specific rockets showed that this can be accomplished by changing the type of nose or by streamlining the afterbody.

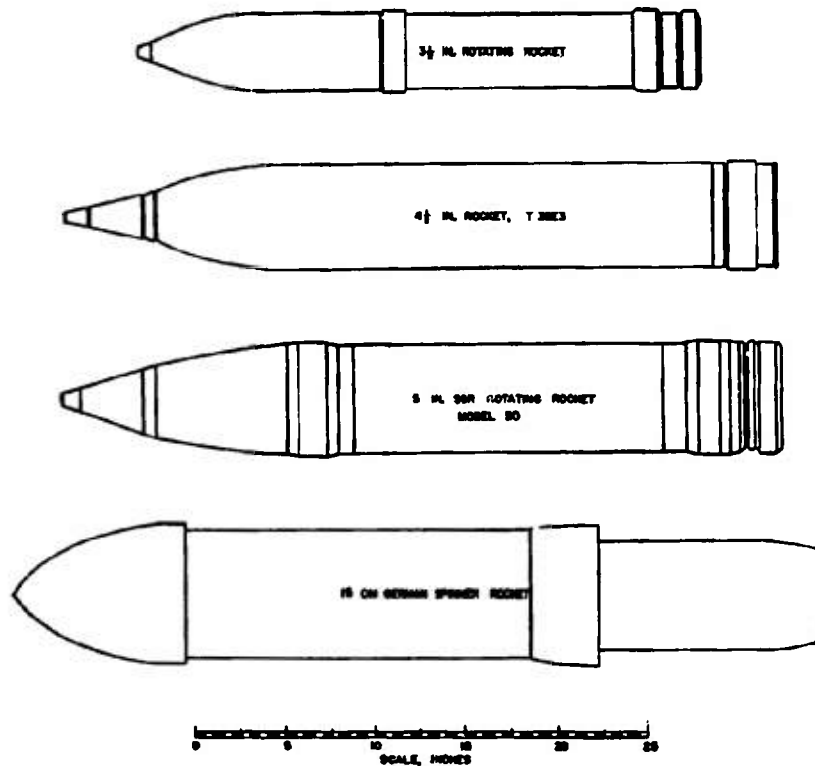


FIGURE 1. Outline drawings of spin-stabilized rockets.

15.2 REVIEW OF SPECIFIC TESTS

The rockets investigated included the 3.5-in. rotating rocket; the 4.5-in. T38E3 rocket; the 5-in. SSR rotating rocket, and the 15-cm German spinner rocket. Outline drawings of these are shown in Figure 1. A review of their specific characteristics follows.

15.2.1 3.5-in. Rotating Rocket

This rocket^{60,61} has the following physical characteristics (without propellant):

Diameter	3.5	in. = 1 caliber
Overall length	24.87	in. = 7+ calibers
Distance, nose to CG	0.443	X length
Rotation	181	rps
Transverse moment of inertia	7.25	lb-ft ²
Transverse radius of gyration	0.576	ft
Polar moment of inertia	0.285	lb-ft ²
Polar radius of gyration	0.117	ft
Weight in flight	21.75	lb
Velocity	760	fps

Figure 2 is a photograph of this rocket and Figure 3 shows several types of afterbodies that were tested. The extent to which slight streamlining of the afterbody is effective in reducing stability near zero yaw is shown in the moment coefficient curves of Figure 4. It has been found that the type of nose on bullet-shaped projectiles also affects the stability. A rather

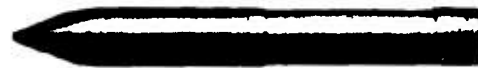


FIGURE 2. SSR rocket (3.5-in.).

blunt tapering nose will produce a slight stabilizing moment at very small yaw angles and this can be eliminated by changing to a long-radius ogive nose, although changing the type of nose is not as effective as streamlining the afterbody.

Tests were made to determine to what extent asymmetry of the nose might affect performance.

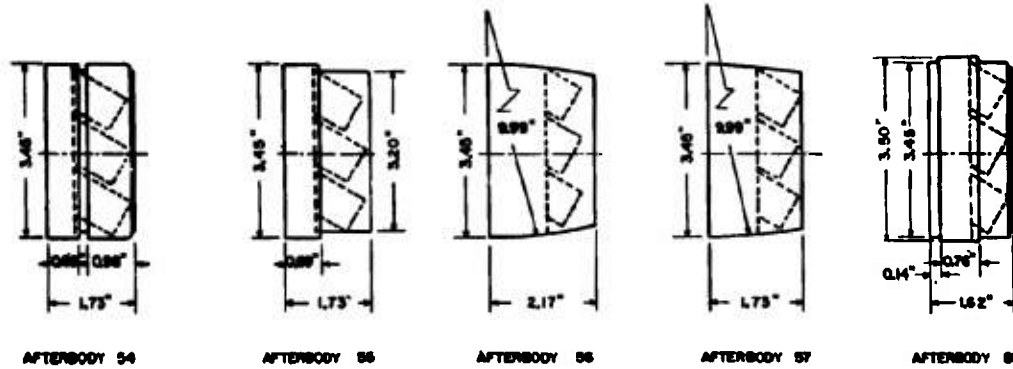


FIGURE 3. Afterbodies for 3.5-in. SSR rocket.

The axis of the nose was deliberately offset so the tip of the nose was displaced a little over $\frac{1}{8}$ in. from its true position. In other words, the axis of the nose made an angle of $1\frac{1}{2}^\circ$ with the axis of the body. The force tests showed that this amount of asymmetry of the prototype nose would not cause a significant change in the fluid forces on the rocket. The effect of this asymmetry in setting up oscillations due to rotational unbalance would probably be much more severe.

15.2.2 15-cm German Spinner Rocket

The physical data for this rocket are as follows:⁶²

Maximum diameter	6.17	in. (= 15cm) = 1 caliber
Overall length	36.18	in. = 5.85 calibers
Weight with propellant	75.3	± 2 lb
Weight without propellant	61.0	± 2 lb
Distance, nose to CG	21.5	in. (= 0.595 × length)
Axial moment of inertia	0.0625	slug-ft ²
Transverse moment of inertia	1.06	slug-ft ²
Jets from aft end	10.48	in. = 1.7 calibers
Velocity		Supersonic

This rocket is a bullet-shaped projectile of novel design although its performance is similar to other spin-stabilized rockets. Figure 5 is a photograph of the model and Figure 6 shows its moment and force coefficients. While this rocket does not have a stabilizing moment for small yaw angles, the destabilizing moment from zero to 1 degree yaw is very small.

It is of interest to note that the performance characteristics shown in Figure 6 are roughly similar to those that have been measured for simple cylindrical projectiles with either ogival or hemispherical noses and square trailing ends. For example, a cylin-

der with hemispherical nose 6 calibers long (note that the spinner rocket is 5.85 calibers long) has a drag coefficient of 0.275 at zero yaw, and increases to 0.40 at 8 degrees. Corresponding figures for the 15-cm spinner are 0.23 and 0.33. The reason for this similar-

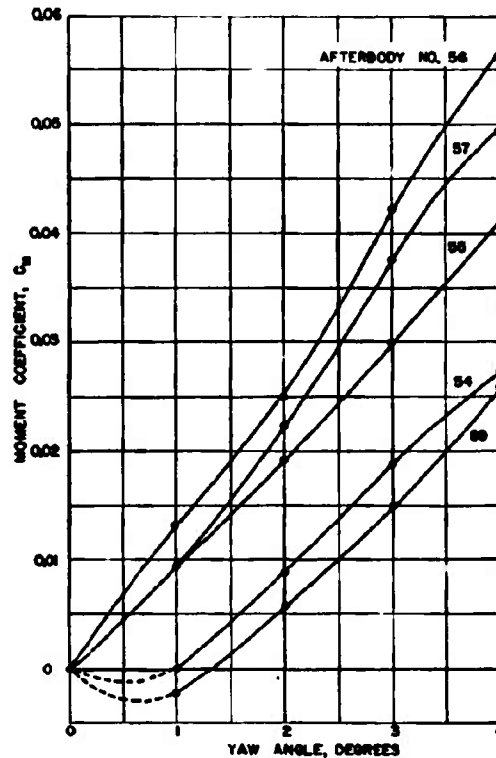


FIGURE 4. Moment coefficients for afterbodies shown in Figure 3; 3.5-in. SSR rocket.

ity is that both the present spinner rocket and the simpler "bullets" have the same general cylindrical shape with rounded nose and blunt trailing end. As the velocity of sound is approached or exceeded, these statements no longer apply since nose shape then becomes of paramount importance. It can be said, as a first approximation, that for simple bullet-shaped bodies traveling at subsonic speeds, the after-body and tail shapes largely determine the aerodynamic forces, whereas for supersonic speeds, the nose shape is the predominating influence.

An interesting indirect measure of the deviation of the subsonic characteristics from those at supersonic velocities can be obtained by making use of the

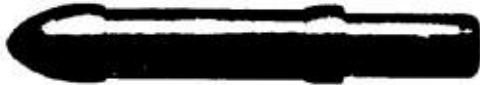


FIGURE 5. German spinner rocket (15-cm).

spinning stability criterion and the propulsive nozzle alignment angle.

According to Hayes,⁴³ the condition for stable motion of a spinning projectile is

$$\frac{A^2 N^2}{4B\mu} > 1, \quad (1)$$

or

$$\frac{A^2 N^2}{4B \frac{C_M}{\psi} \rho \frac{v^2}{2} A_D l} > 1,$$

where A = axial moment of inertia in slug-feet²,
 N = spin in radians per second,
 B = transverse moment of inertia in slug-feet²,
 μ = moment factor in foot-pounds per radian of yaw,
 $= \frac{M}{\psi} = \frac{C_M}{\psi} \rho \frac{v^2}{2} A_D l$,
 ψ = yaw in radians.

For projectiles spun by rocket jets, the stability requirement can be written in terms of the angle which the jet centerline makes with the projectile axis. This is accomplished as follows: the relation between impulse of the jets and the resulting linear and angular momentums can be written

$$\begin{aligned} (F \cos \theta)t &= mv, \\ Tt &= (F \sin \theta)rt = AN, \end{aligned}$$

or eliminating t between the two expressions

$$N = \frac{mrv \tan \theta}{A} \quad (2)$$

where v = maximum velocity reached by rocket in feet per second,

F = jet reaction in pounds,

t = burning time of propellant in seconds,

m = mass of projectile in slugs,

T = torque exerted by jets about projectile axis in pound-feet,

r = radius to centerline of jet ring in feet,

θ = jet alignment angle

If the value for the spin velocity N given by this equation is substituted in the stability relation (1) above and the resulting relation rearranged, the following expression for the required jet angle is obtained:

$$\tan \theta = \frac{1}{mr} \left(2B\rho A_D l \frac{C_M}{\psi} \right)^{1/2} \quad (3)$$

In this equation θ and C_M/ψ are the variables, all other quantities being constant for a given projectile. If values of C_M/ψ from the water tunnel tests are used to evaluate θ , an angle of approximately 6° is obtained as the minimum jet angle for stability at subsonic velocities. Since, as equation (2) shows, N varies directly with $\tan \theta$, the actual nozzle angle of

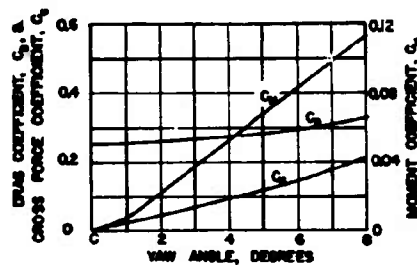


FIGURE 6. Force and moment coefficients; 15-cm German spinner rocket.

14° means that the stability coefficient $A^2 N^2 / 4B\mu$ has a value of about 5.63 instead of the minimum of 1. Although a part of this large excess is undoubtedly needed to provide the desired "stiffness" to the German spinner rocket, it is probable that this high value indicates that, at supersonic velocities, the destabilizing aerodynamic moment coefficient is considerably greater than it is at subsonic speeds.

4.5-Inch HE Rocket, T38E3

This is another example of a bullet-shaped body that has a small stabilizing moment at small yaw angles. The general outline of the projectile⁴⁴ is shown

in Figure 1, and Figure 7 is a photograph of the model. The following physical data apply to this rocket:

Maximum diameter	4.515 in. = 1 caliber
Overall length	31.44 in. = 7— calibers
Distance, nose to CG	0.515 × length
Weight without propellant	42.5 lb
Velocity	830 fps

In Figure 8 are given curves for the drag, cross force, and moment coefficients up to a yaw angle of

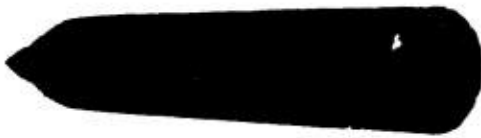


FIGURE 7. HE rocket, T38E3 (4.5-in.).

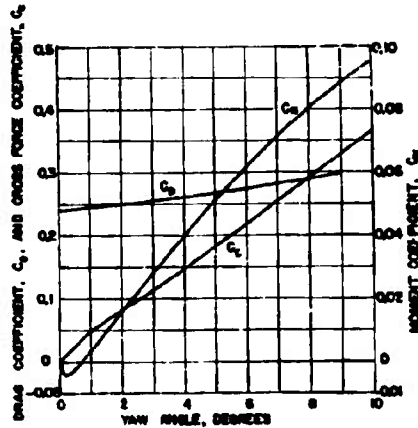


FIGURE 8. Force and moment coefficients; 4.5-in. HE rocket, T38E3.

10°. The drag coefficient for zero yaw is a little less than 0.25, which appears to be the value common to most projectiles of this type.

5-Inch SSR Rotating Rocket

Four models of this rocket²⁶ were tested. Figure 1 gives the outline drawing of model 32 and Figure 9 shows photographs of models 20 and 32, the principal differences between the various models is in the overall length and the type of nose. Table 1 gives data pertaining to these four models.

In Figure 10 are plotted the cross force, drag, and moment coefficients for models 20 and 32. These

TABLE 1. Physical characteristics of the 5-in. SSR rotating rocket.

Model	Max diameter in in.	Overall length in in.	Weight loaded in lb	Weight in flight in lb	Velocity in fps
No. 20	5	28.9	49.7	39.8	1,500
No. 32	5	31.6	51.4	41.3	1,500
No. 25	5	31.7	49.9	44.3	800
No. 21	5	31.7	48.3	42.7	800

models also show drag coefficients of 0.25 or less corresponding to other projectiles of this type. Two tests were made to determine the variation in drag with Reynolds number, the results of which are shown in Figure 11. By extrapolating the curves for



FIGURE 9. Five-inch SSR rotating rocket, models 20 and 32.

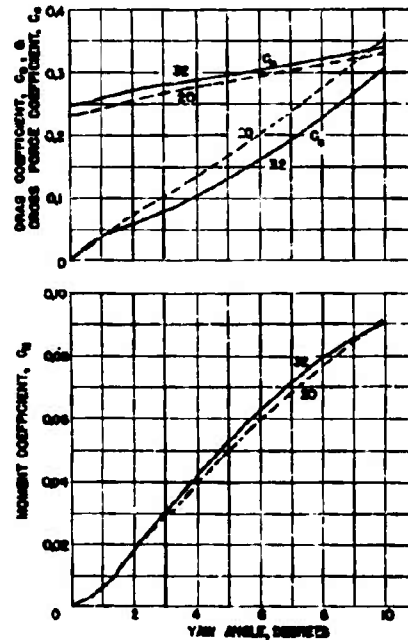


FIGURE 10. Force and moment coefficients. Five-inch SSR rocket, models 20 and 32.

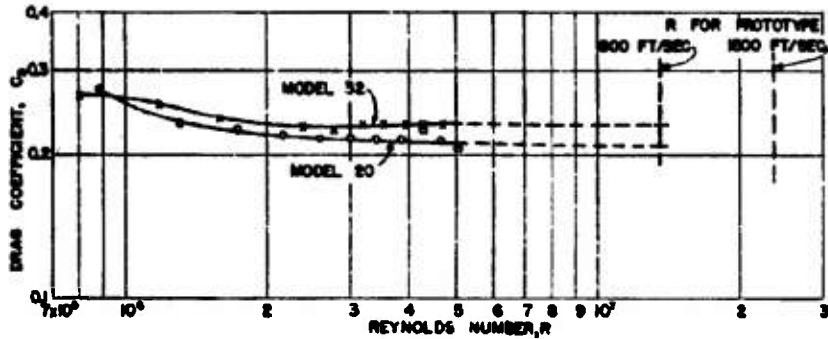


FIGURE 11. Drag versus Reynolds number; 5-in. SSR rocket, models 20 and 32.

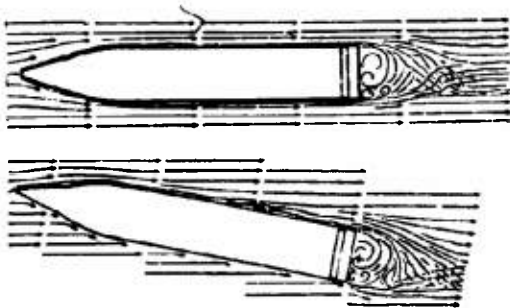


FIGURE 12. Flow line drawings; 5-in. SSR rocket at 0 and 10 degrees yaw.

the model to the Reynolds number of the prototype, it is found that the drag coefficient for the prototype will be between 0.21 and 0.23. Note that this applies only so long as velocity of flight is below the sonic velocity.

By observing the model in the polarized light flume, it is possible to prepare a flow line drawing showing the flow about the model. Figure 12 is a flow line drawing of one of the models showing clearly that there is little or no disturbance along the surface of the body. There is the typical disturbed flow in the wake of the end of the model that is always found with blunt afterbodies.

Chapter 16

DEPTH CHARGES

16.1 GENERAL DISCUSSION

A DEPTH BOMB can be considered as a member of the family of projectiles which also includes air bombs and torpedoes. All are explosive-containing objects which may be launched by aircraft, even though other means are also used. Differences stem, primarily, from the location of the area each is designed to strike. The ordinary air bomb is intended to strike the upper areas of targets at or near the surface of the earth or water. The torpedo is used to attack vulnerable areas of vessels at a point under, but not far under, the water surface. Depth bombs are for use in the general zone from just under the water surface to any desired depth. In consequence, the air bombs will have little or no underwater trajectory; that of the torpedoes will be primarily horizontal, while that of the depth bombs will be mainly vertical. A means of self-propulsion is essential only in the case of the torpedo with horizontal trajectory. High average and terminal velocities are desirable for depth bombs but the evasive action of their targets is relatively slow and, hence, it is less important than the speed of torpedoes which must hit targets that can maneuver much more rapidly than submerged submarines. The relatively low velocities and greater course depths of the depth bombs also make consideration of cavitation less important and do not necessitate extreme streamlining. Furthermore, highly streamlined forms tend toward static instability which is desirable in torpedoes, with their special control devices but is objectionable in depth bombs. Trajectories must be predictable, reliable, and obtainable from the stability inherent in such projectiles. There are other similarities and differences but those mentioned illustrate the general relationships within this family.

16.2 METHODS OF LAUNCHING

Depth bombs are ordinarily launched either by dropping from aircraft in flight over the target or by being shot from a suitable device on a water-supported vessel. Each of these methods has some influence on the design of the bomb.

16.3 DESIGN REQUIREMENTS

Many factors are involved in the design of a depth bomb. Generally, the starting point will be a definite kind and amount of explosive based upon tactical considerations. This determines a tentative minimum volume which must be shaped, specially, to a suitable length-diameter relationship. These dimensions may be subject to restrictions due to previously existing apparatus to be associated with their use, such as the launching or projection devices, as well as to hydrodynamic considerations, such as drag and stability. Further evolution of the design includes requirements of structural strength, such as wall thickness; of functional parts, such as fuses; of manufacturing, such as simplicity of construction; and of handling and storage. There is, finally, the overall requirement that the explosive charge will reach the vicinity of its target with an acceptable minimum of dispersion. It is known that improvement may be had in this respect if lateral travel, introduced when the projectile is ejected, be checked upon water entry. This can be obtained by a nose shape which will produce a large entrance bubble.

16.4 USEFULNESS OF HYDRODYNAMIC TESTS

Hydrodynamic tests are of great usefulness in determining the actual characteristics of the prototype. They permit prediction of full-scale performance to reasonable degrees of accuracy, and detailed study of the various factors involved is greatly simplified and facilitated. Cavitation phenomena may be photographed if desired. Changes which may be suggested by the results of such tests may be incorporated readily and tested anew.

16.5 SPECIFIC DEPTH BOMBS TESTED

The depth bombs tested by this laboratory included those known as the New London and New London Modified; the 7-in. diameter depth charge, also referred to as the X-42; the Mousetrap and Mousetrap Modified; the AN Mark 41; the AN Mark 53; and the British Squid.

Figure 1 shows photographs of the projectile models listed above, and Figure 2 shows their outlines, all of which are to the same scale for the group. The explosive charge weights and other physical characteristics for these projectiles are given in Table 1.

highest ratio, with the original Mousetrap having the greater of the two. Both of these results might have been anticipated. Boom tails give greater static

M.S.1 Small-Charge Group

Figure 3 is a composite graph of yaw angle* tests for five of the depth charges tested early in the program. The data for this group were not corrected for support interference effects. There are three sets of curves in this figure. The group at the top is for center-of-pressure distance against yaw angle. The difference between the center-of-pressure distance and the center-of-gravity distance may be used to indicate the degree of static stability instead of curves of moment coefficient about center of gravity. The ordinate scale is the ratio of X divided by L , where L is the length of the projectile, and X is the distance of the center of pressure from the nose. It may be seen that the Mousetrap projectiles had the

TABLE 1. Physical characteristics of depth bombs tested.

Projectile	Diameter in in.	Over-all length in in.	Weight of explosive in lb	Total weight in lb	CG distance from nose divided by over-all length
New London	6.0	40.0	30		
Mousetrap	7.2	35.75	30	about 60	0.295
7-in. diameter bomb	7.0	38.5	40	70.94	0.310
Modified Mousetrap	7.2	35.5	30		0.347 (approx)
Modified New London	6.0	50.75	40	80	0.315
AN Mark 41	15.0	52.0	227	330	0.317 from nose fuse
British Squid	11.75	55.0	198	386.4	0.364—air 0.335—sea water
AN Mark 53	13.5	52.5	225.46	323.8	0.375 from nose fuse 0.353

* Definition of term and symbols are given in Appendix.

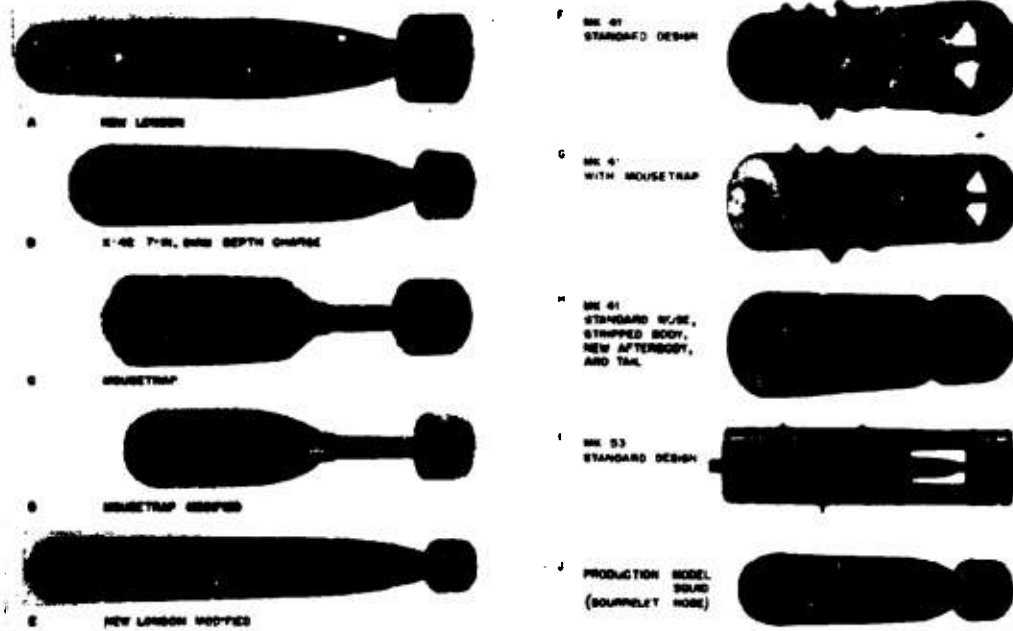


FIGURE 1 Photographs of specific depth charges tested. A-J incl.

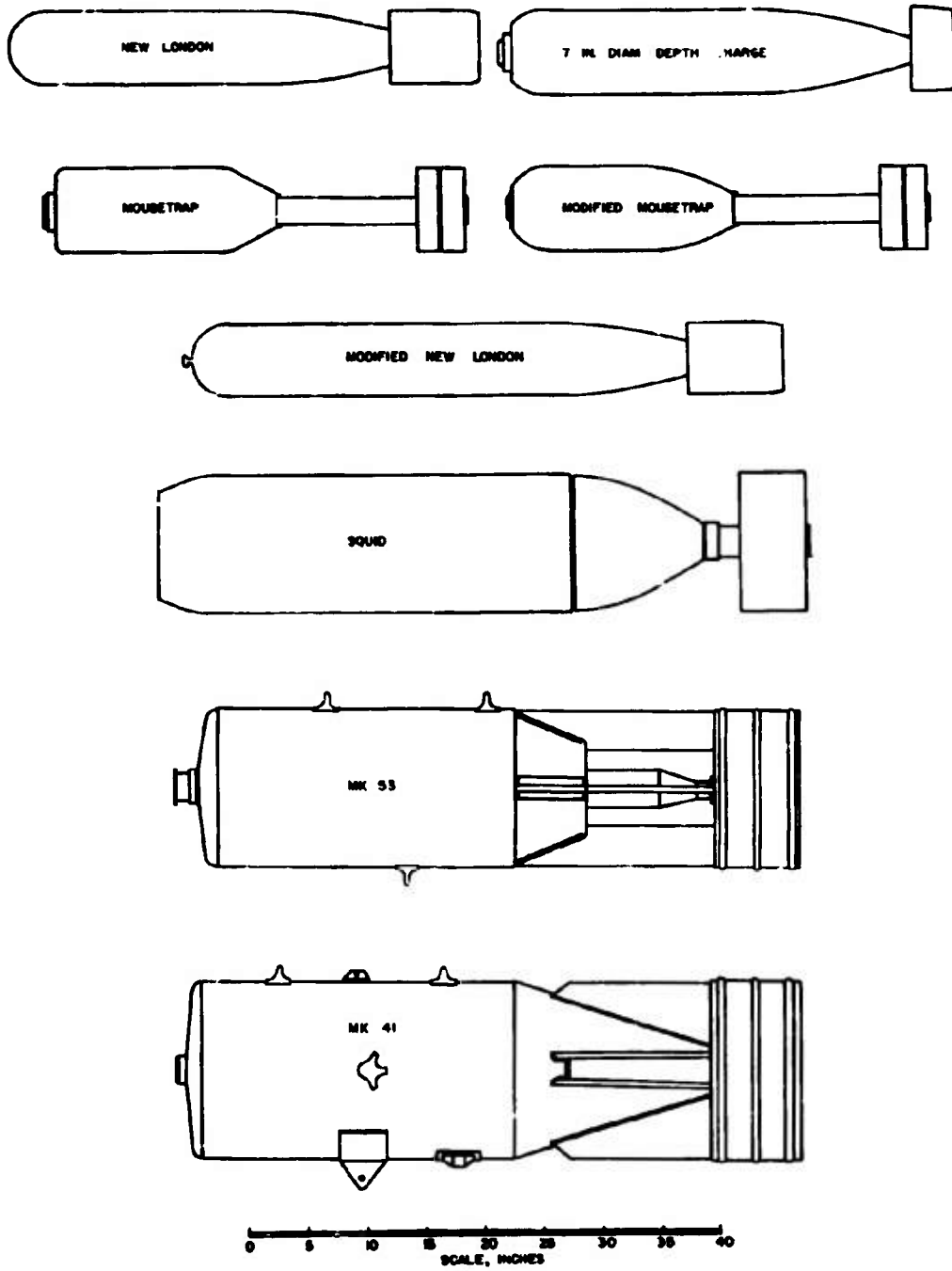


FIGURE 2. Depth charge group. Outline drawings.

CONFIDENTIAL

stability and so does bluntness of nose as compared with less blunt noses, other things being equal. However, the decrease in static stability in the case of the Modified Mousetrap was relatively immaterial and the reduction in the drag coefficient from the highest to the lowest in the group, as shown in the middle set of curves, was much more important. The New London types, particularly the Modified New London, had the least static stability. Their shape approaches that of the torpedo which should have little or no static stability, since it must be amenable to the ac-

zero yaw angle and vary practically linearly with yaw.

14.5.2 AN Mark 41 Bomb

Figure 4 shows the effect of yaw angles on C_D , C_C , and C_M for the AN Mark 41 Bomb⁶⁴ and various modifications which further illustrate the effect of various projectile components on these coefficients.

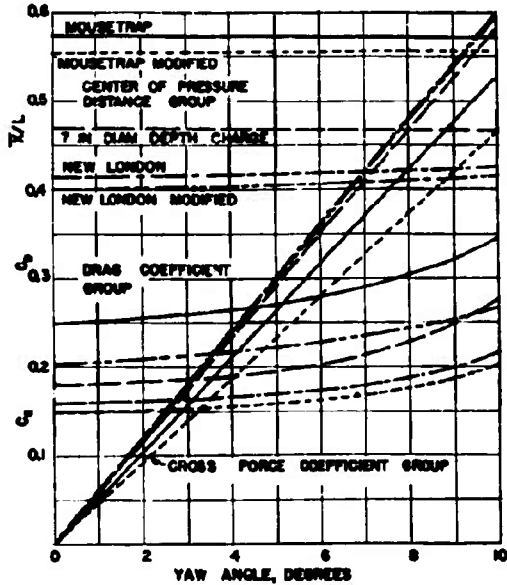


FIGURE 3. Effect of yaw on C_D , C_C , and X/L for group of small charge depth bombs.

tion of control devices. The higher stability of the 7-in. diameter depth charge, of the same general shape as the New London projectiles, is presumably due to its blunter nose.

The drag coefficient curves are also consistent with experience. Very blunt noses have, in themselves, a high degree of drag. The Mousetrap with the bluntest nose gave the highest readings. The Modified Mousetrap gave the lowest because the gain from its nose shape, which was like that of the 7-in. diameter depth charge and less fine than the New London noses, was not offset by the skin friction drag due to greater wetted surface in these other projectiles.

The cross force coefficient curves have zero value at

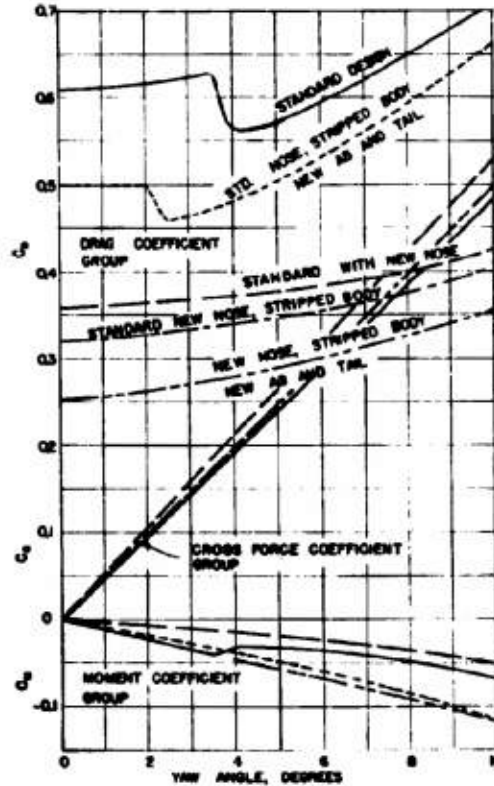


FIGURE 4. Effect of yaw on C_D , C_C and C_M for the AN Mark 41 bomb and modifications.

These data are also uncorrected for support interference. The top curve in the top group is the drag coefficient for the standard (or original) design model at yaw angles to +10 degrees. An unusual dip may be seen to occur between approximately 3½ and 4 degrees. This appears to be a characteristic associated with this particular prototype nose and the sharp reduction in the drag coefficient is presumably due to a change in flow conditions over that yaw angle range.

The drag coefficient was markedly reduced by the substitution of the new afterbody and tail, shown in Figure 1H. The stripping of body protrusions did not contribute any of this reduction as the flow separation from this nose caused the high-velocity water to flow in a region beyond their effective extension from the body as may be seen in Figure 5. The dip in the drag curve still appears although shifted toward zero yaw by $1\frac{1}{2}$ degrees. The long-dash curve shows the results obtained by merely substituting a somewhat smoother nose on the prototype. The reduction of C_D at 0-degree yaw was about 41 per cent, and its rate of increase with yaw angle was smoothed out and reduced. Separation of flow at the nose was also

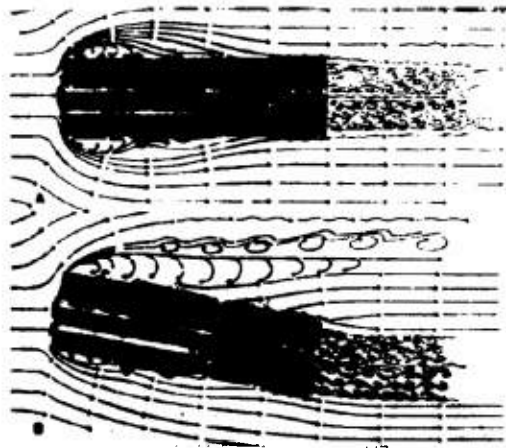


FIGURE 5. AN Mark 41 prototype. Flow line diagram for (A) 0- and (B) 10-degree yaw angles.

reduced and high-velocity water was close enough to the body surface to strike protrusions, as shown in Figure 6. When they were removed, an additional reduction of drag coefficient resulted so that, at 0-degree yaw, the total reduction was $47\frac{1}{2}$ per cent of the original total C_D . The one long-two short-dash curve shows the results with the Squid nose, stripped body, and new afterbody and tail with a C_D reduction at zero yaw of 59 per cent. Such a reduction would increase the terminal velocity in water from 15 to 23 fps, approximately. It is probable that a still further reduction of 10 per cent or better could be obtained in C_D merely by rounding all the leading edges of the fins and shroud ring of the tail.

The cross force coefficient was affected only slightly by any of the changes made. All curves were on or within the limits shown in the group which extends

from zero to the upper right of the graph. The substitution of a finer nose increased the cross force coefficient as it normally does in the absence of other factors.

All moment coefficient curves indicate static stability, the degree increasing with the size of the angle the curve makes with the horizontal axis. Thus, it may be seen that the model with the new nose, stripped body, new afterbody, and tail had the greatest static stability, and the prototype with new nose had the least of the group. The prototype itself shows a radical change between $3\frac{1}{2}$ and 4 degrees of yaw similar to that observed in the drag curve. This indicates a condition of uncertainty of action in this region, which is somewhat objectionable.

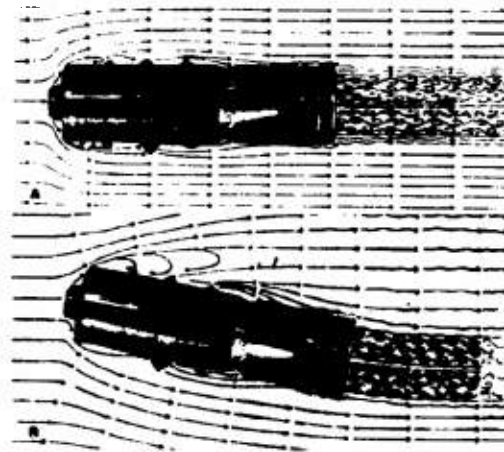


FIGURE 6. AN Mark 41 with new nose. Flow line diagrams for (A) 0- and (B) 10-degree yaw angles.

20.5.3

British Squid

Figure 7 shows the influence of yaw angle on C_D , C_C , and C_M for the British Squid with five different noses.⁴⁷⁻⁴⁹ All these noses except the No. 131 were truncated spherogives with different flat areas. In all cases the overall length and maximum diameter were the same. The noses, designated in the laboratory by Nos. 42, 45, and 46 were ogives with a radius of 12.5 in. and a constant horizontal length of 5.77 in. The center of the ogive was shifted to give flat areas on the front of the nose of 7.90, 8.93, and 9.95 in. diameter, respectively. The prototype nose is shown in Figure 1J. It is similar to those described immediately above except that the flat area had a diameter of 8.75 in. and there was a bourrelet on the nose im-

CONFIDENTIAL

mediately before its junction with the body. This nose, together with the No. 45 nose and a special nose, laboratory designation No. 131, may be seen in outline in Figure 3, Chapter 9. The contour of the No. 131 nose is based on the formula

$$\left(\frac{x}{1.5}\right)^2 + y^2 = 1$$

where x is measured along the axis from the base of the nose and y is the distance from the axis to the nose surface.

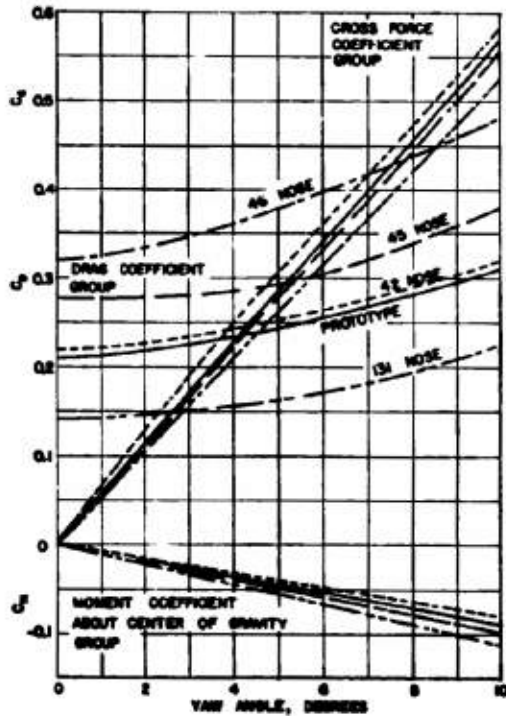


FIGURE 7. Effect of yaw on C_D , C_C , and C_M for the British Squid with several noses.

The C_D curves for the Nos. 46, 45, and 42 noses show the progressive reductions due to reducing the size of the flat leading face or, in other words, of reducing nose bluntness in this manner. The prototype nose is very similar to the No. 45, and the drag coefficient obtained with it would be only slightly under that for the No. 45 had all other conditions been similar. The additional reduction shown in the graph was due to thinner material in the fins and rounded leading edges. The curve for the No. 131, or special

nose, shows the additional reduction from further streamlining. This model also had the thin tail with rounded leading edges.

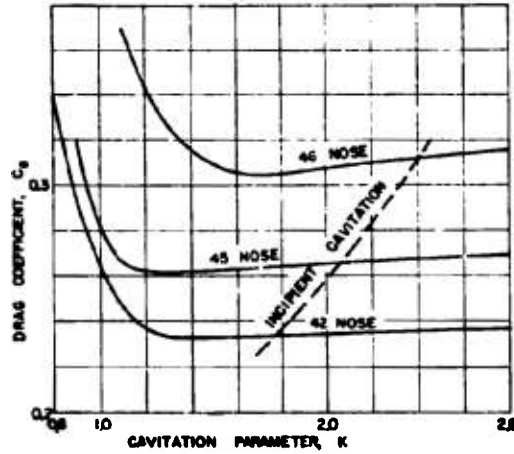


FIGURE 8. Influence of cavitation parameter on drag coefficient for the British Squid depth charge with three noses.

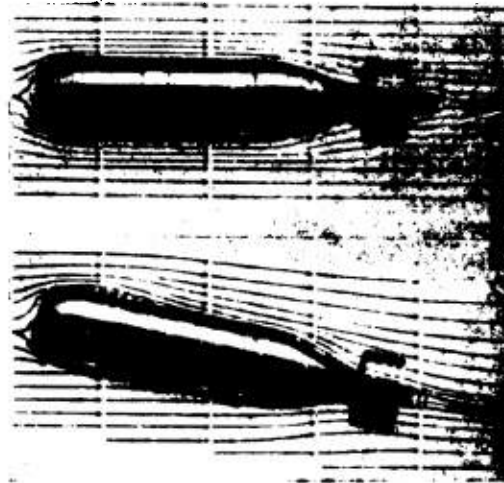


FIGURE 9. British Squid with No. 45 nose. Flow line diagram for 0- and 10-degree yaw angles.

The curves for the cross force coefficient for the Nos. 45 and 46 noses were identical within limits of measurement. The No. 42 nose had a higher C_C as is general for less blunt noses, but the finest nose of the

group had a smaller value which is an anomaly unless attributable to the slight differences in tail structure.

The moment coefficient curves indicate static stability for all models, that for the prototype with special nose having the highest.

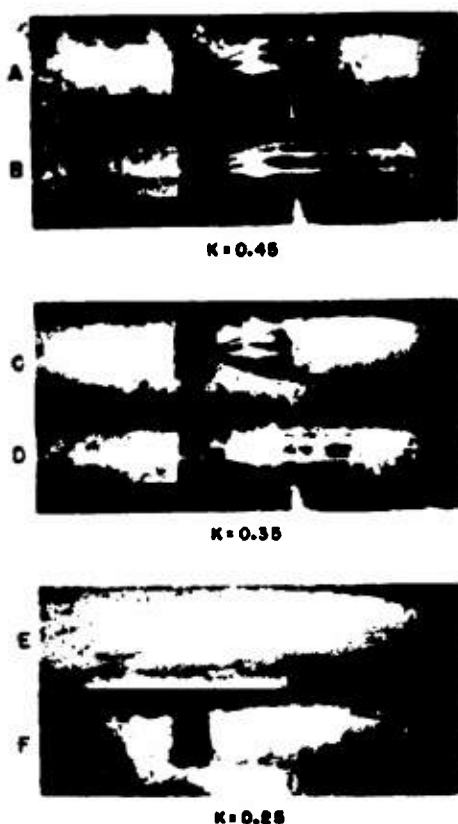


FIGURE 10. British Squid. Cavitation: $K = 0.45, 0.35, 0.25$. Upper view in each set is for prototype. Lower view is for prototype with special nose, (A)-(F) incl.

Figure 8 shows the effect of cavitation parameter K on the drag coefficient for the Squid with Nos. 42, 45, and 46 noses. There is a slight progressive decrease in C_D as the K value is lowered, until and after incipient cavitation is established. When the cavitation "collar" has a width of about $\frac{1}{4}$ in. on the model, the drag coefficient increases sharply and continues this trend with further reduction of K values.

Figure 9 shows the flow line diagrams for the Squid with original nose for zero and 10 degrees of yaw. Separation on the nose and afterbody is apparent.

Figure 10 shows cavitation with the prototype Squid and prototype with the special nose described above. The complete prototype is the upper view in each set. Values of K were 0.45, 0.35, and 0.25. These

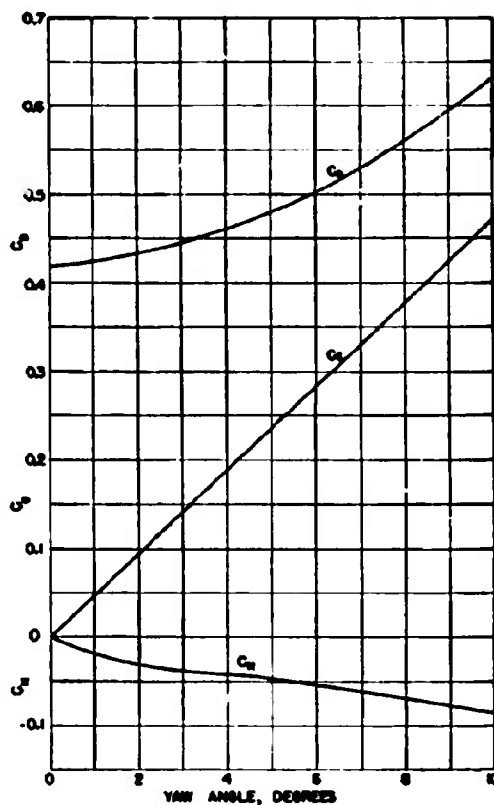


FIGURE 11. Effect of yaw on C_D , C_C , and C_M for the AN Mark 53 bomb.

photographs show clearly the greater cavitating tendency of the prototype nose.

2.2.4

AN Mark 53 Bomb

Figure 11 shows the drag, cross force, and moment coefficients for positive yaw angles to 10 degrees for the AN Mark 53 bomb to the same scale as used for the AN Mark 41, Figure 4. The relatively high drag coefficient (0.42) is due, primarily, to the blunt nose shape. The cross force coefficient is a linear function

of the yaw within the test range and is comparable to that of the AN Mark 41. The moment coefficient about the center of gravity is also comparable and shows a greater slope between 0 and 2 degrees than between 2 and 10 degrees.

The pressure distribution was measured on this projectile in order to determine a suitable place for the hydrostatic fuze connection and for cavitation characteristics. Details of these findings may be obtained from the report.⁷¹

Chapter 17

AIR BOMBS

17.1 INTRODUCTION

THE TERM "AIR BOMBS," as here used, refers to projectiles whose trajectory is wholly in air. As distinguished from rockets, they contain no propellant, the initial trajectory conditions being determined wholly by the magnitude and direction of the launching velocity. They are distinguished from projectiles such as depth charges and aerial torpedoes whose trajectory is wholly or partly in water by the following characteristics:

1. They have many times the density of the fluid medium and in consequence the damping forces are low. Air bombs, therefore, require large stabilizing fins not only for static stability but also to supply the damping necessary for dynamic stability.
2. A higher drag usually is permissible since high terminal velocities are seldom important.
3. Cavitation does not occur, but extending lugs, fuzes, and other irregularities may induce supersonic effects before the bomb as a whole attains sonic velocity.

17.2 REVIEW OF TEST RESULTS

17.2.1 Bombs Tested and Scope of Tests

The following air bombs have been investigated by model test in the water tunnel of the Hydrodynamics Laboratory:⁷²

1. The 100-lb concrete practice bombs, with three designs of stabilizing fins.
2. The M38A2 100-lb practice bomb.
3. The AN-M43 GP 500-lb bomb.
4. The AN-M56 LC 4,000-lb bomb.

Figure 1 shows outline drawings of the above bombs, all to the same scale. Figures 2 to 7 are photographs of the models, and Table 1 gives the principal dimensions.

All the bomb bodies are of the same type, with cylindrical midsections, ogival noses either rounded or blunt at the tip, and afterbodies in the form of truncated cones.

All the stabilizing tails are of the square box type with fins extending outward from the box corners,

except for one of the concrete practice bombs, which has a drum-type or shroud-ring tail.

The water tunnel models were accurate reproductions of the prototype except that the arming fuzes were omitted. The tests were made under steady-state conditions and the results gave the hydrodynamic forces and moments for steady-state conditions only. No tests were conducted to determine the damping forces on the bombs when oscillating in free flight or fall.

17.2.2 Force and Moment Coefficients

Figure 8 shows the force and moment coefficients determined by tests of the model of the AN-M43 GP 500-lb bomb. The general shape of the coefficient curves is characteristic of all the models tested. For comparison the principal hydrodynamic characteristics of all the bombs, as determined from the model tests, are given in Table 2. Definitions of terms and symbols used in both Figure 8 and Table 2 are given in the Appendix.

The drag coefficient of the air bombs investigated is more than double that of more fully streamlined shapes, such as torpedoes and certain types of depth bombs having dimensions of the same order of magnitude and approximately the same surface areas.

For air bombs whose density is many times that of air, a sufficient condition for dynamic stability is that the resultant of the steady-state hydrodynamic forces should fall aft of the center of gravity of the projectile.⁷² For all of the bombs investigated this condition was satisfied. However, the magnitude and frequency of the damped oscillation following a perturbation cannot be determined without knowledge of the damping forces.

17.2.3 Effect of Asymmetry

None of the bombs has complete structural symmetry about its longitudinal axis, due principally to the manner of construction and assembly of the tails. The result of asymmetry, particularly in the fins, is to produce a rudder effect in flight resulting in deviation of the trajectory of a truly symmetrical projectile. The effect of asymmetry on moment and

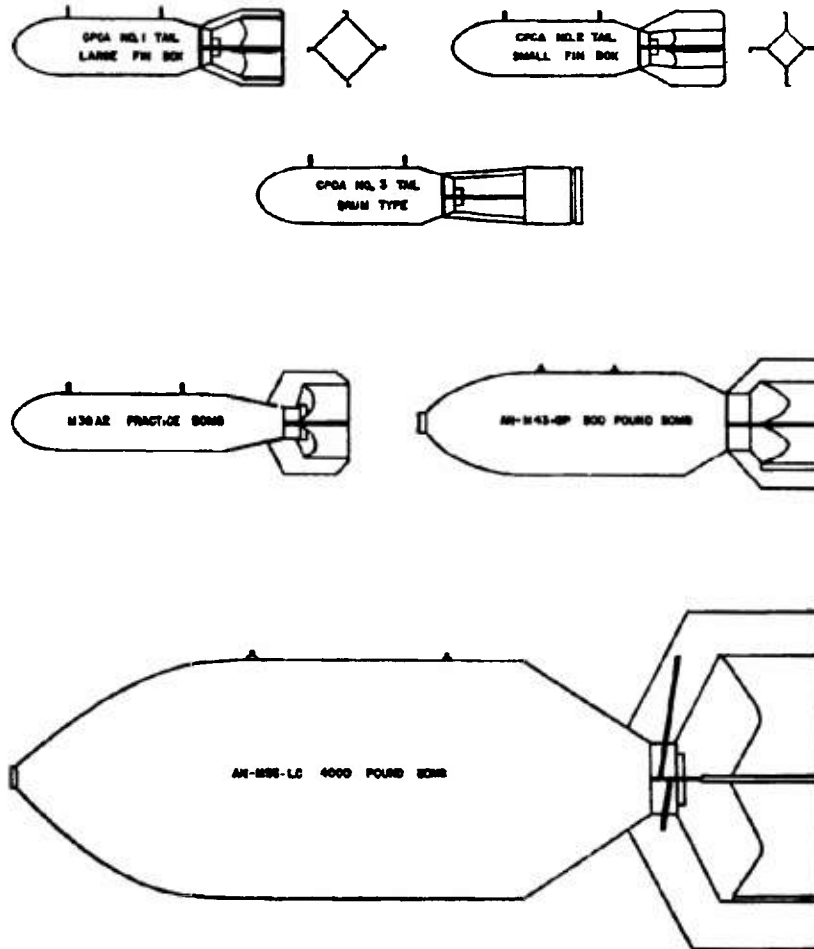


FIGURE 1. Outline drawings of air bombs.

TABLE 1. Principal prototype dimensions.

	Concrete practice bombs			M38A2 100-lb practice bomb	AN-M43 GP 500-lb bomb	AN-M56 LC 4,000-lb bomb
	Large box tail CPCA-1	Small box tail CPCA-2	Drum tail CPCA-3			
Maximum diameter in in.	8	8	8	8	14	34
Overall length in in.	38.50	38.50	45.50	47.50	58.14	116.06
Body length in in.	30.10	30.10	30.10	40.66	48.33	96.12
Afterbody taper in degrees from longitudinal axis	10.3	10.3	10.3	15.7	24	30
Side of fin box in in.	6.00	4.75	8 (dia)	6.00	7.60	22.56
Max span of fins in in.	11.00	11.00	8 (dia)	10.77	18.94	47.62
Weight in lb	103.25	103.25	104	100	508	4,200
Nose tip to CG in in.	14.75	14.75	15.50	18.15	24.00	49.20
Scale ratio, prototype to model	4/1	4/1	4/1	4/1	7/1	1/1

CONFIDENTIAL



FIGURE 2. CPCA No. 1 tail. Large fin box.

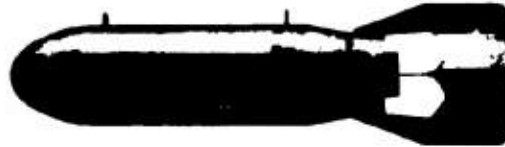


FIGURE 3. CPCA No. 2 tail. Small fin box.



FIGURE 4. CPCA No. 3 tail. Drum type.



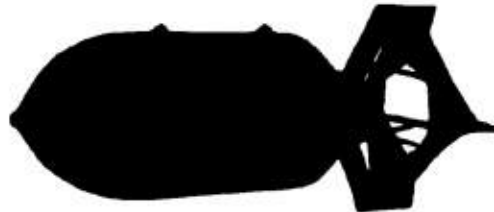
FIGURE 6. AN-M43 GP 500-lb. bomb.



FIGURE 5. M38A2 practice bomb.



FIGURE 7. AN-M56 LC 4,000-lb. bomb.



cross force is illustrated in Figure 8, which shows the variation of moment and cross force with yaw as actually determined for the model of the AN-M43 500-lb bomb. Neither the cross force nor the moment is zero at zero yaw. At a yaw of about 1 degree, the moment is zero, but the cross force has a considerable magnitude which acts to deflect the trajectory. The

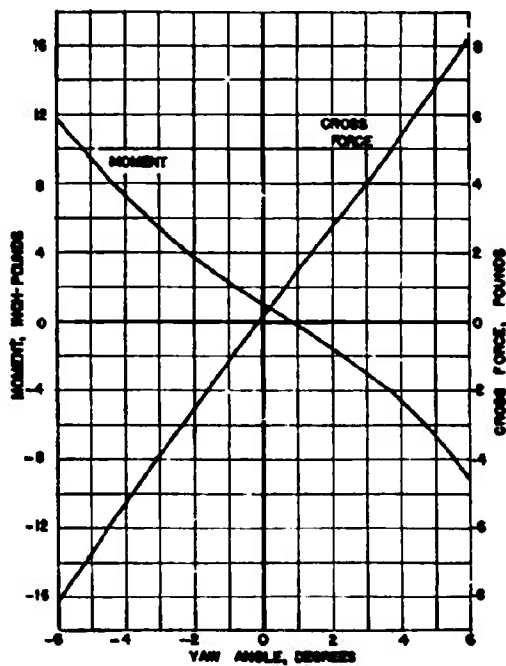


FIGURE 8. Effect of asymmetry on force and moment coefficients. AN-M43 GP 500-lb bomb.

consequence of asymmetry is a dispersion which is unpredictable. Tests at various orientations of the tails with respect to the yaw plane showed varying degrees of asymmetry.

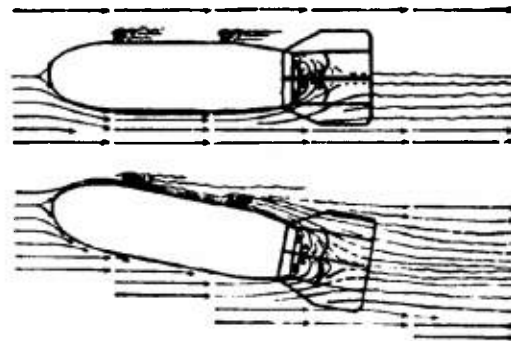


FIGURE 9. CPCA No. 1. Flow line drawings; 0- and 10-degree yaw.

The coefficient curves of Figure 8 and the coefficient values given in Table 2 are obtained from force measurements averaged for 180-degree differences in orientation and represent the characteristics of symmetrical projectiles.

17.2.4

Conclusions

The high drag results mainly from separation and turbulence on the afterbody. This is illustrated clearly by Figures 9 to 12 which are drawings of the flow patterns observed in the polarized light flume.*

* The polarized light flume and methods of obtaining flow diagrams are described in Chapter 2.

TABLE 2. Comparison of hydrodynamic characteristics.

	Concrete practice bombs			M38A2	AN-M43	AN-M56
	Large box tail CPCA-1	Small box tail CPCA-2	Drum tail CPCA-3	100-lb practice bomb	GP 500-lb bomb	LC 4,000-lb bomb
Drag coefficient, C_D						
At zero yaw	0.285	0.250	0.240	0.270	0.220	0.287
At $\pm 6^\circ$ yaw	0.315	0.305	0.290	0.295	0.260	0.325
Cross force coefficient C_C						
C_C per degree, zero to $\pm 1^\circ$ yaw	0.062	0.065	0.050	0.055	0.060	0.056
C_C at $+6^\circ$ yaw	0.450	0.460	0.335	0.440	0.380	0.355
Moment coefficient C_M						
C_M per degree, zero to $+1^\circ$ yaw	-0.008	-0.006	-0.009	-0.008	-0.009	-0.005
C_M at $+6^\circ$ yaw	-0.085	-0.081	-0.058	-0.074	-0.065	-0.041
Center-of-pressure eccentricity e at $+6^\circ$ yaw	-0.189	-0.176	-0.173	-0.168	-0.171	-0.115
Reynolds number $\times 10^{-6}$						
Model in water at 32 fps	2.4	2.4	2.8	2.9	2.0	1.7
Prototype in air at 600 fps	12	12	14	14	18	35

CONFIDENTIAL

Comparing Figures 9 and 10, it will be noticed that the eddies formed by separation on the afterbody practically fill the interior of both the fin box on the CPCA No. 1 and the drum tail on CPCA No. 3, con-

siderably reducing the stabilizing effect. On the drum-type tail of Figure 10, even though the drum or shroud ring is located farther aft than is the fin box of Figure 11, it is less effective except near zero yaw. The greater effectiveness of the box tail at larger yaws may be attributed to the fins which project from the corners of the box to a span greater than the projectile diameter and extend into undisturbed fluid.

Note that the water tunnel tests are all for a lower range of Reynolds numbers than the prototype reaches in air flight. The measured cross force and moment coefficients probably apply to the prototype conditions without correction, although the drag coefficients may be subject to some scale effect. It is

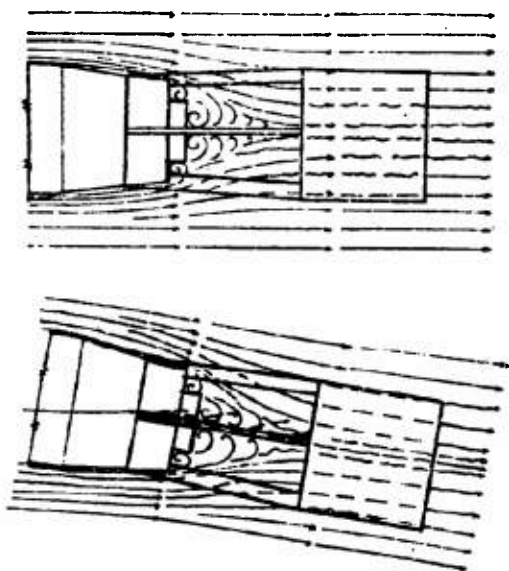


FIGURE 10. CPCA No. 3. Flow line drawings; 0- and 10-degree yaw.

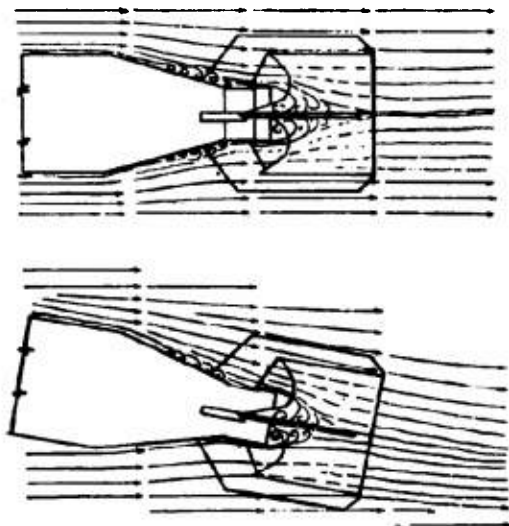


FIGURE 12. M32A2 practice bomb. Flow line drawings. Afterbody 102 at 0- and 10-degree yaw.

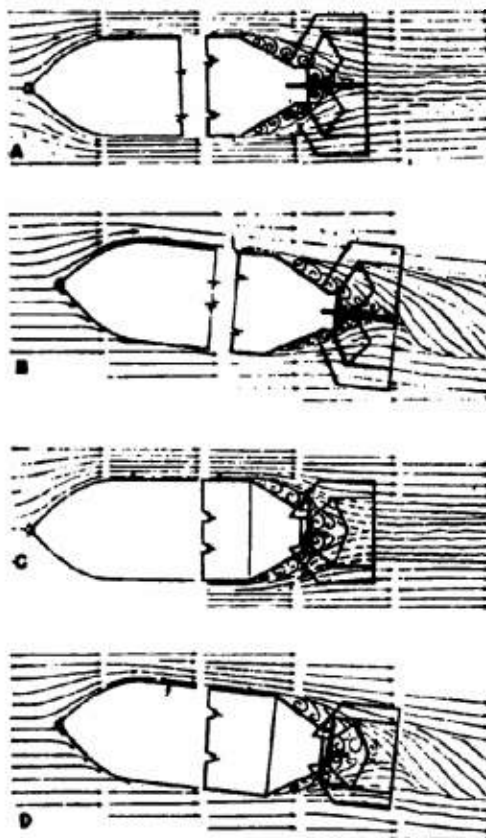


FIGURE 11. AN-M56 LC 4,000-lb bomb. Flow line drawings; 0- and 10-degree yaw. Tail fins in upper two drawings are oriented parallel and normal to projection plane; in lower drawings, fins are inclined 45 degrees to plane.

estimated that this effect is small because the drag is primarily form drag caused by the harmful effect of the separation at the afterbody.

Low dispersion and low drag are both desirable for the highest aiming accuracy, particularly with the very heavy bombs which may be launched singly. To accomplish this, a construction is indicated which is completely symmetrical about the longitudinal axis and has a streamlined shape to minimize drag.

There is considerable qualitative evidence to indicate that the random dispersion which remains after aiming errors are accounted for is less than would be expected on the basis of the average misalignment of the tail structure. There is also qualitative evidence to show that most bombs rotate during the air flight,

probably due to chance asymmetries or to the effect of the stiffener angle at the fin tips. The effect of the rotation is to average the steering error due to tail structure misalignment or body damage and thus sensibly reduce the dispersion. It is believed that even lower dispersions could be obtained by introducing a planned rather than a chance amount of rotation.

Tests on a variety of models having such characteristics (see Chapter 9) lead to a suggested bomb shape with a rather blunt nose, a very short cylindrical section, if any, and a long tapering afterbody with a shroud-ring tail as far aft as practicable. For a given volume and maximum diameter, such a shape would be perhaps ten to fifteen per cent longer than the shapes illustrated in Figure 1.

Chapter 18

TWO-DIMENSIONAL BODIES

18.1 CHARACTERISTICS OF HYDROFOILS —THE NACA 4412 SECTION

18.1.1 Scope of Investigation

THE PERFORMANCE DATA of most profiles which are used as hydrofoils in the design of underwater devices have been determined in wind tunnels and in general include only the hydrodynamic forces and moments as functions of angle of attack and of Reynolds number. Aside from approximating the pressures and velocities at which cavitation will first appear (with the aid of measured pressure distributions along the surface of the shape), no information is obtained about the beginning and growth of cavitation nor about the forces acting on the hydrofoil during cavitation. Such data can be obtained only in a water tunnel. This chapter includes a typical set of water tunnel measurements of hydrofoil characteristics including forces and moments without cavitation and photographic observations of the development of cavitation.⁷⁴ The results are also compared with the available wind tunnel data on the same shape.⁷⁵⁻⁷⁸

18.1.2 Installation and Tests

The profile tested is identical to the 4412 airfoil section of the National Advisory Committee for Aeronautics, and is called the NACA 4412 hydrofoil here. Its dimensions are shown in Figure 1 where the profile is sketched in the zero angle-of-attack position. For the experiments, solid stainless steel test sections* with a chord of 3 in. were supported at one tip by the water tunnel balance spindle and cantilevered into the working section. By rotating the spindle, the hydrofoil angle of attack could be changed. A special arrangement of the working section was used where a 3.33 aspect ratio hydrofoil test unit spanned a 10-in. gap between parallel tunnel walls. This installation, which gave approximately two-dimensional flow, is shown in Figures 2 and 3. Two different hydrofoil installations were used, permitting measurements of the hydrodynamic forces

and moments acting on the complete 10-in. span or on only one-half the span. The latter was obtained by splitting the hydrofoil at the tunnel centerline and supporting one-half independently of the tunnel balance. For measurements at angles of attack both halves were rotated through the same angle.

Two types of experiments were made. The first was the determination of the hydrodynamic lift, drag, and pitching moment as functions of the angle of attack for cavitation-free operation at Reynolds

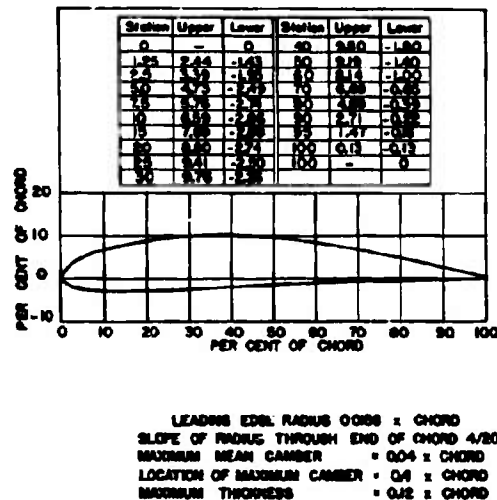


FIGURE 1. Dimensions of the NACA 4412 airfoil.

numbers of from 287,000 to 903,000. The second was the observation of the inception and growth of cavitation at different angles of attack as functions of velocity and pressure. The effect of cavitation on the lift and drag was investigated qualitatively but detailed investigations were postponed because of the limited time available for the tests.

18.1.3 Infinite Aspect Ratio Characteristics of the NACA 4412 Hydrofoil

Because of the two-dimensional character of the water tunnel test installation, the measured hydrodynamic forces and moments approximate without

* These test sections were supplied by the David Taylor Model Basin.

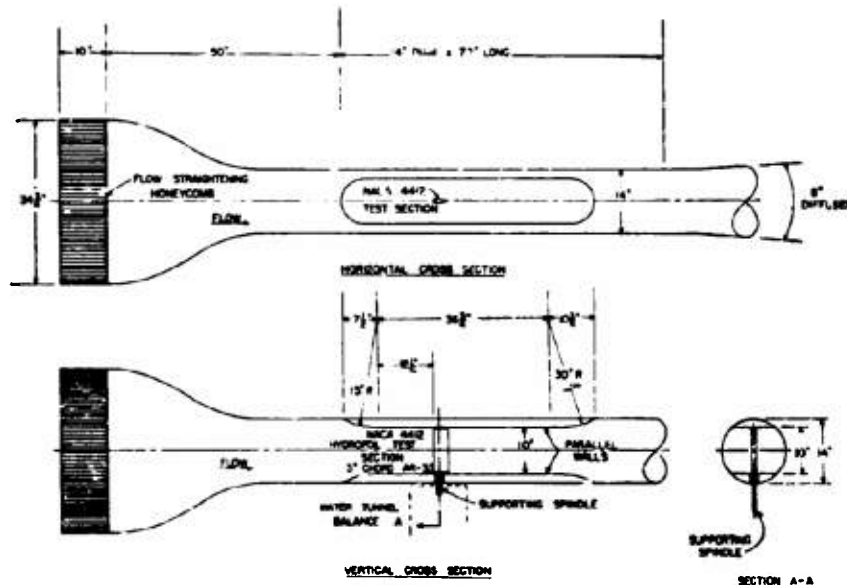


FIGURE 2. Hydrofoil test installation.

further correction the characteristics of a hydrofoil section with infinite aspect ratio. Infinite aspect ratio characteristics differ from those obtained by



FIGURE 3. View looking downstream into tunnel working section with the parallel walls and hydrofoil test span in place.

tests of a finite span airfoil or hydrofoil because of the occurrence for the finite span of the so-called "induced" effects.^{7,8,9}

These effects, which arise because of the large "leakage" of fluid at the tips of the foil from the high-pressure bottom surface to low-pressure top surface, reduce the lift and increase the drag at given angles of attack. The magnitude of the effects is different for changing aspect ratios, plan form, and twist of the section. Because of the absence of these secondary influences, infinite aspect ratio results are also called "section characteristics," denoting that they represent the basic behavior of the profile shape of the foil independent of aspect ratio or other geometrical configurations. Data in this form are particularly useful to the designer of wings, propeller blades, or other lifting or pumping devices. Several methods have been developed for converting section characteristic data into the performance of finite span units with either uniform or varying sections.^{7,8,9}

§ 1.4

Terms and Symbols

The terms and symbols most widely used for describing infinite aspect ratio characteristics are those developed for the aeronautics field. These differ in some respects from those normally used for reporting water tunnel data and, consequently, must be defined here. The following list includes all the definitions used in this chapter:

- α_0 = angle of attack between hydrofoil and the mean flow direction of the water, in degrees.
- d_0 = drag force per unit length of hydrofoil span, in pounds.
- l_0 = lift force per unit length of hydrofoil span, in pounds.
- m_{ac} = pitching moment per unit length of hydrofoil span, in foot-pound, measured about the aerodynamic center.
- v = relative velocity between the water and the hydrofoil, in feet per second
- ρ = density of water, in slugs per cubic foot.
- μ = absolute viscosity of water, in pounds-seconds per square foot.
- c = chord of hydrofoil section, in feet.
- b = span of hydrofoil test unit, in feet.
- b/c = aspect ratio.
- ac = aerodynamic center, the point about which the pitching moment coefficient is independent of lift.
- CP = center of pressure, the point at which the resultant of all the hydrodynamic forces acting on the hydrofoil is applied.

Section Profile Drag Coefficient

$$c_{d_0} = \frac{d_0}{\frac{\rho}{2} v^2 c}$$

Section Lift Coefficient

$$c_{l_0} = \frac{l_0}{\frac{\rho}{2} v^2 c}$$

Section Pitching Moment Coefficient (about aerodynamic center)

$$c_{m_{ac}} = \frac{m_{ac}}{\frac{\rho}{2} v^2 c^2}$$

Reynolds Number

$$R = \frac{vc\rho}{\mu}$$

Cavitation Parameter

$$K = \frac{P_L - P_b}{\frac{\rho}{2} v^2}$$

where in addition to terms defined above

P_L = absolute pressure in the undisturbed flow, in pounds per square foot,

P_b = pressure in the cavitation bubble (taken as equal to the vapor pressure of water for these tests), in pounds per square foot.

4.1.5 Measured Characteristics

The hydrodynamic characteristics without cavitation are shown in Figure 4, which is a diagram of angle of attack, drag, and pitching moment coefficients as functions of the lift coefficient. These data are derived directly from the water tunnel measurements without corrections of any kind. They include the Reynolds number range from 287,000 to 903,000 and were obtained with the semispan installation. Tests with the full span which were limited to Reynolds numbers below 388,000 gave the same results and were not included in the diagram. The magnitudes for the important characteristics for both semi- and full-span installations are given in Table 1.

The curves show certain consistent changes in performance with Reynolds number. With increasing Reynolds number the maximum lift coefficient increases while the angle of attack for zero lift and the profile drag both decrease. The pitching moment about the aerodynamic center remains essentially independent of Reynolds number up to a lift coefficient of about 0.8 (angle of attack of +4 degrees). Moreover, its magnitude is essentially constant in this range.

4.1.6 Deviations from True Infinite Aspect Ratio Characteristics

The only deviations of these results from real two-dimensional characteristics will be caused first, by variation of velocity along the span of the hydrofoil from the center of the working section on through the boundary layer to the tunnel wall; second, by flow through the clearance spaces between the ends of the foil and the tunnel walls or between the two halves of the split-span installation; and third, by interference from the tunnel walls.

Deviations from a uniform velocity distribution will tend to make all the coefficients numerically high. However, as shown in Figure 2, the hydrofoil test unit was located in the measuring section about one "diameter" downstream from the final contraction of the flow. With so short a distance the boundary layer growth should be small. Consequently, along most of the hydrofoil span the flow should have the full velocity of the central uniform portion of the velocity profile, and the resulting hydrodynamic forces and moments should be reasonably accurate for infinite span.

CONFIDENTIAL

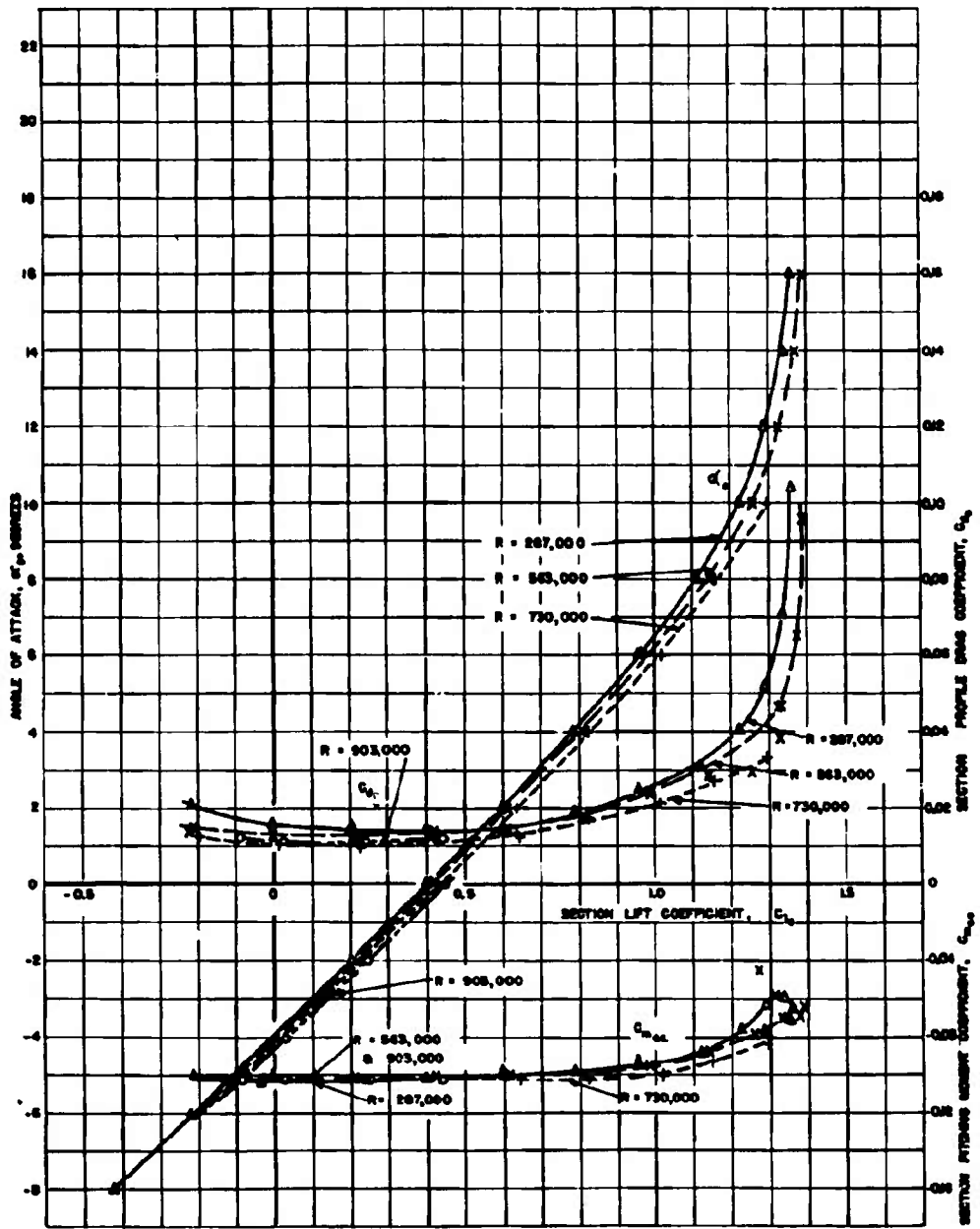


FIGURE 4. Infinite aspect ratio characteristics of the NACA 4412 hydrofoil section.

CONFIDENTIAL

TABLE 1. Principal section characteristics of the NACA 4412 hydrofoil from two-dimensional tests in water tunnel.

	Test Reynolds number	Attack angle for no lift	Lift curve slope	Max lift coefficient	Min drag coefficient	Pitching moment	Aerodynamic center	
		α_1 , in degrees	$c_{l\alpha}$ per degree	C_{lmax}	$C_{d0 min}$	C_{mom}	Ahead of $c/4$ in per cent of c	Above chord in per cent of c
Semispan installation	287,000	- 3.95	0.098	1.36	0.014	- 0.102	5.47	- 0.26
	563,000	- 4.06	0.102	1.39	0.013	- 0.101	4.92	- 4.52
	730,000	- 4.15	0.104	0.0105	- 0.102	5.53	- 3.84
	903,000	- 4.25	0.106	0.011	- 0.101	5.39	1.68
Full-span installation	299,000	- 4(approx)*	0.098	1.38	0.014	- 0.100	5.12	- 0.38
	388,000	- 4(approx)*	0.101	0.014	- 0.102	5.12	- 0.39
Theoretical values for infinite aspect ratio		- 4.58	0.120	- 0.137	0	0

*These values for α_1 are obtained after correction for error in initial alignment of hydrofoil chord with tunnel axis.

The principal effect of leakage flow through the gaps between the tunnel walls and the hydrofoil and between the ends of the split hydrofoil will be to reduce the actual angle of attack at the hydrofoil for high lifts. All clearance gaps were held to approximately 0.005 in., so that the resistance to flow through them was high. At small angles of attack the influence on the measured forces and moments should be negligible. However, as the lift increases, enough leakage flow may occur to reduce the maximum lift coefficient appreciably. This is an error in lift and moment that would be reduced by using end plates set into the tunnel walls instead of clearance gaps. However, such a setup would not be as satisfactory an arrangement for measuring drag. It should be emphasized that the clearance gap effect is important so that good control of the gap is essential. Measurements made with the clearance varied indicated that for a moderate range of the lift coefficient the errors in measurements made with 0.005-in. gap were probably not more than 2 per cent.

Tunnel wall interference changes the streamline pattern around the hydrofoil from that in a free stream. The walls parallel to the pitching axis are important for two-dimensional flow and it was with this in mind that the maximum dimension normal to the hydrofoil axis was held to the full 14 in., as shown in Figure 1. Wall interference, including the so-called "blocking" or actual restriction of the passage by the test unit itself, is negligible at low lift (small angles of attack). At high lifts it is much more important and should show greatest effect at the maximum lift. The actual magnitude of the wall interference has not been evaluated.

To summarize, it appears that these tests give accurate results in the low-lift range, the normal range of application for hydrofoils. At high lifts, the

accuracy is lower but good comparative results are still obtainable.

2.1.7 Theoretical Characteristics

It is of interest to compare these water tunnel measurements with the characteristics that can be calculated from theoretical consideration of an infinite-span section in a nonviscous fluid.^{2c} Such a treatment gives, for small angles of attack, a lift coefficient proportional to the angle of attack, an attack angle for zero lift proportional to the amount of camber, and a moment coefficient constant about the quarter-chord point. Since frictionless flow is assumed, the theoretical values are independent of Reynolds number. Also, because of the zero friction assumption, this treatment gives zero drag and gives no information about the maximum lift coefficient to be obtained. Comparison in Table 1 of the theoretical values with the measured values shows that the former are slightly higher (numerically) in each case.

2.1.8 Comparison with Wind Tunnel Measurements

The 4412 profile has been thoroughly tested in the NACA variable-density wind tunnel and its characteristics reported in a series of technical reports.^{2d} These measurements were made on finite rectangular span sections having an aspect ratio of 6 and the data were then corrected to get the infinite aspect ratio or section characteristics. In Figure 5, two of the water tunnel tests are compared with two of the wind tunnel tests for comparable Reynolds numbers. The wind tunnel data are not corrected for turbulence or scale effects and should not be confused with final characteristics, presented in the later NACA re-

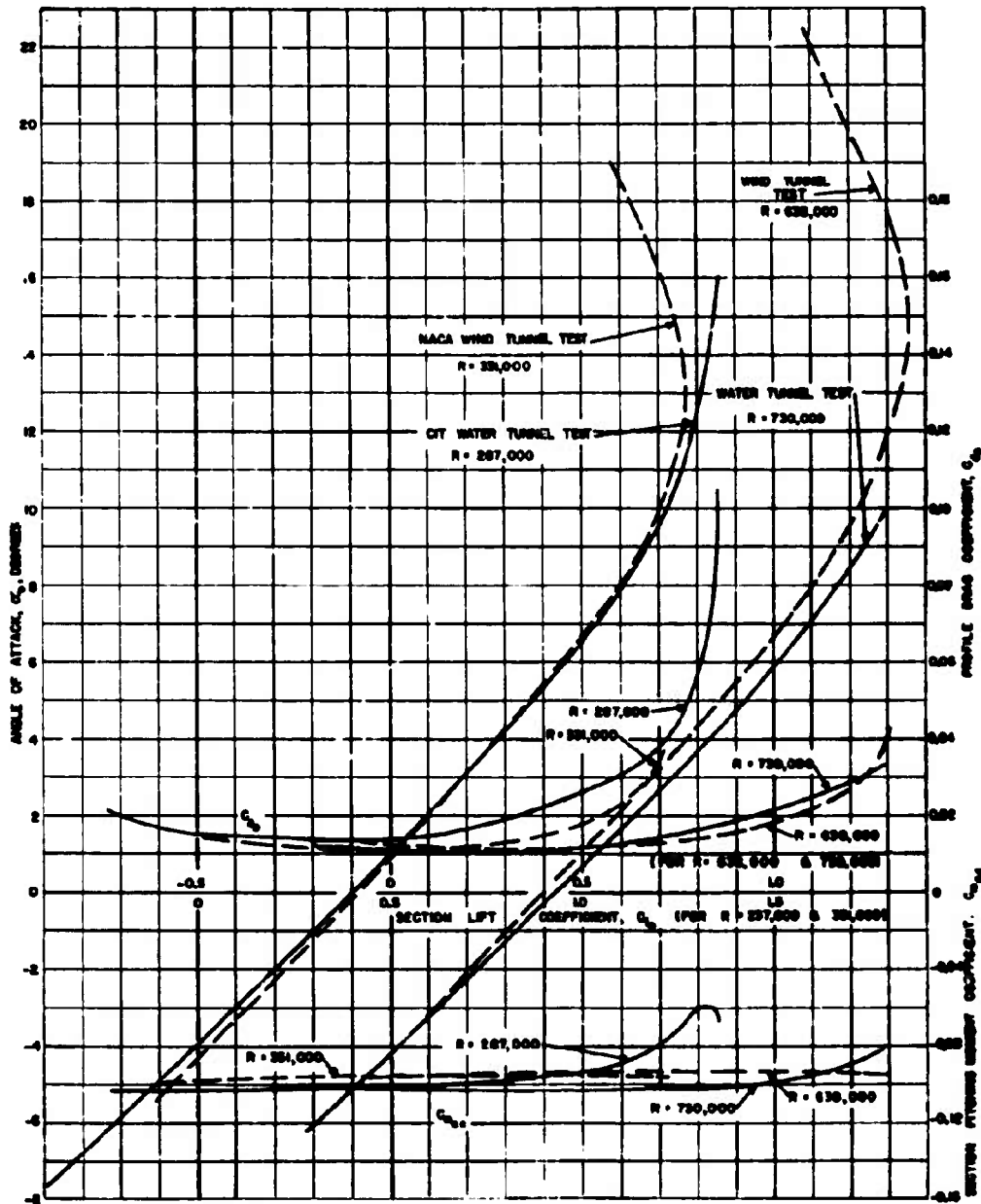


FIGURE 5. Comparison of NACA 4412 hydrofoil characteristics from wind tunnel and water tunnel tests.

CONFIDENTIAL

TABLE 2. Principal section characteristics of the NACA hydrofoil from wind tunnel tests of rectangular airfoils with aspect ratio = 6^o.

Test Reynolds number	Attack angle for no lift α_0 , in degrees	Lift curve slope a_0 , per degree	Max lift coefficient C_{lmax}	Min drag coefficient $C_{d0 min}$	Pitching moment C_{m0}	Aerodynamic center Ahead of $c/4$ in per cent of c	Above chord in per cent of c
331,000	- 4.35	0.094	1.27	0.011	- 0.096	1.1	- 8.0
638,000	- 4.25	0.094	1.36	0.012	- 0.094	1.0	- 10

*Wind tunnel data were taken from Figure 7 of the NACA Technical Report 869, and corrected by the methods outlined on pages 17 and 18 of that reference to give so-called "second approximation" characteristics.

ports,²⁵⁻²⁸ which have been extrapolated to full-scale aircraft flight Reynolds numbers. In Table 2, the principal characteristics from the wind tunnel tests for these two Reynolds numbers are listed for comparison with the water tunnel values given in Table 1. Both the figures and tabulations show some differences between the two sets of measurements. The angles for zero lift are comparable, while the minimum drag coefficient, the rate of change of lift with angle of attack, and the moment coefficient are all about 10 per cent lower in the case of wind tunnel measurements. The latter two represent more marked deviation from the theoretical values than shown by the water tunnel characteristics. The wind and water tunnel minimum drag coefficients are comparable at the higher Reynolds number but differ considerably at the lower R values. The maximum lift coefficient is higher for the water tunnel tests.

It is seen that the water tunnel results are as good or better than the corresponding wind tunnel data. Furthermore, they are obtained directly from tunnel measurements without corrections of any kind, whereas the finite span tests must be treated elaborately to obtain approximate infinite aspect ratio characteristics. Even at large attack angles where the water tunnel data may be in error, the results are as satisfactory as those from the other type of tests.

2.1.3 Reynolds Number and Turbulence Effects for Tests and Applications

The range of Reynolds numbers covered by the water tunnel tests includes the values characteristic of many hydrofoil applications. For very large propellers, R will exceed 1,000,000, but for many pump, turbine, and small propeller applications, R is less than that figure. For application outside the range of the tests the data must be extrapolated and corrected. For test Reynolds numbers up to about 3,000,000, wind tunnel measurements have indicated

that the lift curve slope increases only 1 or 2 per cent beyond its value at $R = 1,000,000$. The angle for zero lift and the pitching moment coefficient are also affected only slightly. However, the maximum lift coefficient increases 10 per cent to 20 per cent and the profile drag coefficient decreases at approximately the same rate as the turbulent skin-friction drag on flat plates. By judicious application of such rules the useful range of these results can be extended appreciably.

Actually, the performance measured in the tunnel will differ from free-stream behavior because of differences in turbulence. High turbulence in the tunnel working section will cause high maximum lift coefficients and will influence the boundary layer transition on the hydrofoil and hence c_{d0} . There are methods proposed for compensating for tunnel turbulence by assuming the results apply at higher than test Reynolds numbers, but these procedures are of questionable accuracy for all but c_{lmax} corrections and were not applied to the water tunnel data.

2.1.4 Cavitation Characteristics

The continuity of the behavior of airfoils when used in the normal range of velocities below the sonic is limited by "separation" of the flow for large angles of attack. For the same shape used as a hydrofoil in a liquid instead of a gas, the continuity in behavior can be interrupted by cavitation as well as by separation. Cavitation first occurs when, because of flow accelerations caused by the curvatures of the hydrofoil, the local pressure at any point on or near the hydrofoil is reduced to the vapor pressure of the liquid. This results in local boiling and vapor bubble formation. These bubbles collapse as they are swept into higher pressure zones. As the flow velocity is increased or as the general pressure level is reduced, the extent of the low-pressure zone is enlarged and the volume occupied by cavitation bubbles increases.

The interest in cavitation lies in the fact first, that when it begins, the lift on the hydrofoil (or thrust for propellers) drops off sharply and the drag simultaneously increases; second, prolonged cavitation causes physical damage to the hydrofoil blade itself. Cavitation erosion of propellers and turbine impellers are two outstanding examples of this latter.

CAVITATION PHOTOGRAPHS

Figures 7 to 13 inclusive make up a photographic study of the inception and growth of cavitation on the NACA 4412 hydrofoil. These flash photographs

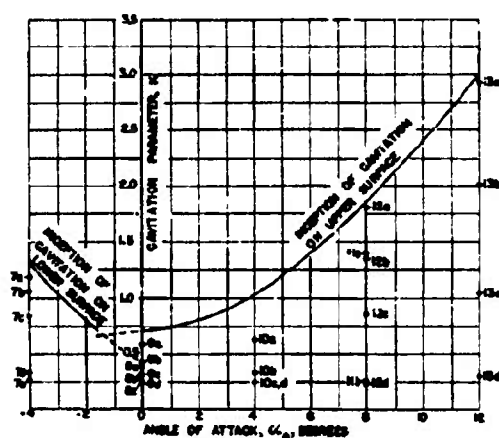


FIGURE 6. Diagram showing cavitation test conditions for each photograph in Figures 7 to 13.

of about 20 μ sec exposure were obtained at constant water speed and variable pressure. They include the development of cavitation on one or both faces of the hydrofoil for attack angles ranging from 4 to 12 degrees. The photographs are grouped according to angle of attack, each group arranged to show the development of cavitation as the pressure and hence the cavitation parameter K is reduced. Figure 6 is a diagram that will be useful in discussing the significance of the pictures. It is a graph of the cavitation parameter K plotted against the angle of attack α_0 . A curve marks the inception of cavitation on the upper and the lower surface of the hydrofoil. In the area above this curve there is no cavitation, while everywhere below the curve cavitation exists in varying degrees, increasing with the reduction of K below the incipient value. The numbers of 7A to 13D

appearing on the diagram refer to figures in the report and the coordinates of the points marked by the numbers indicate the attack angle and K value at which each picture was taken. Thus the relationship between conditions for inception of cavitation and the conditions for each figure is shown graphically.

ANGLE OF ATTACK AND CAVITATION INCEPTION

It will be noted in Figure 6 that for both large positive and large negative angles of attack, cavita-



FIGURE 7. Cavitation on lower surface. $\alpha = -4^\circ$. $V = 45$ feet per second. Flow right to left.

tion occurs "early," that is, at high pressures or low velocities and hence high K values. At angles near zero, cavitation is delayed, the minimum critical K falling at about 0.66 at $\alpha_0 = -1.4^\circ$. Thus, Figure 12A shows cavitation soon after inception at $K = 1.8$ for $\alpha_0 = +8^\circ$, while Figure 9A shows an early stage of cavitation at $K = 0.57$ for $\alpha_0 = 0^\circ$. This is caused by the fact that with increasing attack angle the leading edge of the hydrofoil, where the profile curvature is large, is turned at an angle to the flow and the water

must curve sharply to follow it. Consequently, the local acceleration of the fluid is large and the vapor pressure is reached locally even with high static pressure in the main flow. Cavitation occurs first on the top surface of the hydrofoil for all positive angles and for negative angles down to -1.4° because it is the low-pressure side for those attack angles. At negative angles beyond -1.4° , however, the higher pressure is obtained at the top and cavitation occurs first on the lower surface. Thus in Figure 7A, for $\alpha = -4^\circ$, the beginning of cavitation is shown near the leading edge of the lower side of the hydrofoil.

It is interesting to note that the best cavitation performance does not occur at the angle of attack for



FIGURE 8. Cavitation on lower surface. $\alpha = 0^\circ$. $V = 45$ feet per second. Flow right to left.

zero lift. At $\alpha_0 = -1.4^\circ$, which has the minimum value of $K = 0.66$ for incipient cavitation, the lift coefficient is 0.26 ($R = 287,000$) whereas at $\alpha_0 = -3.95^\circ$, which is the attack angle for zero lift, the K for incipient cavitation is 1.30.

At high angles of attack cavitation occurs only on one surface of the hydrofoil. There is a sufficient dynamic pressure increase on the surface pitched into the stream to suppress cavitation completely. Figures 11A to 12D show that for $\alpha_0 = 8^\circ$, no cavitation is obtained on the lower surface of the hydrofoil even though K is reduced to 0.26, while on the upper surface cavitation is well established at $K = 1.8$. For angles near zero, cavitation occurs first on the upper or low-pressure surface and then also occurs on the high-pressure surface as K is reduced. For example, at $\alpha = 0^\circ$, the lowest pressure occurs on the top of the hydrofoil and Figure 9B shows well developed cavi-

tation there with $K = 0.42$. By contrast, Figure 8A shows the bottom surface at $K = 0.37$ with cavitation in an early stage. There the beginning of cavitation on the lower side is seen with trailing wisps of the more fully developed cavitation from the top appearing at the left.

CAVITATION BUBBLE GROWTH

A certain similarity exists for each sequence of photographs for one angle of attack. Cavitation be-



FIGURE 9. Cavitation on upper surface. $\alpha = 0^\circ$. $V = 45$ feet per second. Flow left to right.

gins on the forward part of the hydrofoil as a narrow zone of small bubbles. The bubbles are individually distinguishable in some cases but coalesce to form "sudsy" zones in others. The limit of the zone of bubbles is a rough measure of the extent of the low-pressure area on the hydrofoil surface. As the pressure is reduced the low-pressure area is broadened and the vapor bubbles are swept farther back before collapsing, until they form a sheet hiding the hydrofoil and extending downstream more than 6 or 8 chord lengths, completely past the limits of the working-section windows. (See Figures 9D, 101, etc.) For any given pressure and velocity the cavitation bubble grows until the rate of vapor entrainment by the water balances the rate of vapor formation within the bubble. Thus the magnitude of the cavitation zone in

each of the photographs represents a "steady-state" condition for the given value of K .

As Figures 7A to 8C show, the fine-grain sudsy type of bubbles are obtained where the minimum pressure is caused by a sharp curvature such as occurs at the leading edge of the lower hydrofoil surface. Figures 9A to D, on the other hand, show the formation of transparent, relatively large individual bubbles on the upper surface. Here the minimum pressure is obtained where the profile has a more gentle curvature. As the hydrofoil is given large angles of attack

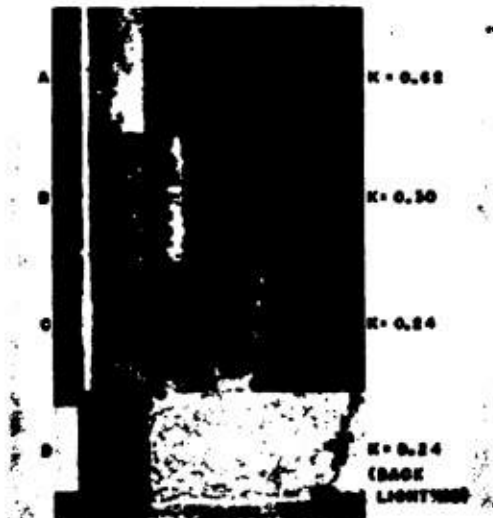


FIGURE 10. Cavitation on upper surface. $\alpha = +4^\circ$. $V = 45$ feet per second. Flow left to right.

(Figures 13A to D at $\alpha = +12^\circ$), the minimum-pressure point moves forward to a place where the curvature of the upper surface is sharper and the sudsy bubbles are again obtained.

Under some conditions the forward portion of the large enveloping bubble for fully developed cavitation is transparent. That is, the interface between the cavitating zone and the surrounding water is a smooth surface, free of disturbances. An example of this is shown in Figure 7E where the hydrofoil itself and the disturbance from cavitation on the opposite face of the hydrofoil are clearly visible through the bubble enveloping the near surface. The smooth interface is an indication that very little vaporization is occurring through that surface. Most of the vapor that is being supplied to the bubble comes from the

turbulent boiling zone near the downstream end of the envelope. Figure 9D shows how the bubbles tend to coalesce as the pressure is reduced to form the single large transparent envelope. The transparency



FIGURE 11. Cavitation on lower surface. $\alpha = +8^\circ$. $V = 45$ feet per second. Flow right to left.



FIGURE 12. Cavitation on upper surface. $\alpha = +8^\circ$. $V = 45$ feet per second. Flow left to right.

cannot always be reproduced, but rather seems to occur randomly unless some external disturbance, such as a piece of trash hanging to the foil or a nick in its surface, is introduced to accelerate the formation. Figure 8B shows the effect of small disturbances at the leading edge in forming long, extended bubbles. Such disturbances also cause cavitation to occur at higher pressures (or lower velocities).

Note that the individual bubbles grow from the time of their formation until they collapse. In Figure

IOC measurements of the average bubble size showed that growth was rapid for the first quarter chord length of travel, attaining 60 to 75 per cent of what appears to be the final diameter. Beyond this the

growth of the bubbles is probably evidence of continual vaporization into each bubble cavity until the bubble itself is swept into a higher pressure zone.

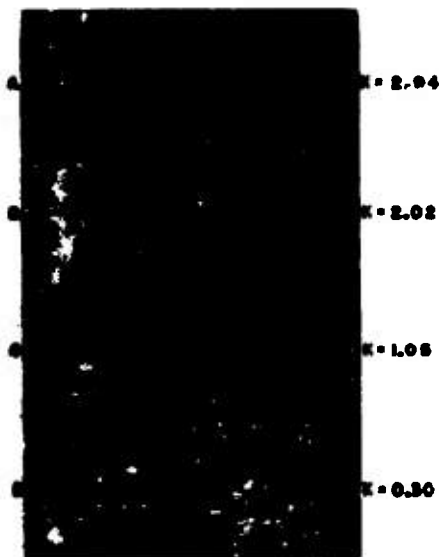


FIGURE 13. Cavitation on upper surface. $\alpha = +12^\circ$. $V = 32$ feet per second. Flow left to right.

bubbles grow more slowly until they interfere with their neighbors and finally are entrained and collapse. The interior of the cavitation bubble is at the vapor pressure of the water and is maintained at this pressure by the "pumping" action of the water. The

CRITICAL K COMPARED WITH PREDICTIONS FROM WIND TUNNEL DATA

Figure 14 is another diagram showing values of the cavitation parameter K for incipient cavitation

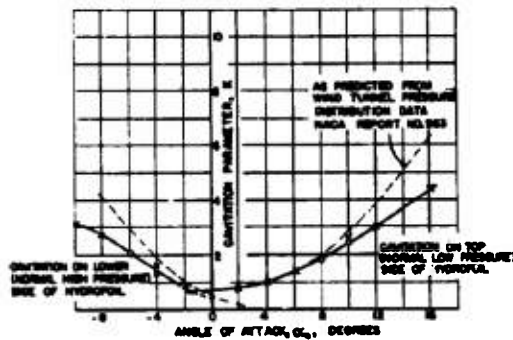


FIGURE 14. Values of K at which cavitation begins versus angle of attack.

versus the angle of attack α_0 . This diagram covers a much wider range of angles than Figure 6 and includes, in addition, a curve predicted from wind tunnel measurements of the pressure distributions on the 4412 profile.⁷⁸ The agreement between the water tunnel curve and the predicted curve is good only for small positive angles of attack, while for increasing

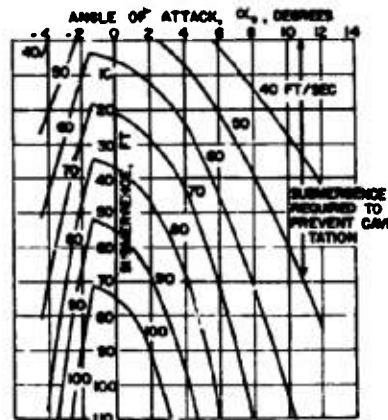
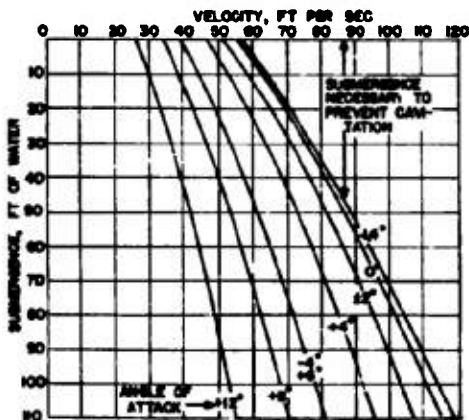


FIGURE 15. Submergence required to prevent cavitation on NACA 4412 hydrofoil.

α_0 , either negatively or positively, the water tunnel tests indicate a "delay" in reaching the inception point. A similar deviation from pressure-distribution predicted values for inception has been observed in case of some projectile shapes. As discussed in Chapter 6, the reason for the deviation is not known definitely, but may be associated with the ability of the fluid to stand a slight tension.

SUBMERGENCE REQUIRED TO PREVENT CAVITATION

Figure 15 shows the submergence required to prevent cavitation on the 4412 hydrofoil as a function of velocity and angle of attack. The term "submergence" means the vertical depth below the water surface (e.g., ocean surface). The curves are calculated for

fresh water at 60 F and 14.7 psi atmospheric pressure. In each of the two diagrams the vertical distance down from the horizontal axis represents the submergence required to prevent cavitation at a given attack angle or given velocity. All points below the constant α_0 or constant v curves represent cavitation-free operation.

It is clear from the left diagram that for any velocity, the minimum submergence will be required for cavitation-free operation if $\alpha_0 = -1.4^\circ$. For all other angles of attack, the necessary submergence is greater. In the right diagram the limiting range of angles at given velocities and submergences are emphasized. For example, at 60 fps and 15 ft submergence, cavitation-free operation is possible only within the limits of -2.4° and $+2.6^\circ$.

Chapter 19

MISCELLANEOUS INVESTIGATIONS

19.1 FLUID FRICTION LOSSES IN 0.50-CALIBER GUN BARRELS

19.1.1 Purpose of Investigation

TWO ASSOCIATED problems in the internal ballistics of guns arise from the rapid expansion of the powder gases. One is the reduction in effective force applied at the projectile as a result of the pressure drop caused by fluid friction, and the other is the influence of the friction effects on heat transfer. The measurements described here were made to determine the effect of rifling on the friction pressure drop and to determine by analogy with the fluid friction laws the effect on turbulence and, hence, on heat transfer.

19.1.2 Material Tested

Test measurements were recorded for two barrels. These barrels were standard except that one had no rifling. Their comparative dimensions and conditions are indicated as follows:

	Rifled Barrel	Unrifled Barrel
Bore diameter	0.500 in.	0.500 in.
Maximum diameter	0.507 in.	0.500 in.
Rifling groove depth	0.0035 in.	None
Rifling groove width	0.125 in.	None
Land width	0.071 in.	None
Area of cross section normal to barrel axis	0.1999 sq in.	0.1964 sq in.
Equivalent diameter	0.5045 in.	0.500 in.
Twist of rifling	1 turn in 30.5 calibers	None
Surface condition	Spiraled boring tool marks on lands were not so deep as for unrifled barrel. Broaching tool marks along length of each groove	Close spaced, spiraled boring tool marks throughout barrel length
Barrel length	3.349 ft	3.349 ft
Distance between pressure taps	3.646 ft	3.646 ft

19.1.3 Friction Factor

The friction factor was evaluated for both barrels from the equation

$$H_f = f l v^2 / 2dg \quad (1)$$

where H_f = friction loss in feet of the fluid flowing,
 f = friction factor,

l = length in feet of the barrel or tube between pressure taps,
 v = mean velocity in feet per second,
 g = acceleration of gravity in feet per second per second,
 d = diameter of the tube in feet or $= (4A/\pi)^{1/2}$ for the rifled barrel, when A is the actual cross-sectional area.

The Reynolds number is calculated from the equation

$$R = \frac{vd\rho}{\mu} = \frac{vd}{\nu}$$

where $\nu = \mu/\rho$ = kinematic viscosity in square feet per second.

19.1.4 Results Obtained

Figures 1, 2, and 3 are graphical representations of the results obtained.

Figure 1 shows that, for the same rate of flow, the unrifled barrel offers approximately 4 per cent more resistance than hydraulically smooth tubing* of 0.500-in. diameter, while the rifled barrel offers about 3 per cent less. Several factors contribute to this difference. The effective area of the rifled barrel normal to the centerline is greater than for an 0.500-in. diameter tube and this lowers the velocity and resistance. In addition, the unrifled barrel is hydraulically rougher and shows boring tool marks which appear to be deeper than any of the boring or longitudinal broaching marks on the rifled piece. Apparently, because of this very gradual twist, the rifling grooves do not constitute roughness in the normal sense. Note that they did not cause enough rotation of the water to affect the pressure at the downstream measuring point. The friction factors for both barrels approach that of a smooth tube so closely that, for practical purposes, they can be assumed to be smooth tubes.

Figure 2 presents the relation of the friction loss to the Reynolds number.

Figure 3 presents the relation of the friction factor to the Reynolds number. The curve for the unrifled

* The resistance for hydraulically smooth tubing is calculated from the Kármán-Nikuradse equation $(1/\sqrt{f}) = -0.8 + 2.0 \log_{10} (R\sqrt{f})$.

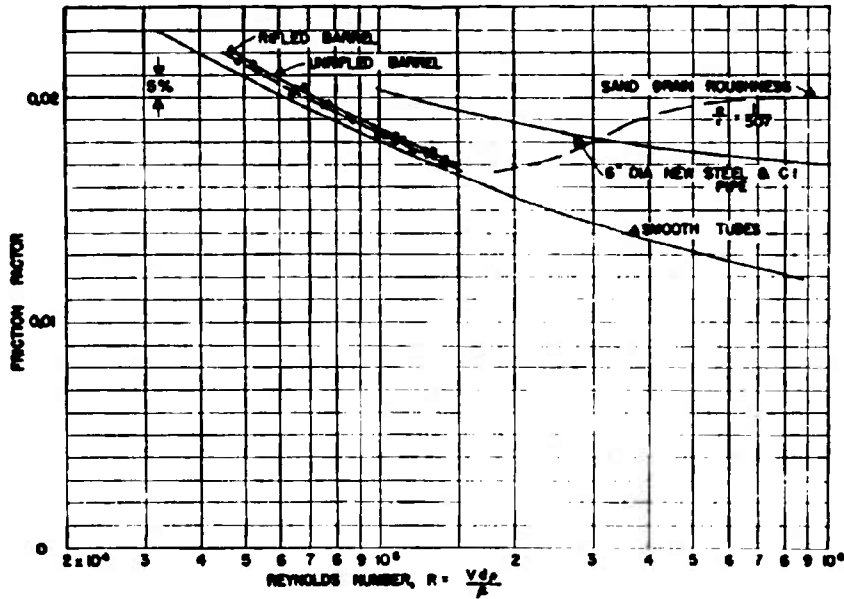


FIGURE 1. Friction factor versus Reynolds number for 0.50-caliber rifled and unrifled gun barrels.

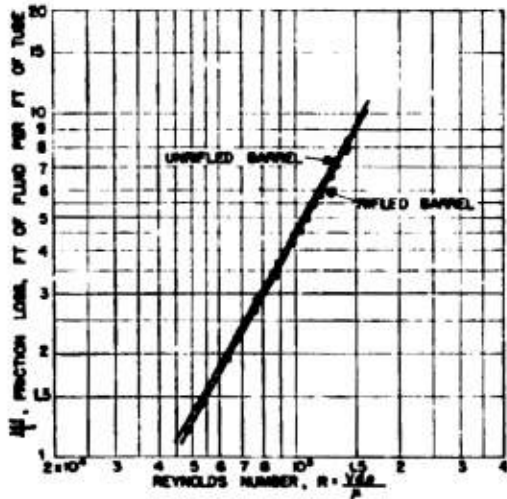


FIGURE 2. Friction loss per unit length of tube versus Reynolds number. For 0.50-caliber rifled and unrifled gun barrels.

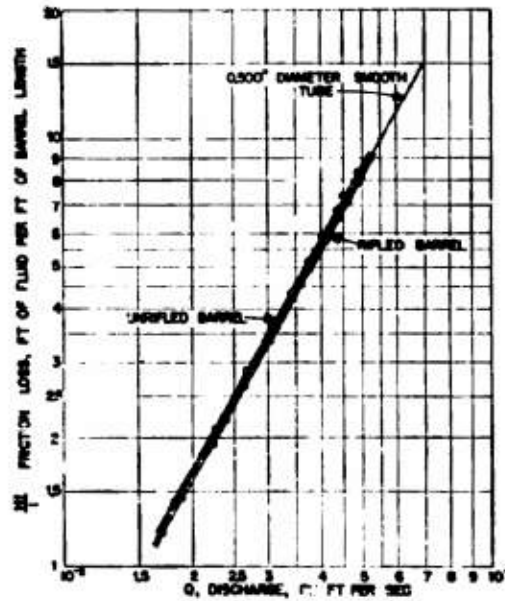


FIGURE 3. Friction loss per unit length of tube versus discharge in cubic feet per second for 0.50-caliber rifled and unrifled gun barrels.

barrel has the same position relative to that for smooth tubes as in the previous figures. However, the curve for the rifled barrel also falls above the smooth-tube curve. This is to be expected when it is considered that Figure 3 is for the friction factor calculated for the actual cross section which is larger in this case.

The results of many investigations of friction loss of different types of tubes have shown that the friction pressure drop at Reynolds numbers between 100,000 and 1,000,000 depends on the type of surface roughness.^{19,22} If the roughness is produced by irregular projections randomly spaced, f becomes constant as Reynolds number is increased. However, if the roughness is produced by waviness in the pipe wall, the curve of f vs R continues approximately parallel but above that of the hydraulically smooth tube. At extremely high Reynolds numbers, most experiments show that rough tubes and pipes assume a constant value of f . Because of these differences, the relation observed in Figure 3 between the curves for smooth tubes and for the gun barrels may not hold exactly if R is further increased. It is possible that the actual friction drop curve for the gun barrels may pass through a transition to give a constant f of

approximately the measured value or possibly slightly higher or, as R increases, it may continue parallel to the smooth-pipe curve. In Figure 3 are shown values for new steel pipes which might be considered to have a wavy-type surface. A curve is also shown for artificially roughened pipe having an irregular type of roughness produced by sand grains whose diameters averaged 1/507 times the tube radius. These two curves are shown as an indication of the trends which could be expected and not as a measure of extrapolated values. Actually, the deviation of the curves for the gun barrels is so slight and the character of the surface is so different from sand-grain roughness, it may be expected that f will continue parallel to the smooth-tube curve in a manner similar to that of the steel pipe curve shown.

The similarity between the fluid friction factor curves in Figure 3 for the rifled and unrifled barrels indicates a similar degree of development of the boundary layer and of friction turbulence. It is not expected, therefore, that the law of heat transfer should be materially different with rifling than without. Assuming the continued agreement of friction factors at higher Reynolds numbers, this conclusion should also hold under actual firing conditions.

APPENDIX

DEFINITIONS OF SPECIAL TERMS AND FORMULAS

The purpose of this Appendix is to present the definitions of special terms and the formulas used frequently throughout this volume in a compact and convenient form for ready reference. Any additional definitions may be found in the Glossary.

DEFINITIONS

YAW ANGLE, ψ

The angle, in a horizontal plane, which the axis of the projectile makes with the direction of motion. Looking down on the projectile, yaw angles in a clockwise direction are positive (+) and in a counterclockwise direction, negative (-).

PITCH ANGLE, α

The angle, in a vertical plane, which the axis of the projectile makes with the direction of motion. Pitch angles are positive (+) when the nose is up and negative (-) when the nose is down.

LIFT, L

The force, in pounds, exerted on the projectile normal to the direction of motion and in a vertical plane. The lift is positive (+) when acting upward and negative (-) when acting downward.

CROSS FORCE, C

The force, in pounds, exerted on the projectile normal to the direction of motion and in a horizontal plane. The cross force is positive when acting in the same direction as the displacement of the projectile nose for a positive yaw angle, i.e., to an observer facing in the direction of travel, a positive cross force acts to the right.

DRAG, D

The force, in pounds, exerted on the projectile parallel with the direction of motion. The drag is positive when acting in a direction opposite to the direction of motion.

MOMENT, M

The torque, in foot-pounds, tending to rotate the projectile about a transverse axis. Yawing moments

tending to rotate the projectile in a clockwise direction (when looking down on the projectile) are positive (+), and those tending to cause counterclockwise rotation are negative (-). Pitching moments tending to rotate the projectile in a clockwise direction (when looking at the projectile from the port side) are positive (+), and those tending to cause counterclockwise rotation are negative (-).

In accordance with this sign convention a moment has a destabilizing effect when it has the same sign as the yaw or pitch angle.

In all model tests the moment is measured about the point of support. Moments about the center of gravity of the projectile have the symbol, M_{cg} .

NORMAL COMPONENT, N

The sum of the components of the drag and cross force acting normal to the axis of the projectile. The value of the normal component is given by the following:

$$N = D \sin \psi + C \cos \psi \quad (1)$$

in which N = normal component in pounds,

D = drag in pounds,

C = cross force in pounds,

ψ = yaw angle in degrees.

CENTER OF PRESSURE, CP

The point of intersection of the axis of the projectile and the resultant of all forces acting on the projectile.

CENTER-OF-PRESSURE ECCENTRICITY, e

The distance between the center of pressure (CP) and the center of gravity (CG) expressed as a decimal fraction of the length (l) of the projectile. The center-of-pressure eccentricity is derived as follows:

$$e = (l_{cp} - l_{cg}) \frac{1}{l} = \frac{1}{l} \frac{M_{cg}}{N} \quad (2)$$

in which e = center-of-pressure eccentricity,

l = length of projectile in feet,

l_{cg} = distance from nose of projectile to CG in feet,

l_{cp} = distance from nose of projectile to CP in feet.

COEFFICIENTS

The three force and moment coefficients used are defined as follows.

Drag coefficient:

$$C_D = \frac{D}{\frac{\rho}{2} V^2 A_D}, \quad (3)$$

Cross force coefficient:

$$C_C = \frac{C}{\frac{\rho}{2} V^2 A_D}, \quad (4)$$

Lift coefficient:

$$C_L = \frac{L}{\frac{\rho}{2} V^2 A_D}, \quad (5)$$

Moment coefficient:

$$C_M = \frac{M}{\frac{\rho}{2} V^2 A_D l}, \quad (6)$$

in which D = measured drag force in pounds,
 C = measured cross force in pounds,
 L = measured lift force in pounds,
 ρ = density of the fluid in slugs per cubic foot = w/g ,
 w = specific weight of the fluid in pounds per cubic foot,
 g = acceleration of the gravity in feet per second per second,
 A_D = area in square feet at the maximum cross section of the projectile taken normal to the geometric axis of the projectile,
 V = mean relative velocity between the water and the projectile in feet per second,
 M = moment, in foot-pounds, measured about any particular point on the geometric axis of the projectile,
 l = overall length of the projectile in feet.

RUDDER EFFECT

The total increase or decrease in moment coefficient, at a given yaw or pitch angle, resulting from a given rudder setting. This change in moment coefficient is measured directly from the graph of the moment coefficient curves for neutral rudder setting and various fixed rudder settings.

REYNOLDS NUMBER

In comparing hydraulic systems where the predominating forces are due to friction and inertia, a factor called Reynolds number is of great utility.

This is defined as follows:

$$R = \frac{lV}{\nu} = \frac{lV\rho}{\mu}, \quad (7)$$

in which R = Reynolds number,
 l = overall length of projectile in feet,
 V = velocity of projectile in feet per second,
 ν = kinematic viscosity of the fluid in square feet per second = μ/ρ ,
 ρ = mass density of the fluid in slugs per cubic foot,
 μ = absolute viscosity in pound-seconds per square foot.

The following numerical example is for the Mark 13-2A torpedo operating in sea water at a temperature of 50 F.

$$\begin{aligned} V &= 33 \text{ knots} = 55.7 \text{ ft/sec} \\ \nu &= 1.46 \times 10^{-4} \text{ sq ft/sec (for salt water)}^* \\ l &= 161 \text{ in.} = 13.42 \text{ ft} \\ R &= \frac{13.42 \times 55.7}{1.46 \times 10^{-4}} \\ &= \frac{13.42 \times 55.7 \times 100,000}{1.46} = 51.2 \times 10^6 \\ &\quad (51,198,200) \end{aligned}$$

Two geometrically similar systems are also dynamically similar when they have the same value of Reynolds number. For the same fluid in both cases, a model with small linear dimensions must be used with correspondingly large velocities. It is also possible to compare two cases with widely differing fluids provided l and V are properly chosen to give the same value of R .

CAVITATION PARAMETER

In order to describe quantitatively the conditions under which cavitation occurs, the dimensionless cavitation parameter, K , has been defined as follows:

$$K = \frac{P_L - P_n}{\frac{\rho}{2} V^2}, \quad (8)$$

in which P_L = absolute pressure in the undisturbed liquid,
 P_n = absolute pressure in the bubble or cavity,
 V = velocity of the projectile with respect to the undisturbed liquid,
 ρ = density of liquid.

* Tables of kinematic viscosity for salt water with an average salinity of 3.5 per cent are given in Rowell and Chapman *Principles of Naval Architecture*, Society of Naval Architects and Marine Engineers, 1941, Vol. II, p. 114.

Note that any homogeneous set of units can be used in the computation of this parameter. It is often convenient to express this parameter in terms of the head, i.e.,

$$K = \frac{h_L - h_B}{V^2/2g} \quad (9)$$

where h_L = the submergence plus the barometric head in feet of fluid,
 h_B = absolute pressure in the bubble in feet of liquid,
 g = acceleration of gravity in feet per second per second,
 $V^2/2g$ = the velocity head in feet of liquid.

Any length unit can be used in equation (9) instead of feet. It will be seen that the numerator of both expressions is simply the net pressure or head acting to collapse the cavity or bubble. The denominator is the velocity pressure or head. Since the pressure reduction at any point on the body is proportional to the velocity pressure, this may be considered as a measure of the pressure available to open up a cavity. From this point of view, the cavitation parameter measures the ratio of the pressure available to collapse the bubble to the pressure available to open it. P_B is the vapor pressure of the fluid if the cavity contains no air or other gas. For normal cases of cavitation this is assumed to be true.

If the K for incipient cavitation (K_i) is considered, it can be interpreted to mean the maximum reduction in pressure on the surface of the body, from the pressure in the undisturbed fluid, measured in terms of the velocity pressure. From this it follows that, if a body starts to cavitate at the cavitation parameter of one, it means that the lowest pressure at any point on the body is one velocity pressure below that of the undisturbed fluid. It will be seen that K_i is a measure of the resistance of the body to cavitation, or in other words, an indication of the excellence of the shape. Thus, the lower the K for incipient cavitation, the greater the cavitation resistance, and the better the shape from this viewpoint.

If the operating conditions (submergence and velocity in a given fluid medium) are such that the numerical value of K is greater than K_i the body will not cavitate. For values less than K_i more advanced cavitation will exist to the limit of a completely enveloping cavity with an "infinite" length when K becomes zero.

Using the Mark 13 torpedo as an example, consider how cavitation on the nose is affected by operation at 33 knots and 40.5 knots in sea water at a temperature of 50 F and a submergence of 15 feet.

At 33 knots

$$\begin{aligned} P_L &= P_{\text{atmos}} + h_{\text{sub}} W \\ &= 14.7 \times 144 + 15 \times 64 = 3,080 \text{ lb/sq ft} \\ P_B &= 0.98 \times \text{vapor pressure of pure water at same} \\ &\quad \text{temperature.}^b \\ &= 0.98 \times 0.178 \times 144 = 25.6 \text{ lb/sq ft} \\ \rho &= \frac{64 \text{ lb/cu ft}}{g} = 1.99 \text{ slugs/cu ft} \\ V &= 33 \text{ knots} = 55.7 \text{ ft/sec} \end{aligned}$$

so that

$$K = \frac{3,080 - 25.6}{1.99 \frac{(55.7)^2}{2}} = \frac{3,054.4}{3,080} = 0.99$$

This is greater than K_i for the nose of this projectile, so cavitation will not exist.

At 40.5 knots

$$V = 40.5 \text{ knots} = 68.3 \text{ ft/sec}$$

so that

$$K = \frac{3,080 - 25.6}{1.99 \frac{(68.3)^2}{2}} = \frac{3,054.4}{4,640} = 0.66.$$

This is slightly below K_i for this nose so a small ring of cavitation will exist.

Figure 1 gives the relation among absolute pressure, velocity, and cavitation parameter for fresh water at 70 F whereas Figure 2 shows the relation among submergence, velocity, and cavitation parameter for sea water at 50 F.

CORRECTIONS TO WATER TUNNEL TEST DATA

The test data obtained from the water tunnel is in the form of forces and moments which indicate the actual hydrodynamic conditions to which the model is subjected in the tunnel working section. These in general, however, are not the conditions which would exist if the model were moving freely in an infinite body of water. Consequently, in reducing the data to coefficients applicable to the free-stream conditions, the following corrections are considered.

TARE DRAG

The clearance between the model and the shield is less than 0.005 inch. With this small gap it appeared that the hydrodynamic force applied directly to the

^b This approximation is obtained from Sverdrup-Johnson-Fleming, *The Oceans*, Prentice-Hall, 1942, pp. 67, 115. Standard properties of pure water are given in Keenan and Keyes, *Thermodynamic Properties of Steam*, Wiley, 1936.

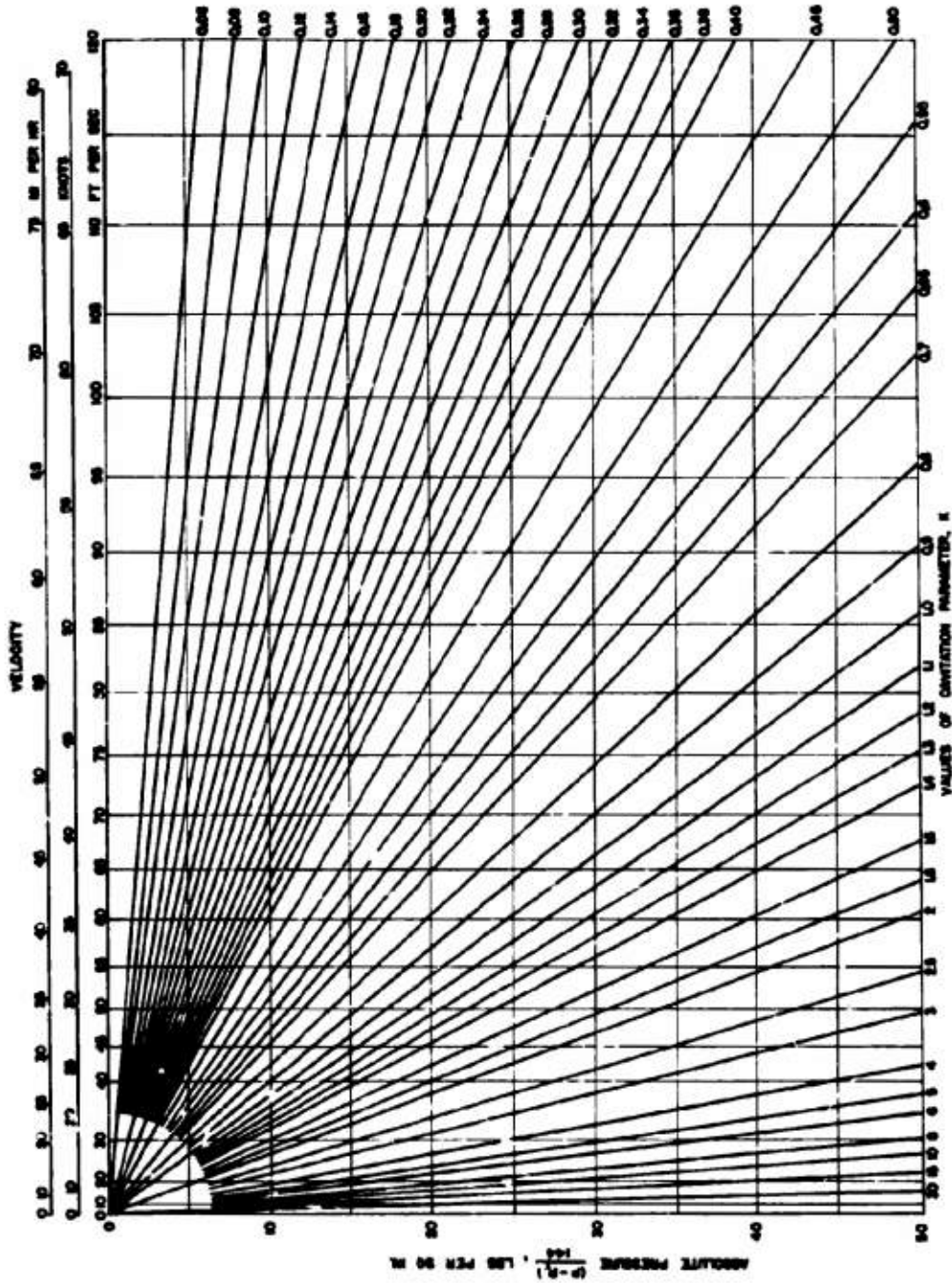


FIGURE 1. Relation among absolute pressure, velocity, and cavitation parameter for fresh water at 70 F.

CONFIDENTIAL

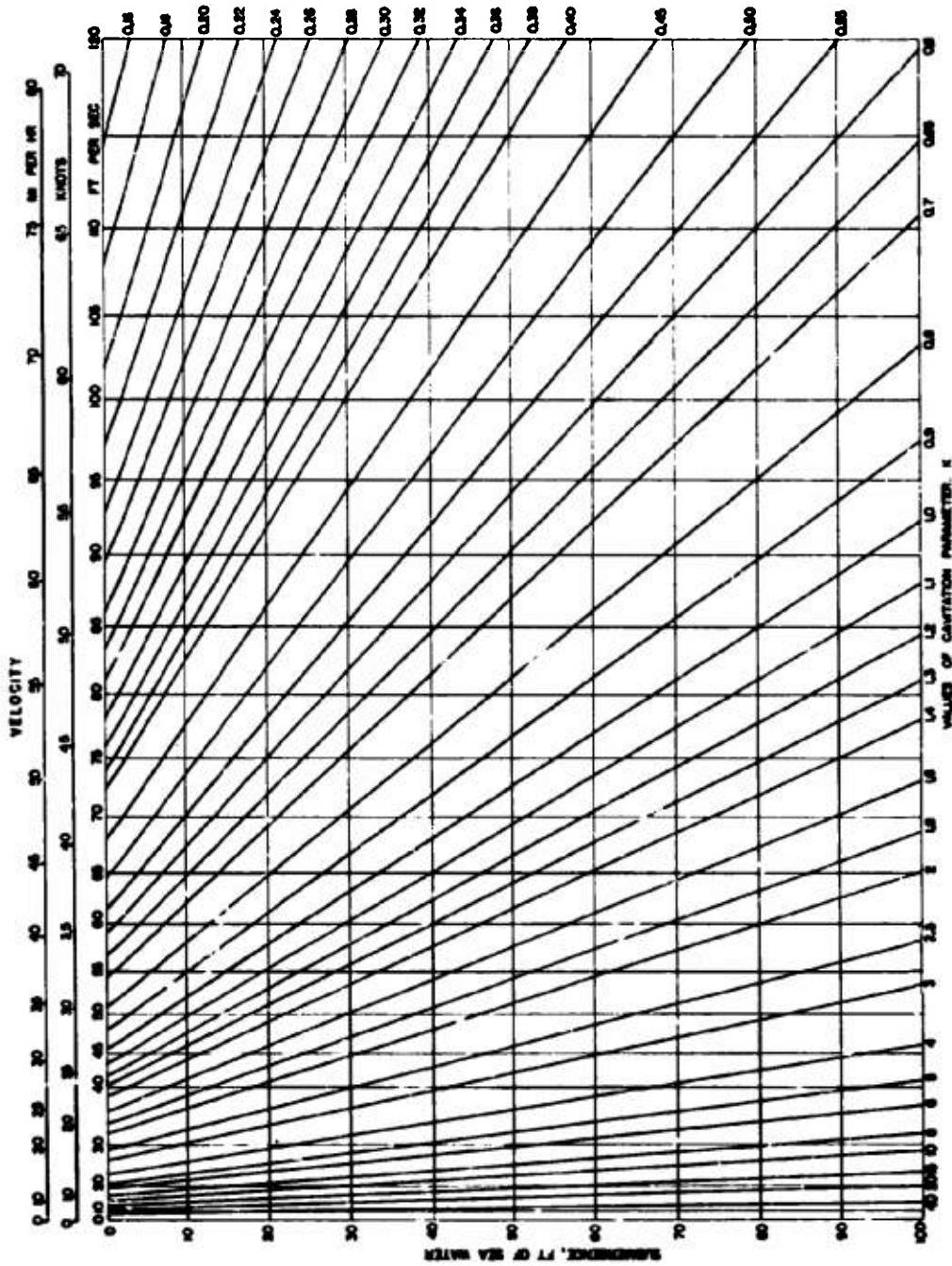


FIGURE 2. Relation among submergence, velocity, and cavitation parameter for sea water at 50 F.

CONFIDENTIAL

spindle would be negligible. Consequently, no tare corrections are applied to the measured forces.

SUPPORT SHIELD INTERFERENCE

In order to correct for the effects of interference with the flow around the model caused by the supporting spindle and its protecting shield, tests are normally made in pairs, one with and one without a dummy image shield on the side of the model opposite the support. The differences between the coefficients thus obtained from each pair of tests is subtracted from the run made without image shield.

For normal cavitation-free operation this procedure produces a result believed to be a good approximation of free-stream conditions. With the onset and development of cavitation, however, the shield and its image produce different results depending upon the degree of the cavitation obtained at various values of K . For very low K 's the shield itself cavitates. As a result, the corrections determined by the above method vary in magnitude and, without doubt, in accuracy. For the full cavity stage, corrections apparently are small. In general, for the material included in this volume the normal corrections were applied for all tests which covered the incipient or the early stages of development. For tests which included only the full cavity stage, such as those described in Chapter 6, no corrections were applied.

TUNNEL PRESSURE GRADIENT

The tunnel pressure gradient correction to be applied to the measured drag for noncavitating or slightly cavitating conditions is evaluated by measuring the pressure gradient existing in the working section of the tunnel in the absence of the model. The pressure gradient dp/dx at each station is multiplied by the cross-sectional areas of the model at that station and the product is plotted against distance along model. The area under this curve gives

$$\int_0^L s \frac{dp}{dx} dx = \int_0^L S dp$$

For models which are five or more diameters in length the calculation can be simplified by writing

$$\frac{dp}{dx} \int_0^L S dx = \frac{dp}{dx} (\text{volume}),$$

i.e., by using the (average pressure drop) \times (volume). It is this expression that has caused the correction to be termed "horizontal buoyancy."

SCALE EFFECT

Tests made in the range of 20 to 70 feet per second (Reynolds numbers from about 2×10^6 to 7×10^6) have shown that lift, cross force, and moment coefficients are unaffected by the scale of the tests, but that the drag coefficient does vary with Reynolds number. Extrapolation of C_D to full-scale Reynolds numbers depends upon the type of body and hence the form drag layer growth over the body. For some streamlined bodies, such as those with very fine noses, the transition between the laminar and turbulent boundary layers may shift position with change in Reynolds number. For these the C_D vs R curve may be irregular or even rising so that extrapolation is very difficult. In such cases it is customary to provide some disturbance such as a small ring or a roughened surface at the nose of the projectile to assure turbulent conditions at all velocities. Extrapolation is based on the resulting "turbulent" curve.

For bodies which do not indicate a shifting transition region, as well as those whose boundary layers are made turbulent artificially, a linear extrapolation of C_D vs R on a log-log plot has been found to give, in general, results that are satisfactory within the accuracy of the measurements. This method assumes that the drag coefficient (after correction for tunnel pressure gradient) varies inversely as the n th power of Reynolds number. For a projectile whose boundary layer is predominantly turbulent and whose afterbody is well streamlined, n should be close to $1/5$. Deviations from this value are the result of different degrees of streamlining and consequent effects on the boundary layer and portion of total drag represented by skin friction. Of course, for a projectile whose drag is almost completely form resistance, C_D should be nearly independent of Reynolds number.

GLOSSARY

- a.c.** Aerodynamic center, point about which pitching moment is independent of lift.
- ACOUSTIC FREQUENCIES.** See sonic frequencies.
- A_D.** Area of projectile at maximum diametrical cross section (square feet).
- AFTERBODY.** That portion of the projectile between the cylindrical body section and the forward edge of the tail structure.
- AIR BOMBS.** As here used, the term applies to any projectile which contains no propellant, is not fired from a gun, and whose trajectory is wholly in air.
- ANGLE OF ATTACK, α .** The angle between some arbitrary axis-of-reference in the body and its direction of motion.
- ASPECT RATIO.** Ratio of span to mean chord of hydrofoil section.
- a.** Span of hydrofoil section (feet).
- b/c.** Aspect ratio of hydrofoil section.
- BODY.** The main portion of the projectile; the projectile less any boom and tail surfaces. Also used frequently herein to refer only to the cylindrical portion of the projectile between the nose and afterbody.
- BOOM.** A small diameter, cylindrical extension from the afterbody generally used to house a rocket motor as well as to place the tail farther aft.
- BOUNDARY LAYER.** For simplicity, it may be considered that the boundary layer is the relatively thin layer of fluid, any part of which is dragged forward by the moving projectile.
- BOURRELET.** That portion of a projectile immediately aft of the nose, especially any part slightly larger in diameter than the body section following. Its function is to center the forward part and provide a bearing or guide during travel through the bore of the projecting device.
- BROACH.** To rise, break through, and spring clear of the water surface.
- c.** Velocity of sound in medium (feet per second); chord of hydrofoil test section (feet).
- C_C.** Cross force coefficient.
- C_D.** Drag coefficient.
- C_L.** Lift coefficient.
- C_M.** Moment coefficient, generally referred to *CG*.
- CB.** Center of buoyancy.
- CG.** Center of gravity.
- CP.** Center of pressure.
- CALIBER.** The maximum diameter of a projectile body.
- CAVITATION PARAMETER, K .** The ratio of the difference between the absolute pressures in the undisturbed liquid and in the bubble to half the liquid density times the velocity squared. $(P_L - P_B)/\frac{1}{2}\rho V^2$.
- CAVITY.** In this volume, the entrance bubble formed by the projectile at water entry.
- CENTER OF PRESSURE, CP .** The point of intersection of the axis of the projectile and the resultant of all forces acting on the projectile.
- CENTER OF PRESSURE ECCENTRICITY, e .** The distance between the center of pressure and the center of gravity expressed as a decimal fraction of the length of the projectile.
- CONE ANGLE.** As used herein, the angle formed in any plane section of the projectile which includes the horizontal axis, by the intersection of the cone sides at the vertex.
- CROSS FORCE, C .** The force exerted on the projectile normal to the direction of motion and in a horizontal plane. It is positive when acting to the right for an observer facing in the direction of travel. C is measured in pounds.
- db.** Decibel, measure of sound pressure level above unit pressure.
- DEPTH CHARGES.** Projectiles used to attack subsurface targets.
- DIRECTIVITY INDEX.** A measure of the directional properties of a transducer. It is the ratio, in decibels, of the average intensity, or response, over the whole sphere surrounding the projector, or hydrophone, to the intensity, or response, on the acoustic axis.
- DISPERSION.** In ballistics, the scattering of shots about the target.
- DRAW, D .** The force exerted on the projectile parallel with the direction of motion. It is positive when acting in a direction opposite to the motion. D is measured in pounds.
- e.** CP eccentricity, expressed as decimal fraction of length of projectile.
- FINENESS OR SLENDERNESS RATIO.** The ratio of the length to the maximum diameter of a projectile.
- g.** Acceleration due to gravity (feet per second).
- GT.** A crystal showing a zero temperature coefficient over a very wide range of temperature—the frequency variation is less than 1 part in 1,000,000 throughout a temperature range of 100 degrees centigrade.
- H.** Hull moment (foot-pounds).
- h_B .** Pressure in the bubble (feet of water).
- h_L .** Pressure in the undisturbed liquid, submergence plus barometric head (feet of water).
- HVAR.** High-velocity aircraft rocket.
- HYDROPHONE.** An underwater microphone.
- INCIPIENT CAVITATION.** Generally, cavitation developed to the point where it may first be seen as a steady phenomenon. Sometimes, when so stated, the point at which the noise produced begins to increase from this cause.
- ISOPIESTIC SURFACE.** A surface over which the pressure is constant.
- JOUKOWSKI STREAMLINED SHAPES.** A family of airfoil sections derived from a circle by a mapping function invented by N. Joukowski.

- K.** Cavitation parameter.
- KARMAN TRAIL.** The wake trailing certain two-dimensional bodies and consisting of vortices shed alternately from opposite sides of the body.
- K_i . K value for incipient cavitation.
- KINEMATIC VISCOSITY, ν .** The ratio of absolute viscosity to the density.
- . Overall length of projectile (feet).
- l/d . Fineness or slenderness ratio.
- LAMINAR FLOW.** The type of flow in which there are no local velocity fluctuations so that each fluid layer slips smoothly over layers nearer the projectile.
- LATTICE EFFECT.** As used herein, refers to modifications of the velocities and pressures around a single vane or airfoil in a lattice or row of vanes, compared to the velocities and pressures when the vane is alone in an infinite body of fluid.
- LIFT.** Force exerted on a projectile normal to the direction of motion and in a vertical plane. It is positive when acting upward. Lift is measured in pounds.
- M.** Moment (foot-pounds).
- $M_{a.c.}$. Pitching moment per unit length of hydrofoil span, measured about a.c. (foot-pounds).
- M_{cg} . Moment about CG (foot-pounds).
- N.** Normal component (pounds).
- NOSE.** The curved portion of the projectile forward of the cylindrical main section.
- P_B . Vapor pressure in entrance bubble, corresponding to the water temperature (pounds per square foot).
- P_L . Absolute pressure in undisturbed liquid (pounds per square foot).
- PITCH ANGLE, α .** The angle in a vertical plane between the projectile axis and the direction of motion. It is positive for nose-up positions.
- R.** Reynolds number.
- ρ . Mass density of fluid (slugs per cubic foot).
- SONIC FREQUENCIES.** Range of audible frequencies, sometimes taken as from 0.02 kc to 15 kc.
- SONIC VELOCITY.** The velocity of sound in air, about 1,100 fps (750 mph).
- SUBSONIC VELOCITIES.** Velocities below the sonic velocity.
- SUPERSONIC FREQUENCIES.** Range of frequencies higher than sonic. Sometimes referred to as ultrasonic to avoid confusion with growing use of the term supersonic to denote higher-than-sound velocities.
- SUPERSONIC VELOCITIES.** Velocities above the sonic velocity.
- SSR.** Spin-stabilized rocket.
- TAIL.** The fin, or fins, and ring structure with supporting parts at the aft end of the projectile. It includes rudders, if any.
- TURBULENT FLOW.** That type of flow in which there are irregular fluctuations distinct from vortex motion in general. It results in continuous interchange of particles between streamlines with different velocities.
- V . Mean relative velocity between water and projectile (ft per sec).
- VISCOSITY, μ .** The fluid property which resists relative motion between adjacent sections, often called absolute viscosity. See also kinematic viscosity.
- W.** Specific weight of fluid (lb per cu ft).
- WIMP.** The change at water entry in the angular velocity of the projectile in the vertical plane.
- YAW ANGLE, ψ .** The angle, in a horizontal plane, between the projectile axis and the direction of motion. It is positive when clockwise as viewed from above.

BIBLIOGRAPHY

Numbers such as Div. 6-712-M2 indicate that the document listed has been microfilmed and that its title appears in the microfilm index printed in a separate volume. For access to the index volume and to the microfilm, consult the Army or Navy agency listed on the reverse of the half-title page.

1. *Measurements of the High Frequency Noise Produced by Cavitating Projectiles in the High Speed Water Tunnel*, Robert T. Knapp, NDRC 6.1-*sr*207-924, Hydrodynamics Laboratory, Aug. 31, 1943.
2. *Cavitation Noises from Underwater Projectiles*, James W. Daily and Howard Baller, NDRC 6.1-*sr*207-1910, Hydrodynamics Laboratory, Mar. 21, 1945.
3. *Flow Diagrams of Projectile Components*, Robert T. Knapp, Garrett Van Felt, and Elizabeth A. Thorne, NDRC 6.1-*sr*207-1649, HML Report ND-3C, CIT, Sept. 15, 1944. Div. 6-712-M2
4. *Underwater Behavior of 3.5' Aircraft Rockets*, I. S. Bowen, JBC 23, CIT, Dec. 6, 1943.
5. *Fluid Mechanics for Hydraulic Engineers*, Hunter Rouse, McGraw-Hill Book Company, New York, 1938.
 - 5a. *Ibid.*, p. 228.
 - 5b. *Ibid.*, p. 248.
 - 5c. *Ibid.*, p. 251.
6. *Modern Developments in Fluid Mechanics*, Vols. I and II, edited by S. Goldstein, Oxford University Press, 1938.
7. *Aerodynamic Theory*, Vols. 1 to VI, edited by W. F. Durand, Julius Springer, Berlin, 1934.
 - 7a. Vol. I, Div. C, Chap. III.
 - 7b. Vol. VI, Div. Q, Sec. 9.
 - 7c. Vol. II, Chap. II.
8. *Applied Hydro- and Aeromechanics*, L. Prandtl and O. G. Tietjens, McGraw-Hill Book Company, New York, 1934.
9. *The High Speed Water Tunnel at the California Institute of Technology*, Robert T. Knapp, Vito A. Vanoni, and James W. Daily, OEMsr-207, CIT, June 29, 1942. Div. 6-711-M1
10. *Entrance and Cavitation Bubbles*, Robert T. Knapp and Harold L. Doolittle, HML Report ND-31, NDRC 6.1-*sr*207-1900, Dec. 27, 1944. Div. 6-712-M3
11. *Centrifugal Pump Performance as Affected by Design Features*, Robert T. Knapp, Trans. A.S.M.E., Vol. 63, 1941, pp. 251-260.
12. *Experimental Investigations of Design and Operating Features of Centrifugal Pumps with Reference to the Grand Coulee Irrigation Project*, Part II, a report submitted by the Hydraulic Machinery Laboratory of the California Institute of Technology to the U. S. Bureau of Reclamation, 1942.
13. *Cavitation Tests on a Systematic Series of Torpedo Heads*, NDRC Nos. 6.1-*sr*1353-2191, Feb. 28, 1945, *Hemispherical Head*; 6.1-*sr*1353-2192, Mar. 5, 1945, *Blunt Head*; 6.1-*sr*1353-2195, Mar. 21, 1945, [The] *1-Caliber Ogival Head*; 6.1-*sr*1353-2196, Mar. 26, 1945, [The] *2-Caliber Ogival Head*; Hunter Rouse, John S. McNowa, and En-Yun-Hsu, State University of Iowa. Div. 6-712-M5, M6, M8, M9
14. *Further Experiments on the Flow Around a Circular Cylinder*, ARC Reports and Memoranda 1309, A. Fage and V. M. Faulkner, February 1931.
15. *An Investigation of Fluid Flow in Two Dimensions*, ARC Reports and Memoranda 1194, A. Thom, November 1928.
16. *Torpedo Launching Project Report for Year Ending November 30, 1944*, F. C. Lindvall, OSRD 2346, Report CIT/JHC-5, CIT, Feb. 1, 1945. Div. 6-700-M1
17. *Underwater Trajectories and Ricochet Tendencies of Rockets*, I. S. Bowen, Proceedings of the Second Conference on Underwater Ballistics, January 29-31, p. 39.
18. *Measurements on C11-A1 Hydrophone with an Ellipsoidal and Spherical Reflector*, Report C-64, OEMsr-30, UCDWR, Oct. 30, 1944. Div. 6-713-M3
19. *Experimental and Theoretical Investigation of Cavitation in Water*, J. Ackoret, Report of the Kaiser Wilhelm Institute für Strömungsforschung, Göttingen, Tech., Mechan., und Thermodynamik, Vol. 1, January 1930, pp. 1-22.
20. *Application of Practical Hydrodynamics to Airship Design*, R. H. Upson and W. A. Klikoff, NACA Report 406, 1931.
 - 20a. *Ibid.*, Part III.
21. *The Aerodynamic Forces on Airship Hulls*, Max M. Munk, NACA Report 184, 1923.
22. *Hydrodynamics*, Sir Horace Lamb, Cambridge University Press, 1932, p. 155.
23. *Tests of 5" HVAR Projector with Fin and Ring Tails*, Robert T. Knapp and Harold L. Doolittle, OSRD 6094, NDRC 6.1-*sr*207-2241, HML Report ND-37, CIT, Aug. 20, 1945. Div. 6-722.6-M2
24. *Water Tunnel Tests of the 60-mm Mortar Projectile*, Robert T. Knapp, OSRD 1860, NDRC 6.1-*sr*207-926, HML Report ND-2C, CIT, Sept. 2, 1943. Div. 6-713-M2
25. *Water Tunnel Tests of a 4.5" Rocket Projectile*, Robert T. Knapp, NDRC 6.1-*sr*207-1312, HML Report ND-12, CIT, Feb. 22, 1943. Div. 6-722.5-M1
26. *Water Tunnel Tests of the 4.5" Rocket Projectile with Three Different Fin Tails and with One Ring-Type Tail*, Robert T. Knapp, NDRC 6.1-*sr*207-1304, HML Report ND-12.1, CIT, May 23, 1943. Div. 6-722.5-M2
27. *Water Tunnel Tests of the 7.5" Chemical Rocket*, Robert T. Knapp and Harold L. Doolittle, NLKc 6.1-*sr*207-1261, HML Report ND-22, CIT, Dec. 22, 1943. Div. 6-722.7-M4

28. *Water Tunnel Tests of the Mark 13-1, Mark 13-2, and Mark 13-2A Torpedoes with Shroud Ring Tails*, Robert T. Knapp and Joseph Levy, OSRD 3008, NDRC 6.1-sr207-939, HML Report ND-15.1, CIT, Nov. 24, 1943.
Div. 6-721.2-M2
29. *Water Tunnel Tests of a 2.57" Rocket Projectile with Collapsible Type Tails*, Robert T. Knapp, OSRD 3193, NDRC 6.1-sr207-1314, HML Report ND-11.1, CIT, Jan. 20, 1943.
Div. 6-722.3-M1
30. *Water Tunnel Tests of the M-7, 2.36" Antitank Rocket Showing a Comparison of Performance with a Folding Fin Tail, a Shroud Tail Ring, Two Hemispherical Ogive Noses of Different Profile and a Conical Pointed Nose*, Robert T. Knapp, OSRD 3074, NDRC 6.1-sr207-276, HML Report ND-11.3, CIT, June 26, 1943.
31. "Turbulence and Skin Friction," Th. von Kármán, *Journal of the Aeronautical Sciences*, Vol. 1, No. 1, January 1934.
32. *Hydraulics*, R. L. Daugherty, McGraw-Hill Book Company, New York, 1937, p. 335.
32a. *Ibid.*, p. 305.
33. *Analysis of Ship Turning and Steering with Statement of Theory*, members of the staff and Dr. L. I. Schiff, Experimental Towing Tank, Stevens Institute of Technology, Hoboken, New Jersey, prepared for DTMB under Contract bs 22087.
34. *Force and Cavitation Tests, Mark 14-1 and Mark 15-1 Torpedoes*, Robert T. Knapp and Joseph Levy, OSRD 5474, NDRC 6.1-sr207-2238, HML Report ND-18, CIT, July 15, 1945.
Div. 6-721.3-M1
35. *Tests of the Mark 13-1 Torpedo with Various Noses*, Robert T. Knapp and Harold L. Doolittle, OSRD 4765, NDRC 6.1-sr207-1909, HML Report 15.4, CIT, Feb. 1, 1945.
Div. 6-721.2-M7
36. *Air Propellers in Yaw*, E. P. Leslie, G. F. Worley, and S. Moy, NACA Report 597, 1937.
37. *Water Tunnel Tests of the Mark 13-1, Mark 13-2, and Mark 13-2A Torpedoes*, Robert T. Knapp, OSRD 2060, NDRC 6.1-sr207-936, HML Report ND-15, CIT, Nov. 9, 1943.
Div. 6-721.2-M1
38. *Water Tunnel Tests of the Mark 13 Torpedo with Spade and Stabilizer Ring Noses*, Harold L. Doolittle, HML Report ND-15.2, Hydrodynamics Laboratory, CIT, June 5, 1944.
Div. 6-721.2-M3
39. *Pressure Distribution Measurements on the Mark 13-1, 13-2, and 13-2A Torpedoes*, Robert T. Knapp and Joseph Levy, OSRD 3035, NDRC 6.1-sr207-1643, HML Report ND-15.3, CIT, June 23, 1944.
Div. 6-721.2-M4
40. *Underwater Performance Characteristics of the Mark 13-2A Torpedo with Suspension Fittings*, Robert T. Knapp and Joseph Levy, OSRD 4096, NDRC 6.1-sr207-1650, HML Report 15.5, CIT, Aug. 18, 1944.
Div. 6-721.2-M5
41. *Pressure Distribution on the Mark 13 Series Torpedoes with Shroud Ring Tails*, Robert T. Knapp and Joseph Levy, NDRC 6.1-sr207-1905, HML Report ND-15.3, CIT, Jan. 15, 1945.
Div. 6-721.2-M6
42. *Force Tests of Mark 13-1 Torpedo with Suspension Bands*, Robert T. Knapp and Gerald B. Robison, NDRC 6.1-sr207-2231, HML Report ND-15.7, Hydrodynamics Laboratory, CIT, May 17, 1945.
Div. 6-721.2-M8
43. *Water Tunnel Tests of the Mark 25 Torpedo with Gas Exhaust through a Vertical Fin*, Robert T. Knapp and Harold L. Doolittle, OSRD 3664, NDRC 6.1-sr207-1275, HML Report ND-30, Service Project NO-176, CIT, May 8, 1944.
Div. 6-721.4-M1
44. *Water Tunnel Tests of the Mark 25 Torpedo with a Gas Exhaust through a Horizontal Pipe*, Robert T. Knapp and Harold L. Doolittle, NDRC 6.1-sr207-1640, HML Report ND-30.1, CIT, June 5, 1944.
Div. 6-721.4-M2
45. *Water Tunnel Tests of the Mark 25 Torpedo with Expanding Exhaust Pipe*, Robert T. Knapp and Harold L. Doolittle, NDRC 6.1-sr207-1642, HML Report ND-30.2, CIT, June 20, 1944.
Div. 6-721.4-M3
46. *Mark 25 Torpedo Exhaust Gas Investigation*, Robert T. Knapp and Harold L. Doolittle, OSRD 5119, NDRC 6.1-sr207-1916, HML Report ND-30.4, CIT, Apr. 12, 1945.
Div. 6-721.4-M4
47. *Mark 25 Torpedo with Various Exhaust Pipes*, Robert T. Knapp and Harold L. Doolittle, OSRD 5381, NDRC 6.1-sr207-2236, HML Report ND-30.3, CIT, July 14, 1945.
Div. 6-721.4-M5
48. *Pressure Distribution Measurements on the Mark 25 Torpedo*, Robert T. Knapp and Joseph Levy, OSRD 6313, NDRC 6.1-sr207-2248, HML Report ND-30.5, CIT, Aug. 31, 1945.
Div. 6-721.4-M6
49. *Pressure Distribution Measurements on the Mark 14-1 and Mark 15-1 Torpedoes*, Robert T. Knapp and Joseph Levy, OSRD 6092, NDRC 6.1-sr207-2244, HML Report ND-18.1, CIT, Aug. 15, 1945.
Div. 6-721.3-M2
50. *Force and Cavitation Tests of the Mark 26 Torpedo*, Robert T. Knapp and Robert M. Prabhdy, OSRD 6423, NDRC 6.1-sr207-2249, HML Report ND-38, CIT, Aug. 31, 1945.
Div. 6-721.3-M3
51. *Water Tunnel Tests of the Hydrobomb*, Robert T. Knapp and Harold L. Doolittle, NDRC 6.1-sr207-1276, HML Report ND-29, CIT, May 13, 1944.
Div. 6-722-M2
52. *Force and Cavitation Tests of the Westinghouse Hydrobomb*, Robert T. Knapp and Robert M. Prabhdy, OSRD 5965, NDRC 6.1-sr207-2234, HML Report ND-40, CIT, June 27, 1945.
Div. 6-722-M3
53. *Force Tests of the United Shoe Machinery Corporation No. 3 Hydrobomb*, Robert T. Knapp and Gerald B. Robison, OSRD 6093, NDRC 6.1-sr207-2247, HML Report ND-29.1, CIT, Aug. 25, 1945.
Div. 6-722-M5
54. *Development of the High Speed Water Tunnel and Summary of Results*, NDRC 6.1-sr207-2251, CIT, Aug. 31, 1945.
Div. 6-711-M2
55. *Analysis of Aircraft Launchings of Torpedoes Equipped with Shroud Rings*, K. H. Kelle, M. Gimprich, and W. H. Wilson, NDRC 6.1-sr1131-1857, Columbia University Special Studies Group, Mar. 26, 1945.

56. *Water Tunnel Tests of the 2 1/4" Antiaircraft Projectile*, Robert T. Knapp and James W. Daily, NDRC 6.1-sr207-927, HML Report ND-13.1, CIT, Dec. 28, 1943.
Div. 6-722.1-M2
57. *Water Tunnel Tests of a 2.5" Rocket Projectile with Hemispherical Noses and Ring Tails*, Robert T. Knapp, OSRD 3068, NDRC 6.1-sr207-1303, HML Report ND-11.2, CIT, Feb. 19, 1943.
Div. 6-722.3-M2
58. *Water Tunnel Tests of the M-6, 2.36" Antitank Rocket Showing Comparison of Performance with the Conical Pointed Nose Combined with Three Types of Shroud Ring Tail and with Shroud Rings of Various Lengths*, Robert T. Knapp, NDRC 6.1-sr207-920, HML Report ND-11.4, CIT, July 20, 1943.
Div. 6-722.2-M2
59. *Water Tunnel Tests of the M-6, 2.36" Antitank Rocket with Fire Designs of Shroud Ring Tail*, Robert T. Knapp, OSRD 3003, NDRC 6.1-sr207-934, HML Report ND-11.5, CIT, Nov. 4, 1943.
Div. 6-722.2-M3
60. *Water Tunnel Tests of the 3.5" Rotating Rocket*, Robert T. Knapp and Harold L. Doolittle, NDRC 6.1-sr207-1270, HML Report ND-27, CIT, Apr. 21, 1944.
Div. 6-722.4-M1
61. *3.5" Rotating Rocket Tests with Various After-bodies*, Robert T. Knapp and Harold L. Doolittle, NDRC 6.1-sr207-1903, HML Report 27.1, CIT, Jan. 4, 1945.
Div. 6-722.4-M2
62. *Water Tunnel Tests of the 15-cm German Spinner Rocket*, Robert T. Knapp, NDRC 6.1-sr207-932, HML Report ND-23, CIT, Nov. 11, 1943.
Div. 6-722.7-M3
63. *Elements of Ordnance*, Col. Thomas J. Hayes, John Wiley and Sons, Inc., New York, 1938.
64. *Force Tests of the 4.5" Rocket, T-38E3*, Robert T. Knapp and Gerald B. Robison, OSRD 5113, NDRC 6.1-sr207-1919, HML Report ND-41, CIT, May 1, 1945.
Div. 6-722.5-M3
65. *Tests of Four Models of the 5" SSR Rotating Rocket*, Robert T. Knapp and Harold L. Doolittle, OSRD 5473, NDRC 6.1-sr207-2239, HML Report ND-33, CIT, July 24, 1945.
Div. 6-722.6-M1
66. *Memorandum on Water Tunnel Tests of the AN MK 41 Bomb*, Robert T. Knapp, NDRC 6.1-sr207-735, Mar. 3, 1943.
67. *Water Tunnel Tests of the British Squid Projectile, Type C*, Robert T. Knapp, NDRC 6.1-sr207-933, HML Report ND-24, CIT, Oct. 29, 1943.
68. *Water Tunnel Tests of the British Squid Projectile, Type C, with Two Alternate Flat Noses*, Robert T. Knapp and Harold L. Doolittle, NDRC 6.1-sr207-938, HML Report ND-24.1, CIT, Nov. 29, 1943.
Div. 6-721.5-M2
69. *Drag Tests of the British Squid*, Robert T. Knapp and Gerald B. Robison, NDRC 6.1-sr207-1904, HML Report ND-24.2, CIT, Jan. 8, 1945.
Div. 6-721.5-M3
70. *Force Tests of the Squid with New Afterbody, Tails, and Noses*, Robert T. Knapp and Gerald B. Robison, OSRD 5529, NDRC 6.1-sr207-2243, HML Report ND-24.3, CIT, July 30, 1945.
Div. 6-721.5-M4
71. *Tests of the AN-Mark 53 Aircraft Depth Bomb*, Robert T. Knapp and Harold L. Doolittle, OSRD 6091, NDRC 6.1-sr207-2350, HML Report ND-41, CIT, Aug. 31, 1945.
Div. 6-723-M6
72. *Force Tests of Concrete Practice Bombs, M3A2 Practice Bomb, AN-M43 General Purpose 500-lb Bomb, AN-M56 LC 4000-lb Bomb*, Robert T. Knapp and Robert M. Peabody, OSRD 5757, NDRC 6.1-sr207-2245, HML Report ND-32, CIT, Aug. 14, 1945.
Div. 6-723-M4
73. *Dynamic Stability of Bombs and Projectiles*, M. A. Biot, NDRC 3.2-sr418, CIT, Sept. 6, 1943.
74. *Force and Cavitation Characteristics of the NACA-4412 Hydrofoil*, Robert T. Knapp and James W. Daily, NDRC 6.1-sr207-1273, HML Report ND-19, CIT, June 10, 1944.
Div. 6-712-M1
75. *The Characteristics of 78 Related Airfoil Sections from Tests in the Variable Density Wind Tunnel*, E. N. Jacobs, K. E. Ward, and R. M. Finkerton, NACA T. R. No. 460, 1933.
76. *Calculated and Measured Pressure Distributions over the Midspan Section of the NACA 4412 Airfoil*, R. M. Finkerton, NACA T. R. No. 563, 1936.
77. *Airfoil Section Characteristics as Affected by Variations of the Reynolds Number*, E. N. Jacobs and A. Sherman, NACA T. R. No. 566, 1937.
78. *Airfoil Section Data Obtained in the NACA Variable-Density Tunnel as Affected by Support Interference and Other Corrections*, E. N. Jacobs and I. H. Abbott, NACA T. R. No. 669, 1939.
79. *Aerodynamics of the Airplane*, C. B. Millikan, Wiley, 1941.
80. *Determination of the Characteristics of Tapered Wings*, R. F. Anderson, NACA T. R. No. 572, 1936.
81. *The Design of Propeller Pumps and Fans*, M. P. O'Brien and R. G. Folsom, University of California, Publication in Engr. Vol. 4, No. 1, University of California Press, 1939.

CONTRACT NUMBERS, CONTRACTORS, AND SUBJECT OF CONTRACT

<i>Contract Numbers</i>	<i>Name and Address of Contractor</i>	<i>Subject</i>
OEMar-20	The Trustees of Columbia University in the City of New York New York, N. Y.	Studies and experimental investigations in connection with and for the development of equipment and methods pertaining to submarine warfare.
OEMar-1123	The Trustees of Columbia University in the City of New York New York, N. Y.	Conduct studies and experimental investigations in connection with and for the development of equipment and methods involved in submarine and subsurface warfare.
OEMar-207	California Institute of Technology Pasadena, California	Construction and operation of a high speed water tunnel, and use of such water tunnel in research and experimental investigations involving underwater projectiles and detection equipment.
OEMar-1353	The Iowa Institute of Hydraulic Research of the University of Iowa Iowa City, Iowa	Conduct studies, experimental investigations, observations, and tests of pressure distribution about underwater structures of varying form, together with photographic records of the character of the flow, especially with reference to the onset and continuance of the phenomena of cavitation, all at varying speeds and under selected conditions of operations.

SERVICE PROJECT NUMBERS

The projects listed below were transmitted to the Executive Secretary, NDRC, from the War or Navy Department through either the War Department Liaison Officer for NDRC or the Office of Research and Inventions (formerly the Coordinator of Research and Development), Navy Department.

<i>Service Project Number</i>	<i>Subject</i>
NO-141	Hydrodynamic characteristics of projectile forms
NO-176	Torpedoes for high speed aircraft
OD-99	Determination of the dynamic characteristics of specified bomb and projectile shapes
NS-294	Cavitation research

INDEX

The subject indexes of all STR volumes are combined in a master index printed in a separate volume.
For access to the index volume consult the Army or Navy Agency listed on the reverse of the half-title page.

- AA rocket, 2¼ inch, 234
ADP hydrophone (ammonium dihydrogen phosphate), 64
Aerodynamics, terms and symbols, 260-261
Afterbody
 see Projectile afterbody
Air bombs, 253-256
 effect of asymmetry, 253-256
 hydrodynamic characteristics, 253, 256
 physical dimensions, 254
 types, 253-256
Air bubble formation
 see Bubbles, entrance; Cavitation, bubble formation
Air separator, free-surface water tunnel, 54-56
Aircraft torpedoes, 203-207
 dimensions, 203
 hydrobombs, 203, 205-207, 214, 217, 225
 Mark 13 series, 135, 178, 203, 226-229
 Mark 25; 203, 205, 222
 trajectory, 3
 water-entry studies, 209
Air-launched projectiles
 nose shapes, 73-75, 77
 trajectory, 4
 water-entry studies, 201-202, 209
AN-M43 air bomb, 263-256
 hydrodynamic characteristics, 253, 256
 physical dimensions, 254
AN-M56 air bomb, 253-256
 hydrodynamic characteristics, 256
 physical dimensions, 254
AN Mark 41 depth charge
 effect of nose shape on drag force, 185
 hydrodynamic characteristics, 248-249
 physical characteristic, 246
AN Mark 53 depth charge, 251-252
Artillery projectiles, nose shapes, 71-73
Ashcan (depth charge), 1
Aspect ratio, hydrofoils, 260-263
AX 90 hydrophone, 64

Basooka (rocket), 235-237
 collapsible fin tails, 235
 fore-and moment coefficients, 235-236
 ring tails, 236-237
Bentonite, use in flumes, 2
 characteristics, 27
 purification, 34

sensitivity to mineral content of water, 33
streaming double refraction, 33-34
Bernoulli equation, conservation of energy, 98
Bombs, air
 see Air bombs
British Squid (depth charge), 249-251
 drag coefficient, 189-190
 physical characteristics, 246
Bubbles, cavitation
 see Cavitation, bubble formation
Bubbles, entrance, 96-97, 107-111
 comparison with cavitation bubbles, 107-108
 cross force, 110
 decay, 109
 desirable characteristics, 115
 effect of nose shape, 115-116
 equilibrium yaw angles within bubble, 110-111
 formation, 108-109
 maximum diameter, 109
 projectile entrance velocity, 109
 significance of bubble shapes, 109-110

California Institute of Technology, 1
Cameras for hydrodynamic studies, 44, 56-60
Cavitation, 96-117
 coarse-grained, 103, 119, 121
 definition, 96, 98
 degrees of cavitation, 101-103
 desirable characteristics, 113-115
 effect of projectile nose shape, 116, 126
 effect on projectile trajectory, 104-105, 109-111
 effect on projectile yaw, 110-111, 123-129, 136-137
 fine-grained, 103, 119-122
 formula for velocity, 101
 gas cycles, 105-107
 location of point of inception, 98-100
 parameter, 100-101, 118, 261, 276, 278-279
 photography, 119, 127-133, 266
 projectile nose cavitation, 111-133
 projectile resistance, 100
 sources, 99
 tests, 11, 22-23, 26-27, 62-63
 torpedoes, 126, 152-153, 224-226
 types, 103-104, 119-122, 156-180
Cavitation, bubble formation, 107-111
 see also Bubbles, entrance

comparison with entrance bubbles, 107-108
 conclusions from studies, 133
 cross force, 110
 desirable characteristics, 115
 effect of projectile nose shapes, 131-133
 equilibrium yaw angles within bubble, 110-111
 hydrofoils, 263-270
 location on projectile nose, 119
 physical dimensions from photographs, 127-130
 significance of bubble shapes, 109-110
Cavitation, effect on hydrodynamic forces, 134-154
 air-water entry of projectiles, 133
 conclusions from studies, 151-154
 cross force and moment, 147-151
 drag, 134-147
 hydraulic machinery, 154
 lifting surfaces, 153
 torpedoes, 152-153
Cavitation noise, 155-170
 background noise, 156-159
 body shape, 159
 correlation with growth of cavitation, 159-160
 frequency distribution, 169-170
 location of noise source, 167-169
 magnitude, 166, 169
 measuring apparatus, 62-63, 155-156
 sound pressure and bubble collapse, 165
 sound pressure versus cavitation growth, 160-165
 surface conditions, 165
 velocity of projectiles, 165-166
 visible cavitation and the noise source, 167
Cavity drag, 140-147
 comparison with calculated drag, 146-147
 cross forces, 147
 description of cavity, 141-143, 146
 drag versus cavitation parameter, 144, 146
 effect of body shape, 141-144
 form drag formula, 140-141
 noncavitating drag, 147
 of a cylinder, 144-147
 wall effects, 147
Cavity formed by water entry of projectile
 see Bubbles, entrance

- Chemical rocket, 7.2 inch, 220
- Controlled-atmosphere launching tank
see Launching tank for projectiles
- Cross force
definition, 185, 275
effect of projectile components, 192
formula, 185
influence of yaw, 192
- Cross force, effect of cavitation, 110, 111, 147-151
cavity symmetry versus nose shape, 147-148
conclusions from studies, 151-153
description of cavities, 149-150
measured coefficients, 149-151
- Cross force coefficient of projectiles
see under name of projectile
- Crystals, use in producing light paths, 30-33
bentonite, 33-34
requirements, 30-33
tobacco mosaic virus, 34
- Damping force, 193-195
coefficients, 194-195
definition, 193
effect of projectile components, 199-200
mechanics of damping, 193-194
theoretical force distribution, 193
- Data analyzer, 37-38, 51-52
- Depth and roll recorder, 223-224
- Depth charges, 1, 245-253
7 inch, 240-241, 246
afterbody shape, 82
air-launched, 77
Ashran, 1
blunt nose shape, 136
British Squid, 189-190, 249-251
design requirements, 245
general features, 245
hydrodynamic tests, 245
Mark 41; 188, 246, 248-249
Mark 53; 251-252
methods of launching, 245
mousetrap, 245-246
New London, 245-246
small-charge group, 246-248
yaw angle tests, 246
- Differential pressure gauge, 21
- Drag, 186-192
definition, 185, 275
form drag, 186, 187
formula, 140-141, 185, 188
in relation to flow, 187
influence of yaw, 192
skin-friction, 137-140, 186-187, 189
total drag coefficient, 186
variation with Reynolds number, 213-215
- Drag, effect of cavitation, 110, 134-147
blunt-nosed bodies, 136, 139
cavitation parameter, 144, 146
cavity drag, 140-147
conclusions from studies, 151-152
effect of yaw, 136-137
effect on boundary layer and skin friction, 137-140
hemisphere projectile nose, 134-135
separation of flow, 137-139
square-end cylinder projectile nose, 135
torpedo noses, 135-136
- Drag, effect of projectile components, 186-192
body, afterbody, and tail, 189-192
effect of ring tail, 228, 236-237
nose shape, 189-192, 248
- Drag coefficient of projectiles
see under name of projectile
- DRR (depth and roll recorder), 223-224
- Dynamic stability of projectiles
see Projectile stability
- Dynamometer for high-speed water tunnel, 12
- Eyrite
see M. S. Eyrte
- 15-cm German spinner rocket, 239, 241-242
- Fin tails, projectiles, 175-181, 232-233
collapsible, 183-184, 232, 235
comparison with ring tails, 175-176
184, 232
effectiveness, 178
fixed fins, 176-177
influence of body interference, 176
moment, 176-177
rockets, 84-85, 183-184, 235
torpedoes, 85
- 5-inch HVAR rocket, 230-232
- 5-inch SSR rotating rocket, 243
- Flow diagrams of projectile, 69-95
60-mm mortar, 238
afterbodies, 70-83
application to projectile design, 93
nose shapes, 69-79
rocket booms, 80, 89-90
tails, 83-92
- Flow studies, equipment
see Polarized light flume
- Flume, polarized light
see Polarized light flume
- Force measuring equipment, 9, 16-18
- Forces on projectile bodies
see Hydrodynamic forces
- Form drag
cause, 186
coefficient, 187
effect of projectile tail, 190
formula, 140-141
projectile nose shape, 190-192
4½ inch non-rotating rocket, 232-234
4½ inch rotating rocket, 242
- Free-surface water tunnel, 52-56
air separator, 53-56
comparison with polarized light flume, 27
purpose, 5-6
working section, 53
- Gauges
see Pressure gauges
- German spinner rocket, 15-cm, 239, 241-242
- Gorton pantograph machine, 67
- Guns, fluid friction losses in barrel, 271-273
friction factor, 271
relation to smooth tubes, 273
test results, 271-273
- Hayes, stability requirement for spinning projectiles, 242
- High-speed water tunnel
see Water tunnel, high-speed
- Hydraulic machinery, effect of cavitation, 154
- Hydraulic Machinery Laboratory, 1
- Hydrobombs (jet-propelled torpedoes)
cavitation, 225, 226
dimensions, 203
lift and pitching curves, 211-214
moment coefficient, 214
power, 217
United Shoe Machinery Corporation, 206-207
Westinghouse, 205-207
- Hydrodynamic forces, 171-174
see also Lift force
cross force, 147-151, 185, 192
damping, 193-195, 199-200
distributed and resultant forces, 171-173
drag, 134-147, 186-192
dynamic stability, 195-200
ideal fluid, 171-172
moment, 172-183
nose cavitation, 134-137
real fluid, 172
ring tail, 178, 228, 236-237
theoretical moment, 173
yaw, 192
- Hydrodynamics, CIT laboratory, 1-6
equipment, 4-6
history, 1-3
- Hydrodynamics, laboratory apparatus, 7-68
controlled-atmosphere launching tanks, 5, 35-52
electrical accessories, 61-62
free-surface water tunnel, 52-56

- high-speed water tunnel, 4, 7-27
 hydrophones, 62, 64
 photographic equipment, 42-51, 56-61
 polarized light flume, 1, 5, 27-35
 shop facilities, 66-68
 sound-measuring equipment, 62-65
 Hydrodynamics, tests, 25-27
 cavitation, 11, 22-23, 26-27, 62-63
 depth charges, 245-246
 force, 25
 powered model and exhaust tests, 27
 pressure distribution, 26
 speed, 26
 Hydrofoil tests, 259-270
 cavitation, 265-270
 dimensions of hydrofoil, 259
 hydrodynamics, 261
 infinite aspect ratio, 259-263
 installation, 259
 Reynolds number and turbulence, 265
 theoretical characteristics, 263
 tunnel wall interference, 263
 wind tunnel measurements, 263-265, 269
 Hydrophones for hydrodynamic studies, 62, 64
 ADP, 64
 AX 90; 64
 free-field calibrations, 64
 Jet-propelled torpedoes
 see Hydrobombs
 Karman trail (wake trailing), 147, 216
 Kopf stabilizing ring, 75-77
 Launching tank for projectiles, 5, 35-62
 atmospheric pressure, 35-36
 design specifications, 37
 density of air, 36
 purpose, 2, 5, 35
 requirements, 35-36
 surface tension, 36
 variable-pressure launching tank, 2
 Launching tank for projectiles, construction, 35-62
 data analyzer system 37-38, 51-52, launcher, 40-42
 main tank, 38-40
 recording camera, 44
 trajectory recording system, 42-51
 Lift force
 coefficient curves for hydrobombs, 214
 definition, 185, 275
 effect of projectile components, 192
 finless bodies, 198-194
 formula, 185, 261
 influence of yaw, 192
 relation to moment, 172-173
 torpedoes, 211-215
 Light flume, polarized
 see Polarized light flume
 M38A2 practice bomb, 253
 hydrodynamic characteristics, 256
 physical dimensions, 254
 Manometer, multiple differential, 21-22
 Mark 3 acoustic unit (amplifying system), 64
 Mark 13 torpedo, 135-136, 203, 226-229
 cavitation, 136, 225
 dimensions, 203
 effect of ring tail, 178, 228
 modifications, 226
 moment coefficient, 178
 pitch angle and rudder setting, 219
 power, 217
 shroud-ring tail, 226
 Mark 14 torpedo, 197-198
 cavitation, 225
 dimensions, 205
 hydrodynamic properties, 198
 pitch angle and rudder setting, 219
 power, 207, 217
 pressure distribution, 220-222
 stability, 197
 Mark 15 torpedo, 203, 207, 217, 219
 dimensions, 203
 equilibrium conditions, 219
 power, 217
 pressure distribution, 221-222
 Mark 25 torpedo, 205
 dimensions, 208
 pressure distribution, 221-222
 Mark 26 torpedo, 208-209, 228-229
 cavitation, 225
 dimensions, 208
 modifications, 228
 pitch angle and rudder setting, 219
 power, 217
 Mark 41 depth charge, 245-249
 characteristics, 246
 drag force, 185
 Mark 53 depth charge, 251-253
 Massachusetts Institute of Technology, bentonite studies, 33
 Moment coefficient of projectiles, 261
 see also under name of projectile
 Moment of force, 173-183
 damping moment, 193-195
 effect of cavitation, 147-151
 effect of projectile fin tail, 176-177
 effect of projectile length, 182
 effect of ring tails, 178, 236-237
 evaluation of theoretical moment, 173-174
 relation to lift, 172-173
 Mortar, 60-mm, 237-238
 flow-line drawings, 238
 force coefficient curves, 238
 physical characteristics, 237-238
 stabilizing device, 238
 Mousetrap depth charge, 245-248
 M. S. Eyring (bentonite), use in flumes, 2
 characteristics, 27
 purification, 34
 reaction with metals, 27
 sensitivity to mineral content of water, 34
 streaming double refraction, 33-34
 NACA 4412 hydrofoil
 see Hydrofoil tests
 Naval Ordnance Laboratory, 64
 New London depth charges, 245-246
 Noise from cavitating projectiles
 see Cavitation noise
 Normal force on projectile body, 171
 Nose shapes of projectiles
 see Projectile nose shapes
 Pantograph machine, 67
 Photocell
 use in pressure gauges, 19
 use in projectile launching tank, 42
 Photographic equipment for hydrodynamic studies, 56-61
 portable camera, 56-60
 processing facilities, 58, 60-61
 trajectory recording system, 37, 42-51
 Photography of cavitation, 127-133, 264
 bubble dimension measurement, 127-130
 ogive projectile nose, 119
 spherogive projectile nose, 130-131
 Pitch angle, definition, 275
 Polarized light flume, 1, 5, 27-35
 applications, 29
 bentonite, 27, 32-34
 circulating pump, 27-29
 comparison with water tunnels, 27
 construction, 27-29
 diffuser section, 29
 light source, 29
 mechanisms for studying fluid flow, 29
 operation, 27, 35
 polarized screens, 27, 29
 streaming double refraction, 30-33
 tobacco mosaic virus, 34
 working section, 29
 Pressure distribution tests, 26
 measuring equipment, 21-22
 torpedoes, 220-222

- Pressure gauges, 19-21**
 balance sensitivities, 21
 control panel, 20
 differential pressure gauge, 21
 hydraulic transmission system, 20-21
 photocell control, 19
 principle of operation, 19
 sensitivity and range of system, 20
- Projectile, air-launched nose shapes, 73-75, 77 trajectory, 4 water-entry studies, 201-202, 209**
- Projectile afterbody, 79-83**
 booms, 80
 conical tapers, 80
 damping and stability, 199
 depth charges, 83
 drag force, 189-192
 fin afterbodies, 83
 flow diagrams, 79-83
 ogives, 79-80
 recessed, 80
 rocket nozzles, 83-83
 spherogives, 80
 torpedo, 82
- Projectile design**
 finless bodies, 171-174
 flow diagrams, 93
 spherogive nose shape, 126-127
- Projectile dynamics within cavitation, 104-106, 109-111**
see also Cavitation
 cross force, 110, 111
 curvature of path, 111
 drag force, 110
 effect of body shape, 111-114
 effect of nose shapes, 111-117
 equilibrium yaw angles within bubbles, 110-111
 significance of bubble shapes, 109-110
- Projectile entrance into water**
see Bubbles, entrance
- Projectile launching tank**
see Launching tank for projectiles
- Projectile nose cavitation, 111-123, 151-153**
 bubble formation, 119, 123, 126, 131-133
 cavity symmetry, 147-148
 effect of sphere size, 123
 effect of yaw angle, 123-129
 effect on hydrodynamic forces, 134-137
 ellipsoidal nose, 113
 hemispherical nose, 113, 120-129, 134-135
 incipient cavitation, 118
 measurements from photographs, 123
 method of testing, 118
 ogive shape, 113, 118-126, 131-133
 recommendations, 117
 resistance to cavitation, 113, 117
 selection of nose shape, 115
 spherogive shape, 126-123
 square-end cylinder, 125
- Projectile nose shapes, 69-79**
 air-launched projectiles, 73-75, 77-78
 characteristics, 111-117
 conical tapers, 73
 damping and stability, 199, 240, 246-248
 drag force, 187-192, 248
 ellipsoids, 70, 112
 flow diagrams, 69-79
 hemispherical, 75, 112
 high-velocity projectiles, 78
 Kopf ring, 75-77
 modified square-end cylinders, 77
 modified tapers, 77
 noses with common length, 78
 ogives, 71, 73-79, 113
 pickle barrel, 75
 selection of shape, 69
 spherogive, 71-73, 76, 114-117
- Projectile stability, 195-200**
 criteria for stability, 195-197
 definition, 195
 dependent factors, 197
 effect of various components, 179, 190-200
 formulae, 196-197, 242
 Mark 14 torpedo, 197
 nose shape, 199, 240, 246-248
 propellers, 200
 rudders, 196
 spinning projectiles, 239, 242
 tail structure, 197, 199, 246-248
- Projectile tails, 83-92, 173-184**
 body length, 176, 181-183
 damping, 190-203
 design variables, 173-184
 drag force, 189-192
 effectiveness, 173-176
 fin tails, 84-85, 173-181, 183-184, 223-223
 flow diagrams, 83-92
 form and action, 173
 form drag, 186
 moment coefficient, 176
 non-rotating projectiles, 173-184
 operation, 83-84
 propellers, 200
 purpose, 83, 173
 ring tails, 85-92, 177-184, 226-226, 223-227
 rudders, 192
 square tails, 92
 stability, 197, 199-200, 246-248
- Projectile trajectory recording system, 37, 42-51**
 camera drive motor, 45-47
 light source, 48-51
 magazine loader, 47
 optical coverage of cameras, 43-44
 recording speed, 44-45
 spherical windows, 42-43
- Projectile yaw**
 depth charges, 245
 effect of cavitation, 110-111, 123-129, 136-137
 effect on hydrodynamic characteristics, 192
 torpedoes, 220
- Refraction, double, of crystals, 20-24**
 bentonite, 33-34
 requirements, 30-32
 tobacco mosaic virus, 34
- Reynolds number, 163, 261, 270**
- Ring tails, projectiles, 85-92, 177-184, 226-226, 232-237**
 advantages, 226, 232
 body length, 177, 181-183
 boom mounting, 86-90, 177-178, 224
 comparison with fin tails, 173-176, 184, 232
 force coefficient curves, 181
 high-drag ring tails, 92, 181
 hydrodynamic forces, 178, 226, 236-237
 mounted on extended fins, 90-92
 shroud ring, 226
 with exhaust stack, 92
 with ogival afterbodies, 95
- Rockets, 80-90**
 collapsible fins, 81-85, 183-184
 fixed fins, 84-85
 low-velocity, 77
 moment coefficient, 178, 235-236
 nozzles, 83-83
 rings on rocket booms, 89-90
 use of booms, 80
- Rockets, non-rotating, 220-227, 226-241**
 2½ inch AA rocket, 224
 2.26 inch rocket (bazooka), 225-227
 4½ inch rocket, 223-224
 5 inch HVAR rocket, 220-222
 7.2 inch chemical rocket, 220
 general features, 220
 hydrodynamic characteristics, 226-226, 229-241
- Rockets, rotating, 229-244**
 3.5 inch rocket, 240-241
 4.5 inch HE rocket T26F3; 242
 5 inch MMR, 243
 13-cm German spinner rocket, 241-242
 general features, 229
 hydrodynamic characteristics, 229
 propellant burning, 229

- stability, 239, 242
water tunnel tests, 239
- Roll recorder for projectiles, 223-224
- 7 inch depth charge, 245-246
- 7.2 inch chemical rocket, 230
- Shear force on projectile body, 171
- 60-mm mortar, 237-238
flow-line drawings, 238
force coefficient curves, 238
physical characteristics, 237
stabilizing devices, 238
- Skin-friction drag, 186-187, 189-192
cause, 186
coefficient, 186-187
effect of cavitation, 187-189
effect of projectile tail, 189
formula, 186-187
projectile body length, 189
turbulent flow, 188
- Sound measuring equipment, hydrodynamic studies, 62-65
amplifying and filtering equipment, 64-65
cavitation noise, 62
free-field calibrations, 64
hydrophone, 62
internal receivers, 64
sound reflectors, 63
- Sound pressure, effect of cavitation, 180-185
- Sound reflectors for hydrodynamic studies, 63
- Specifications for controlled-atmosphere launching tank, 37
- Specifications for high-speed water tunnel, 7-11
balance equipment for force measurements, 9
requirements for cavitation studies, 11
velocity, 8
working section, 8-9
- Spin-stabilized rockets
see Rockets, non-rotating
- Liquid (British depth charge), 249-251
drag coefficient, 189-190
physical characteristics, 246
- NSR rocket, 5 inch, 243
- Stability of projectiles
see Projectile stability
- Streamline body, definition, 188
- T3813 rocket, 242
- Tails of projectiles
see Projectile tails
- Tank, controlled-atmosphere launching
see Launching tank for projectiles
- Taylor Model Basin, 24
- 3.5 inch rotating rocket, 240-241
- Tobacco mosaic virus, 34
- Torpedo, aircraft
see Aircraft torpedoes
- Torpedoes, 203-229
adjustable rudders, 85, 175
afterbody shape, 82
aircraft, 3, 75, 203-207
cavitation, 126, 152-153, 224-226
dimensions, 203
fin tails, 85
hydrobombs, 203-207, 214, 217, 225
Mark 13; 135-136, 226-229
Mark 14; 197-199, 203, 217, 219-222, 225
Mark 15; 203, 207, 217, 219, 221
Mark 25; 203, 205, 222
Mark 26; 208-209, 228-229
modifications, 226-229
nose shape, 135-136
pitch angle and rudder settings, 217-219
power, 216-217
purpose of tail, 83
shroud-ring tail, 228
trajectory, 3
water-borne, 203, 207-209
water-entry studies, 209
- Torpedoes, force measurements, 198, 200, 209, 219
cross force coefficient, 211-215
dependent factors, 211-215
drag and power requirements, 216-217
drag coefficient, 215-217
equilibrium running conditions, 217-219
lift and moment, 211-215
- Torpedoes, pressure distribution, 219-224
application of measured data, 223
effect of component shape, 221
effect of yaw, 221
method of measuring, 219
test results, 220
- Trajectory recording system for projectiles
see Projectile trajectory recording system
- 2 1/2 inch AA rocket, 234
- 2.26 inch rocket, 235-237
collapsible fin tails, 235
force and moment coefficients, 235-236
ring tails, 235-237
- Underwater projectile design
see Hydrofoil tests
- United Shoe Machinery Corporation, 206-207
- Variable-pressure launching tank, 2
- Water entry of projectiles
see Bubbles, entrance
- Water tunnel, 155-159
see also Hydrofoil tests
background noise, 156-159
cavitation noise measurement, 155-156
comparison with polarized light flume, 27
corrections to test data, 277-278
directivity pattern of hydrophone system, 155-156
focusing reflectors, 155-156
noise from circuit variables, 157
purpose, 1
- Water tunnel, free-surface, 52-56
air separator, 53-56
comparison with polarized light flume, 27
purpose, 5-6
working section, 53
- Water tunnel, high-speed, 4, 7-27
air removal and flow straightening, 14
balance system, 16-18, 21
circulating pump and drive, 11
comparison with polarized light flume, 27
cooling circuit, 16
dynamometer, 12
essential components, 7-8
flow circuit, 11
nose, 14
operating techniques, 24-27
operating variables, 25
pressure distribution measuring equipment, 21-23
pressure gauges, 19-21
pressure regulating circuits, 15-16
purpose and specifications, 7-11
speed control, 12-13
tests, 25-27
types of measurements, 4
working section, 15
- Water-borne torpedoes, dimensions, 203
Mark 14 and 15 series, 207
Mark 26 torpedo, 208-209
- Westinghouse, 205-206
- X-42 depth charge, 245-246
- Yaw angle, definition, 275

~~CONFIDENTIAL~~

ATI- 37690

TITLE: Fluid Dynamics

AUTHOR(S): (Not known)

ORIGINATING AGENCY: Columbia University, New York, N. Y.

PUBLISHED BY: Office of Scientific Research and Development, NDRC, Div 6

REVISION

(None)

ORIG AGENCY NO

Vol-20

PUBLISHING AGENCY NO

(Same)

DATE	DOC. CLASS.	COUNTRY	LANGUAGE	PAGES	ILLUSTRATIONS
1946	Conf'd' 1	U.S.	Eng.	293	photos, graphs, drwgs

ABSTRACT:

A summary technical report, published by the NDRC on fluid dynamics, comprises some 19 chapters. Development of the laboratory and facilities is described. Results are discussed of investigations of cavitation and entrance bubbles, nose cavitation of ogives and spherogives, hydrodynamic forces resulting from cavitation of underwater bodies, and cavitation noise. Other topics covered are finless body shapes, stabilizing surfaces of projectiles, effects of projectile components on drag, cross force, and lift, and various tests of torpedoes, rockets, depth charges, air bombs, and other miscellaneous studies.

U
over

DISTRIBUTION: Copies of this report obtainable from Air Documents Division; Attn: MCIDXD

DIVISION: Ordnance and Armament (22)
SECTION: Ballistics (12)

22
416

SUBJECT HEADINGS: Ballistics, Underwater (15615); Hydrodynamic theory (49850)

ATI SHEET NO.: C-22-12-30

Air Documents Division, Intelligence Department
Air Materiel Command

AIR TECHNICAL INDEX

Wright-Patterson Air Force Base
Dayton, Ohio

~~CONFIDENTIAL~~

U Authority: Order Sec Army By
VAC PER J205213 dtd 17 July 58